The University of Sheffield

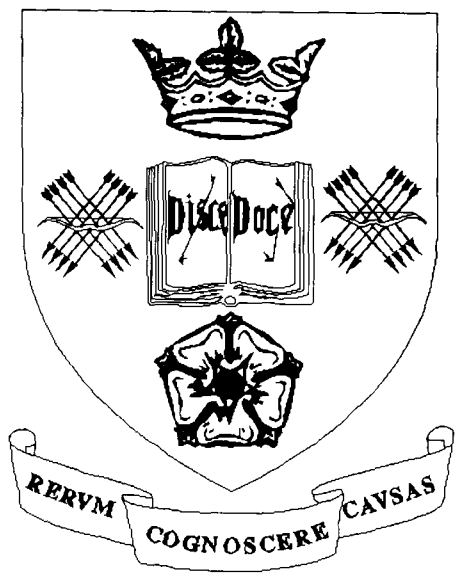

ACOUSTIC NOISE AND VIBRATION OF SWITCHED RELUCTANCE MACHINES

by

Stephen Andrew Long

A Thesis submitted for the degree of Doctor of Philosophy in the Department of Electronic and Electrical Engineering, University of Sheffield.

November 2001

Summary

This thesis describes a systematic investigation into the sources of acoustic noise and vibration in switched reluctance machines, and encompasses the vibrational behaviour of the stator, the influence of control parameters, and an evaluation of the effectiveness of active vibration cancellation.

The influence of leading design parameters, such as the width and number of poles and the yoke thickness, and geometric asymmetries, such as lamination notches in the stator core, and the effect of the stator windings, the frame, the end-caps and the mounting assembly, on the natural frequencies and modes of vibration are investigated, Chapter 3. Both two-dimensional and three-dimensional finite element analyses are employed, the predicted results being validated by measurements on various experimental models, which consequently highlights the limitation of the finite element technique for highly complex structures with discontinuities in their fabrication. The influence of the mass and stiffness of the laminated stator core and the stator windings on the natural frequencies and vibration modes is investigated, and effective material properties are deduced for the analyses. It is found that the number of poles and lamination notches on the stator influence the number of vibrational modes which occur in the audible frequency range due to the introduction of dual natural frequencies, viz. symmetrical and anti-symmetrical modes, which are shown to separate further in value as the asymmetries become more profound. As the diameter of the stator yoke is reduced the natural frequencies increase, whereas increasing the thickness of the yoke and the adding of a frame and end-caps significantly increase the natural frequencies. The effect of the stator poles is to significantly reduce the stator natural frequencies, which are irrespective to a variation to the width of the poles, a variation in their mass being annulled by the resulting change in stiffness. Similarly, it is shown that the winding mass and stiffness offset each other so that their influence is also relatively small, whereas, although quantification of the damping is not within the aims of this thesis, it is apparent that the windings introduce a high level of damping which consequently limits the magnitude of the vibrations and hence acoustic noise. Finally, the laminated nature of the core is quantified and is shown to affect the effective material properties compared to an equivalent solid core, and to increase the effective damping.

Previous investigations have studied the influence of the drive control parameters, but generally limit the analysis to either the frequency or time domain or to measurements of

the sound pressure level, and are generally carried out in isolation. Therefore, the influence of alternative operating modes and their associated control parameters on the acoustic noise and vibration of an SR machine is thoroughly investigated, the results being analysed in both the frequency and time domains, and compared with measurements of the sound pressure level, Chapter 4. The noise and vibration which results when the SR machine is operated under both voltage and current control, with both hard and soft chopping techniques, and various switching angles, and for various sampling and switching frequencies, is measured. The influence of speed and load is also investigated, and the vibration and noise are also investigated under single pulse mode operation. It is found that hard chopping results in a noisier operation than with soft chopping due to increased current ripple, especially under current control. The noise and vibration is clearly shown to differ under current control compared to voltage control and single pulse mode, due to the random switching of the phase voltages resulting in wide-band harmonic spectra, thereby increasing the levels of all the mechanical resonances. Further, it is found that the noise and vibration increase with both speed and load. In general, the increases in noise and vibration are attributed to an increase in the rate of decay of current at phase turn-off, regardless of the control parameter under investigation.

Finally, the effectiveness of active vibration cancellation for noise reduction is investigated under typical operating modes in Chapter 5, which, for the first time, is analysed in both the frequency and time domains, and validated by measurements of the sound pressure level. It is found that active vibration cancellation is less effective for machine stators which have more than one dominant vibration mode within the audible frequency range, since the technique is only capable of applying active cancellation for a single vibration mode, thus any further resonances remain unaffected. Further, during chopping control, especially current control which results in random switching, it has been shown, for the first time, that the effective time-delay varies to that applied, thus rendering the technique less effective. This is found to be attributed to the asynchronism of the final chopping edge and point of phase turn-off, therefore preventing the vibrations from being excited in anti-phase, as explained in section 5.6.

Acknowledgements

I would like to express my sincere thanks to my supervisors, Professor Z.Q.Zhu and Professor D.Howe for their invaluable guidance and support throughout the duration of this Ph.D.

I would also like to thank members of the Electrical Machines & Drives Group, especially Damyn Musgrave, Nigel Schofield and Philip Churn for their advice and discussions, and also the technical support staff.

Finally, I would like to thank my family and friends for their support and encouragement during the course of this Ph.D.

Contents

Chapter 5: Reduction of Noise and Vibration

Chapter 6: Conclusions

Appendices

List of acronyms

2D	2-dimensional
3D	3-dimensional
ADC	Analogue-to-digital converter
DSP	Digital signal processor
EMF	Electro-magnetic force
ET	Element type
FEA	Finite element analysis
GPT	General purpose timer
ISR	Interrupt service routine
PWM	Pulse width modulation
QEP	Quadrature encoder pulse
SLM	Sound level meter
SPL	Sound pressure level
SRM	Switched reluctance machine

Chapter 1

Acoustic Noise and Vibration of SR Machines

1.1 Introduction

Advances in power silicon technologies and device availability in terms of volume and cost, have fostered an expansion in variable speed drive applications over the last two decades. The facility to electronically control the magnitude and phase of the supply to the stator windings of electrical machines has made electromagnetic speed variation a viable design option for the application engineer over more established but less efficient mechanical techniques. Additionally, it has opened the market to machine technologies previously limited in application, the switched reluctance machine being such a technology, the fundamental operation of which was demonstrated as a variable speed traction machine for an electric vehicle as far back as the late 1890's, [SCH97]. However, switching of the machine stator supply of these early machines was realised mechanically which imposed limitations on switchable current magnitudes and frequency. For induction and brushless permanent magnet machine technologies, the stator excitation is generally implemented to ensure a continuously rotating stator magnetic field. However, for the switched reluctance case, the stator windings are, by virtue of the machine magnetic design, switched discretely the consequence of which is acoustic noise generation due primarily to deformation of the stator iron core.

1.2 Fundamentals of Acoustic Noise and Vibration

A typical cross-section of an SR machine outlining its main components is illustrated in **Fig. 1.1**. The stator is comprised of salient poles which carry concentrated windings, whereas the rotor is a simple laminated salient structure. Due to its doubly salient nature, the current waveform, i_{ph}, for torque production, is neither sinusoidal nor a square wave, taking a typical form as illustrated in **Fig.1.2**, depending on the rotational speed and winding inductance which varies with position. The corresponding coil flux linkage, ψ_{ph}, is also shown in **Fig. 1.2**. The radial force in electric machines is defined by equation (1.1) where μ_0 is the permeability of air, x is the length of overlap between stator and rotor poles, as described in **Fig. 1.3**, and B is proportional to the coil flux linkage. Consequently, the variation in radial force can be considered analogous to force applied to the stator mechanical structure, which excites its natural frequencies.

$$F_r = \frac{B^2 xL}{2\mu_0} \tag{1.1}$$

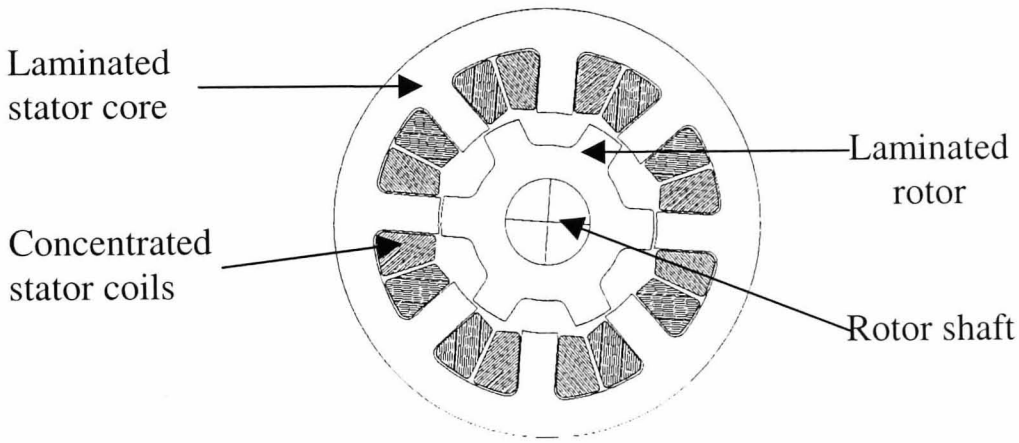

Fig. 1.1 *Switched reluctance machine*

It will be discussed later that the peak radial force occurs at the point of greatest pole overlap which coincides with the instant of phase winding turn-off. This reduction of phase current at turn-off results in a reduction of the flux density and hence radial force releasing the stator from its compressed state to vibrate according to its natural frequencies. Essentially, the stator core can be thought of as a spring being released from its compressed state at point 'B', **Fig. 1.2**, and being set into vibration. As a consequence, the acceleration, a, behind the pole of the excited phase, will have a typical form as illustrated in **Fig. 1.2**, the frequency of which is the dominant vibration mode of the stator core.

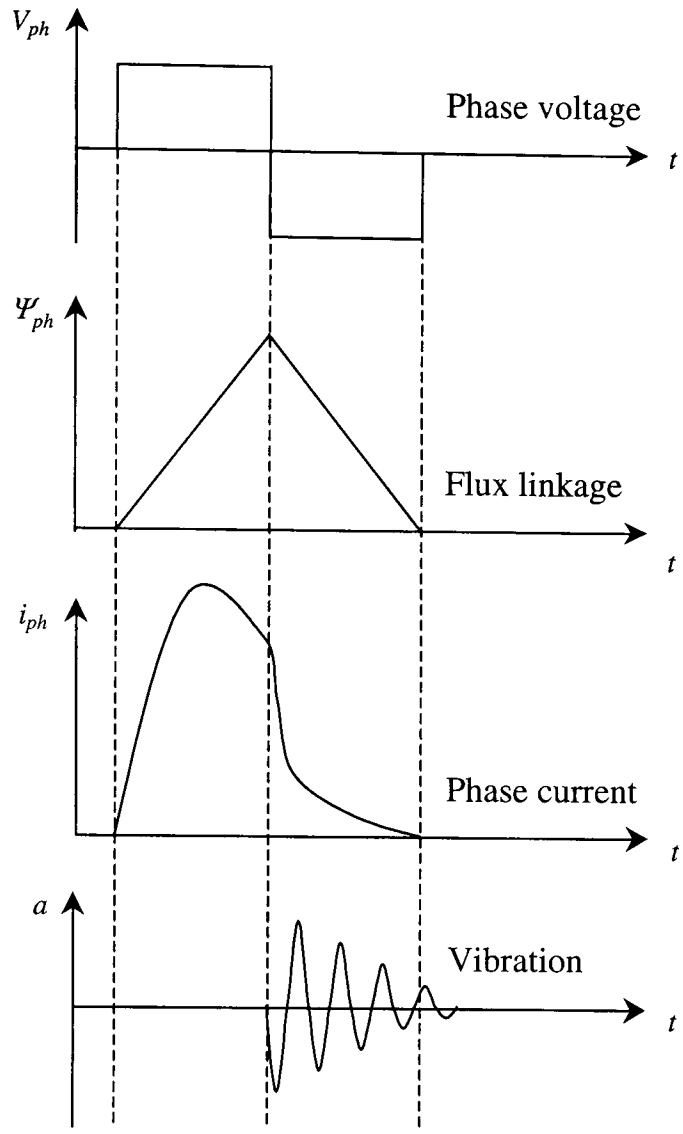

Fig. 1.2 *Operating characteristics*

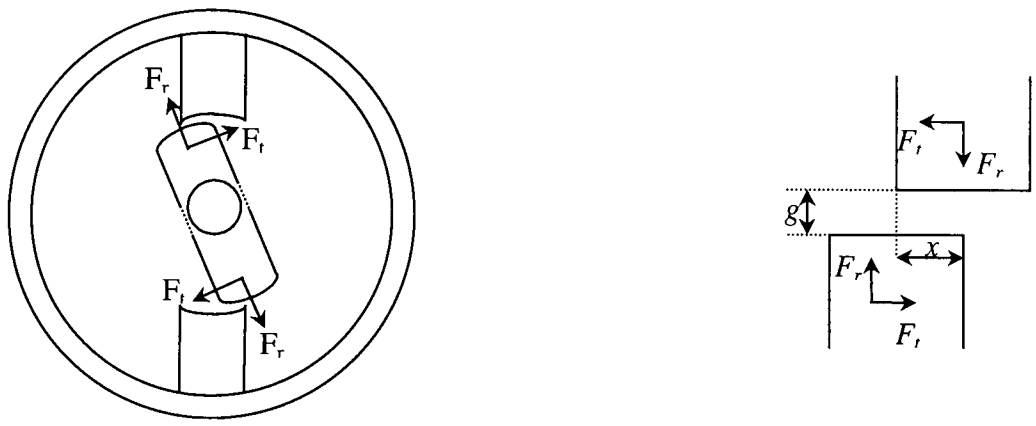

Fig. 1.3 *Definition of radial and tangential forces*

It is the coincidence of the electro-magnetic forces with the natural frequencies (and their associated mode shapes) that excites the stator into resonance and hence induces the most severe vibration and acoustic noise. However, the extent of the severity of the vibration and noise emissions at resonance is limited by the damping of the structure. The damping is a measure of the ability of a structure to absorb vibrational energy due to its internal friction. Thus, the higher the damping, the lower the magnitude of the acoustic noise since it reduces the ability of the structure to propagate vibrations to the

surrounding air. The damping therefore determines the magnitude of the resonant frequencies and thus the sound pressure of the noise peaks, although in the case of excessive damping the values of the frequencies may be altered, but in the case of electric machines such high levels of damping are not present. Determination and characterisation of damping is not within the remit of this thesis, although its importance with regard to acoustic noise emissions cannot be dismissed.

When addressing acoustic noise, the perception of the noise by the person upon which it is inflicted is of great importance. The human ear can detect frequencies in the range 20Hz to 20kHz, but more importantly the sensitivity of the ear changes with frequency and sound pressure, as illustrated **Fig. 1.4**, showing the 'equal loudness' contours. If you take for example a sound emitted at a frequency of 50Hz, its sound pressure must be 15dB higher than a frequency emitted at 1000Hz for the human ear to detect the same subjective 'loudness'. Thus, when addressing the issue of acoustic noise it is important that the spectra of the noise is analysed to identify the pure tones to which the ear is most sensitive. Furthermore, in order to establish whether a noise source is perceived as 'loud' by the human ear, the sound pressure meter used for measurement must account for the variation in sensitivity. Typically, the industry standard is to use the A-weighted sound pressure for comparative studies, [BRU84].

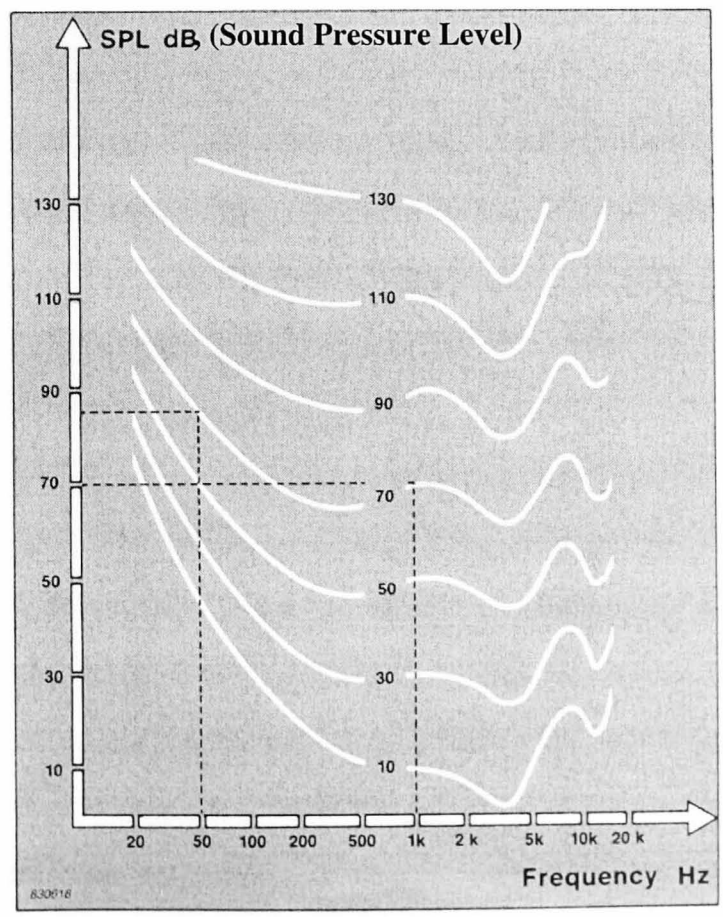

Fig. 1.4 *Equal loudness contours [BRU84]*

1.3 Review of acoustic noise and vibration

The following sections present a comprehensive review of publications that address the noise and vibrational behaviour of SR machines. Due to the multi-disciplinary nature of this research area, they cover a range of topics, viz. sources of noise and vibration, influence of control parameters, structural issues, and both active and passive noise reduction methods. Early conclusions regarding the dominant cause of acoustic noise by Cameron and Umas, [CAM92], and the correlation between the noise level and the rate of change of current highlighted by Wu and Pollock, together with their noise reduction technique, [WU95], are discussed. In addition, more recent advances, such as the development of simulation tools to enable the machine designer to physically predict and hear the noise before a machine is made, [RAS99], are described.

1.3.1 Sources of noise and vibration

a) Electromagnetic, mechanical and aerodynamic noise [CAM92, PIL99]

The various sources of noise and vibration of SR machines, some of which are common to other machine types, are outlined in **Fig. 1.5**. Of these, it is well established that electromagnetically induced noise is by far the most dominant in SR machines.

Mechanical sources of noise and vibration in SR machines are similar to those for other machine types, such as induction machines and permanent magnet machines, in that they include the machine bearings and couplings to inter-connecting shafts/loads.

Aerodynamic noise exists due to the salient nature of the rotor, on which the poles are not dissimilar to the blades of a fan, and, therefore, become more of an issue at high operating speeds. Clearly, the aerodynamic noise produced by SR machines is more significant than that for machines which have a cylindrical rotor.

The noise emissions which are of an aerodynamic and mechanical in nature are generally insignificant compared to that of the dominant noise source. By way of example, one of the experiments which has been carried out entailed accelerating a 4-phase 8/6 machine, [CAM92], to a high speed by a dynamometer, whilst unexcited, and then exciting the machine and accelerating it to the same speed and allowing it to coast to a standstill. During this test, it was observed that the noise which was emitted when the machine was unexcited was insignificant compared to that which resulted when the machine was excited.

Electromagnetic noise may result from a number of sources, such as magnetostrictive forces within the laminations, forces imposed on the windings due to the interaction of the winding currents with the local magnetic field, and the vibration of the rotor and stator due to fluctuating airgap forces. However, magnetostrictive forces are negligible compared to that of the dominant source noise, as highlighted by measurements at a number of locations around the periphery of a 4-phase 8/6 machine, [CAM92]. Further, the magnetic field in the winding slots is greatest when the stator and rotor poles are misaligned, when minimum noise emissions were observed. Thus, the interaction of the current in the stator windings with the local magnetic field is generally a negligible cause of noise, [CAM92].

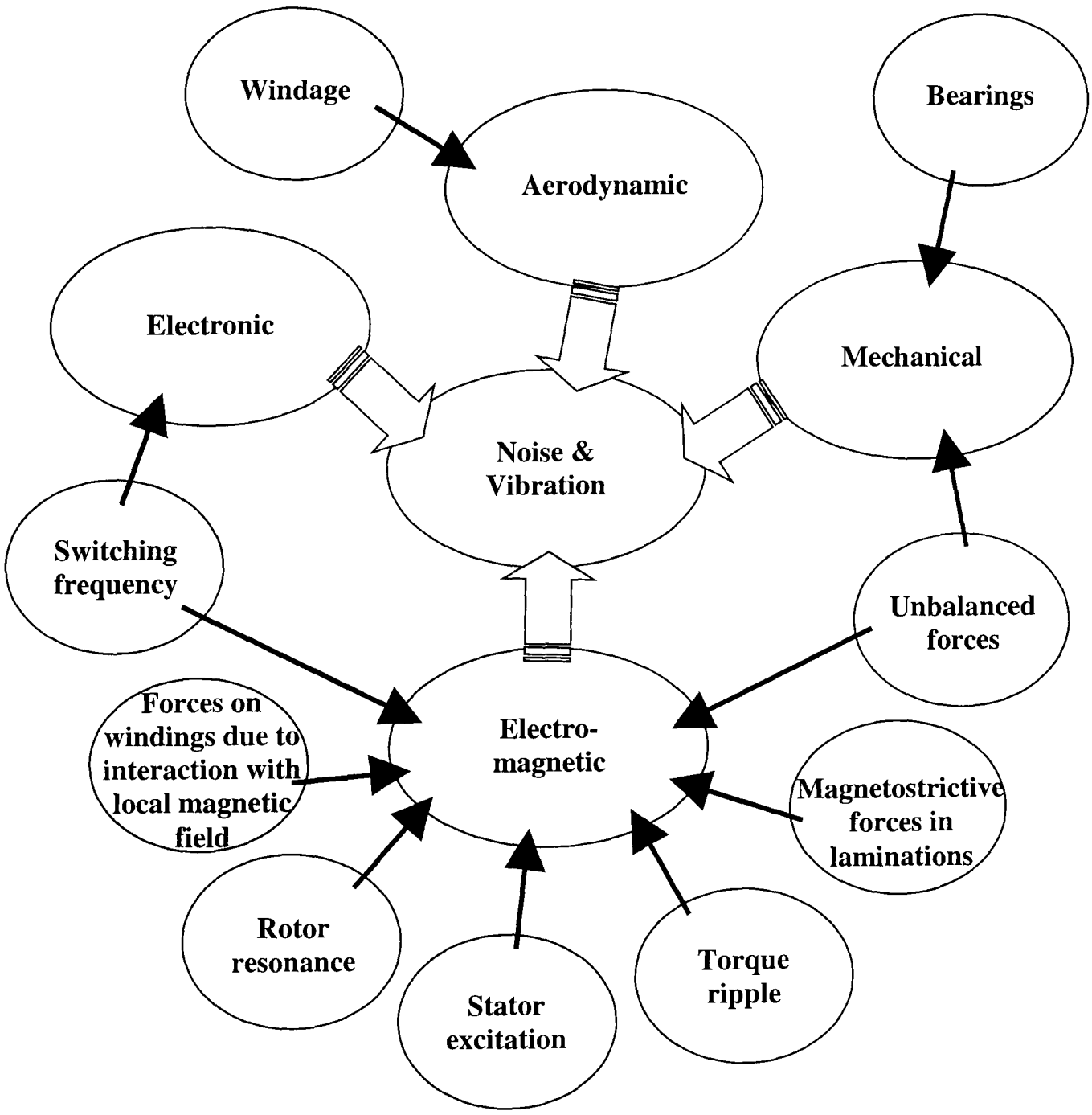

Fig. 1.5 *Sources of noise and vibration*

b) Unbalanced magnetic pull [MIL95, HUS00, AYA99, WU96, CAM92]

Unbalanced magnetic pull results from eccentricity of the rotor, and causes a magnetic asymmetry and, therefore, a higher air-gap flux at the side of the machine with the smallest airgap. Poor machining of the stator bore diameter and the rotor outside diameter, and manufacturing tolerances related to the bearings may cause rotor eccentricity. In addition, unbalanced magnetic pull will result during certain fault conditions, for example a winding short circuit, which is generally more severe than the unbalanced forces caused by rotor eccentricity.

However, measurements on a 4-phase 8/6 SR machine eliminated rotor unbalance as a significant source of noise, [CAM92]. However, rotor unbalance can enable natural frequencies associated with odd vibration modes to be excited during machine operation, a typical example of which is shown in **Fig. 1.6**, whereas for a well balanced rotor only even vibration modes are excited due to the symmetrical forces inherent with the machine structure. For example, acceleration measurements on the stator of a 3-phase 6/4 machine with rotor eccentricity, compared to measurements without rotor eccentricity, showed a significant increase in the vibration, whose spectrum comprised of additional harmonics, [AYA99]. Further, excitation of rotor vibrations has been shown to result from unbalance of the rotor due to the resulting centrifugal forces, whose vibrations are transmitted to the stator housings via the bearing supports, [WU96].

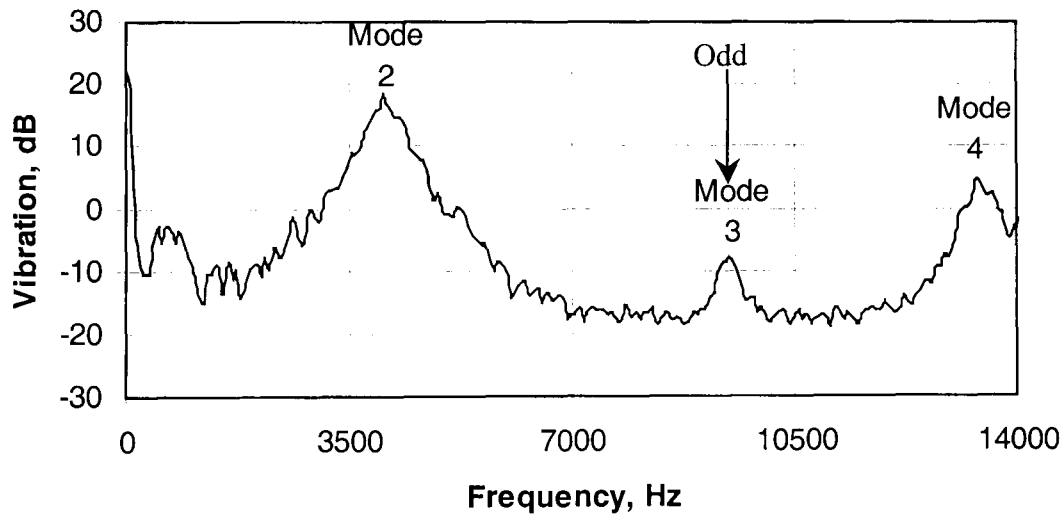

Fig. 1.6 *Typical example of stator resonance at odd vibration mode (Chapter 4)*

As rotor eccentricity increases, the variation of the air-gap will increase further, thus resulting on a bigger difference in the radial force on the diametrically opposite stator poles. Analyses have shown that the variation of the sound pressure level increases almost linearly with rotor eccentricity, [WU96], although ultimately the flux is limited

by saturation of the poles, thus limiting the magnitude of the radial magnetic force, [AYA99]. Based on such knowledge, it follows that unbalanced magnetic pull is less of an issue at high operating currents when a machine will be more heavily saturated. However, it should be noted that as the machine saturates there is potential for additional excitation frequencies.

c) Torque ripple [MEH92, BAR99]

Torque ripple is more significant in the SR machine than in other types of machine, such as induction machines and permanent magnet machines, owing to its doubly salient construction and its non-sinusoidal stator current waveforms.

Numerous methods have been proposed for minimising torque ripple, such as current shaping, [LOV94]. However, current profiling methods are relatively complex and are specific to a particular machine, [TUR98]. The influence of the rotor pole geometry on the torque ripple has been investigated, [MEH92], although any benefit which might be realised was marginal. However, more recently, the use of staggered rotor poles enabled the constant torque producing region associated with a given phase to be extended beyond the region usually associated with torque dips, [BAR99]. However, changes to the stator or rotor pole geometry also influences the machine inductance, and thus the energy conversion, which may be compromised in order to reduce the torque ripple.

The torque, and, hence, the torque ripple, is derived from the tangential force which acts on the rotor poles, rather than the radial force. Therefore, any vibration disturbance induced by torque ripple has an insignificant effect on the noise emitted by a machine, since tangential vibrations are not efficient for propagation from a machine stator to the surrounding medium.

It was found, [CAM92], that the dominant noise peak emitted during static and dynamic tests had the same level, and since torque ripple is not present when a machine is stationary, it was concluded that torque ripple had negligible influence on the generation of noise.

However, the influence of torque ripple may become more of an issue in regard to noise and vibration when the machine is integrated into a system, since the associated vibrations may be transmitted to other components, for example, those coupled to the drive shaft or the stator. These vibrations may then induce resonance of such

components, thereby emitting significant noise, and cannot, therefore be dismissed. However, in this thesis, only the noise and vibration associated directly with the structure of the SR machine is investigated. Therefore, the influence of torque ripple is not addressed any further.

d) Mechanical resonance [CAM92]

It is well established that the dominant cause of noise and vibration is the deformation of the stator due to radial electromagnetic forces. Further, noise and vibration will be most severe when the frequency of the radial electromagnetic force coincides with a natural frequency of the stator geometry, and result in a stator resonance. Thus, over all operating modes of the SR machine, regardless of speed and load, the frequencies of the dominant vibration and noise components do not vary, and are governed by the stator design of the given machine.

By way of example, the rotor of a 4-phase 8/6 machine was held stationary with the poles in the aligned position with a phase excited under hysteresis current control, whilst the other three phases were unexcited, [CAM92]. The excitation frequency of the phase current was swept over a large range of frequencies, so as to simulate a range of operating speeds, and at three distinct excitation frequencies dominant noise peaks occurred, having the frequencies of the excitation frequencies. In addition, the phase and amplitude of the stator vibration was observed to follow that of the acoustic noise. This provides strong evidence that stator vibrations are magnetically induced, and that these are responsible for the emitted noise which occur at particular excitation frequencies. In addition, this was supported by the observation that during normal machine operation the sound pressure level was significantly higher than the background level at three different speeds, which were not specified, at which dominant narrow peaks of noise were observed, whereas when unexcited insignificant noise was measured, [CAM92]. This is a very effective method to ascertain the correlation between the phase excitation frequency, and hence speed, with the stator resonance, but since it was only for single phase excitation, did not account for the interaction between vibrations induced by the excitation of successive phases.

Measurement of the amplitude and phase of the vibrations at a number of positions around the periphery of the stator enable the vibrational mode shapes to be identified, [EWI00]. Such techniques, applied by Cameron et al [CAM92], revealed that SR machine vibrations correspond to stator resonances.

e) Radial magnetic attraction [WU93, WU95, CAM92, PUL93]

A number of important issues relating to the noise and vibration of SR machines become apparent when analysed in the time domain that would otherwise be overlooked with frequency domain analysis.

Firstly, the stator acceleration may be observed with respect to the instantaneous phase current, which shows that the major vibration oscillations are induced at phase turn-on and turn-off.

This is due to the radial attractive magnetic forces, which result at the excited stator poles and, attract the stator to the rotor. These become more significant as the rotor and stator poles approach alignment, and, therefore, the vibration is generally much more severe at phase turn-off, as observed by Wu and Pollock, [WU93].

Utilising measured current waveforms and electromagnetic finite element analysis, radial and tangential stresses on the stator may be calculated, and, hence, the radial and tangential forces which act on the stator poles may be obtained over an electrical cycle, as shown by [PUL93]. This information showed a radial force pulse, which is phase shifted with respect to the instantaneous torque, and was consequently emphasised as the key to the production of acoustic noise, [PUL93]. Calculation of the Maxwell Stress curves showed a very predominant radial force for the rotor position corresponding to the end of phase excitation and it was, therefore, suggested that this radial force level needs to be reduced to limit excitation of the stator structure by rapidly reducing the phase current at phase turn-off, [PUL93].

Although the reduction of the radial force is of benefit, rapid reduction of the phase current is not, since this causes a rapid change in the radial force. When attracted to the rotor, the stator can be thought of as a spring in its compressed state. When released slowly, little or no oscillation will occur. However, if reduced quickly the converse results. Thus, the rate of change of stator current relates strongly to the stator vibration, which is particularly large when the phase voltage is switched from a positive to zero, zero to negative or positive to negative, as observed by Wu and Pollock, [WU93].

Due to the inherent symmetric nature of the radial forces in an SR machine, during phase excitation for the case of 2 active stator poles per phase, the most dominant vibrations

induced behind a stator pole at 90° mechanical to the excited stator poles are in anti-phase to those behind the excited stator poles, since a pair of radial compressive forces occur behind the excited stator poles as the stator is attracted to the rotor, as was observed by [WU93] during single phase excitation of a machine. Thus the action of the stator is similar to a symmetric elastic cylinder, when subjected to a radial force at two diametrically opposite points, the points at 90° to these being forced out, causing an ovalisation. Similar observations were made by Cameron et al, [CAM92] during vibration measurements using two accelerometers mounted radially opposite at points mid-way along a stator core. This is due to the stator resonating at its fundamental vibrational mode shape, mode 2. In addition, noise measurements provided conclusive evidence of the strong radial magnetic attraction of the stator to the aligned rotor poles, and the resulting deformation of the stator.

1.3.2 Control parameters and noise

The drive parameters of a variable-speed SR machine system include the dc supply voltage, the required shaft torque, the operational speed, the turn-on and turn-off angles, the current chopping level for operation in the current limited mode, and the frequency and duty cycle for operation under pulse width modulation voltage control.

a) Operating speed [WAL90, CAM92, BLA94, PIL95, COL96]

Mathematical relationships between the sound power level, the shaft power, the speed and the PWM duty cycle have been obtained through the analysis of measured data over a range of operating conditions, [PUL93]. Application of these relationships enabled a set of contours for the sound power level to be obtained for a range of speeds and shaft powers, from which it was concluded that maximum noise levels do not necessarily coincide with maximum power output.

It is well established that for a given machine, the harmonic content of the acoustic noise remains constant throughout the whole operating range, regardless of load, due to the fact that it is determined by the natural frequencies and, hence, the assembled stator geometry and the materials employed for its fabrication.

However, the magnitude of the vibration at the stator natural frequencies varies over the machine operating speed. For example, during investigations carried out on a 4-phase 8/6 machine, it was observed that the noise emissions were more significant at particular rotational speeds and appeared to be suppressed at others, although no quantitative results were provided, [CAM92]. This phenomena was attributed to the relationship between the fundamental phase excitation frequency and the stator natural frequency. Similar observations were made during investigations by Colby et al [COL96] in that an SRM was substantially quieter at 3930rpm than at 5432rpm, which was attributed to the significantly higher vibration peak observed for the fundamental vibration mode for the 'louder' speed.

It is also well established that in the linear operating region, the radial force is proportional to the square of the phase current and, therefore, the harmonic content of the phase current, and, hence, the harmonics of the square of the phase current, are influential on noise emissions. For example, during investigations made by Cameron et al [CAM92] on a 4-phase 8/6 machine it was observed that the noise emissions were lower at phase excitation frequencies that contained no current harmonics at the phase

excitation frequency and multiples thereof, however, again no supportive results were shown.

The absence of particular current harmonics was attributed to the duty cycle of the phase voltage. For a 4-phase machine employing a nominal dwell period, i.e. a dwell period equal to that of the stroke angle, the duty cycle of the phase voltage is 25%, and therefore does not contain 4^{th} harmonics or multiples thereof, although, in the spectrum presented for the square of the phase current, these harmonics were clearly present, with magnitudes similar to those of other harmonics, [CAM92]. Nevertheless, for single phase excitation, the fundamental excitation frequency was fixed at a value whose 7^{th} harmonic coincided with the natural frequency of vibration mode 2, during which the machine was held stationary. The duty cycle was varied, and it was observed that the noise emission was lower for duty cycles that resulted in 'squared' currents without a 7^{th} harmonic.

Similar observations were made for a 3-phase 6/4 machine in that larger vibrations were induced when the speed was such that an odd harmonic of the excitation current coincided with a stator natural frequency, than those which were induced by an even harmonic [WU93]. This, however, draws a correlation between the noise and the phase current, rather than the square of the current, and again no quantitative results were provided to support the observations. However, if a similar analysis to that discussed above, [CAM92], is applied to a 3-phase 6/4 configuration employing a nominal dwell angle, the duty cycle of the phase voltage is 33% and, therefore, the machine would be expected to have lower vibrations when running at speeds which yield 3^{rd} harmonics and multiples therefore that coincide with the stator natural frequency.

It should be noted, however, that such relationships with the harmonics of the square of the phase current are not supported by clear evidence, and that conflicting observations exist in the literature. In addition, such analyses are more complex when a machine is working in its saturated region, since the radial force is then no longer proportional to the current squared.

At high operating speeds, such that the SR machine is in single pulse mode the back-EMF, limits the initial rate of change of current during phase de-magnetisation. It is for this reason that single pulse mode operation associated with high rotational speeds is generally quieter than current limited machine operation associated with lower rotational speeds. However, an investigation on a 3-phase 6/4 machine by [WU93] showed that a

higher peak vibration is induced during the single pulse mode than that during hysteresis control. It should be noted, however, that this comparison was made whilst the machine was stationary and, therefore, did not account for the greater back-EMF which would result in single pulse operation, which would limit the rate of change of current and, therefore, the vibration.

For lower speed operation, it is usually beneficial to include an additional chopper in the dc link in order to limit the available dc voltage, as proposed by [PIL95]. However, the exact nature of their investigations is not clearly explained, and since they employed a split dc converter, which without the additional chopper circuitry is similar to that of the Outlon circuit, Appendix A, they could only achieve hard chopping strategies. Thus, during turn-on and the subsequent dwell period, the additional chopper is of no additional benefit, compared to a machine supplied from an inverter which is capable of providing soft chopping control. Therefore, it can only be assumed that the additional chopper continues to operate during the de-magnetisation period, thus limiting the available de-magnetisation voltage and, hence, the rate of change of current.

b) Voltage control, current control and single pulse mode

Voltage control is often considered to result in quieter operation of an SR machine in the current limited region, rather than current control. However, published results are sparse, and explanations regarding this issue are rather limited. An investigation by Gabsi et al [GAB97] compared the vibration of a machine operating under hysteresis control to that with PWM voltage control, employing a switching frequency of 20kHz, concluded that the random nature of the switching frequency associated with hysteresis control excites many resonant modes, and thus produces greater acoustic noise. However, this does not provide a clear explanation for the higher noise emissions which result under current control, since the same vibration modes are generally excited regardless of the control technique.

c) Soft and hard chopping

Soft chopping has occasionally been referred to in the literature as a means for achieving quieter machine operation. However, limited evidence of this has been provided to support this claim. Soft chopping, as opposed to hard chopping, provides the benefit of switching only half the available dc supply voltage across a phase, thus resulting in a lower rate of change of current and, therefore, noise. However, at phase turn-off, when the major vibrations are induced, the rate of change of current is similar for both hard

and soft chopping and, hence, it is probable that it is the reduction in current ripple throughout the dwell period which reduces the vibration and, hence, noise.

One investigation [GAB97] compared acceleration measurements for both soft and hard chopping, but this was only under voltage control, for which the operating conditions were not specified, and the associated phase current waveforms were omitted, and, furthermore the sound pressure level was not considered. Thus, within this thesis a comparison of the noise and vibration under soft and hard chopping is made, utilising time domain and frequency domain measurements of noise and vibration, together with the associated phase current waveforms and the measured sound pressure levels.

d) Switching angles

The turn-on and turn-off angles which were employed can be varied widely depending on the desired operating performance, for example, maximum efficiency, minimum torque ripple, etc. It follows, therefore, that a particular set of switching angles exists for minimum noise. However, for any given machine design these angles will differ, and in order to obtain the required performance a rigorous method is required to map out the machine performance over a range of switching angles.

For a fixed rotational speed, and assuming that the phase current waveform is rectangular, if both the turn-on and turn-off angles were advanced, such that the dwell angle remains fixed, then the value of inductance and flux-linkage at turn-off will be lower than for the initial angles. Thus, the current must have a higher magnitude so as to maintain the rotational speed. Due to this higher current and lower inductance, it follows that the rate of change of current at turn-off increases, although the radial component of force would also reduce, since the poles are further from full alignment at turn-off.

Similarly, for a fixed rotational speed, assuming the current waveform is rectangular, for a fixed turn-on angle and advancing the turn-off angle, such that the dwell angle is reduced, the current must attain a higher magnitude for the same reason given above, which, therefore, results in a higher rate of change of current.

The dependence of the noise and vibration on the switching angles was recognised by Besbes et al, [BES94], who suggested the possibility of optimising these angles to reduce the noise. However, no experimental details or results were provided, only the observation that the acoustic noise increases when the turn-on angle is increased for a

fixed dwell angle, and when the dwell angle is reduced whilst the turn-on angle is maintained constant. However, based on the switching angle discussion above, such a suggestion appears reasonable. Nevertheless, in contrast, during single phase excitation of a 3-phase 6/4 machine, [WU93], it was observed that switching the angles further ahead of the aligned position reduced the stator vibration, which was attributed to a reduction of the radial component of force. However, the machine was maintained stationary throughout this test, and the current level remained fixed, whereas, had the machine been rotating, the phase current would have been higher at the point of turn-off, thus influencing its rate of decay.

An investigation on a 6/4 SR machine [BLA94] applied a fixed turn-off angle whilst the turn-on angle was advanced, but little explanation of the results was provided. When the machine was operating on no-load under voltage control, the sound pressure level was observed to reduce as the turn-on angle was advanced, whereas on load, no variation in the sound pressure level occurred. Further, under current control, regardless of load, no variation in sound pressure level occurred as the turn-on angle was increased.

However, in general, if the turn-on angle is increased for a fixed turn-off angle, the current level will not increase and, therefore, the rate of change of current at turn-off will not vary over the range of turn-on angles. In addition, if the range of turn-on angles lies within the vicinity of the unaligned inductance, such that the demanded current level is reached prior to the onset of magnetic overlap, no change will occur in the rate of rise of current at turn-on. However, it should be noted that since the current waveform changes, its harmonic content alter, thus influencing the noise emissions.

An investigation into the influence of the current switching angles on the vibration of a 4-phase 8/6 SR machine, [NEV97], compared the force harmonics for two sets of switching angles with a fixed dwell angle. It highlighted that the spectral peaks in the radial force spectrum for the earlier switching angles had a lower magnitude compared to those associated with later switching angles, which accounted for the lower noise emissions when the machine was operated with the earlier switching angles. However, this study was based purely on simulations, and provided no experimental validation of the findings.

1.3.3 Structural vibration behaviour

Since the dominant source of vibration is attributed to the radial deformation of the stator core, a number of studies have addressed the natural frequencies of SR machines, [COL96, SAD96, TAN97, MAH96, NEV97, NEV99, NEV01, PIL99], many of which have coupled mechanical analyses with the electrical drive circuit, [SAD96, TAN97, NEV97, BES98, GAB99b]. However, to-date, the majority of the mechanical finite element analyses are limited to 2D analyses, exceptions being [KAC98, PIL99, CIA99], and many of the analyses omit details of the finite element discretisation or material data, [MAH96, NEV97, SAD96, NEV99, KAC98, PIL99, CAI99, BES98].

a) Stator yoke

It is well established that the yoke thickness is one of the most influential parameters as regards the stator natural frequencies since it contributes significantly to the stator stiffness. A number of researchers have studied the influence of the yoke thickness, with either finite element analyses, [BES98, CAI99] or analytical formulae, [COL96, PIL99]. These generally increase the yoke thickness whilst maintaining a fixed outer diameter, which naturally results in an increase in the natural frequencies. In addition, the values of the natural frequencies decrease almost linearly with an increase in the mean radius of the stator yoke. The accuracy of analytical formulae is limited, and they are generally only applied to predict the frequency of vibration mode 2, and, furthermore, they cannot account for anti-symmetrical modes introduced by geometric asymmetries, which will be highlighted in Chapter 3.

b) Stator frame

It follows from the influence of the yoke thickness that the addition of a frame will also significantly influence the stator natural frequencies. The addition of a smooth frame to the FE model of an 8-pole stator [CAI99, PIL99] showed that the natural frequencies increase when perfect contact is assumed between the stator and the frame, whereas if it is assumed that contact occurs only at the point of the interface keys, the natural frequencies can increase or decrease, and additional frequencies may be introduced. Further, the addition of a ribbed frame induces additional frequencies associated with the cooling ribs, and more complex mode shapes occur when the terminal box is included. However, this investigation was not validated experimentally, and did not account for the end-shields, which are often omitted from frame analyses, [NEV99], or simply modelled separately, [MAH96].

c) Stator windings

The stator windings are generally neglected when determining the stator natural frequencies, and, consequently, have received little attention, one exception being [YON97], in which the winding mass and stiffness were included in an analytical formulae, together with the poles, frame and cooling ribs, for the determination of the stator natural frequencies. However, the materials were treated as being homogeneous, and the formulae did not take account of the end-windings, whilst limited validation was provided.

d) Stator stack

The earliest application of finite element analyses for predicting the stator natural frequencies and associated mode shapes was to a 4-phase 8/6 SR machine, using a 2D model of the stator core, [COL96]. Surprisingly good correlation was achieved considering that the assembly of the stator was neglected, although the presence of an additional vibration peak in the presented vibration response, which may be due to stator asymmetry, was overlooked owing to the simplified nature of the stator model. Such techniques were also applied to a 12-pole stator from a 3-phase 12/8 machine, [TAN97].

Application of analytical formulae for calculating of stator core natural frequencies have treated the stator core as a uniform cylindrical shell, [COL96], the winding and pole mass being lumped with that of the yoke, whilst any further features, such as notches and key-ways, were only considered to influence the mass, [PIL99]. Again, these formulae have limited accuracy and cannot account for asymmetries in the stator geometry.

e) Damping ratio

The damping ratio, which is generally associated with SR machine stators is relatively low, and, therefore, does not significantly influence the value of the natural frequencies. Thus, damping is generally neglected when determining the modal characteristics. However, it is important when determining the magnitude of the induced vibrations and assessing the subsequent decay of these vibrations.

Experimental methods together with modal analyses have been applied to obtain the damping of a given machine structure, [GAB99b, NEV99]. Owing to the highly complex structure of the machine assembly, however, determination of the damping is not possible without prior knowledge of the characteristics of the structure, i.e. requires the machine to be built before it can be characterised. In addition, the damping ratio is

complicated further by the stator assembly, winding and the mounting which is employed.

f) Increasing vibration mode order

A novel SR machine which was designed with the intention to improve torque capability also yielded a stator with an 'effectively' higher stiffness, [PHI90]. This was achieved since the design comprised of 12 stator poles and 4 rotor poles whilst maintaining the properties of a classical 6/4 machine. The design utilised all 4 rotor poles during torque production, thus rendering a force wave excitation pattern, n, of 4, as opposed to 2 which is usually associated with a 6/4 machine. The stiffness of the ring, which is proportional to n^4, is increased by a factor of 16. Similarly, the dominant stator vibration peak of 3-phase 12/8 machines was recognised to relate to mode 4, [WU96, RAS99]. This is in contrast to 8/6 and 6/4 machines which are usually associated with mode 2. Therefore, the significance of modes is attributed to the configuration of a machine and its associated magnetic field distribution.

1.3.4 Electro-mechanical analyses

a) Calculation of airgap forces

Stator phase current waveforms may be applied to electro-magnetic models to calculate the tangential and radial force waveforms, and subsequently enable the force harmonics to be derived with reference to the stator natural frequencies. This technique has been employed in a number of investigations [BES94, SAD96, MAH96, NEV97].

To measure such forces in an SR machine is very difficult, and, therefore, in order to validate the force calculation it was suggested [MAH96] that the forces should be applied to a validated mechanical model of an SR machine. Subsequent comparison of the resulting vibrations to those measured on an actual machine, therefore, provides an indirect means of evaluating the accuracy of the force calculation. However, in order to assess the influence of these forces from a mechanical model, the magnitude of the stator response is required. This would necessitate an accurate knowledge of the damping ratio, which is a high complex parameter to characterise accurately. Therefore, it follows that the calculation of the forces cannot be validated accurately.

b) Influence of radial force harmonics

An investigation on a 3-phase 6/4 SR machine showed, through the application of force calculations, that the vibrations are more severe when force harmonics coincide with stator natural frequencies, [SAD96], although no explanation is provided. Further, a similar investigation, also on a 3-phase 6/4 machine topology, observed maximum vibrations only when odd force harmonics coincided with the natural frequencies, [BES94], although, again, there was no indication of the damping ratio employed for determining the vibration magnitudes.

A more recent study [GAB99b] outlined the development of a model of a complete SR drive system, incorporating the dynamic nature of the converter and SRM, which was linked to the magnetic and mechanical systems. This utilised measurements of the stator excitation to establish a transfer function of the machine modal characteristics, which was incorporated into the software, together with the magnetic forces determined form electromagnetic FEA, to enable computation of the stator acceleration. However, this is based on a single phase model, and the model was validated for only one particular working point. There are clear differences between the predicted and measured acceleration and vibration spectra, although the predicted values do exhibit similar trends

to those which were measured. Further, they omit the variables calculated from the transfer function as well as the value derived for the damping ratio.

c) Mass-spring-damper system

The idea of employing a mass-spring-damper model for fast computation of the stator response has been used in a number of investigations, [TAN97, AND97, MAH96, WU93].

By way of example, [TAN97] employed a simple damped spring mass system together with calculated radial force spectra to facilitate a computer simulation of the stator displacement, velocity and acceleration. Previously, the idea of modelling the vibration response through the use of a 2^{nd} order mass-spring damper system was suggested, [WU93]. It was claimed that the results supported all those obtained from measurements on the machine, but no results obtained from the model were shown and no model details were provided. More recently, the use of a simple oscillation model, together with a dynamic model of the SRM, was reported as sufficient to enable the stator vibration to be simulated, although the dynamic model required measured flux-linkage charateristics from the experimental machine, [AND97]. A 4^{th}-order spring mass damper system was preferred over finite elements, [MAH96], for faster computation, from which the calculated stator vibration was compared to that obtained experimentally, although no axes are given.

d) Noise prediction

More recent publications have addressed the issue of noise emission, notably an acoustic noise simulation method has been developed, [RAS99], whereby the electromagnetically induced noise can be estimated and even heard, thereby allowing comparison between different machine designs and control schemes. The simulated noise spectra showed similar trends to those measured, except for an offset in the dBA level owing to the assumptions and other intrinsic errors. However, although it is usually sufficient to neglect damping when predicting the amplitudes of non-resonant vibrations, it is not adequate to do so when resonances occur. Further, for all SR machines, the dominant noise peaks are induced due to resonance of the stator at its natural frequencies and, therefore, it is imperative that the damping ratio is known for accurately predicting the vibration magnitudes and, hence, noise. However, as mentioned earlier, prediction of the damping ratio is a difficult task, in that it is influenced by the machine assembly and mounting, etc. Thus, although the proposed method, [RAS99], predicted the noise trends

for the given machine, the damping ratio is based on that particular machine. It follows, therefore, that correlation of such noise predictions will be less accurate for other machines.

1.3.5 Noise reduction techniques

In addition to the investigations cited earlier, numerous different methods have been proposed for reducing acoustic noise. These embrace design considerations, [COL96, WU96] and active control techniques, [CAM92, WU95, BLA94, GAB97, GAB99a].

a) Random turn-on and turn-off

One of the earliest suggestions for reducing the noise and vibration of SR machines was that of 'dither', proposed by Cameron et al [CAM92], which entails randomly changing the switching angles at both turn-on and turn-off by 0° or ±l° mechanical, thus reducing the level of excitation of the stator frequencies. Despite the fact that no results were shown, the method was claimed to be effective. This method was also assessed during an investigation carried out by [BLA94] with a voltage controlled 3-phase 6/4 machine, using a random switching band of ±l.5° mechanical. It was claimed a small reduction in the resonant peaks resulted, but the natural frequencies of the stator were not clearly identified, and no significant reduction in the vibration and noise peaks was observed, whilst the sound power level was not reduced. Further, since the earlier discussion on the switching angles highlighted that the turn-on and turn-off angles do not significantly influence the noise, it follows that little if any benefit would be gained by their random variation.

b) Random PWM

This can be achieved by one of two methods, viz. by variation of the PWM switching frequency within a defined frequency range - which spreads the switching noise and, also results in a lower average switching frequency and, thus an increased inverter efficiency. – or by varying the pulse width modulation between the leading and lagging edge. However, in general, random PWM can only reduce the switching noise, which could otherwise be eliminated from the audible frequency range simply by selecting a PWM switching frequency above 20kHz at the expense of increased switching losses. Hence, random PWM does not reduce the noise emissions attributed to stator resonances, as can be observed by the sound power measurements presented in [BLA94].

c) Active cancellation technique

The method proposed by Wu and Pollock, [WU95], is possibly the most notable in terms of active noise reduction. However, it does not prevent the occurrence of stator vibrations, rather it ensures that vibrations are induced which oppose existing vibrations, such that the net vibration level is reduced. This is achieved by controlling the step

changes of the applied voltage in such a way, that together with a knowledge of the stator natural frequencies, anti-phase stator vibrations are induced. The technique, therefore, involves switching off a phase in two stages, whereby the first switching event reduces the phase voltage from the positive supply to zero voltage by means of opening either switch in an asymmetric half bridge inverter whilst the other remains closed. This initiates a vibration, the magnitude of which is lower than that during normal commutation due to the reduced step change in voltage and, hence, reduced rate of change of current. The acceleration is negative, in that the stator accelerates away from the rotor radially and reaches a maximum negative value one quarter of a resonant cycle after the switch is opened. Subsequently, this peak reduces and returns to zero after half a resonant cycle before growing to a maximum positive value. It is when the first vibration oscillation reaches zero that the second switch is opened to induce a second vibration, whose acceleration is negative and, therefore, in anti-phase with the first vibration, which is currently entering the positive section of its cycle, **Fig. 1.7**. This is known as the 'OV loop' or '2-stage' cancellation technique, and although this was demonstrated using an asymmetric half bridge circuit, it was noted that other inverters, for which the zero-voltage loop cannot be produced, are still capable of applying active vibration cancellation, [POL97], although they are less effective.

With reference to the technique developed by Wu and Pollock, [WU95], the idea of active vibration cancellation was applied to a 3-phase 6/4 SR machine, [BLA94], to cancel vibrations at turn-on, rather than turn-off. From the results provided by [WU93] it is clear that at phase turn-on the acceleration begins once the peak current is reached, **Fig. 1.8**. Therefore, in order to induce a delay of half a resonant cycle after the onset of vibration, the time from turn-on to maximum current, t_c, is determined by equation (1.2), where θ_{on}, θ_o and ω_r are the turn-on angle, the angle at which magnetic overlap commences and the rotor speed, respectively [BLA94]. It is also clear that any reduction of stator vibration using this technique is limited by two issues. Firstly, it is well established that smaller stator vibrations are induced at turn-on, and secondly the time delay is dependent on the shaft speed, equation (1.3) and, therefore, on the speed calculation, the accuracy of hardware providing the speed feedback, and the control system providing the speed calculation.

$$t_c = \frac{\theta_{on} - \theta_o}{\omega_r} \tag{1.2}$$

$$t_d = t_c - \frac{1}{2f_n} \tag{1.3}$$

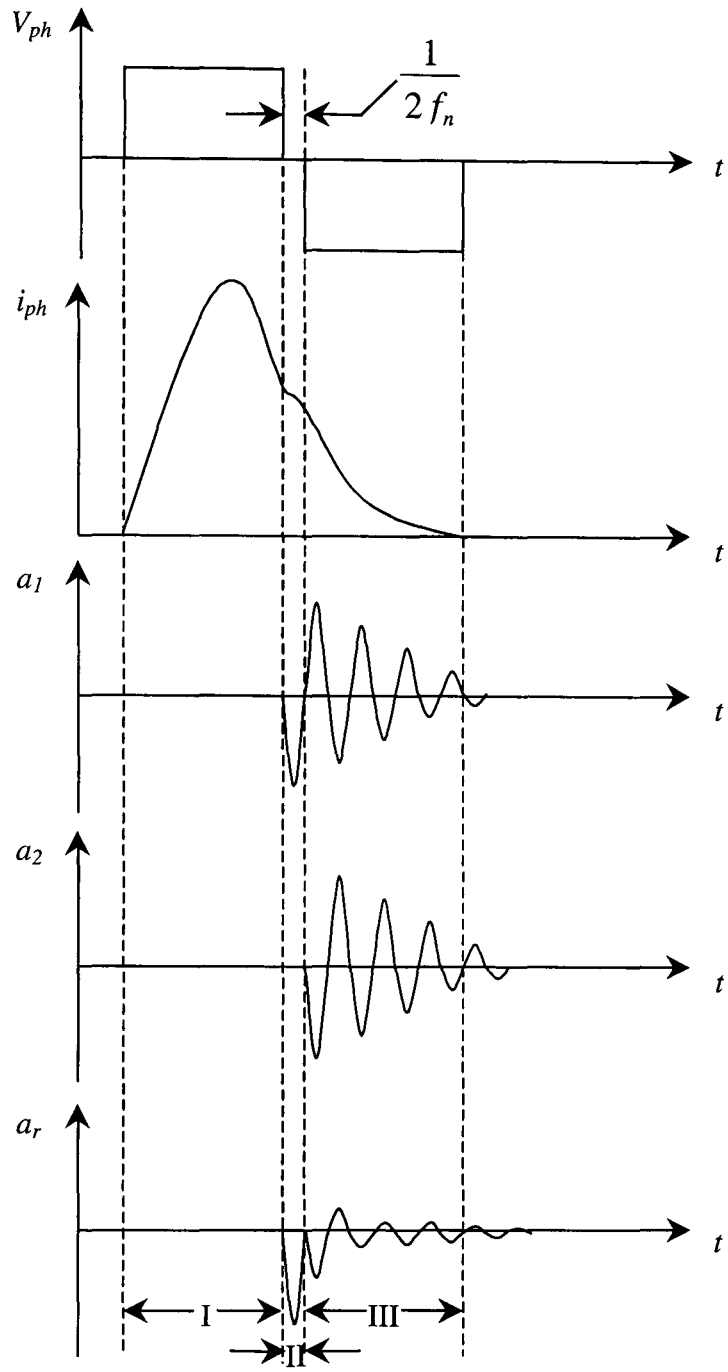

Fig. 1.7 *Representation of '2-stage active cancellation technique' during single pulse operation*

The observations in [BLA94] show that active cancellation at phase turn-on reduces the sound pressure level at all rotational speeds under current control. However, with voltage control the sound pressure level which results with active vibration compensation is generally higher than that which results with normal control, although no explanation is given. In order for the noise level to increase under voltage control, it can only be assumed that the calculation carried out by the controller is less accurate, possibly inducing the second vibration in phase with the first. This could occur if voltage control was more demanding on the machine controller than current control.

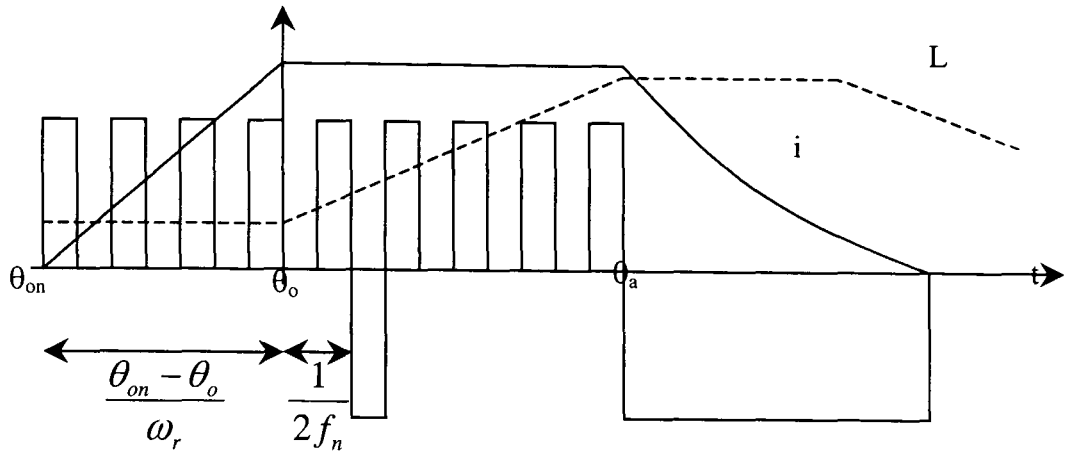

Fig. 1.8 *Definition of variables for active delay at turn-on, [BLA94]*

d) Current shaping

An early investigation by Cameron and Umas [CAM92] suggested the possibility of shaping the squared current to eliminate any offending force harmonics and, thus, reduce noise emissions. In addition, subsequent studies, especially those of Wu and Pollock, [WU93] highlighted the relationship of the stator vibration to the rate of change of current at turn-off. This led to the idea of applying current shaping algorithms at turn-off to limit the rate of change of current, and, thus, the radial force and vibration. Current shaping requires a pre-determined current shape to be defined in the control software, usually in the form of a look-up table comprising of the normalised current shape versus angular position. When summed with the demand signal, be it torque or speed, the current demand ensures that the controller switches the phase voltage accordingly to achieve the desired shape. A typical implementation of the current shaping technique is shown in the control schematic, **Fig. 1.9**, whilst **Fig. 1.10** shows a typical desired current waveform, superimposed with a natural current waveform.

A comparison of a natural current waveform with a shaped current waveform, having a lower rate of change of current at turn-off, shows that the associated radial force waveform has a much smoother gradient. Although limited results are available, it is claimed that the vibration and, hence, noise are reduced without affecting the machine performance. The application of this method is described for a 3-phase 6/4 machine, and is based on controlling the flux gradient, for any operating point, such as at start-up, during overload and during phase magnetisation and de-magnetisation, [GAB99a]. This is achieved through the implementation of an additional control algorithm between the current controller and inverter to control the average voltage across the phase, as desired. The presented noise and vibration spectra, for the machine operating with and without flux variation control, shows that a significant reduction can be achieved for operation at

2000rpm. Further, over a range of operating speeds from 500-2000rpm, the SPL is observed to reduce between 11-13dB with application of the instantaneous flux controller.

Similarly, stator accelerations were compared for a square current wavefrom, characteristic of classical control, to one with rise and decay gradients based on the shape of a sinusoid, [GAB99b]. It is stated that the two currents produce the same torque and result in similar copper losses, and it is observed that the stator vibration is significantly reduced when the control strategy employs quasi-sinusoidal currents. Furthermore, it is shown that the influence of the shape of the rise period of the current is insignificant to the stator vibration compared to that of the current decay period.

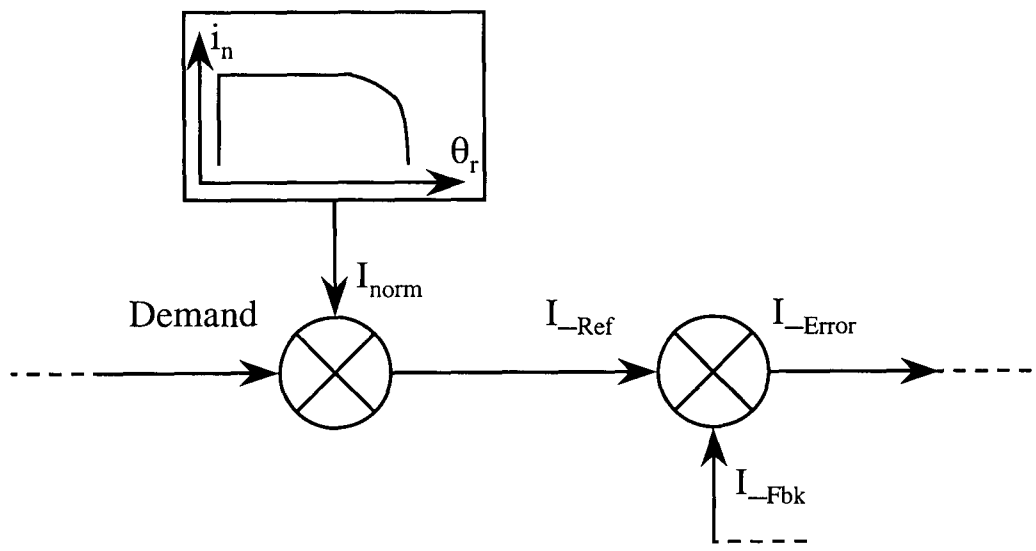

Fig. 1.9 *Implementation of current shaping*

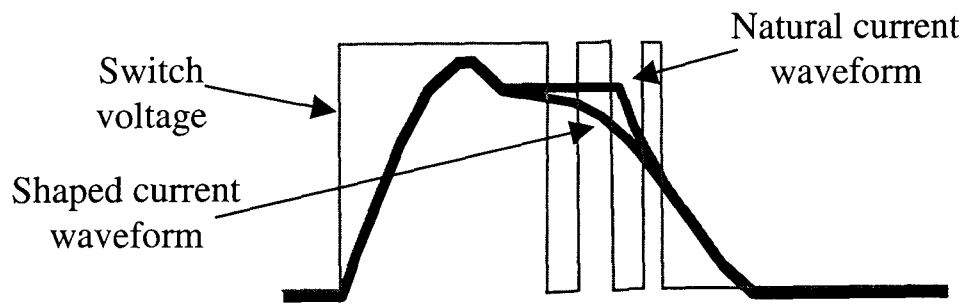

Fig. 1.10 *Example of desired and natural current shape, together with switch voltage*

e) Geometric design criteria

As a result of investigations to-date, various geometric 'optimal' design criteria have been suggested for SR machine designs with the aim of reducing the acoustic noise. It is obvious that the stator yoke should be as thick as possible, in order to increase the stator

stiffness and hence raise the natural frequencies. It was observed [WU96] that the stiffness of a stator stack is increased significantly by the addition of end-shields. Thus, it was suggested that an increase in yoke thickness is only required in the central section to suppress vibrations, [WU96]. Also a thicker yoke leads to increased thermal dissipation distance for heat transfer from the windings to the frame, [COL96], but, it does decrease the core flux density, which will reduce both the core loss and, to some extent, the acoustic noise.

Pole shaping has also been suggested as a means of reducing noise, although no insight is given [PUL93]. Other issues, such as the location of the bearings as close as possible to the rotor to achieve good concentricity, have been suggested, [WU96], and the general need for high machining tolerances.

1.4 Scope of research and contribution of thesis

To date, although finite elements have been employed to identify stator natural frequencies, little has been reported in regard to assessing the influence of the stator geometry on the natural frequencies. Further, analyses have generally neglected the laminated nature of the stator core, omitted the stator windings, the frame and the end-caps, and often do not define the materials which were employed in the motors under consideration. Numerous investigations have been undertaken to assess the influence of control parameters on the noise and vibration of SR machines, but the analyses are generally limited to either the frequency domain, the time domain or measurements of the sound pressure level, and are generally carried out in isolation to the machine design.

The research which is reported in this thesis is concerned with a comprehensive investigation of the acoustic noise and vibration of SR machines, accounting for the strong relationship of the noise and vibration with both the mechanical structure of the machine and its control parameters. Both issues were reported in detail. The main contents of the thesis are as follows:

Chapter 2 briefly describes the experimental SR machine on which the mechanical investigations are based, and which was employed for all the experimental investigations on noise and vibration. The design of the associated inverter and DSP controller software, for implementation of the machine operating modes, are also described.

Chapter 3 describes a rigorous and systematic investigation into the influence of the leading dimensions and geometric asymmetries of the stator of the SR machine on its natural frequencies. These parameters include the yoke thickness, the width and number of stator poles, the lamination notches, the stator windings, the stator frame, the end-caps, and, finally, the mounting of the assembled machine. The investigation encompasses both 2D and 3D finite element analyses, together with experimental validation. Finite element analysis is employed to deduce effective material properties for the laminated stator core and windings to enable the influence of their mass and stiffness on the natural frequencies and vibration modes to be quantified.

Chapter 4 examines the influence of the control parameters on the vibration and acoustic noise of SR machines. Operation of the SR machine under voltage control and current control, on no-load and load, for various operational speeds, switching frequencies, chopping methods, switching angles and with single pulse mode operation,

is considered. Vibration analyses in both the frequency and time domains are presented and the noise is analysed in the frequency domain, complimented by measurements of the sound pressure level.

Chapter 5 evaluates the effectiveness of active vibration cancellation for noise and vibration reduction with the SR machine operating on both no-load and load, under voltage and current control, and during single pulse mode operation. Again, the results are analysed in the frequency and time domains, and measurements of the sound pressure level are presented. The investigation includes an assessment of the effectiveness of the time-delay duration on the emitted noise, and highlights the limitation of the technique on machines having multi-resonant machine stators, and during operation under current control.

Chapter 6 draws conclusions from the previous five chapters and suggests a number of criteria for reducing the noise of an SR machine, at the early machine design stage to the machine control strategy.

The major contributions of the research which is described in the thesis may be summarised as follows:

1. The effect of the leading dimensions and geometric asymmetries on the natural frequencies and associated mode shapes of SR machines is systematically investigated. The influence of the laminated stator core and the mass and stiffness effects of the stator windings, including the end-windings, on the natural frequencies of SR machines is quantified. The influence of the frame and end-caps on the natural frequencies is also investigated highlighting the limitations of finite element analyses for such complex mechanical systems, (Chapter 3).

2. The influence of the control parameters of SR machines is investigated systematically, (Chapter 4), and the effectiveness of the active vibration cancellation method for reducing noise and vibration is, for the first time, investigated in both the time and frequency domains, and validated by measurements of noise and vibration spectra and the sound pressure level. The limitation of the technique for use with SR machines having multi-resonant stators is also highlighted, as is the sensitivity to the accuracy of the time-delay, which is shown to be problematic during current control, (Chapter 5).

Chapter 2
Drive and Hardware Development

Fig. 2.1 shows a schematic of the experimental system, which comprises an SR machine, a power MOSFET inverter, and a TMS320F240 DSP development kit, all of which will be described in this chapter. Firstly, the experimental SR machine, on which all the investigations and analyses which are to be described in this thesis were undertaken, will be described. The design of the inverter is then described, and this is followed by an overview of those features of the DSP system which are relevant to the operation of the machine.

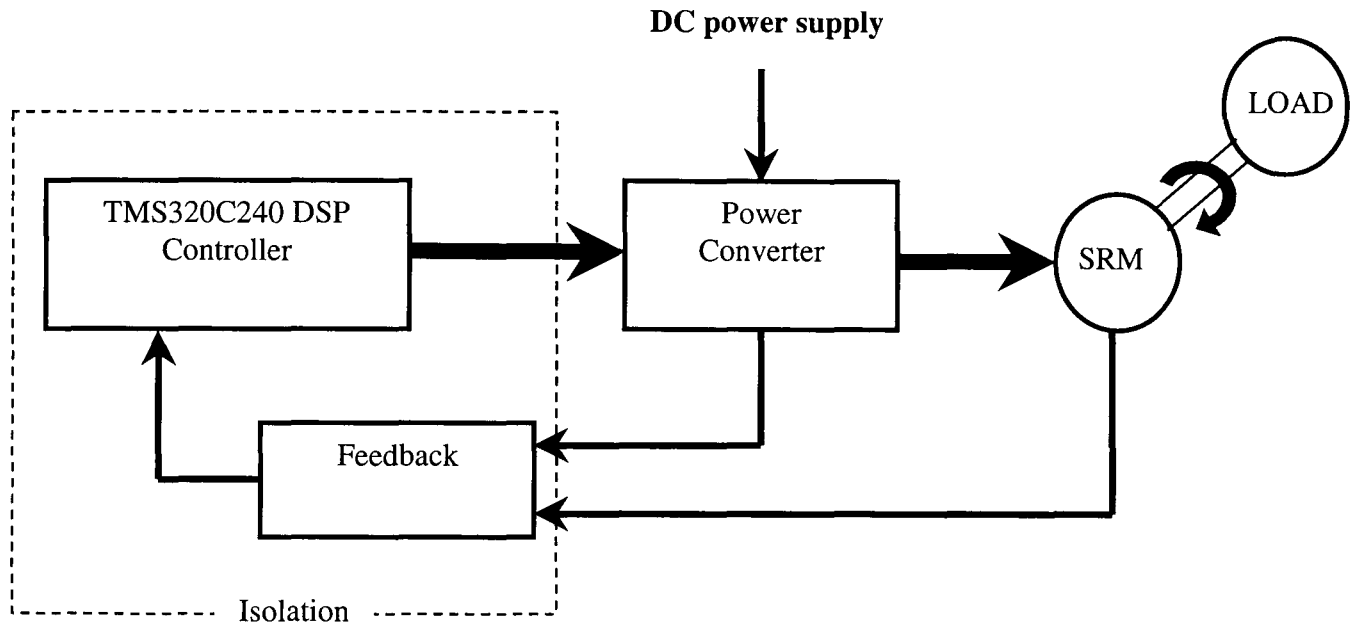

Fig. 2.1 *Schematic of system configuration*

2.1 Machine description

The machine which was employed for the investigation is representative of a typical 3-phase SR machine having 6 stator poles and 4 rotor poles, as shown in **Fig. 2.2**. Each phase is formed by connecting in series the concentrated coils on diametrically opposite stator poles, which comprise of 31 turns, so as to create a NNN-SSS winding configuration. The lamination geometry and winding design is similar to that of the 6/4 SR topology described by Miller, [MIL93], whose performance specification is given in **Table 2.1**, and for which the parameters are given in **Table 2.2**, the variables being defined in **Fig. 2.3**.

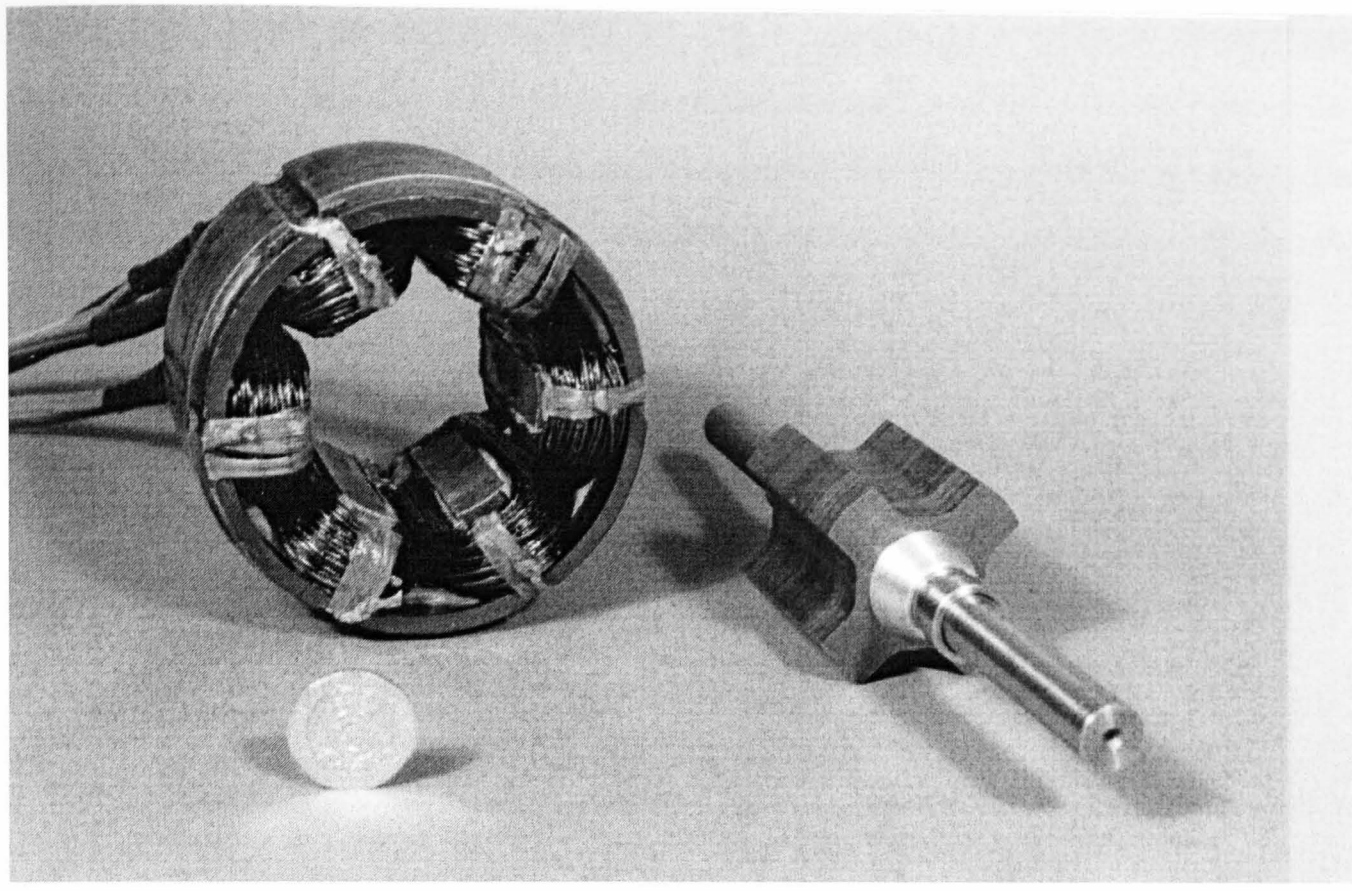

Fig. 2.2 *Photograph of manufactured experimental machine*

Table 2.1 *Specification of experimental machine*

Torque, T	1.1Nm
Speed, N	2000rpm
Supply Voltage, V_s	$24V_{dc}$

The SR machine is a doubly salient, reluctance machine, which operates on the principle of minimising the reluctance between the excited stator poles and the rotor poles, i.e. the machine rotates so as to maximise the inductance of the excited phase winding, which occurs when a pair of rotor poles align with the stator poles of the excited phase. The variation in inductance as the rotor and stator poles move from the unaligned position to the aligned position is generally represented by flux-linkage versus current characteristics, (ψ-i), for a number of equally stepped intermediate rotor positions. The ψ-i characteristics are fundamental to evaluating the performance of an SR machine, since they enable the maximum possible energy conversion and, hence, the average torque produced by the machine to be determined. Electromagnetic finite element analysis (FEA) is the only accurate method of determining the ψ-i characteristics. **Fig. 2.4** shows the ψ-i characteristics obtained for the 6/4 experimental machine, deduced from 2-D FEA. The B-H characteristic of the stator and rotor lamination material, M300-35A, is shown in **Fig. 2.5**. The mechanical properties of M300-35A, which are necessary for vibration analyses of the machine, are given in Chapter 3. Typical flux plots,

generated by FEA, are shown in **Fig. 2.6**. They correspond to each of the 16 rotor positions shown in **Fig. 2.4**, for a fixed current density of 3.0MAm^{-2}, (Current, *I=13.5A*). These highlight the intense saturation which occurs at the pole-tips, as evidenced by the higher density of flux lines, which is characteristic of SR machine operation, and also the existence of flux leakage.

Table 2.2 *Experimental machine parameters*[#]

Parameter	symbol	Value	Unit
Stator diameter	D_s	93.8	mm
Stator pole width	t_s	12.3	mm
Stator pole arc	β_s	30	°
No. of stator poles	N_s	6	mm
Stator slot depth	d_s	14.85	mm
Stator yoke thickness	y_s	8.1	mm
Notch radius	N	3.0	mm
Slot area	A_{slot}	309	mm^2
Stator bore radius	r_1	23.95	mm
Airgap	g	0.5	mm
Number of phases	m	3	
Stack length	L_{stk}	46.9	mm
Rotor pole width	t_r	12.95	mm
No. of rotor poles	N_r	4	
Rotor diameter	r_3	46.9	mm
Rotor pole arc	β_r	32	°
Rotor slot depth	d_r	6.15	mm
Rotor yoke thickness	y_r	8.6	mm
Shaft diameter	D_{sh}	17.4	mm

[#]Refer to **Fig. D3**, Appendix D, for details of the frame and end-caps

The complex non-linear nature of the SR machine necessitates some form of computer based modelling to enable the dynamic performance of a given design to be predicted. This needs to account for the saturation of the pole-tips which is characteristic of partially overlapping stator and rotor poles. Further, the torque is a function of both the phase current and the rotor position, with the current itself being a function of rotor position. Therefore, the average torque can only be determined by the integration of the

co-energy over a working stroke. Software developed in the Electrical Machines and Drives Group at the University of Sheffield incorporates a piecewise linear function of the flux-linkage against rotor position characteristic, with the current as an undetermined parameter, [MIL87a, MIL90], to facilitate such an analysis, although it does not account for the losses in the power converter. A typical example of the phase current waveform, the working (ψ-i) trajectory and the instantaneous torque waveform as predicted by this software for the experimental SR machine are shown in **Figs. 2.7, 2.8 & 2.9**, respectively, for a speed of 2000rpm, and a supply voltage of 24V, 45° corresponding to the full alignment of a pair of rotor poles with the excited stator phase.

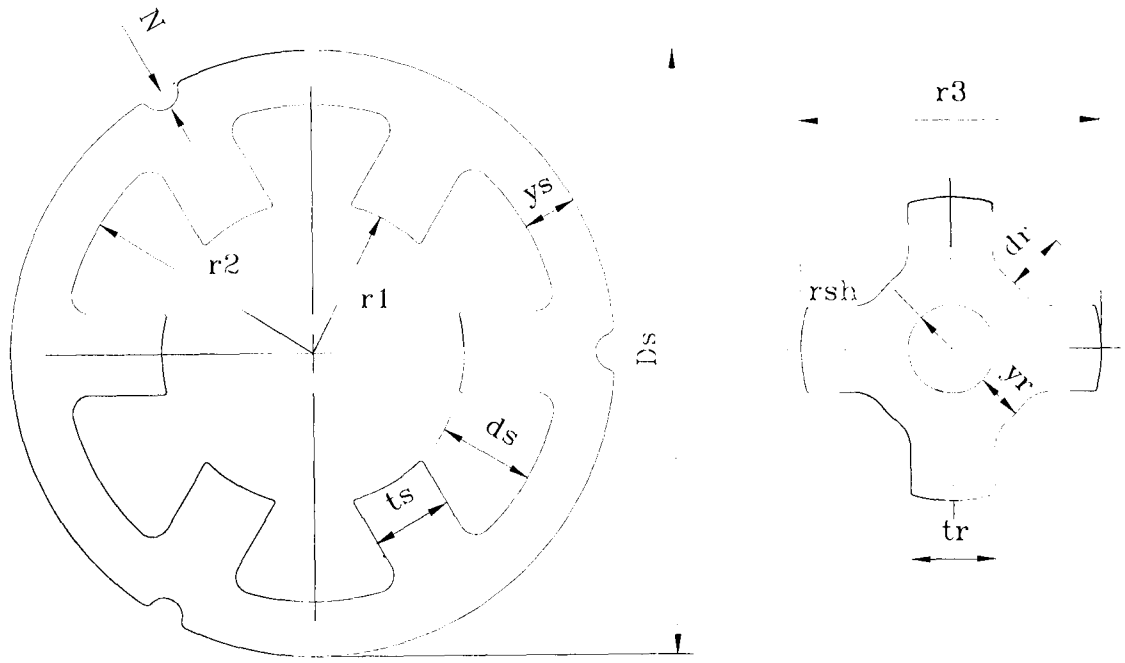

Fig. 2.3 *Definition of dimensional parameters*

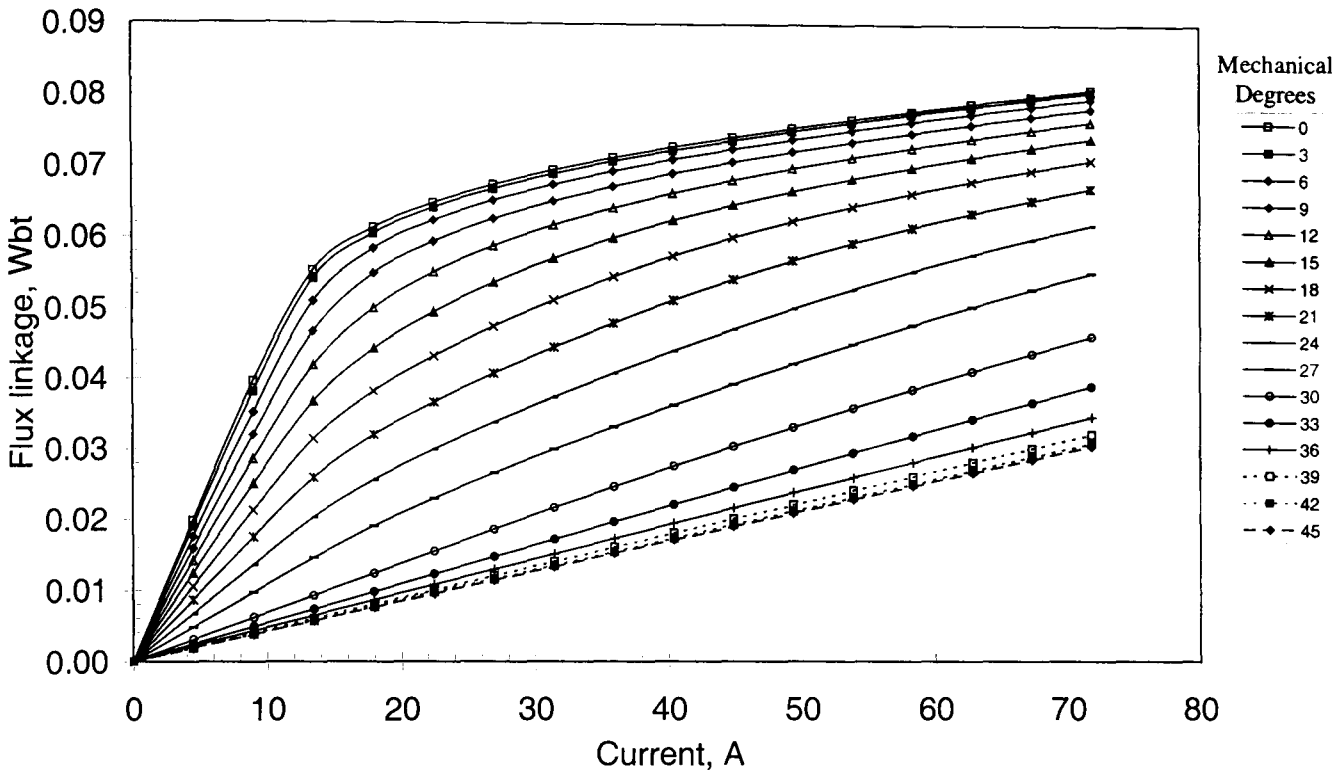

Fig. 2.4 *ψ-i characteristics for experimental SR machine*

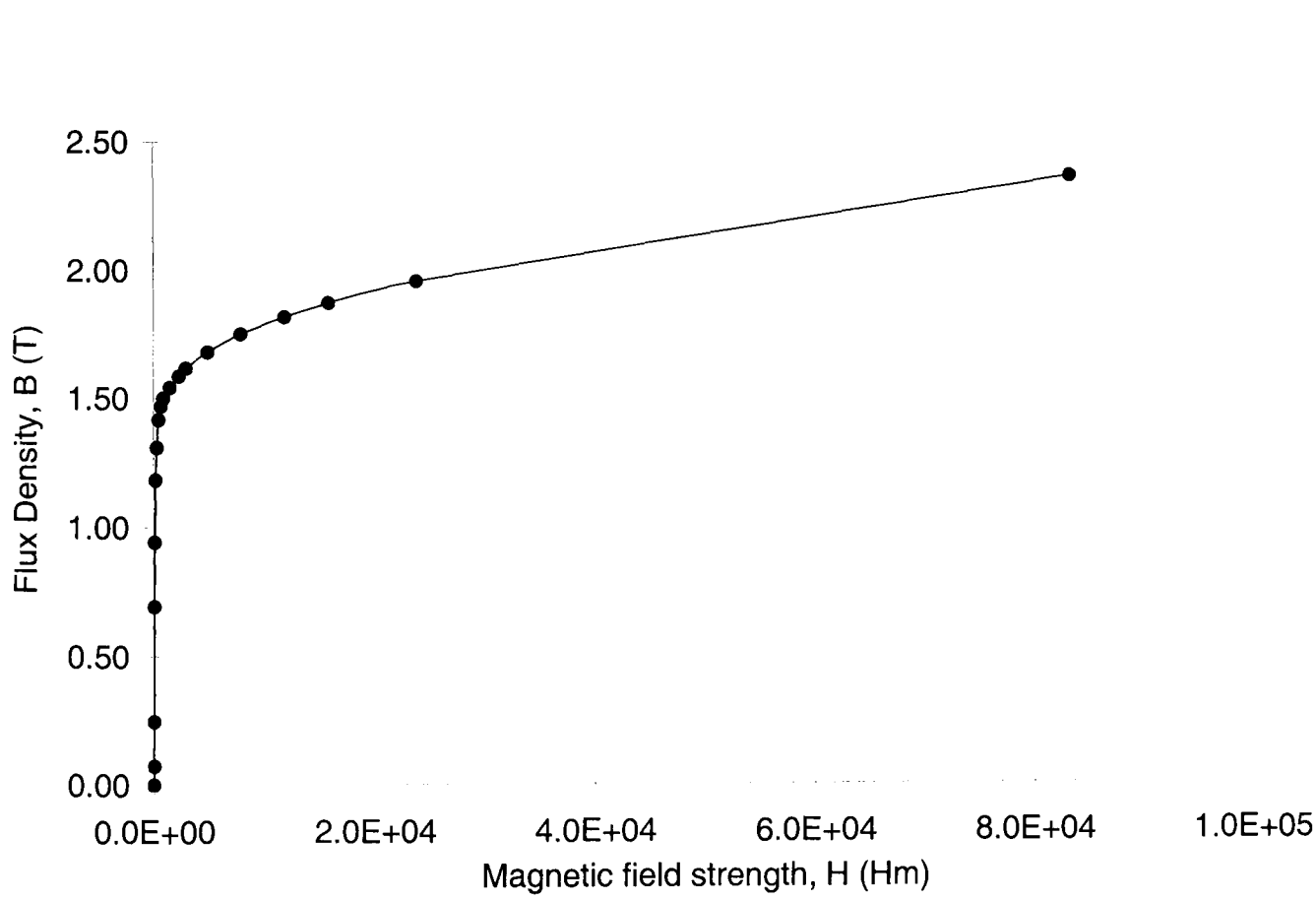

Fig. 2.5 *B-H characteristic of lamination material, M300-35A*

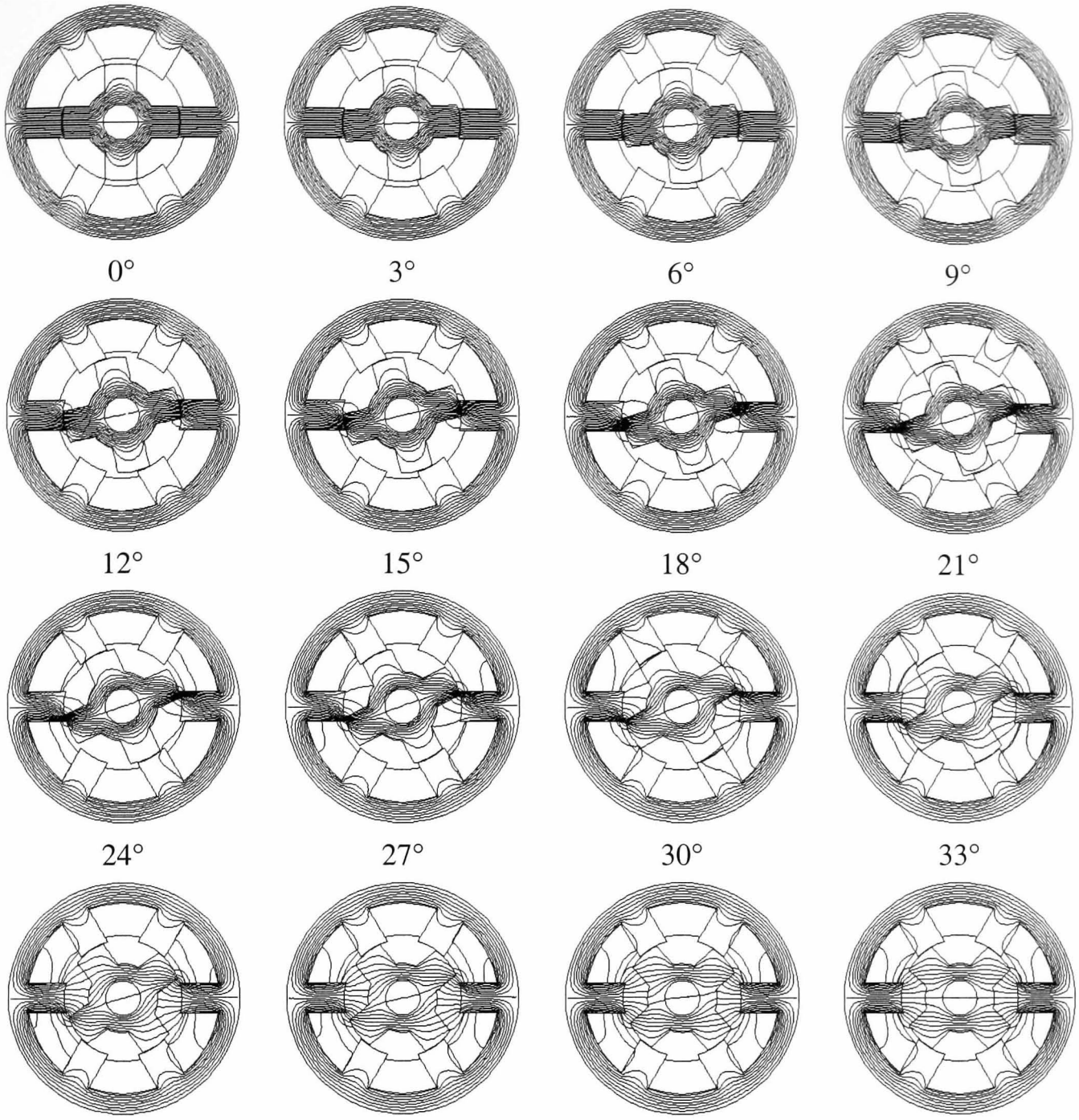

Fig. 2.6 *Typical flux plots for SR machine as rotor moves form the aligned position (0 °) to the unaligned position (45 °)*

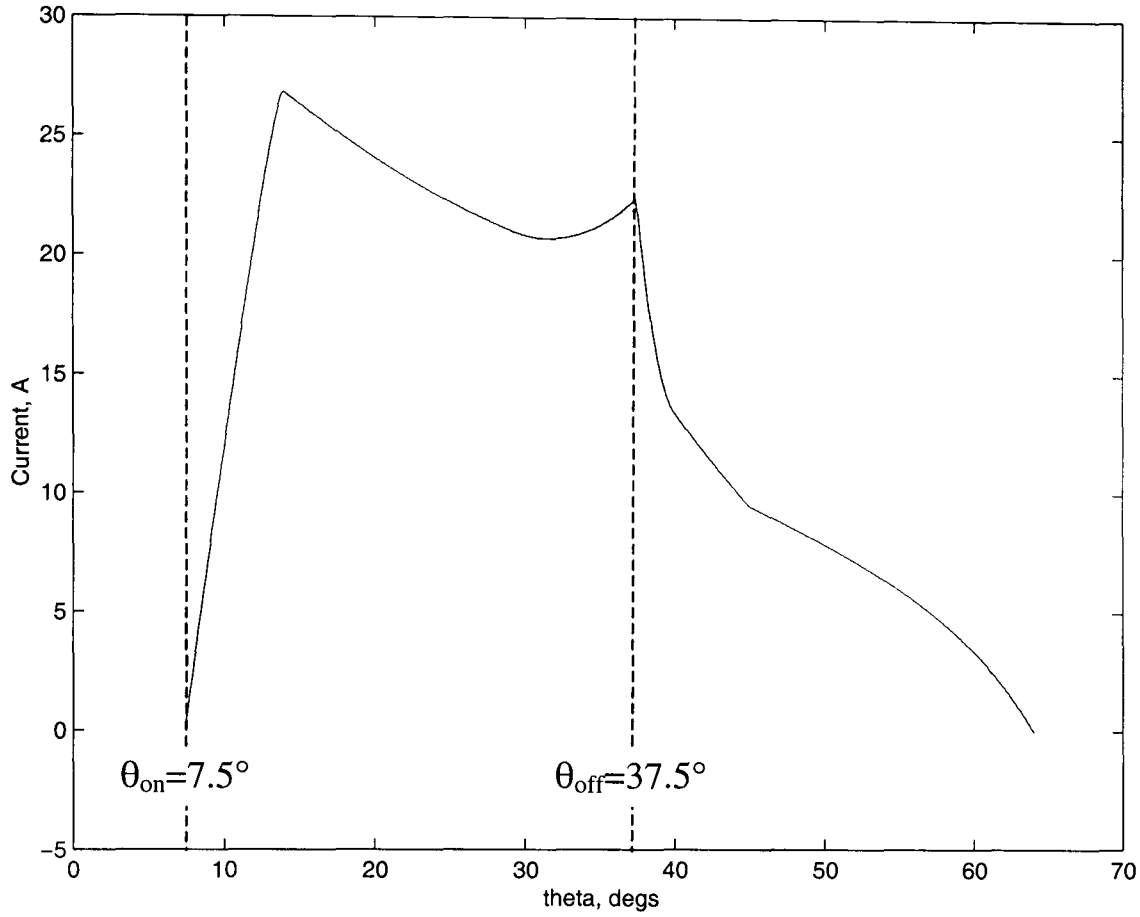

Fig. 2.7 *Typical phase current at 2000rpm*

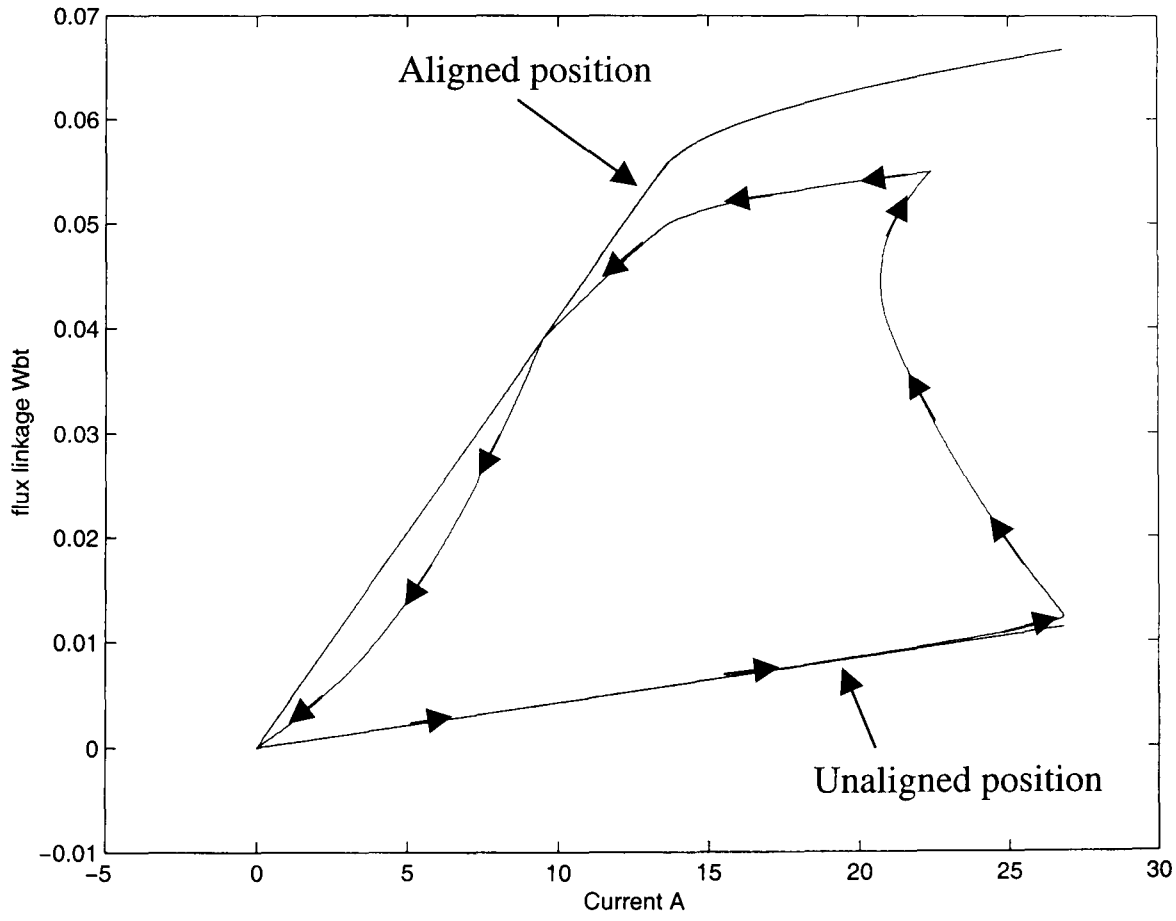

Fig. 2.8 *Typical ψ-i trajectory over working stroke at 2000rpm*

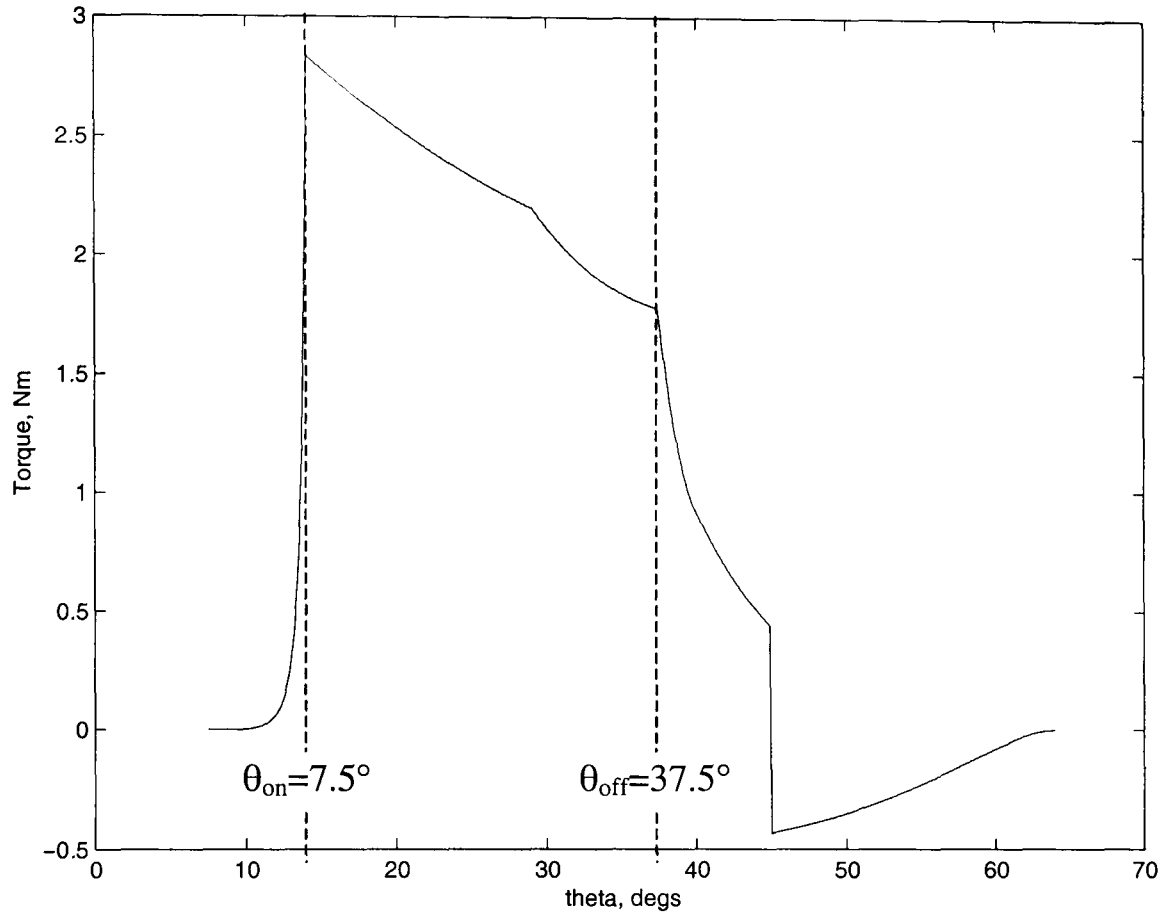

Fig. 2.9 *Typical torque waveform at 2000rpm*

2.2 Inverter and gate drives

The drive system for the experimental SR machine was not developed for any specific application. It was realised purely for research purposes, to enable acoustic noise and vibration measurements and analyses to be carried out under the typical operating modes for an SR machine. For this reason, the design of the system was not crucial in terms of space limitations, it only had to provide stable operation during various steady-state speed and load conditions, its transient response not being critical.

There are several possible inverter topologies for SR machines, some of which are outlined in Appendix A. Since the active power MOSFET's are separated by a machine phase winding, the problem of 'shoot through' is not an issue, and, hence, there is no requirement for 'dead-time' generation. Since several control techniques were to be implemented during the course of the investigation, the classic drive circuit, comprising of two power switches and two diodes per phase-leg, was deemed to be the most appropriate. As the experimental system is low power, power MOSFET switching devices were employed. These enable switching frequencies >20kHz to be used, thus providing flexibility when investigating the various control algorithms. Fast recovery diodes were employed for the free-wheeling devices, to ensure that the current tail at turn-off was a minimum. In order to dissipate heat from the power switching devices, they were mounted on aluminium bars which were attached to an aluminium heat sink, as shown in the photograph of **Fig. 2.10**, together with the gate drive module boards.

In order to minimise the risk of damage to the inverter during development of the controller, the sizing of the inverter components was rather generous, as will be seen in **Table 2.3**. Optical isolation of the DSP from the inverter hardware was provided by the use of a number of H11L1 opto-couplers. The H11L1 configuration and the developed isolation board are shown in **Figs. 2.11(a) & (b)**, respectively.

Table 2.3 *Rating of inverter components*

Device	Description	Rating
Power MOSFET's	BUZ22	100V, 34A
Free-wheeling diodes	Fast recovery, RURP3020	200V, 30A
D.C. link capacitors		6800μF, 34V

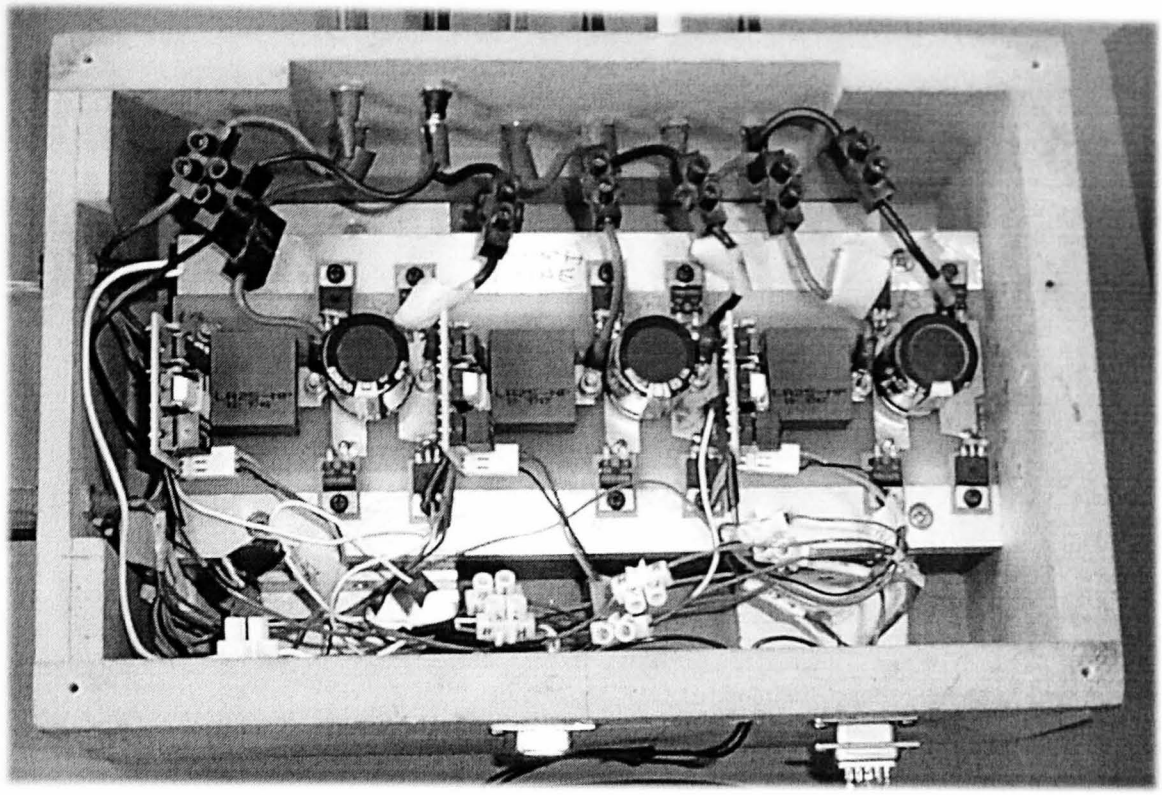

Fig. 2.10 *Photograph of inverter with gate drives*

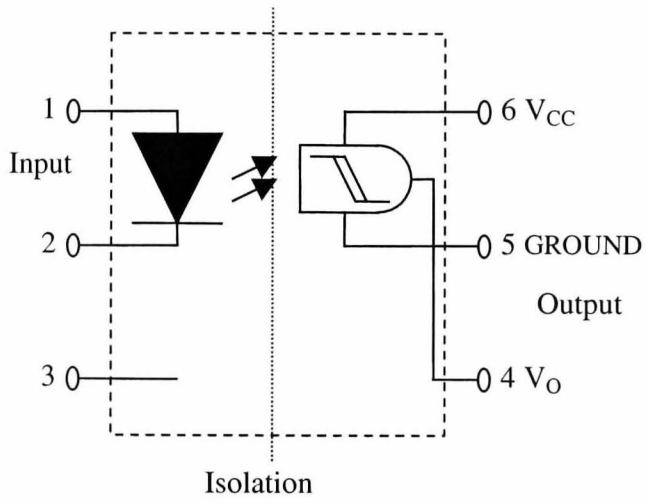

(a)

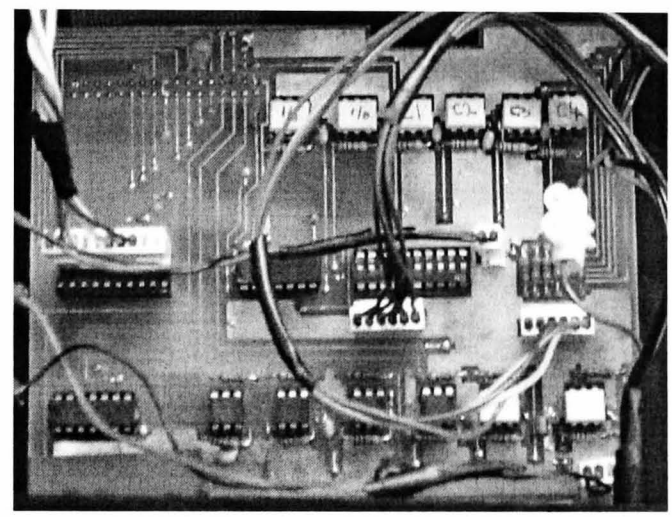

(b)

Fig. 2.11 *Opto-isolation;* **(a)** *configuration of H11L1,* **(b)** *developed isolation board*

In order to provide feedback of the individual phase currents to the digital controller, a standard PCB mount Hall effect transducer was integrated into each phase-leg of the inverter, as shown in **Fig. 2.12**. These devices allow a maximum current of 25A to be measured, with a corresponding output current of 25mA to an accuracy of ±0.6%. A 160Ω resistor was selected for the sense resistor, R_M, so that an output voltage of 4V would represent the peak current of 25A, due to the fact that the input to the spectrum analyser, HP35660A, which was used to analyse the phase current was limited to 4V.

The circuit diagram for the gate drive, for switching the power MOSFET's, and the completed gate drive board are shown in **Figs. 2.13 & 2.14**, respectively. Fast switching

is desirable so as to minimise any time delay during commutation of the phase currents. Therefore, high speed MOSFET drives, TC4433, were employed, since they are capable of providing up a 2A continuous current to charge the MOSFET gate, as they are designed for high power MOSFET's and are, therefore, more than capable of driving the 100V, 34A devices which were employed.

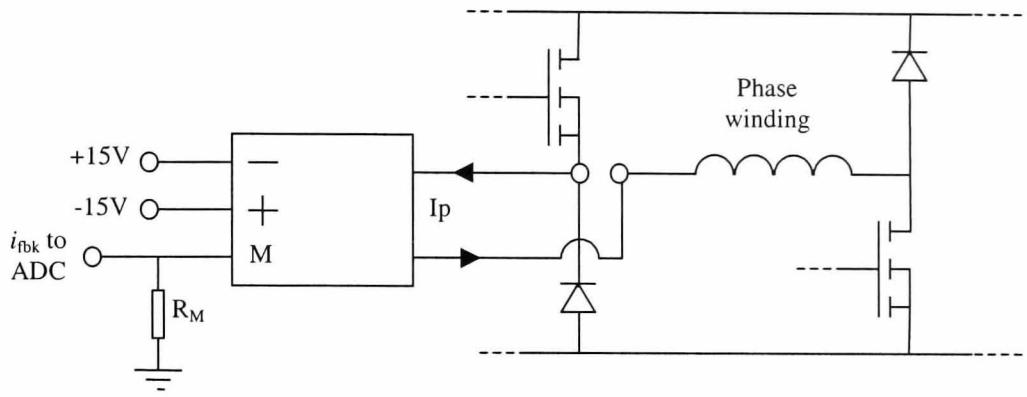

Fig. 2.12 *Implementation of current transducer to derive current feedback signal*

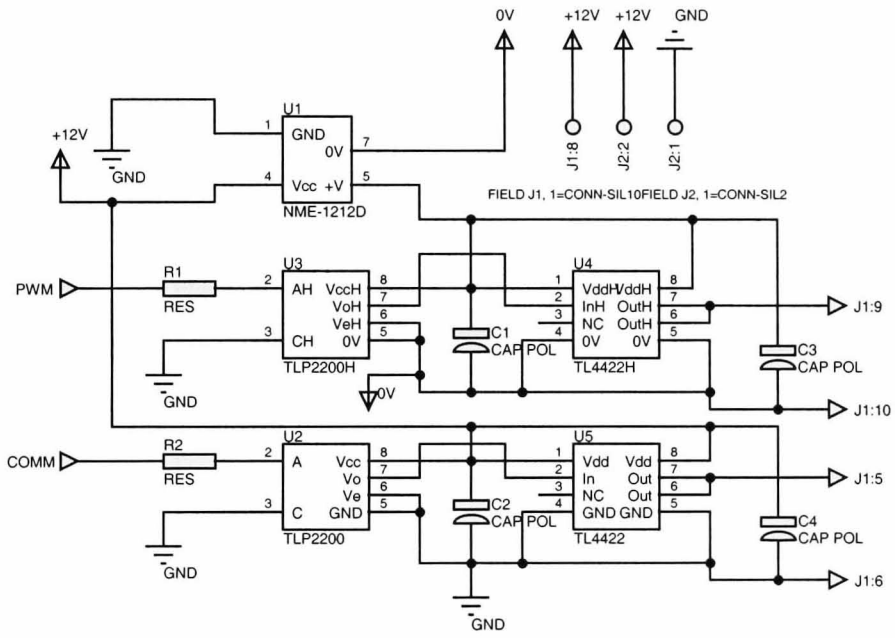

Fig. 2.13 *Gate drive circuit*

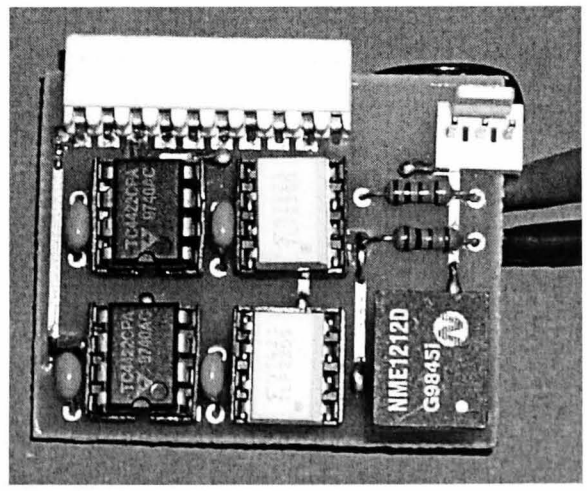

Fig. 2.14b *Gate drive board*

2.3 DSP control of switched reluctance machine

The control system is an essential facet of variable-speed SR machine drives, which require accurate rotor position sensing and, at low operating speeds, some means of controlling the magnitude of the phase currents, due to the fact that the available back-emf is insufficient to limit the peak phase current. It is well established that the vibration and acoustic noise emissions from SR machines are related to the switching of the phase currents and, therefore, depend on the method of control. Whilst an analogue controller is often a very practical and cost effective solution for commercial SR drives, the cost of DSP systems is continually reducing and the technology is improving. Thus, they are an increasingly popular solution for motion control systems. Further, DSP-based control systems provide an ideal environment for research investigations, their versatility enabling alternative control techniques to be implemented and the control parameters to be varied by software.

2.3.1 Overview of TMS320C24x

There are a wide range of technologies available within the DSP market. However, the majority of these are for the control of general purpose systems and would require additional interfacing to enable the transfer of information between a machine drive system and the control software. The TMS320F240 series was selected since it was developed specifically for motion control applications, and, therefore, provides additional peripherals, both within the processor and within the development board, for interfacing with drive systems, **Fig. 2.15**. The C24x is classed as a member of the C2xx series based on the standard 16-bit, fixed-point TMS320 family, and offers 20 million instructions per second (MIPS), which was an adequate speed for the research to be undertaken. The feature which makes it ideal for motion control applications is the 'Event Manager', which comprises of three 16-bit General Purpose Timers (GPT), three full compare/capture units, three simple compare/capture units, pulse-width modulation (PWM) circuits, four edge triggered capture units, quadrature encoder pulse (QEP) circuit designed specifically to interface with a digital encoder and a range of interrupt functions.

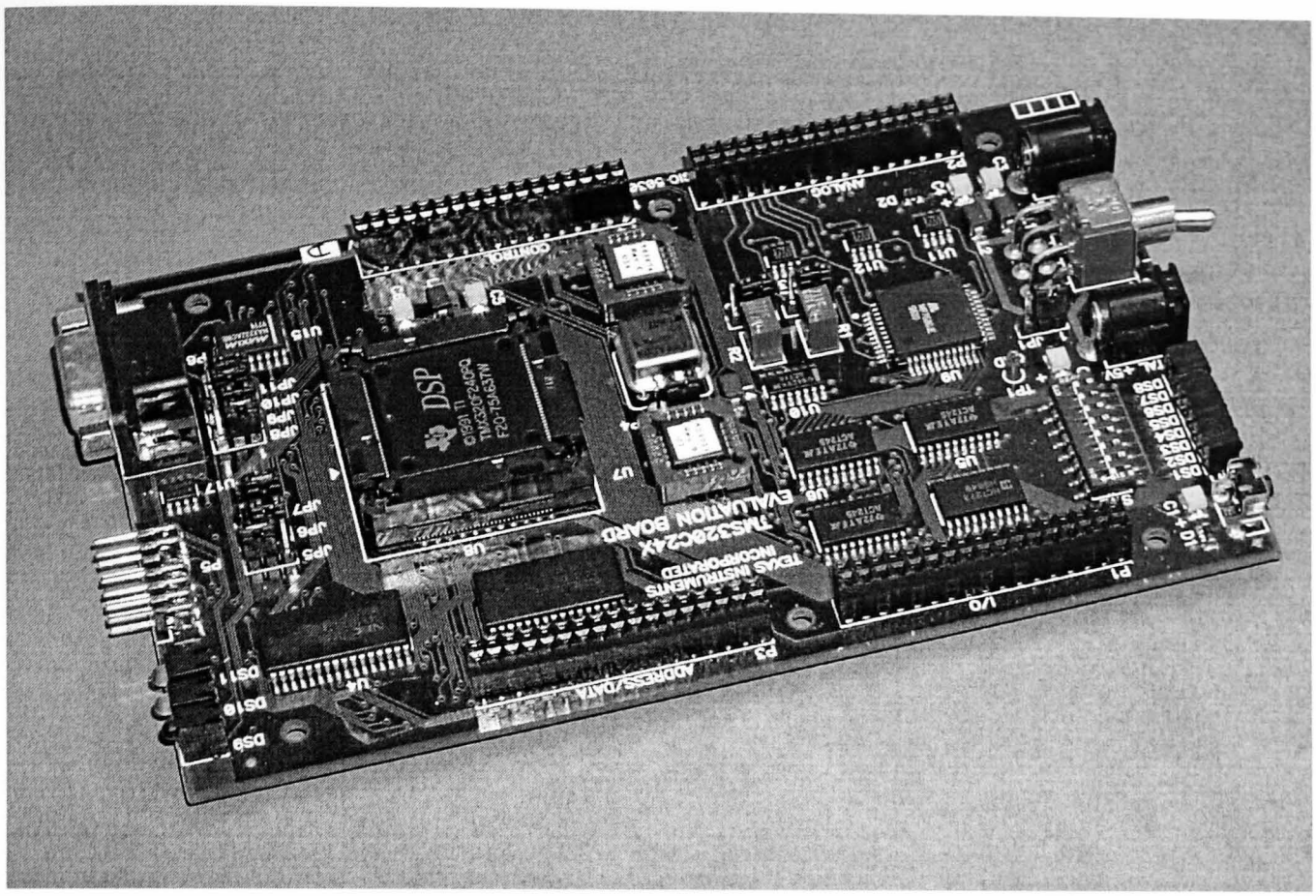

Fig. 2.15 *Photograph of TMS320F240 DSP development kit*

2.3.2 System features

The simplified control loop of **Fig. 2.16** shows the main inputs and outputs of the developed SR drive system, and the features which are relevant for the various control strategies, blocks 1 to 3. Block 1 is utilised for the fixed frequency PWM control scheme, and is a simple proportional-integral (PI) gain. Block 2 is the current regulator which comprises of a simple bang-bang controller. Finally, block 3 provides the output to the power switching devices, which are configured for fixed frequency PWM operation when operated under the voltage control scheme and are configured so as to chop appropriately during current control operation according to the output of the current regulator. These control blocks, and the outer speed loop, are implemented through a number of algorithms in the software which is based around four main interrupt service routines (ISR's) that enable position feedback, speed feedback, speed demand and commutation advance, encoder count reset, and voltage and current control, **Fig. 2.17**.

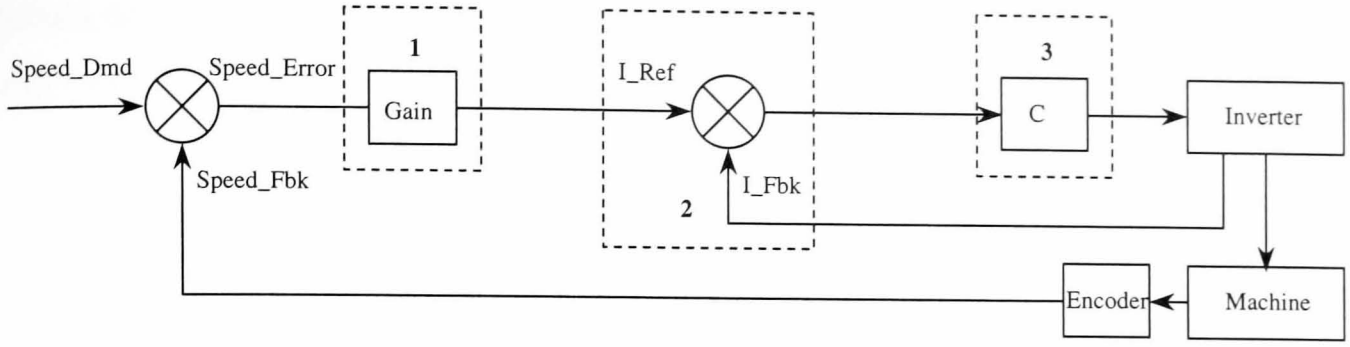

Fig. 2.16 *Control loop for experimental drive system*

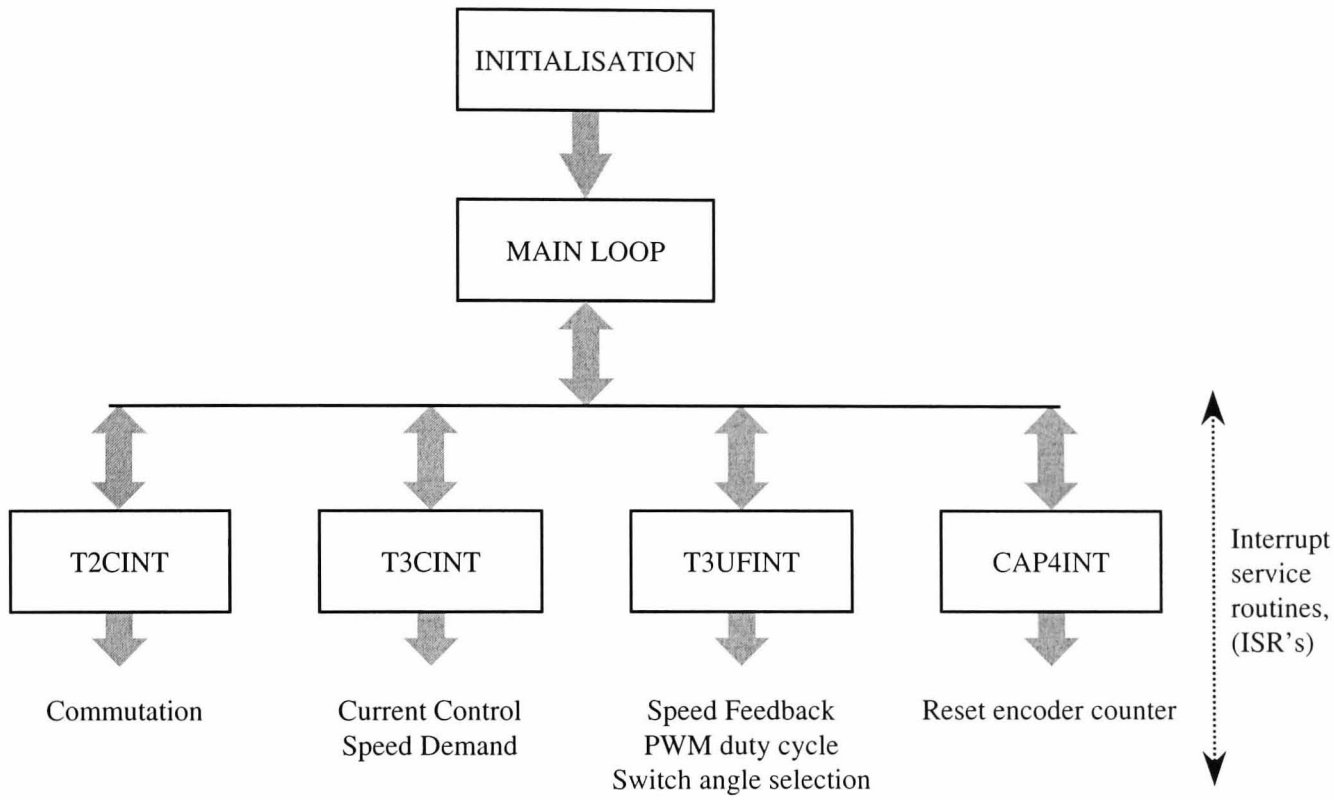

Fig. 2.17 *Flow chart outlining software structure*

The software flow chart shown in **Fig. 2.17** outlines the main blocks which are used to perform the system functions, which are executed through the use of interrupt service routines (ISR's). The DSP 'Event Manager' has a hierarchical interrupt system which links in with the main DSP core interrupt network. This provides a variety of interrupts that can be initialised by a timer value matching that in the corresponding compare register, by a timer reaching its maximum period value and by a timer being reset to zero. Interrupts can also be configured to trigger on the rising and/or falling edges of signals interfaced to the capture units, and similarly for the compare/PWM units. The corresponding registers are all treated as 16-bit memory-mapped registers, allowing the flags to be used independently of the interrupt system if preferred. All interrupts are maskable directly within their corresponding interrupt mask registers, and/or by their corresponding interrupt level within the DSP core. Furthermore, there are three 16-bit general purpose timers (GPT's) which can be configured to operate independently or in synchronism. These are used to provide the time-base for a number of applications

within the software, such as the sampling period for the ADC's, operation of the capture units and the QEP circuit, and the use of compare units associated with PWM generation.

The PWM implemented for the voltage control scheme utilises one of the DSP timers configured in a continuous up counting mode, which resets to zero when the timer counter value matches that specified by the timer period register, TxPR. Once the timer counter resets to zero, the counter starts incrementing for the following period. Thus, a continuous ramping of the timer counter is achieved, **Fig. 2.18**. The value loaded into the timer period register, together with the selected frequency of the timer, defines the PWM frequency, equation (2.1). Thus, the generation of the PWM to the output pins operates continually in the background during software execution.

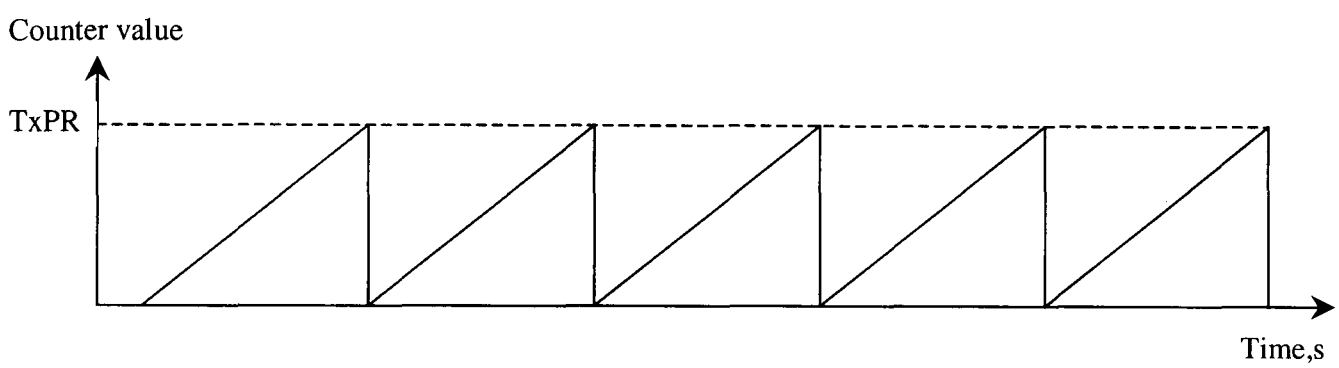

Fig. 2.18 *Configuration of timer for PWM generation*

$$f_s = \frac{1}{\text{period register} \times \text{timer period}} \tag{2.1}$$

The DSP event manager provides six main compare output pins, whose outputs, when configured for PWM operation, can be forced high or low, or can be configured for active high or low. When configured for 'active' operation the state of the output pins switches high or low depending on the compare match event and timer reset, as outlined in **Fig. 2.19**. In the given system, the output pins which are employed for PWM operation are configured for active high and, therefore, when the timer count matches that in the compare register the output goes high and remains in this state until the timer count resets at the timer period. Thus, the value stored in the compare register determines the duty cycle of the PWM, which is derived from the speed error, the value of which is updated every time the speed ISR is executed, and is loaded into the compare register on execution of the commutation ISR. The 'forced high' state is used for the lower switch of a phase-leg when soft chopping is employed, such that it is continually on during phase excitation, whilst the other switch, configured to 'active high', provides

the PWM. The state 'forced low' is utilised for both switches of a phase-leg at phase turn-off to disable phase excitation.

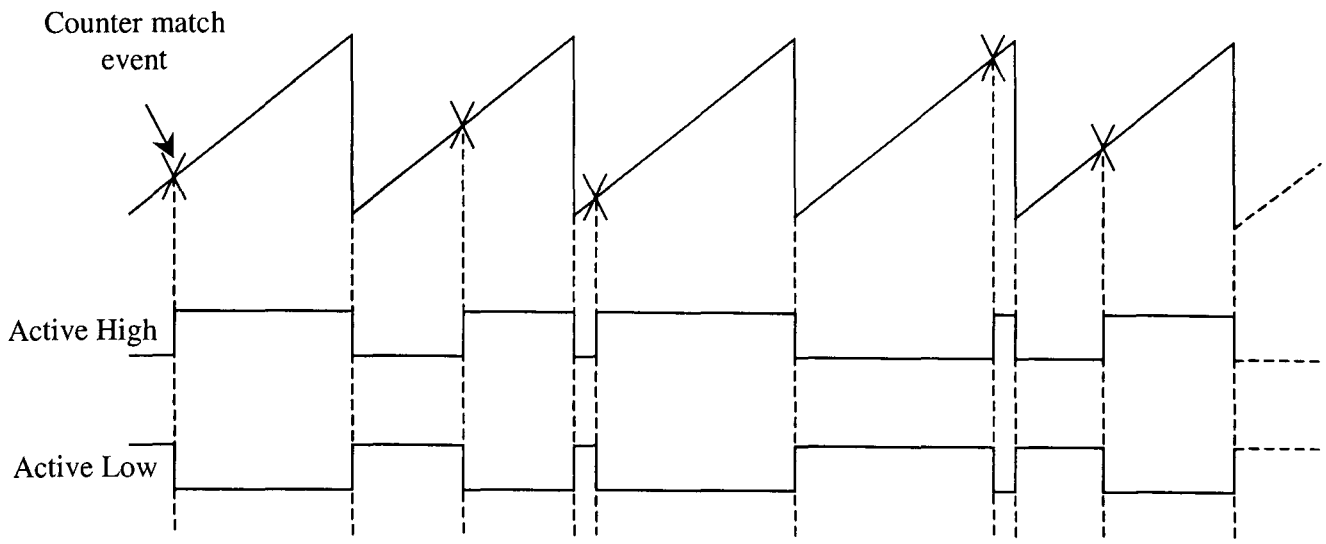

Fig. 2.19 *PWM generation,* [TEX97]

On start up of the software, the initialisation routine ensures that the control variables are loaded into the appropriate registers, and that the timers and other necessary peripherals are configured. At the end of the initialisation routine, a fixed low value duty cycle is output to the gate drives to excite the machine phases sequentially using a time delay, such that open loop commutation is used to crank the machine, i.e. operating as a stepper motor. Once the index pulse of the incremental encoder is detected, the main software loop is entered and closed-loop operation is commenced, **Fig. 2.20**.

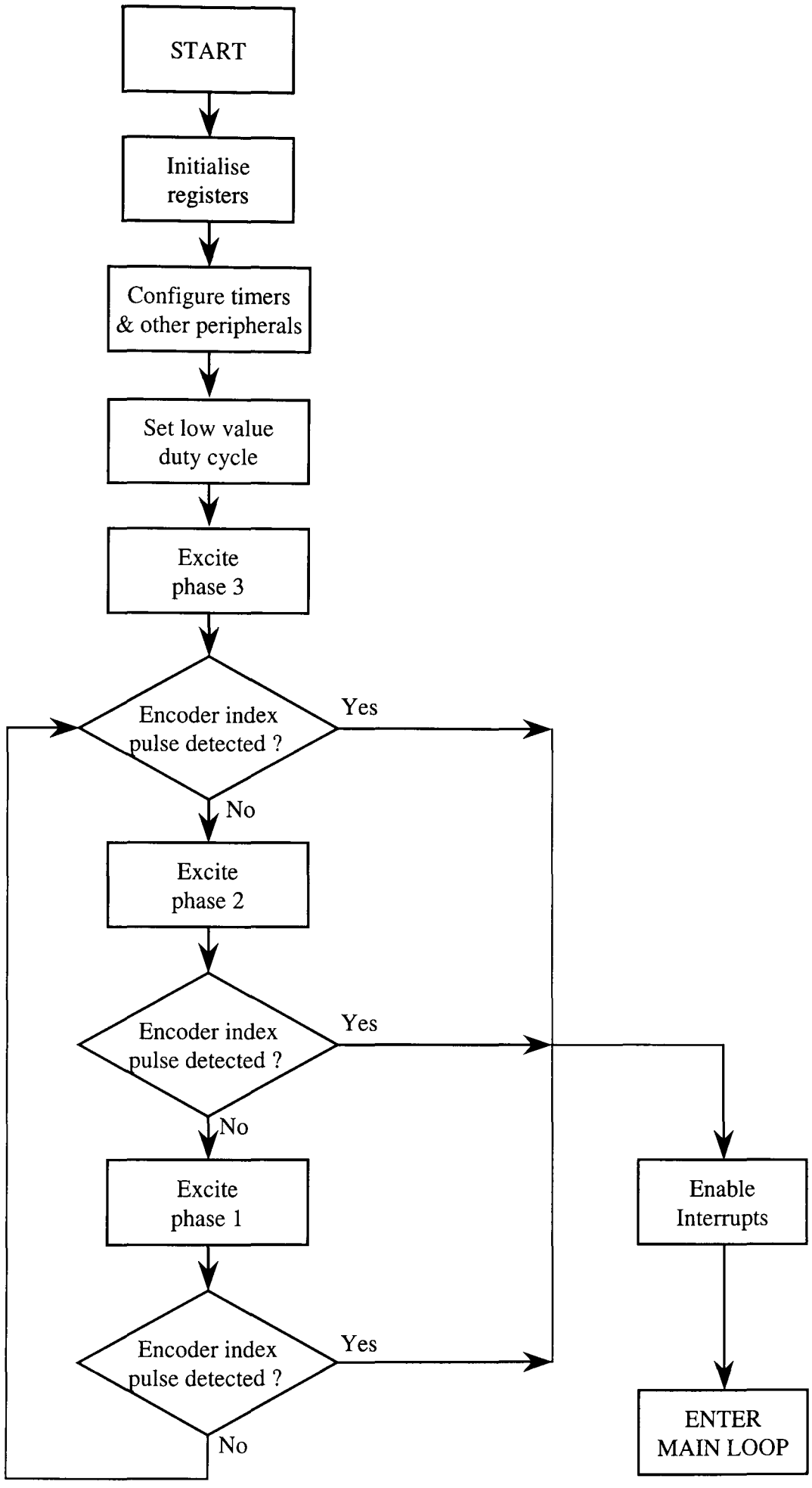

Fig. 2.20 *Flow chart of initialisation routine*

2.3.2.1 Commutation ISR

In order to commutate SR machines, the position of the rotor pole-pairs relative to each stator phase is required, whether it is derived from a slotted disc, a resolver, an absolute or incremental encoder, or even some from of sensorless technique. An incremental encoder with an output of 2048 pulses per revolution was employed for the experimental drive system, owing to the fact that the DSP development kit provides the necessary interfacing hardware. The encoder produces 2048 pulses per revolution for lines A and B, whose respective pulses are phase shifted by 90 degrees and similarly for their complementary lines A' and B'. The encoder also provides an index pulse, Z, and a complementary index pulse, Z', once every revolution to provide a means of determining the position of the rotor, see section 2.3.2.2. The A and B signals interface to the DSP via a quadrature encoder pulse circuit, (QEP) that is configured as the input for one of the three available timers of the processor to produce a counter which counts upwards or downwards relative to the direction of rotation of the shaft. The commutation of phases is provided by an interrupt service routine, which is executed when the encoder count matches the value stored in the compare register, which is updated each time the ISR is entered to ensure the phases are switched in the desired switching sequence. The ISR, therefore, configures the appropriate bits of the PWM control register to set the state of the power switching devices for each phase as required, i.e. active high, forced high, or forced low. Further, for the voltage control scheme, the duty cycle of the PWM is updated in this ISR, and the ADC channels are set for the appropriate phase for the current controller.

In order to investigate the influence of the switching angles on the noise and vibration some means was required for varying the turn-on and dwell angles. However, since these were to be assessed purely for noise purposes and not for specific torque speed profiling of the machine, only a simple implementation method was required. Thus, a single set of switching angles was chosen prior to code execution, and once the machine had been running for a pre-determined time duration these angles come into effect. The switching signals for the 3-phases are shown in **Fig. 2.21** where Z=1 represents the respective position of the index pulse and Z_{off} the offset value between the index pulse to the first switching event. The variable τ represents the duration between consecutive turn-on and turn-off angles of successive phases, the value of which remains fixed and is equal to the maximum dwell period without phase overlap. In addition, the variable θ represents the angle over which no phase overlap exists.

Thus, to achieve commutation advance, whilst maintaining a fixed dwell period, Z_{off} is reduced, whereas for the extension of the dwell period, the variable α_a is introduced. This enables the commutation ISR to determine whether the previous phase is to remain on whilst the subsequent phase is switched on. The operation of the commutation ISR is summarised in the flow chart of **Fig. 2.22**.

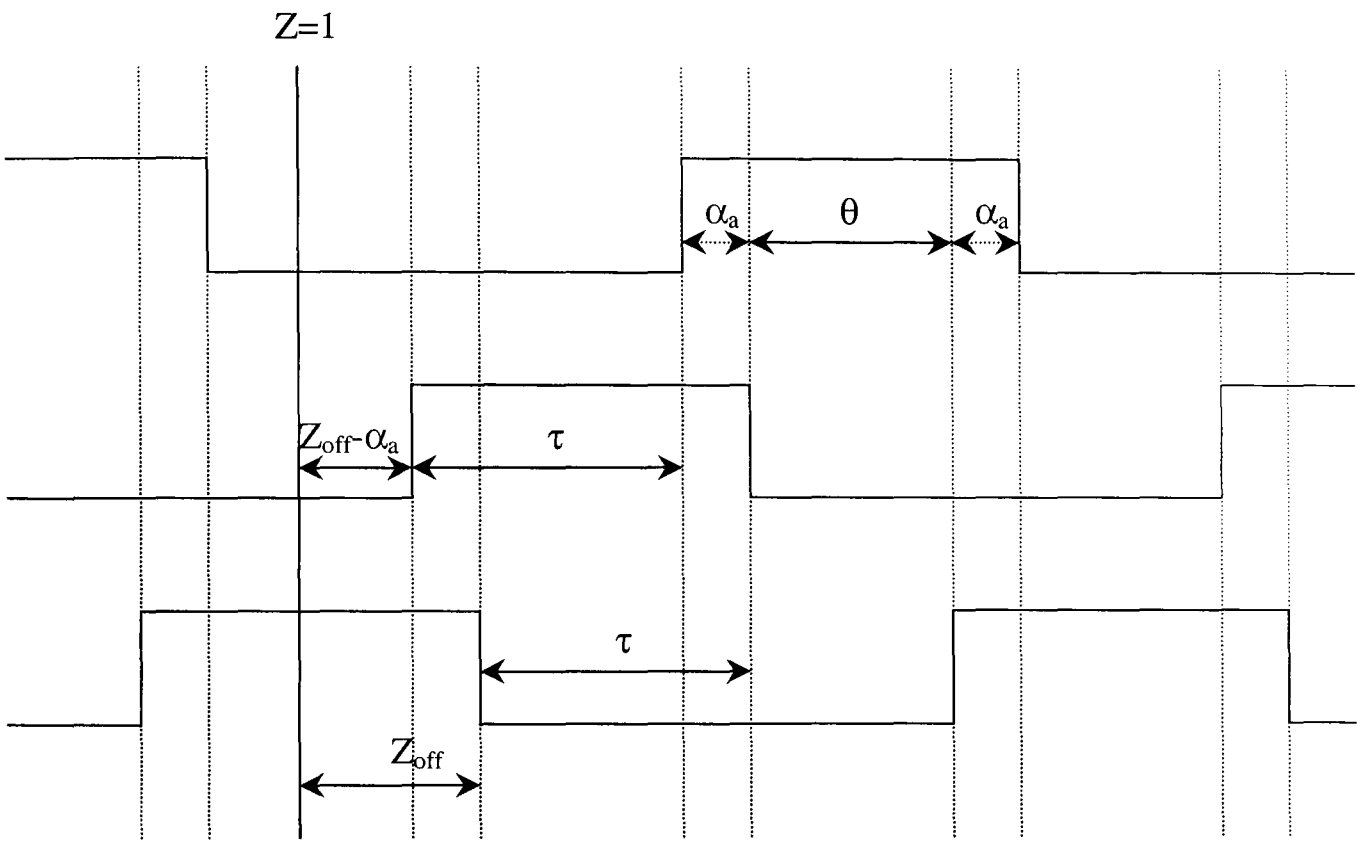

Fig. 2.21 *Gate signals with the existence of phase overlap*

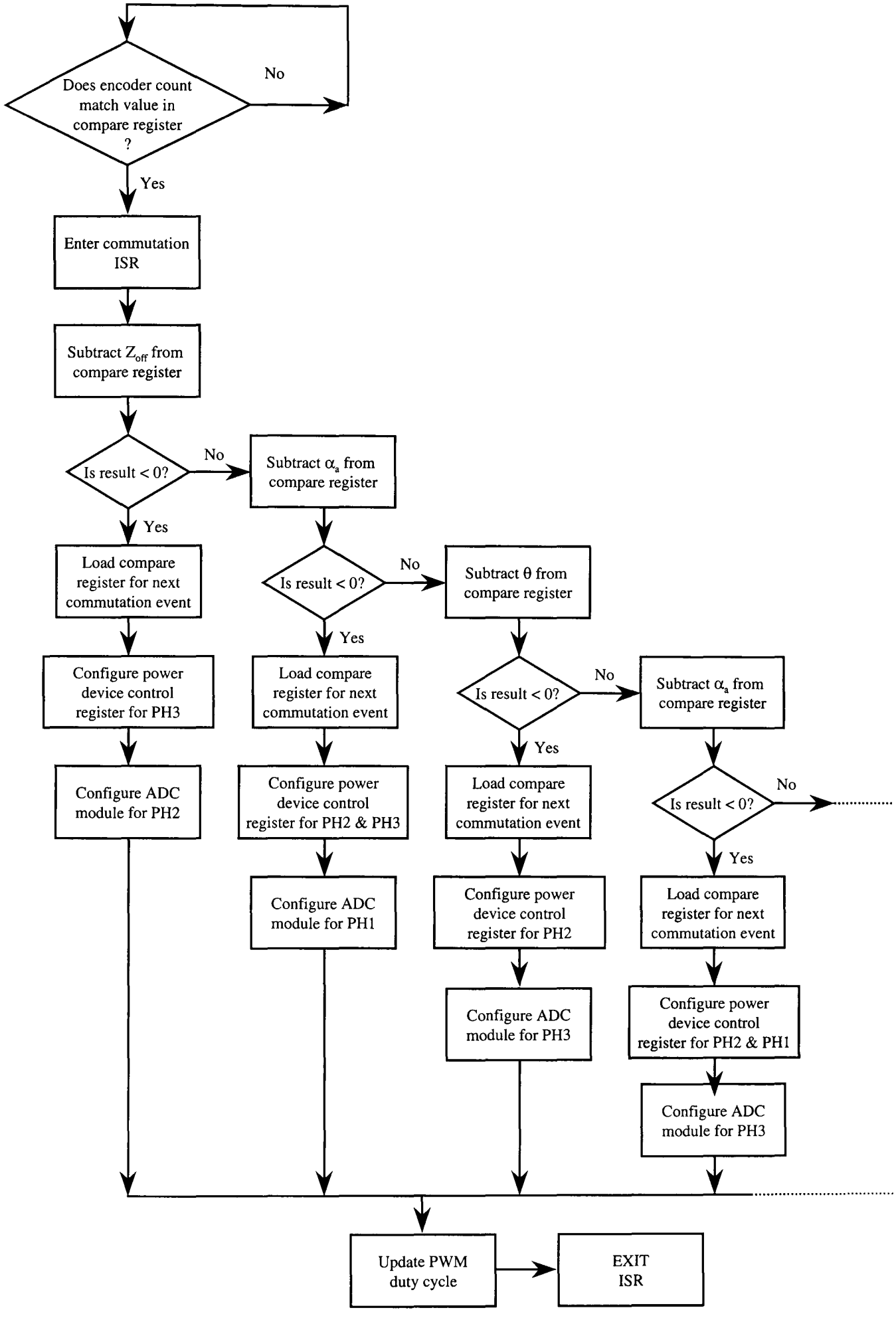

Fig. 2.22 *Flow chart for commutation control algorithm*

2.3.2.2 Encoder reset ISR

The encoder shaft was attached to the rotor of the SR machine at an angular position such that the index pulse corresponded to the alignment of a pair of rotor poles with the stator poles of phase A. Thus, the rotor was rotated, by hand, until the index pulse was captured on an oscilloscope. The counter, which is interfaced for counting the encoder pulses, was then activated in the DSP system and phase A of the machine was excited to bring the rotor poles into alignment with phase A. The angular position swept by the rotor from the position of the index pulse to the aligned position was given by the DSP encoder counter, thereby providing the necessary offset count for calibrating the position of the rotor with respect to the stator. The index pulse is, therefore, a reference point for the rotor and is interfaced to the DSP, during machine operation, via one of the edge triggered capture units, such that on the rising edge of the index pulse the capture unit interrupt flag is raised. This triggers the encoder reset ISR, which is used to reset the counter, produced by the encoder, to zero, **Fig. 2.23**, thus maintaining the position counter within the range required for the commutation ISR.

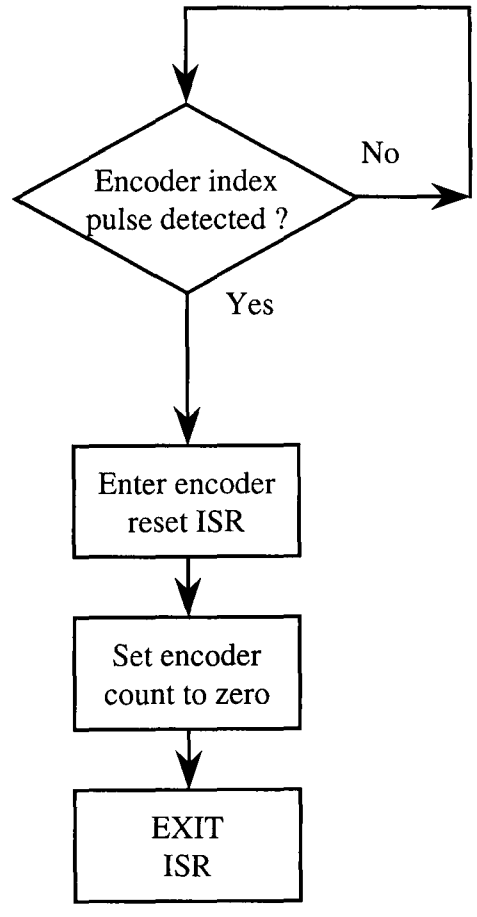

Fig. 2.23 *Flow chart of encoder count reset algorithm*

2.3.2.3 Current controller ISR

The interrupt for initialising the current regulator is based on the same timer as that which is employed for the speed ISR. However, the speed ISR is initiated when the timer reaches zero, and, therefore, only occurs once within the timer period, whereas the current regulator occurs more frequently. Thus, the current regulator ISR is initiated by the counter match between the timer counter and its compare register. Therefore, the sampling period of the current ISR is defined by the frequency of the timer and the value loaded into the compare register on subsequent executions of the ISR. For example, if the desired sampling frequency is 40kHz, then, given the timer clock is operating at a frequency of 20MHz, the value in the compare register is increased by 1f4h on each ISR execution, thus imposing 1f4h (500d) clock counts between successive current regulation ISR's.

The ADC module is configured such that the sample and conversion process of the ADC's is initiated by the timer interrupt that executes the current regulation ISR. It is for this reason that the speed demand is also established within the current regulation ISR, since this is the only other input to the system requiring the use of the ADC module. The ADC Module available on the F240 board comprises of two 10-bit ADC's, with two built in sample-and-hold circuits, and requires a minimum conversion time of 6.6μs. Eight channels are provided for each module via an eight-to-one analogue multiplexer. Therefore, it is capable of performing two simultaneous conversions. The DSP module can only receive input voltages having values between 0 to 5V. Therefore, the speed demand signal, which is derived from a potentiometer connected to a 5V dc power supply, is designed to demand up to 100% PWM duty cycle for a maximum input voltage of 5V. Similarly, for the feedback of the phase currents, the use of an appropriately sized sense resistor on the output of the current transducer, R_M, **Fig. 2.12** section 2.2, enables the phase current to be scaled to a voltage signal varying between 0-4V that is interfaced to the DSP via three ADC channels, thus providing independent current control for each of the inverter phases. Once the current feedback is established, this is compared to the current reference, which is derived using the speed error from the speed control ISR, and the power switching devices are turned on or off as required. The control loop, with feedback for one of the three phases is shown in **Fig. 2.24**, where i^*, i_e and i_{fbk} are the demand current, the current error and the feedback current, respectively. The execution of the current ISR is represented in **Fig. 2.25**.

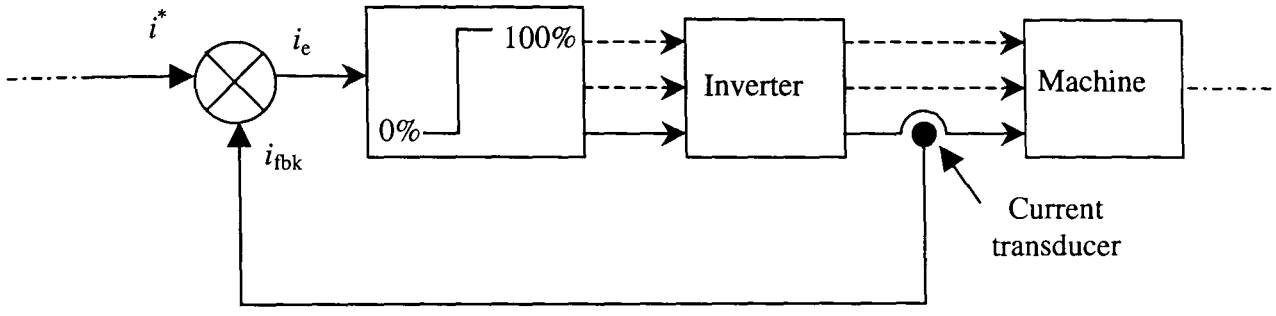

Fig. 2.24 *Current feedback shown for a single phase*

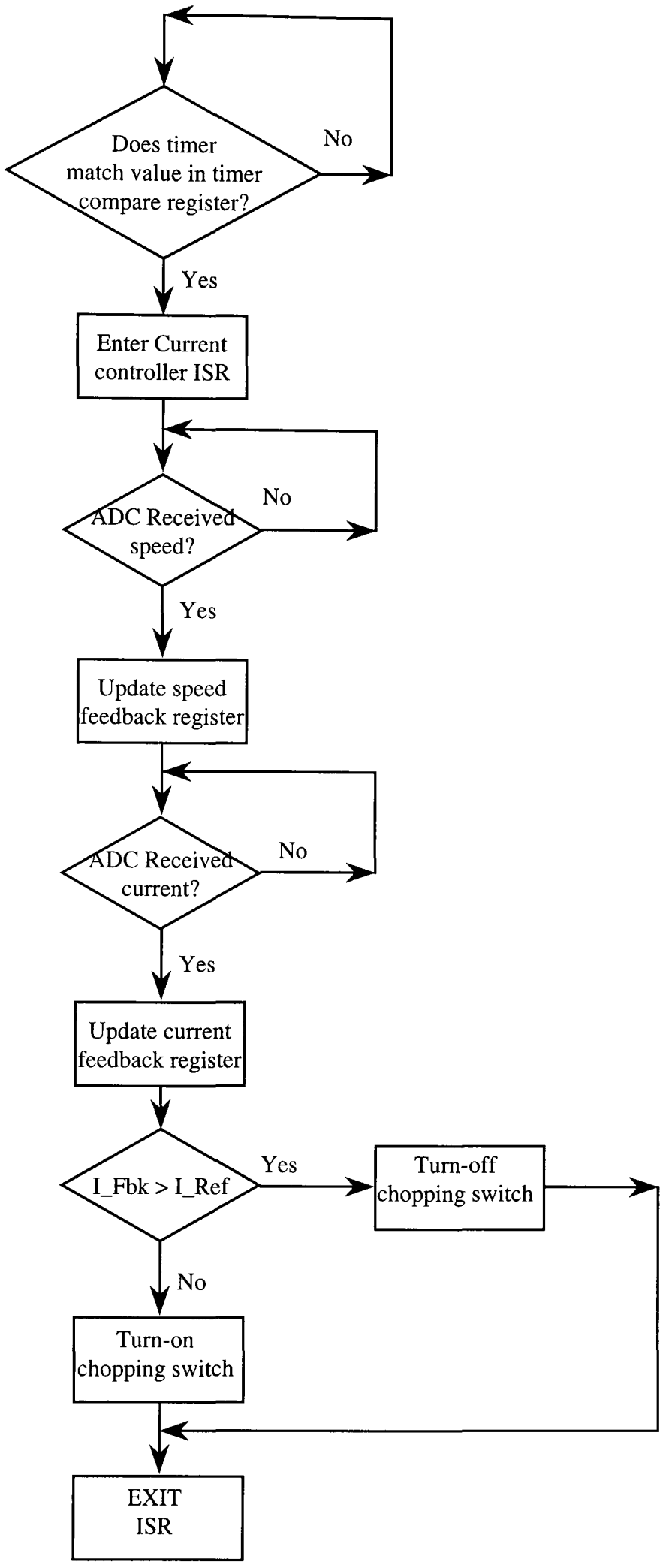

Fig. 2.25 *Flow chart of current control algorithm*

2.3.2.4 Speed control ISR

With a digital velocity loop via digital position feedback, using a sensor such as the encoder which is employed on the experimental drive, it is possible to obtain a velocity measurement by two methods. One involves counting encoder pulses within the period of the sample interrupt clock, whilst the other involves counting timer clock pulses within the period of subsequent encoder pulses. The former method is more appropriate for higher speed operation, due to the larger number of encoder pulses which occur within the sample period, thus increasing the resolution of the velocity calculation. Conversely, the latter method is better suited for low speeds, when the time duration between encoder pulses is longer. The investigations which are reported in the thesis involve the machine operating in a speed range of 500-3500rpm, which is a relatively low. Therefore, the method which involves counting the number of timer clock cycles between subsequent encoder pulses was employed. The speed calculation based on this method is defined by equation (2.2), where *N(K)* and *N(K-1)* represent the current and previous timer counts, respectively, $\Delta\theta$ represents the shaft rotation angle between two subsequent encoder pulses, T_{CLK} the period of the timer clock and ω_r is the shaft frequency, Hz

$$\omega_r = \frac{\Delta\theta}{(N(K) - N(K-1))T_{CLK}} = \frac{\Delta\theta}{\Delta N(K) T_{CLK}} \tag{2.2}$$

This is achieved within the software by interfacing the A' line of the encoder to one of the four available capture units of the DSP system. The capture unit employs one of the three timers as its time-base, and is configured to store the value of the timer, on the rising edge of the encoder pulses, in the 2-level deep first-in-first-out (FIFO) stack associated with the capture unit. The software algorithm implements equation (2.2) by first calculating *ΔN(K)*, simply by subtracting the previous timer count from the subsequent timer count. Before continuing, it must be noted that the ADC modules are 10-bit, and, therefore, for a speed demand of 5V, a full 10-bit number is obtained. Thus, the speed feedback is limited to 10-bits.

The speed control ISR determines the speed feedback, and consequently calculates the speed error utilising the speed demand from the current control ISR. This speed error provides the current reference for the machine when operating under current control, or

is used to derive the PWM duty cycle, using an appropriate gain, for the direct voltage control of the machine. The operation of this ISR is summarised in **Fig. 2.26**.

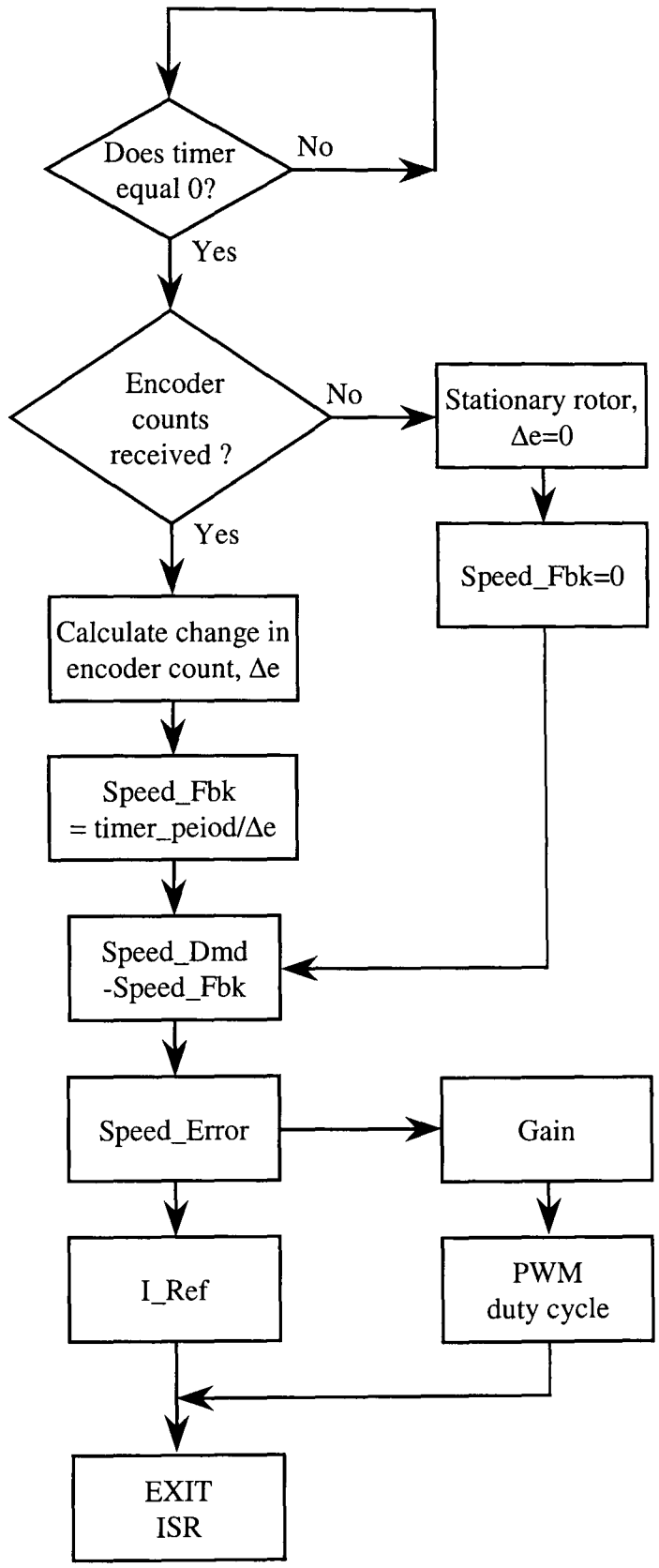

Fig. 2.26 *Flow chart of speed control algorithm*

2.4 Experimental rig

The experimental machine was rigidly mounted in an anechoic chamber, and was mechanically coupled to the load machine, whose specification is outlined in **Table 2.4**, which was mounted in a room adjacent to the anechoic chamber via two flexible couplings and two bearing sets, **Fig. 2.27(a) & (b)**. Clearly the complete system contains a number of bearing sets, so that the experimental machine is constantly under load, due to the frictional torque, which is a constant and not dependent on speed, and the windage loss, which is proportional to speed squared.

Table 2.4 *Specification of wound-field dc load machine*

Power	0.25kW
Speed	3000rpm
Field / Armature current	0.2A / 1.6A
Field / Armature voltage	210V / 180V

The stator of the wound-field dc machine is supported by gimbal bearings affixed to the supporting structure. A torque arm is attached to the swinging stator frame. It extends to a calibrated load cell, which enables the torque to be measured. It should be noted, however, that when the SR machine is loaded by the wound-field dc machine, the load cell measures all the losses within the wound-field machine as well as the electromagnetic torque which it imposes on the shaft of the SR machine. Thus, the torque measured does not account for other losses in the system, such as those associated with the support bearings.

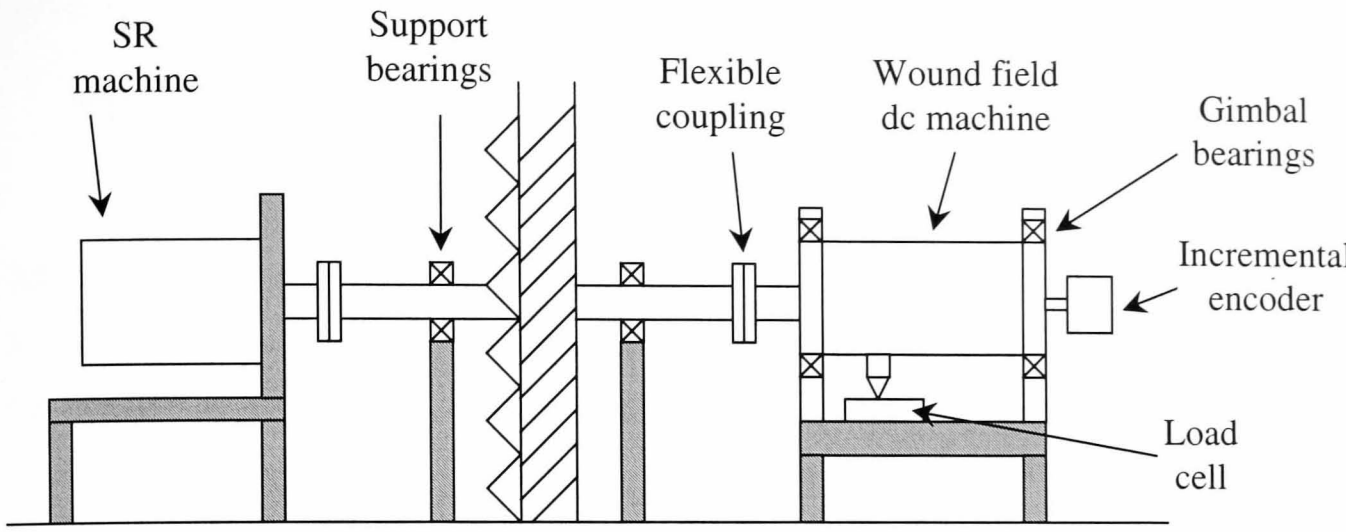

(a)

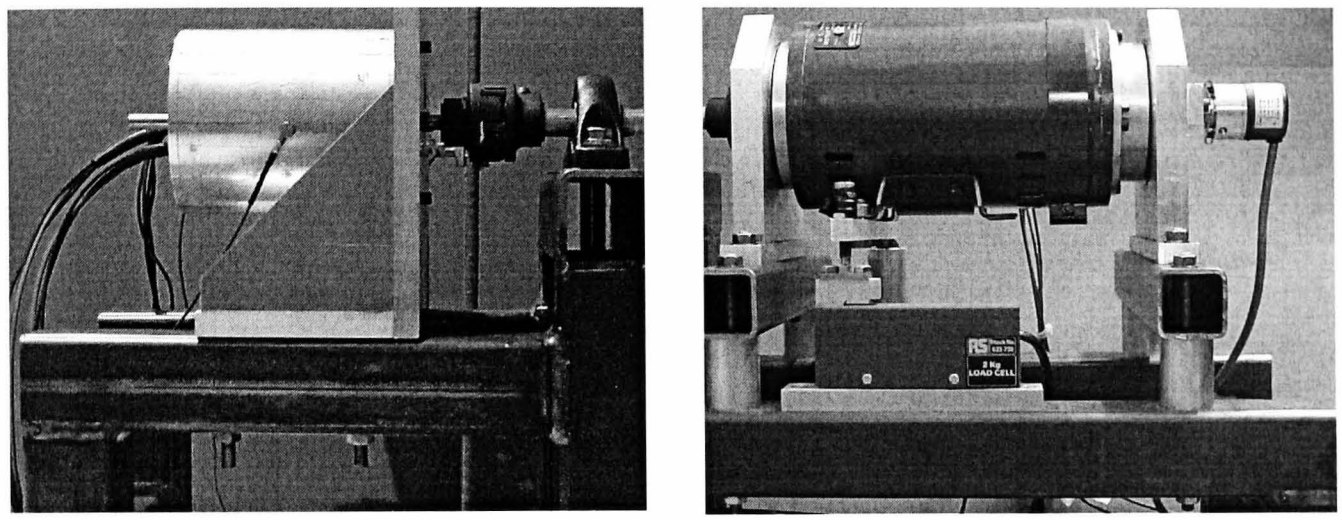

(b)

Fig. 2.27 *Experimental test rig,* **(a)** *schematic,* **(b)** *photograph*

Chapter 3
Vibrational Behaviour of Switched Reluctance Machines

3.1 Introduction

In order to design low noise SR machines it is important to accurately predict the natural frequencies of the stator in order to prevent mechanical resonances, and, hence, large vibrations and acoustic noise emissions. Information on vibrational modes and natural frequencies is essential for improving the mechanical design, and can be used in drive systems that employ some form of vibration cancellation technique, as will be described in Chapter 5. Thus, modal analysis is used to determine the natural frequencies of the experimental switched reluctance machine and the influence of its leading design parameters. The concept of modal analysis is introduced, with the objective of showing that the finite element technique is a viable method for predicting the natural frequencies of the stator of the experimental machine.

This chapter focuses on the vibrational characteristics of the stator of the experimental machine outlined in Chapter 2, with regard to the mode shapes and their associated natural frequencies. This is achieved through 2D and 3D finite element analyses, using the commercial finite element package ANSYS©, and impulse force tests for experimental validation. Firstly, a convergence study is undertaken to establish the mesh density and the appropriate element type to be employed in the finite element modelling, and its compatibility with the available computer processing capability. The chosen mesh and element type are validated against the natural frequencies established in earlier investigations and analytical equations, [YAN78, ZHU87]. Subsequently, the influence of the leading stator design parameters on the natural frequencies is investigated, the predictions being validated against measurements on various experimental models by performing impulse tests. Such design parameters include the stator yoke thickness, the pole width and the fillet radius between the pole root and the stator yoke. The findings are compared with those from earlier numerical analyses [HAR56, YAN78], and a number of interesting issues are highlighted. Furthermore, 3D modelling enables the influence of the nature of the laminated stator core and the stator windings on the natural frequencies to be established and the mass-stiffness effects of the winding to be investigated. Finally, the investigation accounts for the influence of the frame. The problems encountered highlight the limitations of finite element analyses for such highly

complex mechanical systems. The impulse tests which were undertaken in support of the investigations which are described in this chapter are summarised in **Table 3.1**. It should be noted that since the identification of damping is not within the aims of this thesis, and due to the large number of structures under investigation, frequency response functions were not utilised, i.e. all vibration spectra obtained with impulse force tests within this thesis do not account for the applied impulse force.

Table 3.1 *Summary of impulse tests*

	Combination of system components during each test																
Test no. / System components	1	2	3	4	5	6	7	8	9	10	11	12	13	14	15	16	17
Annular ring	√																
Annular ring with single notch		√															
Annular ring with 3 notches			√														
Annular ring with single pole				√													
Annular ring with 6 poles					√												
Full 6-pole stator						√			√					√	√	√	
Annular ring with 8 poles							√										
Full 8-pole stator								√									
Winding									√					√	√	√	
Frame										√	√	√	√	√	√	√	
End-caps											√	√	√		√	√	
Bearings												√	√			√	
Rotor													√			√	
Assembled machine																	√

3.2 Modal analysis

Modal analysis is a technique for determining the vibrational characteristics, (i.e. the natural frequencies and their associated mode shapes), of a structure, and is important for the initial design since it provides information necessary to eliminate and/or avoid possible causes of vibration.

3.2.1 Convergence study

Throughout all the investigations and analyses which are reported in this thesis, the parameter *n* represents purely circumferential modes of vibration in which the cross-section of the machine remains constant throughout its axial length, whilst the parameter *m* represents axial vibration modes, as illustrated in **Fig. 3.1**.

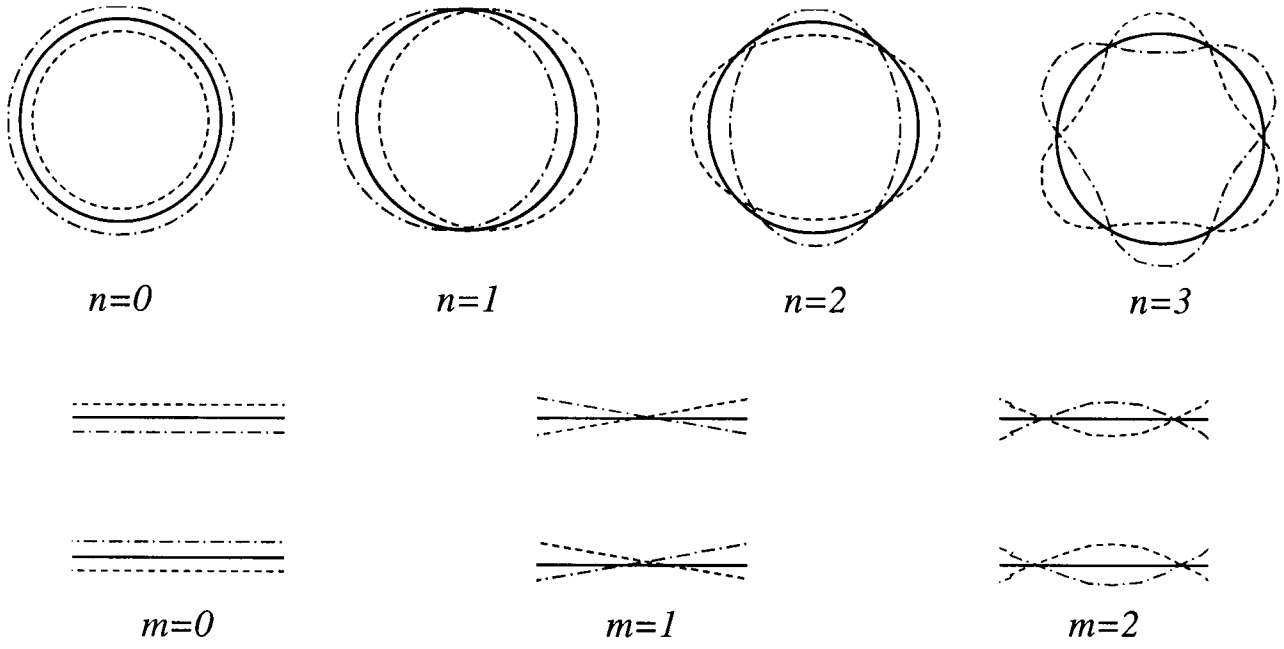

Fig. 3.1 *Definition of circumferential and axial vibration modes*

To ensure that the natural frequencies which are predicted by the ANSYS© package are accurate, whilst at the same time maintaining a reasonable computational time, an appropriate mesh density was established by undertaking a systematic finite element analysis of an annular ring, supported by measurements. The matrix equations which are generated by ANSYS© for a given FE model is based on the 'Wavefront Size', and the RMS Wavefront directly affects the solution time, [ANS99]. It, therefore, enables a comparison to be made between the relative computational times for different mesh densities. Further, whilst it is possible to reduce the size of the FE model, and hence the wavefront size, by modelling only a segment of the structure for cyclic analysis, when applied to modal analysis this limits the order of modes that can be calculated and, therefore may be unappropriate for the detailed investigations which are to be undertaken.

The convergence study is based upon a solid mild steel annular ring, whose leading dimensions are the same as those of the stator back-iron of the experimental machine - as listed in **Table 3.2**. An annular ring was machined from solid mild steel, and its natural frequencies were measured by application of impact force tests, the results being shown in **Fig. 3.2**. The frequency spectra in **Fig 3.2(a)** corresponds to a radial impact at an axially central location. To clarify modes of axial type 1, the ring was also excited radially at one axial end, the corresponding frequency spectra being given in **Fig. 3.2(b)**. The natural frequencies and associated mode shapes are summarised in **Table 3.3**. It is to these natural frequencies that the finite element predictions converged as the density of the finite element mesh was increased.

The FE model of the ring was assigned the properties of solid mild steel as given in **Table 3.2**. A segment of the modelled ring, which illustrates the disposition of the elements for the various mesh densities together with the total number of elements, is shown in **Fig. 3.3**.

Table 3.2 *Properties of Annular Ring*

Property	**Value**	**Unit**
Stator outside diameter, *OD*	93.8	mm
Stator inside diameter, *ID*	77.6	mm
Young's Modulus, *E*	210	GPa
Density, ρ	7800	kgm^{-3}
Poisson's ratio, ν	0.28	

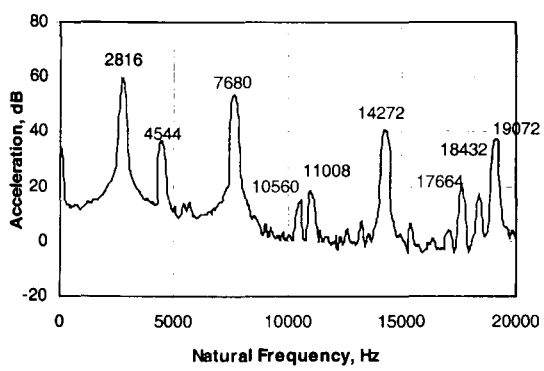

(a)

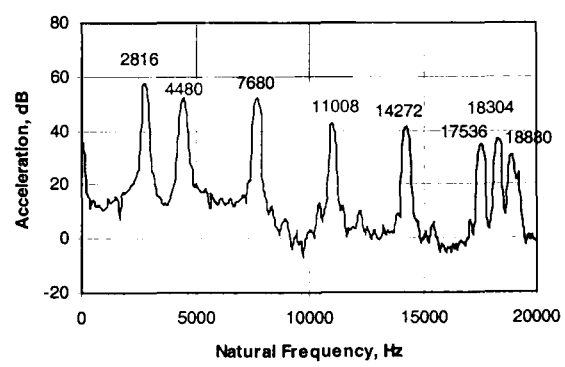

(b)

400 line spectrum analyser, gives:

20kHz/400

=50Hz/line

(Refer to Appendix G)

Fig. 3.2 *Natural frequencies of solid mild steel annular ring;* **(a)** *hit radiallly at an axially central location,* **(b)** *hit radially and one axial end*

Table 3.3 *Summary of measured natural frequencies (Hz) for experimental annular ring*

Circumferential mode, *n*	Axial mode, *m=0*	Axial mode, *m=1*
0	19072	
1		$17536^{\pm 50}$
2	$2816^{\pm 50}$	$4480^{\pm 50}$
3	$7680^{\pm 50}$	$11008^{\pm 50}$
4	$14272^{\pm 50}$	$18304^{\pm 50}$

A number of structural 2D, and 3D, finite element types are available for discretising a finite element model. To ensure consistency of subsequent analyses, it was considered essential that an appropriate element-type be chosen for the 2D and 3D analyses. The element types which are available in ANSYS© are identified by specific numbers, owing to the fact that there are a large number of element types for different engineering problems, (i.e. thermal, structural, electromagnetic, etc). Those available for 2D structural modelling are element types 42 and 82, which are 4-noded and 8-noded elements, respectively, as shown in **Fig. 3.4(a) & (b)**. Element types 45, 73 and 95 are available for 3D structural analyses, element type 45 comprising of 4-nodes and element type 95 having 20 nodes, as illustrated in **Figs. 3.4(c) & (d)**. However, element type 73 is also an 8-noded element that has rotation associated with it. It, therefore, has more nodal freedom than the other element types since it not only enables displacements in the x, y and z directions, but also displacements in θ_x, θ_y, and θ_z. Each black dot in **Fig. 3.4** represents a node which is common to adjacent elements in the finite element model. The higher order elements have larger stress and strain matrices associated with them, since they contain more gauss points and hence require more calculations. As a result, whilst they are more accurate, and necessitate fewer elements in the finite element model, due to the larger matrices, they generally require a longer solution time for the assembled system equations.

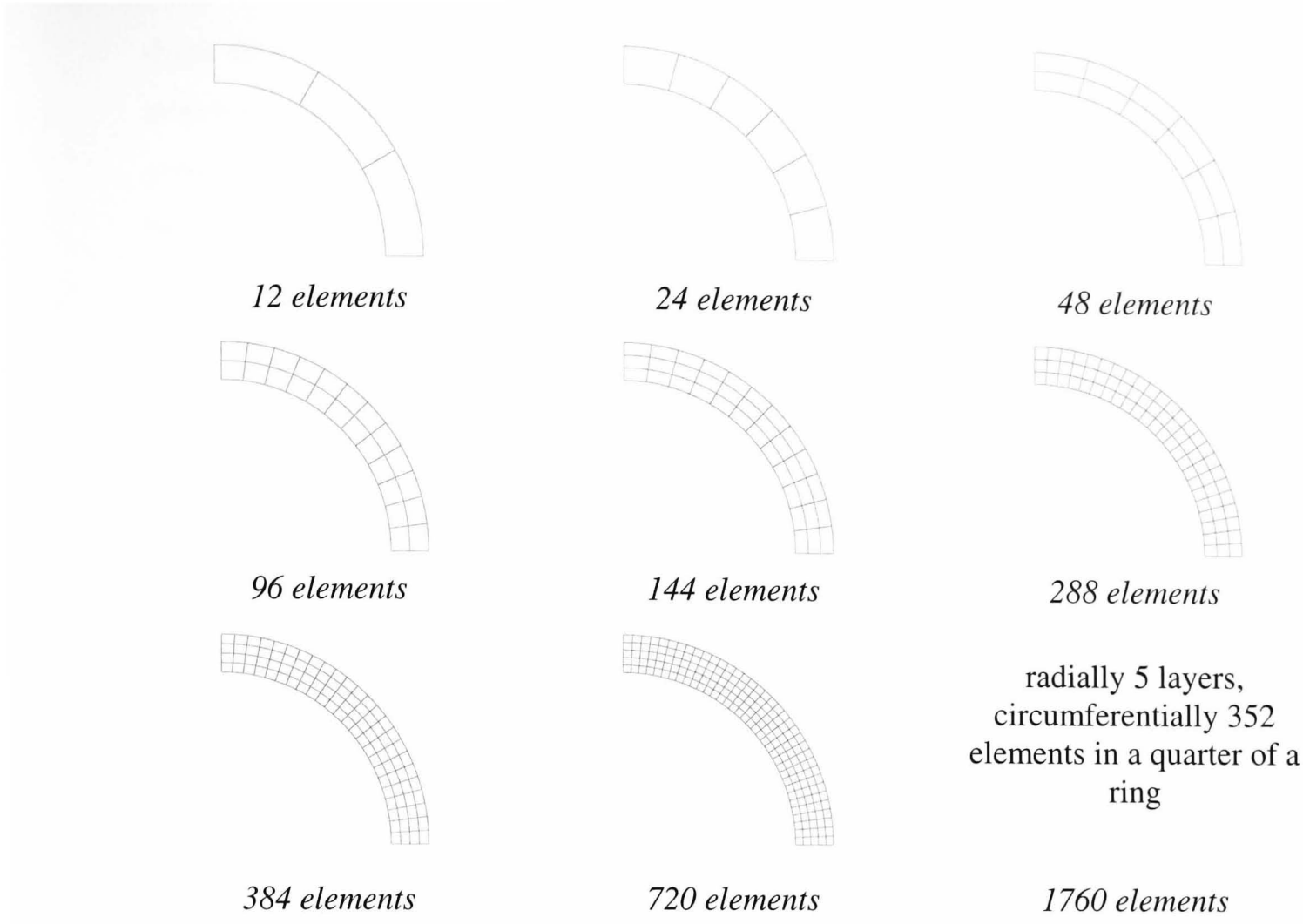

Fig. 3.3 *Mesh discretisation employed for 2D FE model of annular ring*

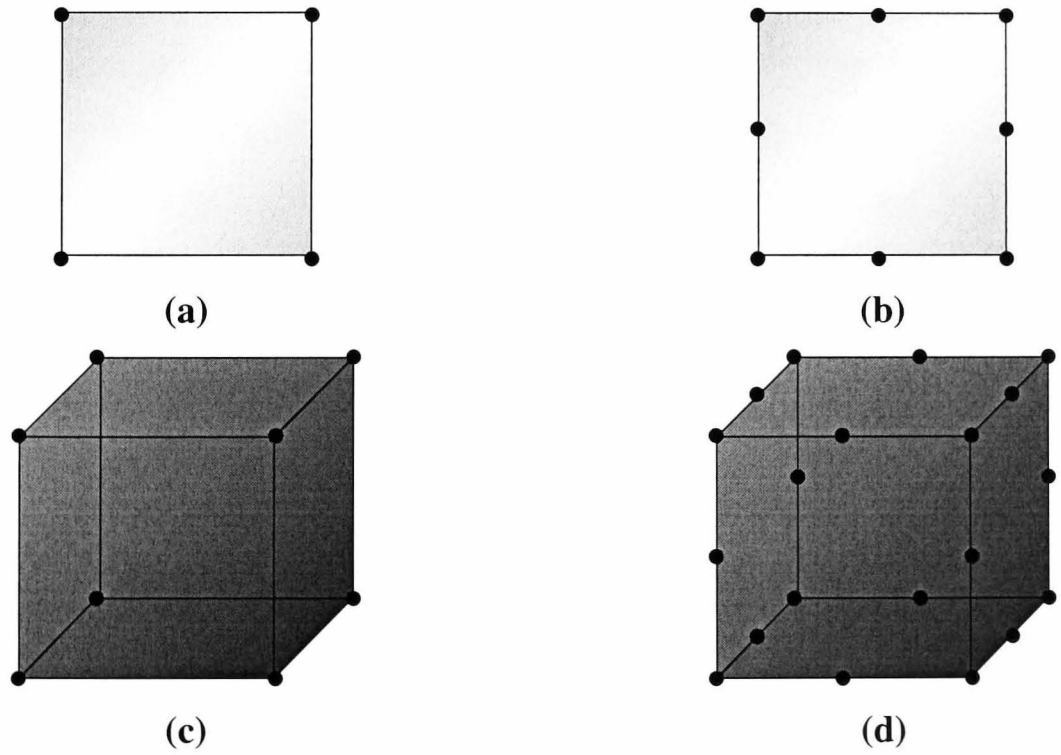

Fig. 3.4 *Element types;* **(a)** *2D 4-node,* **(b)** *2D 8-node,* **(c)** *3D 8-node,* **(d)** *3D 20-node*

Convergence of the natural frequencies for the different vibrational modes, as the number of elements is increased, is shown in **Fig. 3.5** for the 2D and 3D analyses. Since the range of frequencies for the modes considered is quite large, for convenience the predicted natural frequencies have been normalised to those deduced from the impact force tests, i.e. the normalised value is the ratio of the natural frequency of a given mode

shape as predicted by FEA to the measured natural frequency of that mode shape, the measured values being summarised in **Table 3.3**. For the 3D analyses, the results for axial modes types 0 and 1 are presented on separate graphs and all the natural frequencies as predicted by the FE convergence study are summarised in Appendix B. For the 2D analyses, **Figs. 3.5i(a) & 3.5i(b)** shows that significantly fewer 8-noded elements are required for convergence than is required with 4-noded elements. The number of elements employed for the 2D analyses is summarised in **Table 3.4**, together with the RMS error of the relevant modes and the normalised values of the squared wavefront. The RMS error is essentially the accumulative normalised value of the predicted natural frequencies of all modes, i.e. modes 0, 2, 3 and 4, to all the measured modes, i.e. modes 0, 2, 3 and 4. The spread of the RMS error is much smaller for the 8-noded element, element type 82, than for the 4-noded element, element type 42, as expected. Although the wavefront sizes for element type 82 are typically between 50% to 125% of those for element type 42, the values are extremely low, and the difference in the solution times is negligible.

For the 3D analyses, it will be observed that the convergence with element type 73 and element type 93, **Figs. 3.5iii & 3.5iv**, has a lower spread of values predicted for each of the vibrational modes compared to that with element type 45, **Fig. 3.5ii**. The RMS error, **Table 3.5**, for element type 45 with the highest meshing density is 1.028, whereas element type 95 yields 1.029 with the most coarse meshing density, which reflects the higher order of this element type. Their normalised squared wavefronts are 35.73 and 16.0 for element types 45 and 95, respectively, thus element type 95 is the most appropriate. Furthermore, element type 73 results in an RMS error of 1.028 with a normalised squared wavefront of 16.00. With the relation between element types, meshing density and wavefront values, it is clear that although element type 95 converges well with a coarse mesh, for more complex models in which certain areas of the geometry may require a finer discretisation, the solution time may be increased further and, therefore this element type was not appropriate for subsequent analyses. The finite element mesh shown in **Fig. 3.6** is an example of the need for a locally refined mesh density when the geometry of the model is more complex.

Hence, the 8-noded structural element, element type 82, was employed for subsequent 2D analyses, whilst element type 73 was employed for the 3D analyses.

Table 3.4 *2D analyses*

Number of elements	Element Type 42		Element Type 82	
	RMS error	Normalised Wavefront^2	RMS error	Normalised Wavefront^2
12	1.588	1.00	1.089	1.51
24	1.073	1.00	1.020	1.51
48	1.073	1.19	1.002	1.99
96	1.018	1.19	1.000	1.99
144	1.016	1.40	0.997	2.53
288	1.003	1.40	0.997	2.53
384	1.002	1.62	0.997	3.14
720	1.000	1.86	0.997	3.82

Table 3.5 *3D analyses*

Element size	Number of elements	Element Type 45		Element Type 73		Element type 95	
		RMS error	Normalised wavefront^2	RMS error	Normalised wavefront^2	RMS error	Normalised wavefront^2
0.02	72	1.117	4.37	1.048	8.46	1.029	16.00
0.015	96	1.116	5.59	1.048	11.93	1.029	21.92
0.01	180	1.058	6.95	1.028	16.00	1.021	28.77
0.009	216	1.057	8.46	1.028	20.66	1.020	36.55
0.008	576	1.042	15.46	1.020	43.44	1.013	80.59
0.007	672	1.042	18.84	1.020	54.89	1.013	101.37
0.006	960	1.033	22.56	1.016	67.69	1.012	124.53
0.005	1200	1.033	31.00	1.016	97.29	1.012	177.98
0.0045	1584	1.028	35.73	1.014	113.62	1.012	208.28

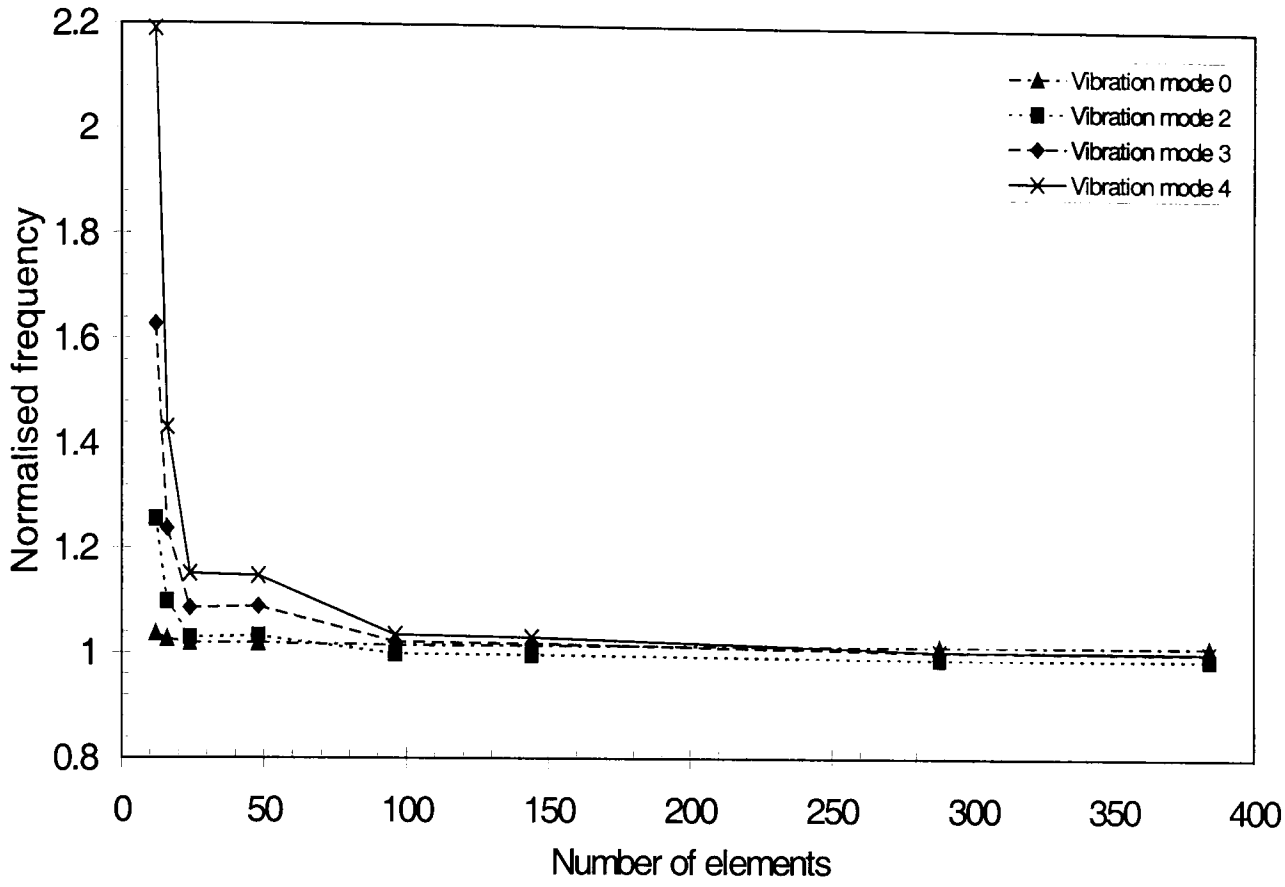

(a)

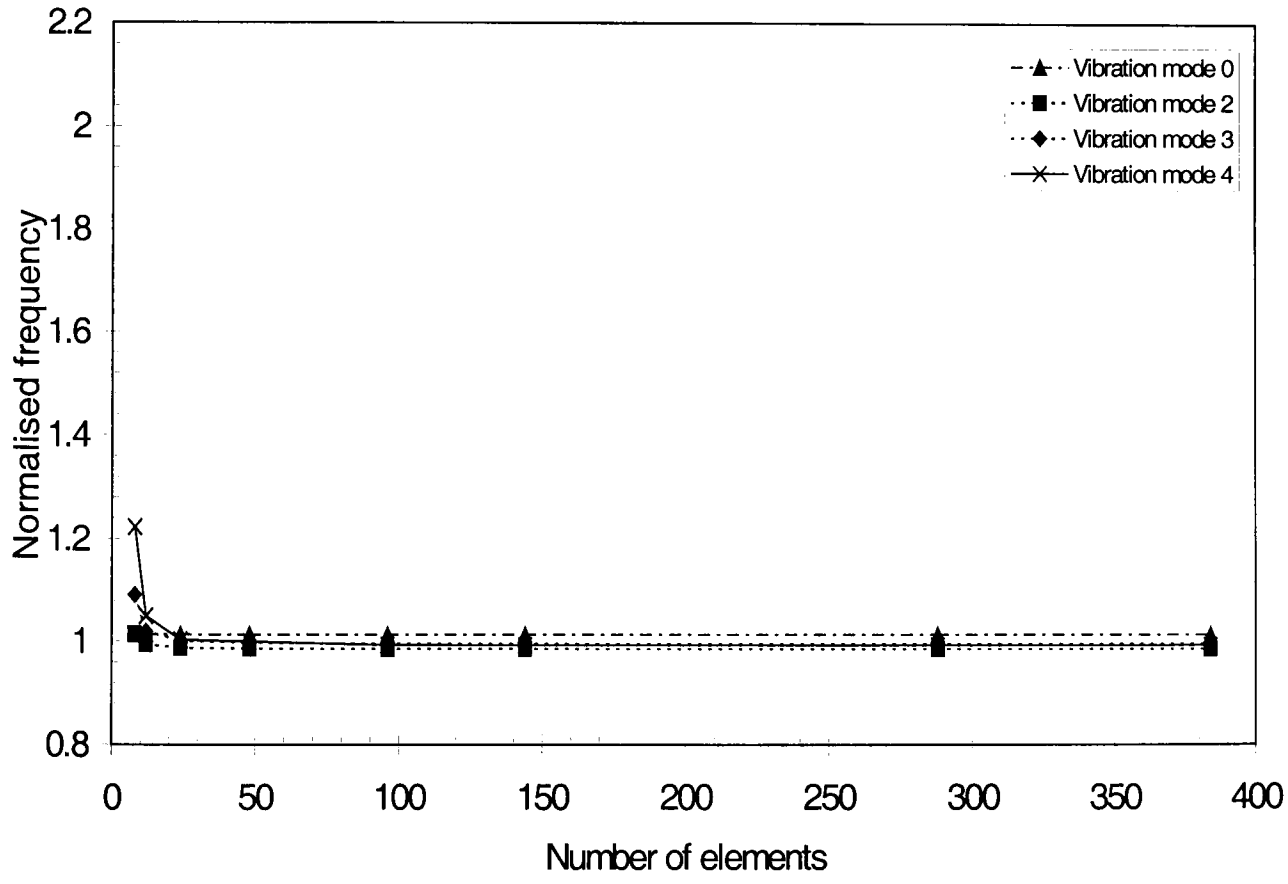

(b)

Fig. 3.5i *Convergence of vibration modes predicted by 2D finite element analyses;* **(a)** *element type 42 (4-noded),* **(b)** *element type 82 (8-noded)*

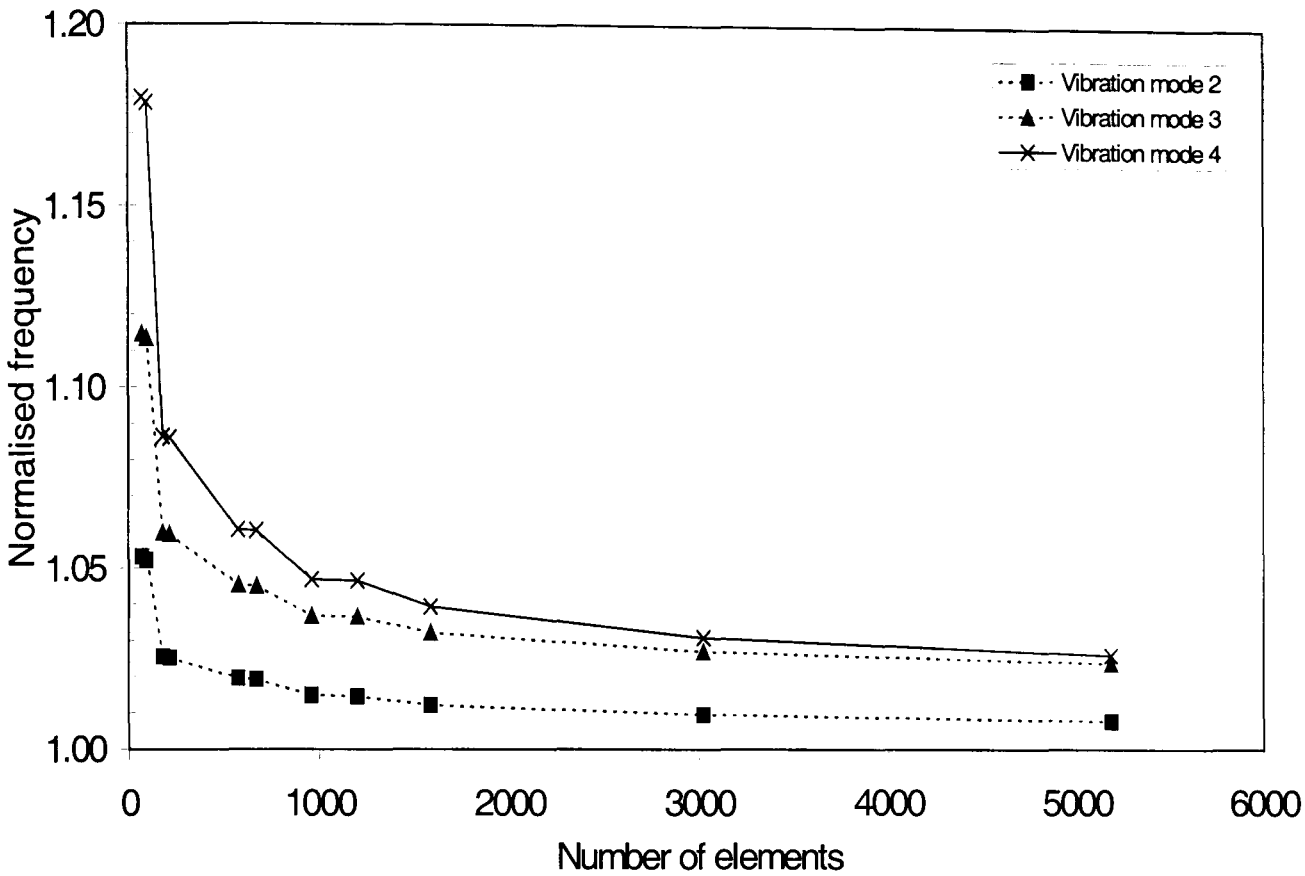

(a)

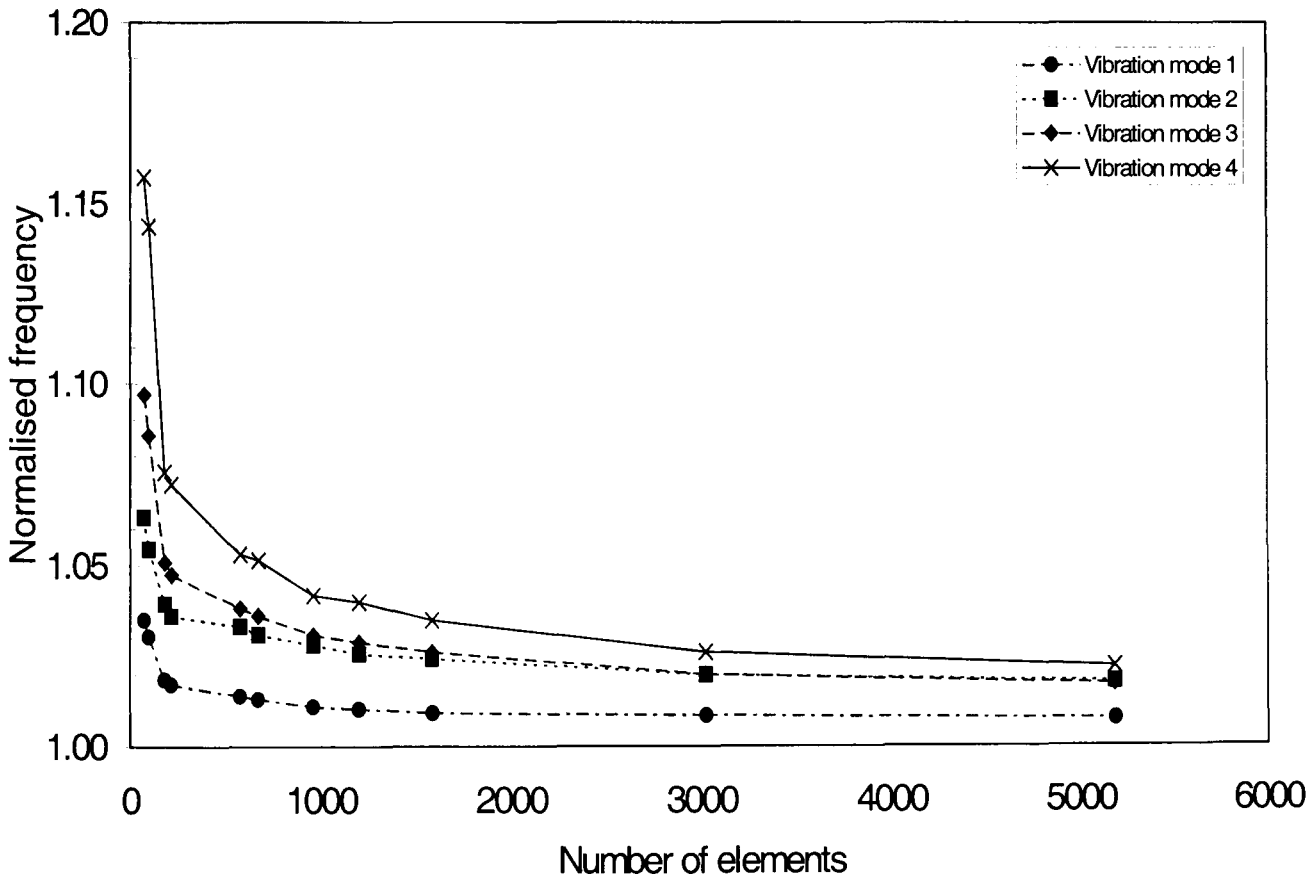

(b)

Fig. 3.5ii *Convergence of vibration modes predicted by 3D finite element analyses, element type 45;* **(a)** *m=0,* **(b)** *m=1*

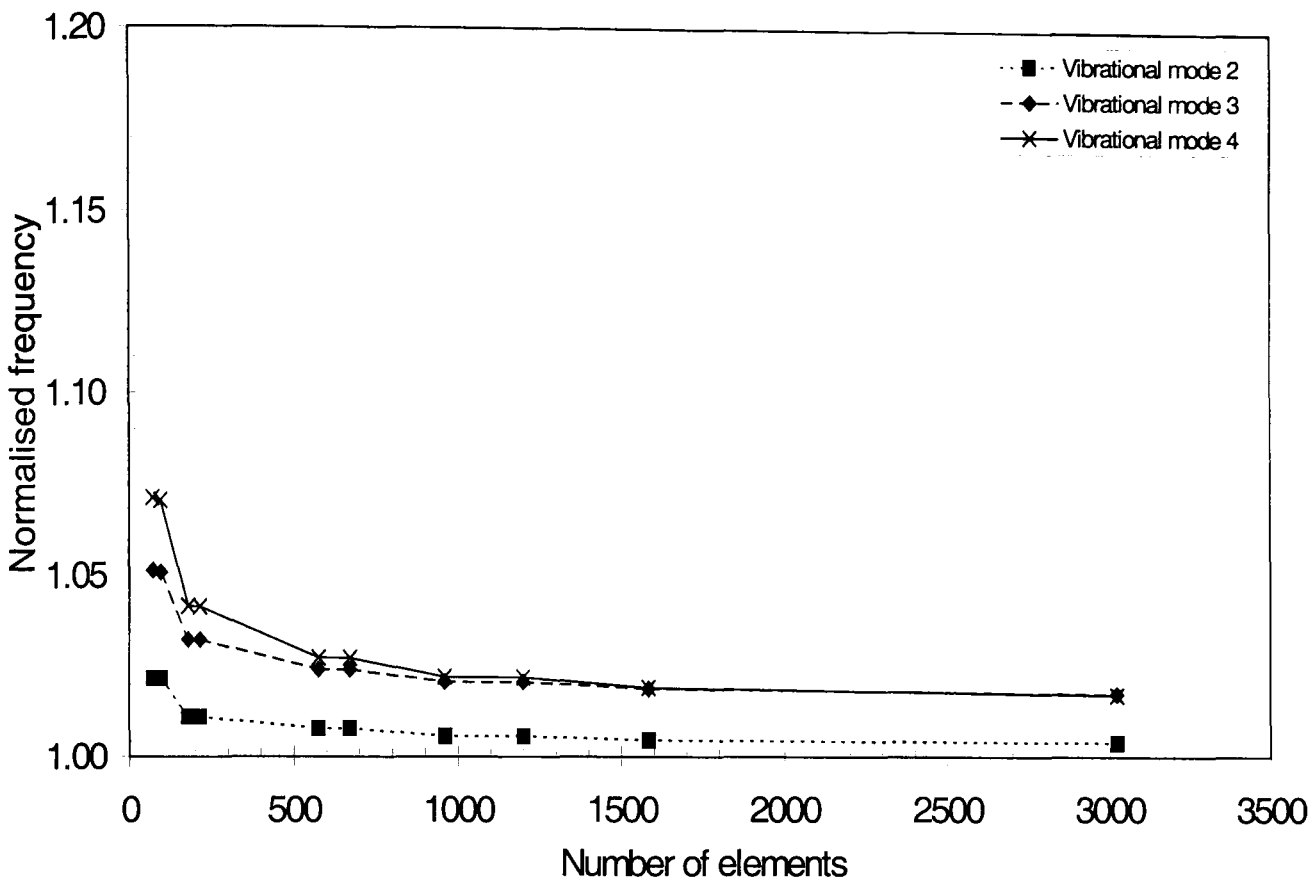

(a)

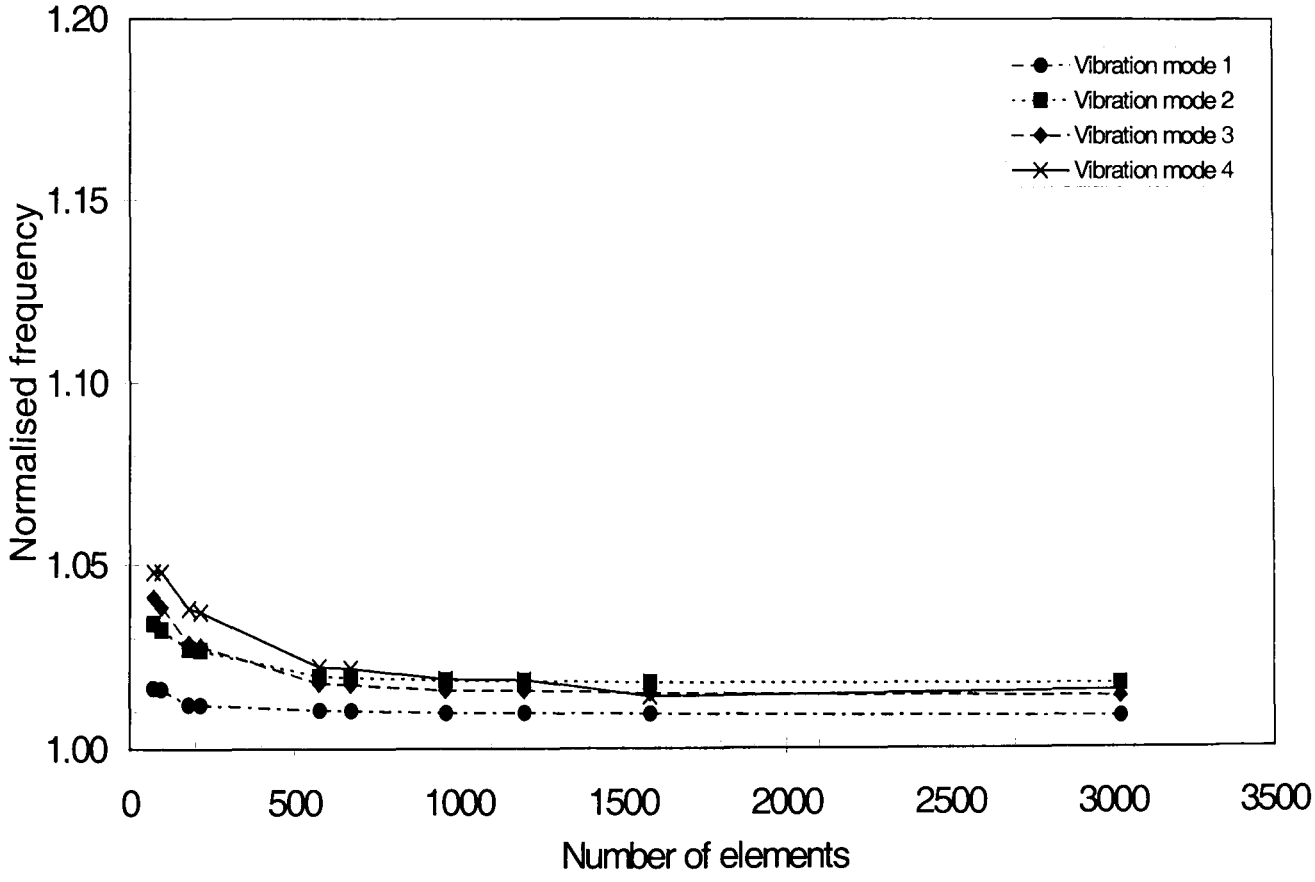

(b)

Fig. 3.5iii *Convergence of vibration modes predicted by 3D finite element analyses, element type 73;* **(a)** *m=0,* **(b)** *m=1*

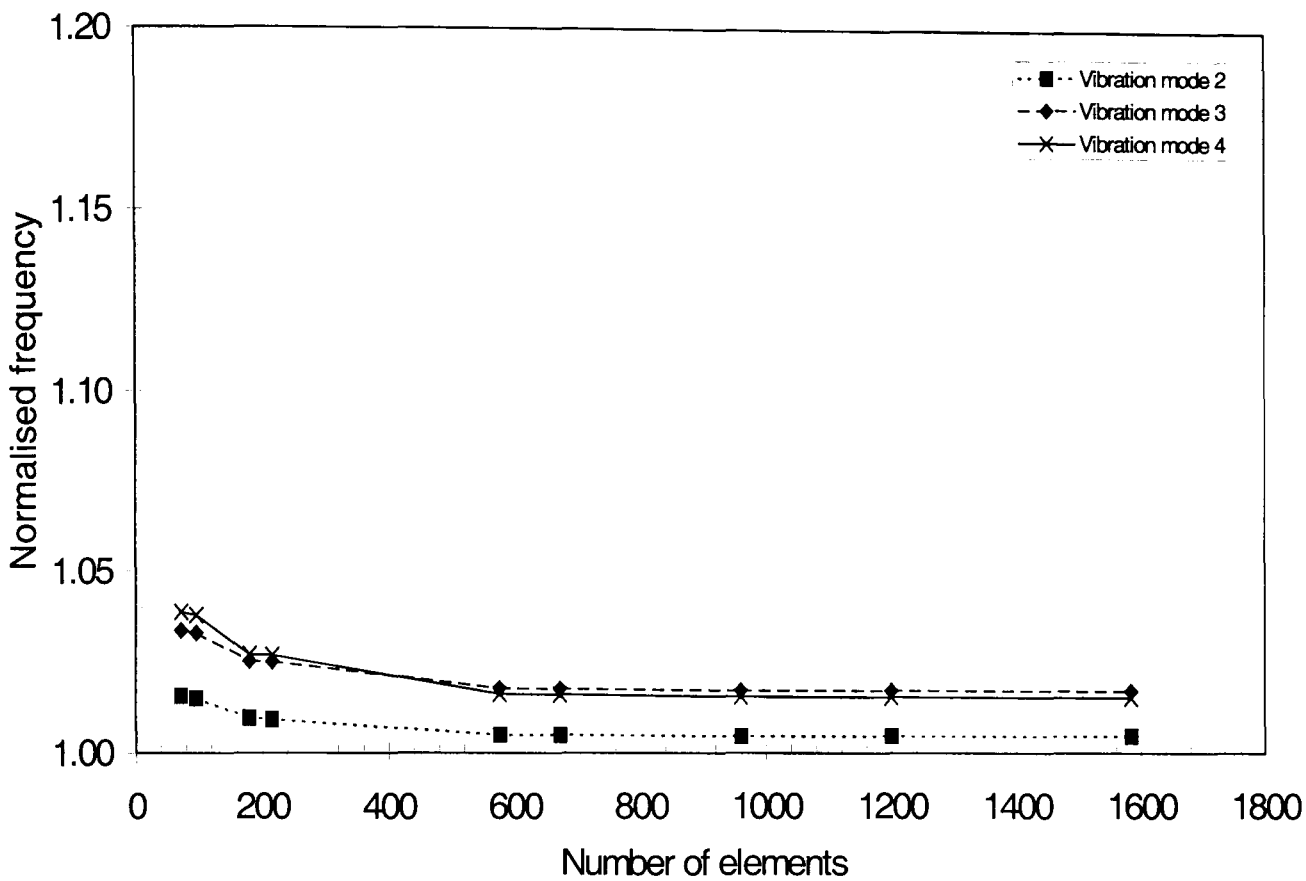

(a)

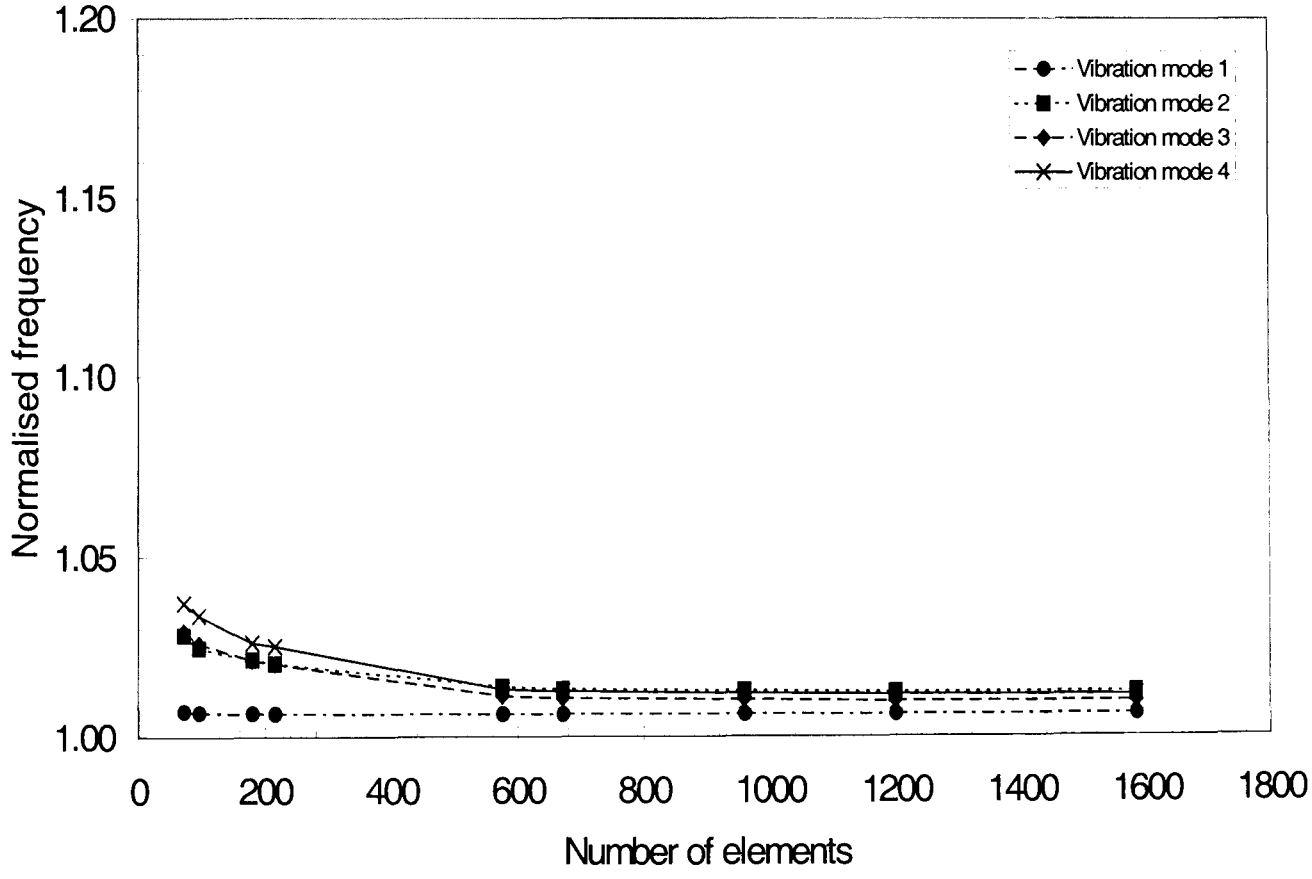

(b)

Fig. 3.5iv *Convergence of vibration modes predicted by 3D finite element analyses, element type 95;* **(a)** *m=0,* **(b)** *m=1*

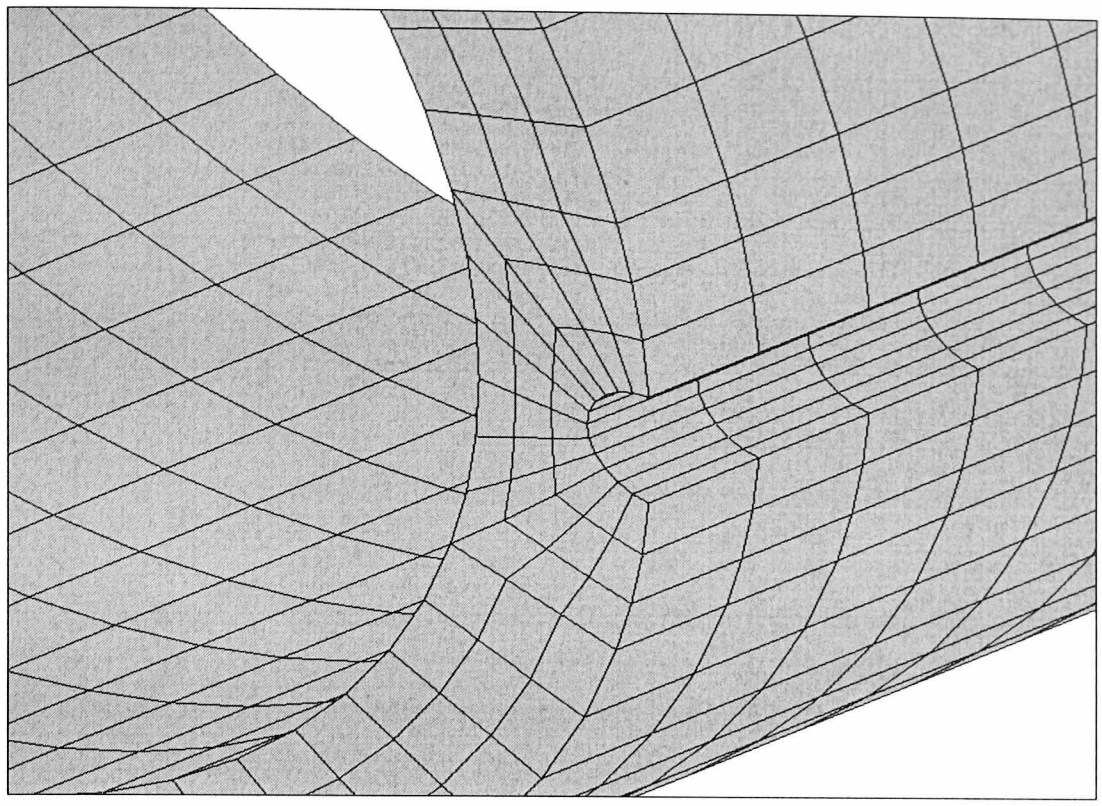

Fig. 3.6 *Example of a locally refined mesh*

The convergence study to this point has considered the influence of the density of the finite element mesh in the plane perpendicular to the axial length of the machine. However, for 3D analyses, the discretisation along the axial length is also a major factor to be considered. Therefore, the number of elements was varied form 1 to 6 and the predicted natural frequencies were again normalised to those which were measured, and are shown in **Fig. 3.7**. It will be observed that when the number of elements in the axial direction is greater than 3, any further increase in the number of elements has negligible influence on the accuracy of calculation of the axial modes, $m=1$. Furthermore, it should be noted that the axial modes $m>0$ are not important to noise produced in an SR machine.

For the 3D analysis, 576 elements were found to be adequate for modelling the annular ring, whereas for 2D analyses 384 elements were employed. These correspond to subsequent simulations in which the element divisions radially and circumferentially are 2 by 96 and 4 by 96 in the x-y plane of the 3D and 2D models, respectively. The corresponding predicted natural frequencies for the annular ring utilising these elements and mesh densities for the 2D and 3D models yielded values of natural frequencies which were within 3% of those which were measured, which is sufficiently accurate for subsequent analyses.

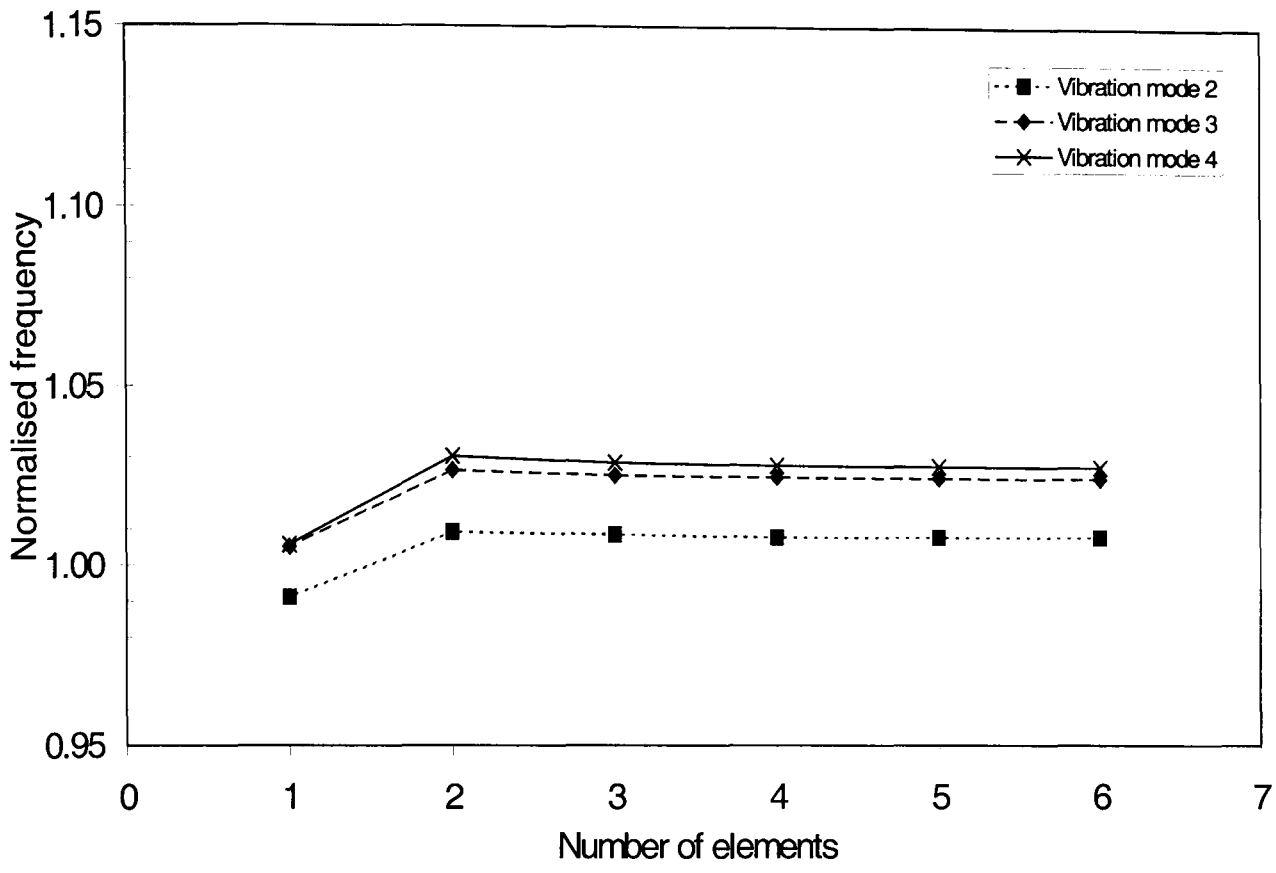

(a)

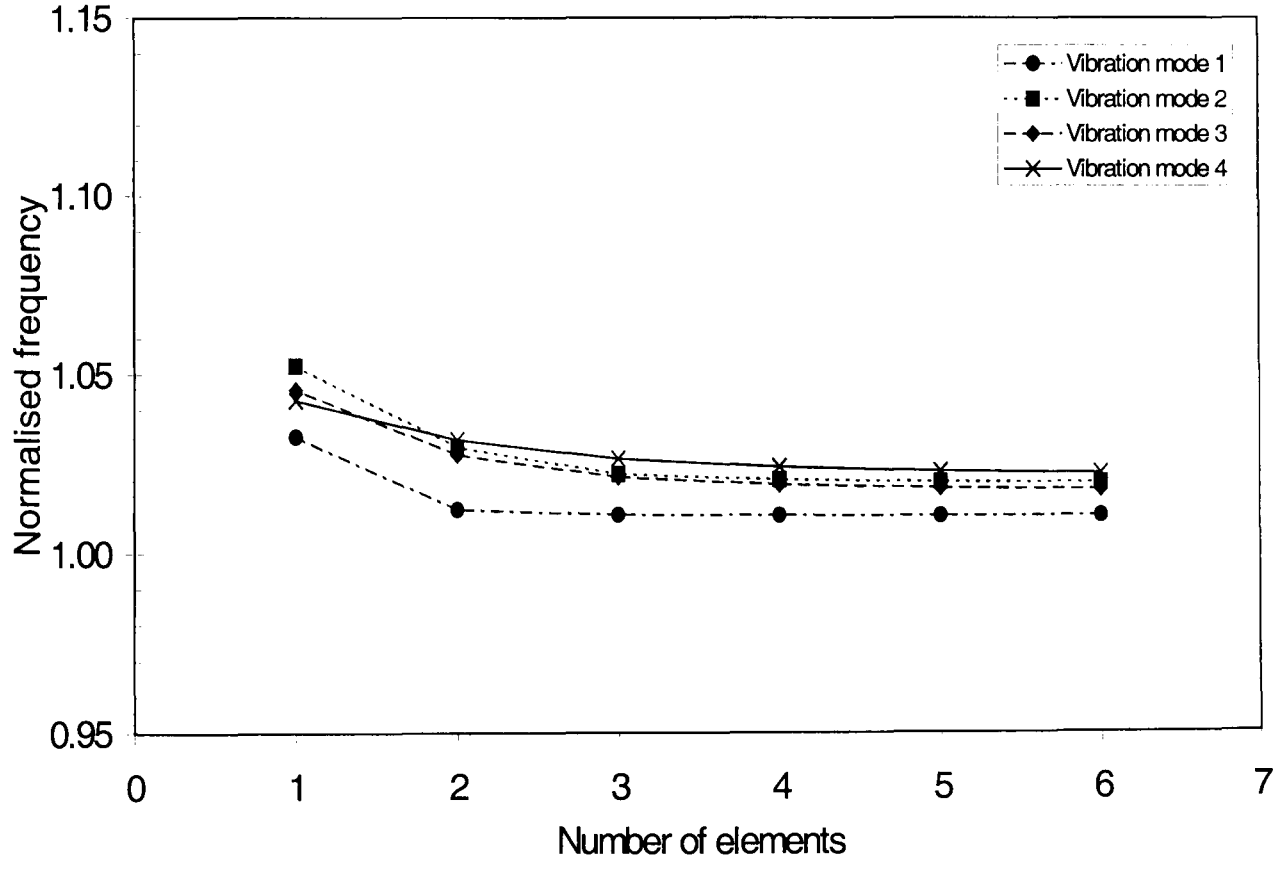

(b)

Fig. 3.7 *Influence of mesh discretisation along axial length of machine on natural frequencies, element type 73;* **(a)** *m=0,* **(b)** *m=1*

3.2.2 Validation of FEA method

In order to further validate the utility of the finite element method with the element types and meshing densities which were chosen for subsequent analyses, a simple dc motor stator geometry was modelled. The natural frequencies of the dc motor are well established, [YAN78], [ZHU87] by way of practical measurements, and finite element and numerical analyses. However, the primary dimensions of the stator of the dc machine are clearly different to those of the SR machine stator under consideration, and, hence, the annular ring, and are defined in **Fig. 3.8**. Therefore, in order to apply the selected number of elements to any model, the meshing density needs to be transformed into a function of the area. An example is scaling the size of the annular ring by a factor of 10, together with the element size, such that the number of finite elements remains the same for the 2D model. The natural frequencies predicted by FEA are given in **Table 3.6** together with those for the original ring.

Table 3.6 *Influence of scaling the leading dimensions of annular ring by factor 10*

Circumferential mode, n	Natural frequencies (Hz)	
	Ring scaled by factor 10	Original ring
2	277.9	2776
3	764.9	7650
4	1417	14170
0	1933	19333

The natural frequencies are observed to reduce by a factor of 10 due to the scaling of the ring geometry, as expected from established analytical formulae, [HAR56, TIM74]. Two leading equations are used for the analytical determination of the natural frequencies of annular rings, since mode 0 is an extensional or 'breathing' mode, whereas modes 2 and above are characterised by a number of sinusoids around the periphery of the ring. Equation (3.1) is used for the extensional mode, and assumes a ring whose cross-sectional dimensions are negligible compared to its mean radius, whereas equation (3.2) is used for modes ≥ 2 and accounts for tangential and radial displacements resulting from their sinusoidal nature. The variable n represents the number of full waves along the circumference of the ring, as defined in section 3.2.1, r is the mean radius, A is the area specified in **Fig. 3.8** and EI is the bending stiffness for which E is the Young's Modulus and I is the inertia specified by equation (3.3), where h is the ring thickness and l_t the

axial length. When the leading dimensions are increased by a factor 10, I increases by a factor 10^3 and Ar^4 by a factor 10^5. Thus, the term $\sqrt{(EI/\rho Ar^4)}$ imposes a factor of 1/10 on the predicted natural frequencies.

$$f_{n=0} = \frac{1}{2\pi}\sqrt{\frac{E}{\rho r^2}} \tag{3.1}$$

$$f_{n\geq 2} = \frac{n}{2\pi}\frac{\left(n^2-1\right)}{\sqrt{n^2+1}}\sqrt{\frac{EI}{\rho Ar^4}} \tag{3.2}$$

$$I = \frac{h^3 l_t}{12} \tag{3.3}$$

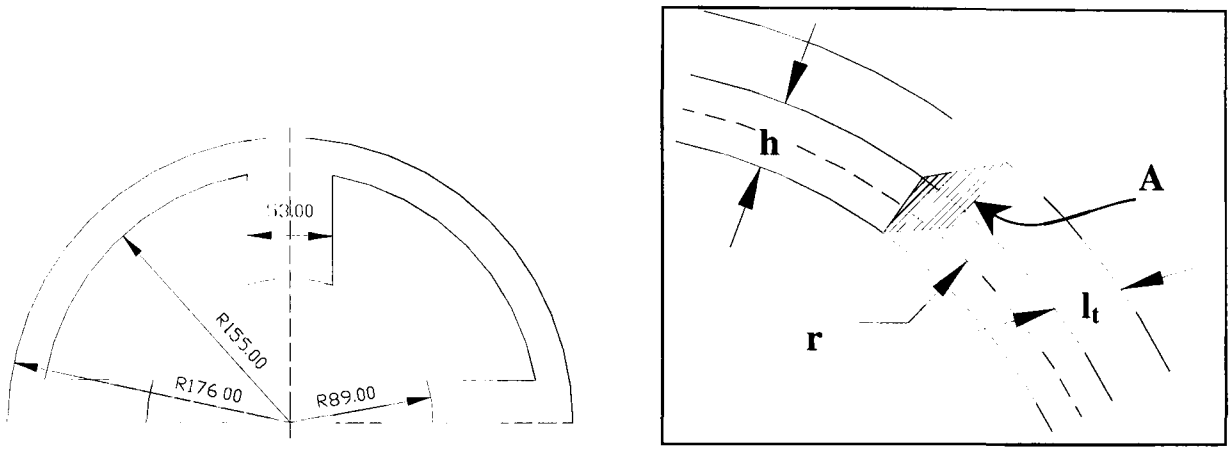

(a) **(b)**

Fig. 3.8 (a) *Dimensions of dc machine stator [YAN78],* **(b)** *definition of variables*

This simple study confirms that the accuracy of the predicted natural frequencies is not compromised by scale, provided that the ratio of the element area to the model area, or the element length to the mean diameter, is consistent, i.e. the number of element divisions remains constant. A constant that relates the ratio of the modelled geometry to the element area was therefore calculated from the annular ring to enable the dc motor to be modelled. The element size of 0.0024m for the annular ring is, thereby, transformed to a value of 0.0075m when scaled appropriately for the dc machine. The scaling procedure is summarised in Appendix C, whilst the predicted natural frequencies are given in **Table 3.7**, together with those established from earlier measurements, FEA and other numerical analyses, [YAN78, ZHU87], and the related mode shapes are shown in **Fig 3.9**. The correlation between the natural frequencies obtained by application of the various methods confirms that the FE method and chosen element size are adequate for subsequent investigations.

Table 3.7 *Summary of natural frequencies established for dc machine [YAN78, ZHU87] together with those predicted by application of chosen ANSYS© mesh*

Vibration Mode, *n*	Measured values		Analytical		Finite element analyses					
	Holtzmann [YAN78]	[ZHU87]	Holzmann's method[1]		[YAN78] 72 elements[1]		ANSYS© 600 elements[1]		[ZHU87][2]	
	f (Hz)	f (Hz)	f (Hz)	error %	f (Hz)	error %	f (Hz)	error %	f (Hz)	error %
2b	358	350	----	----	----	----	350	0	356	0.56
2a	408	415	----	----	----	----	433	-4.34	405	0.74
3	984	965	900	8.54	1007	-2.34	1005	-4.15	978	0.62
4a	1536	1520	----	----	----	----	1546	-1.71	1539	0.2
4b	2082	2080	1685	19.1	2052	1.44	2173	-4.47	2051	1.51
5	2920	3040	2201	24.6	2936	-0.55	2991	1.61	2862	-2.00
6a	3350	3265	3044	9.13	3510	-4.78	3404	-4.26	3239	3.3

[1] *error with respect to measured values, Holzmann*

[2] *error with respect to measured values, [ZHU87]*

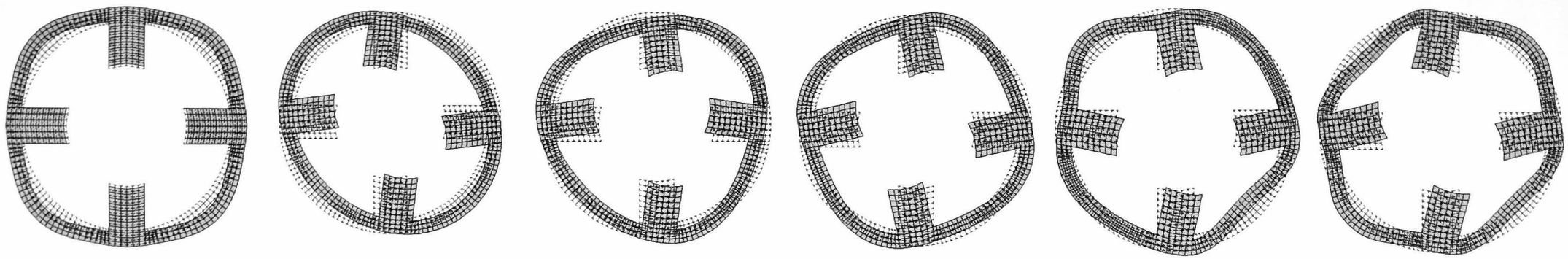

mode 0 *mode 2a* *mode 3a/b* *mode 4a* *mode 5a/b* *mode 6a*

4546Hz *356Hz* *978Hz* *1539Hz* *2862Hz* *3239Hz*

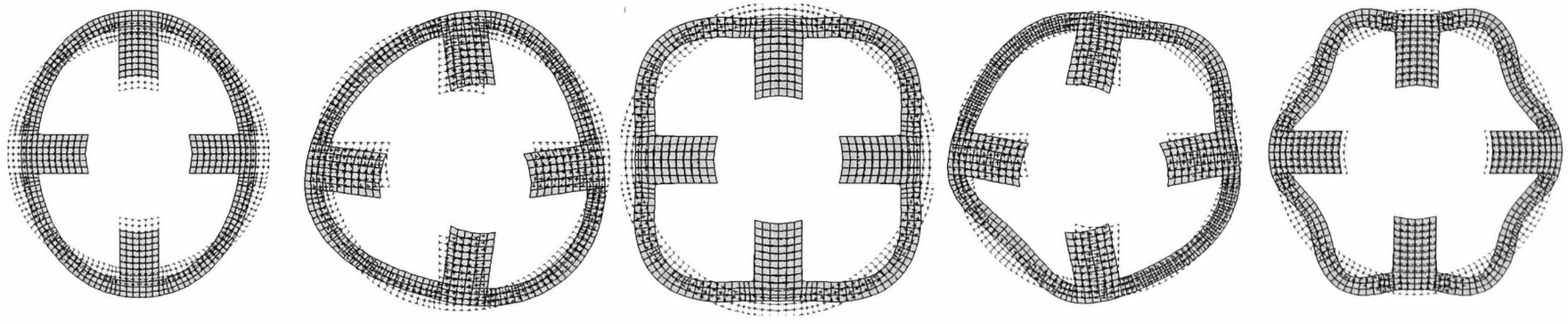

mode 2b *mode 3a/b* *mode 4b* *mode 5a/b* *mode 6b*

405Hz *978Hz* *2051Hz* *2862Hz* *5676Hz*

Fig. 3.9 *Vibrational modes shapes of stator of dc machine*

3.3 Models for investigation

Many of the investigations throughout this chapter are based on eight geometric models, whose primary dimensions are the same as those of the stator of the experimental SR machine. The models represent varying degrees of complexity in construction, as shown in **Fig. 3.10i & ii**, such that the influence of the leading design parameters of the 6-pole SR stator geometry and influence of the geometric asymmetries can be examined. Both solid mild steel and silicon iron laminations are employed for the construction of the various models, the properties of these materials being given in **Table 3.8**, whereas the major dimensions of the models are provided in Appendix D. The features of the various models are outlined below.

Model I is a smooth annular ring, constructed from both solid mild steel and a stack of laminations of the same material as that which was used for the experimental machine, welded at four equi-spaced circumferential points along its axis. This model has two primary objectives. Firstly, to validate the utility of the finite element method for subsequent vibration investigations. Secondly, to investigate the influence of laminating a core on the natural frequencies.

Models II & III have one and three notches, respectively, and are both constructed from solid mild steel, to enable the effects of asymmetries on the natural frequencies to be examined with reference to those of the simple annular ring.

Models IV & V have one and six salient stator poles, respectively, and are again constructed from solid mild steel, to enable investigations into the influence of asymmetry in the stator design and the influence of the mass and stiffness effects of the poles.

Model VI is a complete stator that also includes the fillet radius between the poles and the stator yoke. It was constructed from both solid mild steel and a stack of laminations to form the stator of the 0.25kW experimental machine which was described in Chapter 2. The laminations were welded at six equi-spaced circumferential positions along its axis to further the investigations into the influence of laminating a structure on the natural frequencies. Throughout the course of this chapter, the windings, the frame and the end-caps are added to the laminated stator core to form the complete stator, which is subsequently mounted to the test bench assembly. The masses of these individual stator components are given in Appendix D.

Model VII has eight salient stator poles and is only modelled by finite elements, to further the investigations into geometric asymmetries.

Model VIII is a complete 8-pole stator, which includes the fillet radius between the poles and stator yoke. This is utilised for the same purposes as Model VI and was constructed from both solid mild steel and a stack of laminations which were welded at eight equi-spaced circumferental positions along its axis.

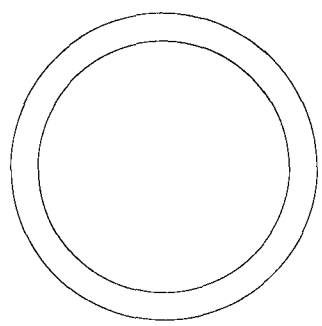

Model Ia – solid
Model Ib –laminated

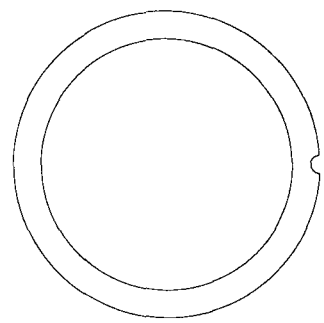

Model II

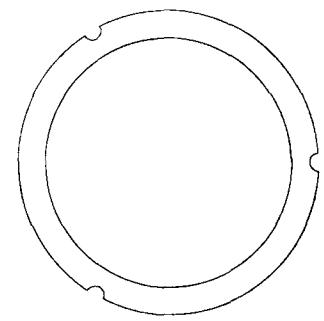

Model III

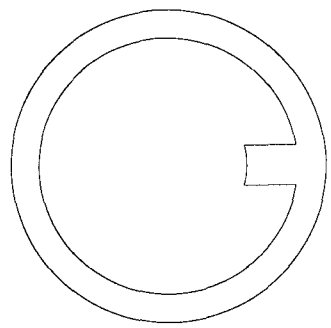

Model IV

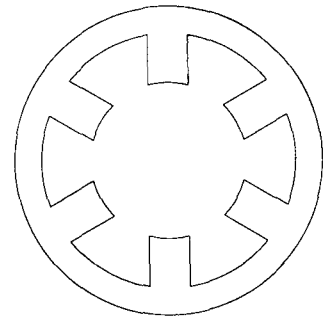

Model V

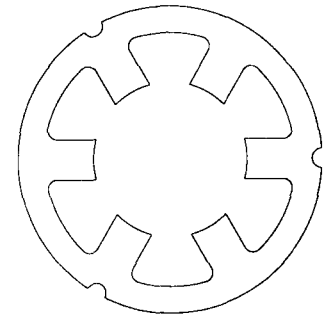

Model VIa – solid
Model VIb - laminated

Fig. 3.10i *Finite element and experimental models*

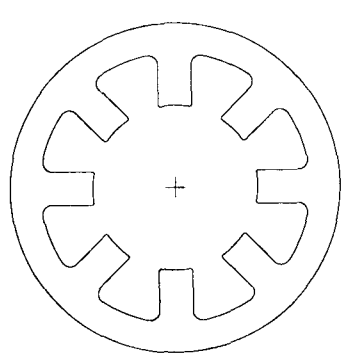

Model VII

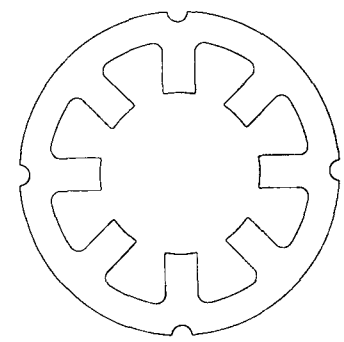

Models VIIIa – solid
Model VIIIb – laminated

Fig. 3.10ii *Finite element and experimental models*

Table 3.8 *Material properties*

Property	Mild Steel	Silicon Iron (M300-35A)
Young's Modulus, E (GPa)	210	215
Poisson's Ratio, ν	0.28	0.3
Density, ρ (kgm^{-3})	7800	7650

Due to the relatively large number of impulse tests which were employed for identifying the mode shapes, a convention was employed to enable the position of impact and the position of the accelerometer to be identified. These positions are indicated circumferentially, relative to the geometric asymmetries, i.e. poles and notches, etc, and axially with respect to the length of the model on which the measurement is taken. The convention is summarised for the circumferential position in **Fig. 3.11(a)**, where the arrow directed towards the model represents the point of application of the impact force, and the arrow pointing away represents the position of the accelerometer. A black dot represents the axial position of the impact and the accelerometer, **Fig. 3.11(b)**, whereas for the case in which the axial position of the accelerometer and the impact force differ, a cross in a circle represents the point of impact and a black dot in a circle represents the position of the accelerometer, **Fig. 3.11(c)**. Furthermore, geometric parameters of the stator, such as poles, notches and weld points, are represented by symbols, as indicated in **Fig. 3.11(d)**.

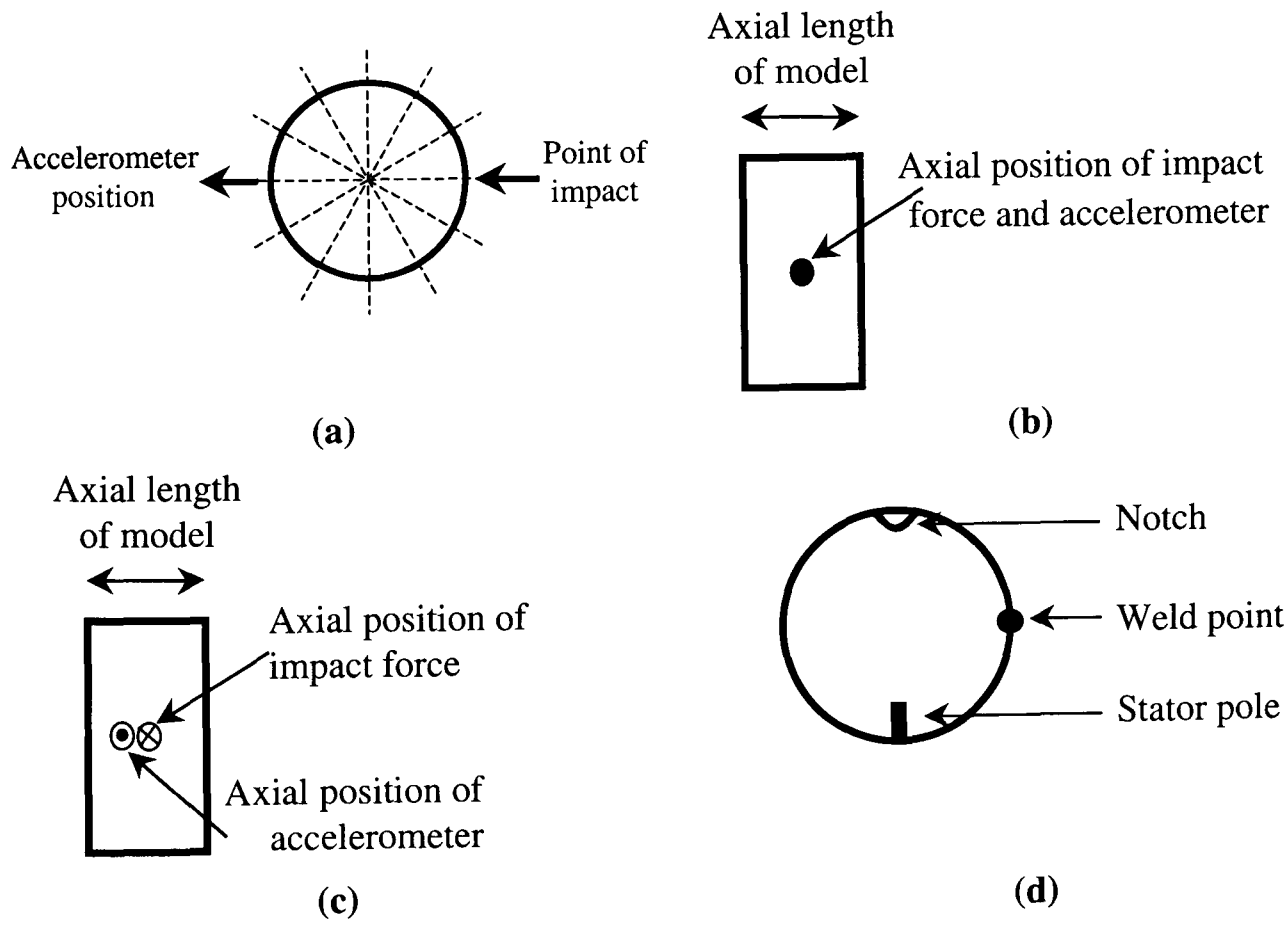

Fig. 3.11 *Convention for identifying measured frequency spectra*

3.4 Influence of geometric asymmetry and cyclic symmetry

The predicted natural frequencies of models I to VI obtained by application of 2D and 3D finite element analyses, employing the material properties for solid mild steel listed in **Table 3.8**, section 3.3, are given in **Tables 3.9 to 3.14**, together with the measured values. The predicted and measured natural frequencies for the 8-pole stator core are given in **Tables 3.15 and 3.16**, both with and without the notches, respectively. The vibration frequency spectra obtained from impulse force tests performed on the various experimental models are shown in **Figs. 3.12 to 3.19**, together with a key to indicate the point of impact and the accelerometer position, whilst the mode shapes determined from the 2D FE analyses are shown in **Figs. 3.20 to 3.27**.

At this stage of the investigation the application of 2D FEA is sufficient for quantifying the influence of the stator geometry on the values of the natural frequencies. However, as will be shown later, when dealing with the non-homogeneous nature of a laminated stator core complete with windings and frame (such that the cross-sectional area of the structure is no longer constant throughout its axial length) 3D FEA is required. For this reason values obtained using 3D FEA are included with those determined from 2D FEA for a comparative evaluation.

From **Tables 3.9 to 3.16**, it is observed that predictions from both the 2D and 3D finite element models correlate well with the measured natural frequencies and vibrational modes. However, it should be noted the values predicted with 2D FEA appear to be more accurate than those using 3D FEA, although it is expected that 3D FEA provides a more accurate representation. Consideration of the accuracy of the spectrum analyser employed for the measurements over the selected frequency range yields a tolerance of ±50Hz as indicated earlier on **Fig. 3.2**, and is therefore indicated in tables. It is well established that the analytic formulae of a thin ring, equations (3.1) and (3.2), yield accurate values of the natural frequencies of homogeneous cylinders such that a correction of less than 1% is required for rings whose ratio of mean diameter, $2r$, to ring thickness, h, **Fig. 3.8(b)**, is 15:8, [KAI53]. The yoke of the stator in this study yields a ratio of 10.6 and the accuracy of the thin ring formula for the stator yoke is further justified by the comparison between thin ring and thick ring formulae presented in section 3.5. Therefore, by way of example, the natural frequencies obtained from equations (3.1) and (3.2) are included in **Table 3.9**, which, together with the margin of experimental error indicate that the 3D FEA is, as expected, more accurate than the 2D

FEA. The measured natural frequencies of the laminated ring, the 6-pole stator and the 8-pole stator are also included in the tables, but these are discussed in section 3.6.

Table 3.9 *Annular ring (Models Ia & Ib[#]), for m=0*

Circumferential Mode, *n*	Natural Frequencies, Hz				
	Measured		FEA		Analytical[##]
	Laminated[#] silicon iron	Solid mild steel	2D Solid	3D Solid	2D thin ring
0	18944 $^{\pm 50}$	19072 $^{\pm 50}$	19333	19282	19272
2	2688 $^{\pm 50}$	2816 $^{\pm 50}$	2776	2838	2822
3	7424 $^{\pm 50}$	7680 $^{\pm 50}$	7650	7865	7982
4	13760 $^{\pm 50}$	14272 $^{\pm 50}$	14170	14662	15304

[#]*Model Ib is detailed in section 3.6, but included in this table for comparison*
[##]*Refer to equations (3.1) and (3.2)*

Table 3.10 *Solid mild steel annular ring with notch (Model II), for m=0*

Circumferential mode, *n*	Natural Frequencies, Hz		
	Measured	2D	3D
0	*	19120	19118
2	2696 $^{\pm 50}$	2673	2738
2	2792 $^{\pm 50}$	2777	2838
3	7468 $^{\pm 50}$	7411	7630
3	7692 $^{\pm 50}$	7643	7853
4	13880 $^{\pm 50}$	13783	14273
4	14288 $^{\pm 50}$	14145	14621

Table 3.11 *Solid mild steel annular ring with 3 notches (Model III), for m=0*

Circumferential mode, *n*	Natural Frequencies, Hz		
	Measured	2D	3D
0	*	18797	18844
2	2640 $^{\pm 50}$	2627	2692
2	2640 $^{\pm 50}$	2627	2692
3	7024 $^{\pm 50}$	6963	7188
3	7664 $^{\pm 50}$	7629	7823
4	13648 $^{\pm 50}$	13540	14009
4	13648 $^{\pm 50}$	13540	14009

Table 3.12 *Solid mild steel ring with 1 tooth (Model IV), for m=0*

Circumferential mode, *n*	Natural Frequencies, Hz		
	Measured	2D	3D
0	*	18626	18684
2	2688 $^{\pm 50}$	2637	2698
2	2752 $^{\pm 50}$	2690	2776
3	7104 $^{\pm 50}$	7057	7282
3	7488 $^{\pm 50}$	7425	7705
4	12736 $^{\pm 50}$	12557	13135
4	13888 $^{\pm 50}$	13755	14337

Table 3.13 *Solid mild steel 6-pole stator with no fillets (Model V), for m=0*

Circumferential mode, *n*	Natural Frequencies, Hz, FEA	
	2D	3D
0	14847 $^{\pm 50}$	14977
2	2250 $^{\pm 50}$	2358
2	2250 $^{\pm 50}$	2358
3	5267 $^{\pm 50}$	5465
3	6548 $^{\pm 50}$	7085
4	10010 $^{\pm 50}$	10758
4	10010 $^{\pm 50}$	10759

Table 3.14 *6-pole stator, (Models VIa & VIb#), for m=0*

Circumferential mode, *n*	Natural frequencies, Hz			
	Measured		FEA	
	Laminated# silicon iron	Solid mild steel	2D Solid	3D Solid
0	*	*	14146	14380
2	2304 $^{\pm 50}$	2352 $^{\pm 50}$	2335	2405
2	2304 $^{\pm 50}$	2384 $^{\pm 50}$	2335	2408
3	5280 $^{\pm 50}$	5488 $^{\pm 50}$	5389	5540
3	7008 $^{\pm 50}$	7216 $^{\pm 50}$	7062	7380
4	10560 $^{\pm 50}$	10896 $^{\pm 50}$	10683	11129
4	10560 $^{\pm 50}$	10896 $^{\pm 50}$	10683	11144

#*Model VIb is detailed in section 3.6, but included in this table for comparison*

Table 3.15 *Solid mild steel 8-pole stator with no fillets (Model VII), for m=0*

Circumferential mode, *n*	Natural Frequencies, Hz
	2D FEA
0	15320
2	2331
2	2331
3	5963
3	5963
4	8847
4	12948

Table 3.16 *8-pole stator (Models VIIIa & VIIIb[#]), for m=0*

Circumferential mode, *n*	Natural frequencies, Hz			
	Measured		FEA	
	Laminated[#] silicon iron	Solid mild steel	2D Solid	3D Solid
0	*	*	14711	14979
2	2176 $^{\pm 50}$	2352 $^{\pm 50}$	2209	2318
2	2304 $^{\pm 50}$	2480 $^{\pm 50}$	2330	2437
3	5760 $^{\pm 50}$	6208 $^{\pm 50}$	5830	6114
3	5760 $^{\pm 50}$	6208 $^{\pm 50}$	5830	6122
4	8672 $^{\pm 50}$	9280 $^{\pm 50}$	8782	9179
4	11968 $^{\pm 50}$	12800 $^{\pm 50}$	12076	12972

[#]*Model VIIIb is detailed in section 3.6, but included in this table for comparison*

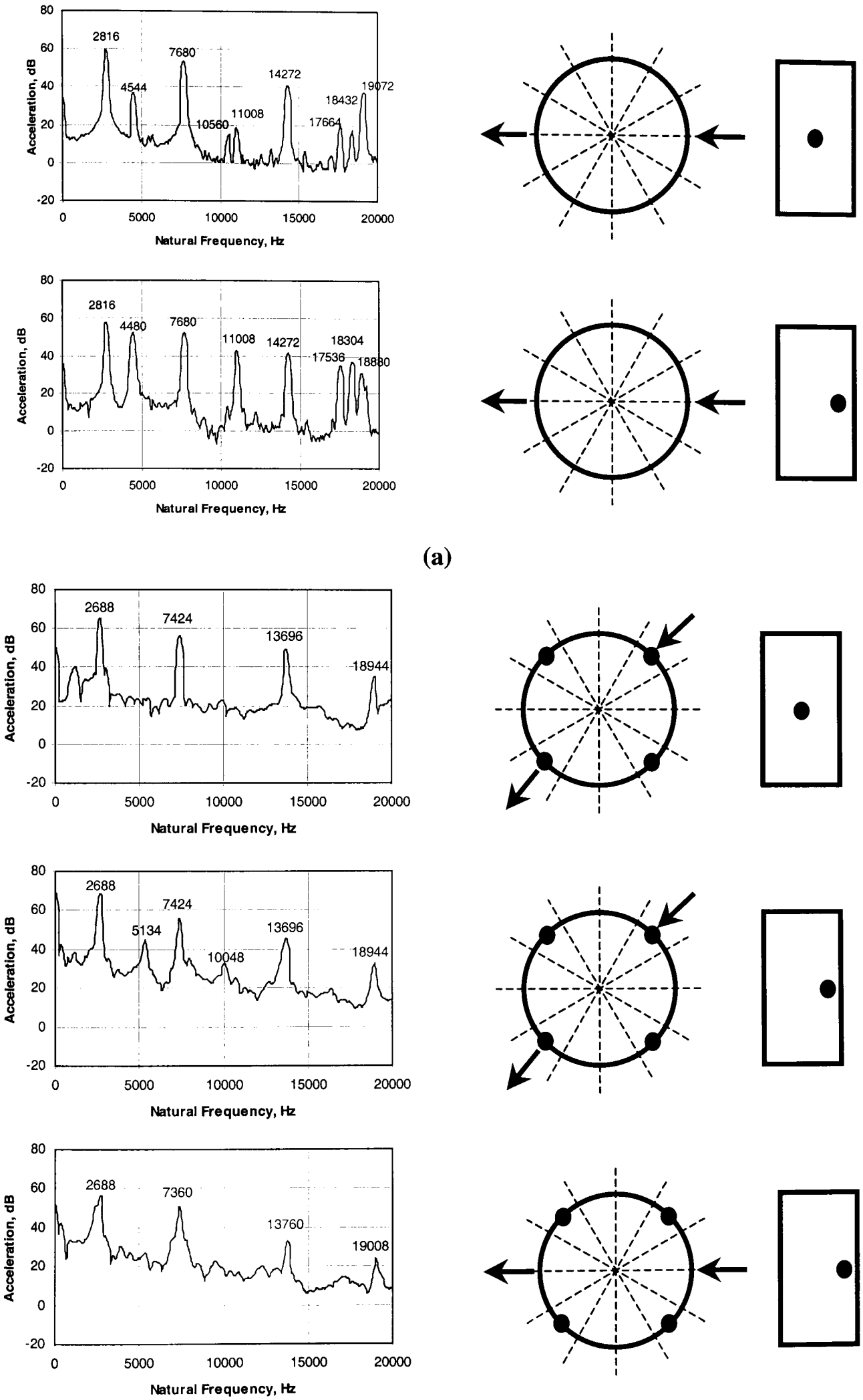

Fig. 3.12 *Impact test – annular ring;* **(a)** *Model Ia, solid mild steel,* **(b)** *Model Ib laminated silicon iron*

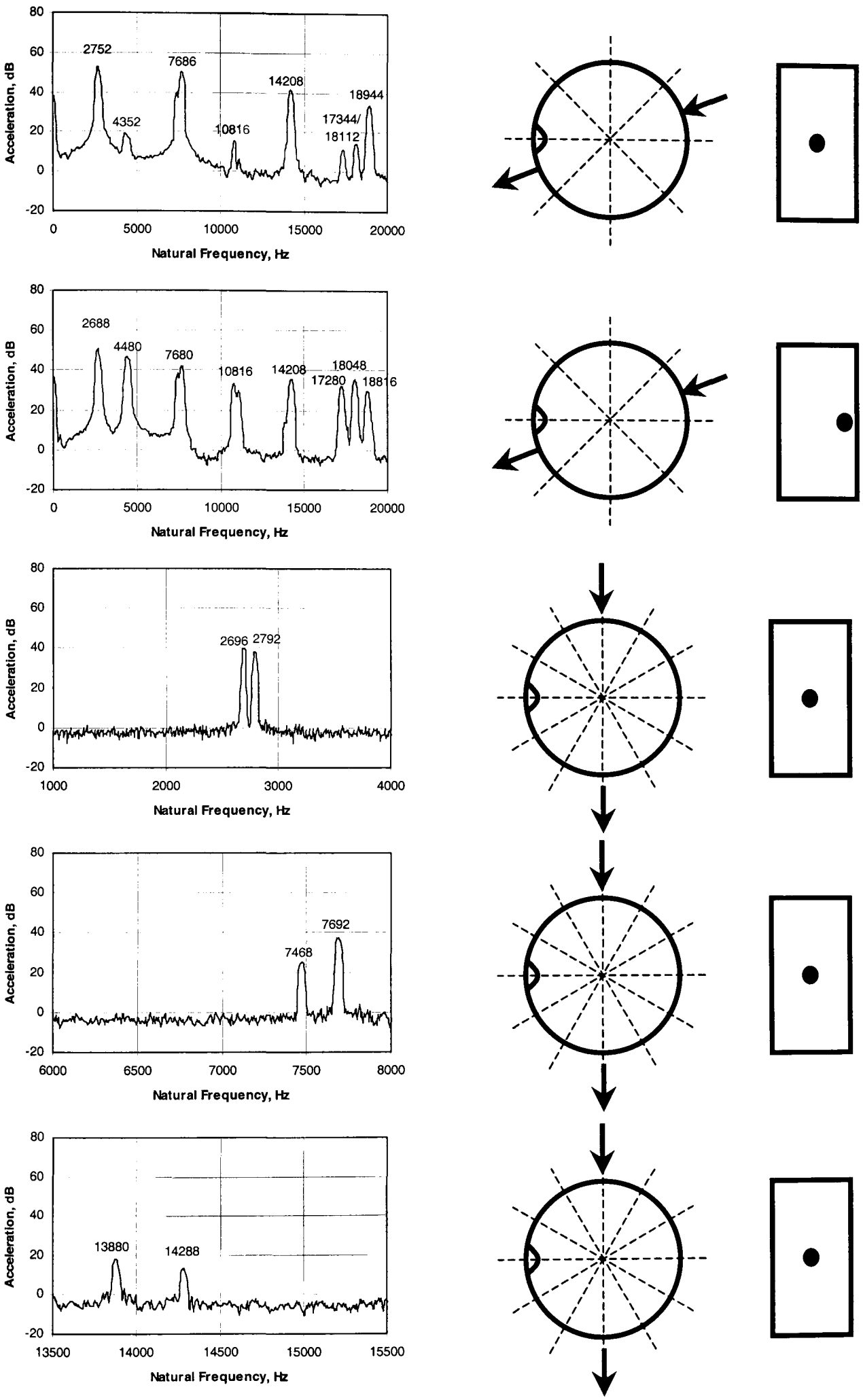

Fig. 3.13 *Impact test – solid mild steel ring with one notch, Model II*

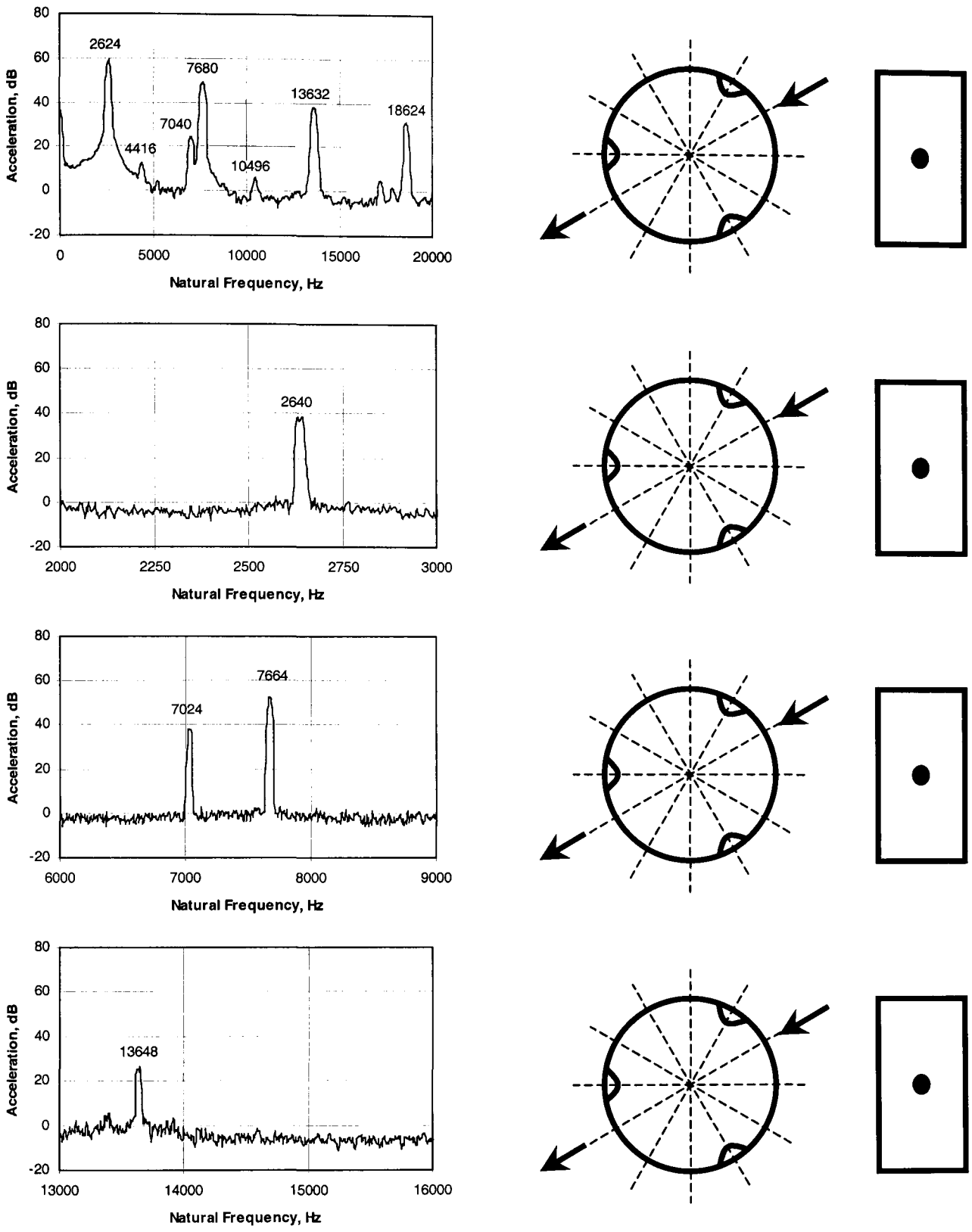

Fig. 3.14 *Impact test – solid mild steel ring with three notches, Model III*

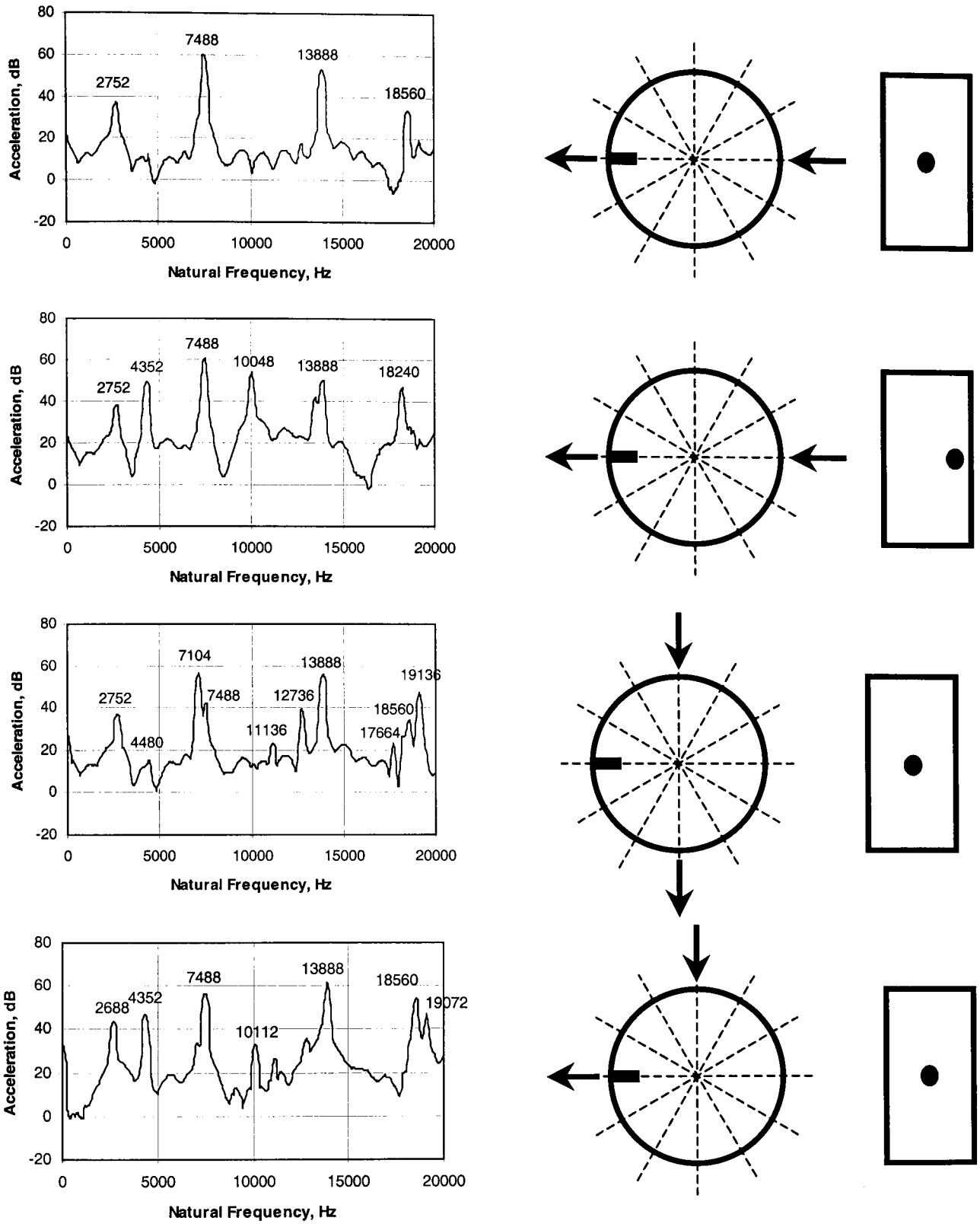

Fig. 3.15 *Impact test – solid mild steel ring with one tooth, Model IV*

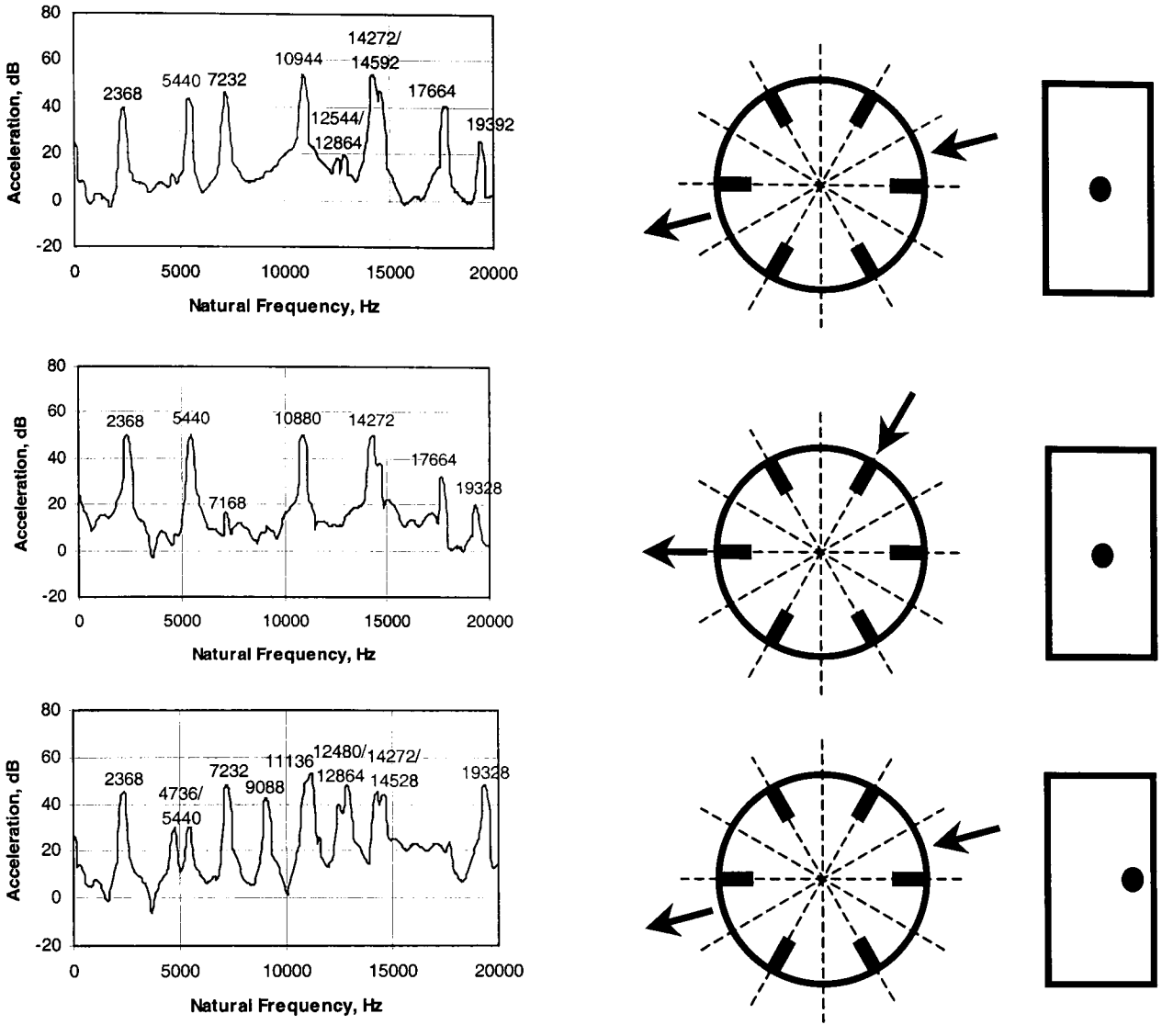

Fig. 3.16 *Impact test – solid mild steel 6-pole stator, Model VIa*

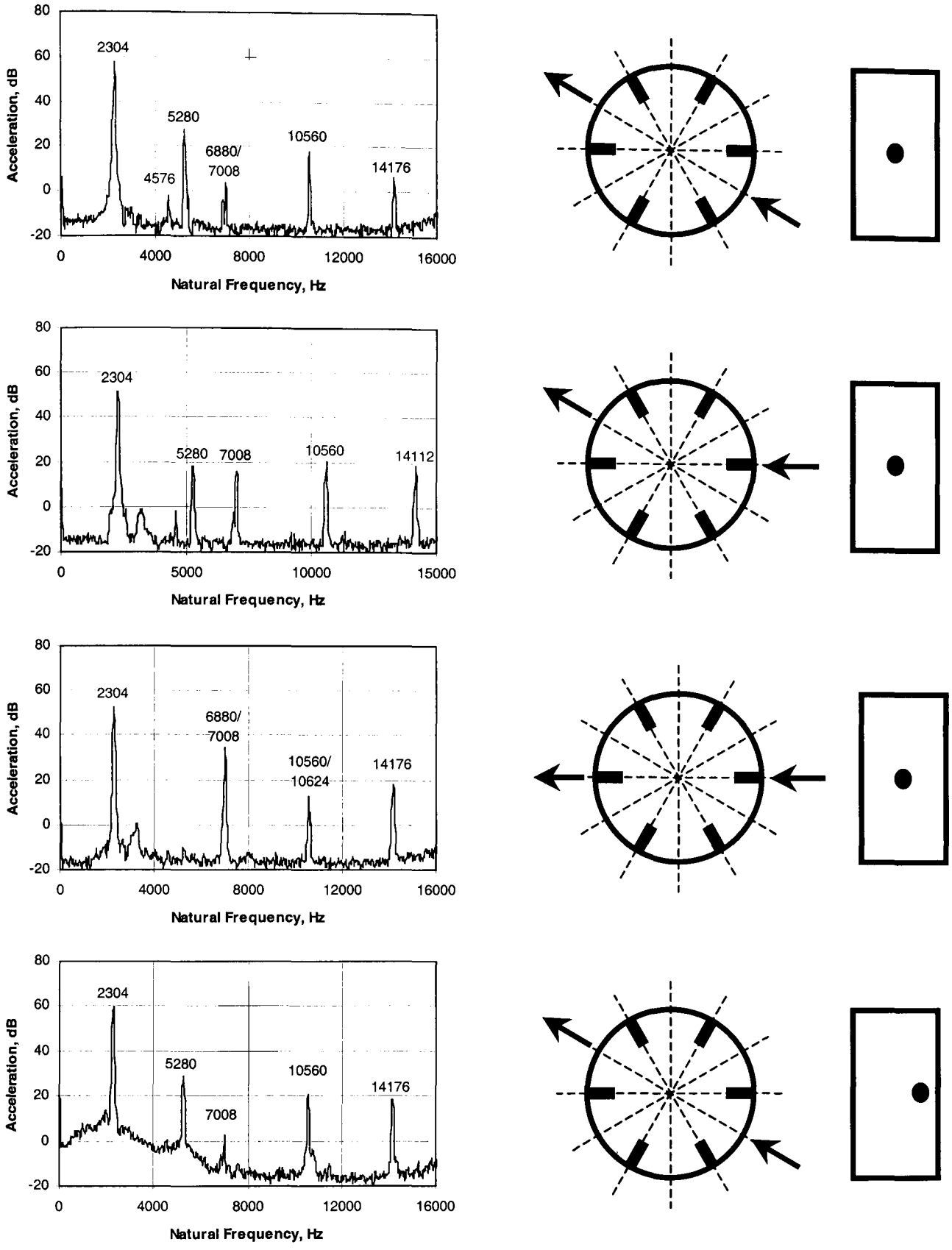

Fig. 3.17 *Impact test – laminated M300-35A 6-pole stator, Model VIb*

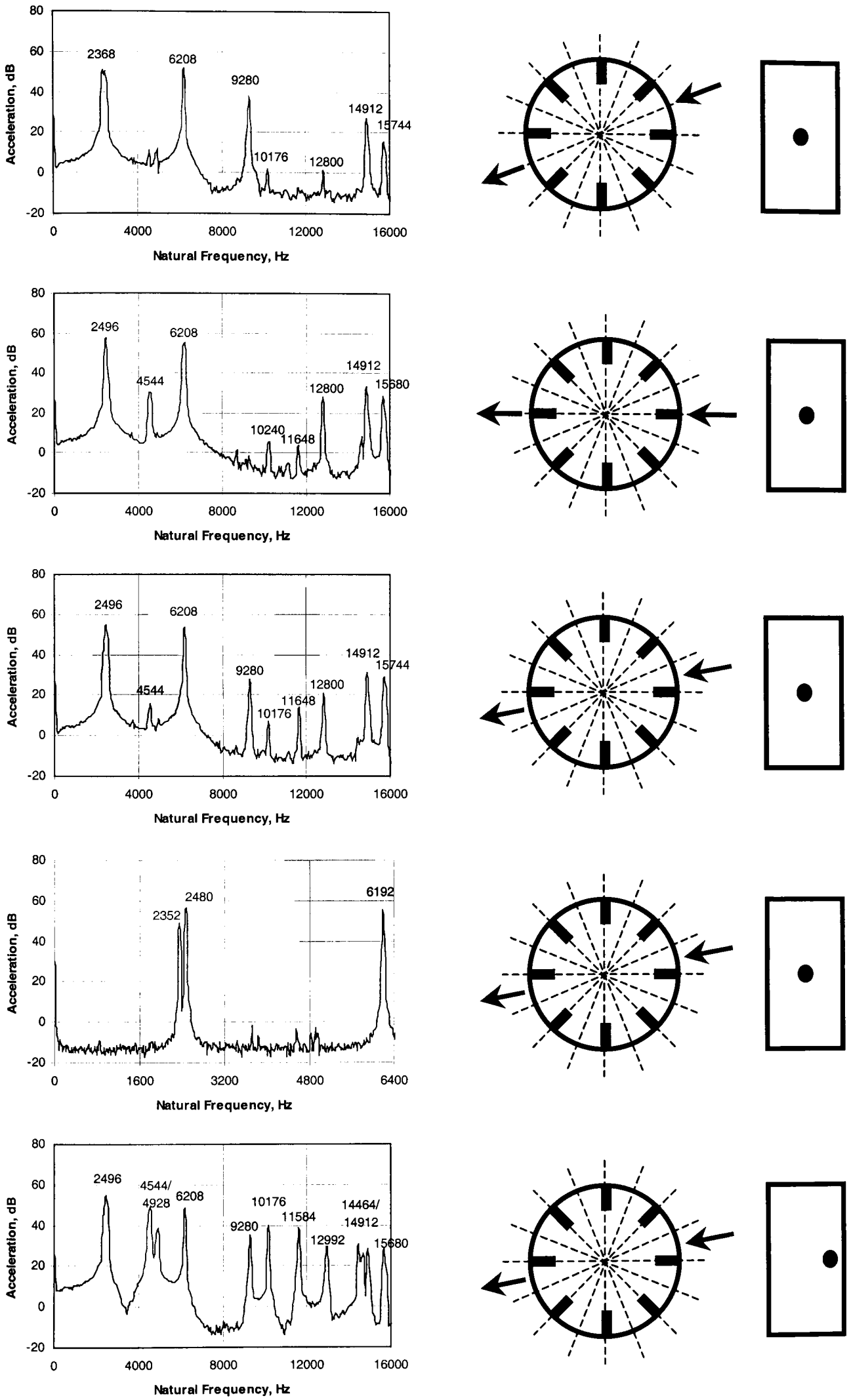

Fig. 3.18 *Impact test – solid mild steel 8-pole stator, Model VIIIa*

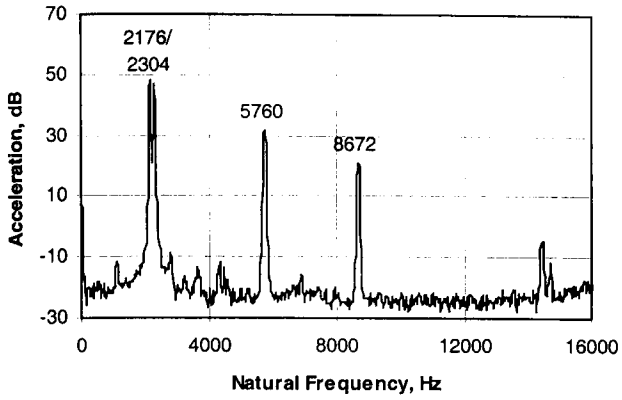

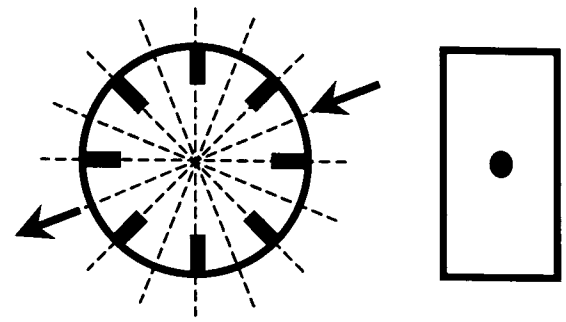

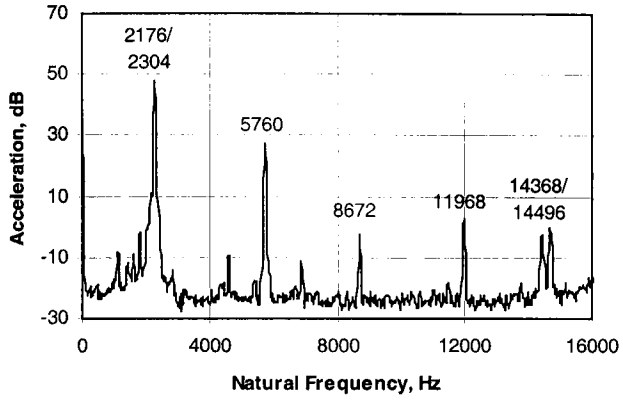

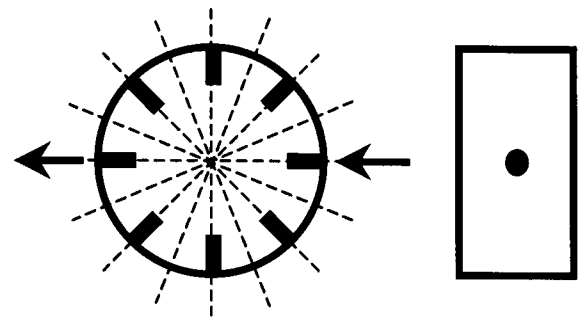

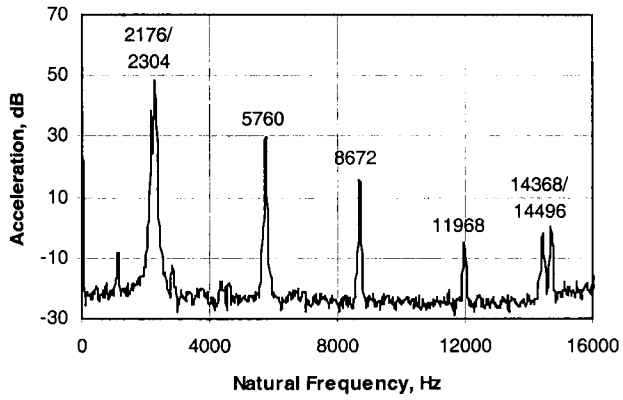

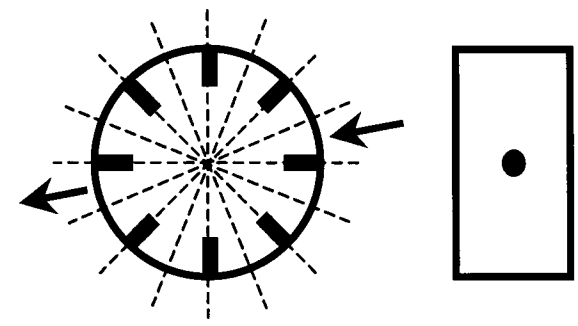

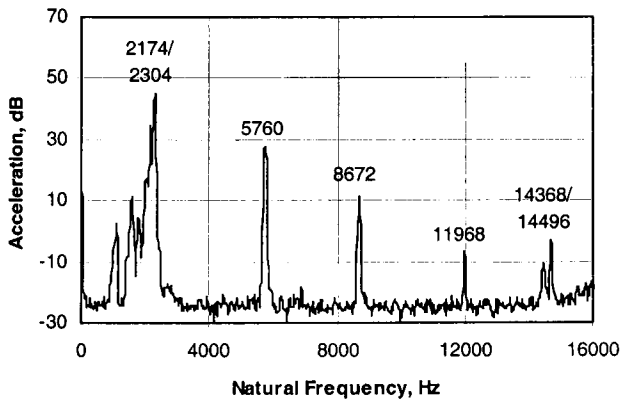

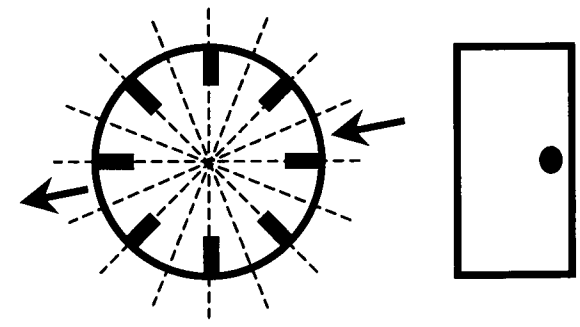

Fig. 3.19 *Impact test – laminated M300-35A 8-pole stator, Model VIIIb*

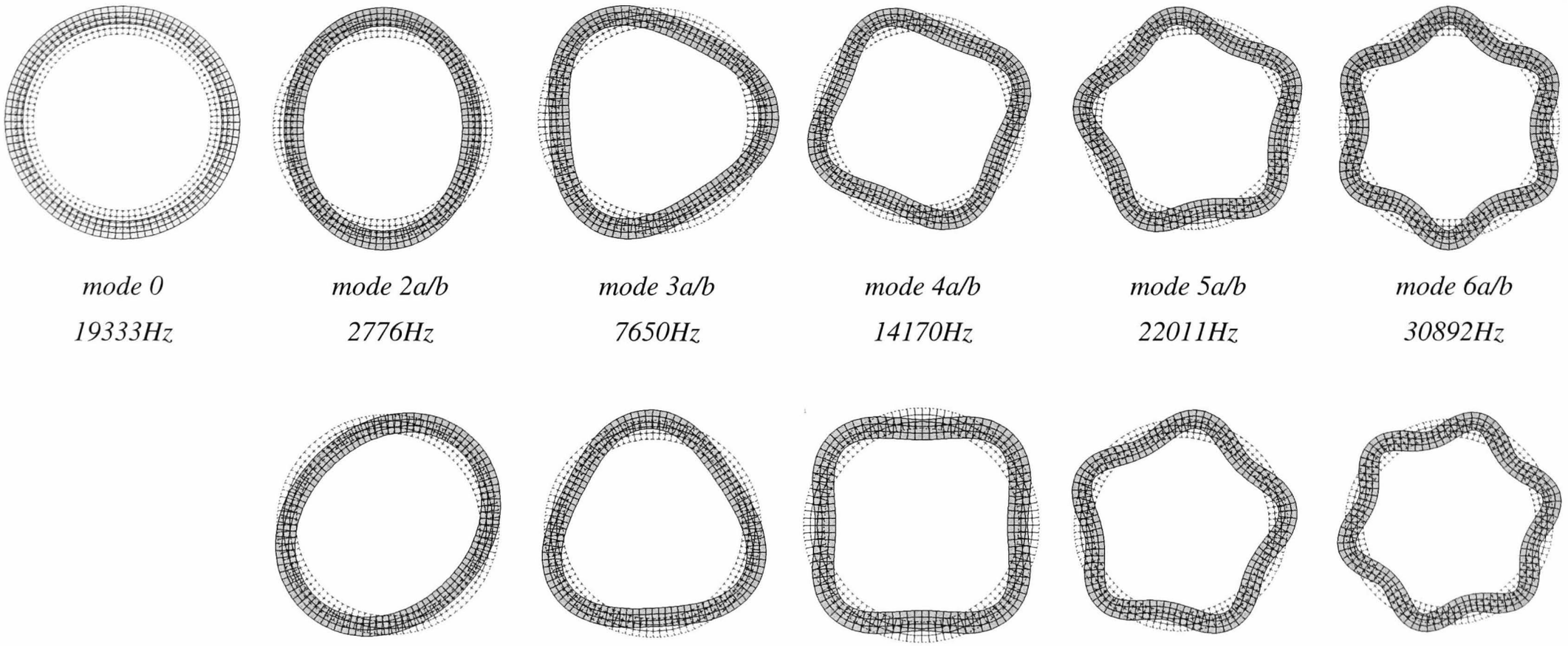

mode 0 *19333Hz*

mode 2a/b *2776Hz*

mode 3a/b *7650Hz*

mode 4a/b *14170Hz*

mode 5a/b *22011Hz*

mode 6a/b *30892Hz*

mode 2a/b *2776Hz*

mode 3a/b *7650Hz*

mode 4a/b *14170Hz*

mode 5a/b *22011Hz*

mode 6a/b *30892Hz*

Fig. 3.20 *Vibrational mode shapes associated with Model Ia*

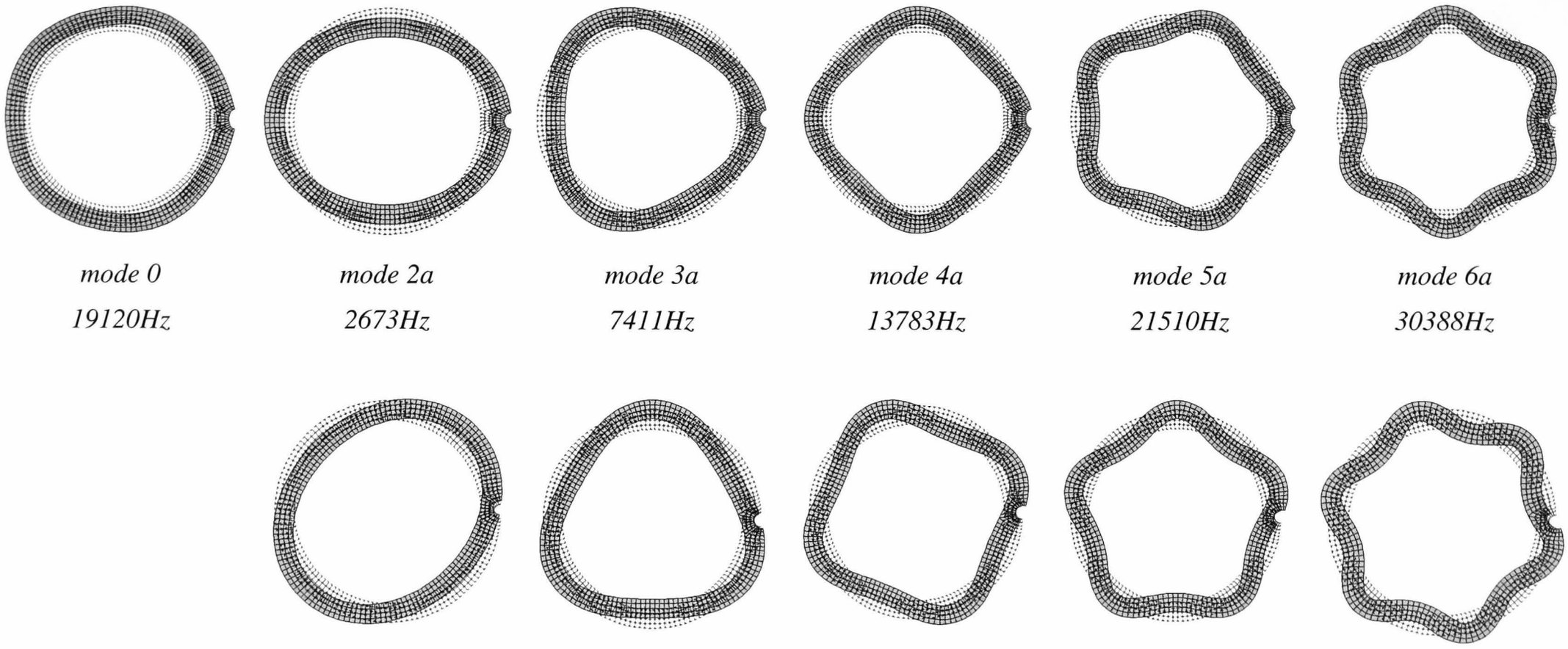

mode 0
19120Hz

mode 2a
2673Hz

mode 3a
7411Hz

mode 4a
13783Hz

mode 5a
21510Hz

mode 6a
30388Hz

mode 2b
2777Hz

mode 3b
7643Hz

mode 4b
14145Hz

mode 5b
21954Hz

mode 6b
30789Hz

Fig. 3.21 *Vibrational mode shapes associated with Model II*

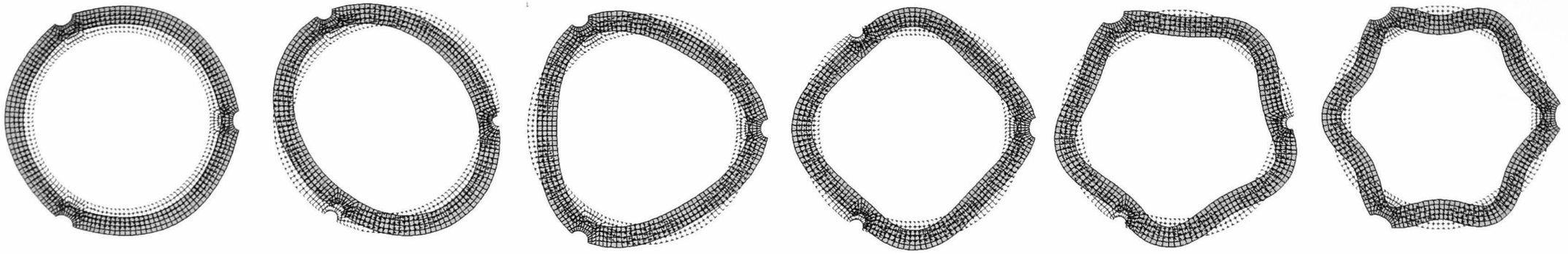

mode 0
18797Hz

mode 2a/b
2627Hz

mode 3a
6963Hz

mode 4a/b
13540Hz

mode 5a/b
21120Hz

mode 6a
29231Hz

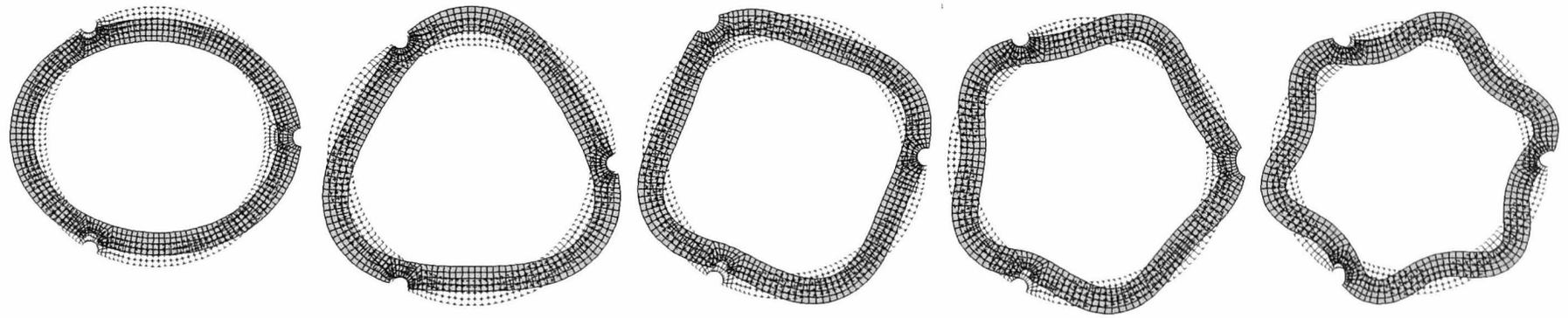

mode 2/b
2627Hz

mode 3b
7629Hz

mode 4a/b
13540Hz

mode 5a/b
21120Hz

mode 6b
30596Hz

Fig. 3.22 *Vibrational mode shapes associated with Model III*

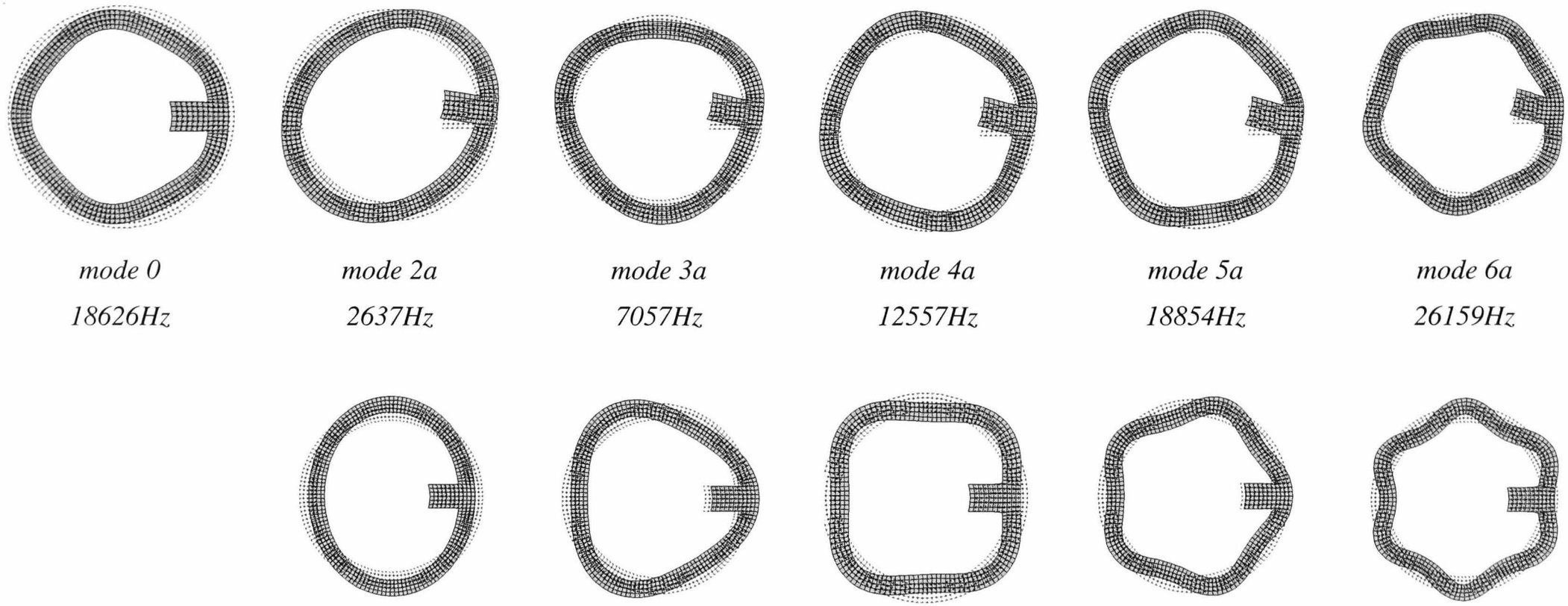

mode 0
18626Hz

mode 2a
2637Hz

mode 3a
7057Hz

mode 4a
12557Hz

mode 5a
18854Hz

mode 6a
26159Hz

mode 2b
2690Hz

mode 3b
7425Hz

mode 4b
13755Hz

mode 5b
21797Hz

mode 6b
30901Hz

Fig. 3.23 *Vibrational mode shapes associated with Model IV*

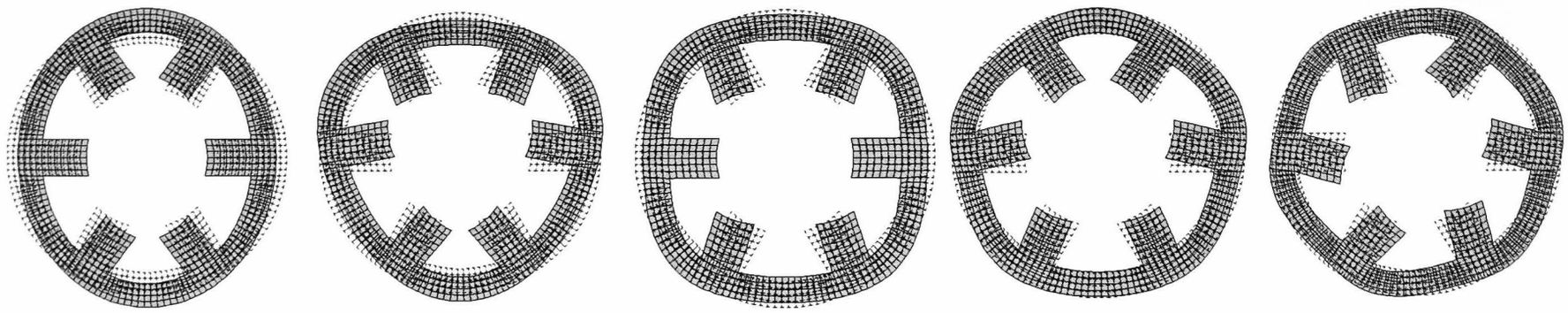

mode 2a/b
2250Hz

mode 3a
5267Hz

mode 4a/b
10010Hz

mode 5a/b
13297Hz

mode 6a
15407Hz

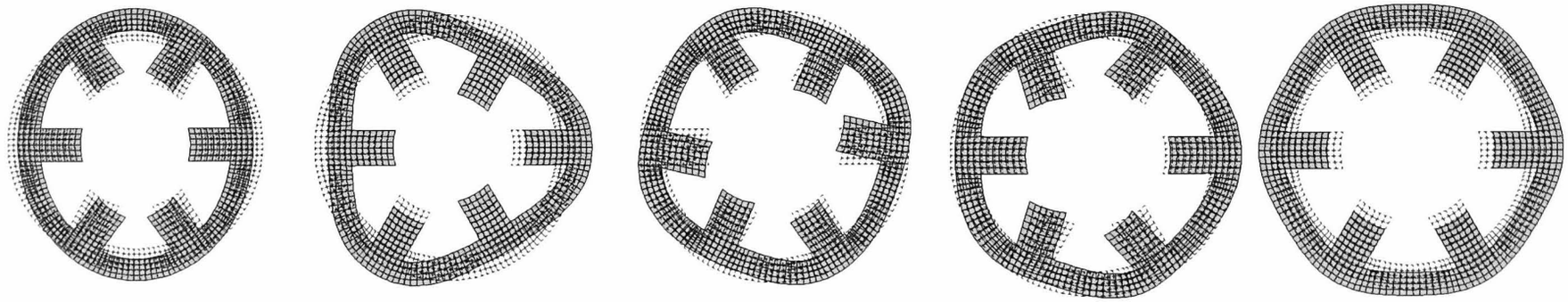

mode 2a/b
2250Hz

mode 3b
6584Hz

mode 4a/b
10010Hz

mode 5a/b
13299Hz

mode 6b
14847Hz

Fig. 3.24 *Vibrational mode shapes associated with Model V*

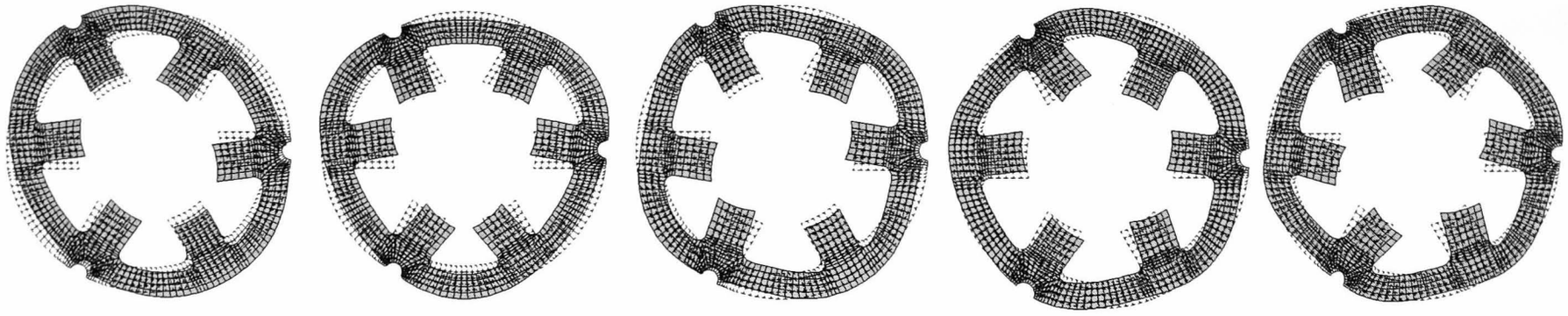

mode 2a/b *mode 3a* *mode 4a/b* *mode 5a/b* *mode 6a*

2335Hz *5389Hz* *10683Hz* *14303Hz* *17259Hz*

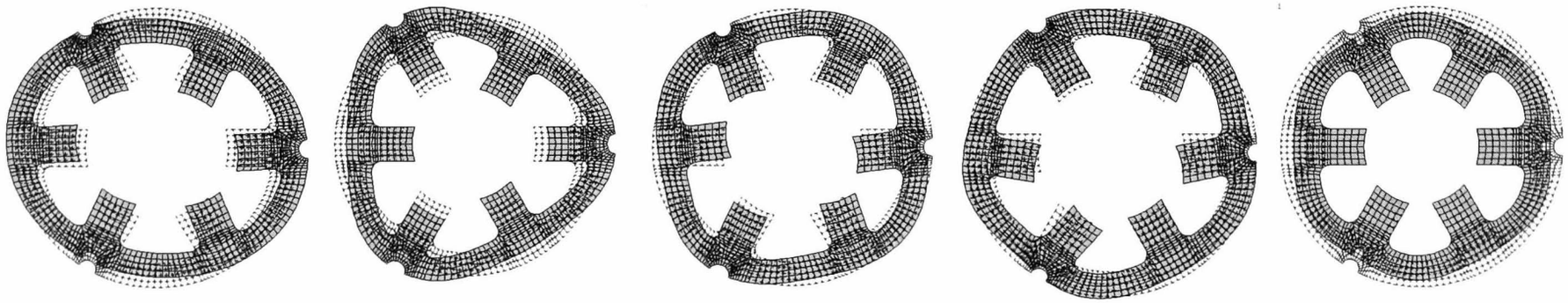

mode 2a/b *mode 3b* *mode 4a/b* *mode 5a/b* *Mode 6b*

2335Hz *7062Hz* *10683Hz* *14303Hz* *14146Hz*

Fig. 3.25 *Vibrational Mode shapes associated with Model VIa*

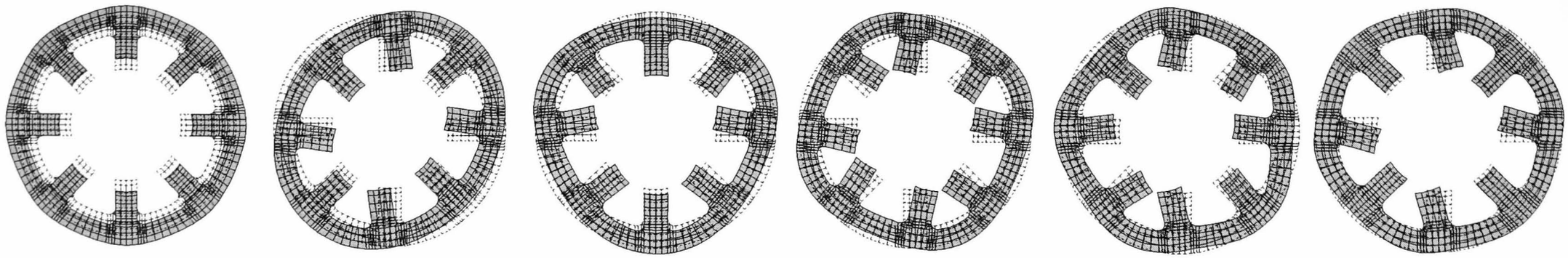

mode 0 *15320Hz*

mode 2a/b *2331Hz*

mode 3a/b *5963Hz*

mode 4a *8847Hz*

mode 5a/b *15509Hz*

mode 6a/b *18185Hz*

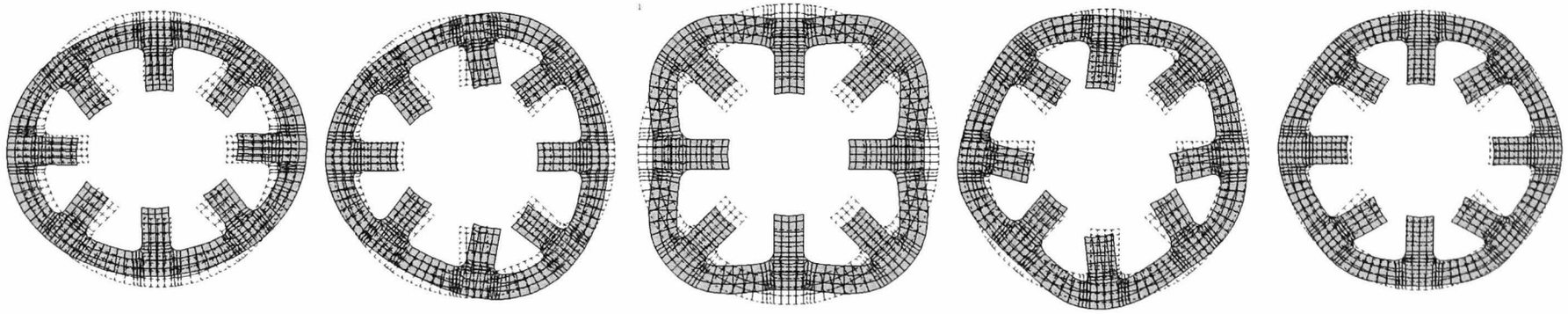

mode 2a/b *2331Hz*

mode 3a/b *5963Hz*

mode 4b *12948Hz*

mode 5a/b *15509Hz*

mode 6a/b *18185Hz*

Fig. 3.26 *Vibrational mode shapes associated with Model VII*

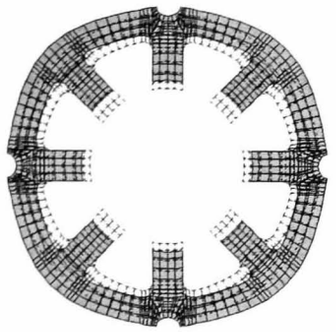

mode 0
14711Hz

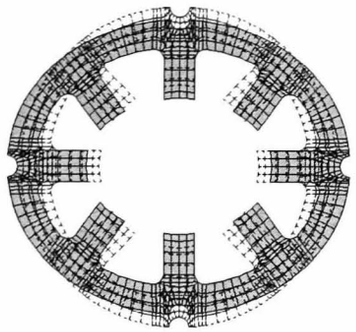

mode 2a
2209Hz

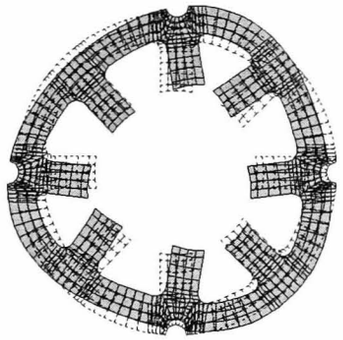

mode 3a/b
5830Hz

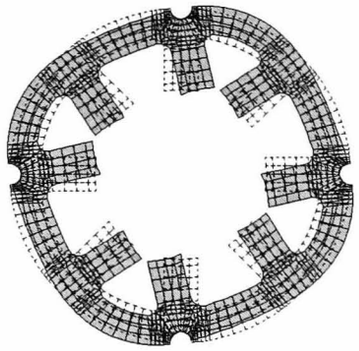

mode 4a
8782Hz

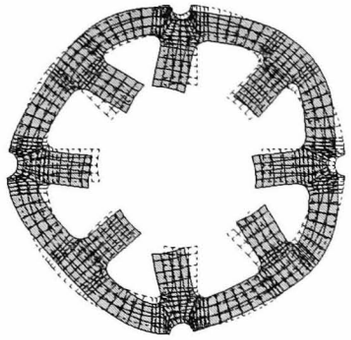

mode 5a/b
14838Hz

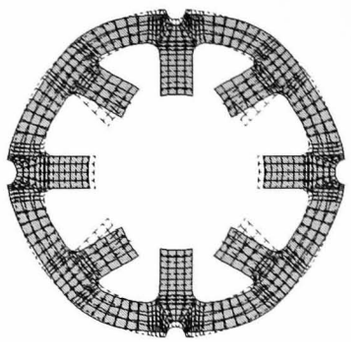

mode 6a
17365Hz

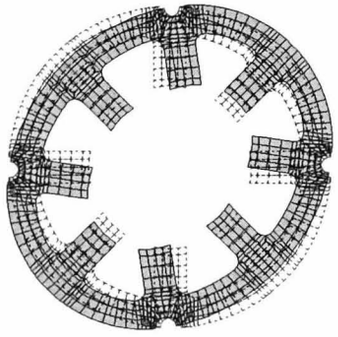

mode 2b
2330Hz

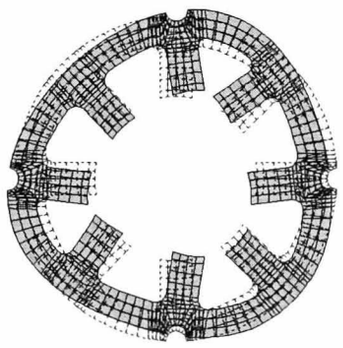

mode 3a/b
5830Hz

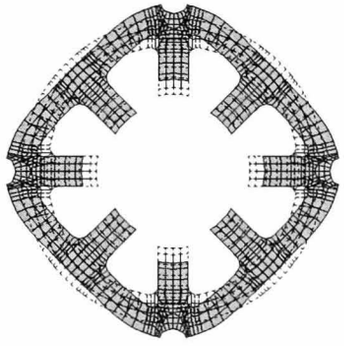

mode 4b
12076Hz

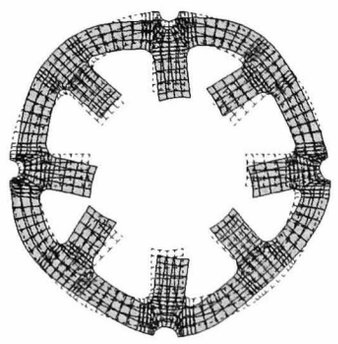

mode 5a/b
14838Hz

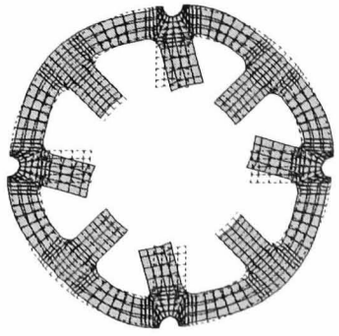

mode 6b
17871Hz

Fig. 3.27 *Vibrational Mode shapes associated with Model VIII*

Finite element analyses of model Ia yields two natural frequencies of equal value for each mode of vibration within the given frequency range, **Table 3.9**. However, for models II to VI, a number of pairs of natural frequencies associated with particular mode shapes differ significantly in value, **Tables 3.10 to 3.16**. These are referred to as dual resonances, [VER81a], two resonances occurring for a particular mode shape as a result of asymmetries in the physical model. However, previous authors, [VER81a] have only associated this with asymmetries which result during manufacture of a machine stator rather than actual asymmetries imposed by the design of the stator, such as poles, and any key-ways used for location of a stator into a frame. Furthermore, the different motions associated with the stator poles, as discussed later, has not previously been recognised, although it has been clarified that the designation of either of the two modes is arbitrary in the case of free vibration, and that the origin of the co-ordinates of one mode will be displaced from the reference mode by a quarter of a wavelength of the mode of vibration. The displacement of a quarter of a wavelength between the two frequencies can be observed in the mode shapes generated by ANSYS©, **Figs. 3.20 to 3.27**, although it is particularly clear for the vibrational modes associated with Model IV, **Fig. 3.23**. For Models II to VIa a number of asymmetries are clearly apparent in their geometry, and, therefore, it was expected that dual frequencies would be present, whereas the absence of any major asymmetries in Model Ia implies that all dual frequencies are equal. This was reported for a dc machine stator, [HAR56], for which two different natural frequencies exist for the mode whose number of half waves around the periphery of the stator is equal to the number of poles. This finding can be extended to account for features which introduce saliency, be it due to a pole or a notch, for example, whereby the part which exhibits a strong stiffness or a high mass is defined as the tooth and the other part is defined as the slot, [YON86], and the two frequencies are observed to characterise two types of waveshape, viz. symmetrical and anti-symmetrical about the reference. The two types of modes are associated with different energies, i.e., for the symmetrical mode the pole is in translational motion, while in the anti-symmetric mode it possesses a lateral 'rocking' motion. Thus, the frequencies previously referred to as dual resonances in [VER81a] exhibit the same characteristics as symmetric and anti-symmetric vibration modes, but such distinction was overlooked due to the minor asymmetries from which they were introduced. Such minor asymmetries in a structures cause a merely a few hertz difference to their corresponding frequencies, and therefore depending upon the resolution of the spectral analysis equipment may only appear as two minor peaks at the apex of one main frequency peak.

In general, if the model under consideration possesses cyclic symmetry, the cyclic symmetry number, S_n is defined as the number of times the symmetry repeats over 2π rads. The natural frequencies associated with each pair of symmetric and anti-symmetric circumferential vibration modes and multiples thereof in the range $0<n<S_n/2$ are identical. However, geometric and/or material asymmetries, as well as asymmetries in automatically generated finite element meshes and rounding errors in the finite element data, may result in two slightly different natural frequencies for each mode shape, [HAR56, YON86, VER81a, VER81b]. This is generally the case, irrespective of whether a full object finite element model or a cyclic symmetric finite element model is used. Thus, for the case of the annular ring with a single notch or a single pole, the cyclic symmetry number, S_n=1 and no symmetry exists, and two different natural frequencies result for each vibrational mode, **Tables 3.10 and 3.11.**

The dual frequencies for the annular ring with a single notch are apparent in the frequency spectra, **Fig. 3.13**. The first two dual frequencies in the spectra corresponding to vibrational modes 2 and 4, have values of 2696Hz and 2792Hz and 7468Hz and 7692Hz, respectively. This could easily be assumed to result merely from experimental error. However, inspection of the frequency response over a narrow frequency range confirms that two individual frequencies exist for each mode, viz. 2, 3 and 4, **Fig. 3.13**. Similarly, for the annular ring with three notches, the frequency spectra exhibits only a single value resonant frequency for modes 2 and 4, but two different values for mode 3, **Fig. 3.14**, for the reasons outlined earlier with regard to model asymmetries.

During early investigations on the vibrational behaviour of the stators of 3-phase induction machines, the stator teeth were treated purely as a mass, [ERD57], and later were considered to move as a solid body as part of the laminated core, [ELL71]. Subsequently, a number of publications considered the effect of the stator poles of electrical machines, but, again, these were restricted to 3-phase induction machines, [VER81a, VER81b, VER89a, VER89b, NOD87, WAT83, GIR79]. However, these papers recognised that the influence of the teeth was more significant than purely a mass-effect, owing to the fact that they were observed to be more influential on the natural frequencies of higher mode numbers, n. Consequently, the derivation of analytical formulae for the determination of natural frequencies treated the poles as cantilevers attached to the stator core, [VER89]. However, the influence of the poles on the symmetric and anti-symmetric mode types has not previously been addressed, although

dual frequencies have been observed, [NOD87]. As discussed earlier, the dual frequencies for the model comprising of a single pole are all different in value, and, therefore, both an anti-symmetric and symmetric mode shape is obtained for each of the vibrational modes, **Table 3.17**. In order to address the significance of the mass and stiffness of the poles and notches on the natural frequencies of a simple annular ring, the parameter, 'pole-ratio' defined as the square root of the ratio of the natural frequency of the model under investigation to the natural frequency of the simple annular ring, is introduced, **Table 3.17**. The pole-ratio for the symmetric type modes in **Table 3.17** is observed to increase slightly with circumferential modes, n, whereas for the anti-symmetric type a gradual decrease in pole-ratio is observed. The reduction in pole-ratio obtained for the anti-symmetric modes is similar to that observed in earlier studies made on the stator of a high power, 3-phase induction machine, [GIR79], for which no distinction was made between symmetric and anti-symmetric shapes and only one frequency was identified for each mode shape. The reduction in the natural frequency for the anti-symmetric mode shapes is attributed to the lateral vibration of the poles about the yoke, **Fig. 3.28(a)**, which results during vibration of the yoke, and increases the rotational inertia of the poles. The increased reduction in natural frequency for the higher circumferential modes n is attributed to the fact that the dimensions of the teeth become comparable to the wavelength of the higher frequencies, [GIR79], whilst more vibrational waves around the periphery means that the tangential movement of the yoke is more pronounced, hence enhancing the lateral movement of the poles. As discussed above, for a symmetric type mode the poles do not possess any lateral movement, purely a radial movement in sympathy to that of the ring motion as illustrated in **Fig. 3.28(b)**. The pole-ratio in **Table 3.17** would be expected to remain constant for all modes if the influence of the poles was purely a mass-effect. This is clearly not the case, and the increase of the pole-ratio for increasing n for the symmetric modes shows that the stiffness is more influential for the higher symmetric modes. For a pure mass-effect, the natural frequencies obtained for the annular ring can be adjusted accordingly by varying the mass density factor, equation (3.4), such that the frequency of Model IV is given by equation (3.5). The effective masses of the respective models are given in **Table 3.18**, together with the effective mass densities assuming such mass is lumped within the annular ring, Model I, and a mass density factor of 0.96 is obtained for Model IV from equation (3.4). However, the mass density factor is in good agreement to that of the pole-ratio of lower modes, derived from the FE analyses, **Table 3.17**, and shows that for low vibrational modes, in the case of a single pole, that the mass-effect dominates the

symmetric vibration mode. The influence of the pole upon the breathing mode, $n=0$, is also dominated by the mass effect in the case of a single pole, although it should be noted that this is a special case in that it only exhibits a symmetric mode, as observed in **Figs. 3.23 to 3.27**, in which the poles only exhibit radial motion.

Table 3.17 *Comparison of 2D predicted natural frequencies of models I, IV and V, for m=0*

Vibration mode, *n*	2D FEA			2D FEA		
	Model Ia	Model IV	Pole-ratio*	Model Ia	Model V	Pole-ratio*
0	19333	18626	0.96	19333	14847	0.77
2a	2776	2637	0.95	2776	2250	0.81
2b	2776	2690	0.96	2776	2250	0.81
3a	7650	7057	0.92	7650	5267	0.69
3b	7650	7425	0.97	7650	6548	0.86
4a	14170	12557	0.89	14170	10010	0.76
4b	14170	13755	0.97	14170	10010	0.76
5a	22011	18854	0.86	22011	13297	0.60
5b	22011	21797	0.99	22011	13299	0.60
6a	30892	26159	0.85	30892	15407	0.50
6b	30892	30901	1.00	30892	----	----

$$^{*}\ Pole\text{-}ratio = \sqrt{\frac{Natural\ frequency\ of\ Model\ IV}{Natural\ frequency\ of\ Model\ I}}$$

(a) **(b)**

Fig. 3.28 *Symmetric and anti-symmetric vibration modes;* **(a)** *anti-symmetric mode,* **(b)** *symmetric mode*

$$\text{mass density } factor = \sqrt{\frac{\text{Annular ring mass density}}{\text{Effective annular ring mass density}}} \tag{3.4}$$

$$frequency_{pole} = frequency_{ring} \times \text{mass density factor} \tag{3.5}$$

Table 3.18 *Mass applied to annular ring and effective annular ring density*

	Model Ia	Model II	Model IV	Model V
Mass, kg	0.7955	0.7909	0.8641	1.2067
Density of Model Ia, kgm^{-3}	7800	7731	8447	11796

The same analysis can be applied to that of the annular ring with six poles, Model V, which not only yields symmetric and anti-symmetric mode types, but also a combination of the two, for the reasons discussed earlier regarding geometric asymmetries. It is observed that all the natural frequencies of the ring reduce with the addition of the poles, **Table 3.17**, and that those associated with the symmetric type show the least reduction, whereas those associated with the anti-symmetric type show the greatest reduction. The influence of 6-poles on the natural frequencies is greater than that of a single pole, and the reduction in frequency for increasing n is also more significant than for the case of a single pole. Furthermore, a mass-factor of 0.81 is calculated from equation (3.4), from which it is clear that the influence of the poles is more significant than purely a mass-effect for the circumferential modes, n.

In order to account for the addition of stator poles to the annular ring, modification factors have been derived for the classic annular ring equation for the two extreme mode types, viz. symmetric and anti-symmetric, [HAR56], equations (3.6) and (3.7) respectively, where M_p is the total pole mass, M_r is the mass of the annular ring and I_{pl} is the inertia of one pole, equation (3.8), where h is the pole height and l_t is the axial length of the poles. However, these modification factors are generally inaccurate, in that they predict natural frequencies for the symmetric modes which are lower than those of the anti-symmetric modes, whereas in practice the frequencies of the symmetric modes are higher. This is due to the fact that only the kinetic energy associated with the mass of the poles is accounted for, the associated potential energy, which relates to the stiffness induced by the poles, being neglected. Thus, analytical methods for determining the natural frequencies of SR machine stators are inherently highly complex, and far less accurate for predicting natural frequencies compared to the FE method. Nevertheless, the analytical equations, based on the different energies associated with the symmetric and anti-symmetric vibration modes, and for which, both modification factors are 1 when no poles are present, i.e. without poles, $f_{na} = f_{ns}$, have been applied to predict the natural frequencies, **Table 3.19**.

$$f_{ns} = \sqrt{\frac{1}{1+\frac{2n^2}{n^2+1}\frac{M_p}{M_r}}} \tag{3.6}$$

$$f_{na} = \sqrt{\frac{1}{1+\frac{n^5}{n^2+1}\frac{4I_{p1}}{M_r r^2}}} \tag{3.7}$$

$$I_{p1} = \frac{h^3 l_t}{12} \tag{3.8}$$

Table 3.19 *Application of analytical modification factors*

Mode, n	2D FE Ring (Hz)	Modification factor, f_{ns} f_{na}	6-poles Using Modification (Hz)	2D FE 6-poles (Hz)
3a	7650	0.999=f_{na}	7644	5267
3b	7650	0.720= f_{ns}	5506	6548
6a	14170	0.993= f_{na}	14064	15407
6b	14170	0.706= f_{ns}	10005	14847

For the case of the annular ring with a single notch, Model II, the pole-ratio is observed to decrease with increasing n for the symmetric mode type, whereas for the anti-symmetric mode, a gradual increase in the pole-ratio is observed, **Table 3.20**, which is opposite to what was observed for an annular ring with a single pole. However, this is expected, since for the case of a notch, the yoke is essentially treated as the pole and the notch as a slot, [YON86]. Furthermore, similar to that of the influence of the poles, it is observed that the natural frequencies of the anti-symmetric modes are influenced more by the addition of a notch than the symmetric modes.

The influence of asymmetries is on the frequency range over which the dual frequencies are separated. It is observed in **Table 3.20**, that for the case of an annular ring with a single notch, this is effectively a minor asymmetry, such that, the existence of dual frequencies due to manufacturing asymmetries, as a result of machining tolerances, for example, are likely to be indistinguishable. It is, therefore, concluded that the presence of the poles is detrimental in terms of acoustic noise and vibration, not only due to the additional modes which are induced by the asymmetry, but also due to the lowering of the natural frequencies that can potentially introduce additional mode shapes within the audible frequency range, **Fig. 3.24**. Consequently, this increases the likelihood of

harmonics in the exciting force coinciding with the natural frequencies of the stator, whereas the notches only introduce additional modes due to the asymmetry.

Table 3.20 *Comparison of predicted natural frequencies of models I and II, for m=0*

Vibration mode, *n*	2D FEA		
	Model Ia	Model II	Pole-ratio*
0	19333	19120	0.989
2a	2776	2673	0.963
2b	2776	2777	1.000
3a	7650	7411	0.969
3b	7650	7643	0.999
4a	14170	13783	0.972
4b	14170	14145	0.998

$$^{*}Pole\text{-}ratio = \sqrt{\frac{\text{Natural frequency of Model II}}{\text{Natural frequency of Model I}}}$$

At this stage it is interesting to consider the cyclic symmetry of the 6-pole and 8-pole stator cores and compare their geometric asymmetries. **Table 3.21** compares the 6-pole and 8-pole stators with and without their associated notches, (3 notches for the 6-pole stator and 4 notches for the 8-pole stator). The cyclic symmetry number S_n is 6 for Model V, and, therefore, the modes which yield two individual natural frequencies are modes 3 and multiples thereof, **Fig. 3.24**. The addition of the three notches, Model VIa, lowers the cyclic symmetry number S_n to 3, **Fig. 3.25**. However, due to the fact that there is no such mode as 1.5, the mode shapes which yield two natural frequencies are the same as those when the notches are omitted, Model V. For the 8-pole stator, Model VII, $S_n=8$, and, therefore, dual frequencies occur for modes 4 and multiples thereof, **Fig. 3.26**. However, the addition of 4 notches, Model VIIIa, lowers S_n to 4, and, therefore, modes 2 and multiples thereof yield dual frequencies, **Fig 3.27**, thus increasing the likelihood of resonant frequencies coinciding with the frequency of the exciting forces. Therefore, it would be more beneficial to manufacture an 8-pole stator with 8-notches such that it maintains $S_n=8$, as the mass/stiffness influence of the notches is minimal, as outlined earlier, and reducing the number of dual frequencies is relatively important. Furthermore, it should be noted, as discussed in Chapter 1, that the electromagnetic excitation forces within SR machines are symmetrical, and, therefore, assuming zero air-gap eccentricity, only the even modes that characterise the pole movements in **Figs. 3.29(a) & (b)** are of significance to noise production, whereas the odd modes that characterise the pole movements shown in **Figs. 3.29(c) & (d)** are not particularly relevant. This implies that, within the frequency range of interest, only four of the natural frequencies of the 6-pole

stator core can potentially coincide with the excitation force of the experimental 6/4 machine, whereas there are six natural frequencies for the 8-pole stator core. Thus, a 6-pole stator core is a more appropriate design in terms of low levels of noise and vibration.

For the solid mild steel stator, Model VIa, the addition of the fillet radii between the pole roots and the stator yoke compensate for the reduction in stiffness induced by the notches. This is due to the fact that although the addition of the notches to Model V would be expected to lower the natural frequencies even further, in fact the natural frequencies are observed to increase, **Table 3.21**, as a result of the enhanced stiffness at the pole roots, Model VIa.

A summary of the natural frequencies predicted by 2D analyses of all the models considered is given in **Table 3.22** together with the associated cyclic symmetry number of the various models.

Table 3.21 *Summary of 2D predicted natural frequencies for the 8-pole stator together with those for the 6-pole stator, for the modes m=0*

Mode, n	Model V	Model VIa	Model VII	Model VIIIa
0	14847	14646	15320	14711
2	2250	2335	2331	2209
2	2250	2335	2331	2330
3	5267	5389	5963	5830
3	6548	7062	5963	5830
4	10010	10683	8847	8782
4	10010	10683	12948	12076
5	13297	14303	15509	14838
5	13299	14303	15509	14838
6	15407	17259	18185	17365
6	*	*	18185	17871
Cyclic symmetry number, S_n	6	3	8	4

Table 3.22 *Summary 2D predicted natural frequencies for m=0*

Mode, *n*	Model Ia	Model II	Model III	Model IV	Model V	Model VIa
0	19333	19120	18797	18626	14847	14646
2	2776	2673	2627	2637	2250	2335
2	2776	2777	2627	2690	2250	2335
3	7650	7411	6963	7057	5267	5389
3	7650	7643	7629	7425	6548	7062
4	14170	13783	13540	12557	10010	10683
4	14170	14145	13540	13754	10010	10683
Cyclic symmetry number, S_n	infinite	1	3	1	6	3

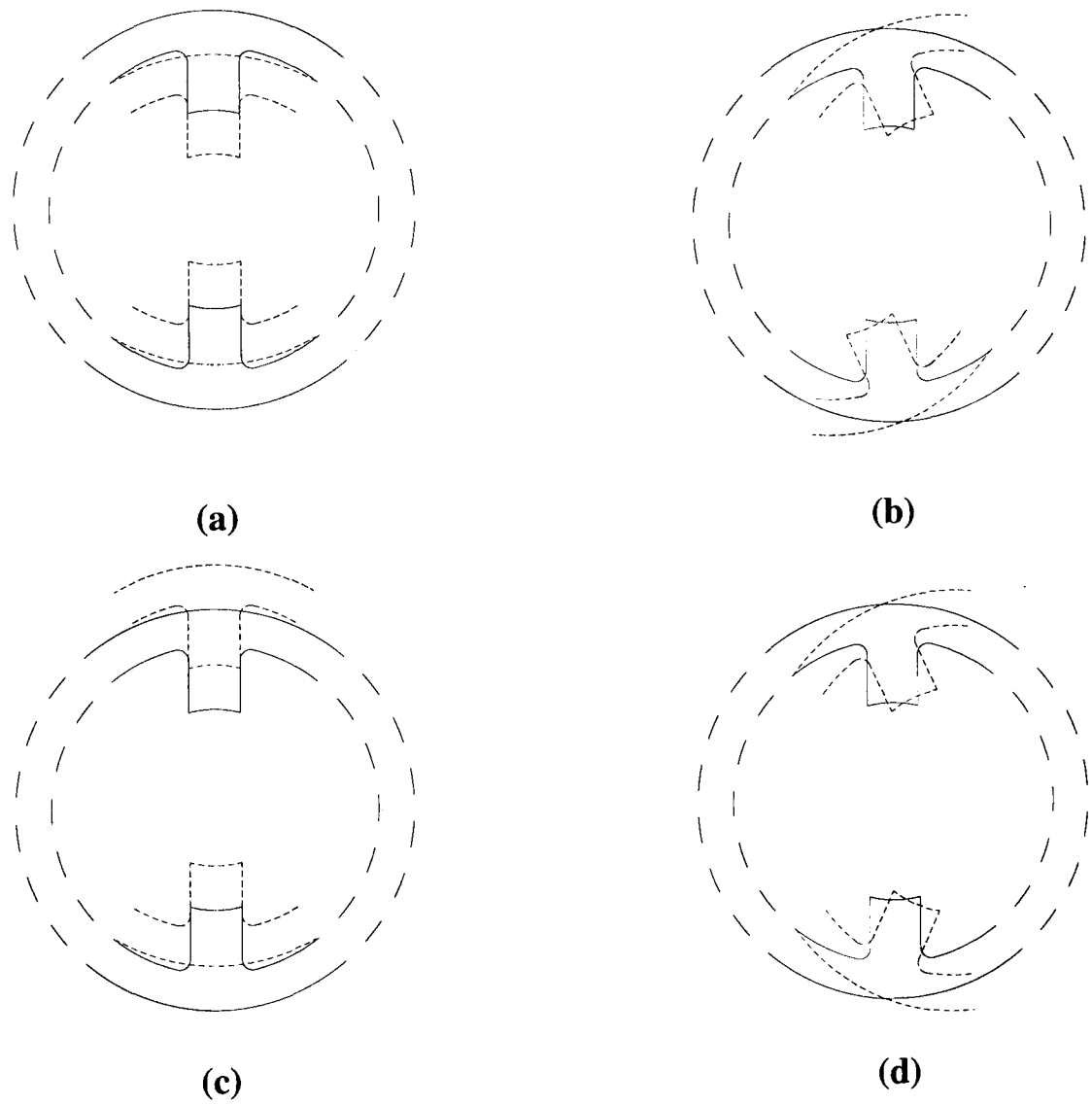

Fig. 3.29 *Pole movement associated with even mode numbers* **(a)** *&* **(b)** *and with odd mode numbers* **(c)** *&* **(d)**

3.5 Influence of geometric dimensions

It is well established that the larger the stator diameter the lower will be the natural frequencies, and that the influence of the stator core length on axial mode 0 of the stator is negligible, except in the case when a frame is used which has a different axial length to that of the core and/or the stator has substantial end-plates. To evaluate the influence of the stator yoke thickness on the natural frequencies, the yoke thickness of Models Ia and V was varied from 50% to 150% of the original value. This was achieved by changing the outside diameter of both Models, whilst maintaining the inside diameter constant. The natural frequencies of Model Ia for all modes $n \geq 2$ were observed to increase significantly with an increase in the yoke thickness, whereas that of mode 0 was observed to gradually reduce, **Fig. 3.30**. The increase in frequency was greatest for the lower mode numbers. For example, an increase in yoke thickness of 50% causes the natural frequencies of modes 2, 3, and 4 to increase by 35%, 31%, and 28%, respectively. The rate of increase of the natural frequencies of modes $n \geq 2$ reduces with further increases in yoke. It is well known [YAN81] that the natural frequency of modes $n \geq 2$ of an annular ring is approximately proportional to its thickness and inversely proportional to the mean radius, as will be evident from equations (3.9) in which $f_{n=0}$ is defined by equation (3.10), i by equation (3.11a) and ϕ_m is defined by equation (3.11b) for the case of an annular ring, where h and r are the yoke thickness and mean radius, respectively.

For mode 0, it is apparent from equation (3.10) that the natural frequency is inversely proportional to the mean radius and independent of the thickness of the yoke, although it should be noted that the mean radius is a function of the yoke thickness. However, for a thick annular ring, [KIR76], whose cross-section exhibits extension, transverse shear and rotational inertia effects, although the influence of the extension is usually negligible, the transverse shear causes rotation against its neutral layer and the shear strain of the cross-section, which contributes to both mass and stiffness effects, but whose modifying effect is essentially the same as a mass increase. The rotational inertia energy also contributes to the mass effect. However, its effect is small compared with that of the transverse shear. Consequently, the natural frequency tends to reduce, compared with that of a thin ring, as the thickness is increased.

The natural frequencies obtained for mode 2 assuming that the yoke thickness incurs only a mass effect, are shown in **Table 3.23**. It will be observed that the natural

frequency values are underestimated for a reduction in yoke thickness and overestimated for an increase in yoke thickness. The derivation of equation (3.2) which is cited in section 3.2.2 for modes $n \geq 2$ is based on an infinitely thin annular ring, whereas equation (3.9), cited below is based on an annular ring comprising of a finite thickness. The natural frequency values calculated from equation (3.9) are plotted in **Fig. 3.31** for the same variation in yoke thickness as was considered in the preceding 2D FE analyses, together with those computed for an infinitely thin annular ring, equation (3.2). It will be seen that that neglect of the thickness of the ring results in an over-estimation of the natural frequencies for increasing yoke thickness and circumferential mode shape, whereas when the ring thickness is taken into account the predicted natural frequencies agree well with those obtained from finite element analysis, **Fig. 3.30**.

Table 3.23 *Influence of pure mass-effect*

Percentage of original yoke thickness	Mass (kg)	Mass-factor	Mode 2 (Mass)	Mode 2 (FEA)
50%	0.3800	0.478	1327	1547
75%	0.5842	0.734	2038	2199
100%	0.7955	1	2776	2776
125%	1.0208	1.283	3562	3286
150%	1.2530	1.575	4372	3736

$$f_{n\geq 2} = \frac{f_{n=0} i n\left(n^2-1\right)\phi_m}{\sqrt{n^2+1}} \tag{3.9}$$

$$f_{n=0} = \frac{1}{2\pi}\sqrt{\frac{E}{\rho r^2}} \tag{3.10}$$

$$i = \sqrt{\frac{1}{2\sqrt{3}}}\frac{h}{r} \tag{3.11a}$$

$$\phi_m = \left[1+\frac{i^2\left(n^2-1\right)\left(5n^2+3\right)}{n^2+1}\right]^{-\frac{1}{2}} \tag{3.11b}$$

The effect of varying the yoke thickness of model V, is shown in **Fig. 3.32**, an increase of 50% of the original yoke thickness, increasing the natural frequencies for modes 2, 3a, 3b, 4, and 5 by 42%, 41.9%, 37%, 35%, and 29%, respectively. Thus, an increase in yoke thickness has a significantly greater influence on the natural frequencies when the

poles are present. However, the natural frequency of mode 6b does not follow the expected trend in that it decreases in value after reaching a maximum value at a yoke thickness of around 8mm.

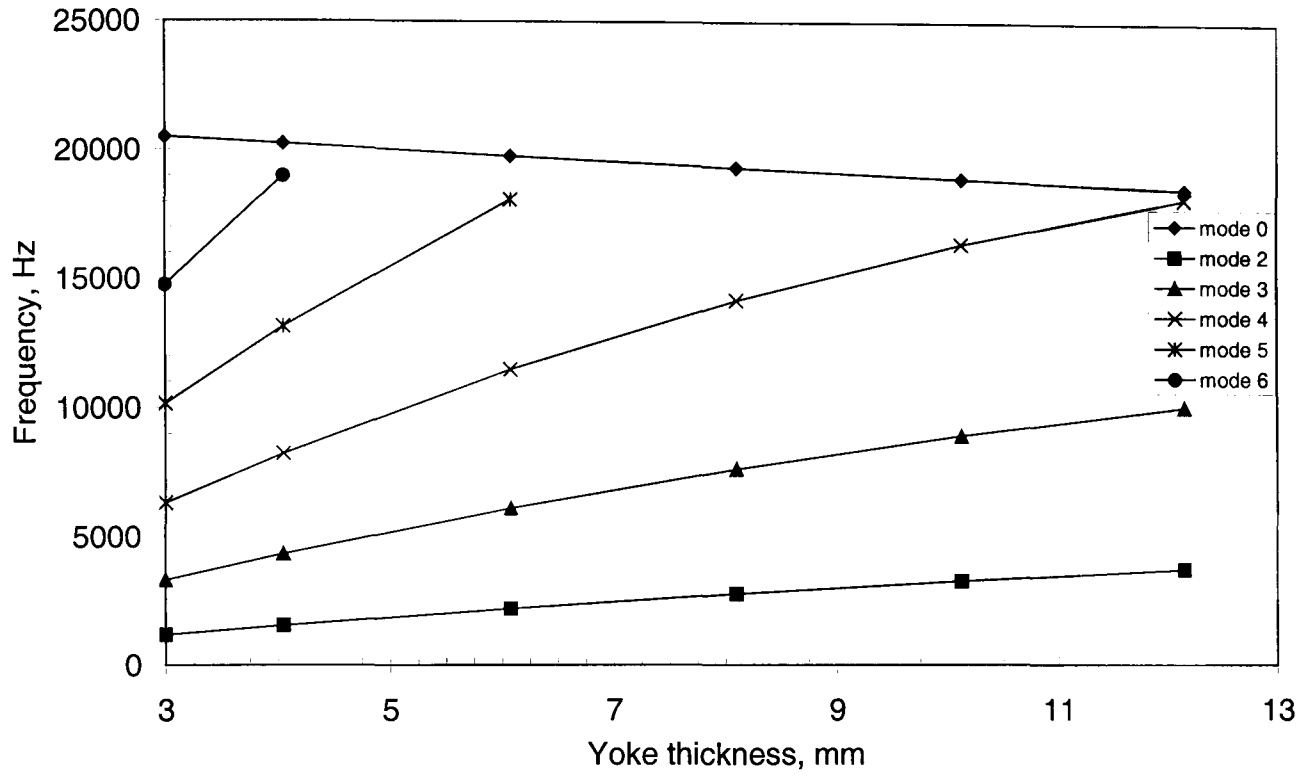

Fig. 3.30 *Effect of variation of yoke thickness, Model Ia*

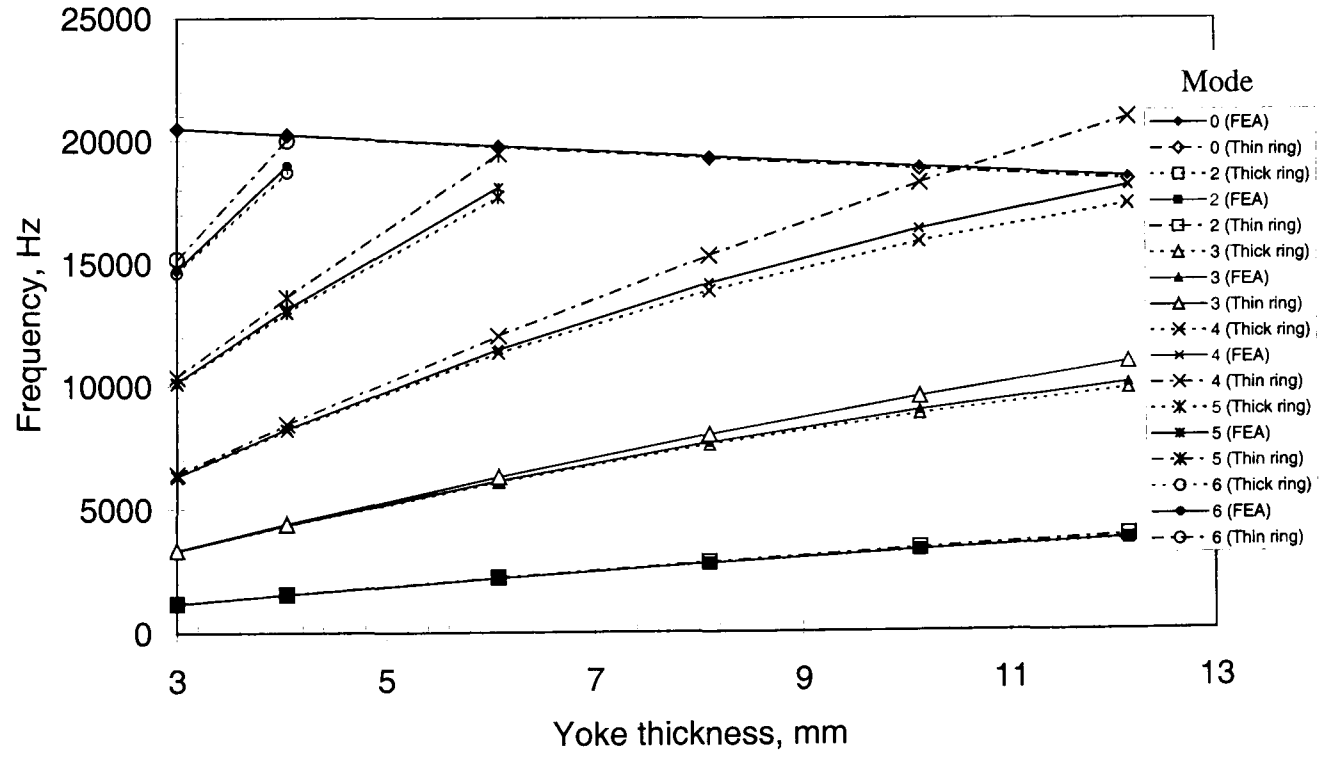

Fig. 3.31 *Effect of variation of yoke thickness, Model Ia*

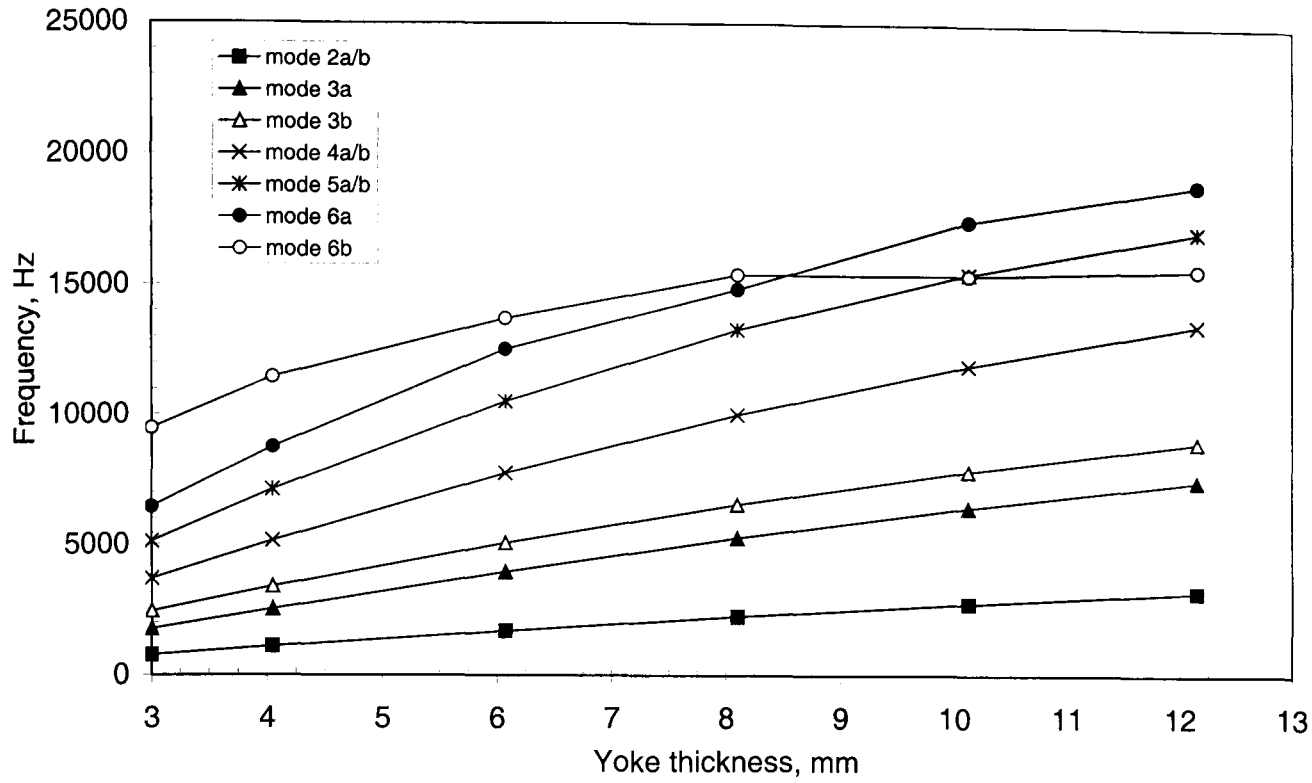

Fig. 3.32 *Effect of variation of yoke thickness, Model V*

In order to investigate the influence of the poles further, the pole width of Model V was varied between 50% and 150% of the value employed in the experimental SR machine. As will be seen in **Fig. 3.33**, the natural frequencies of modes 3 and 6, which are associated with dual frequencies, are observed to be more sensitive to changes in pole width than those for modes 2, 4 and 5 with which only single frequencies are associated. This is expected from a consideration of the influence of the poles on an annular ring as discussed earlier.

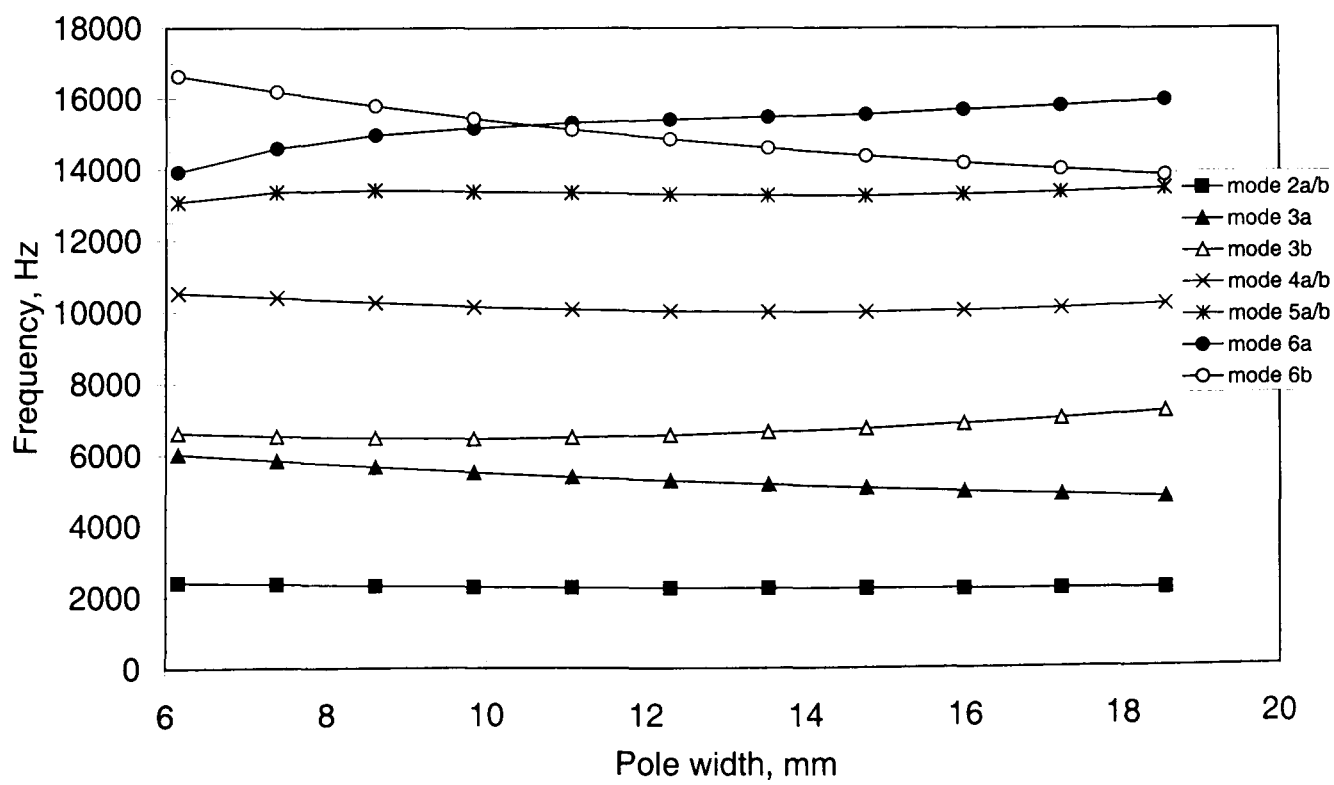

Fig. 3.33 *Effect of variation of pole width, Model V*

A 2D FE investigation was undertaken on Model VIa to quantify the influence of varying the fillet radius from 50% to 150% of that in the experimental machine. however, it showed negligible influence on the natural frequencies, **Fig. 3.34**. The slight increase is attributed to the increased stiffness at the pole root, but it is interesting to note that the fillets are most influential on the frequency of mode 6b, for which no lateral rocking of the poles occurs. Therefore, little benefit would be gained by increasing the fillet radii, since this would compromise the available copper area.

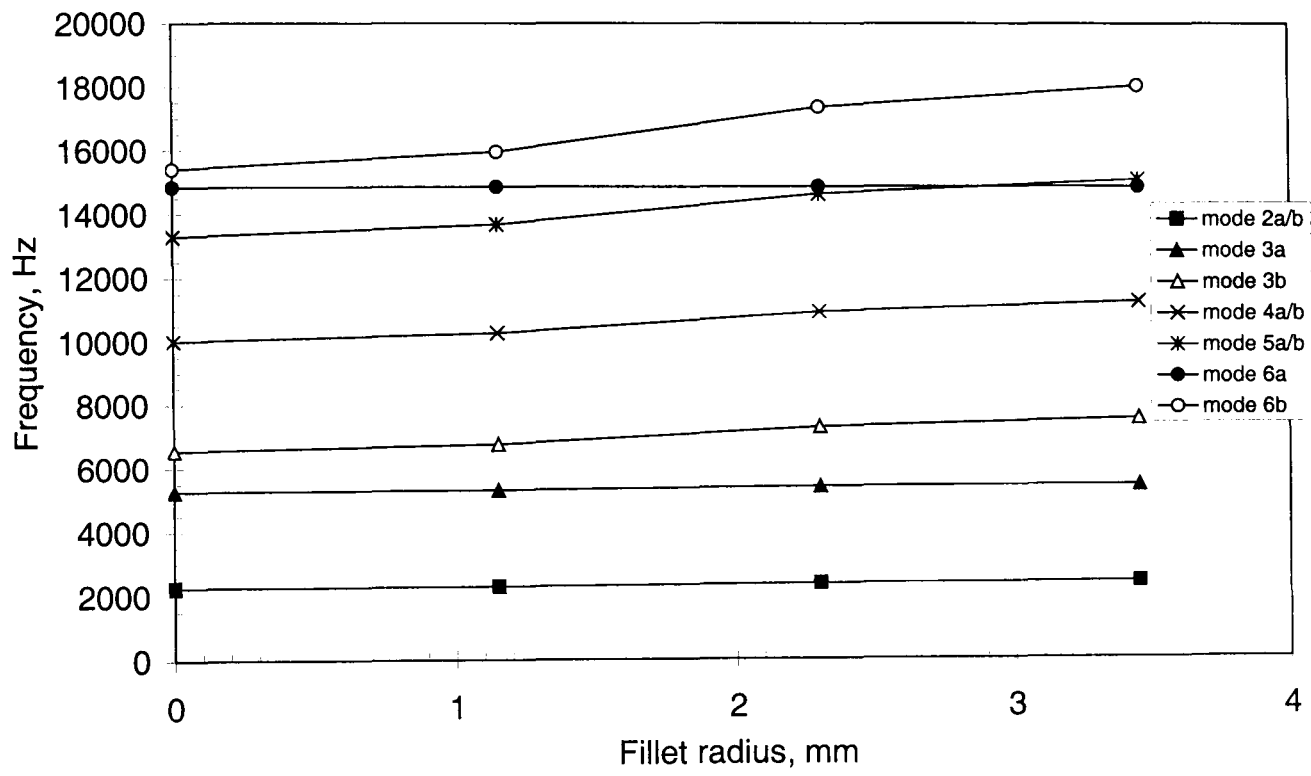

Fig. 3.34 *Effect of variation of fillet radius, Model VIa*

3.6 Influence of laminations

Up to now, the investigations which have been reported in this chapter have, been on solid mild steel models. The stator of the experimental SR machine is constructed from a 0.35mm silicon steel (grade M300-35A) laminations, Model VIb, for which effective material properties need to be deduced to enable subsequent 3D analyses taking due account of the windings and frame.

A limited number of investigations have been reported on the influence of laminated structures with respect to the natural frequencies of electrical machine stators, [GIR79, WAT83, GAR89, WAN97], all of which have been on relatively large 3-phase induction machines. They concluded that treating a laminated stator core as a solid material with isotropic properties was adequate, and that the derivation of complex material properties for the laminated core was not justified, [GIR79], although this was based on a short axial length machine with respect to the stator diameter. A subsequent study was based on two different sized induction motors, [WAT83], one of which was constructed from a segmented laminations due to its physical size. The influence of the clamping pressure was found to be almost negligible on the in-plane modes, and despite the stiffer construction of the segmented core motor it showed no appreciable difference compared to the other motor. A more recent investigation employed an experimental procedure to determine the variation of the modulii of compression and shear in terms of the clamping pressure, with conclusive evidence that a laminated core is more flexible than its solid counterpart, and generally exhibits higher levels of internal damping. Both modulii were observed to increase with clamping pressure, and it was predicted that the values would double for laminations of twice the thickness, [GAR79].

The most recent study involved a systematic investigation into the influence of laminated cylinders, [WAN97], from a single lamination up to a stack comprising of four laminations with a minimum sheet thickness of 7.125mm. It treated the laminated cylinder as a solid homogeneous cylinder with an effective density to account for the lamination stacking factor in the FE analysis. However, it resulted in errors up to 23% in the predicted natural frequencies of the in-plane modes over the frequency range 0-6.4kHz. The transverse vibrations, however, were influenced greatly by all variables to such an extent that the errors incurred for the in-plane modes were considered negligible, since for induction machines many transverse modes are equally as important as the in-plane modes as regards noise production in induction machines due to the skewing

which is inherent in their construction. As a result, it was concluded that the natural frequencies of the in-plane modes are unaffected by the lamination thickness and the clamping pressure. Due to the absence of skew, only the in-plane modes are important for noise production in SR machines, and, therefore, potential errors up to 24% would be unacceptable. Furthermore, the investigation, [WAN97], only considered laminated cores having a low number of laminations, the thickness of which was unrealistically high, such that the natural frequencies could be dominated by a single lamination. However, the laminations employed for the 6-pole and 8-pole experimental SR stator cores are only 0.35mm thick. Thus, with an overall stack length of 46.9mm, the ratio of the lamination thickness to the stack length is ≈0.007, which compares to 0.25 for the induction machine, which was the subject of the earlier investigations, [WAN97].

3.6.1 Initial investigation on laminated annular ring

It is evident from the literature that the elastic nature of a laminated core is relatively complex compared with its solid counterpart, since it is no longer isotropic and homogeneous, and can be considered as having non-linear material properties perpendicular to the plane of the laminations, **Fig. 3.35**. In order to quantify the difference between a solid and laminated core, Model Ia was also constructed from a stack of laminations of the same material as that which was employed for the 6-pole stator lamination stack. In the investigations which were undertaken by Wang and Garvey, [WAN97, GAR79], the laminations were held together by controlled air pressure and bolts, respectively, whereas the laminations of Model Ia were held together by four equi-spaced welds down the axial length of the stack, **Fig. 3.36**. Clearly, the method employed for fabricating a laminated stack adds further complexity to the vibrational behaviour of a laminated structure.

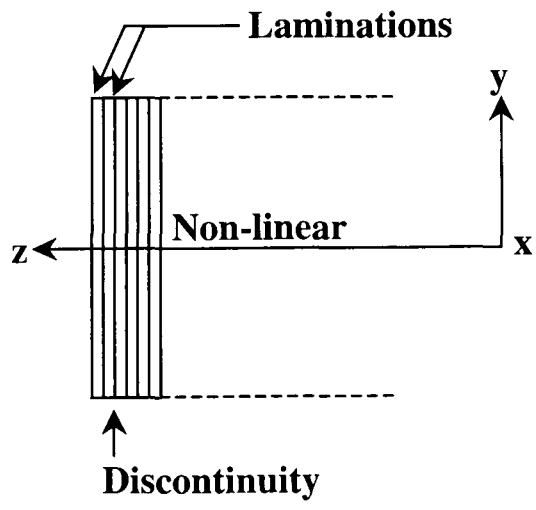

Fig. 3.35 *Schematic of non-homogeneous laminated ring*

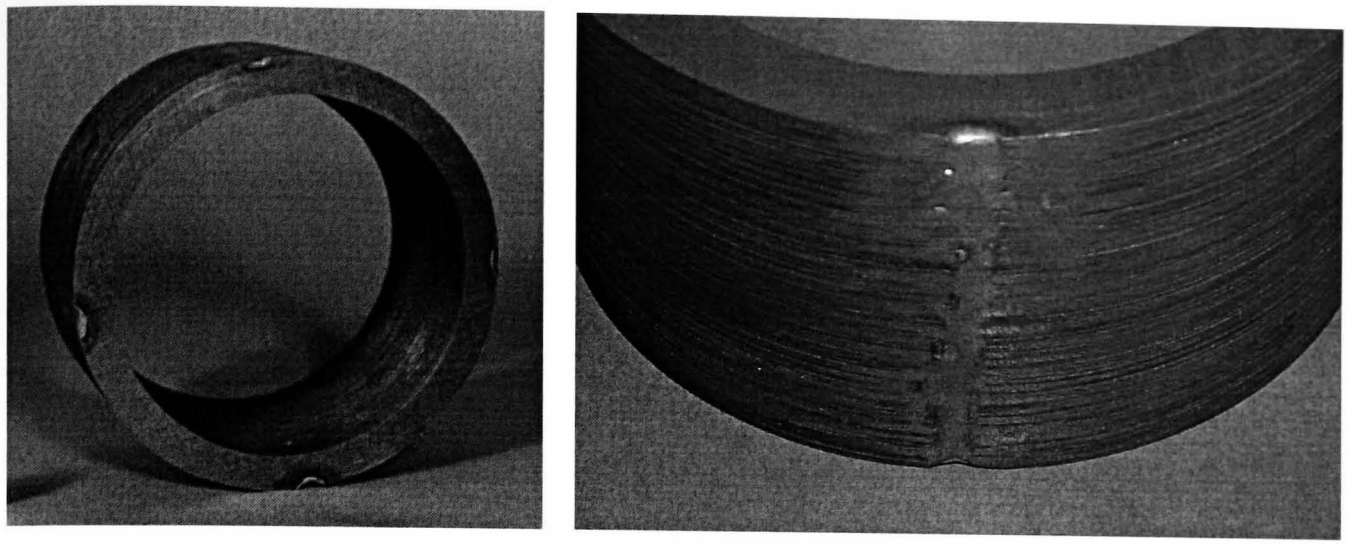

Fig. 3.36 *Laminated ring with associated weld for maintaining the lamination stack*

Initially, the natural frequencies of the laminated ring were predicted using a 3D FE model, which treated the ring as a solid homogeneous structure, by employing published material properties for the material used for the laminated cores, viz. M300-35A, *FEA1*, **Table 3.24**. In addition, impulse tests were employed to measure the natural frequencies of the experimental laminated ring, model Ia. Subsequently, since only the circumferencial modes (*m=0*) are of relevance to noise generation in SR machines and many authors have noted that these are not influenced by the laminated nature of the cores of induction motors, [GIR79, WAN97], the density which was assumed for the solid model was adjusted to account for the packing factor of the experimental laminated ring, *FEA2*, **Table 3.24**. This was achieved by applying of equation (3.12), to account for the packing factor, thereby defining effective material properties, *FEA2*.

$$FEA2 = FEA1 \times \sqrt{\rho_{old} / \rho_{new}} \tag{3.12}$$

Table 3.24 *Material properties*

Property	Solid M300-35A (*FEA1*)	Solid M300-35A* (*FEA2*)
ρ (kgm^{-3})	7650	7305
$E_x = E_y = E_z$ (GPa)	215	215
G_{xy} (GPa)	82.7	82.7
$G_{xz} = G_{yz}$ (GPa)	82.7	82.7
$\nu_{xy} = \nu_{xz} = \nu_{yz}$	0.3	0.3

**Density based on experimental laminated ring, i.e. actual density, taking account of packing factor*

Table 3.25 *Comparison of predicted natural frequencies (Hz) for laminated ring*

Mode	Measured	Solid Transil (*FEA1*)		Solid Transil* (*FEA2*)	
n	Laminated Ring	3D FEA	2D FEA	3D FEA	2D FEA
2a/b	2688	2907	2836	2974	2902
3a/b	7424	8059	7813	8247	7995
4a/b	13760	15025	14469	15376	14807

**Density of experimental laminated ring, i.e. actual density*

The natural frequencies predicted from *FEA1* and *FEA2*, **Table 3.25**, suggest that the influence of laminating a core is more complex than purely a mass density effect. It will be observed that simply employing the actual density of the laminated ring, *FEA2*, results in a greater error in the predicted natural frequencies than those derived by assuming the density for the lamination material alone, **Table 3.25**. The material properties for *FEA1* assume a packing factor of 1.0, whereas *FEA2* takes account of the true packing factor of the experimental laminated ring, and, therefore, is a better physical representation than that of *FEA1*. The natural frequencies are expected to become worse with account of the packing factor since, $\omega_n \alpha \sqrt{1/\rho}$. Comparing the values of the natural frequencies predicted from *FEA2* to measurements on the actual laminated ring, it is observed that an increase of $\approx 11\%$ in the natural frequencies results from laminating the ring, compared to its solid counterpart, **Table 3.25**. Clearly, this error is unacceptable for subsequent analyses to take account of the windings and frame. Furthermore, the four welds which hold the laminations together also have an influence, although this is outside the scope of the current investigation.

3.6.2 Convergence study

The determination of the effective material properties of an anisotropic material is an arduous task, and for the case of the laminated ring it is complicated by the fact that a number of laminations have been welded together under a certain clamping pressure. In order to obtain an acceptable FE model a number of assumptions must be made.

The parameters which are input to ANSYS© to define a material are the Young's Modulii, E_x, E_y, E_z, the Modulii of Rigidity (or Modulii of Shear) G_{xy}, G_{xz}, G_{yz}, the Poisson's ratio, ν_{xy}, ν_{xz}, ν_{yz}, and the density. The Young's Modulus relates the stress in a given direction to the percentage increase of length in that direction. Therefore, considering **Fig. 3.37**, the Young's Modulii in the x- and y-directions are the same, and

assumed to be equal to that of M300-35A which is employed in the experimental laminated annular ring, since they are in the plane of the lamination material. The Young's Modulus in the z-direction, however, is assumed to be lower than that of M300-35A due to the fact that it is perpendicular to the plane of the laminations, and, therefore, accounts for material discontinuities between adjacent laminations.

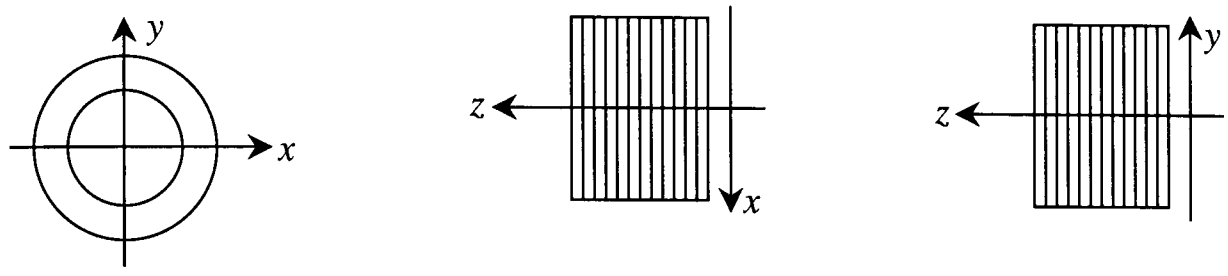

Fig. 3.37 *Orientation of laminations in Cartesian co-ordinate system;* **(a)** *x-y plane corresponds to plane of laminations,* **(b)** *x-z plane is perpendicular to plane of laminations,* **(c)** *y-z plane is perpendicular to plane of laminations*

The Modulus of shear is the relationship between the shear stress acting normal to a plane to the percentage distortion of the angle between the two plane's perpendicular to that plane. Therefore, the shear Modulus, G_{xy}, represents deformation of the x-y plane resulting from stress acting on the y-z plane, in the y-direction. Furthermore, G_{xy} is the same as G_{yx}, which represents deformation in the y-x plane resulting from stress acting on the x-z plane, in the x-direction. Thus, due to the fact that the laminations are stacked in the z-direction, a reduction in the value of G_{xy} from that of M300-35A is assumed. The Shear Modulii, G_{xz} and G_{yz}, represent deformations of the x-z and y-z planes, respectively, and since these planes include the discontinuities of the stack, they are assumed to be lower, but equal in value, than G_{xy} and. The effective density for the model of the laminated ring was deduced, with due account of the lamination stacking factor, as described in section 3.5.1. The Poisson Ratio is assumed to remain the same as that for M300-35A, since this is the relationship between elongation of a material in a given direction to the reduction in cross-sectional area, i.e. transverse strain/longitudinal strain. However, the actual material has not changed and to assess the influence of the clamping pressure and welds on such a parameter would be highly complex. Further, it should be noted that in practice, for a stress in the z-direction, the corresponding longitudinal strain is imposed on the welds, rather than the laminations.

The effective material properties were deduced from a 3D FE model of the laminated ring for which the properties were varied until the predicted natural frequencies

converged to the measured values for circumferential modes 2, 3, and 4, with axial mode = 0. The effective material properties which were deduced in this way are given in **Table 3.26(a)**, (a comprehensive set of convergence data is provided in Appendix E) together with the predicted and measured natural frequencies are given in **Table 3.26(b)**, whilst the corresponding mode shapes are shown in **Fig. 3.38**. It was found that the Young's modulus, E_z, was the same value as for solid silicon iron, for axial mode $m=0$, although it had been expected to reduce slightly. However, this could be attributed to the fabrication of the laminated core, which was frameless and welded at 4 circumferential positions along its axis. The shear moduli were found to have a more significant effect than the Young's Modulii on the natural frequencies, values both in-plane, G_{xy} and normal to the laminations, G_{xz}, G_{yz}, being ≈90% and ≈33% of the values for solid silicon iron, respectively, **Table 3.26(a)**. It can be seen from **Table 3.26(b)** that the correlation between the measured natural frequencies and those obtained with the effective material properties, *FEA3*, is improved considerably, the predicted natural frequencies being within 2% of the corresponding measured values.

Table 3.26(a) *Material properties deduced for laminated core*

Property	Laminated M300-35A (*FEA3*)
ρ (kgm^{-3})	7305
$E_x = E_y = E_z$ (GPa)	215
G_{xy} (GPa)	55
$G_{xz} = G_{yz}$ (GPa)	8.0
$\nu_{xy} = \nu_{xz} = \nu_{yz}$	0.3

Table 3.26(b) *Predicted natural frequencies (Hz) for laminated ring, model Ia*

Mode	Measured	Laminated Transil (*FEA3*)		Error*
n		2D FEA	3D FEA	(%)
2	2688	2598	2640	1.79
3	7424	7419	7560	-1.83
4	13760	13685	14025	0.55

**Between measured and 3D FE prediction*

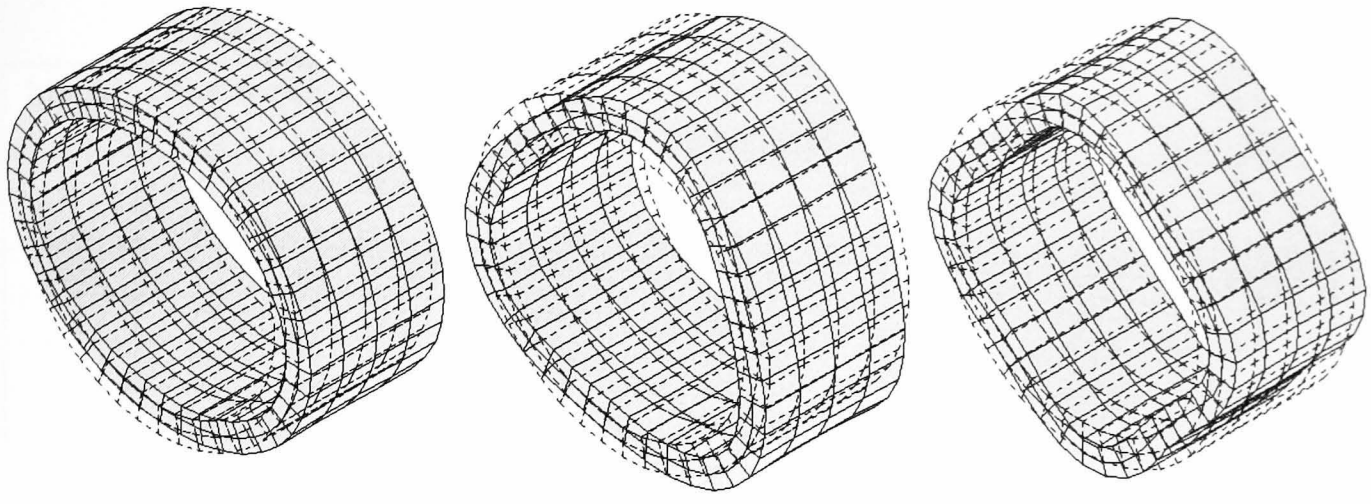

mode 2a/b *mode 3a/b* *mode 4a/b*

Fig. 3.38 *3D FE modes for laminated ring*

3.6.3 Application to laminated stator

The effective material properties which were deduced for the laminated ring were subsequently employed for the analysis of the 6-pole (Model VIb) and 8-pole (Model VIIIb) stators, **Fig. 3.39(a) & (b)**, respectively, for which the predicted natural frequencies are shown in **Tables 3.27 & 3.28**. In both cases, the correlation between the predicted and measured natural frequencies has improved significantly, in that for the 6-pole stator the predicted values are all within 2.3% of the measured values, whilst for the 8-pole stator they are within 3.3%. **Figs. 3.40 & 3.41** show examples of the circumferential mode shapes relating to axial mode 0, obtained from 3D analyses of both stator cores.

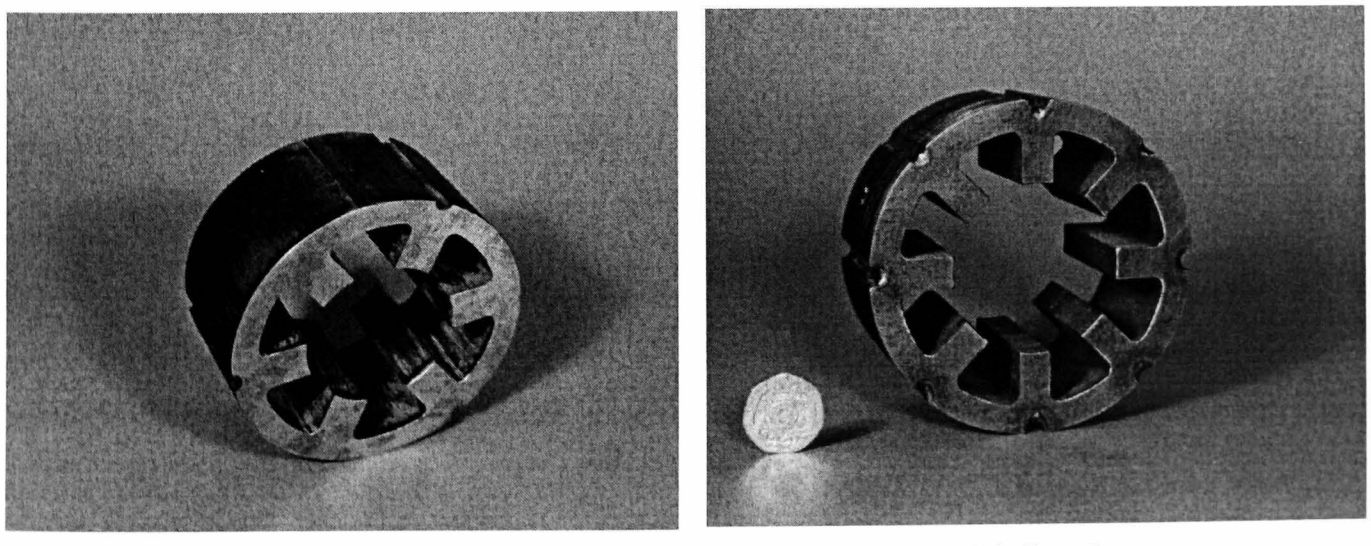

(a) *6-pole* **(b)** *8-pole*

Fig. 3.39 *Experimental 6-pole and 8-pole stator cores*

Table 3.27 *6-pole stator - comparison of natural frequencies (Hz)*

Mode	Measured	Solid Transil (*FEA2*)		Error (3D FEA)	Laminated Transil (*FEA3*)		Error (3D FEA)
n	Laminated Stator	2D FEA	3D FEA	(%)	2D FEA	3D FEA	(%)
2a/b	2304	2442	2525	-9.59	2204	2252	2.26
3a	5280	5633	5815	-10.1	5232	5331	-0.97
3b	7008	7381	7748	-10.6	6852	7095	-1.24
4a/b	10560	11166	11697	-10.8	10338	10673	-1.07

Table 3.28 *8-pole stator - comparison of natural frequencies (Hz)*

Mode	Measured	Solid Transil (*FEA2*)		Error (3D FEA)	Laminated Transil (*FEA3*)		Error of (3D FEA)
n	Laminated Stator	2D FEA	3D FEA	(%)	2D FEA	3D FEA	(%)
2a	2176	2310	2395	-10.1	2194	2246	-3.22
2b	2304	2436	2529	-9.77	2204	2261	1.87
3a	5760	6096	6331	-9.91	5644	5787	-0.47
3b	5760	6096	6338	-10.0	5644	5796	-0.63
4a	8672	9182	9530	-9.89	8514	8762	-1.04
4b	11968	12627	13284	-11.0	11561	12017	-0.41

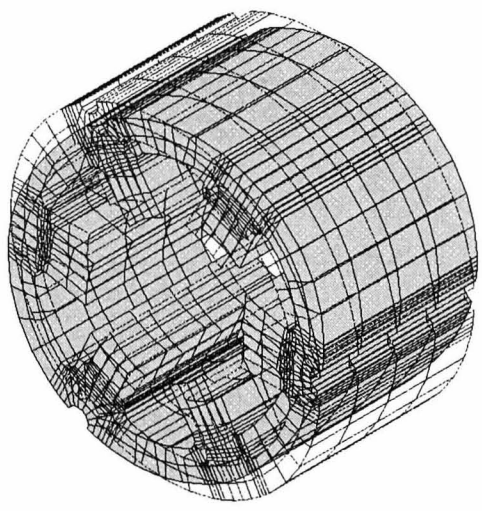

mode 2a/b

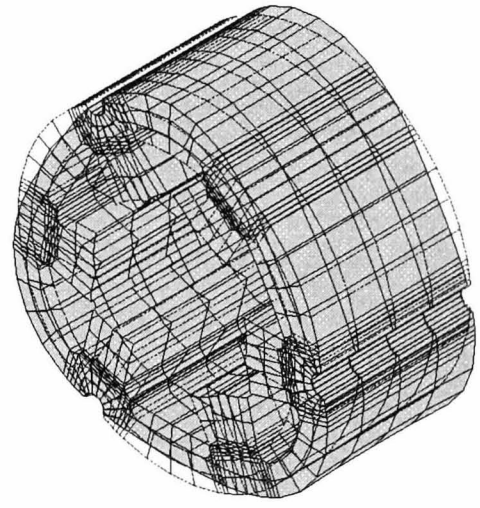

mode 3a

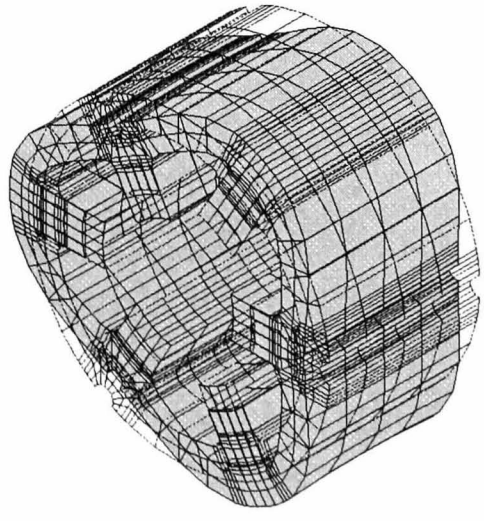

mode 3b

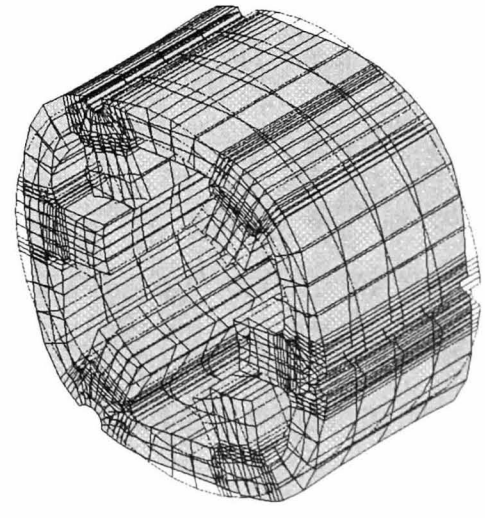

mode 4a/b

Fig. 3.40 *3D FE modes for 6-pole stator core*

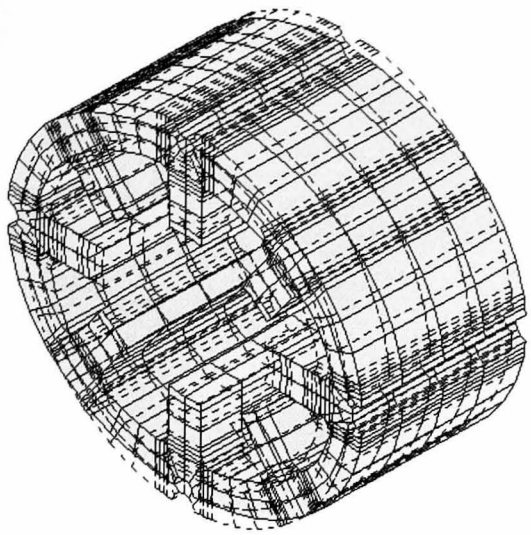

Mode 2a

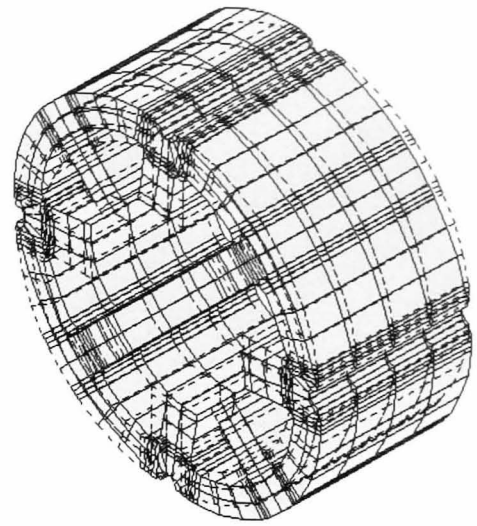

mode 2b

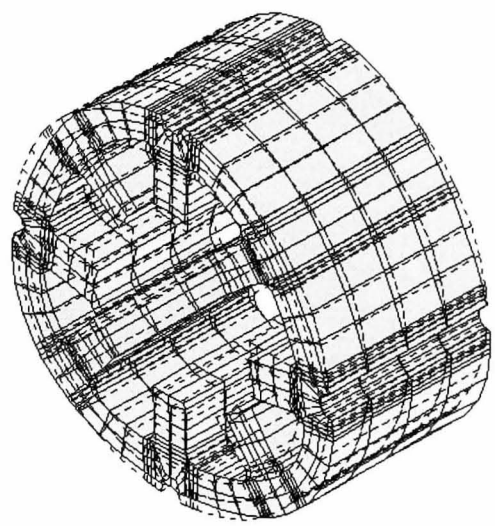

mode 3a/b

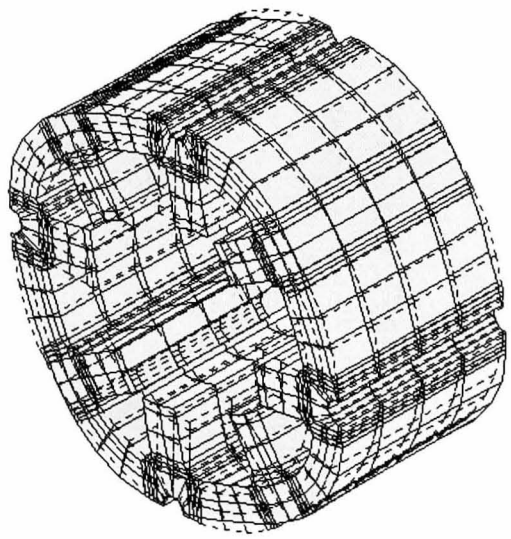

mode 4a

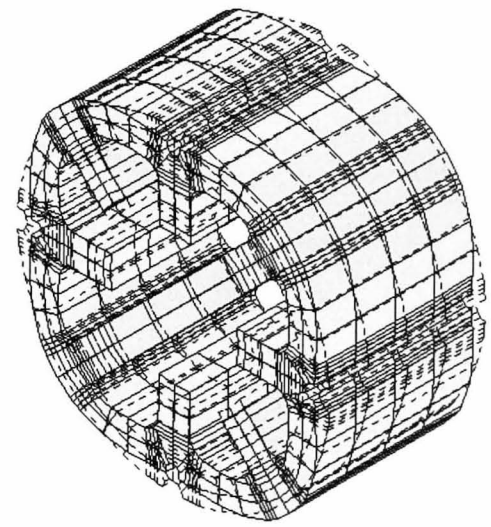

mode 4b

Fig. 3.41 *3D FE modes for 8-pole stator core*

The measured frequency spectra for the annular ring and the 6-pole and 8-pole stators, both solid and laminated, are shown in **Figs. 3.42 & 3.43**, respectively, and indicate that laminating a core suppresses axial modes *m=1*. This is consistent with the observations of Williams and Verma, [WIL89] with regard to laminated induction machine stator cores. The absence of longitudinal modes results from the higher internal damping associated with a laminated structure.

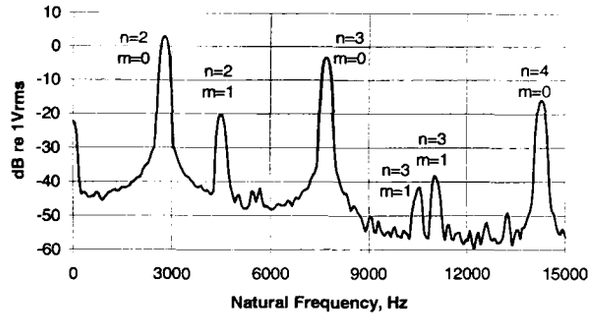

(a) *Annular ring, Model Ia*

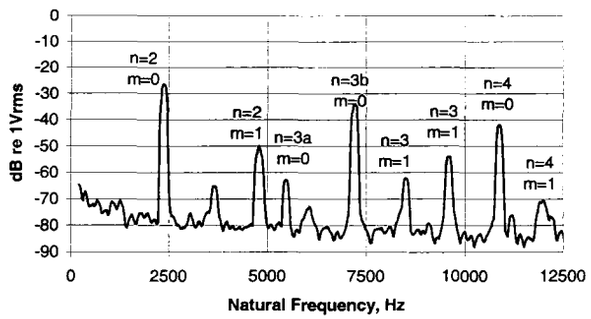

(b) *6-pole stator, Model VIa*

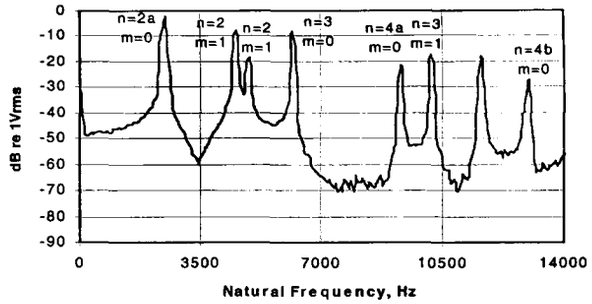

(c) *8-pole stator, Model VIIIa*

Fig. 3.42 *Spectra of solid mild steel specimens*

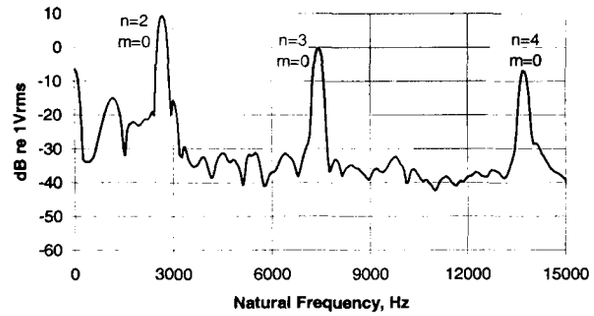

(a) *Annular ring, Model Ib*

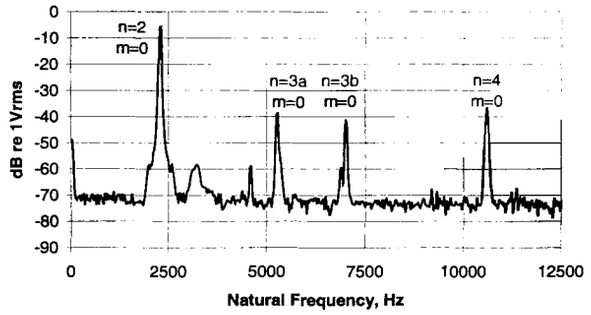

(b) *6-pole stator, model VIb*

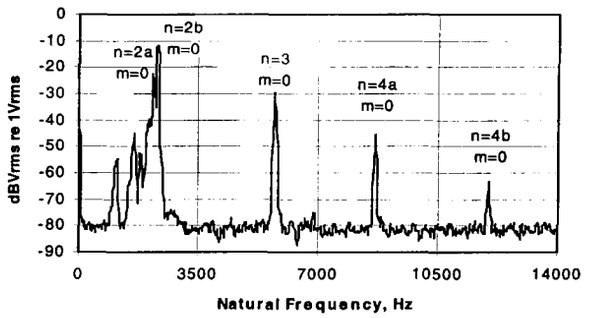

(c) *8-pole stator, Model VIIIb*

Fig. 3.43 *Spectra of laminated M300-35A specimens*

3.7 Influence of stator windings

Several studies have been reported on the influence of the stator winding on the natural frequencies of electrical machines. However, they are almost exclusively restricted to induction motors and synchronous generators [GIR79, NOD87]. The stator core geometry and winding configuration of SR machines are significantly different, in that they have saliency and employ concentrated coils. In this section, therefore, 3D finite element analysis and experimental measurements are again used to investigate the mass and stiffness effect of the stator winding on the natural frequencies of the stator.

3.7.1 Modelling of the windings

Due to the disposition of the conductors within the stator slots and the shape of the end-winding, it is rather difficult to model the windings. It is further complicated due to the presence of the slot liners and the insulation around the copper conductors. Therefore, various assumptions must be made to make it possible to model the windings within the limitations of the finite element technique. These are outlined below.

(a) Intimate contact is assumed to exist between the poles and the coils, as well as between neighbouring coils in the same slot, which were impregnated with resin. Such an assumption is justified, since it was found that modelling adjacent coils in the same slot as being physically separate, i.e. with a physical clearance between them, was not an adequate representation for the stator under consideration, since whilst the coils then contribute mass they present negligible stiffness in the finite element analysis. Furthermore, in the experimental machine there is consistent contact between neighbouring coils throughout the machine, **Fig. 3.44(a)**.

(b) Since each coil comprises of a discrete number of conductors, the cross-section was assumed to have the form shown in **Fig. 3.44(b)**, and that each coil comprises of one equivalent material, having a reduced stiffness compared with that for solid copper, but with the same shear modulus.

(c) Since concentrated windings are generally employed for SR machines, they have non-overlapping end-windings and a relatively short overhang. Thus, the stiffness of the end-windings was assumed to be the same as that of the active section.

(d) The cross-sectional area of the windings, in the x-y plane, was assumed to remain constant throughout their length. Therefore, the cross-section of any plane perpendicular to the orientation of the conductors at any point along the end-windings is the same as that of the active conductors in the slots. Although the formation of the end-windings in the experimental machine does not strictly conform to this assumption they comprise of the same copper area, which is by far the most dominant material within the coils.

(e) The reduced stiffness of the coils was accounted for by assigning an equivalent Young's modulus, the component in the z-direction, E_z, being the same as for solid copper, whilst the x and y components, E_x and E_y, are lower. Assuming E_z to be the same as for solid copper provides an upper bound, but is clearly an over-estimation. Lower bound values for E_x, E_y, and E_z may be estimated by modelling the coils as a composite [HUL96], dependant on the volume ratio of copper and resin, as well as of any air-gaps between the conductors. However, it was considered inappropriate to treat the windings of the experimental machine as a composite material since the resin was applied to the coils manually, whereas had the coils been vacuum impregnated in resin, or potted in Stycast, such a representation would have been more appropriate. Further, finite element calculations showed that the Young's modulus E_z for the coils has little influence on vibration modes $m=0$ and the associated natural frequencies. For example, when E_z, of the coils was reduced to 1/100th of the value for solid copper, the change in natural frequencies is <5%. Clearly, however, a reduction in E_z, would significantly reduce the natural frequencies of the coils alone. In order to simplify the finite element modelling, therefore, E_z for the coils was assumed to be the same as that for solid copper.

(f) The Poisson's ratio of the coils was assumed to be the same as that for copper. In practice, when the volume ratio of a two material composite changes, $\gamma_{zx}(=\gamma_{zy})$ varies linearly between the Poisson ratios of the two materials, $\gamma_{xz}(=\gamma_{yz})$ will be smaller whilst γ_{xy} will be larger than γ_{zx} and γ_{zy} [HUL96].

As mentioned above, the cross-sectional area of the windings is assumed to remain constant throughout the winding length. In addition, the clearance between a pole face at the ends of the core and the inner surface of the end-windings was assumed to be that of the experimental machine, **Fig. 3.45**. Thus, in the finite element model, the end-windings were formed by extruding the cross-sectional area of the slot windings around the axial end of the core, in a semi-circular path whose inner radius was the same as the actual

clearance. Furthermore, for assumptions (e) and (f) to be consistent, the z-component of the conductor was gradually rotated, such that the z-component of the Young's Modulus follows the path of the end-windings, **Fig. 3.46(a)**, as opposed to being orientated in the global z-direction, **Fig. 3.46(b)**. This was achieved by assigning a local co-ordinate system to each set of elements that make up each of the end-windings and orientating the local co-ordinate systems to follow the curvature of the semi-circlular end-windings, **Fig. 3.46(a)**.

The actual end-windings of the experimental 6-pole machine are shown in **Fig. 3.45**, together with the phase connections. Although these are not modelled, it is shown later that the end-windings have negligible influence on the natural frequencies of the stator core. Therefore, this simplification is justified.

The equivalent mass density of the stator windings was deduced from the mass of the windings in the experimental machine and the winding volume as modelled in ANSYS©.

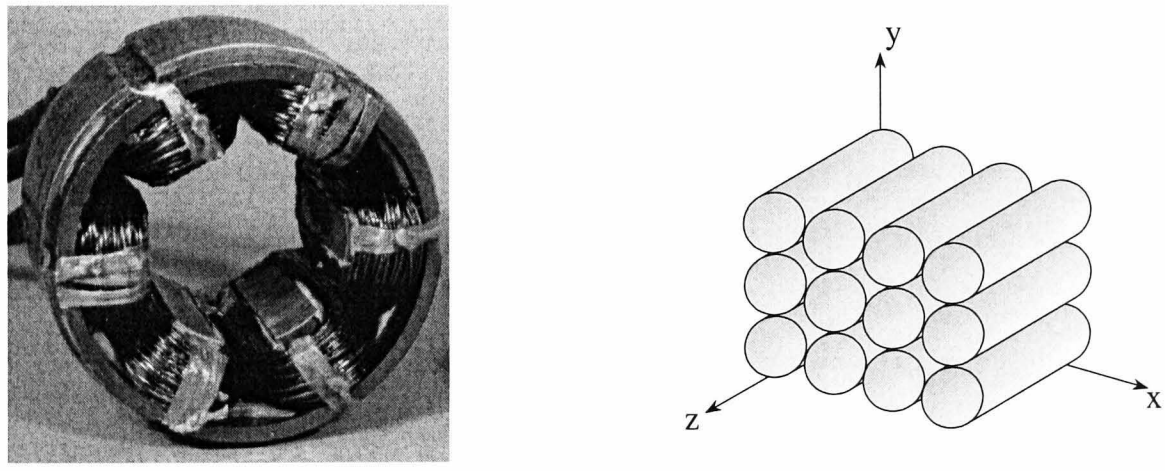

(a) (b)

Fig. 3.44 *Description of coils assumed for FE analyses*

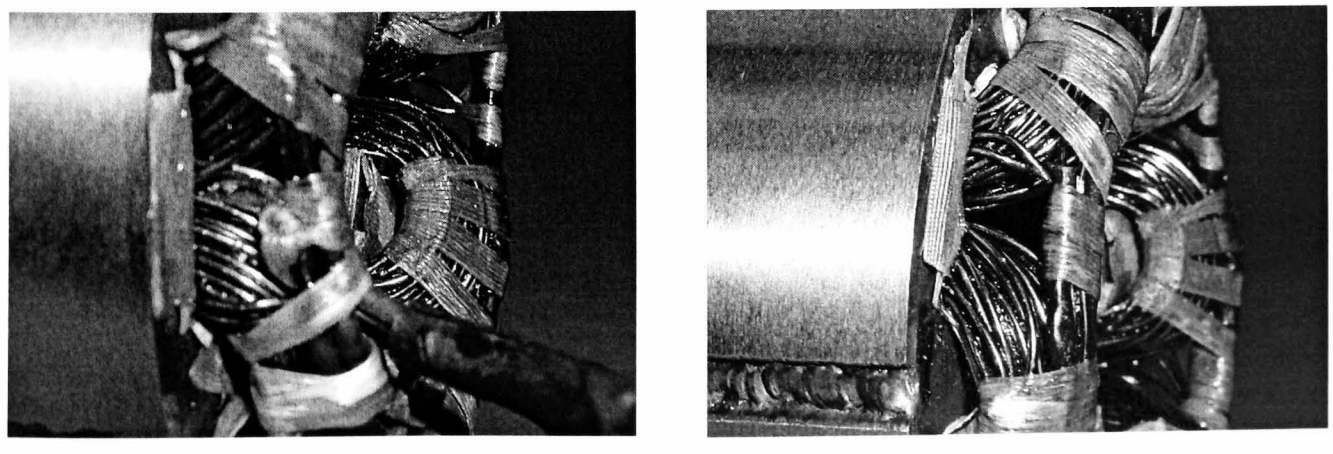

Fig. 3.45 *Formation of end-windings*

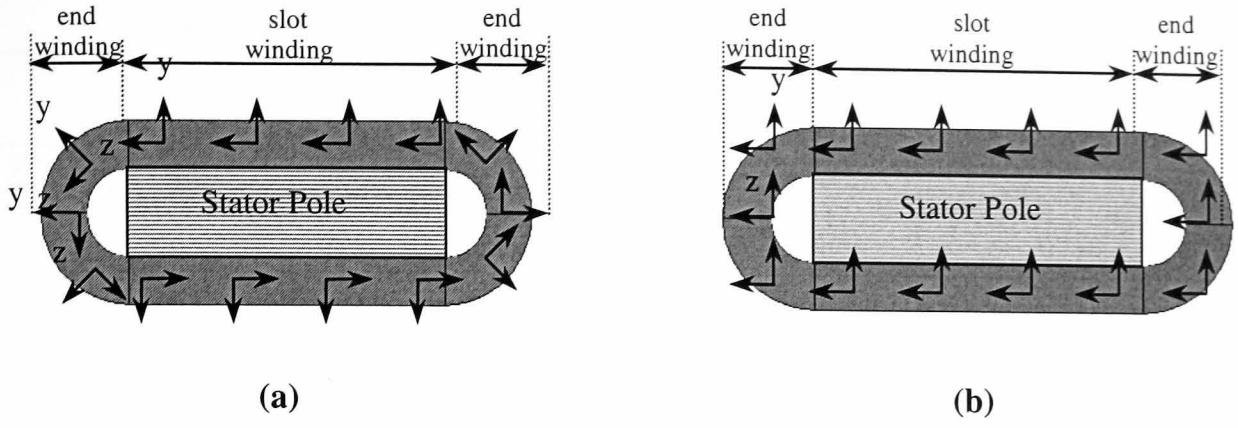

Fig. 3.46 *Schematic of winding model;* **(a)** E_z *in local winding coordinate system,* **(b)** E_z *in global coordinate system*

3.7.2 Convergence study

3D finite element analyses were undertaken using the effective material properties which were deduced earlier for the laminated stator core, *FEA3*. The Young's moduli E_x and E_y of the coils were then varied until the predicted natural frequencies converged to the measured values for circumferential modes 2, 3, and 4, again for axial mode *m=0*. The wound stator, **Fig. 3.44(a)**, was found to be more difficult to excite, due to the damping introduced by the coils, which reduced the vibration response significantly, **Fig. 3.47**. **Table 3.29** shows the effective material properties which were deduced for the coils (a comprehensive set of convergence data is given in Appendix F), together with those for solid copper and the laminated stator core, whilst **Fig. 3.48** shows the variation of the ratio of the calculated natural frequencies to the measured values as the equivalent Young's modulus of the coils is varied. The equivalent Young's modulus in the *x*-*y*-plane of the coils is 1.2eGPa, which is approximately 1/100th of the value for solid copper. Fortuitously, this corresponds to the value which was obtained for induction machine windings [NOD87], when the end-windings and active windings were considered as separate entities with different stiffnesses.

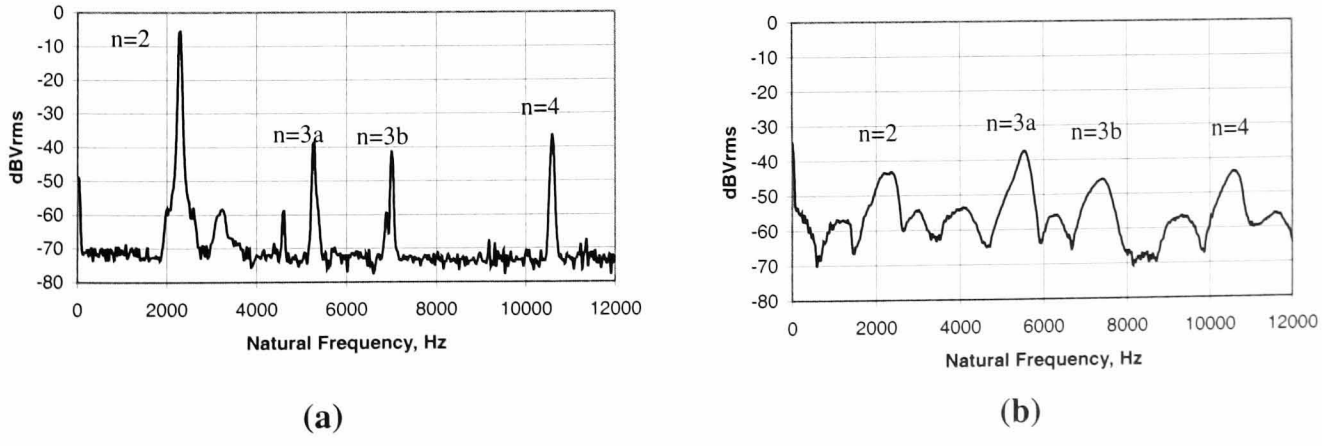

Fig. 3.47 *Impulse force vibration response of 6-pole stator;* **(a)** *without windings,* **(b)** *with windings*

Table 3.29 *Material properties applied to final winding model*

	Copper	Effective Winding	Stack Properties
$E_x = E_y$ (GPa)	120	1.2	210
E_z (GPa)	120	120	210
ρ (kgm^{-3})	8900	4237	7305
$\nu_{xy} = \nu_{xz} = \nu_{yz}$	0.3	0.3	0.3
G_{xz}=G_{yz} (GPa)	------	------	8.0
G_{xy} *(GPa)*	------	------	55

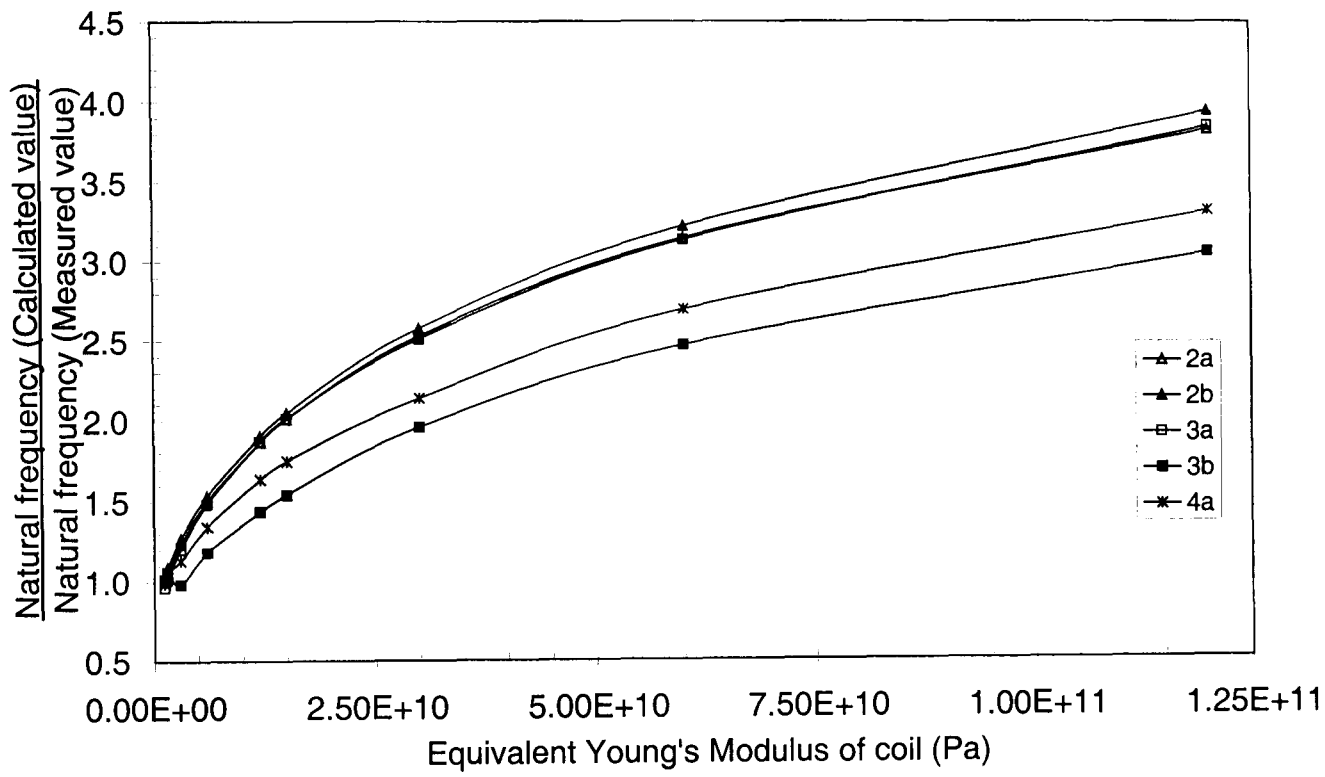

Fig. 3.48 *Convergence for equivalent Young's Modulus*

3.7.3 Investigation of mass-stiffness effect

The derived equivalent Young's modulus for the coils was used to investigate the influence of the mass and stiffness of both the active section of the coils and the end-windings, using various 3D finite element models:

(a) complete wound stator, with end-windings;
(b) stiffness of end-windings neglected, their mass being considered as being distributed over the effective core length;
(c) stiffness and mass of end-windings neglected;
(d) coils removed, but their mass uniformly distributed over stator;
(e) coils considered as an additional mass to that of the stator poles;
(f) stiffness and mass of coils neglected completely.

These are illustrated in **Fig. 3.49**, which also includes the densities of the various stator components. The resultant natural frequencies of the stator core are summarised in **Table 3.30** and **Fig. 3.50**.

Table 3.30 *Predicted natural frequencies from various 3D finite element models (Hz)*

Mode, *n*	Measured	(a)	(b)	(c)	(d)	(e)	(f)
2a/b	2344	2357/2451	2234/2333	2376/2483	1871/1983	1800/1905	2272/2408
3a	5544	5346	5055	5478	4411	4080	5356
3b	7272	7370	6689	7058	5956	5663	7231
4a/b	10600	10464/10470	9590/9617	10469/10482	8916/8955	8087/8128	10825/10872

When the stiffness of the end-windings is neglected, and their mass is considered as an additional mass to the coils over the active core length, as in case (b), the predicted natural frequencies are lower than for the wound stator model with end-windings, case (a). However, when the end-winding mass is removed, case (c), the natural frequencies are almost the same as for case (a), which confirms that the stiffness of the end-windings contributes to the overall stiffness of the stator, but this is offset by their mass. A significant reduction in the predicted natural frequencies occurs when the stiffness is not accounted for and the winding mass is distributed uniformly within the stator core, case (d), and a further reduction is observed when the coil mass is distributed within the stator poles, case (e). This confirms that the winding stiffness has a significant effect on the natural frequencies of the core, and the winding cannot be treated purely as an additional mass. However, when the coils are neglected completely, case (f), a similar result to case (c) is obtained. Therefore, it is concluded that the influence of the winding stiffness is compensated by its mass, and, as a result, the overall effect of the winding on the natural frequencies tends to be relatively insignificant. However, although the example of **Figs. 3.47(a) & (b)** verify that the natural frequencies are within 5.0% of each other, the magnitude of mode 2 shows a reduction of 36dB. Consequently the vibration level and acoustic noise at that frequency will be reduced due to the damping effect of the windings. Due to the complexity of damping this would be a major investigation within itself and therefore is not considered in any further detail, but it is an important area for future research in this field. An investigation on induction motors, [GIR79] arrived at similar conclusions for low vibration modes, but showed that for higher modes (>4) significant changes occur in the natural frequencies. This was attributed to the additional stiffness constraining the movement of the poles. It was found that a large number of

mode shapes, predicted from the 3D finite element analyses were associated purely with movement of the end-windings, as shown in **Fig. 3.51**. Again, this has been observed for induction motors, [NOD87]. However, since the end-windings of SR motors are significantly shorter, the associated modes are of less significance.

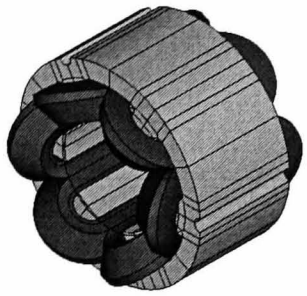

$\rho_{poles} = 7305\ kgm^{-3}$
$\rho_{yoke} = 7305\ kgm^{-3}$
$\rho_{slot\ windings} = 4237\ kgm^{-3}$
$\rho_{end\ windings} = 4237\ kgm^{-3}$

(a) complete wound stator, with end-windings

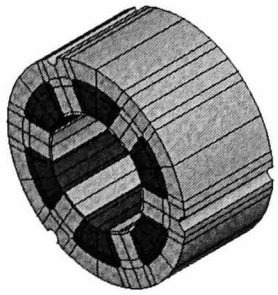

$\rho_{poles} = 7305\ kgm^{-3}$
$\rho_{yoke} = 7305\ kgm^{-3}$
$\rho_{slot\ windings} = 6280\ kgm^{-3}$
$\rho_{end\ windings} = n/a$

(b) stiffness of end-windings neglected, their mass being considered as an additional mass of the coils distributed over the effective core length

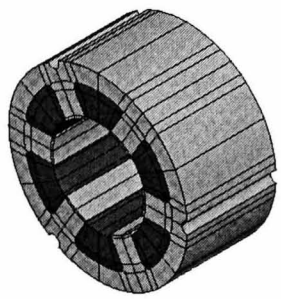

$\rho_{poles} = 7305\ kgm^{-3}$
$\rho_{yoke} = 7305\ kgm^{-3}$
$\rho_{slot\ windings} = 4237\ kgm^{-3}$
$\rho_{end\ windings} = n/a$

(c) stiffness and mass of end-windings neglected

$\rho_{poles} = 10768\ kgm^{-3}$
$\rho_{yoke} = 10768\ kgm^{-3}$
$\rho_{slot\ windings} = n/a$
$\rho_{end\ windings} = n/a$

(d) coils removed, but their mass uniformly distributed over stator

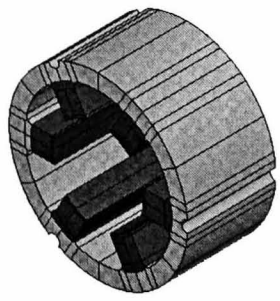

$\rho_{poles} = 17382\ kgm^{-3}$
$\rho_{yoke} = 7305\ kgm^{-3}$
$\rho_{slot\ windings} = n/a$
$\rho_{end\ windings} = n/a$

(e) coils are considered as an additional mass to stator pole

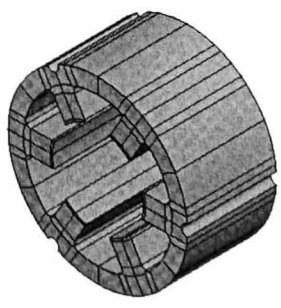

$\rho_{poles} = 7305\ kgm^{-3}$
$\rho_{yoke} = 7305\ kgm^{-3}$
$\rho_{slot\ windings} = n/a$
$\rho_{end\ windings} = n/a$

(f) stiffness and mass of coils neglected completely

Fig. 3.49 *3D finite element models employed for winding investigations*

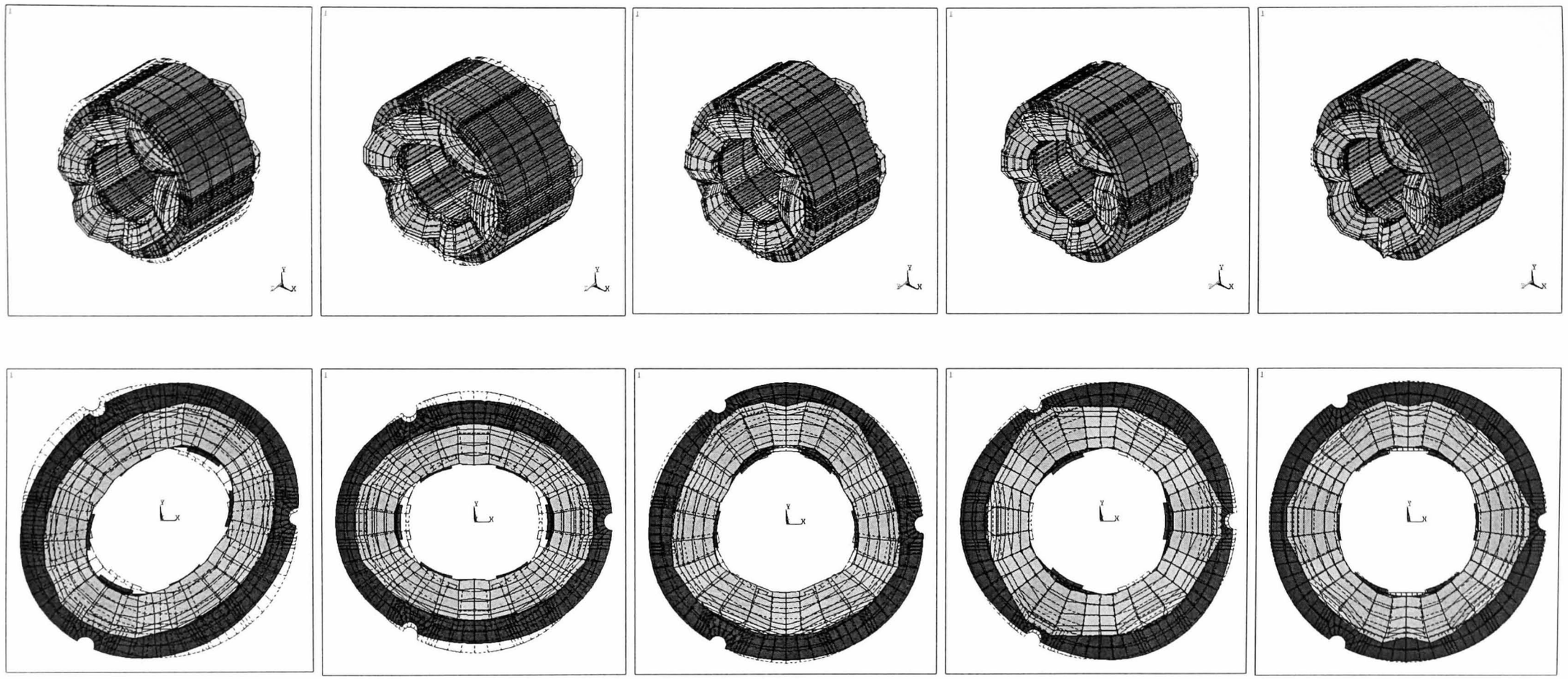

mode 2a: 2302Hz *mode 2b: 2396Hz* *mode 3a: 5204Hz* *mode 3b: 7211Hz* *mode 4a: 10064Hz*

Fig. 3.50 *3D finite element predicted vibration modes for wound 6-pole stator*

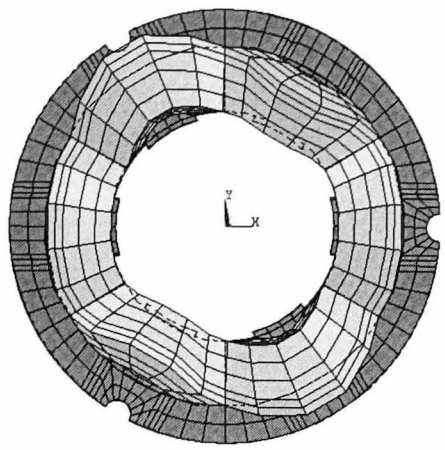

mode 2

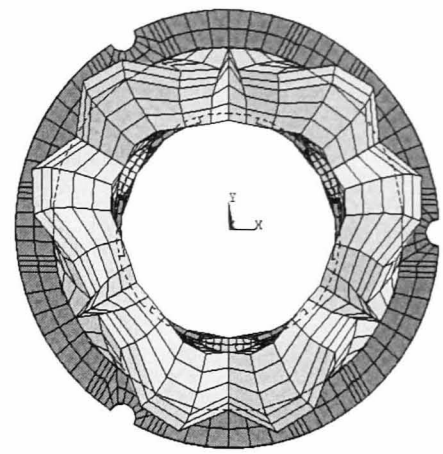

mode 3a

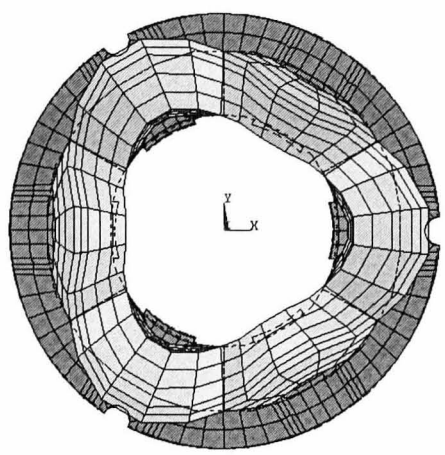

mode 3b

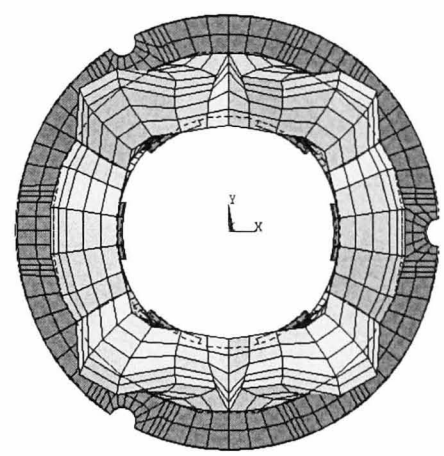

mode 4

Fig. 3.51 *Vibration modes of end-winding*

3.8 Influence of frame and end-caps

A number of analyses have accounted for the influence of the frame, but these were mainly limited to induction machines and permanent magnet machines, [GIR79, WIL89, ZHU93, ZHU89]. From these, however, it is apparent that the presence of the frame significantly increases the effective stiffness of the stator core. It is, therefore, prudent to account for it in noise and vibration analyses of electrical machines. Thus, the influence of a smooth cylindrical frame, and its associated end-caps, on the natural frequencies of the 6-pole experimental SR machine has been investigated.

The frame and end-caps are shown in **Fig. 3.52**. They were machined from aluminium, whose material properties, which were employed in the FE analyses, are given in **Table 3.31**. A tight fit between the frame and end-caps was desirable such that intimate contact between frame and end-caps could be assumed in the FE model. However, this was limited by the machining tolerances. Therefore, a chamfer was introduced on the inner edge of the end-caps to locate them into position, as shown in **Fig. 3.52**. Also shown is the location of the bearing housings, which were neglected in the following analyses, although their influence is considered later. Care was taken to make the frame symmetrical, although it was necessary to employ four equi-spaced screws per end-cap to attach the end-caps to the frame. However, these are shallow relative to the frame length and, therefore, have negligible influnce on the natural frequencies and are neglected in the analyses. Further, a small step was required in the frame to locate the stator core, **Fig. 3.52**. Again, since this is relatively small compared with the rest of the frame it is neglected. A summary of the measured and predicted natural frequencies is given in **Table 3.32** for the frame with and without end-caps, whilst the corresponding frequency spectra are shown in **Fig. 3.53**. The correlation between the measured and predicted natural frequencies of the frame without the end-caps is good, and justifies the omission of the step (for location of the stator core) and screw holes, from the FE model. Comparison between the measured natural frequencies of the frame with and without the end-caps shows that the end-caps increase the stiffness of the frame considerably. The natural frequency of mode 2 is observed to increase to approximately three times its original value, whilst modes 3 and 4 increase by 34% and 12.6%, respectively, **Table 3.32**. However, the natural frequencies predicted for the frame with end-caps do not correlate well with the measured values. This is attributed to the fact that the end-caps of the experimental machine are separate components to the frame, whereas in the FE model intimate contact is assumed between the frame and end-caps, which over-

estimates the stiffness introduced by the end-caps. To account for the fact that intimate contact is not achieved between the end-caps and frame, a FE study was carried out on the sensitivity of the predicted natural frequencies to the contact between the end-caps and frame.

Table 3.31 *Material properties of aluminium employed for FE of frame*

Material Property	Value	Unit
Young's Modulus, E	70	GPa
Poisson's Ratio, ν	0.35	-----
Density, ρ	2760	kgm^{-3}

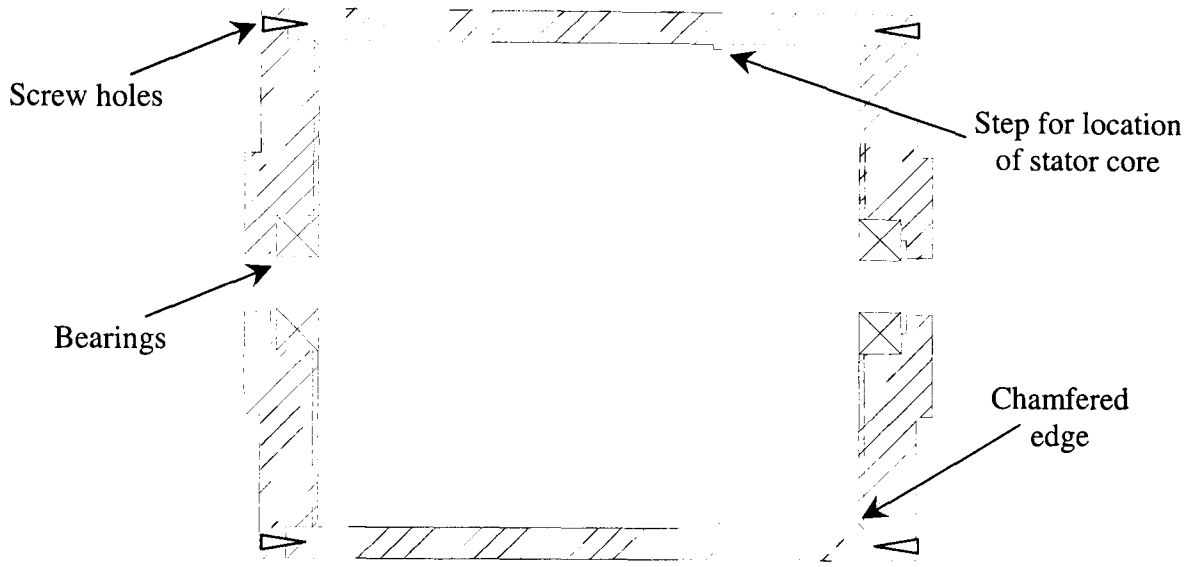

Fig. 3.52 *Schematic of frame and end-caps*

Table 3.32 *Measured and 3D FEA predicted natural frequencies of frame (Hz)*

Circumferential	Frame		Error	Frame with end caps		Error
Mode, n	Measured	3D FE	(%)	Measured	3D FE	(%)
2	1536	1481	3.58	4544	5522	-21.5
2	1536	1481	3.58	4544	5542	-22.0
3	4288	4158	3.03	5760	6339	-10.1
3	4288	4174	2.66	5760	6352	-10.3
4	8128	7937	2.35	9152	9556	4.41
4	8128	7937	2.35	9152	9566	4.52

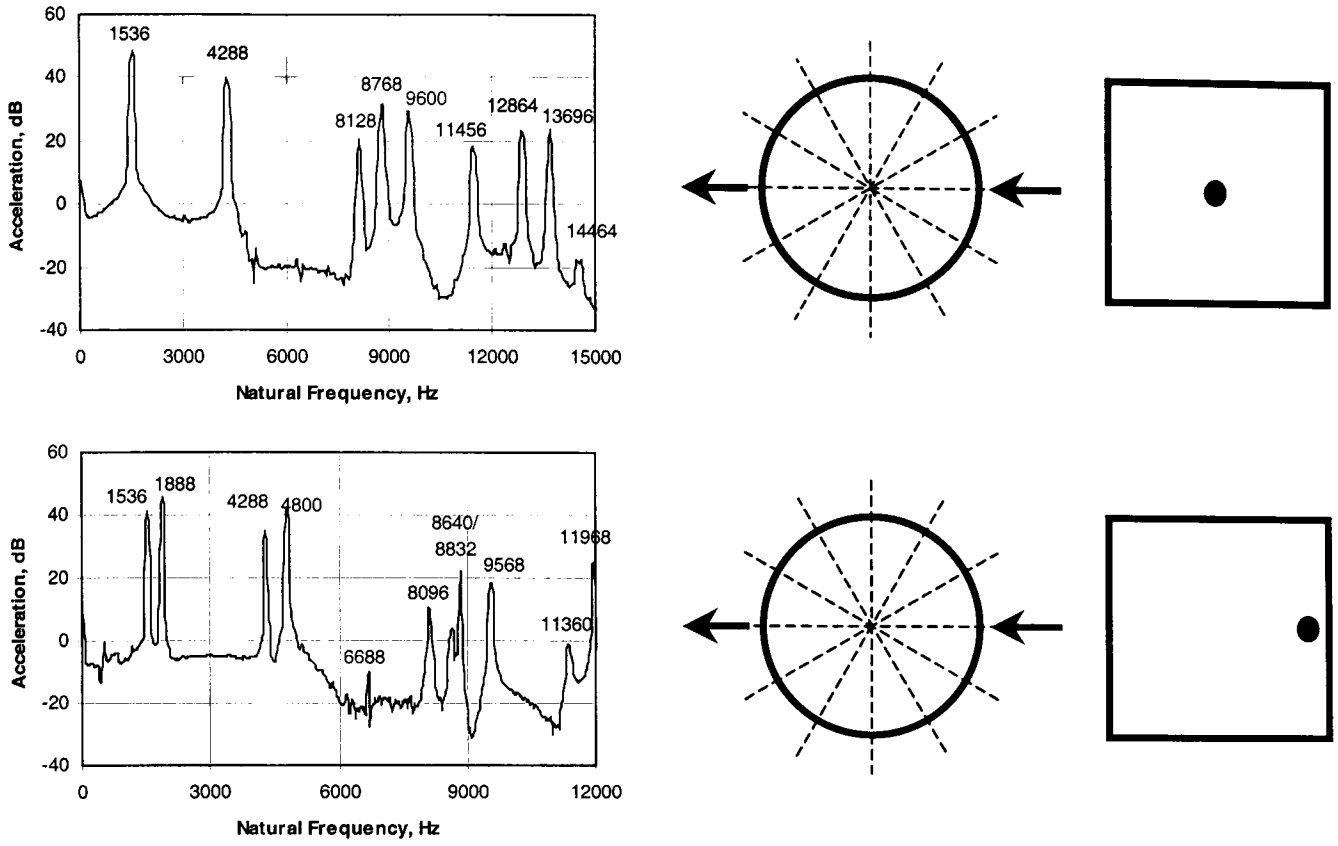

(a)

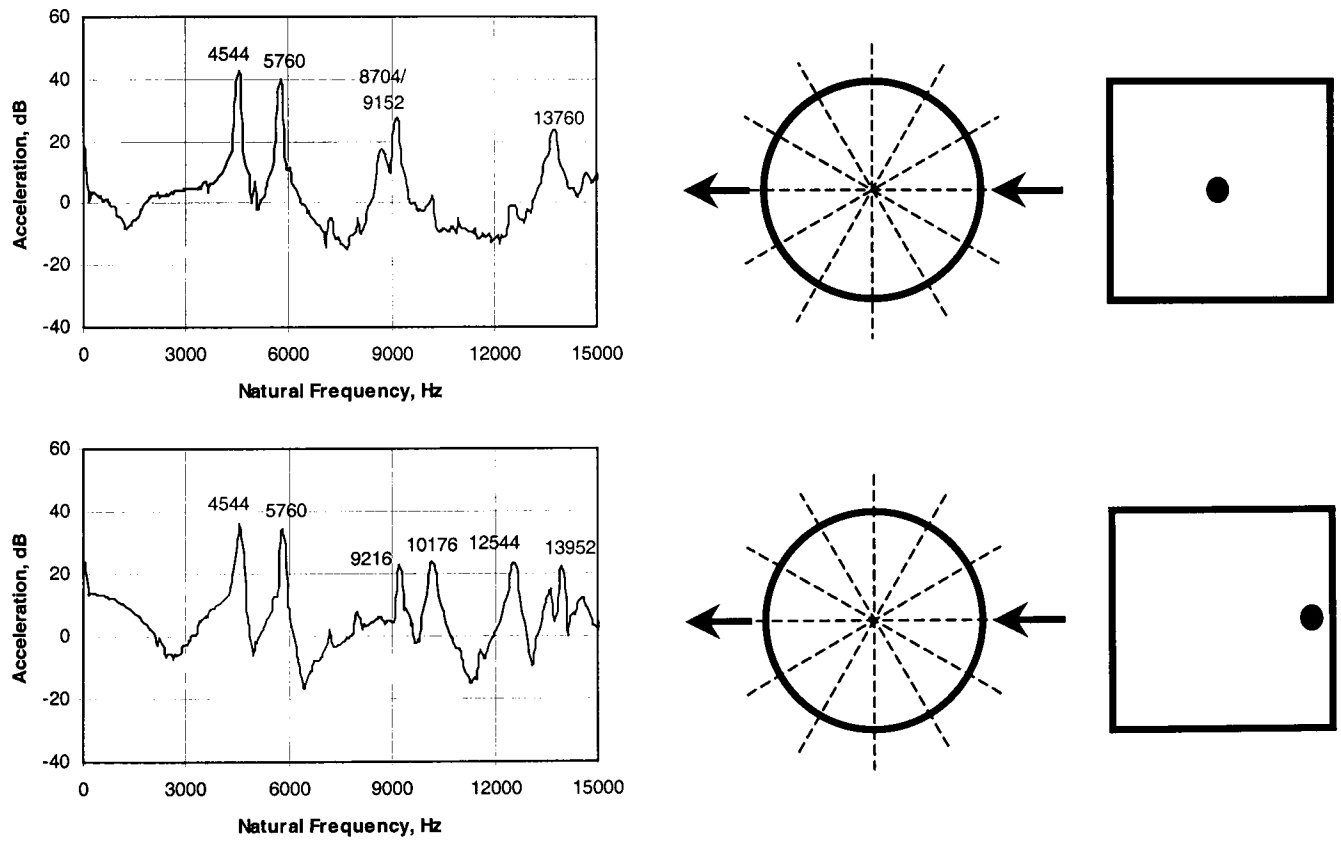

(b)

Fig. 3.53 *Frequency spectra of frame obtained from impact tests;* **(a)** *without end-caps,* **(b)** *with end-caps*

The schematic of **Fig. 3.54(a)** shows the model in which intimate contact between the frame and the end-caps is assumed for the prediction of the natural frequencies in **Table 3.32**. In the schematic of **Fig. 3.54(b)** the contact between the frame and the end-caps, *l*, was varied in the FE model from 6mm, (the original model, **Fig. 3.54(a)**, to 0mm, when

only the axial end-faces of the frame make intimate contact with the end-caps. The radial air-gap introduced between the frame and end-caps was 1mm, since this is sufficient to provide the necessary clearance between the frame and end-caps and small enough to have negligible influence on the mass of the frame. The schematic of **Fig. 3.54(c)** represents the case when there is no intimate contact between the axial end-faces of the frame and the end-caps, the clearance again being 1mm. In this model, the axial length over which intimate radial contact occurs, l, was varied down to 0mm, as in **Fig. 3.54(d)**. The ratio of the predicted natural frequencies from the various FE models to the measured values is shown in **Figs. 3.55 & 3.56**, as the radial contact is varied, both with and without axial contact. In both cases, the accuracy of the predicted natural frequencies improves as the contact between the frame and end-caps is reduced, and it is observed that the natural frequencies predicted by the model which assumes minimal contact, **Fig. 3.54(d)**, results in the best correlation with the measured values, which are summarised in **Table 3.33**, together with the original predictions. This highlights the fact that despite the high machining tolerance to achieve a tight fit between the frame and the end-caps, the stiffness is reduced significantly compared to that which would be achieved if the end-caps and the frame were manufactured as a single component. Thus, in subsequent FE analyses which account for the end-caps, contact between the frame and the end-caps was assumed to be that illustrated in **Fig. 3.54(d)**.

It is important to note that the placement of the end-caps also introduces additional damping into the frame, which is apparent by the broader bandwidth of the measured peaks, **Fig. 3.53(b)**. Thus, although the additional stiffness imposed by the end-caps is not as high as for perfect intimate connection as predicted by the finite element analyses, it may be more beneficial in terms of noise radiation. This is due to the fact that the level of damping, which is introduced by the end-caps, is expected to reduce as the connection with the frame becomes more rigid.

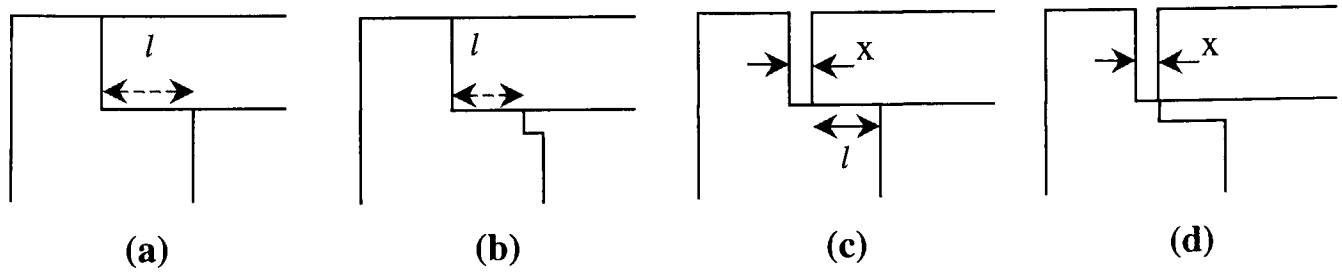

Fig. 3.54 *Schematic of intersections studied*

Having identified the natural frequencies of the frame and the limitations of modelling complex systems with FE analysis, the core was placed inside the frame by shrink fitting the frame onto the core so as to achieve the best possible contact between frame and core such that in the FE analysis intimate contact can be assumed.

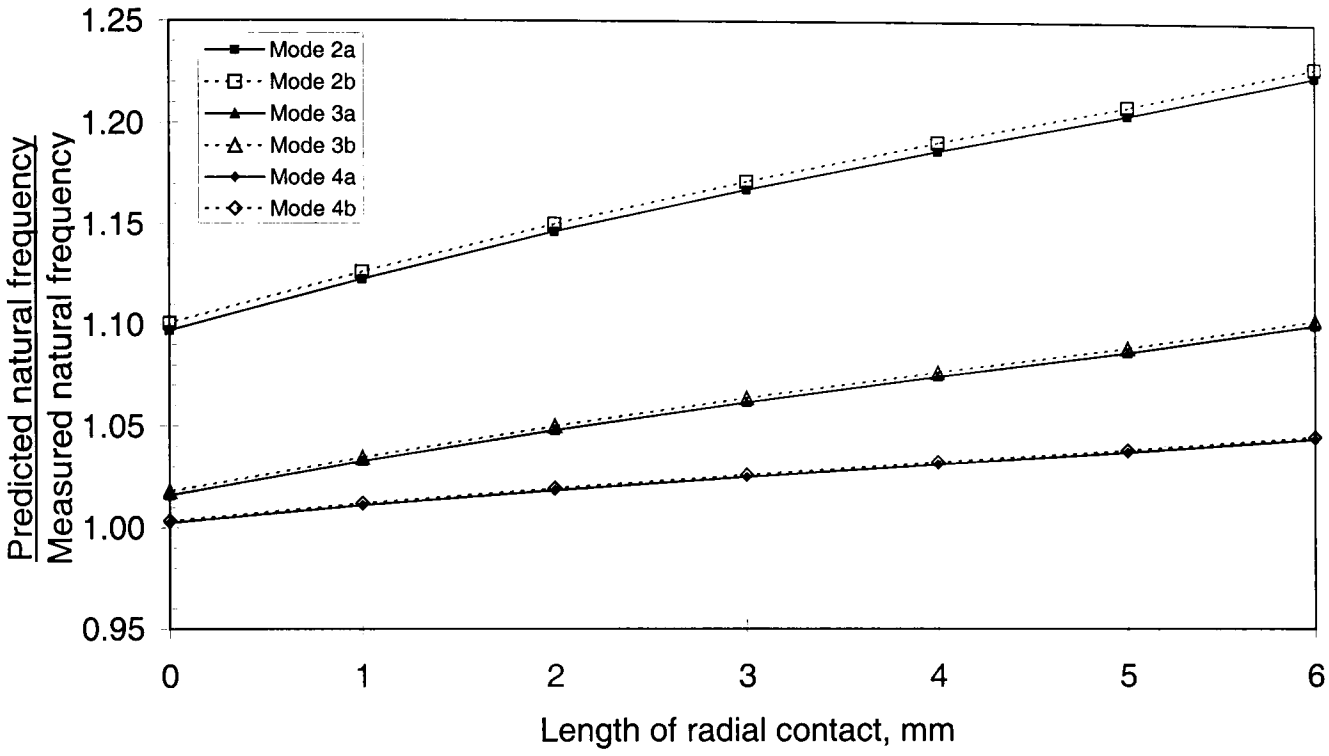

Fig. 3.55 *Variation of length of axial contact with fixed radial contact, model* – **Fig. 3.54(b)**

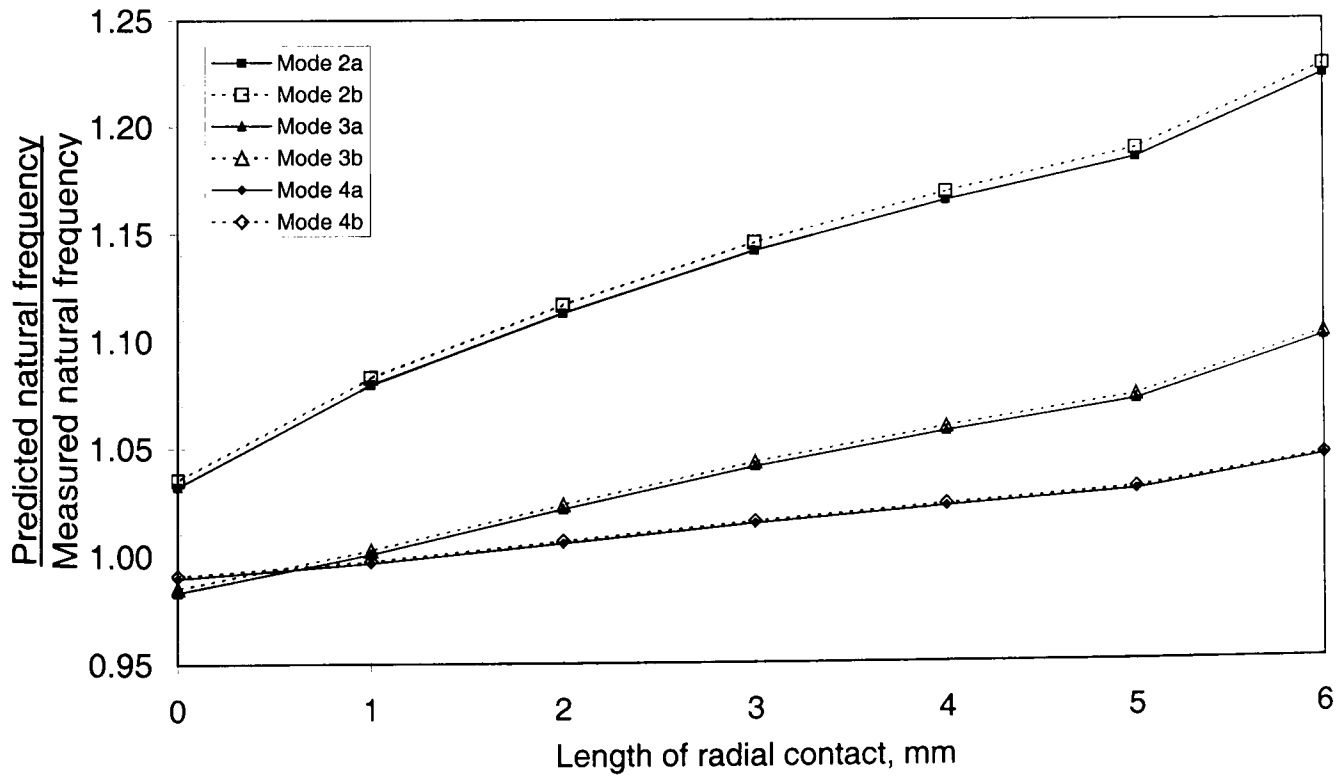

Fig. 3.56 *Variation of length of axial contact without axial contact, model* – **Fig. 3.54(d)**

Table 3.33 *Frame with end-caps (Hz)*

Circumferential Mode, *n*	Measured	3D FE predictions			
		Original **Fig. 3.54(a)**	Error (%)	New **Fig. 3.54(d)**	Error (%)
2	4512	5522	22.4	4656	-3.19
2	4512	5542	22.8	4670	-3.50
3	5760	6339	10.1	5663	1.68
3	5760	6352	10.3	5674	1.49
4	9152	9556	4.41	9058	1.03
4	9152	9566	4.52	9068	0.92

Identification of the measured natural frequencies of modes 2, 3 and 4, with the stator core mounted in the frame without the end-caps proved to be difficult, necessitating very careful impact tests. The spectra which best represents the natural frequencies are shown in **Fig. 3.57**. Two different FE models were employed for the analysis, viz. winding mass and stiffness accounted for, and winding mass and stiffness omitted such that only the stator core is present in the frame. A summary of the predicted natural frequencies with and without the windings is given in **Table 3.34**, together with the corresponding values identified from impact tests. The corresponding mode shapes generated from the finite element analyses are shown in **Figs. 3.58 and 3.59**, both with and without the windings, respectively. The natural frequency of mode 4 was not identified from the measurements, whilst the limitations of the FE analysis make it impossible to assess the influence of the frame on mode 4 of the wound stator, although the accuracy of the FE model is observed to generally improve with higher values of circumferental mode, *n*. Furthermore, four natural frequency values were obtained for mode 3, which implies that the addition of the frame to the wound stator core has induced additional modes. However, the addition of the frame is observed to increase the stator core natural frequency associated with mode 2 since the frame increases the effective stiffness of the wound stator core. Omitting the windings in the FE anaylses results in better correlation with measurements. However, the additional frequencies associated with mode 3 cannot then be predicted. Thus, it is concluded that inclusion of the windings in the model generally results in a more accurate representation, and better correlation with the measured values.

The introduction of the wound core into the frame introduces a higher level of damping to that introduced by the end-caps, as expected due to the damping effect of the windings highlighted in section 3.7. Again, this is apparent from the broader bandwidth of the natural frequency peaks (and lower magnitudes), moreover, it was apparent from the difficulty in exciting the frame for identification of the natural frequencies.

Table 3.34 *Stator in frame without end-caps (Hz)*

Mode, *n*	Measured		FE with frame			
	wound core	wound core in frame	with windings	Error[#] (%)	without windings	Error[#] (%)
2a/b	2344	3264	3000	8.09	3182	2.51
2a/b	2344	3328	3096	6.97	3313	0.45
3a	5544	6592	6418	2.71	6848	-3.88
3b	7272	7232	7478	-3.40	7491	3.40
3a	----	8480	8349	1.54	*	----
3b	----	9888	9623	2.68	*	----
4a/b	10600	*	10333	----	10458	----
4a/b	10600	*	10343	----	10476	----

* *Not identified*; [#] *Compared to measurements made on wound core in frame*

Finally, the frequency spectra were obtained from impulse tests with the end-caps attached to the frame, as shown in **Fig. 3.60**, the corresponding mode shapes obtained from FE analyses of the wound stator core, with and without the end-caps being displayed in **Figs. 3.61i and 3.61ii**, respectively. A summary of the identified natural frequencies is given in **Table 3.35**, together with those predicted from FE analysis and measured values for the wound stator core alone. As will be seen, the FE model results in even greater errors than for the model without the end-caps, an error of 11.7% existing for mode 2, which is of great significance to the noise produced in an SR machine. However, it should be noted that the stiffness which is introduced by the end-caps depends on the method of attachment to the frame. Therefore, the assumption of minimal contact between the frame and end-caps, **Fig. 3.54(d)**, results in the best corrrelation with measured values, the measurements do vary when the end-caps are removed and re-attached. Nevetheless, it is observed that the addition of the fame with end-caps to the wound stator core has a significant influence on the natuaral frequencies of the stator core, the natural frequencies of modes 2, 3a and 3b increasing by 66.6%, 32.8% and 30.3%, respectively, although, unfortunately, mode 4 was not identified.

The spectra shown in **Fig. 3.62**, for excitation of mode 2 and mode 3b, was measured with the stator core in the frame with the end-caps and the bearings. It is observed that the influence of bearings is negligible compared to the error that the FE model introduces, and therefore their omission from the analyses is justified. Further, the change in stiffness of the frame following the removal and subsequent re-attachment of the end-caps, required to insert the bearings, was more influential than the bearings themselves.

The trends observed throughout this chapter highlight the importance of damping on the vibrational response. To obtain further detail into the influence of the damping would require the measurement of frequency response, which were omitted throughout this study since characterising the damping was beyond the scope of research in this study, and thus calculation of the logarithmic decrement. However, considering the three cases outlined in **Fig. 3.63**, it is apparent that the inclusion of the core without windings into the frame without end-caps introduces additional damping due to the coupling at the interface of core and frame. In the case of an impulse force applied at an axially central position on the circumference of the frame, then with the presence of the unwound core **Fig. 3.63(b)**, the transmission of vibration to the outer frame (or frame overhang) will be reduced with respect to that without the core, **Fig. 3.63(a)**, as a result of the additional damping. Further, as for the case when the core comprises of coils, **Fig. 3.63(c)**, the damping is increased further, as apparent from the winding investigation, thus for an impulse force axially centred, the fame overhangs will radiate the vibration less efficiently due to this additional damping. From the forgoing discussion it is clear that there is scope for research into the influence of the damping on the radiation of acoustic noise from electric machines.

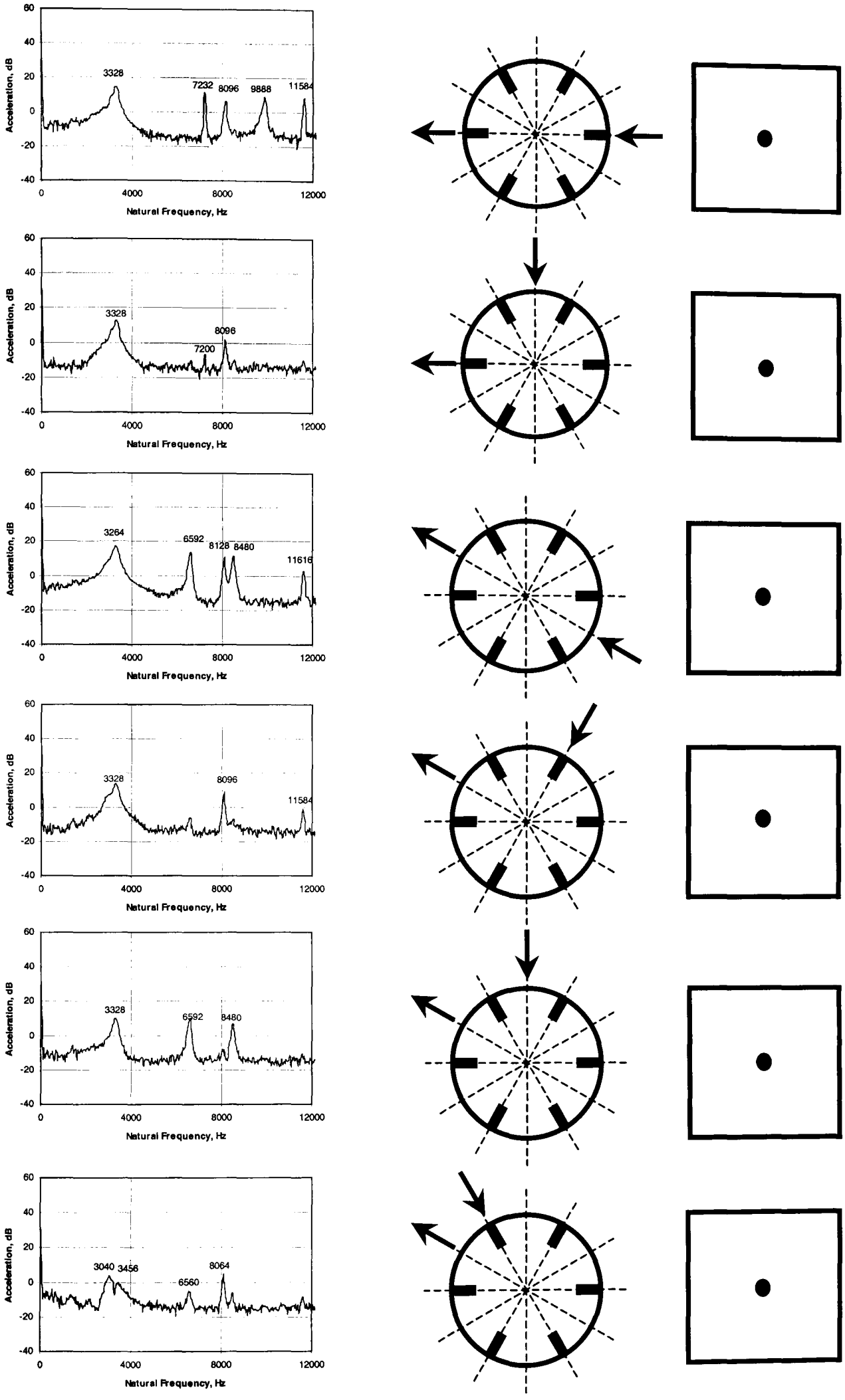

Fig. 3.57 *Frequency spectra of wound stator in frame without end-caps*

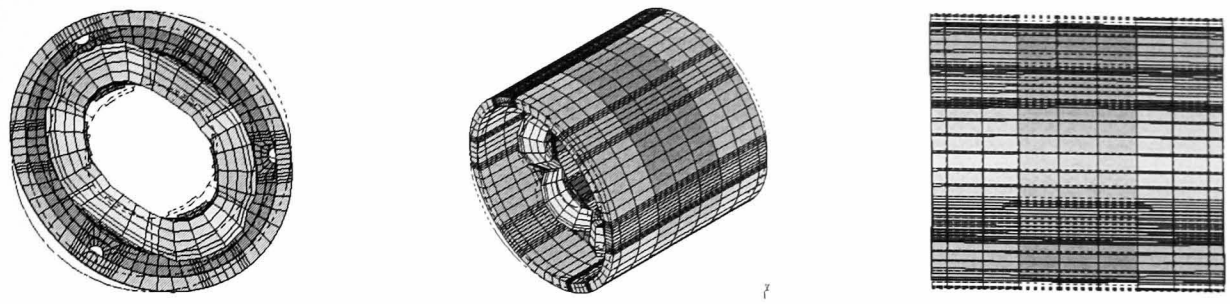

Mode 2 (3000Hz)

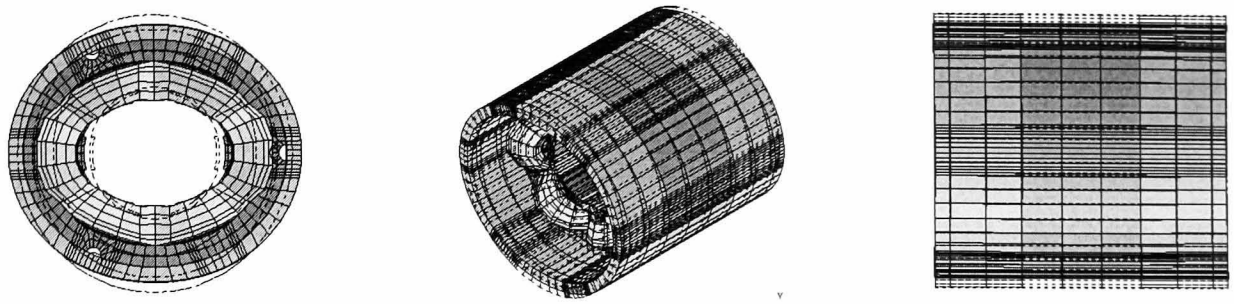

Mode 2 (3096Hz)

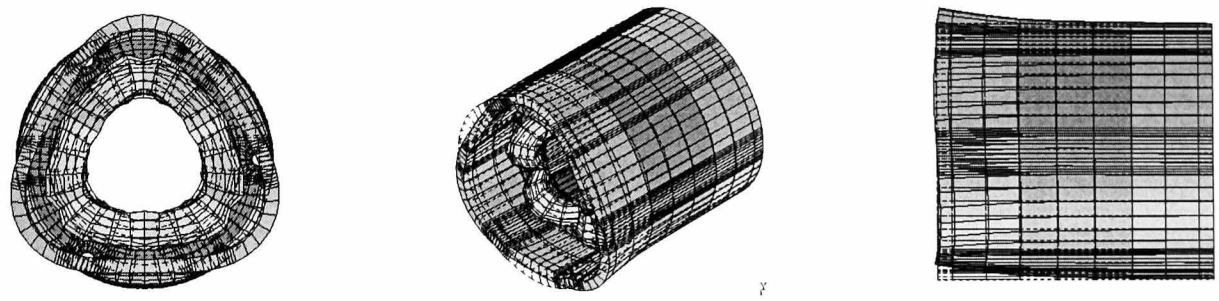

Mode 3 (6418Hz)

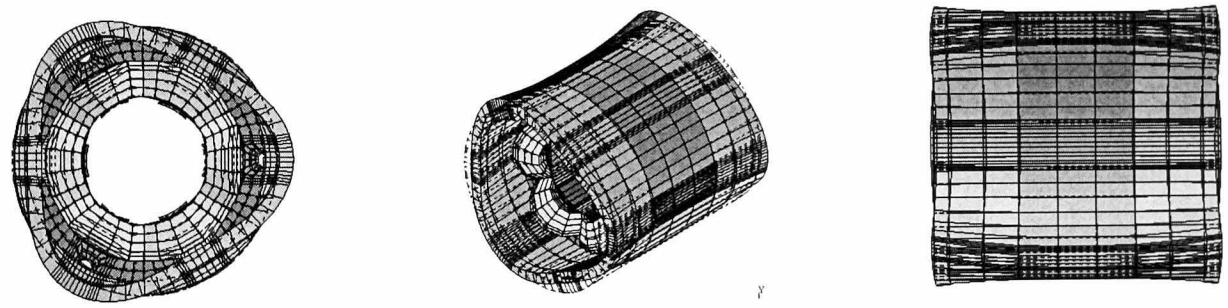

Mode 3 (7478Hz)

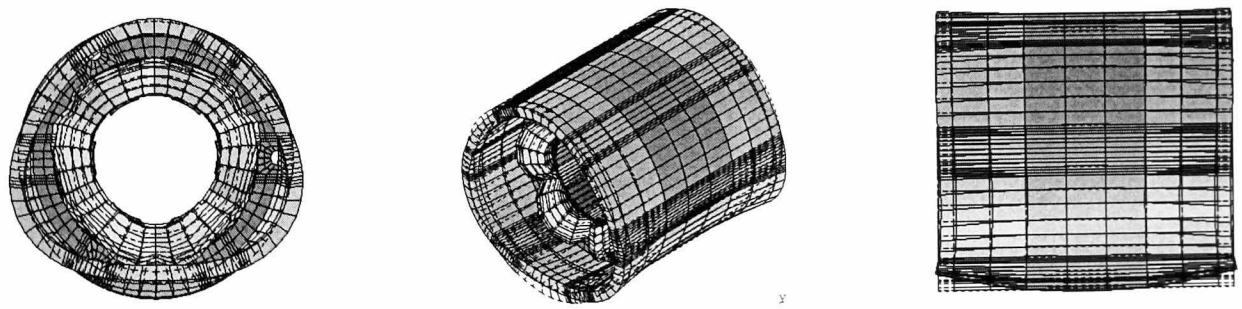

Mode 3 (8349Hz)

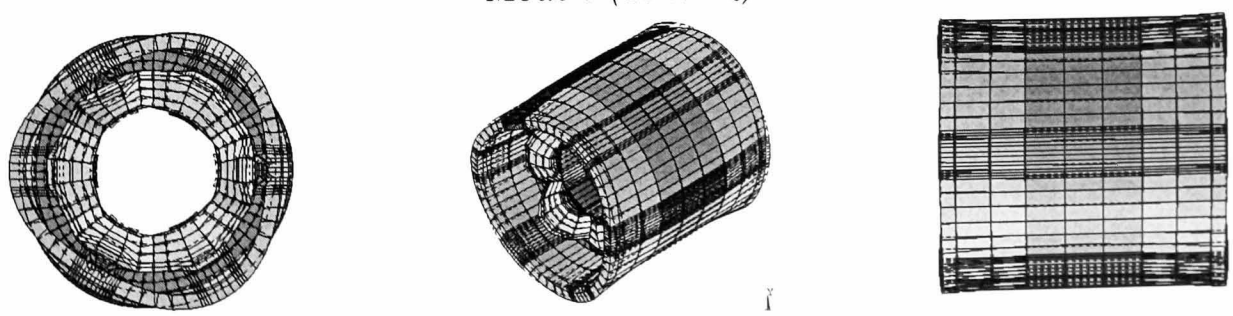

Mode 3 (9623Hz)

Fig. 3.58 *Wound stator in frame without end caps*

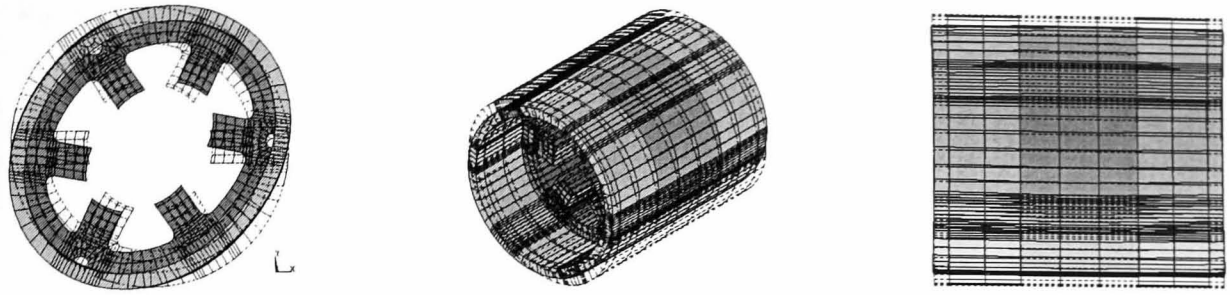

Mode 2a (3182Hz)

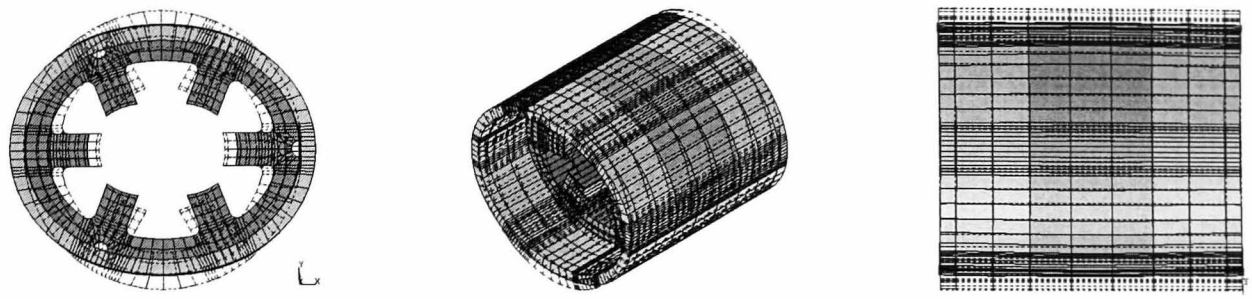

Mode 2b (3313Hz)

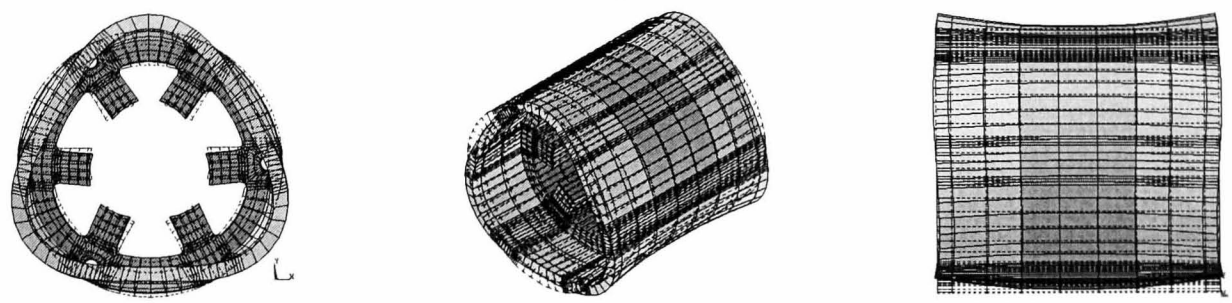

Mode 3a (6848Hz)

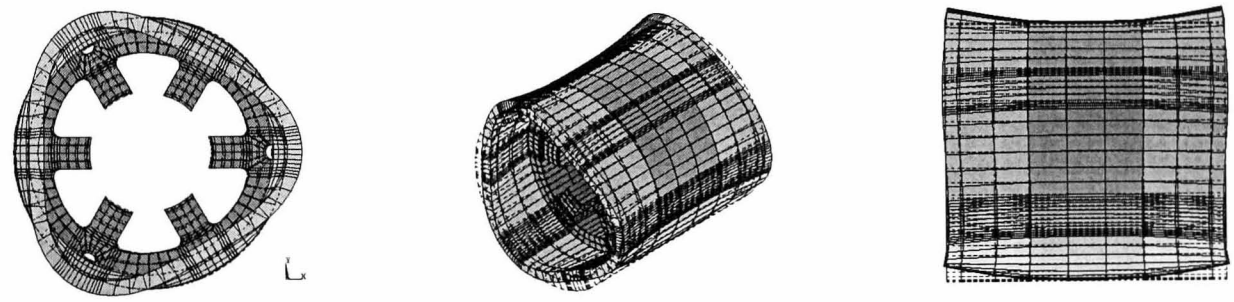

Mode 3b (7491Hz)

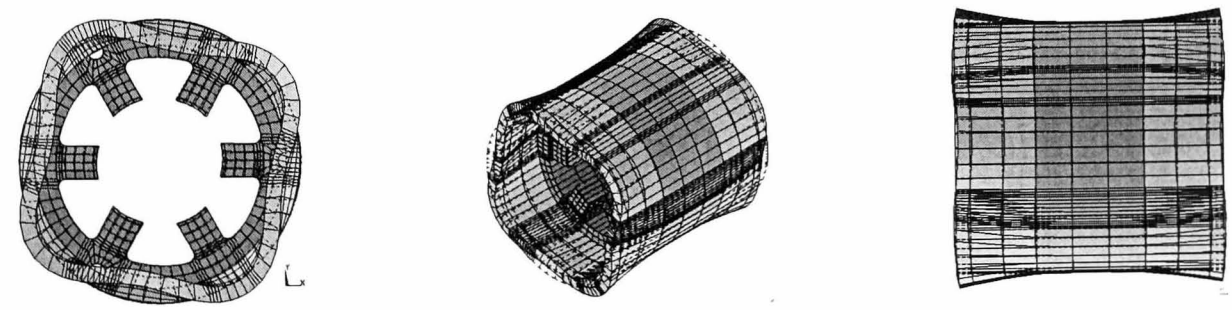

Mode 4 (10458Hz)

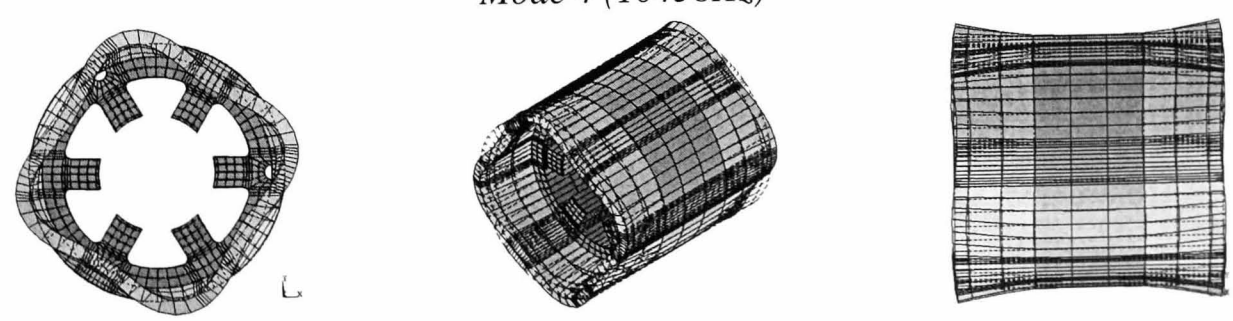

Mode 4 (10476Hz)

Fig. 3.59 *Core no windings, in frame without end-caps (winding mass and stiffness neglected*

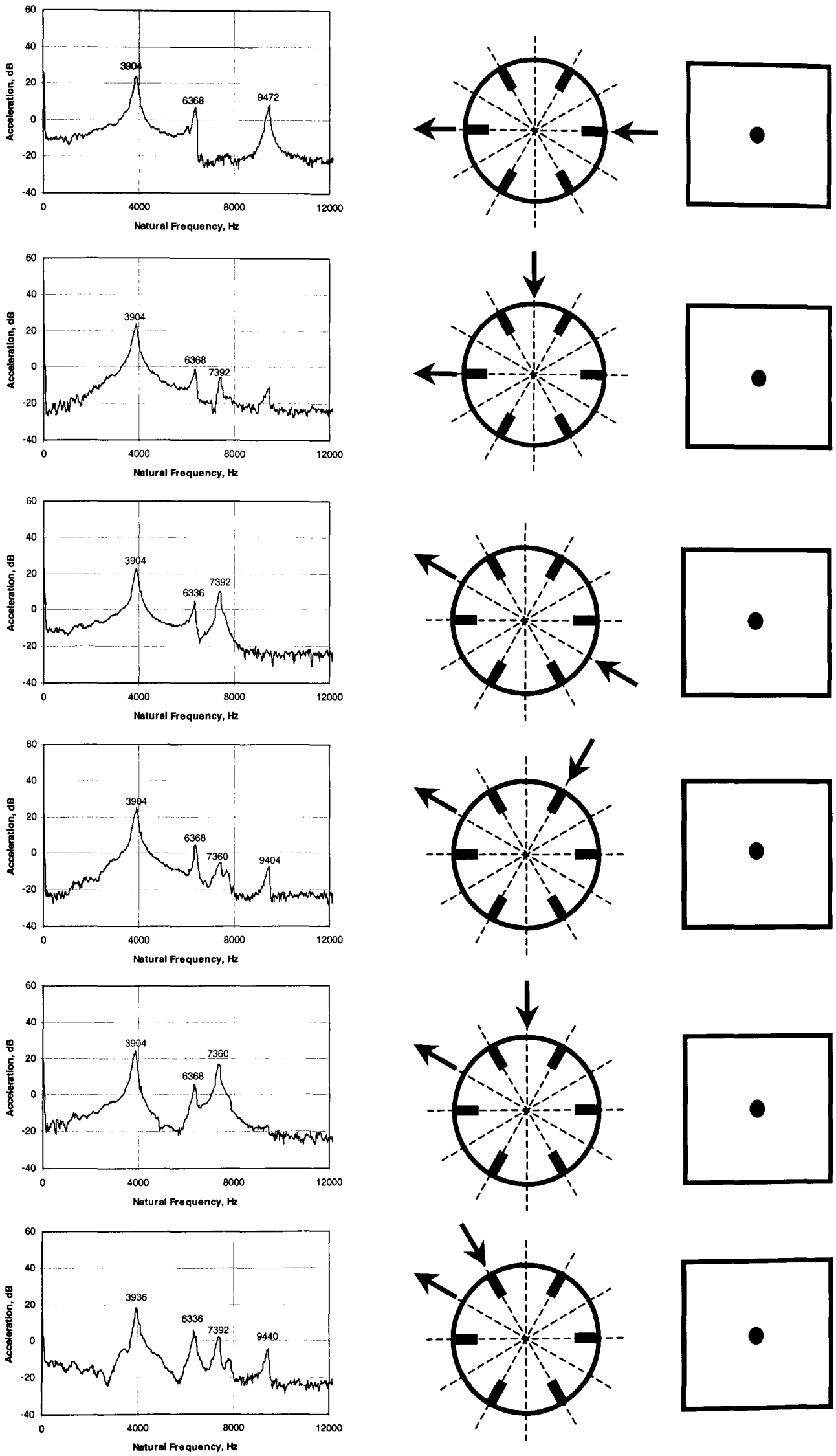

Fig. 3.60 *Frequency spectra of wound stator in frame with end-caps*

Table 3.35 *Wound stator core in frame with end-caps (Hz)*

Mode, *n*	Measured		3D FEA	Error[#]
	wound core	wound core in frame	wound core in frame	(%)
2a/b	2344	3904	3447	11.7
2a/b	2344	3904	3523	9.8
3a	5544	7360	6852	6.9
3b	7272	9472	9050	4.1
4a/b	10600	*	*	----
4a/b	10600	*	*	----

[#] *Compared to values measured on wound core in frame with end caps*

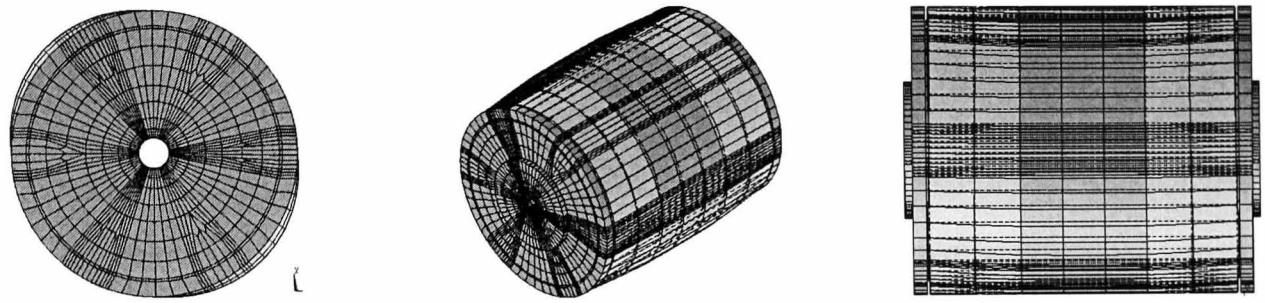

Mode 2 (3447Hz)

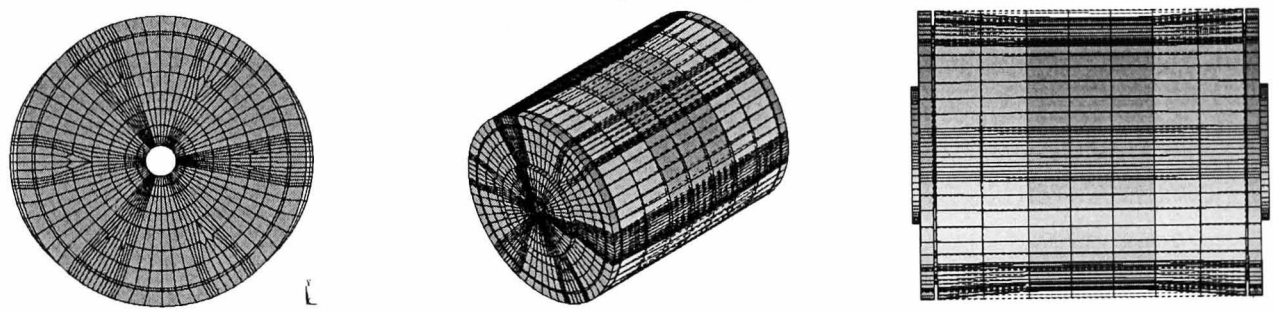

Mode 2 (3523Hz)

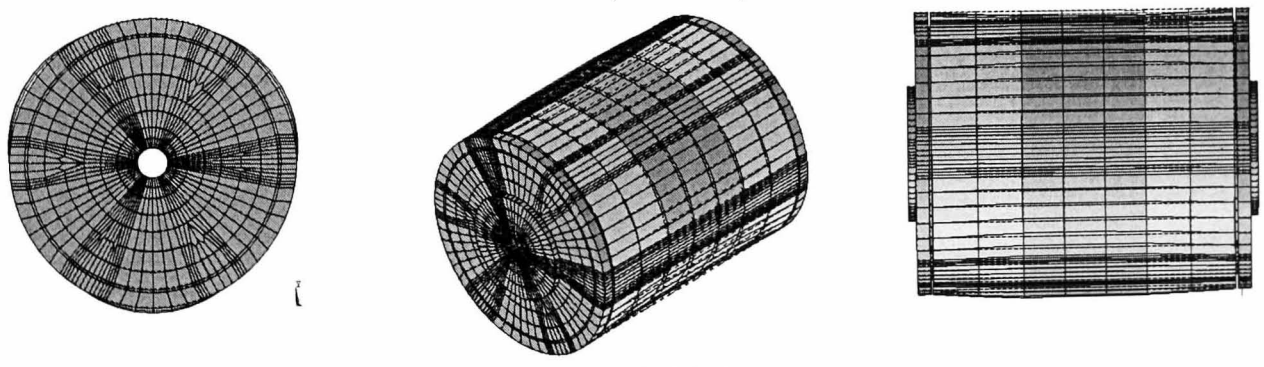

Mode 3 (6852Hz)

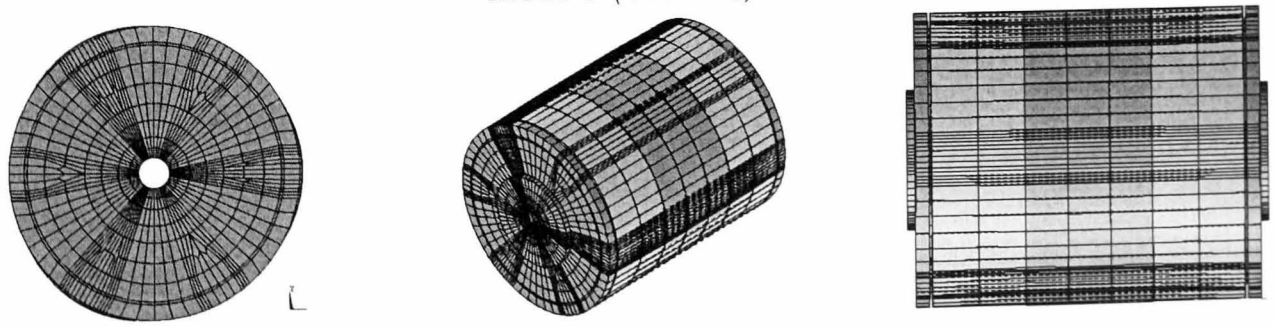

Mode 3 (9050Hz)

Fig. 3.61i *Stator in frame with end-caps – end-caps displayed*

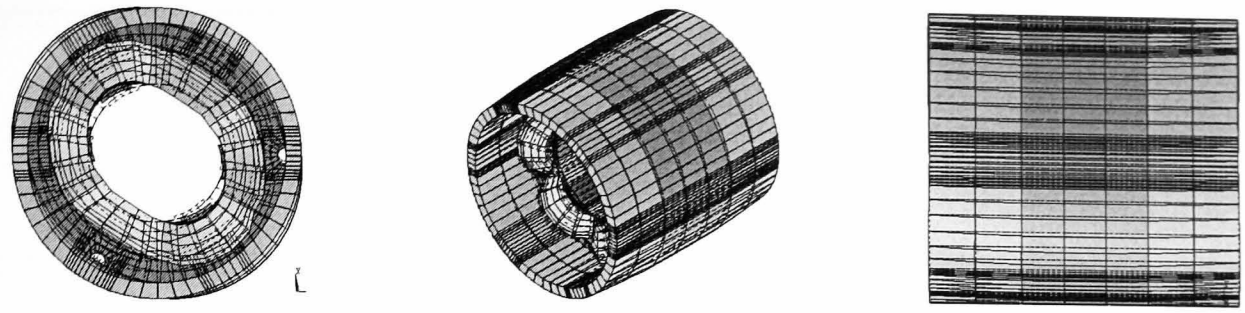

Mode 2 (3447Hz)

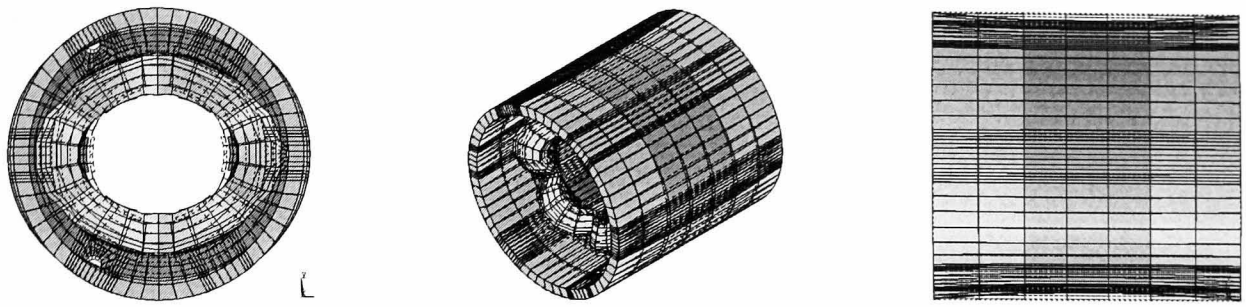

Mode 2 (3523Hz)

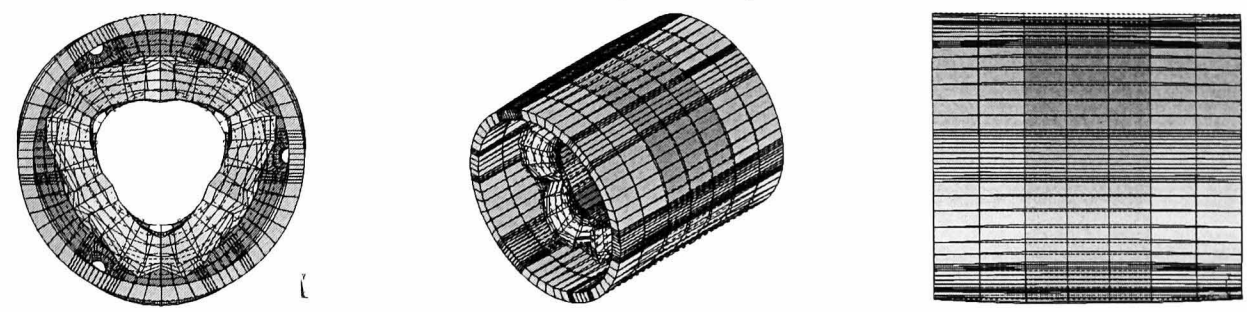

Mode 3 (6852Hz)

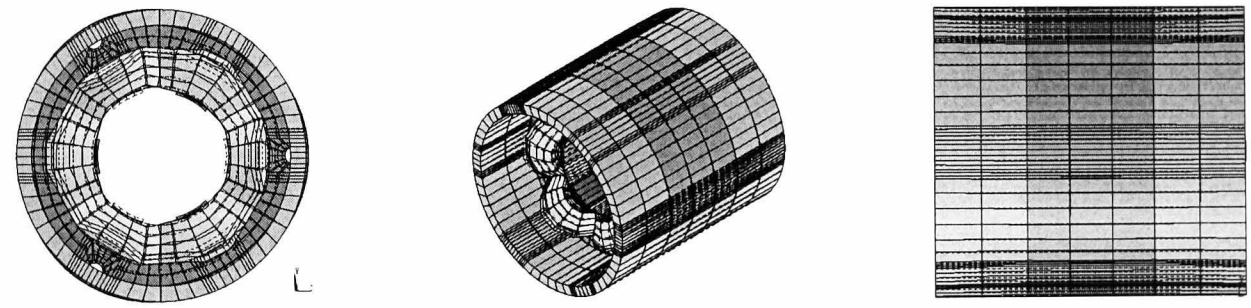

Mode 3 (9050Hz)

Fig. 3.61ii *Wound stator core in frame with end-caps – end-caps not displayed*

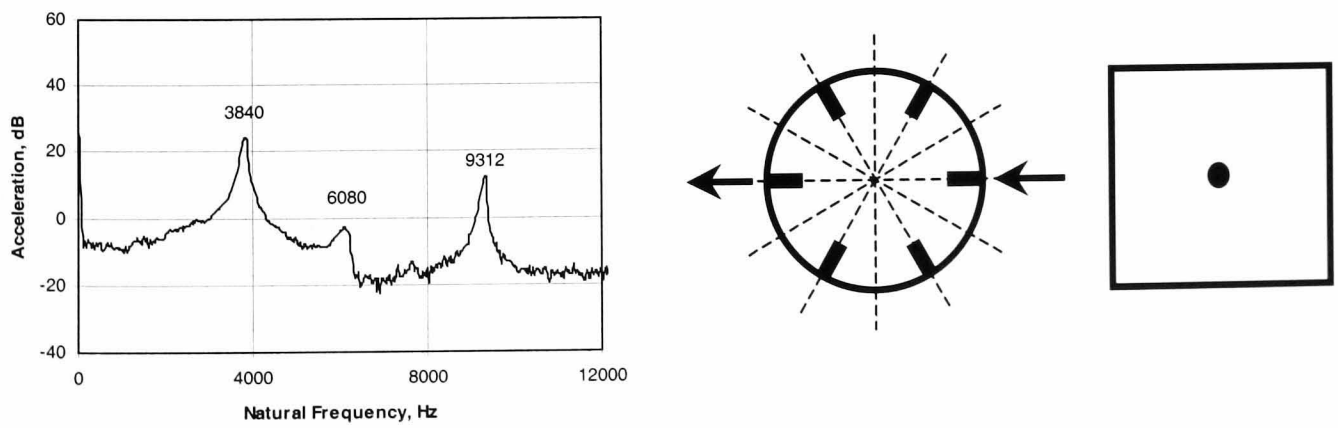

Fig. 3.62 *Frequency spectra of wound stator in frame with end-caps and bearings*

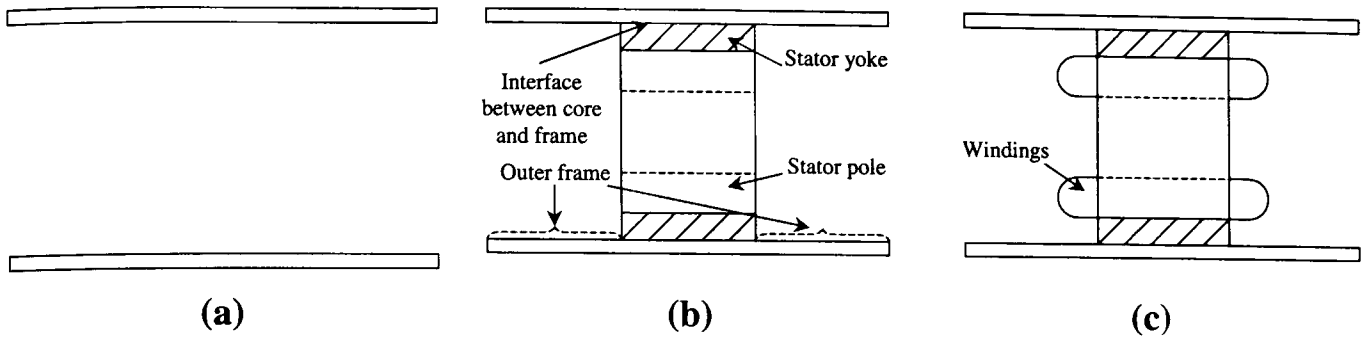

Fig.3.63 *Frame no end-caps; (a) without core, (b) with core, (c) with wound core*

Another important issue when dealing with the acoustic noise is the sensitivity of the human ear which, as highlighted in Chapter 1, varies with frequency and sound pressure. Referring back to the equal loudness contours of in Chapter 1, **Fig. 1.4**,. attention is drawn to the dip in the curves which occurs at approximately 4.2kHz. This implies that the human ear is more sensitive to frequencies in this region. As shown in **Table 3.35**, the frequency measured for mode 2 (3904Hz) is within this sensitive region and therefore the addition of the frame and end-caps have shifted the wound core natural frequencies to a more sensitive frequency for the human ear, thus causing the machine to be effectively 'louder'.

3.9 Influence of motor assembly and mounting

The final parameter which was considered in influencing the stator natural frequencies of the experimental machine was that of the mounting. The machine was mounted to a faceplate by four equi-spaced screws in the periphery of the frame. The resulting frequency spectra are shown in **Fig. 3.63(a) & (b)**, for the assembled machine coupled to the load machine as described in Chapter 2. The natural frequencies identified from the impulse tests are summarised in **Table 3.36**, together with those measured for the wound stator core in the frame with end-caps. It is observed that compared to the influence of the frame and end-caps as observed in the previous section, the mounting has negligible influence on the natural frequencies. However, if the machine was foot-mounted, the natural frequencies would in general, change, [XU99]. However, in this investigation the machine is mounted to a faceplate which contributes only to the radial stiffness of the machine, and that a similar level of radial stiffness is already introduced by the end-caps.

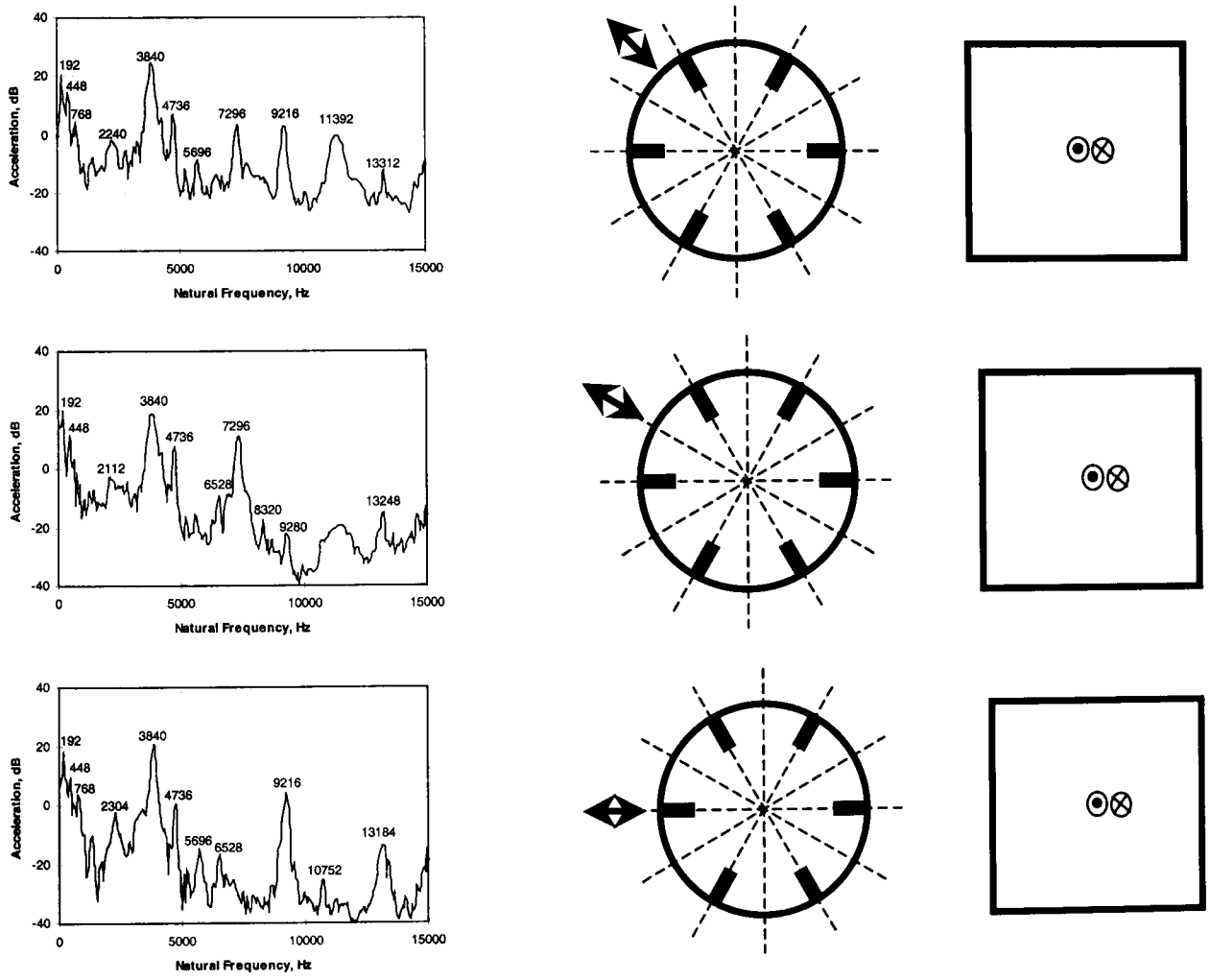

Fig. 3.63(a) *Vibration response of wound stator in frame with end-caps and bearing*

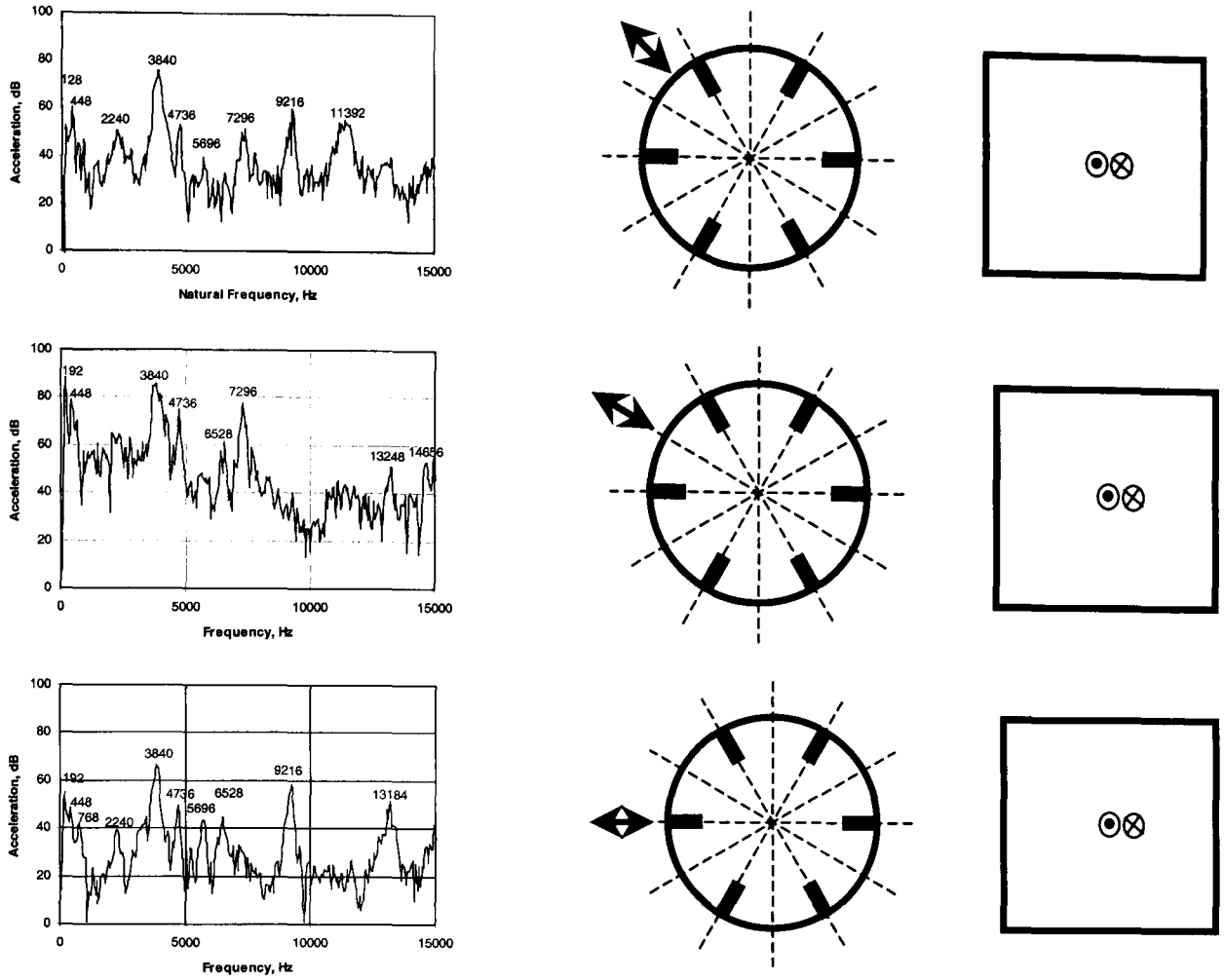

Fig. 3.63(b) *Transfer function of wound stator in frame with end-caps and bearing*

Table 3.36 *Influence of mounting wound core in frame with end-caps*

Mode,	Measured (Hz)		Change
n	Without mounting	Face-plate mounted	(%)
2a/b	3904	3840	1.64
3a	7360	7296	0.87
3b	9472	9216	2.70

3.10 Summary

This chapter presented a systematic investigation into the influence of the leading dimensions and geometric asymmetries of the stator on its natural frequencies and vibration modes. This was achieved by the application of 2D and 3D finite element models of increasing complexity, together with measurements on fabricated models for validation. Consequently, the most influential parameters have been identified and effective material properties have been deduced for the lamination stack and windings of the experimental machine under investigation, to enable 3D modelling to account for the windings and frame.

It has been shown that the influence of geometric asymmetries in the stator are much more significant than those which may be attributed to manufacturing tolerances, and therefore induce more distinctive dual natural frequencies for certain mode shapes. These dual natural frequencies possess greater separation as the asymmetry becomes more profound, and are shown to possess different motions associated with the stator vibration, viz. symmetric and anti-symmetric modes, which are not apparent from manufacturing tolerances due to the resolution of the spectral analysis apparatus. Consequently, the choice of pole number, the placement and number of notches and key-ways have been highlighted as influential factors on the number of natural frequencies a stator may possess in a given frequency range. However, through careful consideration at the design stage, these may be such as to minimise the possibility of stator resonance. For example, a 6-pole stator has been shown to possess a single frequency for modes 2 and 4 and dual frequencies for mode 3, whereas an 8-pole stator has been shown to possess a single frequency for modes 2 and 3 and dual frequencies for mode 4. However, odd vibration modes, i.e., modes 3, 5, etc, are generally not as important as even vibration modes in regard to noise generation in SR machines.

In addition, it has been highlighted that the poles should not be treated purely as an additional mass to the stator yoke, especially when higher mode numbers are of significance, since, firstly, they introduce dual frequencies, and, secondly, although they reduce the stator natural frequencies, their stiffness effect becomes more significant for higher mode numbers. However, a variation to the pole width only influences the symmetric and anti-symmetric mode types of modes 3 and 6, for the 6-pole stator under investigation, due to the nature of their kinetic and potential energies. In addition, it has been shown that the fillet radius has an insignificant effect on the natural frequencies.

It has been shown that the fabrication of a laminated stator core has a very significant influence on its vibrational characteristics, compared to a solid equivalent. The natural frequencies are considerably reduced, despite the reduction in the mass density from that of a solid core, and are influenced by the clamping pressure and the means of affixing the laminations together. It was found that the effective Young's modulus E_z of a laminated silicon iron core had the same value as for solid silicon iron, for axial mode 0, although it had been expected to reduce slightly. However, this was partially attributed to the fact that in the experimental SR machine the laminated stator core was welded at six circumferential points along its axis. In fact, the influence of E_z was found to be insignificant for the in-plane flexural vibration, i.e. axial mode $m=0$. The shear moduli were found to have a more significant effect than the Young's moduli on the natural frequencies, the values both in the plane (G_{xy}) and normal to the laminations (G_{xz}, G_{yz}) being ≈90% and ≈33% of the values for solid silicon iron, respectively. It was also found that laminating a core significantly increases the damping, such that the axial modes, $m=1$, are suppressed significantly, although these modes are not generally relevant to noise production in SR machines.

Due to the relatively short overhang lengths, the end-winding mass and stiffness are as influential as the slot windings, in that the end-windings cannot be treated merely as an additional mass in the slots, or the complete windings as an additional mass in the poles. In fact, the influence of the winding mass is offset by their stiffness, so that their influence on the values of the frequencies of the dominant vibration modes is relatively small. However, it was emphasised that the stator windings impose a high level of additional damping to the stator core, and, therefore, reduce the magnitude of the vibrations and hence acoustic noise. Thus, with the addition of a frame to the wound stator core it is apparent that the damping introduced by the windings will limit propagation of the frame vibrations to the surrounding air, and hence reduce the acoustic noise. Further, for higher modes their stiffness may become more apparent in restraining the lateral movement of the stator poles, although the most important vibration modes are usually those with low orders. It was also found that the presence of the stator winding introduces a large number of additional vibration modes, many of which correspond purely to end-winding movement. These increase the complexity of the winding analyses, but are not relevant to noise generation, as evidenced by the noise and vibration measurements on the experimental SR machine

The addition of a smooth frame to the wound stator core has been shown to increase the core natural frequencies considerably, whilst the addition of end-caps causes a much further increase, due to their very high radial stiffness restraining radial movement of the axial ends of the frame. However, it was found that the assumption of an intimate contact between the end-caps and the frame, for modelling purposes, resulted in a large over-estimate of the predicted natural frequencies, and that this was more severe for the lower mode shapes. This highlighted the limitation of finite element techniques for analysing such highly complex mechanical structures comprising of non-linear material properties and discontinuities in their fabrication, but provided an upper limit to which the end-caps may increase the natural frequencies, if for example, they were to be welded to the frame. However, it was highlighted that the addition of the end-caps introduces additional damping, and that as the rigidity of the end-caps to the frame increases this damping will reduce, thus increasing the potential for higher vibration magnitudes. Finally, the face-plate mounting arrangement which was employed for the experimental SR machine was shown to have an insignificant influence on the natural frequencies, since it added no further radial stiffness to that already provided by the presence of the end-caps. However, the natural frequencies generally change if foot-mounting is employed, [XU99].

Chapter 4
Influence of Control Parameters on Acoustic Noise and Vibration

4.1 Introduction

The SR machine is inherently noisy due to the radial stator deformation which results from the large radial electromagnetic forces which are developed as alternate phases are excited, since, in the absence of saturation, the force is proportional to the square of the airgap flux density. The stator vibration and emitted noise are most severe when the electromagnetic force coincides with a natural frequency of the stator, thereby inducing a mechanical resonance. Furthermore, it is well established that the vibration level is generally greater at turn-off than turn-on due to the larger radial force component which is present as the stator and rotor poles move closer towards the aligned position, such that the excited stator poles are attracted towards the rotor. Therefore, at phase turn-off when the stator is released from the compressed state, it accelerates away from the rotor, inducing vibration and hence acoustic noise. A number of investigations have been carried out that address the control parameters and their influence on the emitted noise, [BES94, NEV97, BLA94, GAB97], from which it is clear that the control parameters have a significant effect on the noise. Investigations to-date encompass issues such as the variation of the switching angles, [BLA94, BES94, NEV97], a comparison of voltage and current control methods, [BLA94, GAB97] and a comparison of soft and hard voltage chopping, [GAB97].

Although numerous investigations have been undertaken, studies on the influence of the control parameters on the noise and vibration of SR machines are far from exhaustive. In general, investigations to-date have been undertaken in isolation and have usually been limited to either frequency or time domain analyses, with limited physical explanations of measured results. Therefore, in this chapter a detailed and systematic investigation, which considers the most common control methods employed for SR machines and in which the results are analysed in both the frequency and time domains, and are complemented by measurements of the sound pressure level, is described. A summary of the investigations which have been undertaken is outlined in **Table 4.1**. These address the influence of speed and load on the noise and vibration, as well as voltage and current control techniques, and the influence of hard and soft chopping techniques. In addition,

the effect of different PWM switching frequencies for voltage PWM control and the sampling frequency, which is employed for current control, is investigated together with single pulse operation. The noise and vibration is assessed whilst the machine is operated under single pulse mode with a reduced dc link supply. Finally, the influence of switching angles, for advanced commutation, is discussed for both voltage and current control methods over a range of operating speeds. Throughout the investigations, both the A-weighted sound pressure levels (SPL) and their associated spectra are analysed, together with frequency and time domain stator vibration measurements.

Table 4.1 *Summary of noise and vibration investigations*

Test Description	Test Condition			
	Voltage PWM Control		Current Control	
	No-load	Load	No-load	Load
Soft chopping	√	√	√	√
Hard chopping	√	√	√	√
Variation of switching f	√	√		
Variation of sampling f			√	√
Advance θ_{on} and θ_{off}	√		√	
Single pulse operation	√	√	√	√

4.2 Initial investigation

The experimental SR machine which was employed for the investigation is that which was described in Chapter 2. It has 6 stator poles and 4 rotor poles, and is encased in a shrunk-fit aluminium frame, which is secured to a solid faceplate. The machine was tested in a non-standard anechoic chamber on a rigid mounting fixture, **Fig. 4.1.** A wound-field dc machine was employed for simulating various load conditions on the SR machine, and was mounted external to the anechoic chamber to ensure that the only sources of noise within the chamber were associated with the SR machine, **Fig. 4.2**. The two machines were coupled via a flexible coupling and a shaft through the wall of the chamber which was supported by RHP self-lube cast iron pillow block unit bearings. Thus, although for many of the experiments the SR machine was operated under no-load, strictly speaking there was always a frictional torque applied to the SR machine from the bearing sets in the system and the frictional torque of the dc machine.

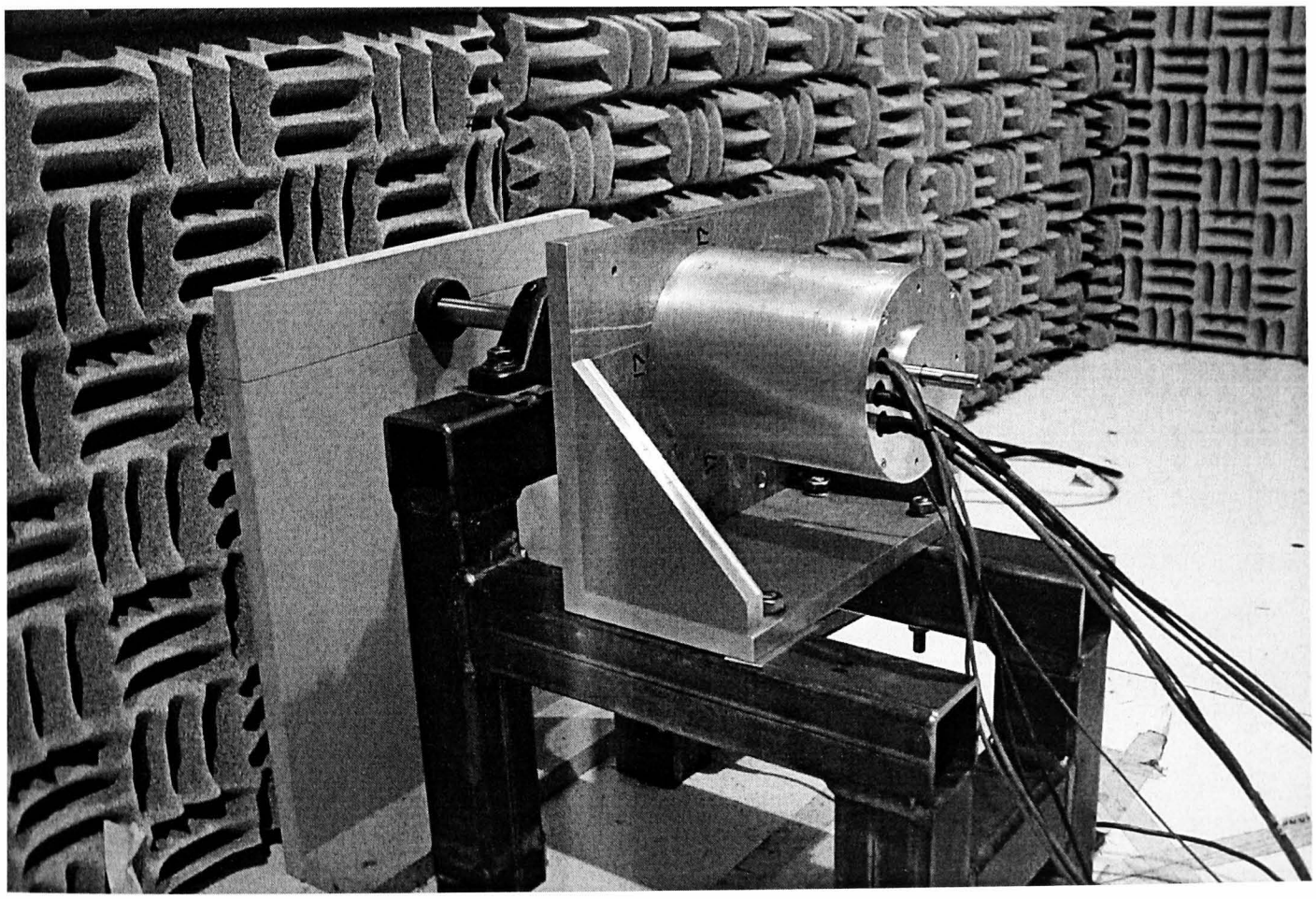

Fig. 4.1 *Non-standard anechoic chamber (with motor & mounting)*

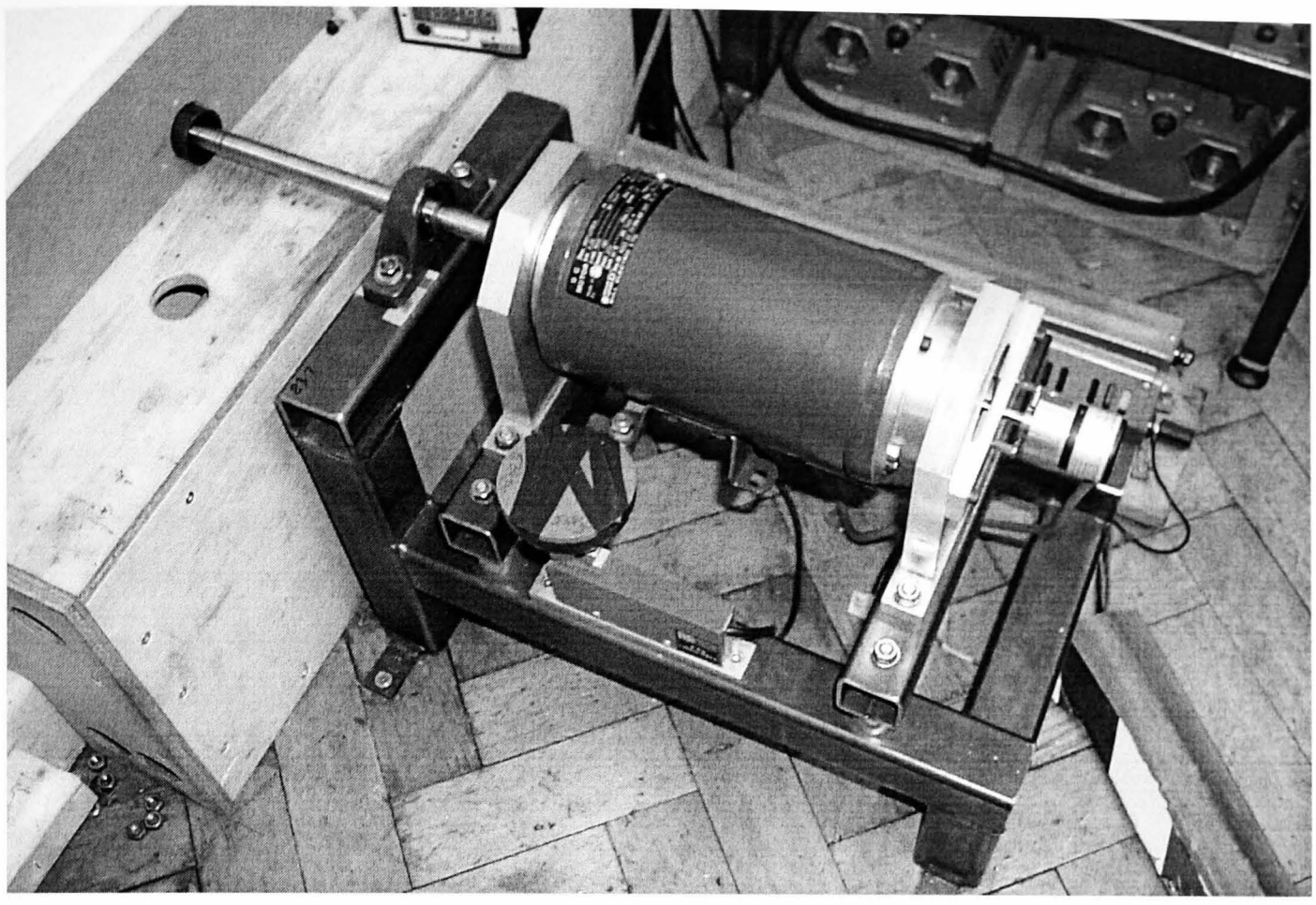

Fig. 4.2 *Adjacent room (with dc load machine & mounting)*

Equipment

The vibration was measured behind a stator pole of a given phase by a PCB Piezotronics ICP accelerometer, Model 353B15, which was calibrated with an output sensitivity of 10mV/g. A calibrated IEC Bruel & Kjaer precision integrating sound level meter (SLM), Type 2221, was employed for all the A-weighted sound pressure level measurements, dBA, and spectral noise data. The output from the accelerometer and SLM was analysed and recorded by a Hewlett Packard dynamic signal analyser, Model HP35660A. The calibration of the equipment and the scaling of the output data is discussed in Appendix G, together with the resolution and sampling associated with the dynamic signal analyser.

Distance of sound level meter (SLM) from centre of SR machine

It is well established that the main source of noise is attributed to the radial deflection of the stator. Thus, for the majority of the experiments, the SLM should be located behind a stator pole. The horizontal distance, '**X**', of the SLM from the experimental machine needs to be determined, **Fig. 4.3**. An anechoic chamber resembles that of a free-field environment, and, therefore, the sound pressure level measured is expected to drop 6dB for each doubling in distance from the noise source. For a range of distances relative to the centre of the experimental machine, both the A-weighted sound pressure level and

the spectrum content of the sound were recorded, **Table 4.2** and **Fig. 4.4** respectively, together with the vibration, **Fig. 4.5**. The SPL measurements relate to location 1 shown in **Fig. 4.6**, with respect to the position of the SLM around the periphery of the machine. For such a small machine important information could be missed if too great a distance is chosen, and in many of the investigations reported to-date, [CAM92], [BLA94], [WU95], distances from the centre of the machine in the range of 1-20cm have been employed. As can be seen, the dominant frequencies in the noise spectra are closely associated with the vibration of the stator, as can be seen clearly by comparing the sound pressure level spectrum at 100mm with the associated vibration spectrum. At a distance of 200mm, the noise peaks associated with the stator vibration lose their clarity, although the sound pressure level is approximately 6dBA lower compared to that at 100mm, confirming a free-field environment. Therefore, a distance of 100mm was chosen as the radial distance for all subsequent measurements, since this provided the best correlation with the vibration measurement.

Table 4.2 *Variation of sound pressure level with distance of SLM from centre of machine (SR machine excited)*

Distance from centre of SRM, **X** (mm)	Sound pressure level (dBA)
100	78.1
150	74.1
200	71.9
250	70.0

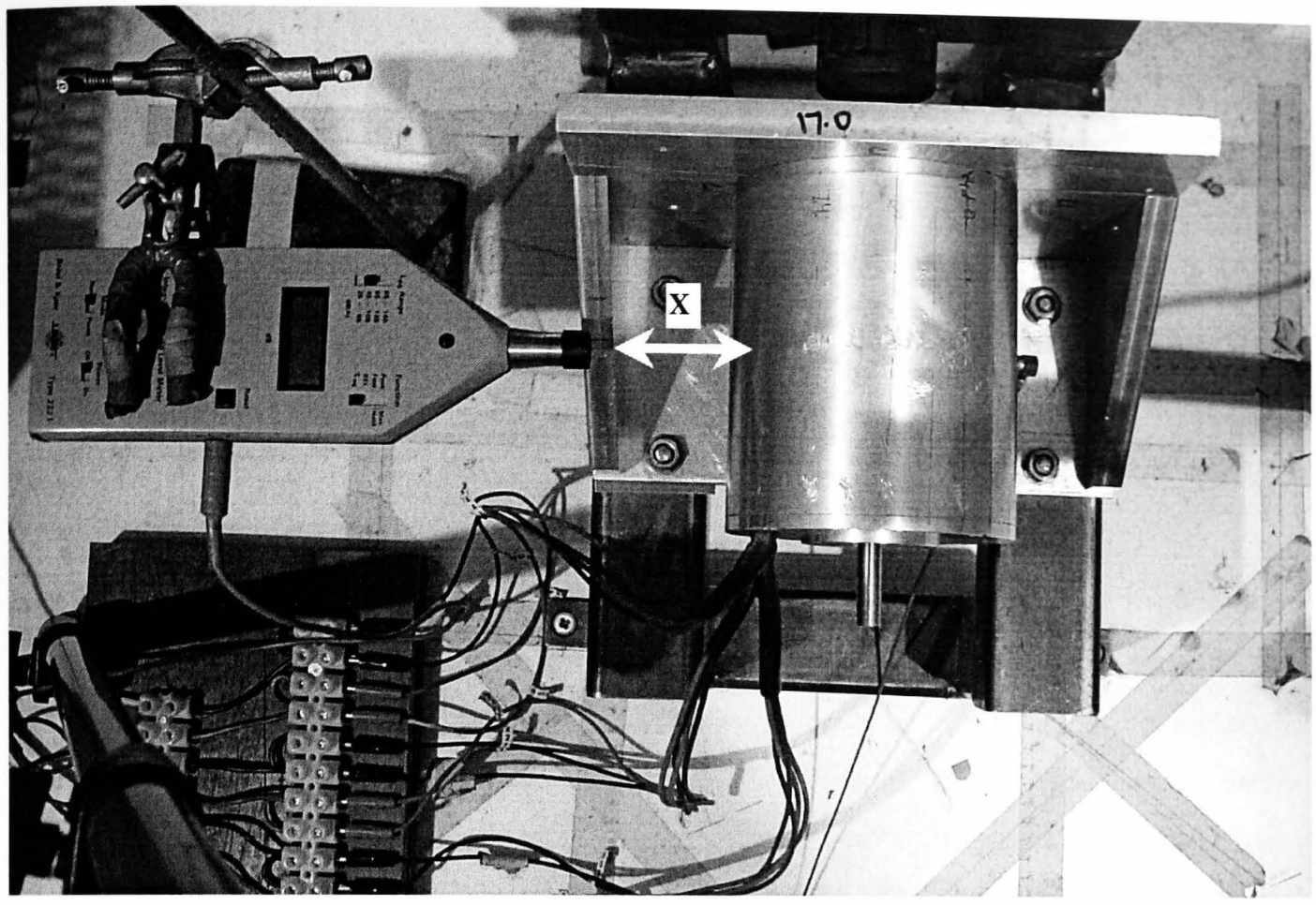

Fig. 4.3 *Distance of sound level meter (SLM) from centre of SR machine, location 1*

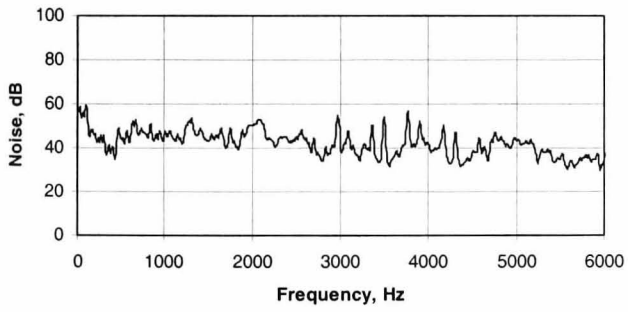

250mm location 1

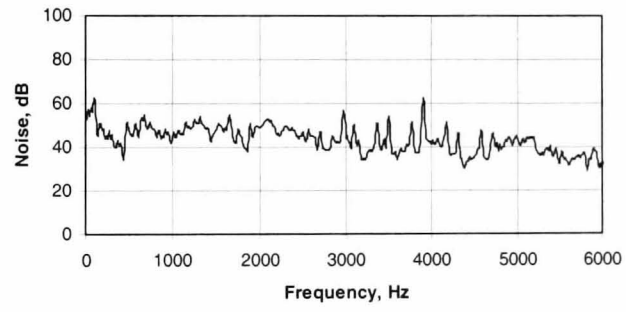

200mm location 1

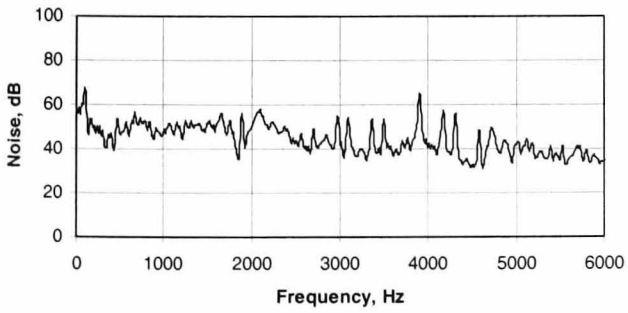

150mm location 1

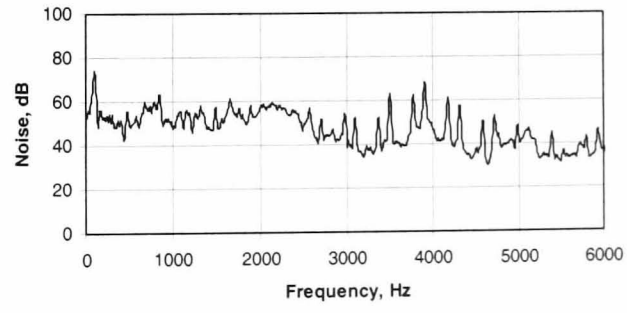

100mm location 1

Fig. 4.4 *Sound pressure level spectra, no-load, 2020rpm*

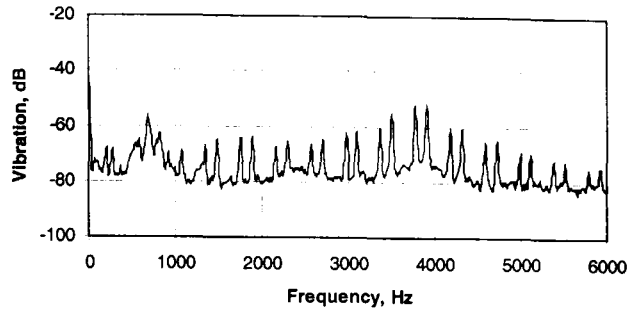

Fig. 4.5 *Vibration spectrum at 2020rpm, no-load*

Peripheral position of SLM

In order to establish whether there were any additional sources of noise, the SLM was located at a number of positions around the periphery of the experimental machine, as indicated in **Fig. 4.6** where location 1 represents that shown in **Fig. 4.7**. The recorded data, **Fig 4.8** and **Table 4.3**, shows the noise is more dominant at the radial location behind the poles, i.e. locations 1 and 5, than at locations perpendicular to the end-shields (point 3) or at ±45° to the end-shields (locations 2 and 4). This observation was expected, and further highlights the dominance of the radial deflection of the stator on the emitted acoustical noise.

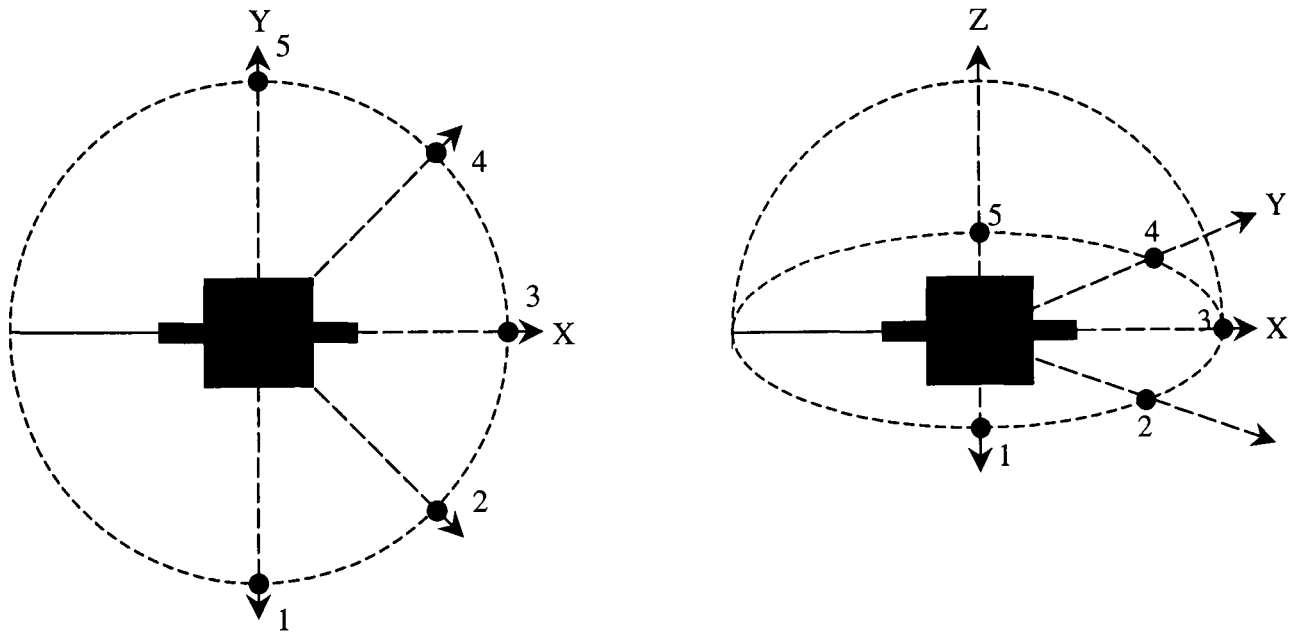

Fig 4.6 *Sound pressure measurement locations around periphery of machine*

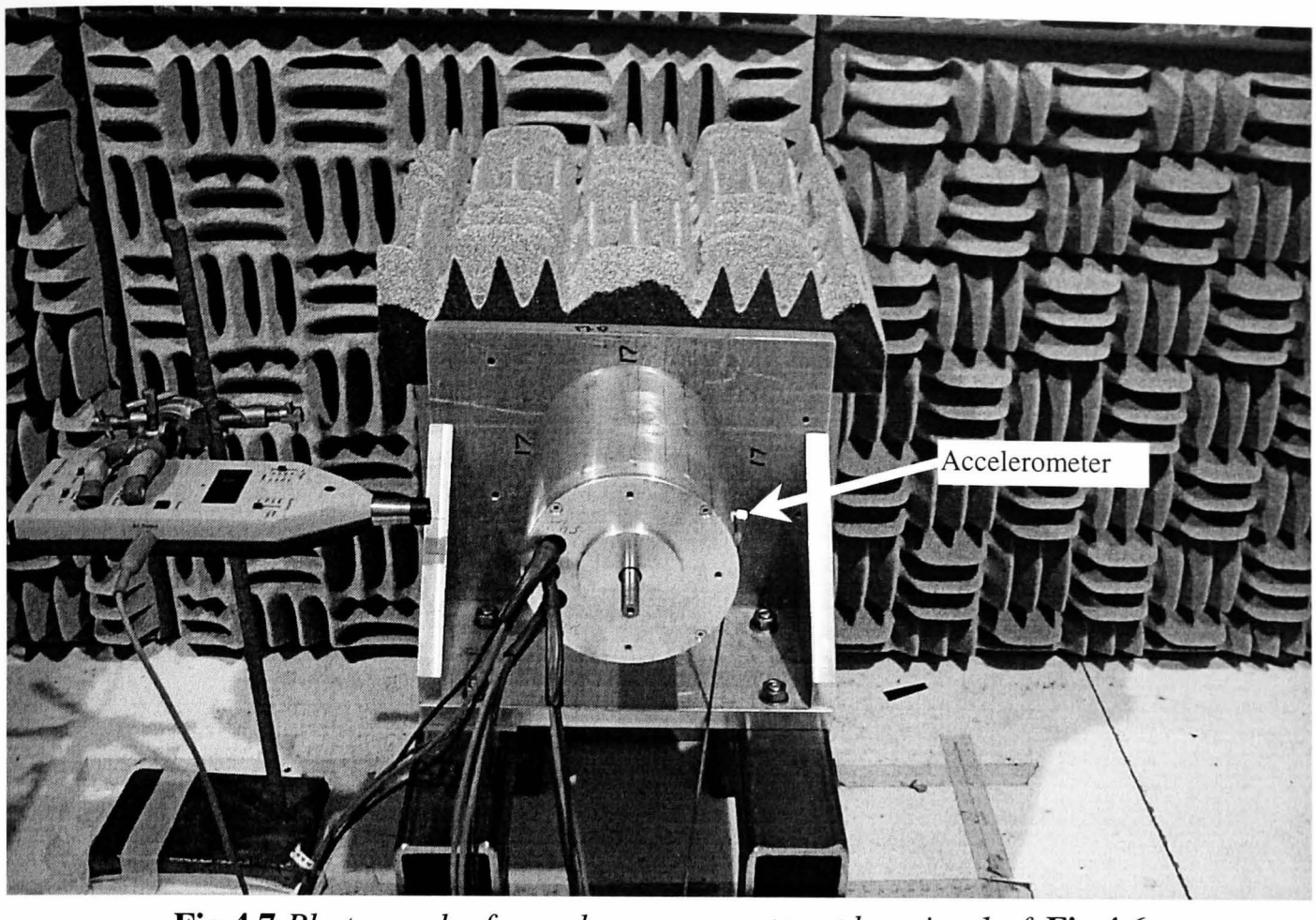

Fig 4.7 *Photograph of sound pressure meter at location 1 of* **Fig 4.6**

Table 4.3 *Variation of sound pressure level pressure for periphery position of SLM*

Location, **Fig. 4.6** relating to **Fig. 4.8**	Sound Pressure Level (dBA)
(1)	78.1
(2)	72.4
(3)	72.7
(4)	74.0
(5)	77.8

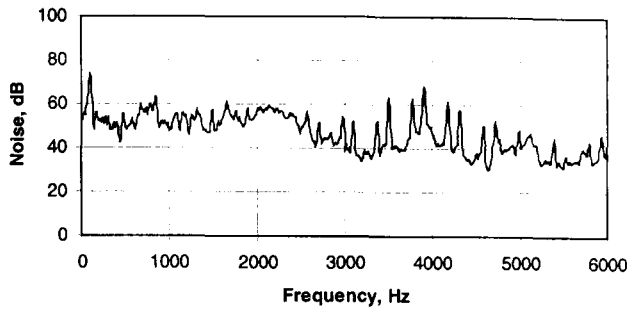

Location (1)

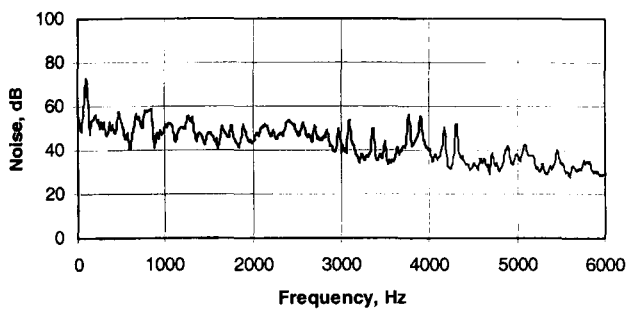

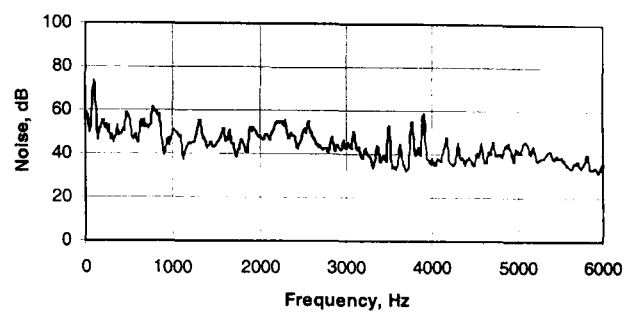

Location (2)

Location (3)

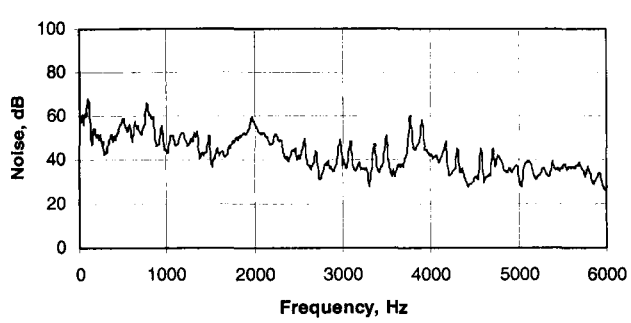

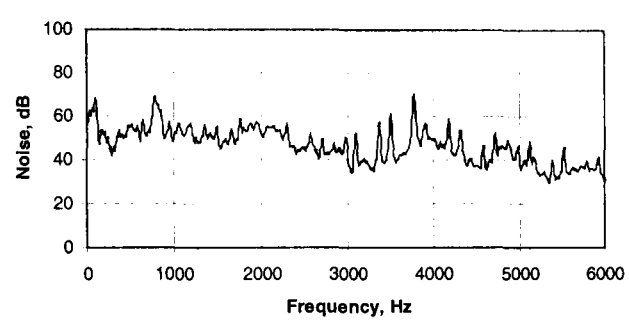

Location (4) *Location (5)*

Fig. 4.8 *Measurements at 100mm from centre of machine, at 2020rpm, no-load (refer to* **Fig. 4.6** *for measurement locations)*

Background Noise

Having confirmed that the radial deformation of the SR machine is the dominant cause of the emitted noise, thereby enabling the most appropriate location of the SLM and accelerometer to be selected, the following measurements were made to highlight any noise sources which were not associated with the excitation of the SR machine, such as the bearings and general background noise.

Firstly, the SR machine was driven by the dc machine with the SR machine unexcited. The SPL was recorded over a range of speeds, **Table 4.4**, with the SLM at location 1 of **Fig. 4.6**, together with the associated stator vibration, **Fig. 4.9**. The natural frequencies of the SR experimental system were also identified, **Fig. 4.10i & ii**, from which it will be seen that the peak vibration at 192Hz coincides with that of peak '1', **Fig. 4.9**. At 500rpm no dominant peaks are present in the vibration and noise spectra, whereas at

1000rpm more pronounced peaks can be observed at the low frequency end of the spectra, with particular reference to peak '1', together with an increase of 7.1dBA in the SPL, **Table 4.4**. Hence, the spectra are limited to a frequency range of 0-6kHz. At 1500rpm, peak '1' is still pronounced in the vibration spectrum, although the sound level has only increased by a further 2.6dBA. At 2000rpm, a dramatic change occurs to both the noise and vibration spectra. A large number of distinct peaks are now present in the vibration spectrum, many of which also occur in the noise spectrum, and the magnitude of peak '1' has increased significantly. This is reflected in the background noise level having increased by 17.9dBA to 86.0dBA. At this speed a loud, deep 'grumbling' noise was heard, which was not evident at the other speeds. This was clearly due to a critical speed of the shaft and/or a system resonance being excited. A further increase of speed to 2500rpm causes the spectra to settle down again, with peak '1' as the only significant peak and the background level reduced, but not as low as that at 1500rpm. The SPL reduces to a value of 74.5dBA, which is significantly lower than at 2000rpm but higher than at 1500rpm, indicating that a rotor/system resonance is no longer being excited.

Secondly, a number of SPL measurements were made at locations at which other sources of acoustic noise might be identified, such as the couplings, the coupling shaft and the bearing housings, etc, as shown in **Fig. 4.11**. The SR machine was again unexcited, and the noise spectra was recorded at speeds of 1500rpm, **Fig. 4.12**, and 2000rpm, **Fig. 4.13,** the associated sound pressure levels being given in **Tables 4.5 & 4.6**, respectively. No significant variation in the noise spectra can be seen at measurement locations (a) to (d) for a speed of 1500rpm, **Fig. 4.12** and the magnitude of peak '1'appears to remain constant. However, at location (d), at which the SLM is directed towards the flexible coupling, the highest SPL is recorded, **Table 4.5**. Furthermore, when the speed is increased to 2000rpm, at which a shaft/resonance occurs, the SPL is seen to increase significantly at location (d), **Table 4.6** and is higher than that at location (a). Observation of the spectra of **Fig. 4.13** shows the magnitude of peak '1' is slightly higher at location (d) than at location (a), which highlights the possibility that there is a shaft resonance. The identification of the source of the additional peaks at around 2000rpm is difficult, and although many of the peaks are present in the transfer function of **Fig. 4.10**, identification of their origin is outside the scope of the investigation and was, therefore, not pursued.

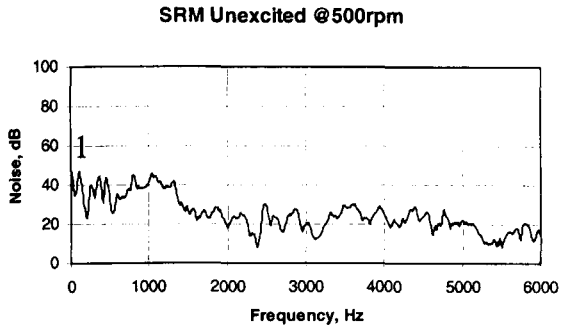

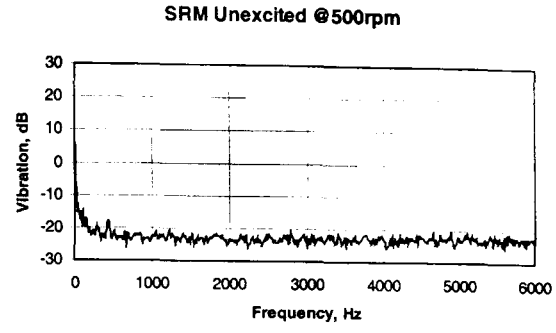

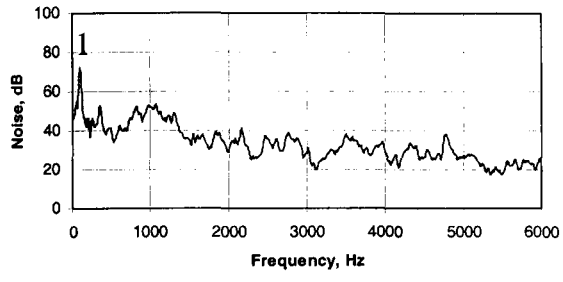

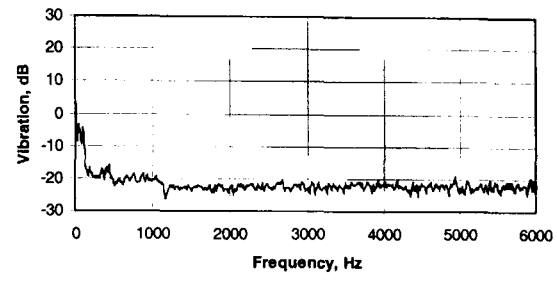

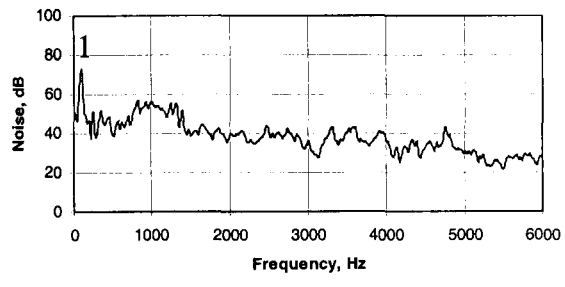

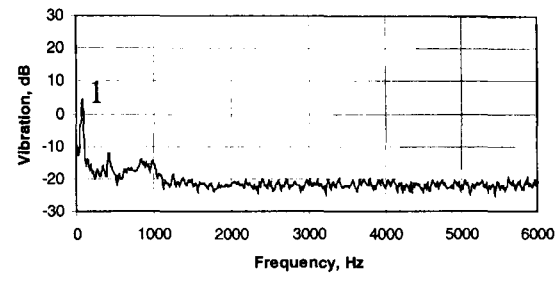

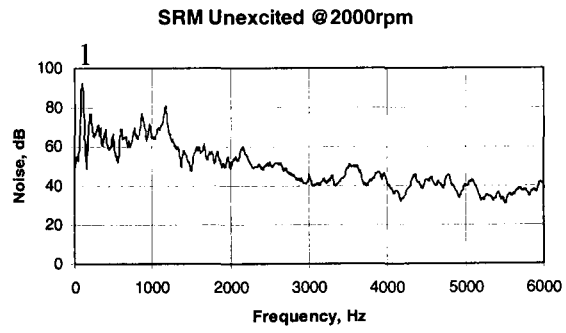

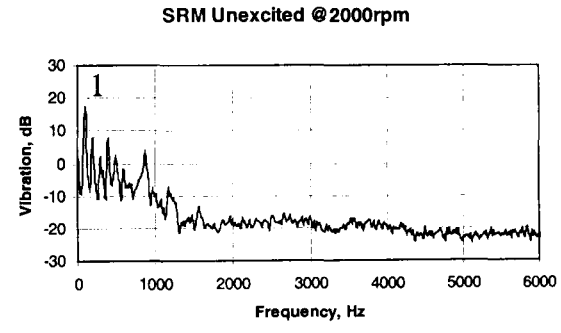

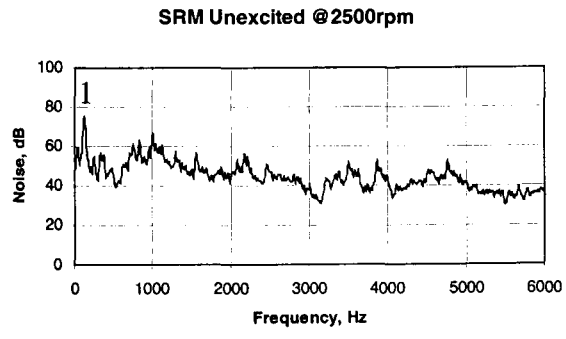

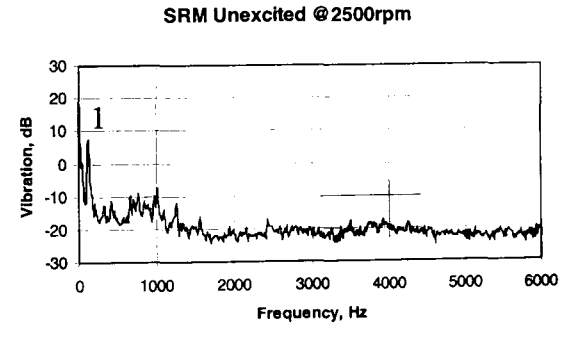

Fig. 4.9 *SR machine driven by wound-field dc machine, noise measured at location 1*

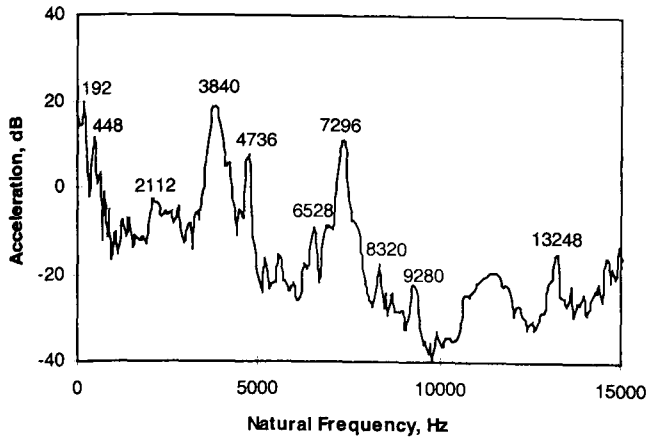

(a) *Between poles*

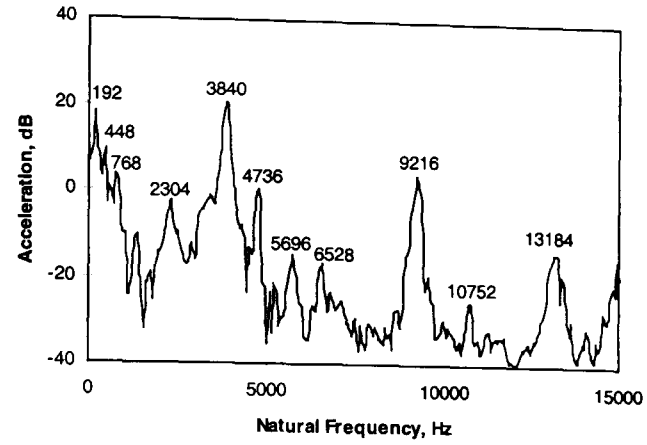

(b) *Behind pole*

Fig. 4.10i *Vibration response of SR experimental system excited at two locations*

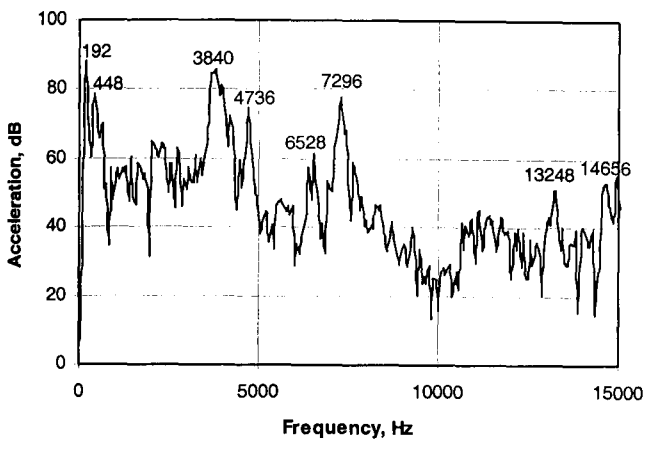

(a) *Between poles*

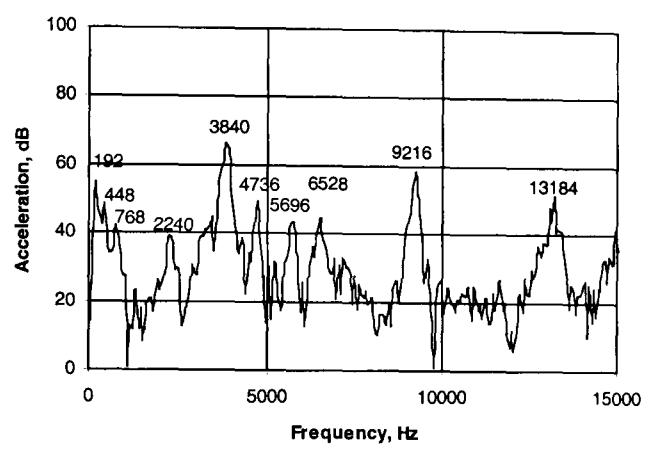

(b) *Behind pole*

Fig. 4.10ii *Transfer function of SR experimental system excited at two locations*

Table 4.4 *Summary of A-weighted SPL for given speeds, PLM at location 1, (SR machine unexcited)*

Speed (rpm)	SPL (dBA)
500	58.4
1000	65.5
1500	68.1
2000	86.0
2500	74.5

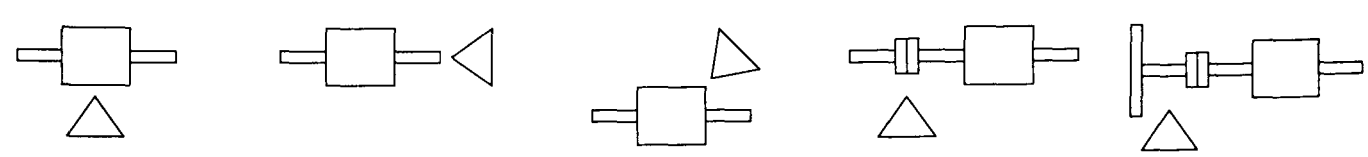

Position (a) *Position (b)* *Position (c)* *Position (d)* *Position (e)*

Fig. 4.11 *Locations of SLM during background noise measurements*

Table 4.5 *Summary of A-weighted SPL for various SLM locations, 1500rpm (SR machine unexcited)*

Position, **Fig. 4.11**	SPL (dBA)
(a)	68.1
(b)	64.7
(c)	66.1
(d)	73.7

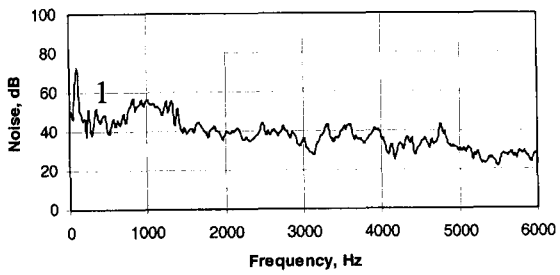

Location (a)

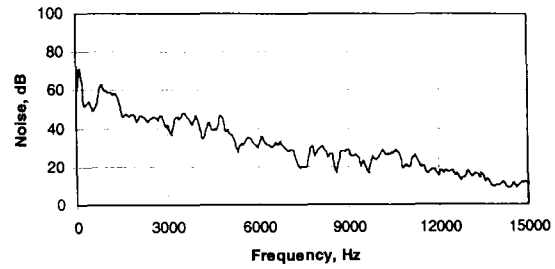

Location (a)

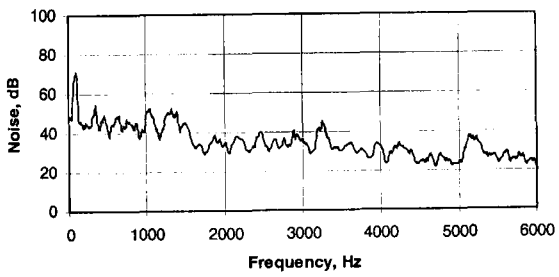

Location (b)

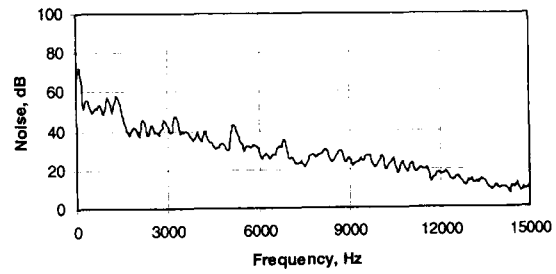

Location (b)

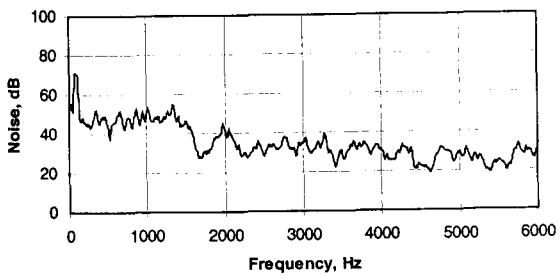

Location (c)

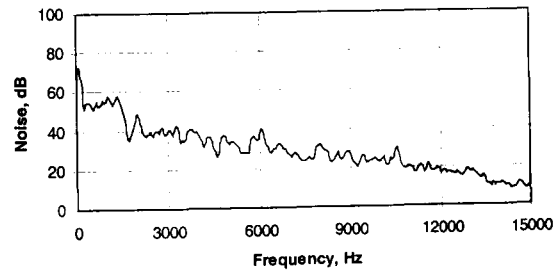

Location (c)

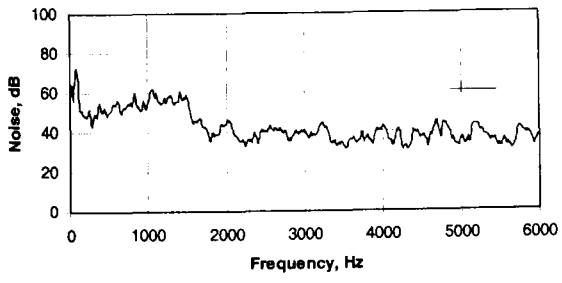

Location (d)

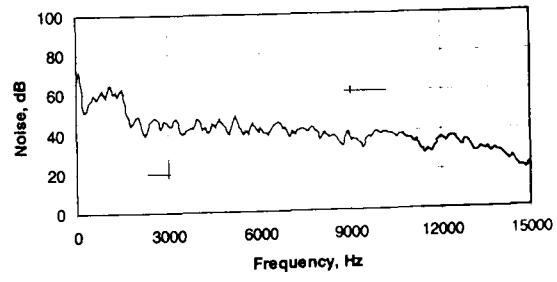

Location (d)

Fig. 4.12 *Measurements at various locations to identify potential noise sources, 1500rpm (SRM unexcited)*

Table 4.6 *Summary of A-weighted SPL for various SLM locations at 2000rpm (SR machine unexcited)*

Position, **Fig. 4.11**	SPL (dBA)
(a)	86.0
(d)	87.0
(e)	85.5

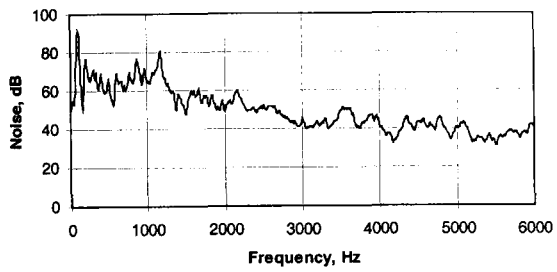

Location (a)

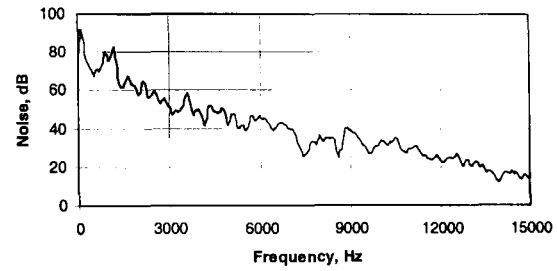

Location (a)

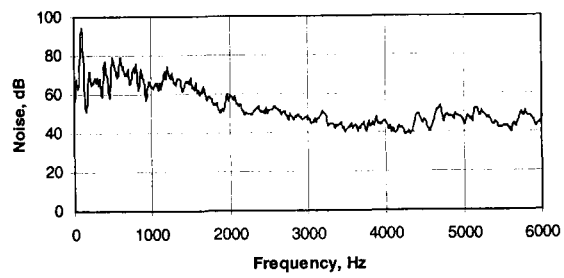

Location (d)

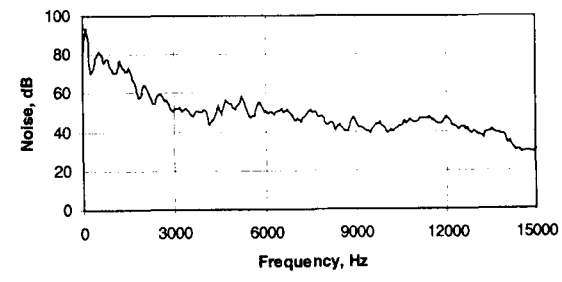

Location (d)

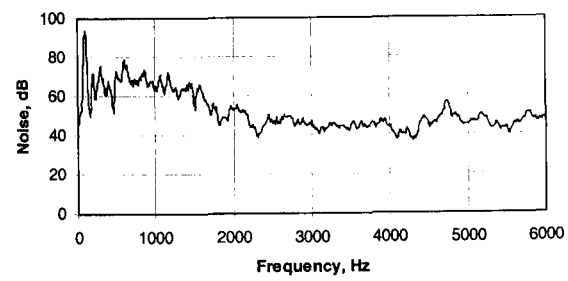

Location (e)

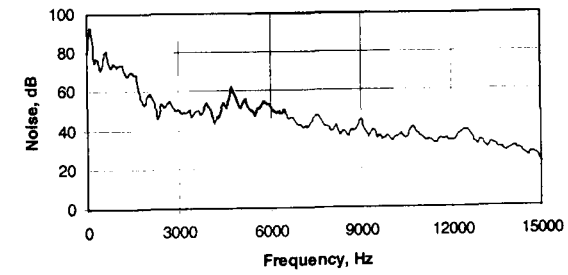

Location (e)

Fig. 4.13 Measurements at locations *to identify potential noise sources, 2000rpm (SRM unexcited)*

The SR machine was subsequently excited, and test data was recorded at three different speeds, viz. 3472rpm, 1991rpm, 460rpm. The harmonic content of the commutation signal and no-load current waveform was then analysed with respect to the associated noise and vibration spectra. The three speeds embraced the nominal speed range of the SR machine, 3742rpm resulting in single pulse mode operation. It is observed that the harmonics in the commutation signal correlate with those in the current waveform, **Fig. 4.14i** and it is noted that the 3rd harmonic and multiples thereof are absent in the commutation signal owing to the fact that it is essentially a pulse train with a duty cycle $\tau/T=1/3$, see Appendix H. This is also the case at 1991rpm, **Fig. 4.14ii**, and 460rpm, **Fig. 4.14iii,** although for the latter the peaks are indistinguishable due to the relatively small increments between the frequency harmonics with respect to the resolution of the dynamic signal analyser for the given frequency ranges.

The rotational shaft frequency of the machine is defined by equation (4.1), where ω_r is the rotational shaft speed in rads^{-1}. Thus, at a speed of 3472rpm the shaft frequency is ≈58Hz. The phase excitation frequency is defined by equation (4.2), where N_r is the number of rotor poles, whilst the dc supply switching frequency is defined by equation (4.3) where m_{ph} is the number of phases. For a shaft speed of 3472Hz, the phase excitation and dc supply switching frequencies are, therefore, 231Hz and 693Hz respectively.

$$f_r = \frac{\omega_r}{2\pi} \tag{4.1}$$

$$f_{ph} = \frac{N_r \omega_r}{2\pi} \tag{4.2}$$

$$f_s = \frac{m_{ph} N_r \omega_r}{2\pi} \tag{4.3}$$

The frequencies of the peaks in the current spectrum (0-6kHz) of **Fig. 4.14i** are listed in **Table 4.7**, in which the corresponding frequencies in the commutation, vibration and noise spectra are also indicated, slight discrepancies between the values of corresponding peaks for each spectrum, due to resolution and experimental errors, being neglected. It can be seen that the 1st harmonic of the current spectrum is 224Hz and the 17th harmonic is 3904Hz, the 1st harmonic being the fundamental excitation frequency and subsequent

harmonics being multiples thereof. Similarly, at 1991rpm the fundamental excitation frequency and the dc supply switching frequency are 132.7Hz and 398Hz, respectively, whilst at 460rpm these are 31Hz and 92Hz, respectively. For all cases the current spectrum is rich in harmonics which are spread over the whole frequency spectrum, as observed in the frequency range 0-15kHz. The 17^{th} harmonic coincides with the natural frequency of mode 2 (3840Hz), taking into account the resolution of the dynamic signal analyser during the measurement of the natural frequencies, **Fig. 4.14i**.

The noise and vibration spectra exhibit a lower harmonic content than that of the commutation signal and current waveforms. Nevertheless, the peaks which are present in the noise and vibration spectra correlate with those in the current and commutation spectra. The peak at 3840Hz, for mode 2, is by far the most dominant in both the vibration and noise spectra, and this is attributed to the fact that it is exciting the natural frequency of mode 2, thus inducing a stator resonance. This is the case at all three rotational speeds. Although the other peaks in the vibration spectrum (0-6kHz) also contribute towards acoustic noise (as can be seen in the noise spectrum), they do not coincide with a natural frequency, and hence their influence is negligible compared to that of mode 2. This is reflected by their relative magnitudes in the noise spectrum, the 3840Hz peak having a magnitude of ≈78dB, whereas the largest of the neighbouring peaks, <3000Hz, has a magnitude of ≈64dB.

In the 0-15kHz frequency range, modes 2 and mode 4 are clearly excited at all three operating speeds. A vibration peak can be observed at 9.2kHz, although it has a relatively low amplitude, and is indistinguishable from the background noise in the noise spectrum, since it corresponds with the natural frequency of mode 3 which was not expected to have a significant influence on the noise due to the fact that symmetrical radial forces are induced, as discussed in Chapter 1. Any significant vibration and/or noise associated with mode 3 would imply that there was an unbalance in the electromagnetic forces resulting from rotor unbalance and/or an uneven airgap, ie eccentricity.

As will be seen, all the current, vibration and noise spectra are very rich in harmonics at all speeds, but due to the fact that the fundamental harmonic is related to the rotational shaft frequency, the frequency increment between successive harmonics decreases as the speed increases, thus increasing the number of harmonics within a given frequency

range. This also causes the harmonic which coincides with a natural frequency to be of a higher order, and may explain why the noise tends to increase with speed.

At 1991rpm, owing to the small frequency increment between successive harmonics, the resolution over the 15kHz frequency range is insufficient, and the harmonics tend to merge. This is particularly noticeable in the commutation signal spectrum. For the 15kHz frequency spectra, **Fig. 4.14**, the spectrum analyser range was actually set to 25kHz, giving a resolution of 50Hz. Whereas the harmonics at 1991rpm are separated by ≈133Hz, at a speed of 460rpm they are separated by only ≈31Hz, and, therefore, even over the 6kHz frequency range, the resolution of the spectrum analyser is inadequate for distinguishing the associated current harmonics at this speed.

It is the coincidence of the electromagnetic exciting force with the natural frequencies of the stator that induces resonance and hence the most severe acoustic noise. From equation (1.1), in the absence of saturation, the radial force is proportional to the square of the flux density and hence in the linear region of the SR machine ψ-i characteristic, flux density is proportional to the phase current. Thus, it follows that the excitation force harmonics will occur at the same frequencies as the harmonics of the square of the phase current. However, since the SR machine phase current is unipolar the phase current waveform will contain the same harmonic content as that of the square of the phase current. By way of example, the phase current and phase current squared at a speed of 3472rpm, (from **Fig. 4.14i**), is shown in **Figs. 4.14iv(a) & (b)**, respectively. A Fast Fourier Transform (FFT) of the currents of **Figs. 4.14iv(a) & (b)** yields their respective harmonic contents, **Figs. 4.14iv(c) & (d)**, confirming that no additional harmonics are introduced, and that there is merely a change of harmonic magnitude. The correlation between the FFT of the phase current and that obtained from the spectrum analyser during machine operation is verified by comparing **Figs. 4.14iv(c) & (e)**.

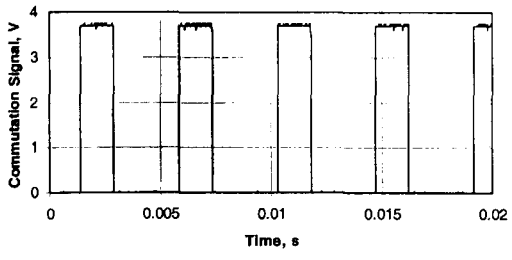

Commutation signal

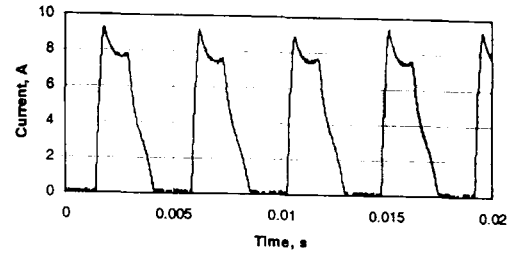

Phase current

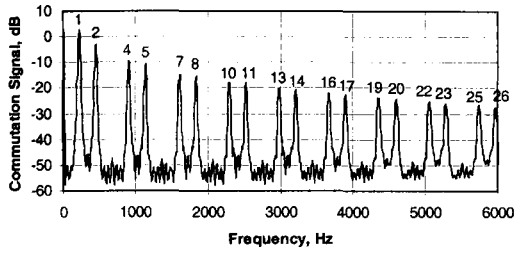

Harmonic content of commutation signal

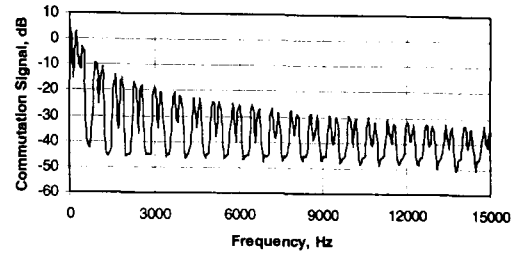

Harmonic content of commutation signal

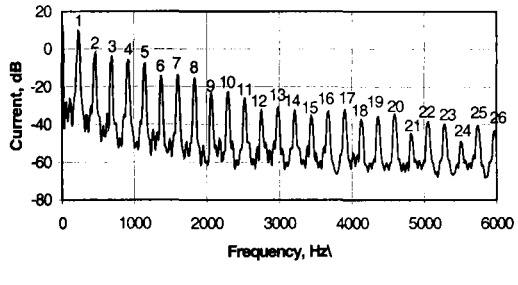

Harmonic content of current waveform

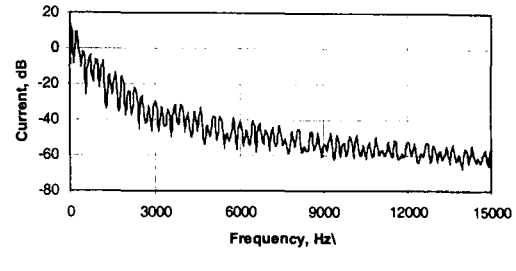

Harmonic content of current waveform

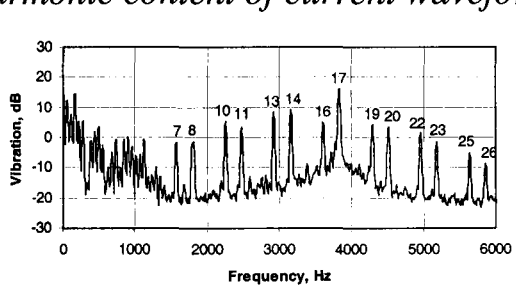

Stator vibration spectra

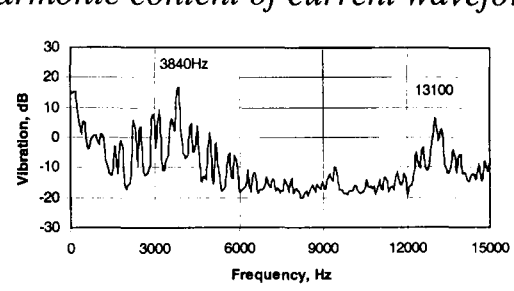

Stator vibration spectra

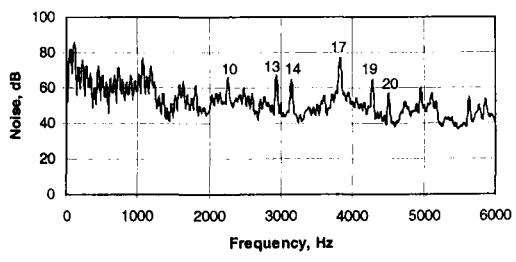

Noise spectra

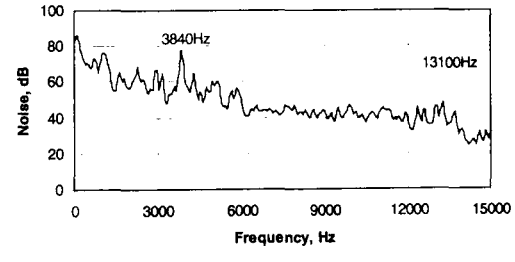

Noise spectra

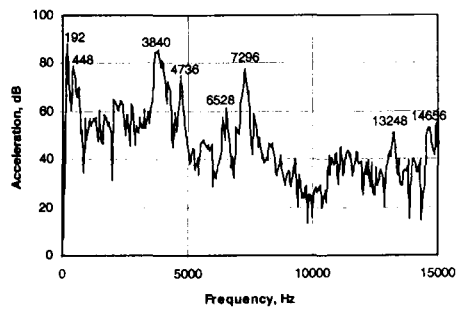

Stator natural frequencies (SRM mounted)

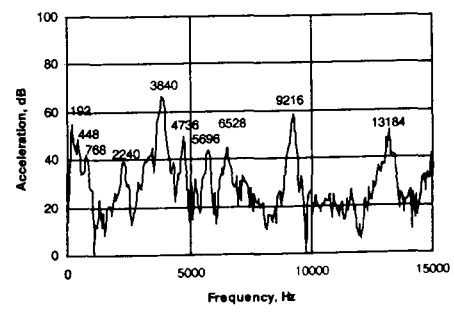

Stator natural frequencies (SRM mounted)

Fig. 4.14i *No-load, 3472rpm*

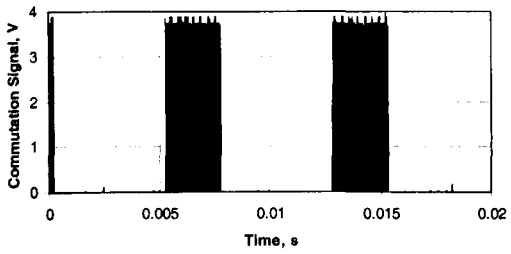

Commutation signal

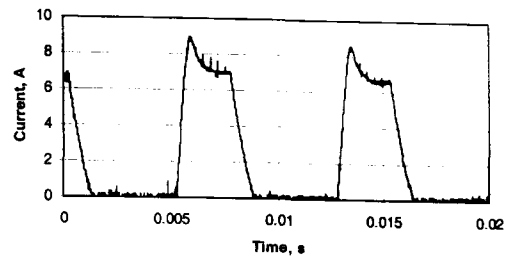

Phase current

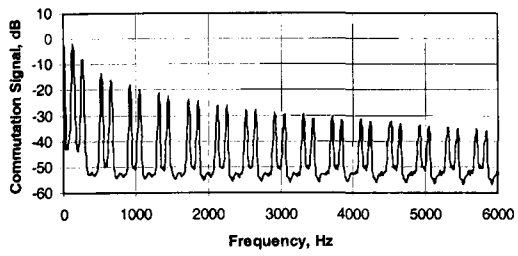

Harmonic content of commutation signal

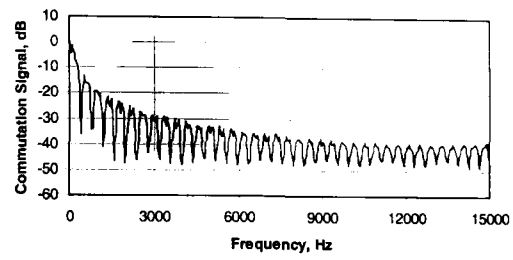

Harmonic content of commutation signal

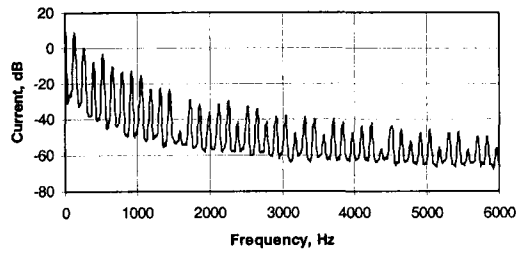

Harmonic content of current waveform

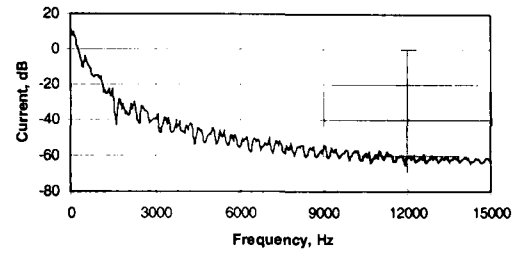

Harmonic content of current waveform

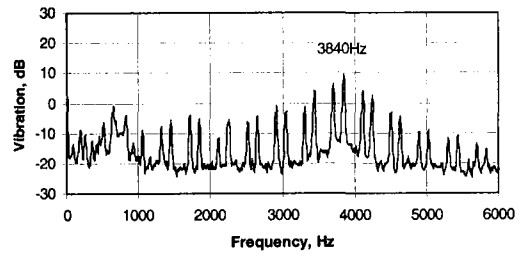

Stator vibration spectra

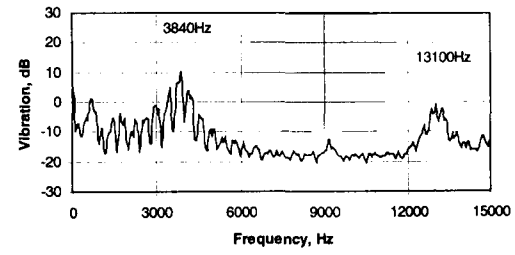

Stator vibration spectra

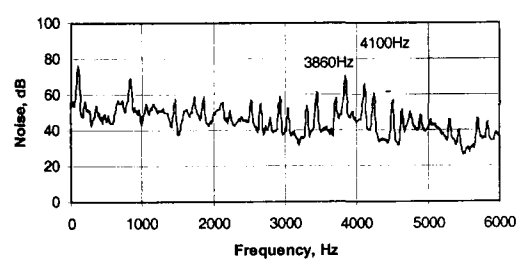

Noise spectra

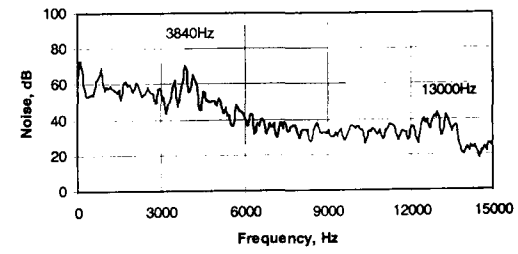

Noise spectra

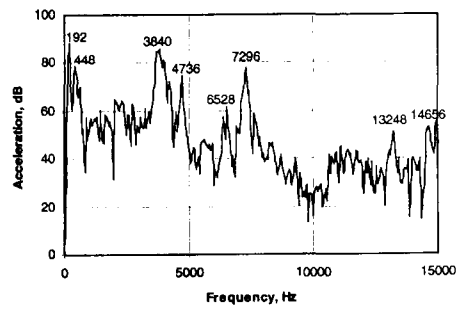

Stator natural frequencies (SRM mounted)

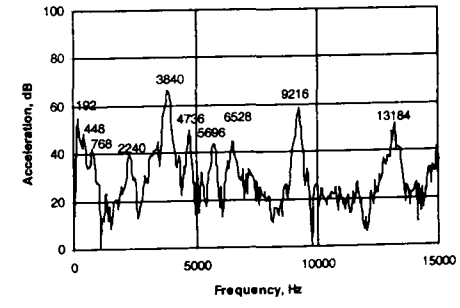

Stator natural frequencies (SRM mounted)

Fig. 4.14ii *No-load, 1991rpm*

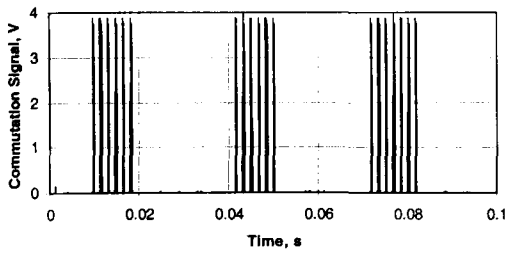

Commutation signal

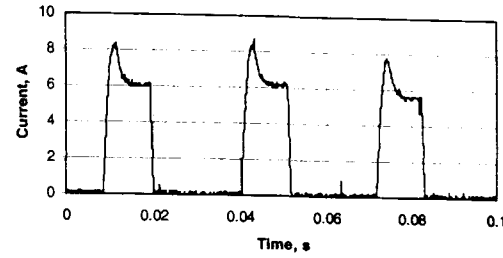

Phase current

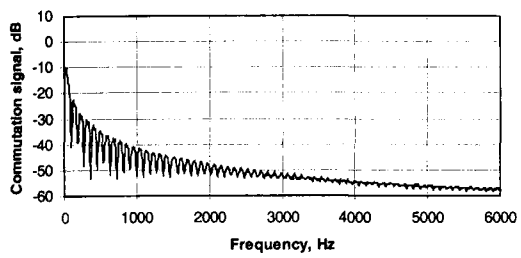

Harmonic content of commutation signal

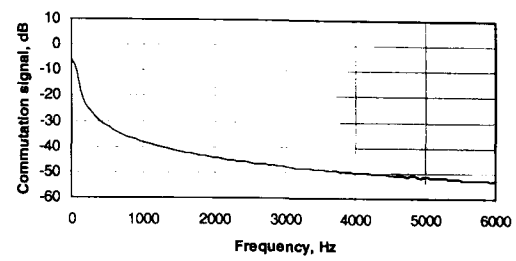

Harmonic content of commutation signal

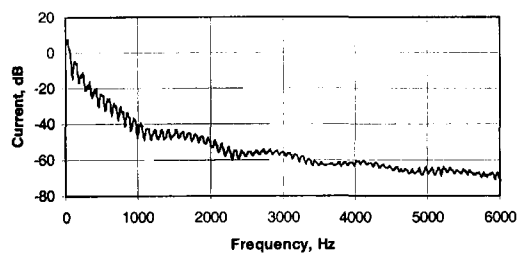

Harmonic content of current waveform

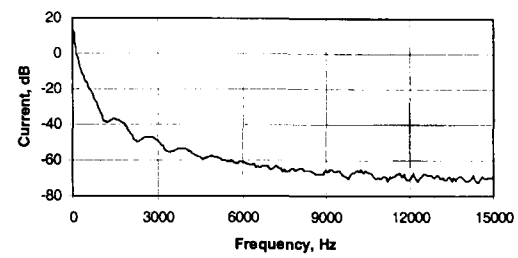

Harmonic content of current waveform

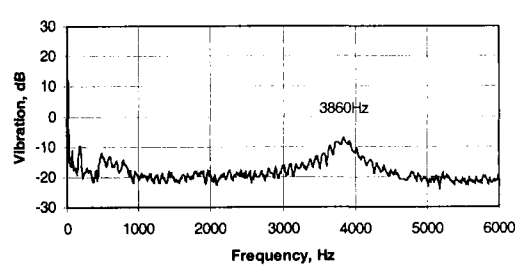

Stator vibration spectra

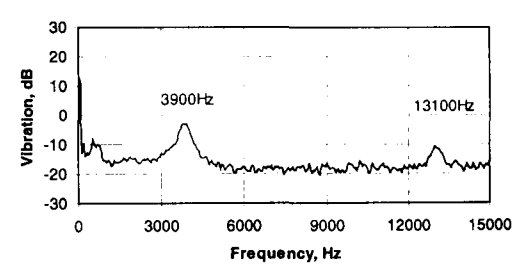

Stator vibration spectra

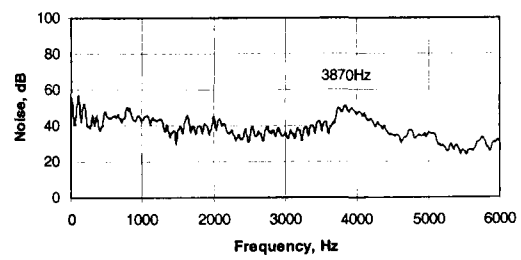

Noise spectra

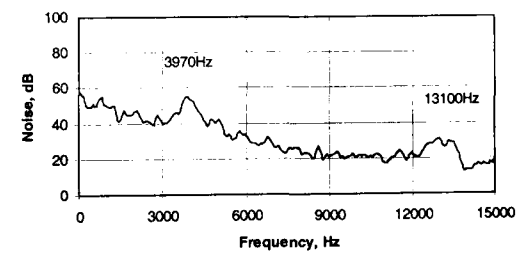

Noise spectra

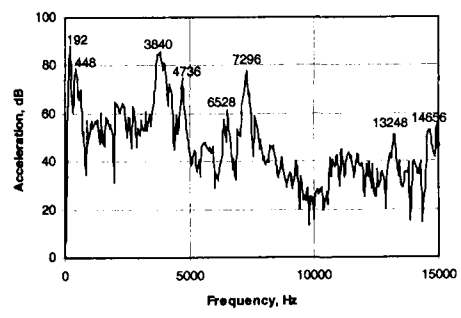

Stator natural frequencies (SRM mounted)

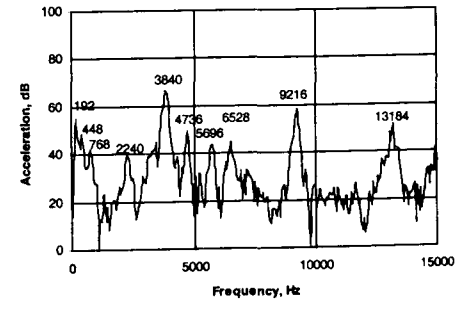

Stator natural frequencies (SRM mounted)

Fig. 4.14iii *No-load, 460rpm*

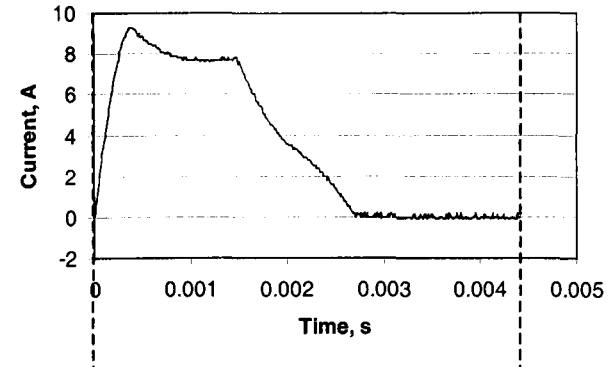

(a) *Measured current*

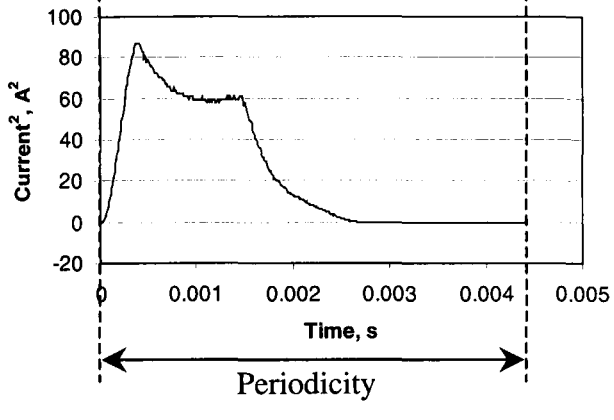

(b) *Current² (calculated from* (a)*)*

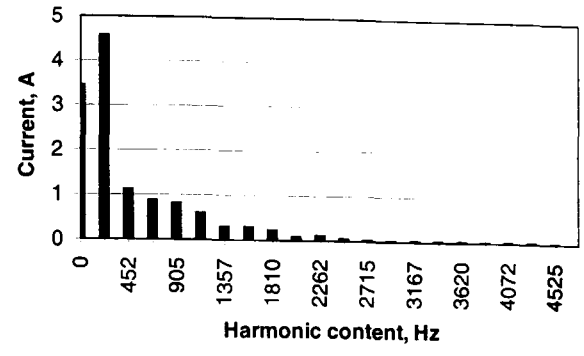

(c) *FFT of current,* (a)

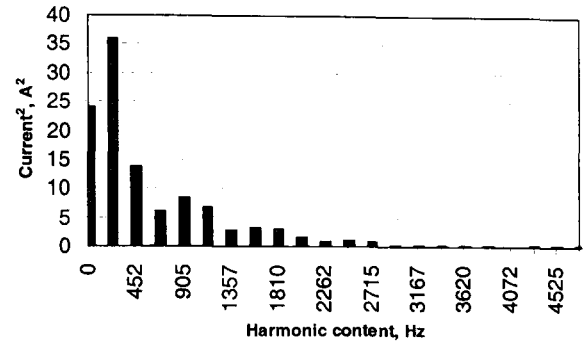

(d) *FFT of current², (b)*

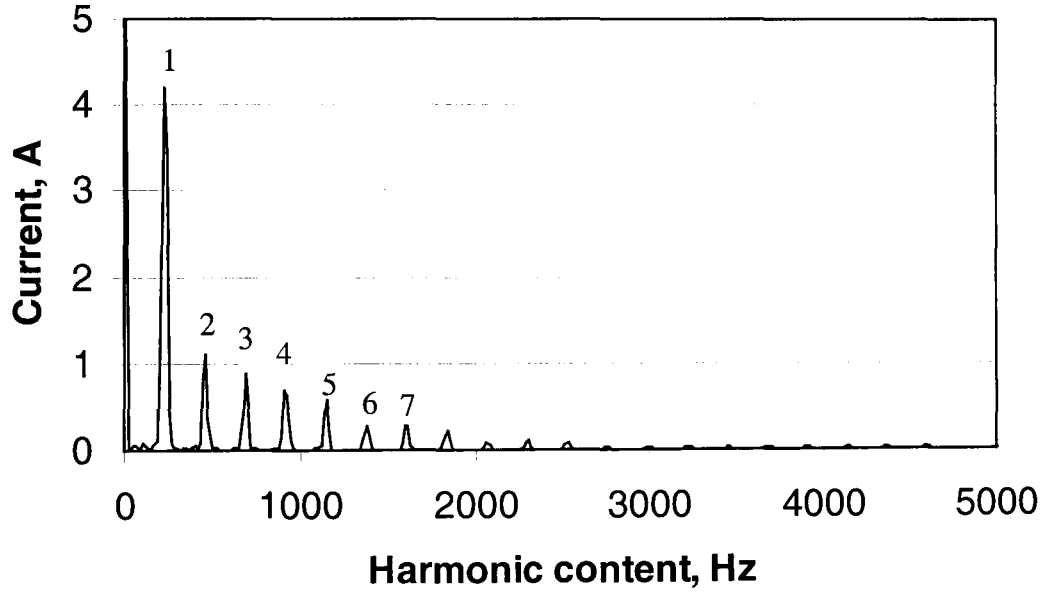

(e) *On-line FFT from spectrum analyser (refer to* **Table 4.7** *for the specific frequencies)*

Fig. 4.14iv *Spectral analysis of phase current and squared phase current, no-load, 3472rpm*

Table 4.7 *Harmonic content at 3472rpm*

Harmonic	Current (Hz)	Commutation	Vibration	Noise
1	224	√		
2	464	√		
3	688			
4	912	√		
5	1152	√		
6	1376			
7	1600	√	√	
8	1840	√	√	
9	2064			
10	2304	√	√	
11	2528	√	√	
12	2752			
13	2992	√	√	√
14	3216	√	√	√
15	3440			
16	3680	√	√	
17	3904	√	√	√
18	4128			
19	4368	√	√	√
20	4592	√	√	√
21	4816			
22	5056	√	√	
23	5280	√	√	
24	5504			
25	5744	√	√	
26	5968	√	√	

4.3 Noise and vibration under voltage PWM control

The following section describes a systematic assessment of the influence of voltage PWM control on the stator vibration and emitted acoustic noise. The effect of soft and hard chopping and the PWM switching frequency are considered, together with the influence of rotational speed and load condition. Initially, these are addressed with regard to the resultant current waveform and the associated vibration and noise frequency spectra and the time-domain vibration. Subsequently, their merits are compared through interpretation of sound level measurements.

4.3.1 Influence of soft and hard chopping

The most common form of voltage PWM control utilises fixed frequency PWM of the dc link voltage, V_s, together with a variable duty cycle. The rotational speed, derived from an incremental encoder, is compared to the speed demand to provide a speed error, which is then used to derive the required duty cycle, between 0% and 100%. For the half asymmetric H-bridge inverter which is employed in the experimental drive system, soft chopping and hard chopping techniques can be applied, whereby V_s or $2V_s$, respectively, is applied to the phase windings, V_s being $24V$ for the experimental system. The operation of the inverter was outlined in Appendix A, and is summarised in **Fig. 4.15**, for a single phase-leg, where the arrows indicate the direction of current flow. By alternating between stages *(i)* and *(ii)*, V_s and $0V$ is applied across a phase winding, thus providing soft chopping, **Fig. 4.16.** The ripple in the flux and current waveforms in **Fig. 4.16** oscillates at the chopping frequency. However, the flux oscillations have been omitted for simplicity. In the case of high frequency PWM, flux ripple will be less significant, and the flux waveform will tend towards the idealised waveform which is shown. By alternating between stages *(i)* and *(iii)*, V_s and $-V_s$ is applied across a phase winding, thus providing hard chopping, **Fig. 4.17**. The ripple in the current waveform is now larger than for soft chopping, since the step voltage change is greater, which results in a higher rate of change of current. Although it has been reported that such hard chopping results in a noisier machine operation, [MIL93, GAB99a], little evidence has been presented, and no reference has been made with regard to the influence which it may have on the dominant stator resonance.

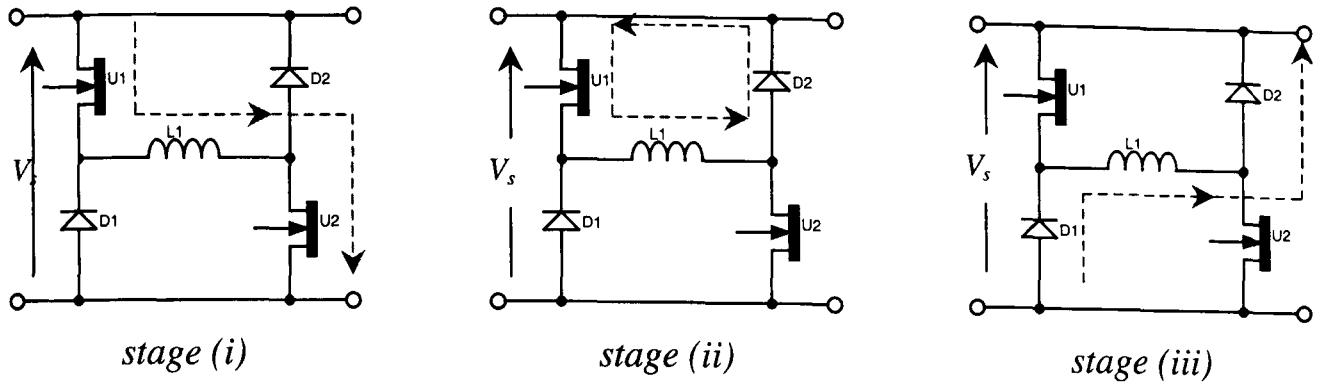

Fig. 4.15 *Switching stages of a half-asymmetric H-bridge to provide soft and hard chopping*

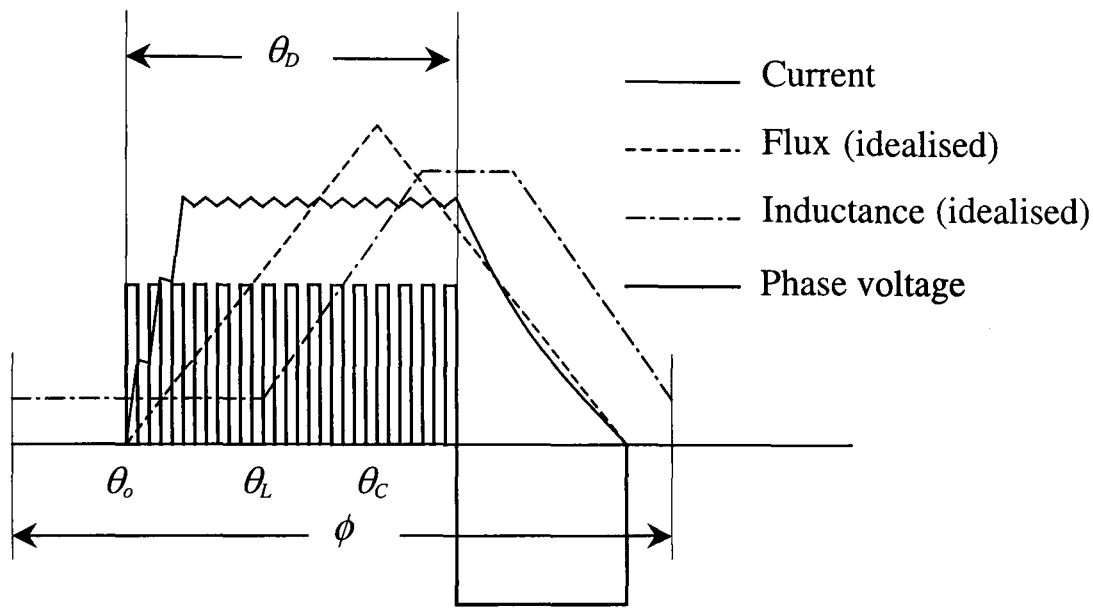

Fig. 4.16 *Soft chopping voltage PWM control*

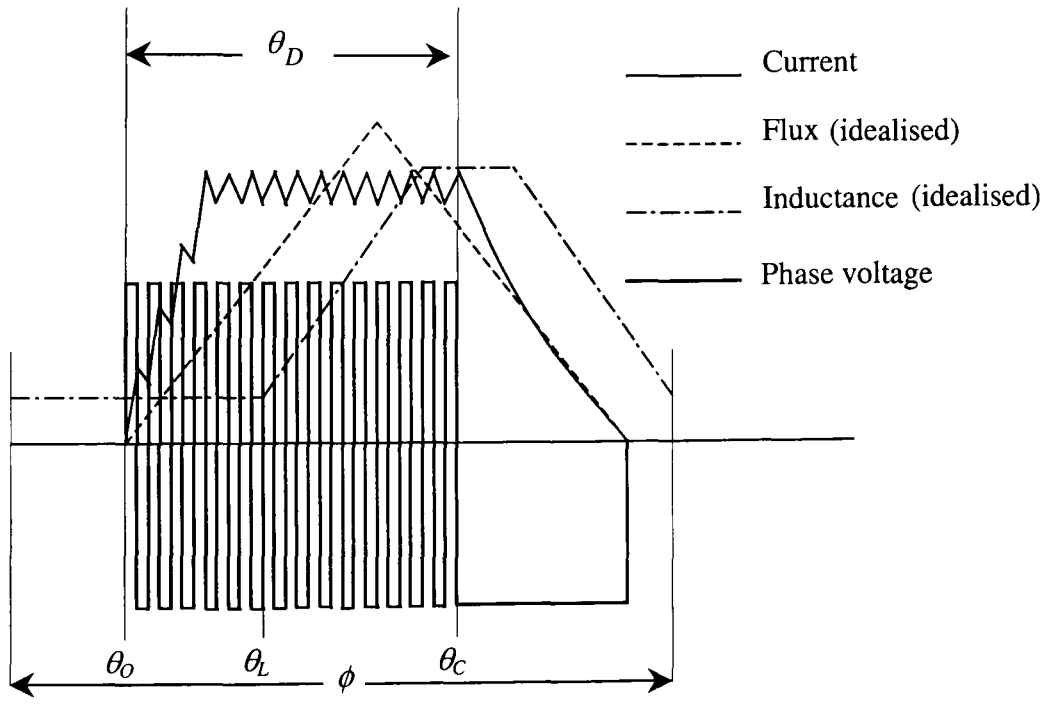

Fig. 4.17 *Hard chopping voltage PWM control*

Results obtained for both soft and hard switching strategies with a PWM switching frequency of 20.6kHz for the SR machine running on no-load at 1000rpm are shown in **Figs. 4.18i(a)** and **4.18i(b)**, respectively. The current waveforms for the two techniques are very similar, and due to the high PWM switching frequency of 20.6kHz which was employed, it is not possible to distinguish any ripple in the current waveforms. The rate of change of current during the current decay periods is similar since the de-fluxing is identical, whereas the rate of rise of current is slightly different due to the different applied voltages.

For both hard and soft switching strategies, significant oscillations are observed in the time domain vibration waveform at the turn-off point of the associated phase current, **Fig. 4.18i**. These oscillations occur due to the SR machine stator resonating at the frequency of vibration mode 2, viz. 3840Hz. Furthermore, additional oscillations at the same frequency are also observed at other instants of time, although these have lower peak amplitudes. These correspond to the turn-off of the other phases, whose associated vibrations appear less severe owing to the fact that the accelerometer is not mounted behind their corresponding stator poles. A typical vibration waveform, measured behind a stator pole of phase 3 is shown in **Fig. 4.18ii**, together with the current waveforms of all three phases, which illustrates that the respective turn-on and turn-off points correspond to the vibration oscillations. The time-domain vibration waveforms show that the peak oscillation associated with vibration mode 2 is similar in magnitude for the two chopping methods, **Fig. 4.18i**, although the oscillations are more prolonged when the machine is operating under hard chopping control. Furthermore, the ripple between successive mode 2 oscillations, induced by turn-off of a given phase current, is larger when the machine is operated under hard chopping control, to such an extent that the mode 2 oscillations induced by the turn-off of neighbouring phases are indistinguishable.

At the three frequencies in the noise spectrum 0-25kHz, which are associated with vibration modes 2 and 4 and the PWM switching frequency, there is a significant increase in magnitude with hard chopping, especially at the PWM switching frequency, although it is also observed that the level of background noise increases. The increase in magnitude of the noise peaks associated with modes 2 and 4 is attributed to the fact that larger forces arise when the applied voltage is doubled, the doubling of the voltage causing a greater voltage ripple and an increase in magnitude of the noise at the PWM switching frequency of 20.6kHz. The vibration spectrum shows a similar trend to that observed for the noise.

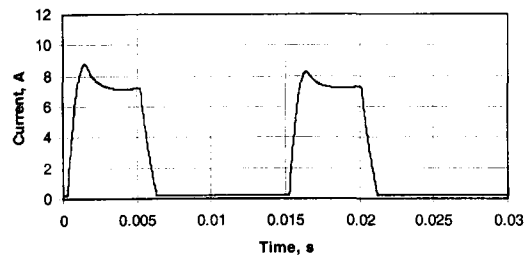

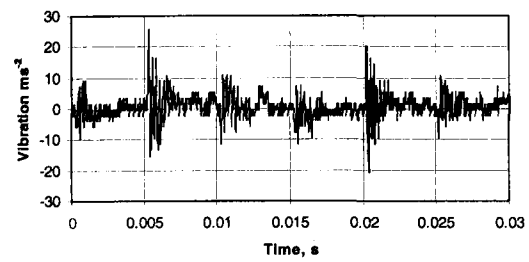

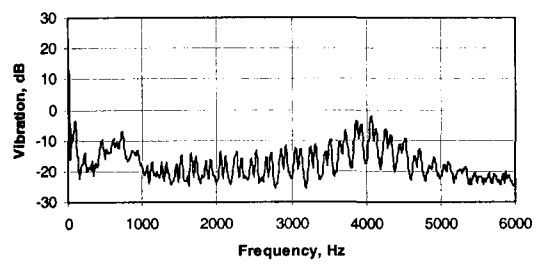

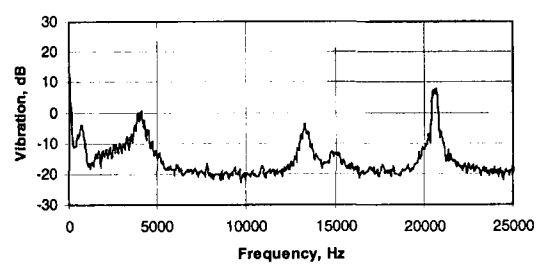

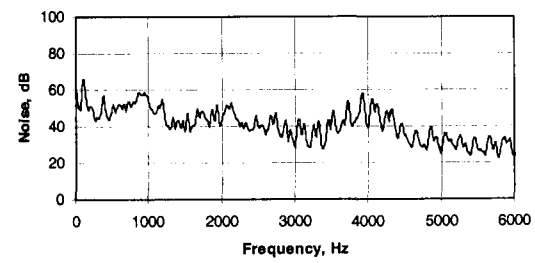

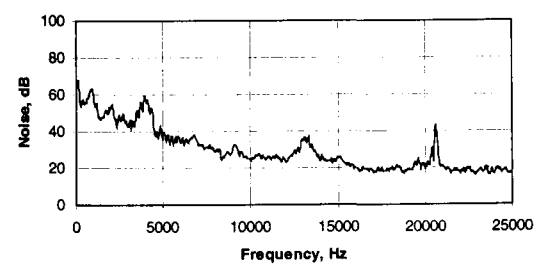

(a) *Soft chopping (PWM f_s=20.6kHz)*

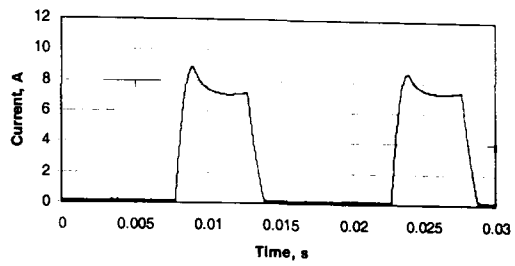

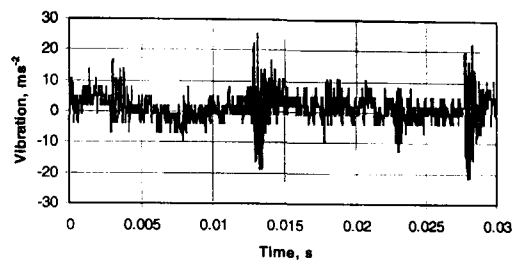

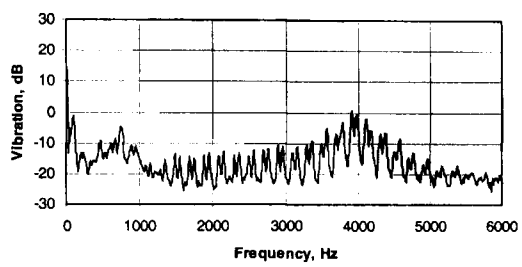

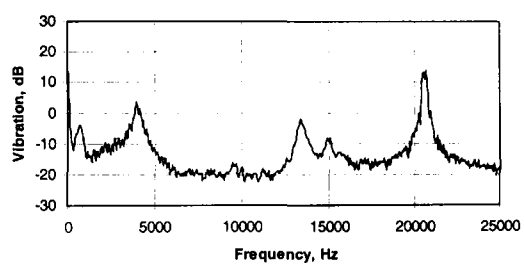

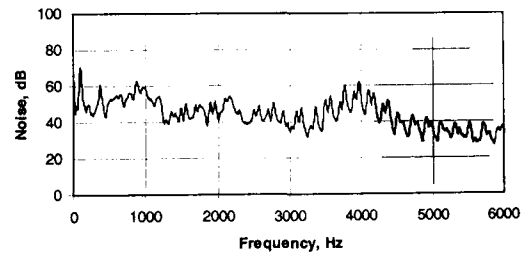

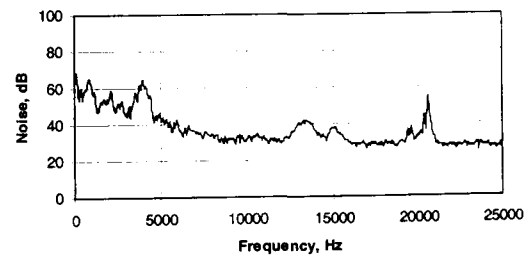

(b) *Hard chopping (PWM f_s=20.6kHz)*

Fig. 4.18i *Influence of soft and hard switching strategies under voltage PWM control, no-load, 1000rpm*

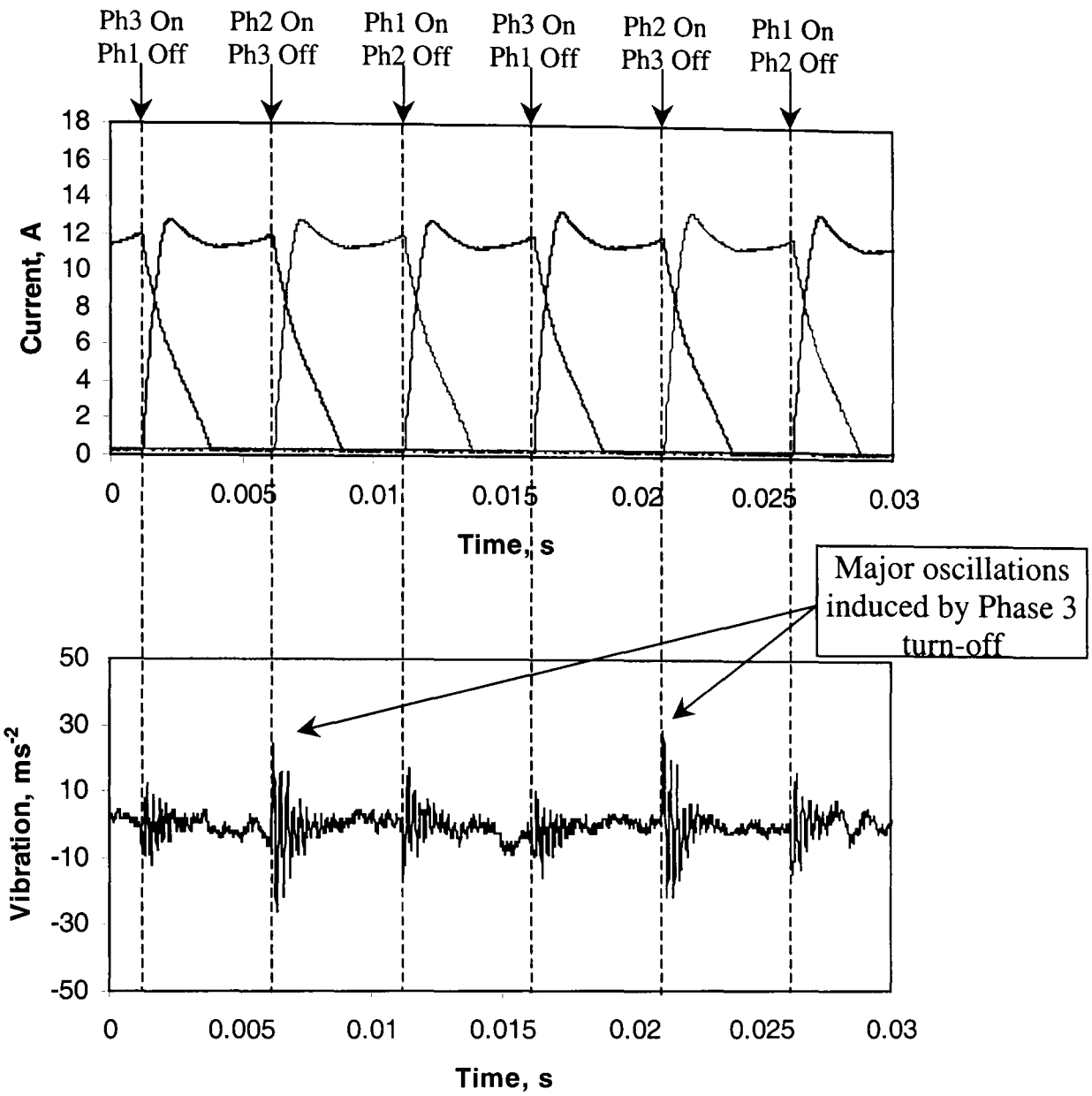

Fig. 4.18ii *Typical three phase current waveforms showing respective phase turn-on and turn-off points, together with a typical vibration response measured behind a stator pole of phase 3*

4.3.2 Influence of operating speed

The SR machine was excited using soft chopping voltage PWM control, with a PWM switching frequency of 20.6kHz, and measurements of the phase current, and the noise and vibration spectra were made on no-load at rotational speeds of 500rpm, 1000rpm and 1500rpm, as shown in **Fig. 4.19i**. The peak value and the turn-off value of the current increases significantly from 500rpm to 1000rpm, after which they remain more or less constant. When operating below base speed, i.e. $back\text{-}EMF<V_{dc}$, the current is expected to remain constant. However, when the SR machine is running, the load-cell measures the frictional loss in the wound-field dc machine as well as the electro-magnetic torque imposed on the output shaft of the SR machine by the wound-field dc machine. Other sources of loss in the system, such as those in the bearing sets which support the shaft which couples the two machines, are not measurable. When the wound-field dc machine is operating the electromagnetic torque, which it develops to overcome frictional losses in the system, is measured by the load-cell since they impose a reaction torque on its swinging stator. Furthermore, the difference between the frictional loss measured when the wound-field dc machine is operating to that which is measured when the SR machine is operating is the frictional loss which is not accounted for in the load-cell reading when the SR machine is operating, and is shown in **Fig. 4.19ii**. It is observed from **Fig. 4.19ii** that a gradual increase in frictional torque occurs as the speed increases, and that at speeds around 1000rpm and 2000rpm a sharp increase in the loss torque occurs. It has already been established that there is a system resonance at ≈2000rpm, section 4.2, and, therefore this is the likely reason for the higher torque at 2000rpm. Furthermore, it is possible that there is a sub-harmonic of the 2000rpm resonance at 1000rpm, which is responsible for the increase in torque which occurs at this speed. These frictional torques are relatively large with respect to the torque rating of the experimental SR machine, and since they are not accounted for in the load-cell measurement during the noise investigations they are responsible for the increase in current which is observed in **Fig. 4.19ii**, even though the SR machine is normally operating on no-load.

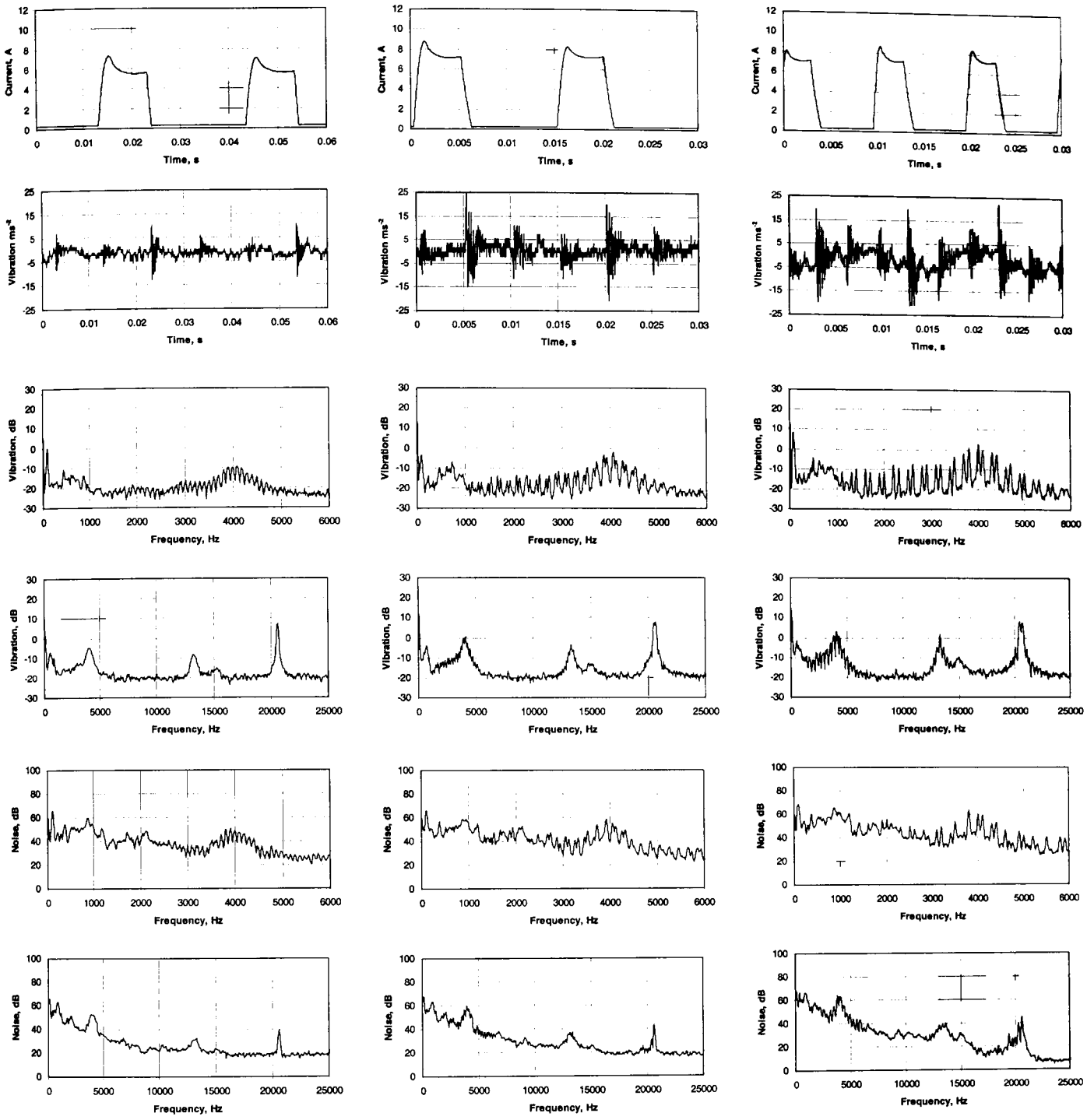

(a) *500rpm* **(b)** *1000rpm* **(c)** *1500rpm*

Fig. 4.19i *Influence of operation speed under voltage PWM control, no-load*

The significant increase in time domain vibration observed from 500rpm to 1000rpm is attributed to the increase in load and hence current, due to the frictional torque increasing with speed. The phase current waveforms for 1000rpm and 1500rpm have similar peak values subsequent to turn-on and similar average values prior to turn-off, which is expected since frictional torque at these two speeds is similar, both being greater than that at 500rpm, **Fig. 4.19ii**. However, it is observed that in the 0-6kHz and 0-25kHz vibration and noise spectra the peaks associated with vibration modes 2 and 4 are slightly higher in magnitude at a speed of 1500rpm.

A low frequency ripple at approximately 80Hz is observed in the time domain vibration waveform, which corresponds to the lowest peak on the 0-6kHz vibration spectrum. This peak is also present in the corresponding vibration spectra for speeds of 500rpm and 1000rpm, at approximately the same frequency, although with a lower magnitude, and is attributed to the rotor/system resonance identified in the initial investigations, section 4.2.

The noise and vibration spectra confirm that the vibration increases with speed, as observed in the time-domain vibration waveforms, although the magnitude of the 20.6kHz peak in the vibration spectrum remains essentially constant since this is associated with the PWM switching frequency, and is independent of speed.

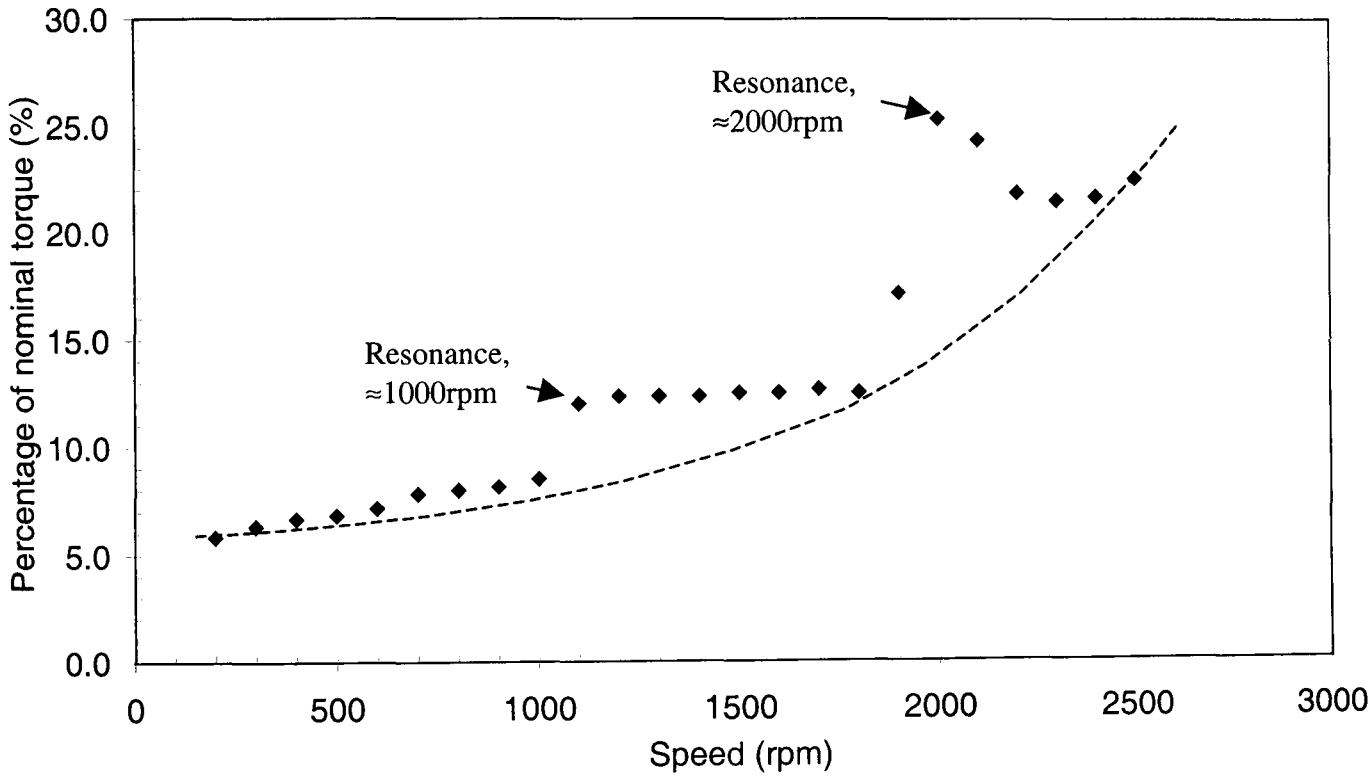

Fig. 4.19ii *Frictional torque not accounted for during testing of SR machine*

4.3.3 Influence of load

The SR machine was again operated at three speeds, viz. 500rpm, 1000rpm and 1500rpm, and a load was applied by the wound-field dc machine. The current, noise and vibration were measured with the machine on no-load and at a load of ≈75% of the nominal rated torque of the experimental SR machine, the measurements being shown in **Figs. 4.20(a) and (b)**, respectively.

The current for a given speed is observed to increase significantly with the load. Again, the increase in current with speed is due to the fact that the torque as measured by the load-cell was maintained constant for all speeds, whilst the frictional torque is not measured by the load-cell, and this increases with speed, as discussed earlier. This effectively results in the SR machine operating at a significantly higher load than ≈75% of nominal rated torque when operating at 1500rpm. This is evident since the peak in the phase current waveform occurs at the point of turn-off, which indicates that the machine is operating well within the saturated region of its flux-linkage characteristic.

At all three speeds, the application of load significantly increases the level of oscillations in the time-domain vibration waveform that arise due to the resonance of the stator at the frequency of vibration mode 2, as well as the magnitude of the vibration and noise peaks associated with vibration modes 2 and 4.

The corresponding rate of rise and rate of decay of the phase currents with the machine operating on no-load and ≈75% of full load, at the three rotational speeds, are given in **Table 4.8**. The rates of change of current are, essentially, average values since it is assumed that the rise of current from the point of turn-on to the peak value is linear, and similarly that the decay from the peak value to zero is also linear. It will be observed that the rate of rise of current increases significantly when the machine is on load, as expected, since the magnetisation voltage is increased. The rate of decay of current also increases, although the available supply voltage for de-magnetisation is unchanged. This is attributed to the fact that the current attains a significantly higher value prior to turn-off, which, therefore, results in a greater rotational back-EMF, and hence a more rapid decay of current. Since the radial component of force which acts on the stator is proportional to the square of the current, the rate of change of the radial force at turn-off is, therefore, greater, thereby releasing the stator from its compressed state more quickly, and inducing vibrations having a higher magnitude. This supports published observations

that the higher the rate of change of current at turn-off, the higher is the noise and vibration of SR machines, [WU93].

Table 4.8 *Comparison of rate of rise and decay of current with machine on no-load and ≈75% of full load*

Speed (rpm)	Rise time (ms)/di/dt (As^{-1})		Decay time (ms)/di/dt (As^{-1})	
	No-load	75% load	No-load	75% load
500	2.3/3052	2.1/4813	1.3/4102	1.4/6149
1000	1.2/6717	1.01/11889	1.1/6450	1.7/7122
1500	0.9/9008	0.74/18909	1.0/6956	2.05/7606

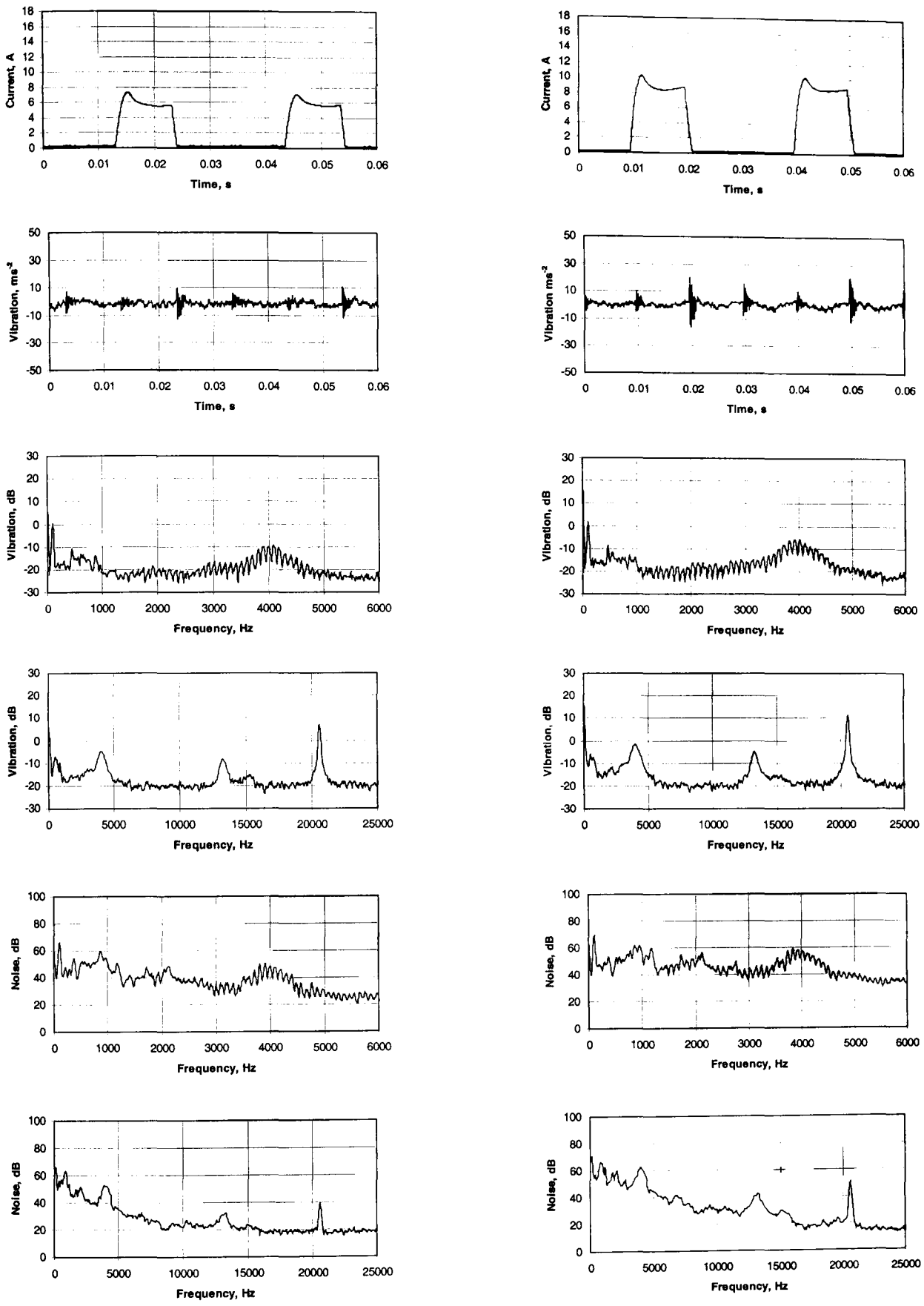

(a) *No-load* **(b)** *≈75% Load*

Fig. 4.20i *Influence of load under voltage PWM control at 500rpm*

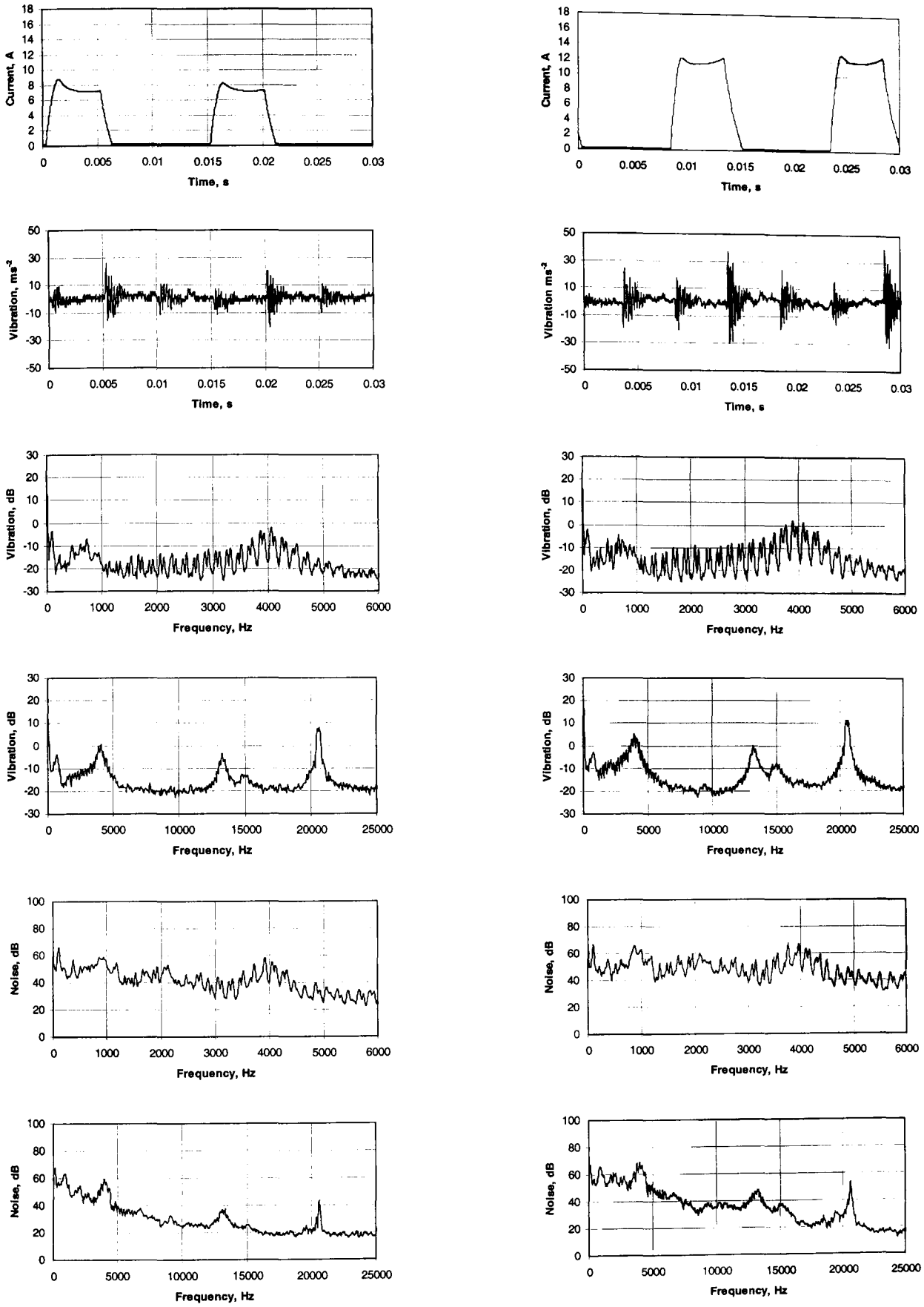

(a) *No-load* **(b)** *≈75% Load*

Fig. 4.20ii *Influence of load under voltage PWM control at 1000rpm*

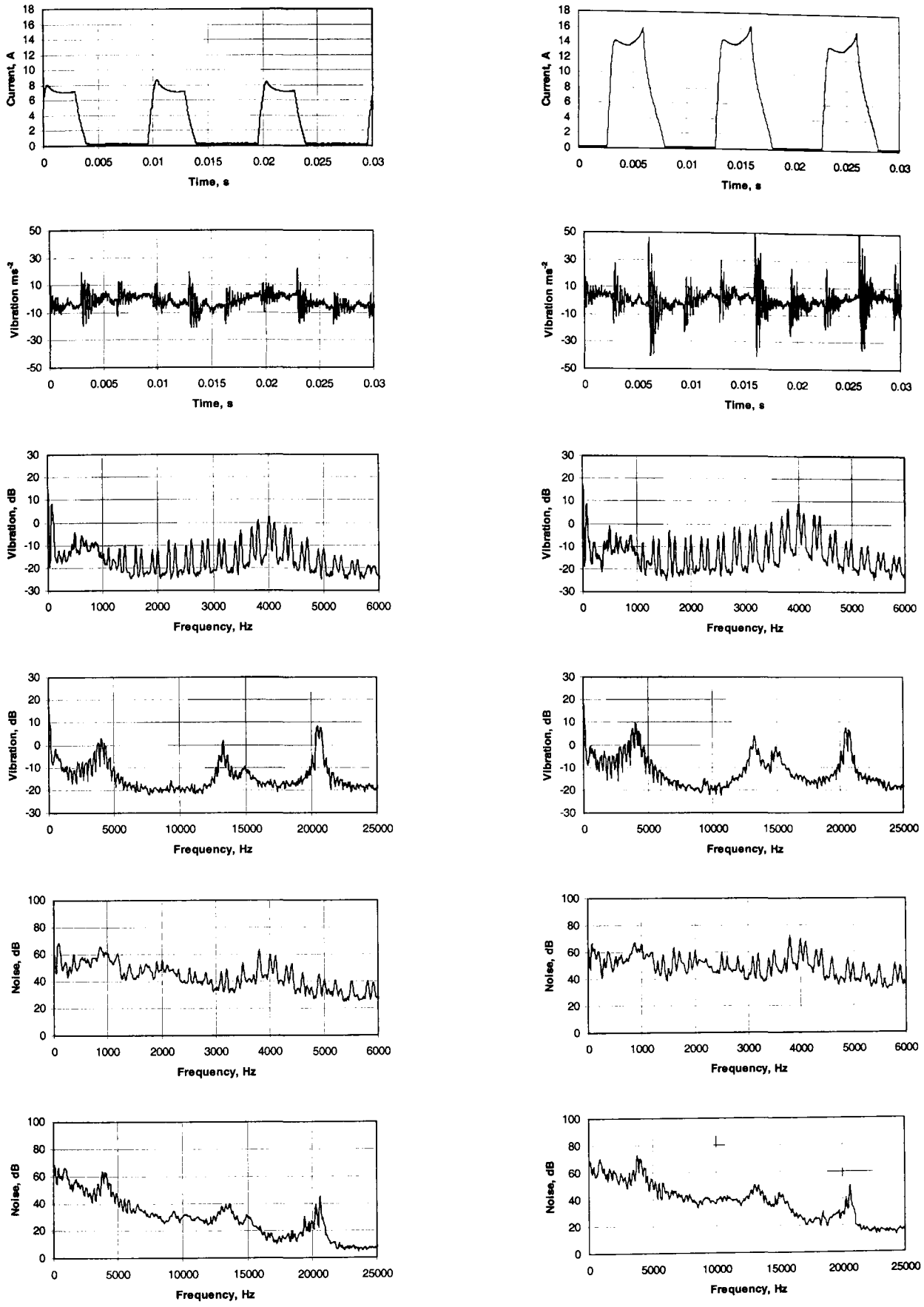

(a) *No-load* **(b)** *≈75% Load*

Fig. 4.20iii *Influence of load under voltage PWM control at 1500rpm*

4.3.4 Influence of PWM switching frequency

Throughout the foregoing investigations, a PWM switching frequency of 20.6kHz has been employed for the experimental system when operated under voltage PWM control. However, a lower switching frequency may have to be employed for high power drive systems due to the limitations of higher power semi-conductor devices and the need to limit switching losses. Therefore, the influence of the PWM switching frequency on the noise emitted under voltage PWM control and the associated sound pressure level was measured at 1000rpm, at both no-load and ≈75% of full load, **Fig. 4.21**. As will be seen, the sound pressure level tends to reduce very gradually as the switching frequency is increased. However, to obtain further insight into the cause of the variation in noise level with the PWM switching frequency, spectra were recorded for PWM switching frequencies of 10.3kHz and 20.6kHz, shown in **Figs. 4.22** and **4.23**, for conditions of no-load and ≈75% of full load, respectively.

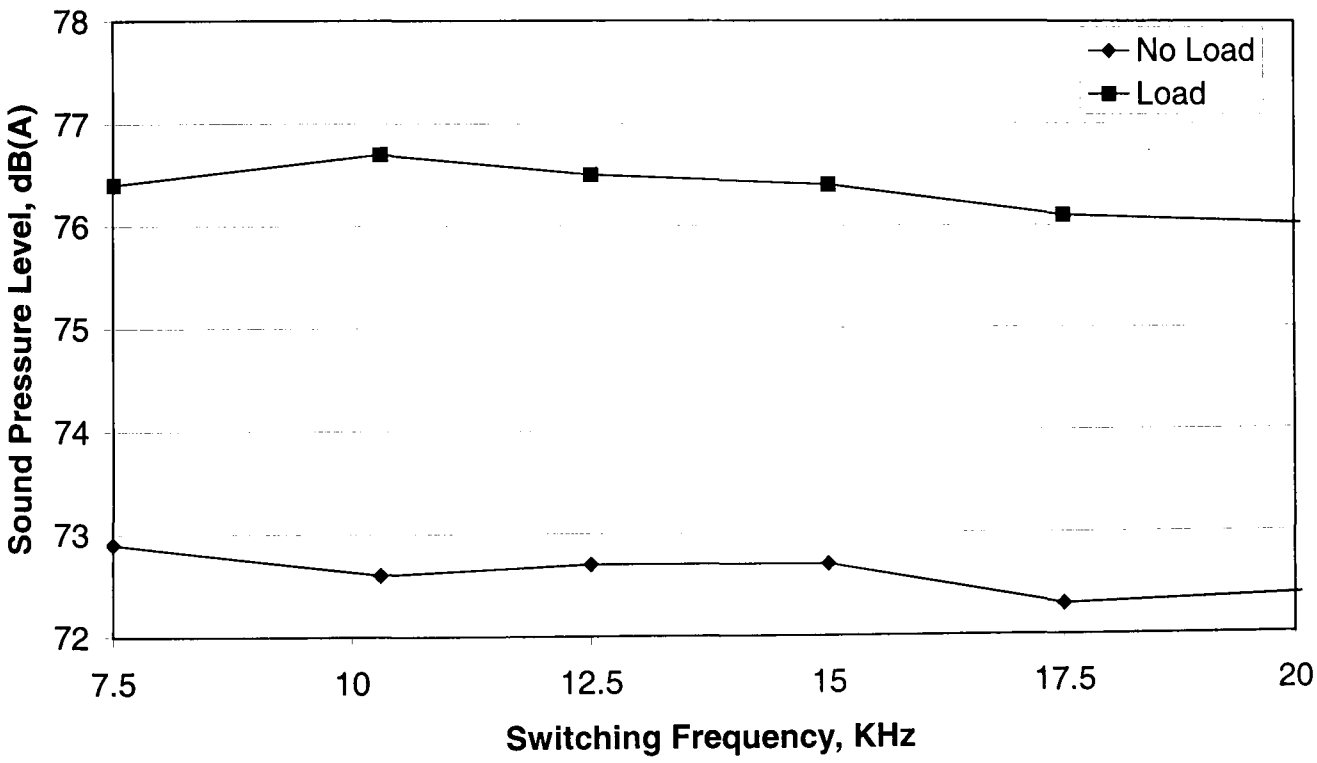

Fig. 4.21 *Influence of PWM switching frequency on emitted sound pressure level for machine operating at 1000rpm, at no-load and ≈75% load.*

As will be seen, the current waveforms are similar irrespective of the PWM switching frequency, although the current ripple is slightly more pronounced at 10.3kHz.

The reduction of the switching frequency to 10.3kHz results in an additional frequency component in the noise and vibrations spectra, **Fig. 4.22(b)**, at 10.3kHz. However, the 20.6kHz component is still present as a second harmonic component, although its

magnitude is lower than that which was present with the original switching frequency of 20.6kHz. The associated vibration spectrum exhibits a slight increase in mode 2 and a significant increase in mode 4, due to the fact that the PWM switching frequency is close to the natural frequency of mode 4, whilst the noise spectrum exhibits a slightly higher pedestal level, and, consequently, slightly higher noise emissions associated with modes 2 and 4. Thus, although the reduction in the switching frequency has a relatively small influence on the resonant modes, the main reason for the higher noise level is the fact that the switching frequency falls within the audible frequency range, and the lower frequency noise components are more heavily weighted by the SLM A-weighted scale than those for a PWM switching frequency of 20.6kHz, i.e. the 10.3kHz noise component is more dominant in the noise spectrum with a switching frequency of 10.3kHz than the 20.6kHz noise peak which results with a 20.6kHz switching frequency, despite the associated vibration magnitudes being similar. This is also the cause of the variation of the SPL in **Fig. 4.21**.

When the machine was loaded, **Fig. 4.23**, the time-domain vibration oscillations are more pronounced, due to fact that the phase current waveform has a higher rate of change of current at the instant of turn-off than that on no-load, as discussed previously. However, the comments which were made in regard to the no-load spectra apply equally for the ≈75% load spectra.

Further interesting features become more apparent when a shorter time base is used for the time-domain waveforms, **Figs. 4.24** and **4.25**. For example, significant oscillations are observed to be present in the time-domain vibration between the dominant vibration oscillations, (these cannot be observed once the stator is resonating at the frequency of mode 2), and although their magnitude is lower when the PWM frequency is 10.3kHz the associated noise emissions are higher. It is also evident that a resonance occurs at 20.6kHz which results in a large vibration amplitude at a switching frequency of 20.6kHz.

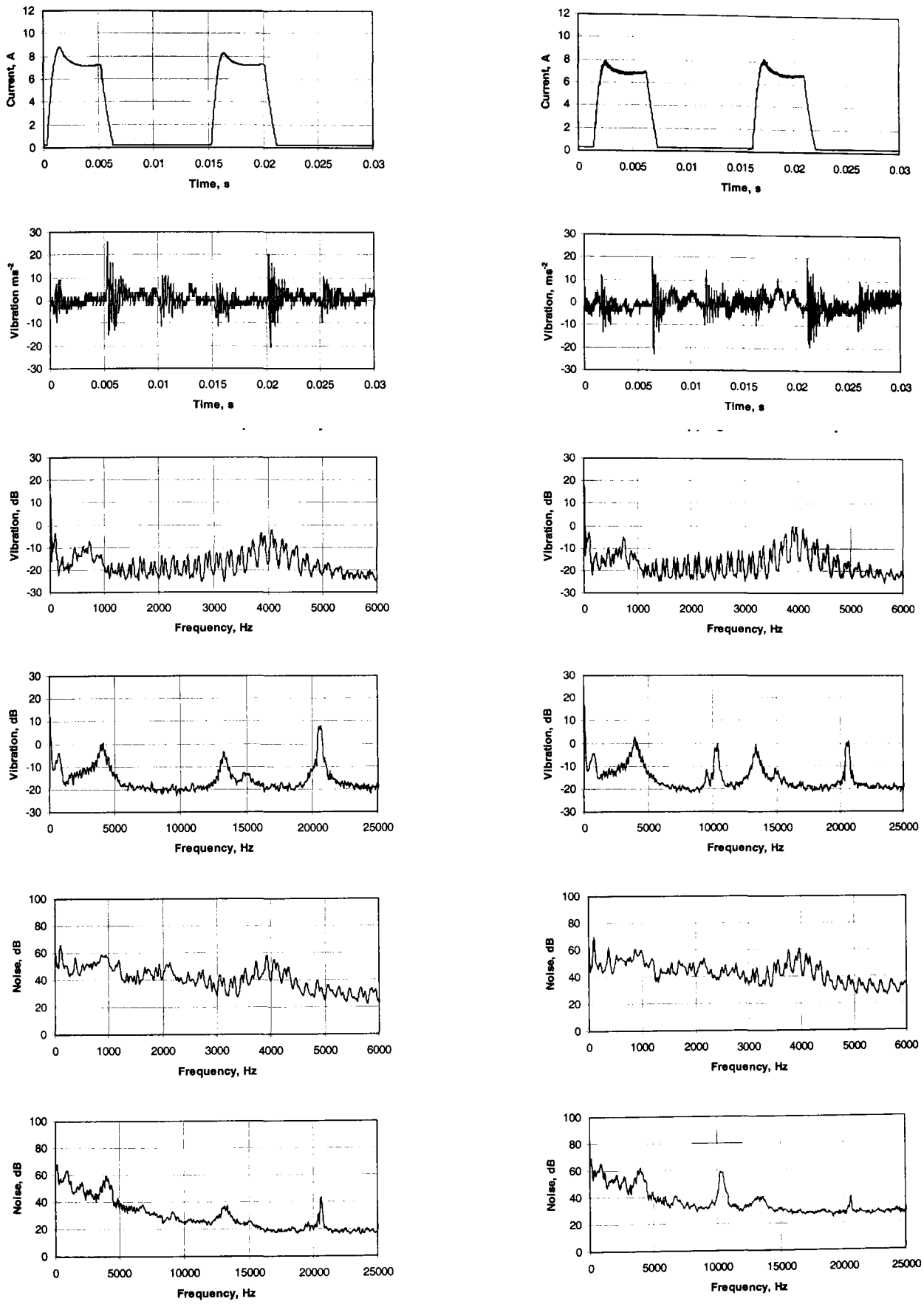

(a) 20.6kHz (b) 10.3kHz

Fig. 4.22 *Influence of PWM switching frequency under voltage PWM control at 1000rpm, no-load*

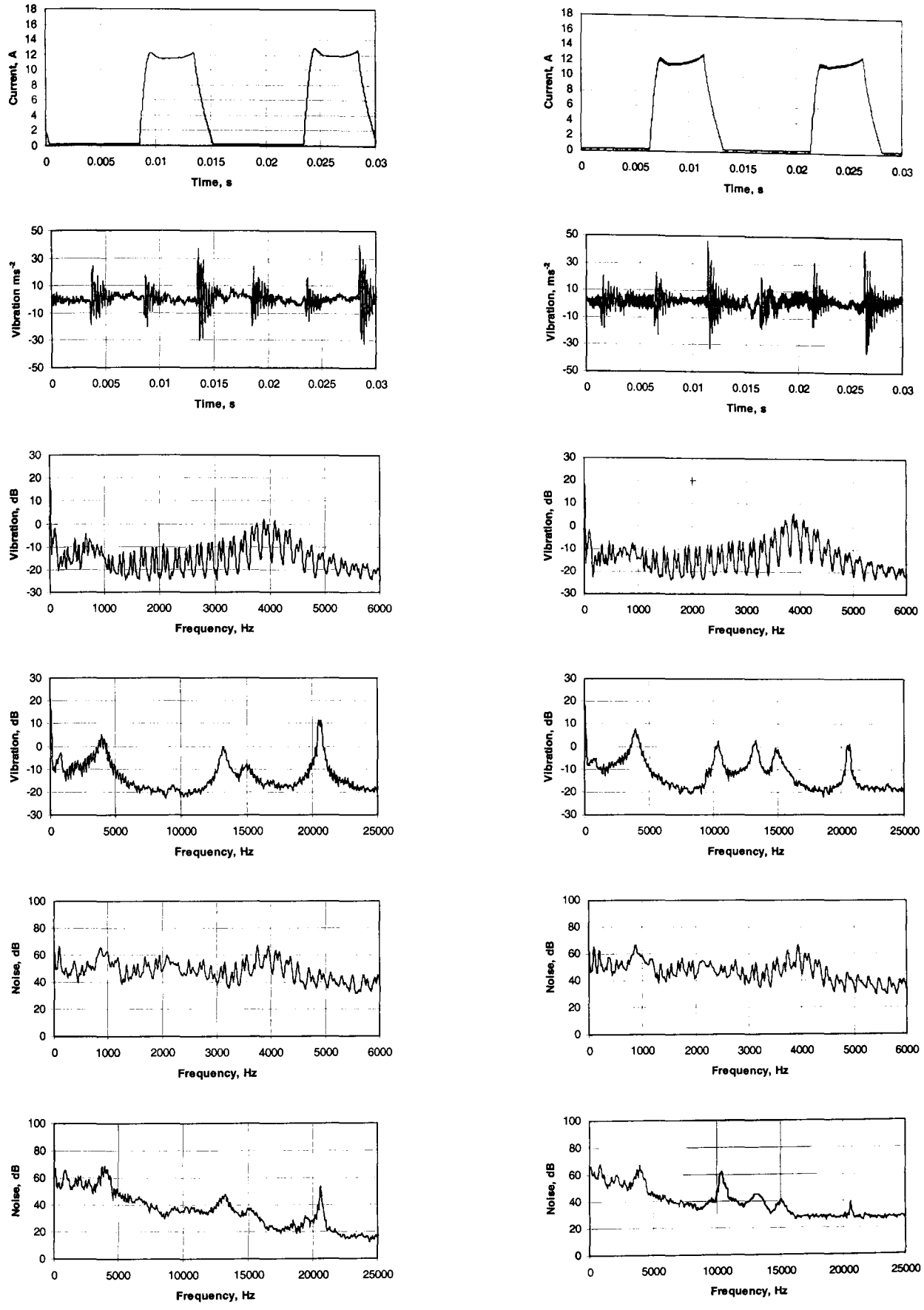

(a) 20.6kHz **(b)** 10.3kHz

Fig. 4.23 *Influence of switching frequency under voltage PWM control at 1000rpm, ≈75% load*

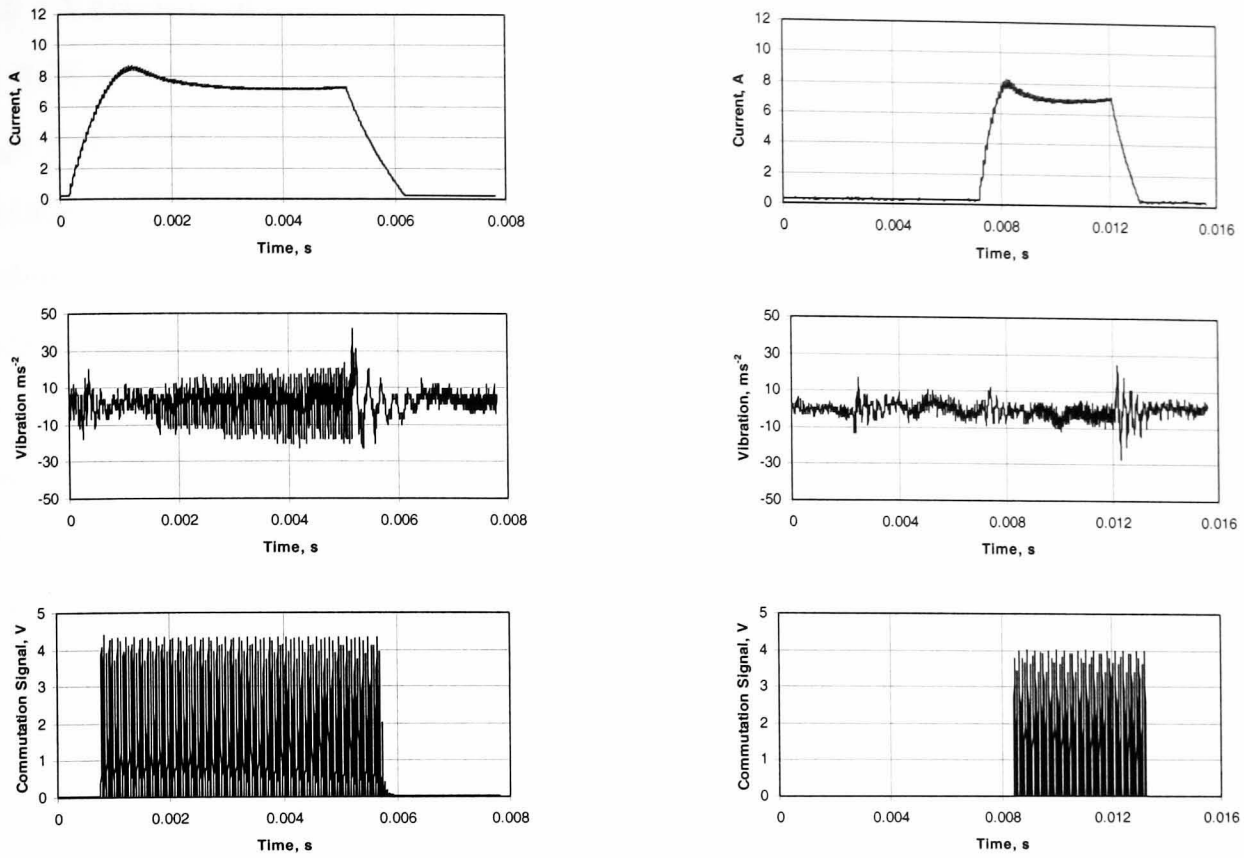

(a) 20.6kHz **(b)** 10.3kHz

Fig. 4.24 *Influence of switching frequency under voltage PWM control at 1000rpm, no-load*

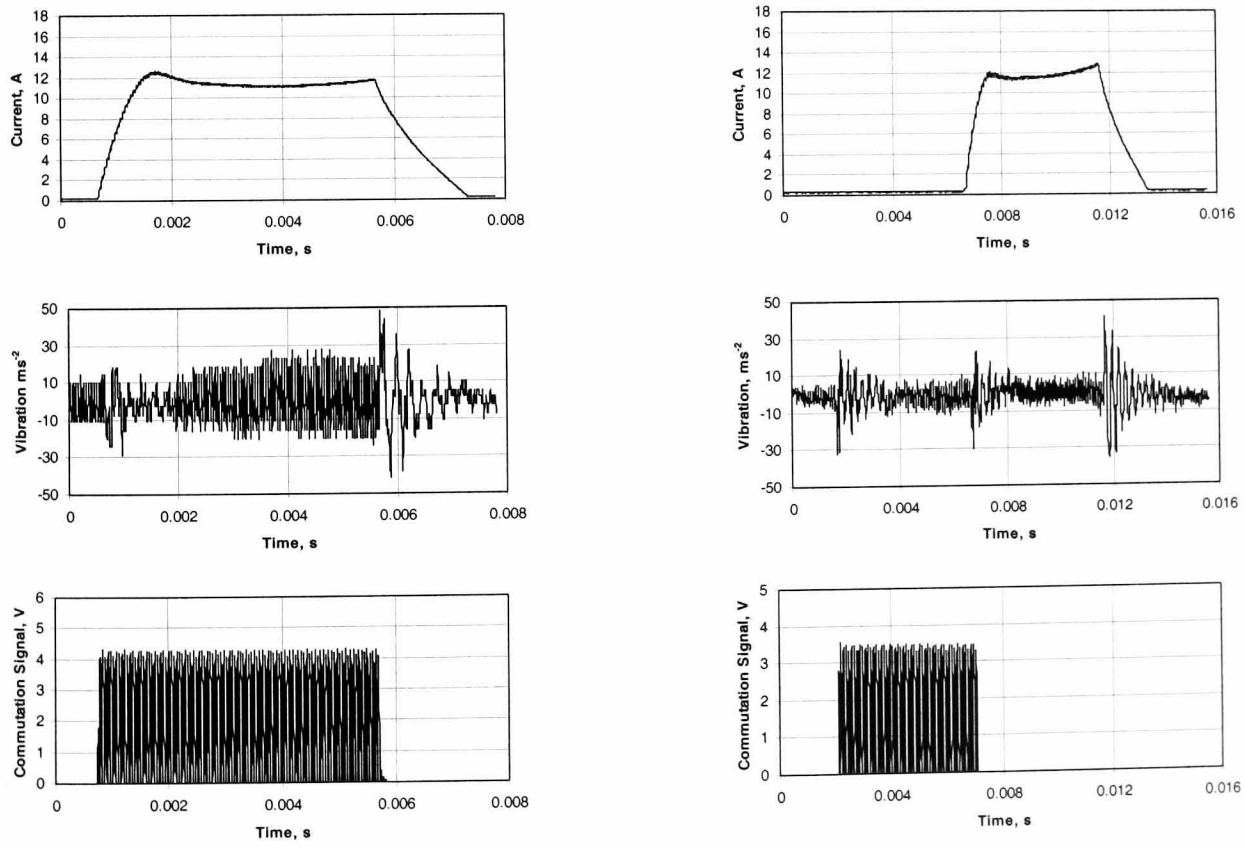

(a) 20.6kHz **(b)** 10.3kHz

Fig. 4.25 *Influence of switching frequency under voltage PWM control at 1000rpm, ≈75% load*

4.3.5 Variation of sound pressure level

Fig 4.26 compares the SPL which results with soft and hard switching over a speed range from 500rpm to 2500rpm, for both no-load and ≈75% load. In general, the SPL increases with speed, which is consistent with earlier observations in section 4.3.2. Furthermore, as discussed in section 4.1, in relation to the harmonic analysis, since the fundamental current increases in frequency as the rotational speed increases, as the speed is increased, the fundamental frequency becomes closer to the natural frequency of mode 2, and thus the resonance induced is expected to become more severe with an increase in speed. Soft chopping, for both on no-load and on load, generally results in a lower SPL than results with hard chopping. However, it will be observed that at 2000rpm a rotor/system resonance exists, and, both on no-load and on load, the machine emits a slightly higher SPL with soft chopping than that with hard chopping. Under all load conditions the SPL is higher than that on no-load, except at 2000rpm, when the SPL on load with hard chopping is slightly lower than that with soft chopping on no-load.

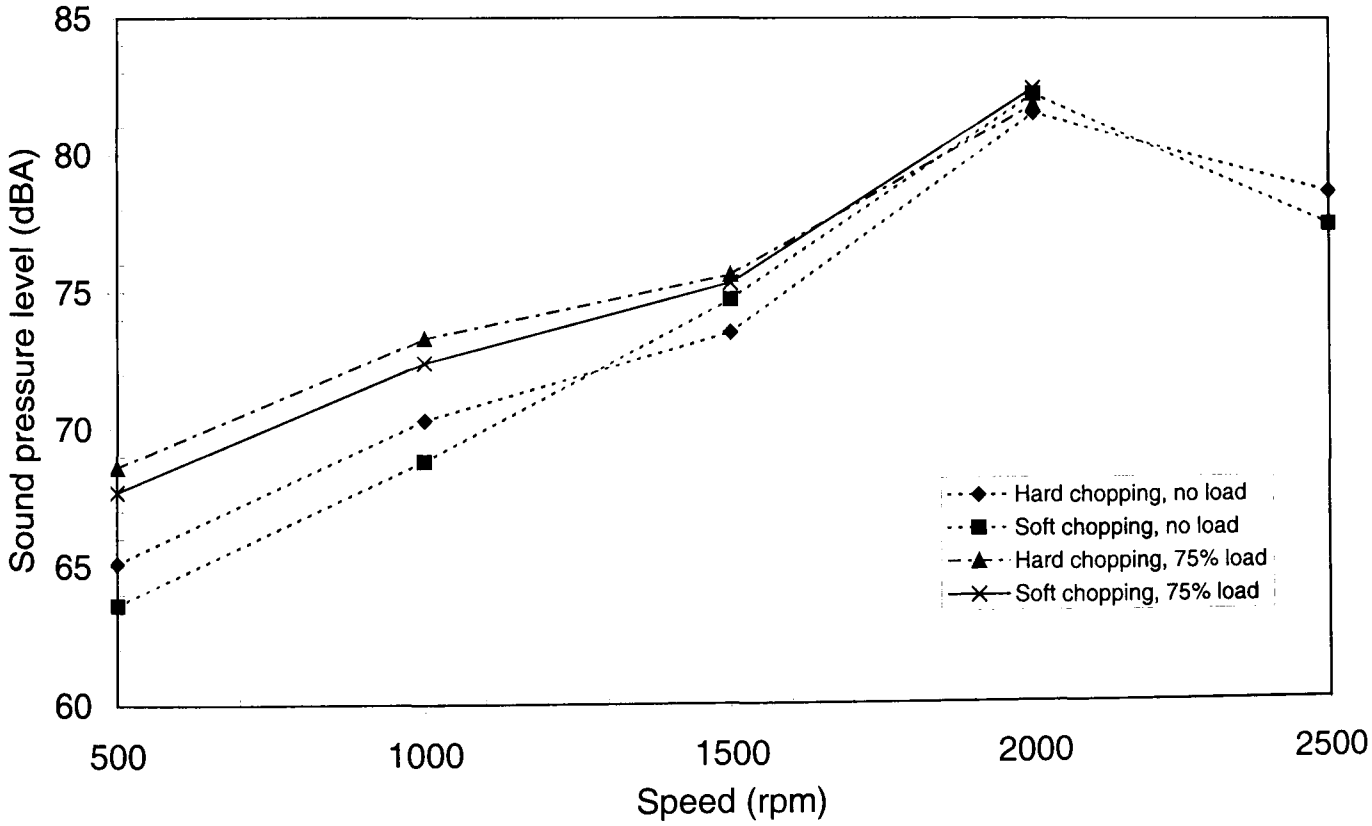

Fig. 4.26 *Variation of sound pressure level under voltage PWM control*

4.4 Noise and vibration under current control

Current control essentially adds another closed loop within the speed loop. The feedback current, derived from a current transducer, is compared to the demanded current (or reference current) at some frequency that is fixed within the control algorithm. A simple 'bang-bang' control scheme is employed such that the switching devices are turned on or off, depending upon whether the current is lower or greater than the reference current, respectively. Due to the limitations of the digital controller, a finite time is required to execute the current control code, which influences the maximum switching frequency for the power devices. Therefore, the control scheme is limited to simple 'bang-bang' control, without the need for hysteresis band control, which would provide little advantage. As with voltage PWM control, both soft and hard switching strategies can be implemented by employing the appropriate combination of stages *(i)*, *(ii)* and *(iii)*, **Fig. 4.15**. An example of hard chopping current control is shown in **Fig. 4.27**. As can be seen, the chopping frequency decreases from turn-on to turn-off. This is due to the inductance being lower at the point of turn-on, and, therefore, the back-EMF being lower, thus resulting in a higher rate of rise of current which requires a faster switching rate to ensure stabiliy. However, as the rotor is pulled into alignment with the excited stator poles, the inductance increases, thereby increasing the back-EMF and consequently limiting the rate of rise of current and reducing the switching frequency whilst maintaining a relatively stable current. However, in the experimental drive system, the current rises so fast that the controller cannot respond sufficiently quickly to limit the initial instantaneous current. This is attributed not only to the sampling frequency but also the conversion time of the ADC's which interface the current feedback signal from the current transducers to the DSP. Furthermore, the commutation interrupt service routine (ISR) is a higher priority than that of the current control, which introduces a delay due to the necessary interrupt flags being reset and the controller responding to the current controller interrupt request.

The investigations, which follow, are similar to those which were carried out when the machine was operated under voltage PWM control, in that the influence of soft and hard chopping, the operational speed, the load, the sampling frequency and thus the switching frequency is investigated. Generally, the observations are similar to those which were obtained with voltage PWM control. Thus, to avoid duplication, only results which are specific to current control will be discussed in detail.

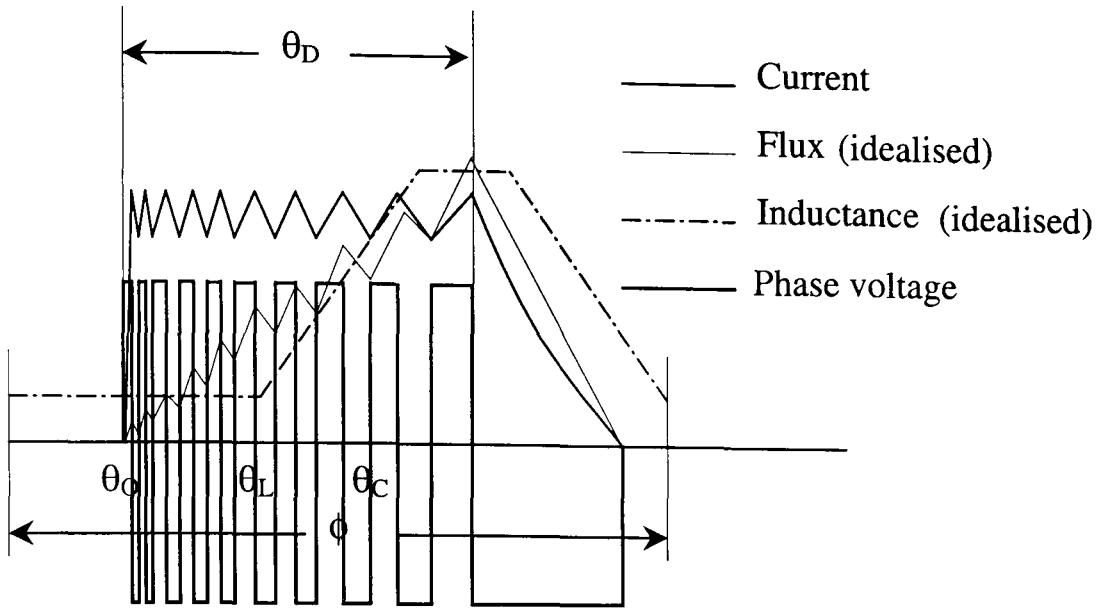

Fig. 4.27 *Hard chopping current control*

4.4.1 Influence of soft and hard chopping

The instantaneous phase current under hard chopping control exhibits a higher overshoot at turn-on than that under soft chopping control, **Fig. 4.28**. This is expected, due to the fact that the step change in applied voltage with hard chopping is twice that which is applied during soft chopping, which results in a greater rate of change of current. A higher sampling rate would be required to ensure more stable operation under hard chopping, which would reduce the current ripple to a level which is comparable to that with soft chopping.

The time domain vibration with hard chopping also exhibits higher oscillation levels. This is reflected in the vibration spectrum, in which higher peaks are associated with modes 2 and 4. Furthermore, the peak of mode 3 is observable in the vibration spectrum, although it is insignificant in the noise spectrum, but it does imply that there are unbalanced forces in the airgap.

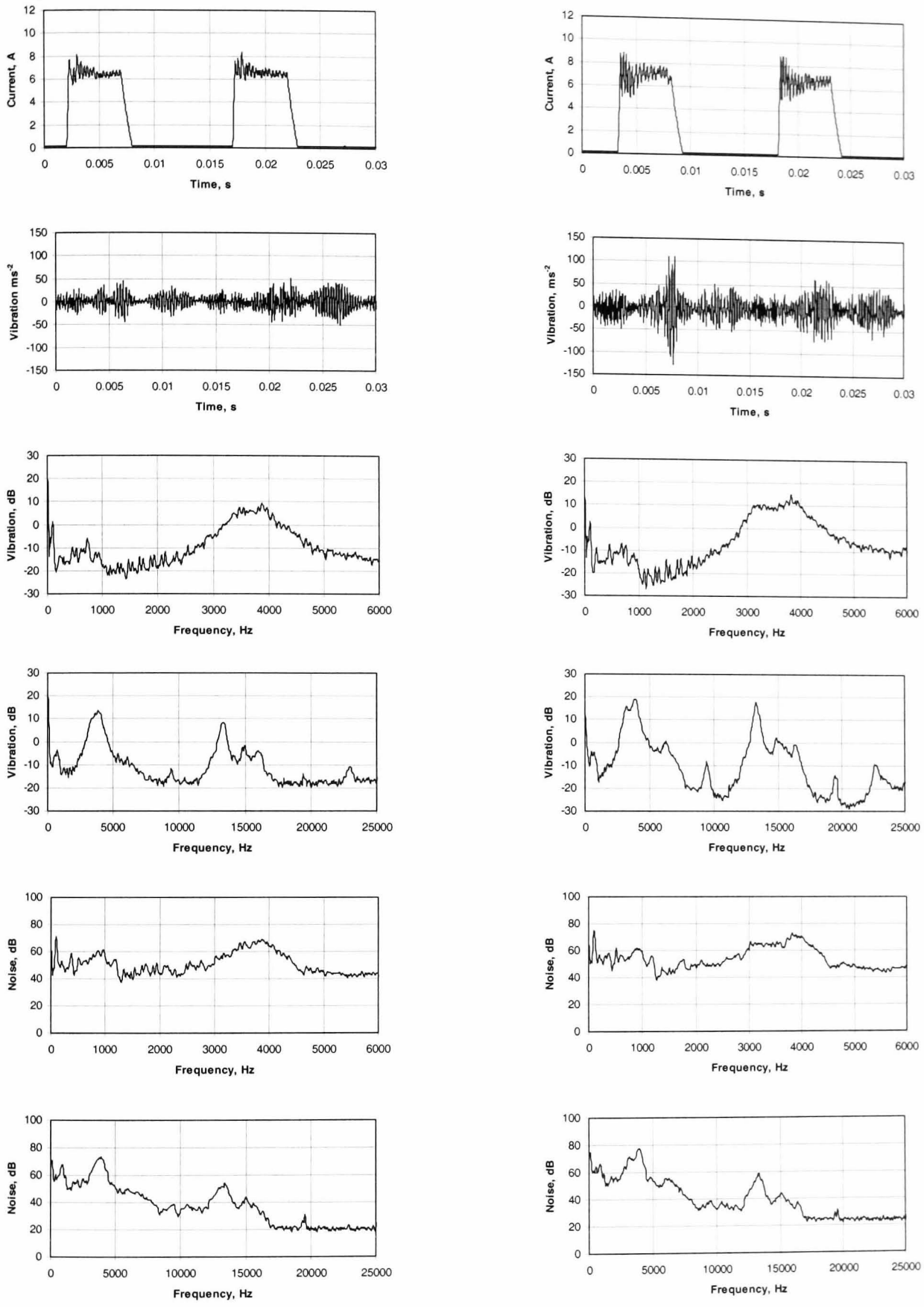

(a) *Soft chopping* **(b)** *Hard chopping*

Fig. 4.28 *Influence of soft and hard switching strategies under current control, no-load, 1000rpm*

4.4.2 Influence of operating speed

The instantaneous phase current and the associated noise and vibration measurements for rotational speeds of 500rpm, 1000rpm and 1500rpm, with the machine operating on no-load, are shown in **Fig. 4.29**.

Generally, oscillations in the time domain vibration increase with speed, although the variation in the magnitude of the peak vibration associated with mode 2 does not remain the same for each of the given speeds. At 1500rpm, the largest vibration peaks are associated with modes 2 and 3, whilst at a speed of 1000rpm mode 4 has the largest value. At a speed of 1000rpm the vibration peak associated with mode 2 is slightly lower than at 500rpm. The noise spectra generally follow trends which are present in the associated vibration spectra.

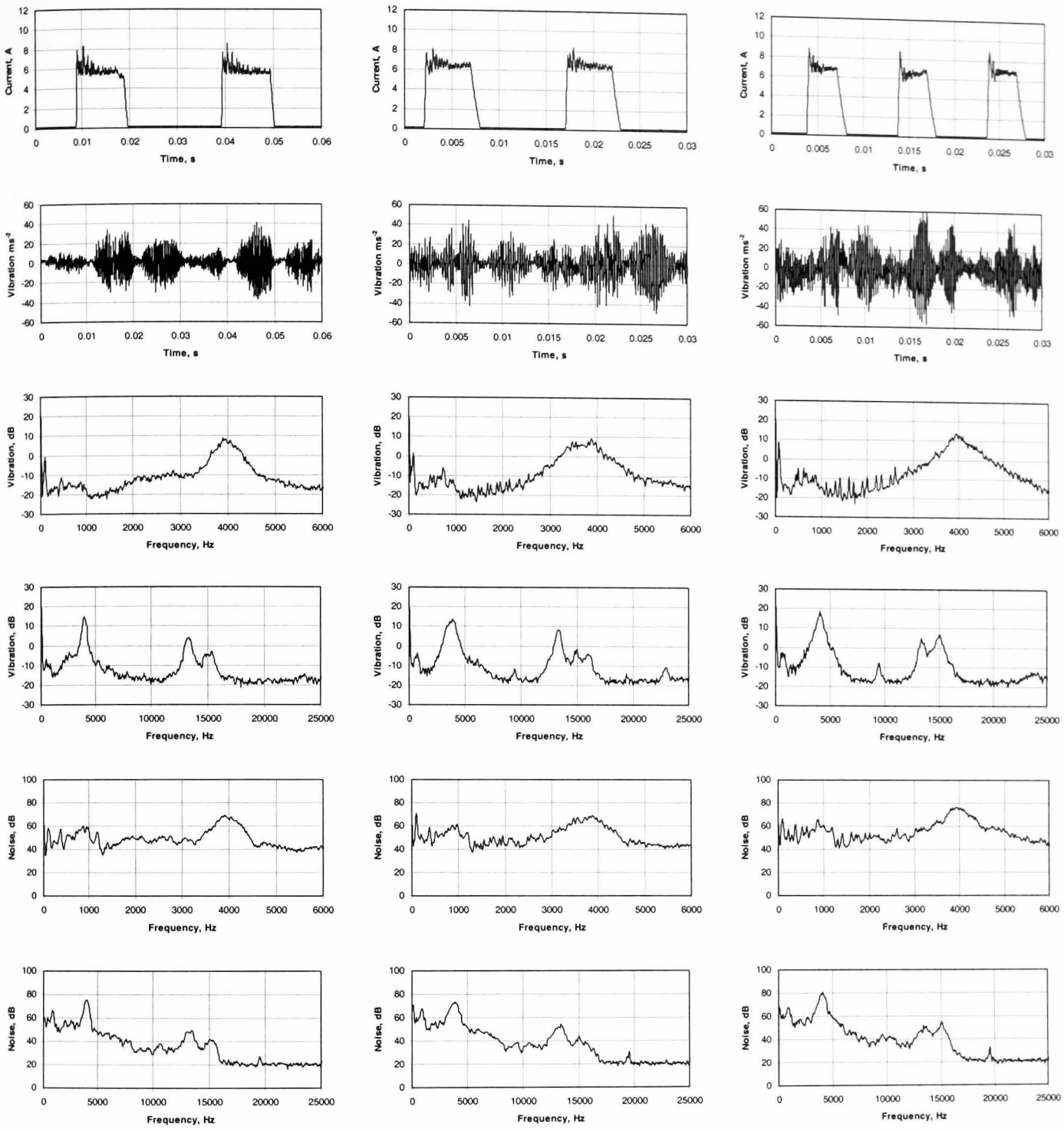

(c) *500rpm* **(b)** *1000rpm* **(a)** *1500rpm*

Fig. 4.29 *Influence of operating speed under current control, no-load*

4.4.3 Influence of load

The SR machine was again run at three speeds, viz. 500rpm, 1000rpm and 1500rpm, with a load applied by the wound-field dc machine. The current, noise and vibration were measured with the machine on no-load and with a load of ≈75% of the nominal rated torque, the measurements being shown in **Figs. 4.30(a) and (b)**, respectively.

At 500rpm the magnitude of the instantaneous phase currents on no-load and load is comparable, whereas at 1500rpm the amplitude of the current almost doubles when the load is applied. At a speed of 1500rpm, on load, the machine operation is observed to approach that of single pulse mode due to the relatively large back-EMF, which reduces the number of switching events in the current waveform of **Fig. 4.30iii(b)**.

At each speed, oscillations in the time domain vibration increased as load is applied, although they are greatest at a speed of 1000rpm.

At 1500rpm, the application of load reduces the amplitude of mode 3 in the vibration spectrum, the load restraining, to a some extent, the oscillations/unbalance of the shaft. However, at 1000rpm the load has insignificant influence on the amplitude of mode 3, whilst at 500rpm the load induces mode 3, which is not present on no-load at this speed. It should be noted that a peak associated with mode 3 is not present in the noise spectrum at any of the rotational speeds, due to the very low magnitude of the vibrational peak of mode 3.

A further observation is that at 1500rpm magnitude of the vibration peak which corresponds to mode 2 is actually reduced when a load is applied. However, this is not reflected in the time domain waveform, which highlights the random nature of the stator vibration when the machine is operated under current control. However, the magnitude of vibration mode 4 is observed to increase with application of the load at this speed, although this is not reflected in the noise spectra.

At 1000rpm, the application of load causes an increase in the peak of mode 2 in both the vibration and noise spectra, due to the higher current, and, hence, force. However, the peak of mode 4, for both the vibration and the noise spectra, decreases, whereas the peak associated with mode 3 slightly increases.

At 500rpm, the application of load has a negligible effect on the peak value of vibration mode 2, but causes a slight decrease in the corresponding noise peak. The vibration peak of mode 4 increases considerably, whereas the associated noise peak is unaffected.

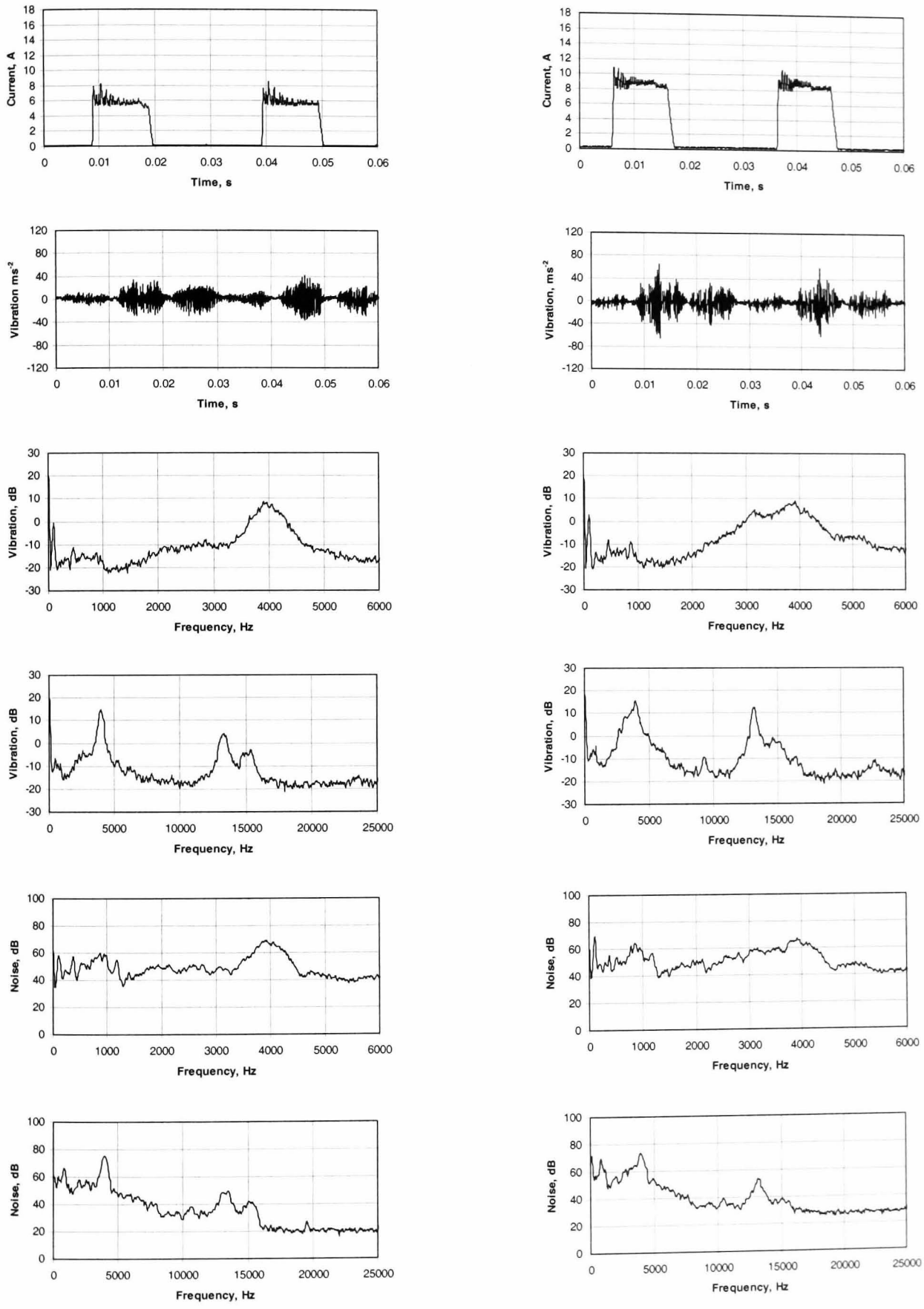

(a) *No-load* **(b)** *≈75% Load*

Fig. 4.30i *Influence of load under current control at 500rpm*

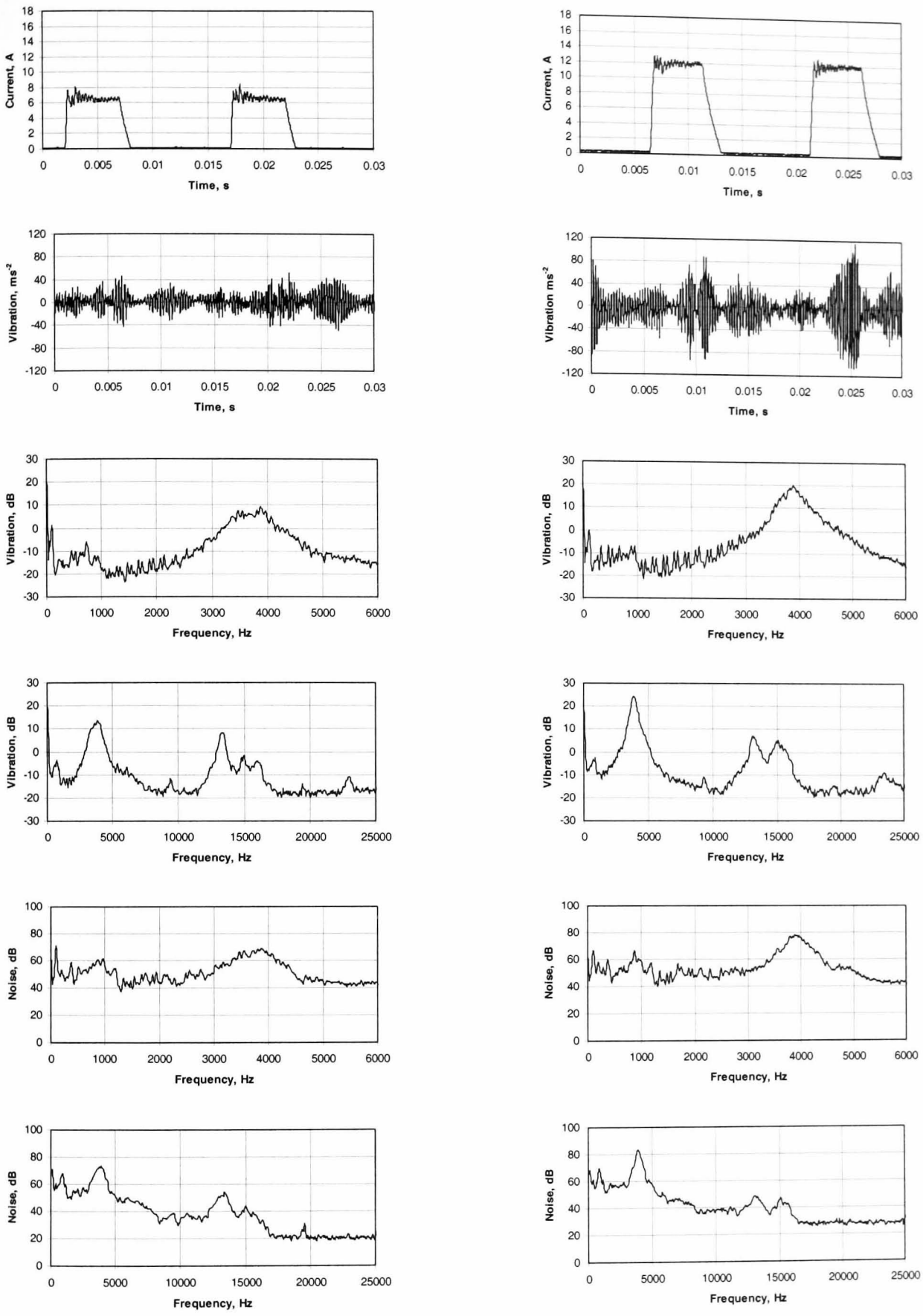

(a) *No-load* **(b)** *≈75% Load*

Fig. 4.30ii *Influence of load under current control at 1000rpm*

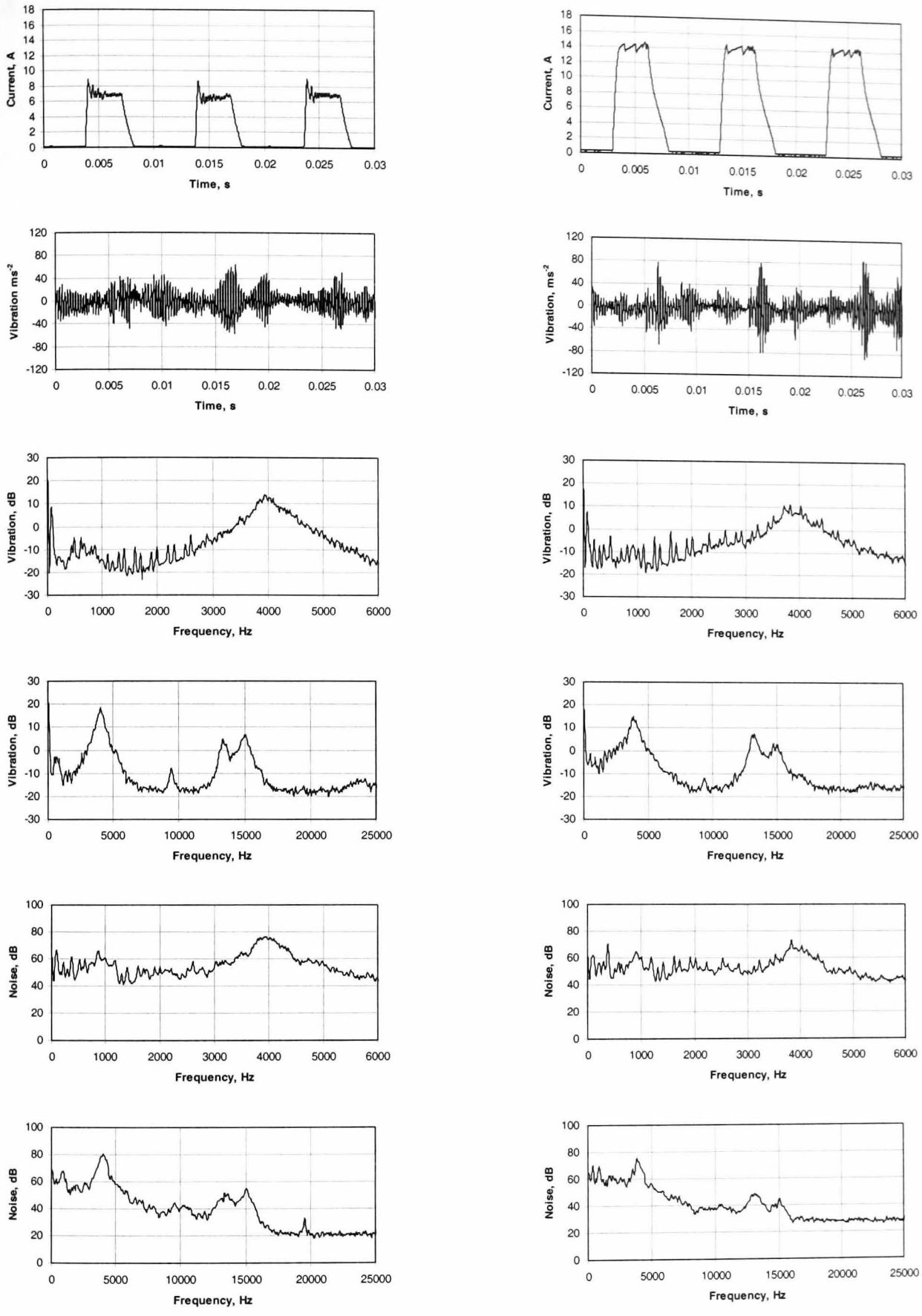

(a) *No-load* **(b)** *≈75% Load*

Fig. 4.30iii *Influence of load under current control at 1500rpm*

4.4.4 Influence of sampling frequency and switching frequency

To investigate the influence of the sampling frequency of the current controller on the emitted noise, sampling frequencies of 10kHz, 20kHz, 30kHz and 40kHz were employed, and the SPL was measured with the machine operating on no-load and ≈75% rated load, as shown in **Figs. 4.31** and **4.32**, respectively.

Over the given speed range, with the exception of 2000rpm, a sampling frequency of 20kHz generally results in the quietist operation, both on no-load and load, **Fig. 4.31(a)** and **Fig. 4.32(a)**. However, it will be observed that the SPL is generally higher when load is applied. A 10kHz sampling frequency results in a slightly higher SPL over the speed range, although at 500rpm it results in the lowest SPL. Increasing the of sampling frequency to 30kHz and 40kHz increases the SPL, although at 500rpm and 2500rpm the SPL is more or less similar.

For each of the sampling frequencies, the SPL varies over the speed range, generally increasing with speed, **Figs. 4.31(b)** and **4.32(b)**. Again, this is expected since the number of switching events varies with both the sampling frequency and speed, as can be seen in the instantaneous current waveforms of **Fig. 4.33**. For a given speed, the average switching frequency varies over the dwell period, as discussed in section 4.4. Furthermore, observation of the instantaneous current waveforms, especially at speeds of 500rpm and 1500rpm, confirms that the rate of change of current at the turn-off point generally becomes more rapid as the sampling frequency is increased, with the exception of the current waveforms approaching single pulse mode. Thus, the higher SPL which results with sampling frequencies of 40kHz and 30kHz is attributed to the higher rate of change of current at turn-off, and an increase in the switching frequencies which fall within more heavily A-weighted region of the audible frequency range.

As observed in section 4.4.2, the number of switching events in the phase current waveform reduces as the speed increases, due to the larger back-EMF and reduced rate of change of current. This is very significant at a speed of 2500rpm when the phase current waveform approaches that of a single pulse. When the sampling frequency is reduced from 40kHz, **Fig. 4.33(a)**, to 10kHz, **Fig. 4.33(d)**, the number of switching events reduces. This is particularly clear at a speed of 1500rpm, **Fig. 4.33iii**, as summarised in **Table 4.9**. The number of switching events is obtained from the phase current waveforms in **Fig. 4.33**, over the dwell period. The chopping region is one third

of the phase excitation period. Thus at an excitation frequency of 100Hz, the portion of the current waveform over which the switching events occur is 33.3ms.

Table 4.9 Number of *switching events at 1500rpm for specified sampling frequencies*

Sampling Frequency (kHz)	Switching Events	Average Switching Frequency (kHz)
40	12	3.6
30	9	2.7
20	8	2.4
10	5	1.5

At sampling frequencies of 30kHz and 40kHz, the noise and vibration peaks associated with modes 2 and 4 have a higher magnitude than those which result with sampling frequencies of 20kHz and 10kHz at all rotational speeds, **Fig. 4.33**. Again, this is attributed to the higher initial rate of current decay at turn-off.

At 500rpm and 2500rpm the vibration and noise peaks associated with mode 2 are similar in magnitude for sampling frequencies of 30kHz and 40kHz, whereas at 1500rpm they are larger with a sampling frequency of 40kHz. Further, at 1500rpm and 2500rpm, the noise and vibration peaks associated with mode 2 are larger with a sampling frequency of 10kHz than those for a sampling frequency of 20kHz. At 500rpm and a sampling frequency of 20kHz a slightly higher noise peak results, whilst the associated vibration peaks are similar.

At 500rpm, the noise peaks associated with mode 4 are similar in magnitude, for sampling frequencies of 30kHz and 40kHz, whereas the vibration peak is larger for the 30kHz sampling frequency. However, at 1500rpm the vibration peaks for mode 4 have a similar magnitude, whilst the noise peak is significantly larger for the 40kHz sampling frequency. Further, at 2500rpm both the noise and vibration peaks are essentially the same for the two sampling frequencies. At a sampling frequency of 10kHz and a speed of 2500rpm, the noise and vibration peaks associated with mode 4 are essentially the same as those for sampling frequencies of 30kHz and 40kHz at a speed of 2500rpm, whereas those for a sampling frequency of 20kHz are significantly lower. At 500rpm a 20kHz sampling frequency results in larger vibration and noise peaks than for a 10kHz sampling frequency. However, at 1500rpm only the vibration peak is greater.

A vibration peak associated with mode 3 is observed for all sampling frequencies at speeds of 1500rpm and 2500rpm. However, at 500rpm it can only be observed for a sampling frequency of 30kHz. This mode is not observed in any of the noise spectra.

At all speeds, a noise peak is present at approximately 19kHz for sampling frequencies of 40kHz and 30kHz. However, it is not present at sampling frequencies of 20kHz and 10kHz, and is not in any of the corresponding vibration spectra.

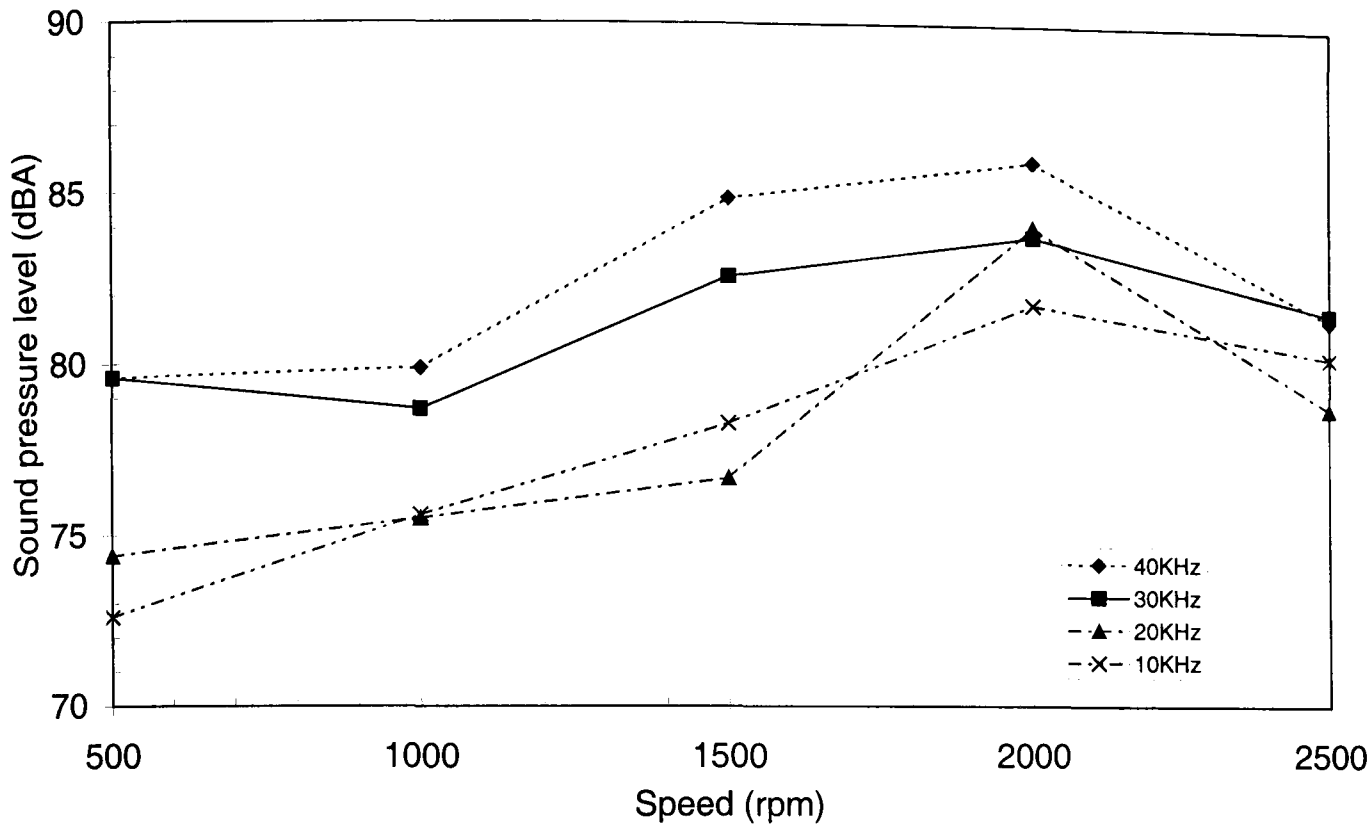

(a)

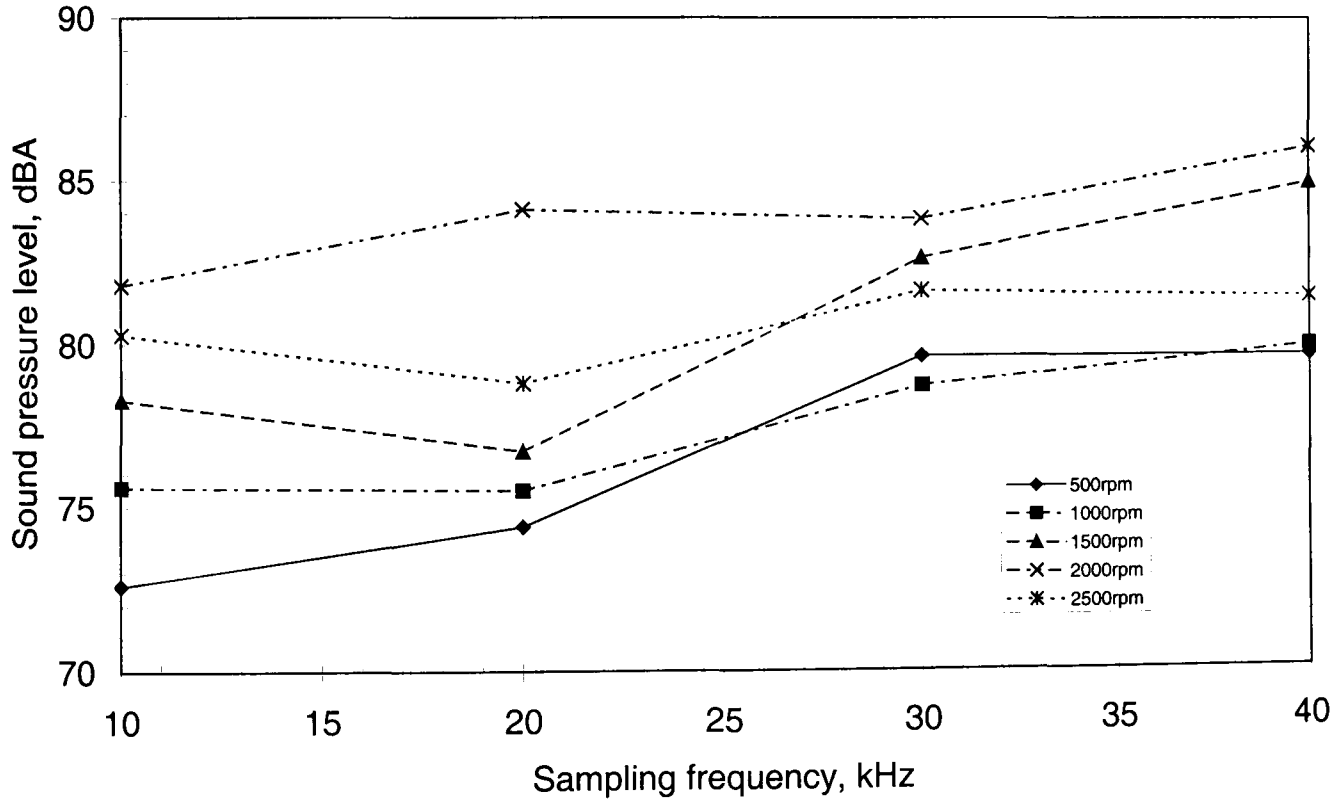

(b)

Fig. 4.31 *Variation of sound pressure level with sampling frequency and operating speed, on no-load*

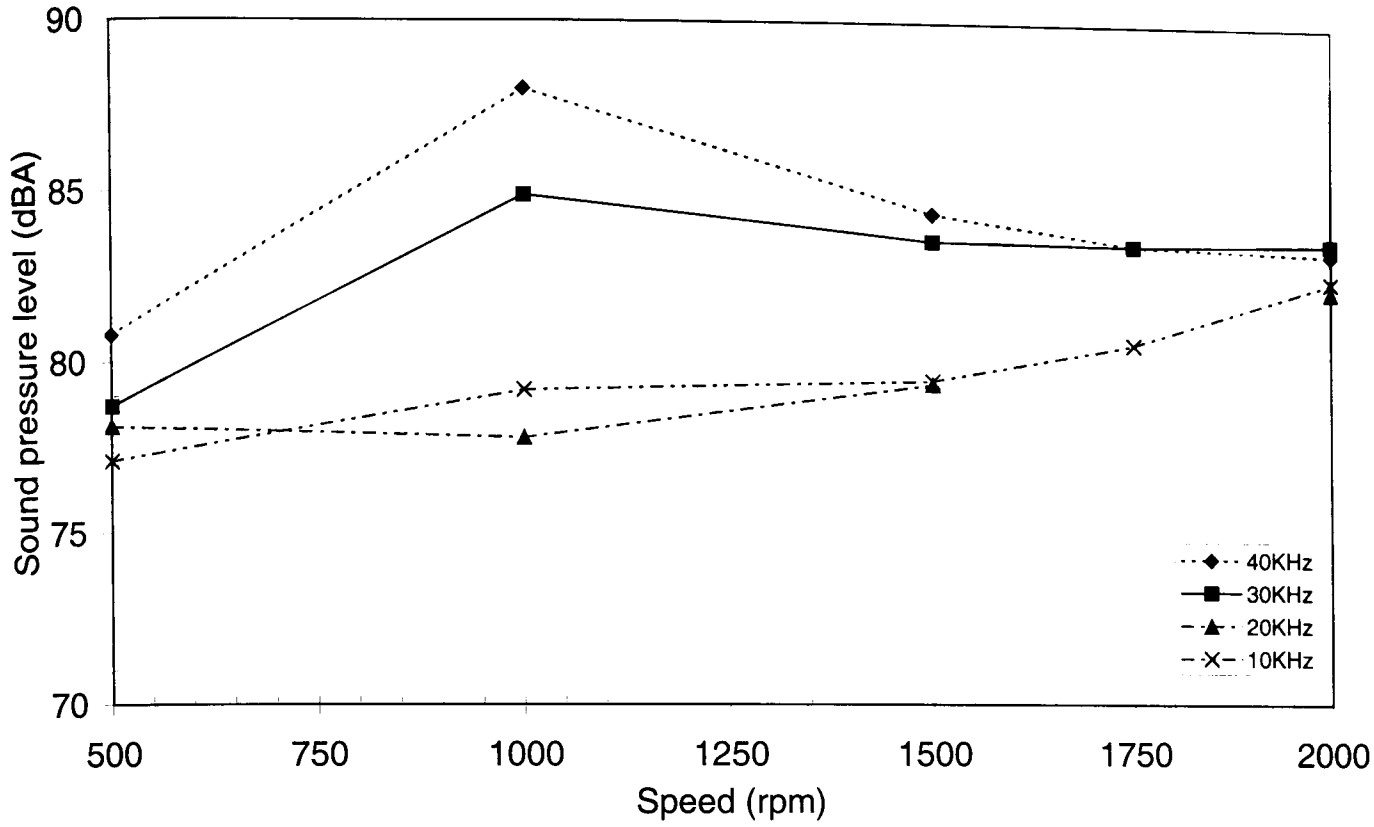

(a)

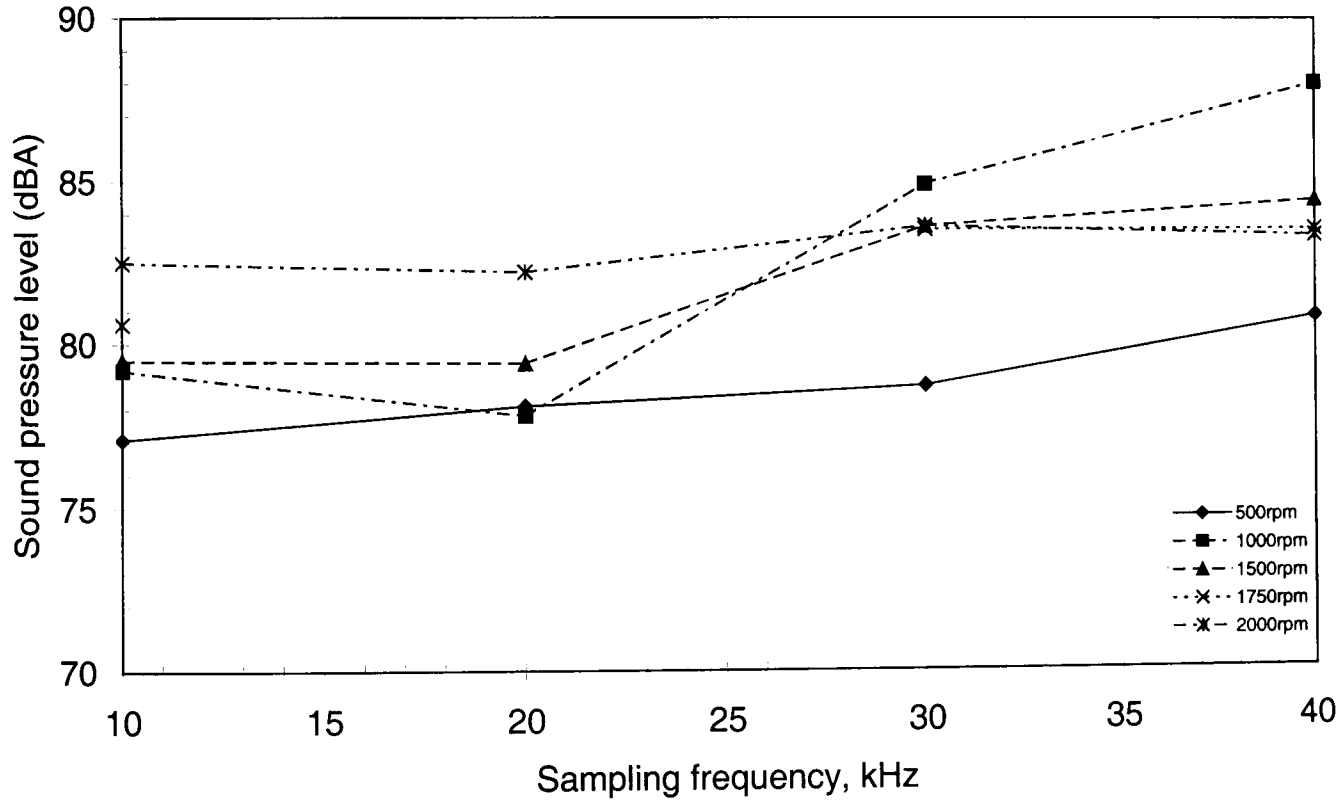

(b)

Fig. 4.32 *Variation of sound pressure level with sampling frequency and operating speed, at ≈75% load*

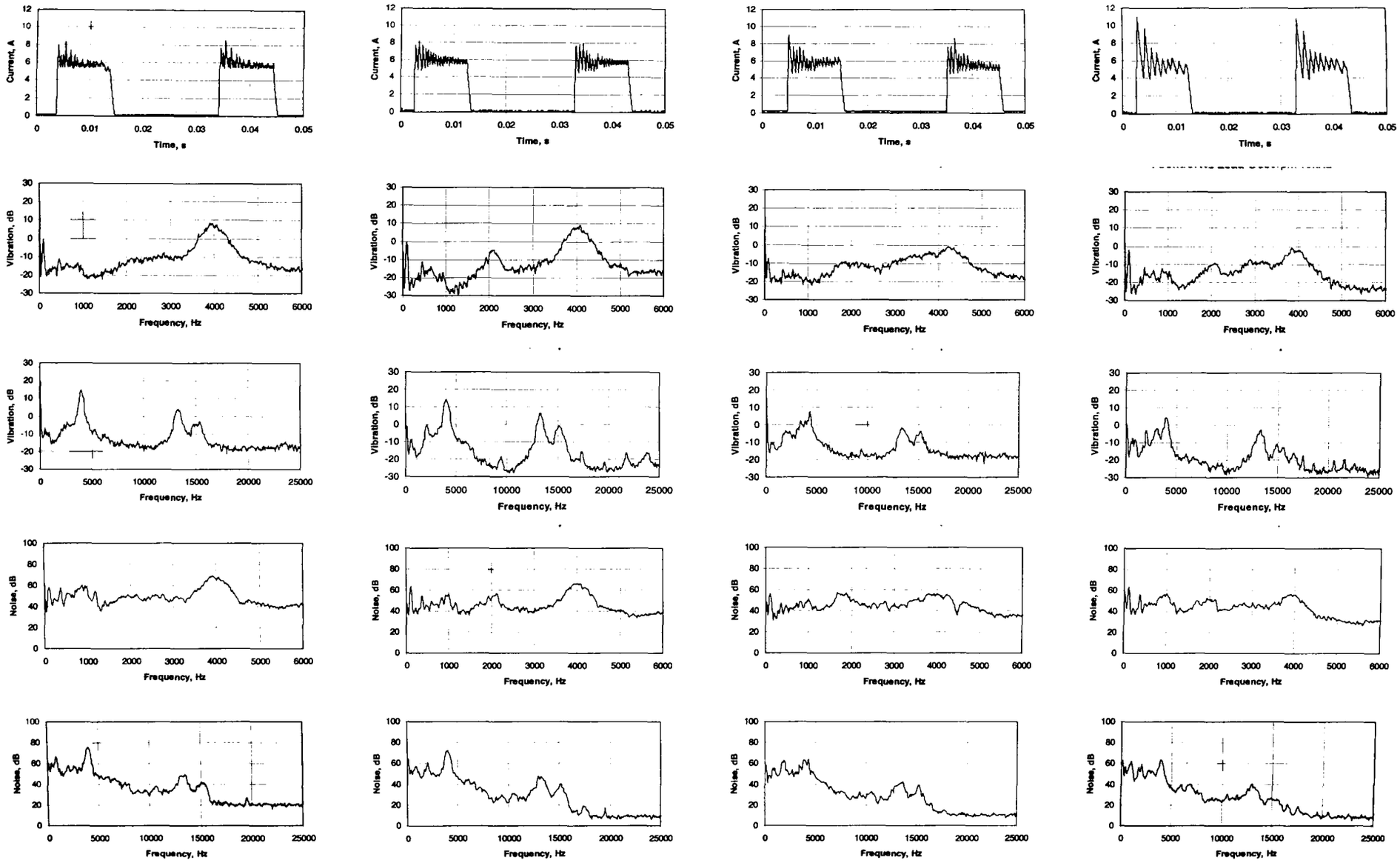

(a) *40kHz* **(b)** *30kHz* **(c)** *20kHz* **(d)** *10kHz*

Fig. 4.33i *Influence of sampling frequency under current control, no-load, 500rpm*

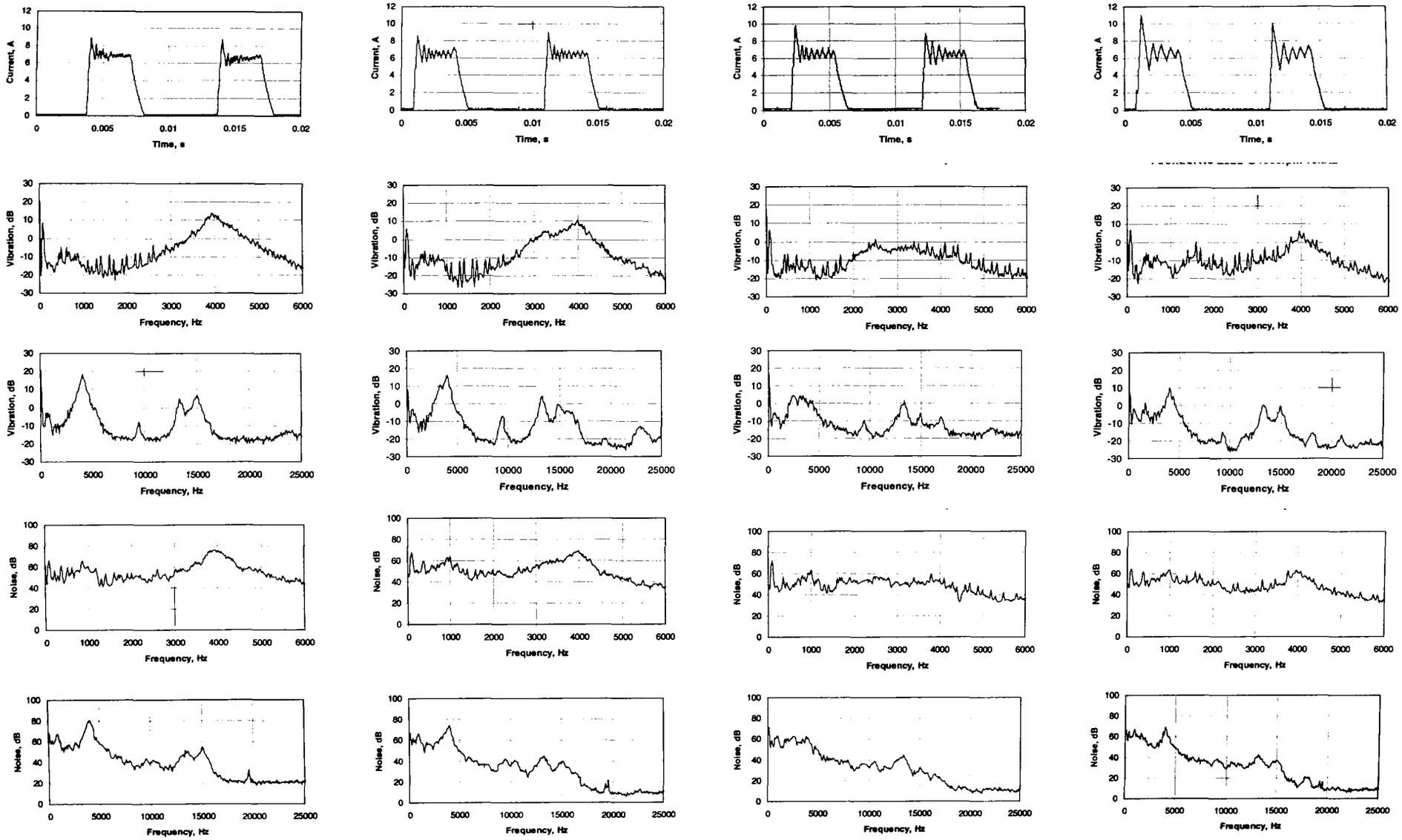

(a) *40kHz* **(b)** *30kHz* **(c)** *20kHz* **(d)** *10kHz*

Fig. 4.33ii *Influence of sampling frequency under current control, no-load, 1500rpm*

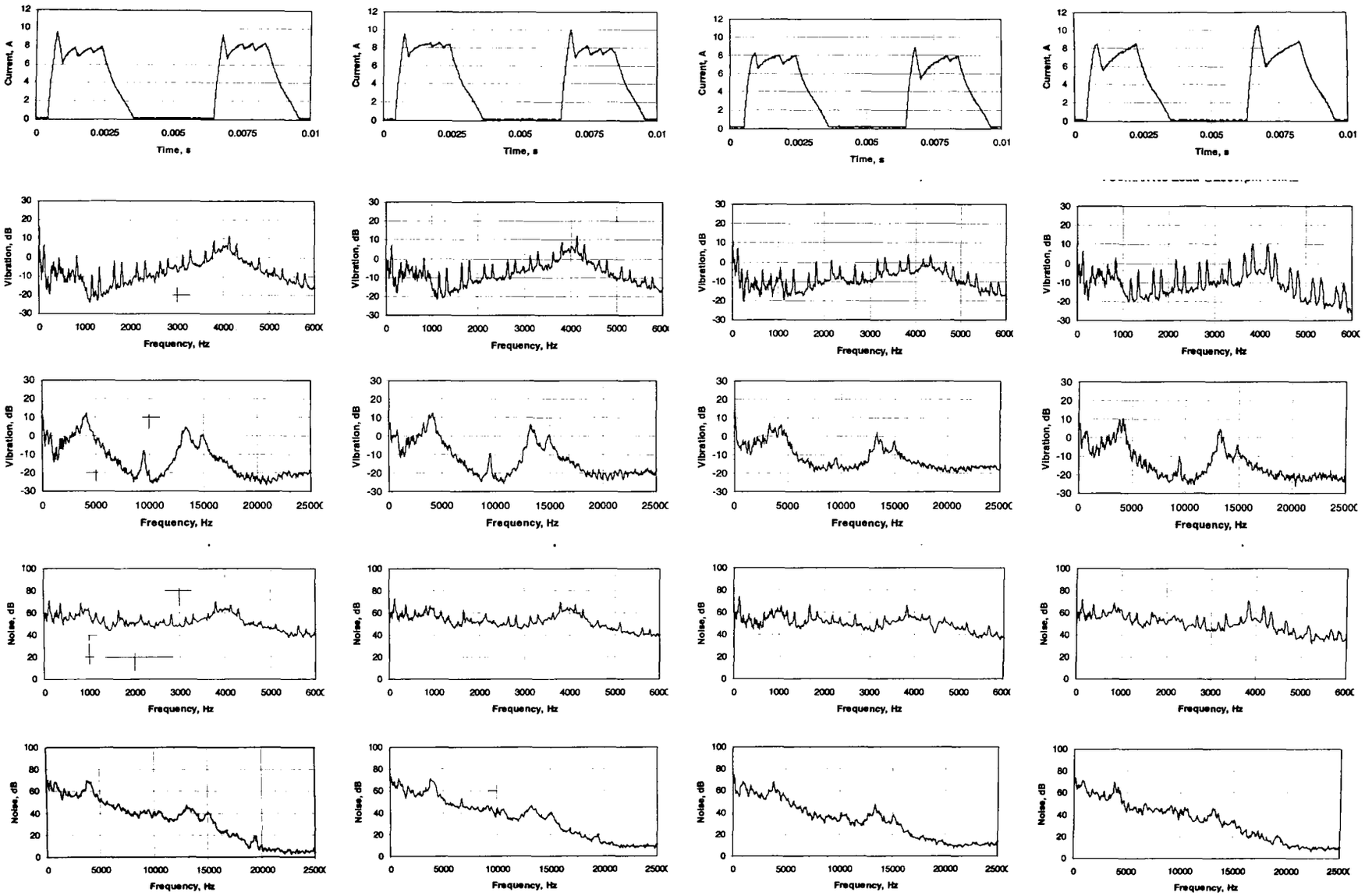

(a) *40kHz* **(b)** *30kHz* **(c)** *20kHz* **(d)** *10kHz*

Fig. 4.33iii *Influence of sampling frequency under current control, no-load, 2500rpm*

4.4.5 Variation of sound pressure level

The variation of the SPL with the machine on no-load and ≈75% load, under both soft and hard chopping control, is shown in **Fig. 4.34**, over the speed range 500rpm to 2500rpm. With the exception of operation at 2000rpm, soft chopping on no-load results in the lowest SPL at all speeds. Soft chopping control also results in the lowest SPL when the machine is loaded. Hard chopping control results in the highest noise emissions, both on no-load and when loaded. The SPL with soft chopping tends to gradually increase with speed, whereas the SPL with hard chopping tends to vary more erratically.

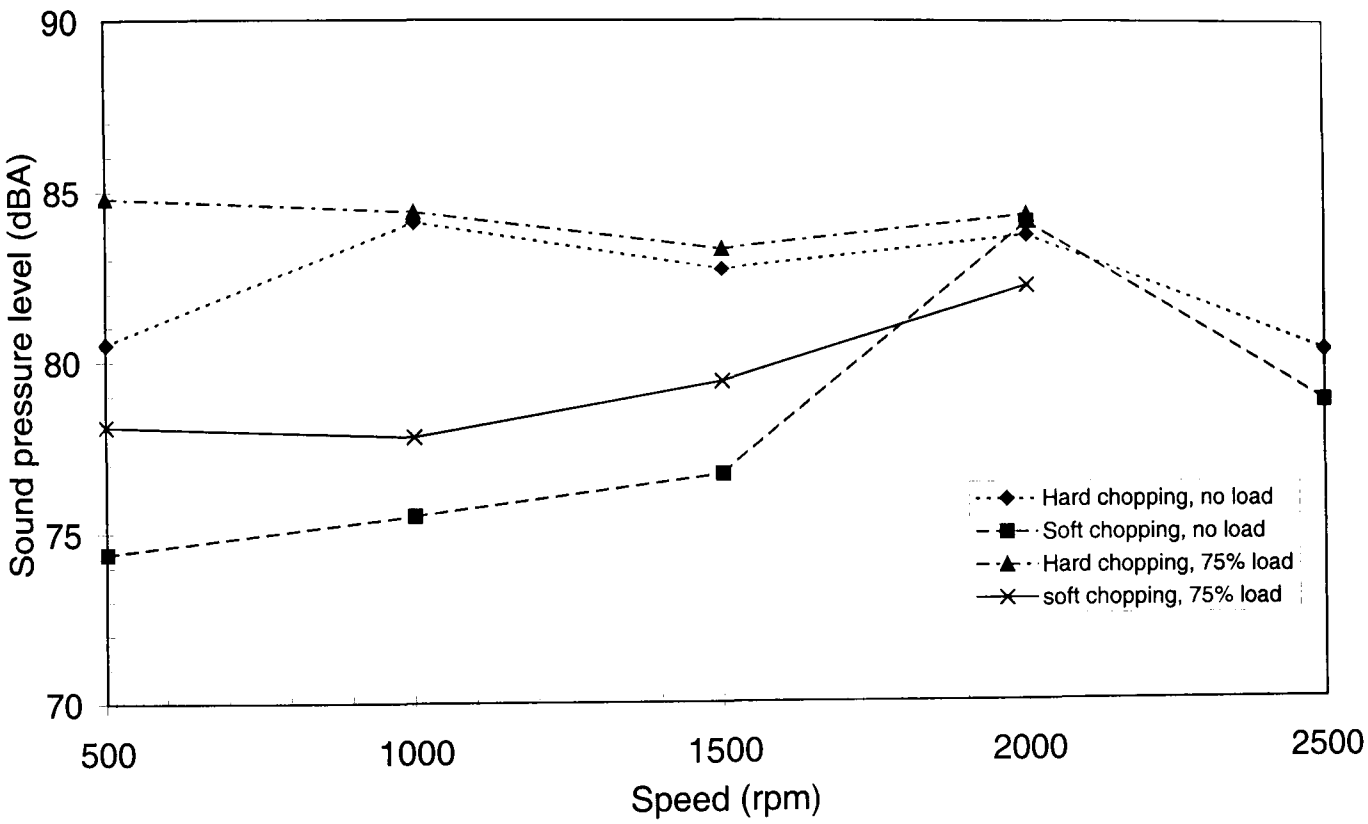

Fig. 4.34 *Variation of sound pressure level under current control*

4.5 Variable DC link voltage PWM control

The following describes an investigation into the influence of varying the dc supply voltage, V_s. Firstly, the machine was operated in single pulse mode, the variable dc supply voltage being used to vary the speed, whilst maintaining fixed switching angles over the speed range. Secondly, the machine was operated at a constant speed of 1000rpm under voltage PWM control, as the dc supply voltage was varied. Thus, the duty cycle of the PWM changed to maintain the required speed. The use of dc chopping, by means of an additional power switching device between the dc supply voltage and the inverter, was reported [PIL95] to reduce acoustic noise emissions from a 4-phase SR machine by reducing the mark-to-space ratio, and hence the rate of change of current. However, it is clear that this would have no more influence on the rate of rise of current compared to that which results with standard voltage PWM control, only affecting the rate of decay of current as a consequence of the reduced de-magnetisation voltage. This is highlighted further in the investigation which follows.

4.5.1 Single pulse operation with variable DC link voltage

Measurements made under the single pulse operated mode, which is employed for the investigation, are compared with those when the machine operates with standard voltage PWM control, for operation on no-load. The measured time domain and frequency domain data are given in **Fig. 4.35**, **(a)** being for voltage PWM control and **(b)** being for the single pulse mode.

At turn-off, the rate-of-change of current when the machine is operating under voltage PWM control is significantly higher than that which results when the machine is under single pulse mode operation when the dc link voltage controls the speed and thereby reduces the de-magnetisation voltage. However, at turn-on the average magnetisation voltage under PWM control is essentially the same as that in the single pulse mode.

Despite the fact that the magnetisation voltages are similar, the current waveforms under voltage PWM control generally have a higher peak and possess a higher value at turn-off than those which result with single pulse mode operation. The rates of change of current, which are summarised in **Table 4.10** for the two methods, highlight the influence of the magnetisation voltages. It will be seen that the rate of rise of current during the magnetisation period is similar for the two control methods at all speeds, which highlights the fact that they result in the same average magnetisation voltage, whereas

with single pulse mode operation rate of change of current is significantly lower during the de-magnetisation period which reflects the reduced de-magnetisation voltage.

At all speeds the time domain vibration contains much higher peak oscillations when controlled by voltage PWM, **Fig. 4.35**, due to the significantly higher rate of decay of the phase current, **Table 4.10**. However, the low frequency ripple is similar, in both phase and amplitude, for the two methods. The reduction in the peak oscillations associated with mode 2 for single pulse mode operation is reflected in the vibration and noise spectra, although the difference between the peak values for mode 2 is observed to reduce as the speed is increased. This is expected, since when operated in single pulse mode, with fixed firing angles, the speed is increased by increasing the dc link voltage. Hence, the de-magnetisation voltage becomes more comparable for both methods. This is also the case for the noise peaks associated with mode 4, whereas the corresponding vibration peaks differ significantly for the two methods.

Table 4.10 *Comparison of rate of change of current under single pulse mode and voltage PWM control for no-load operation.*

Speed (rpm)	Rise time (ms) /di/dt (As^{-1})		Decay time (ms) /di/dt (As^{-1})	
	PWM control	Single pulse mode	PWM control	Single pulse mode
500	2.3/3052	2.2/2928	1.3/4102	3.3/1513
1000	1.2/6717	1.16/6147	1.1/6450	2.4/2364
1500	0.9/9008	0.82/9063	1.3/5359	2.0/3016

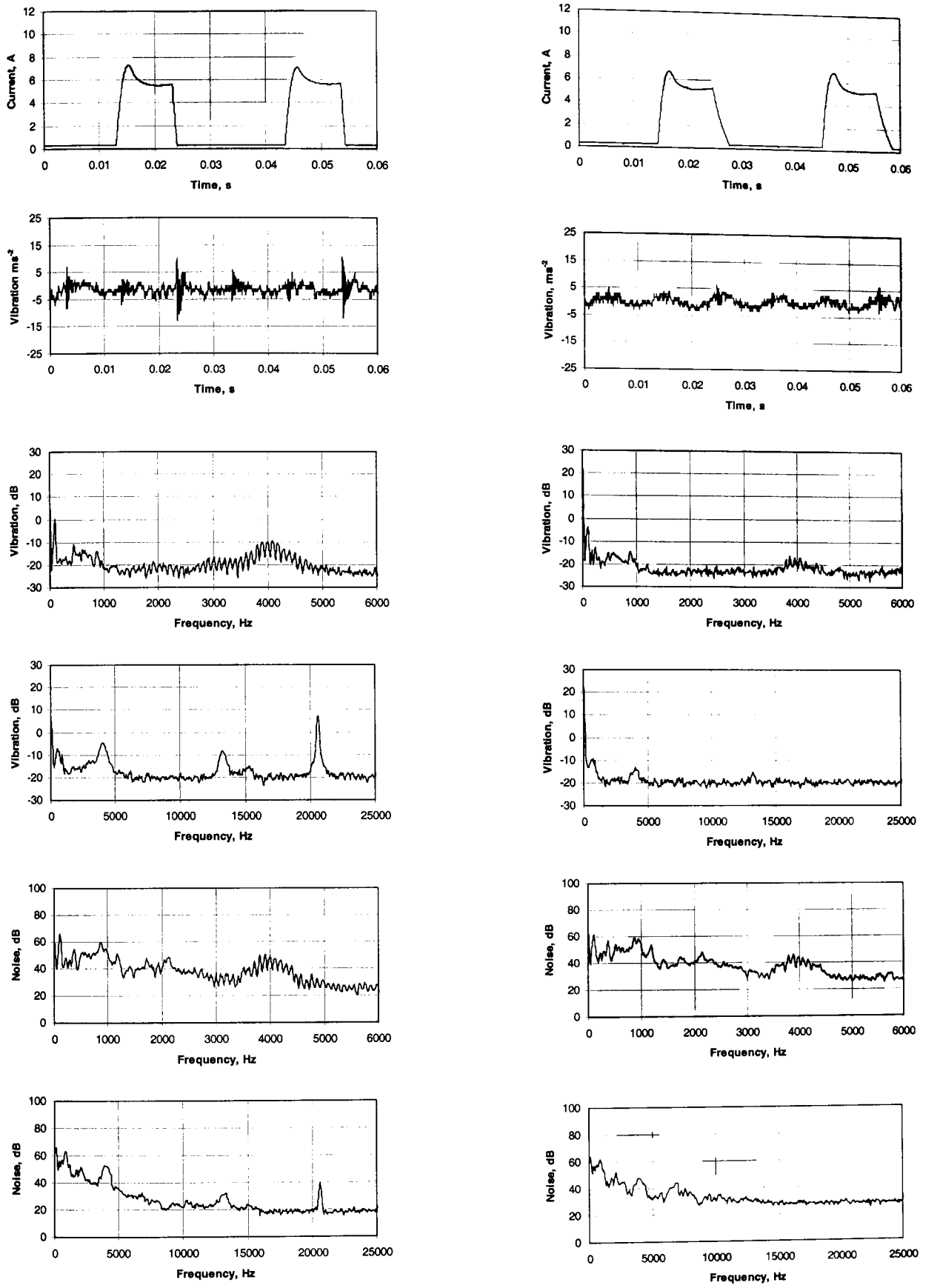

(a) *Voltage PWM control V_s =24V* **(b)** *Single pulse mode V_s =5V*

Fig. 4.35i *Comparison between single pulse mode operation and voltage PWM control operation with a PWM switching frequency of 20.6kHz, no-load, 500rpm*

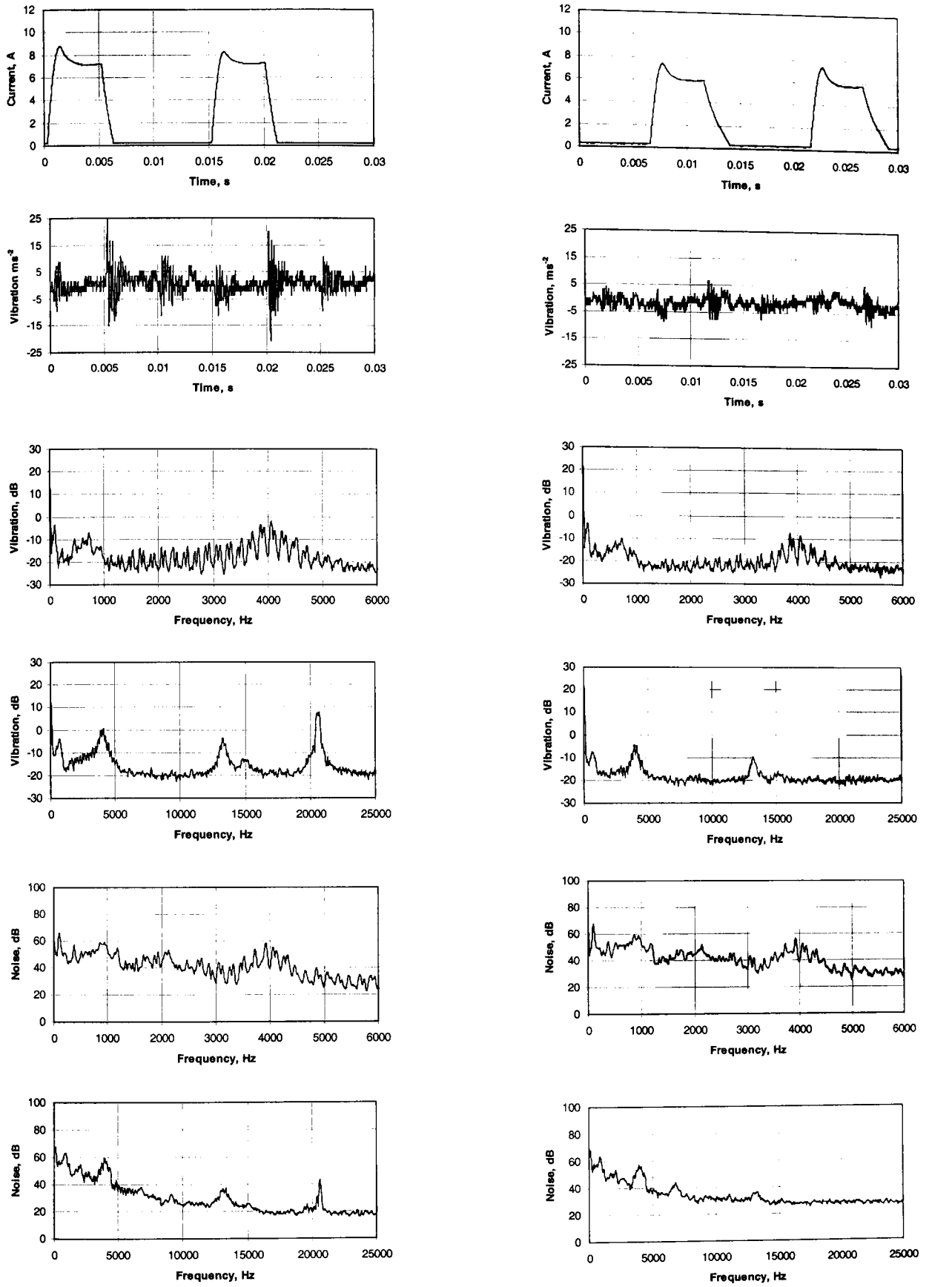

(a) *Voltage PWM control V_s =24V* **(b)** *Single pulse mode V_s =8V*

Fig. 4.35ii *Comparison between single pulse mode operation and voltage PWM control operation with a PWM switching frequency of 20.6kHz, no-load, 1000rpm*

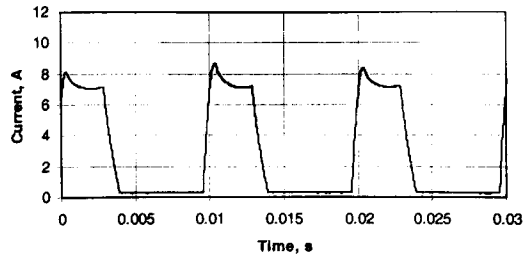

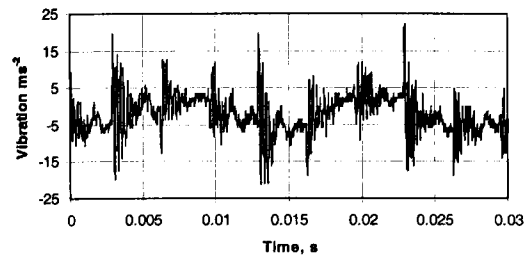

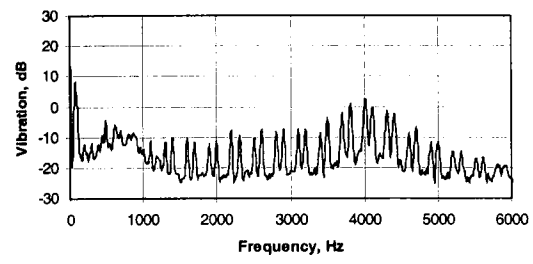

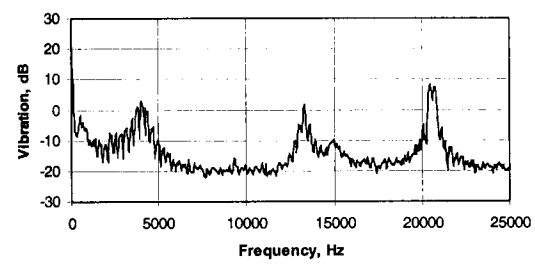

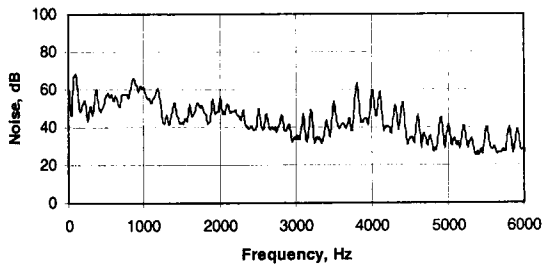

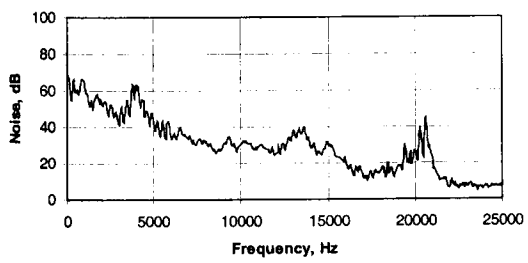

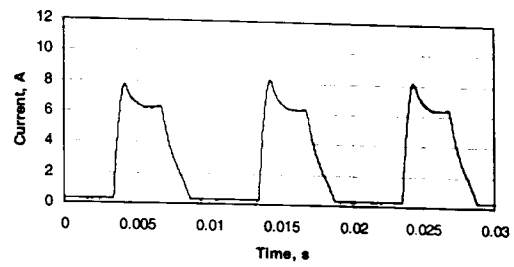

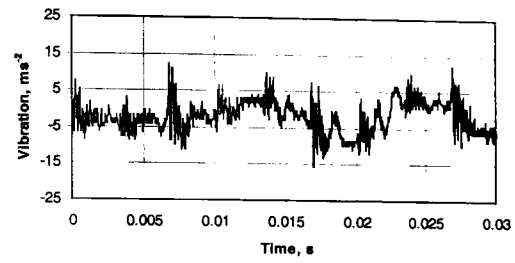

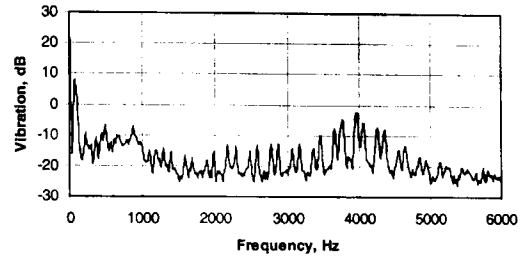

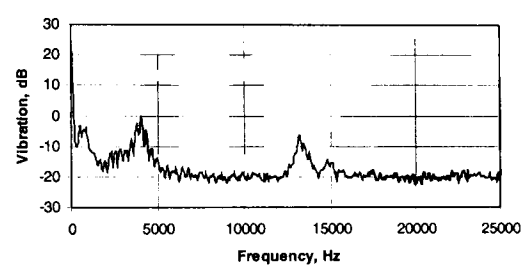

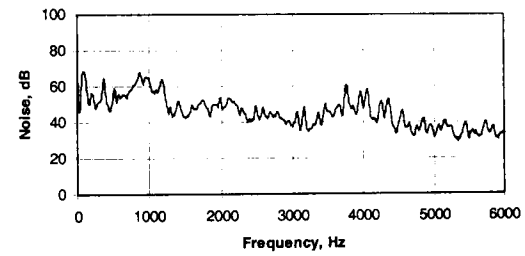

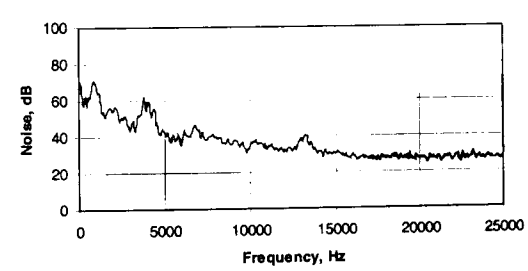

(a) *Voltage PWM control V_s =24V* **(b)** *Single pulse mode V_s =11V*

Fig. 4.35iii *Comparison between single pulse mode operation and voltage PWM control operation with a PWM switching frequency of 20.6kHz, no-load, 1500rpm*

4.5.2 Voltage PWM with variable DC supply voltage

In the preceding section the dc link voltage was varied to provide speed control under single pulse operation. Thus, the magnetisation and de-magnetisation voltages were the same, and varied with speed. This investigation maintained a constant speed under voltage PWM control for various dc link voltages, under both no-load and load conditions, such that the average magnetisation voltage remains constant, but the de-magnetisation voltage varies with the supply voltage.

The current waveforms which result when the machine was operated at four different dc supply voltages, are generally comparable, **Fig. 4.36**, attaining approximately the same peak current and value at the point of turn-off. This is expected, since the speed and load were maintained constant, and, therefore, the average magnetisation voltage is constant. Therefore, the rise times and associated rates of increase of current are similar for the different supply voltages. However, reducing the supply voltage reduces the de-magnetisation voltage, and thereby causes a significant variation in the current decay time and the associated rate of change of current, as can be seen in **Table 4.11** for the four supply voltages which were considered employed.

Table 4.11 *Comparison of current rise and decay times and corresponding rate of change of current, at 1000rpm, no-load, for a number of supply voltages*

V_s	Rise time, (ms)	di/dt (As^{-1})	Decay time (ms)	di/dt (As^{-1})
24	1.2	6717	1.1	6450
20	1.1	7012	1.3	5024
16	1.2	6422	1.5	4318
12	1.2	6606	1.9	3242

It will be observed that in general the time domain vibration oscillations associated with mode 2 reduce as the dc supply voltage is reduced, due to the reduction in the rate of decay of current, **Table 4.11**. Generally, the vibration and noise peaks of vibrational associated with modes 2 and 4 reduce with the dc supply voltage on no-load, **Figs. 4.36i,** whereas any reduction on load is insignificant, **4.36ii**. Further, the variation in the current rise time with the machine operating under different supply voltages is negligible compared to that which was observed with the other control methods. This highlights the

fact that the vibration, and hence noise, is largely dependent on the rate of decay current rather than the rate of rise of current.

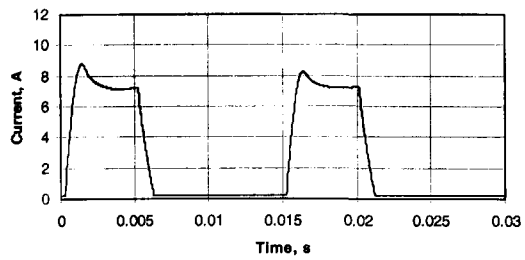

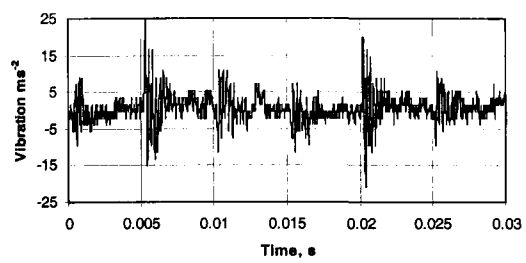

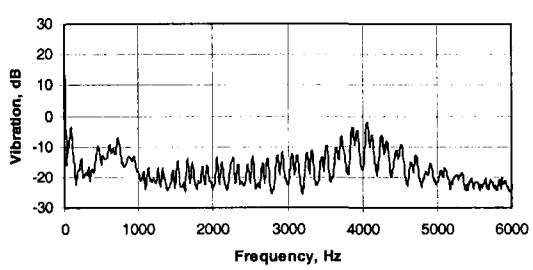

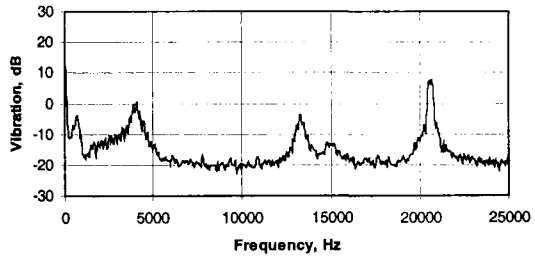

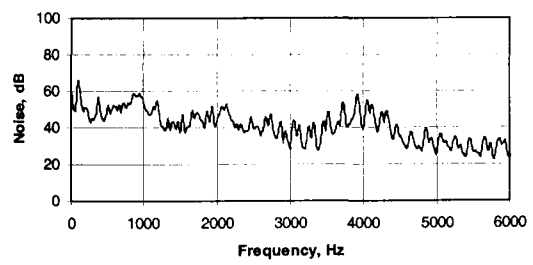

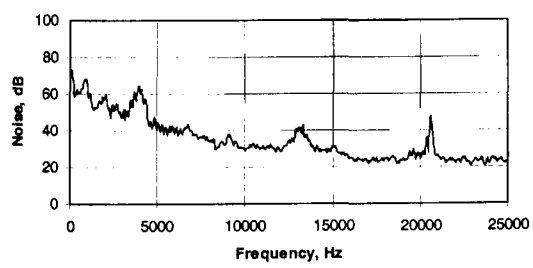

(a) *24V dc supply*

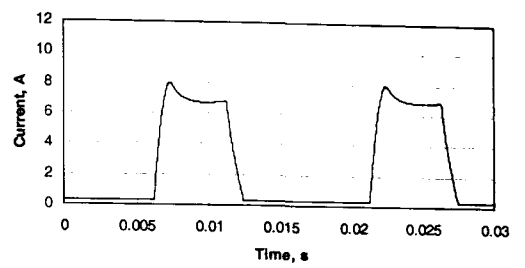

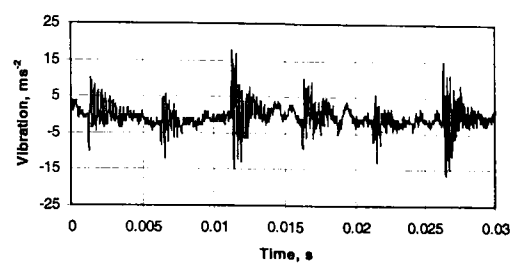

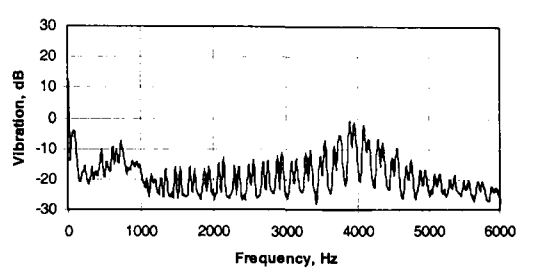

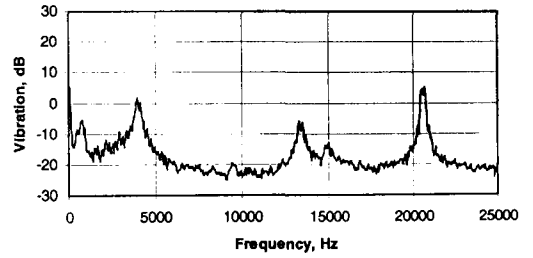

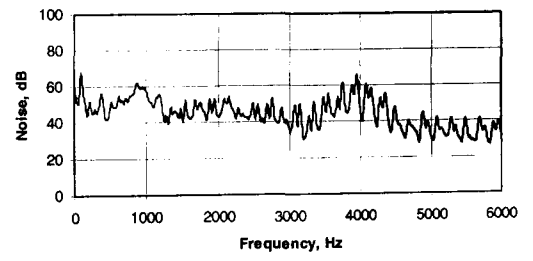

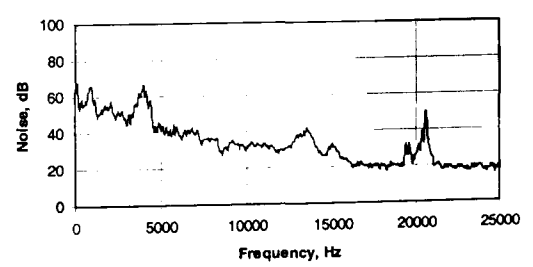

(b) *20V dc supply*

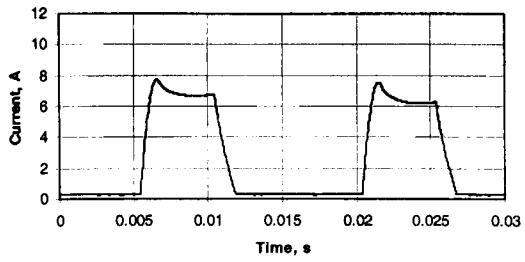

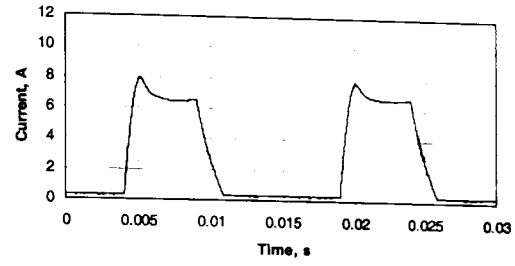

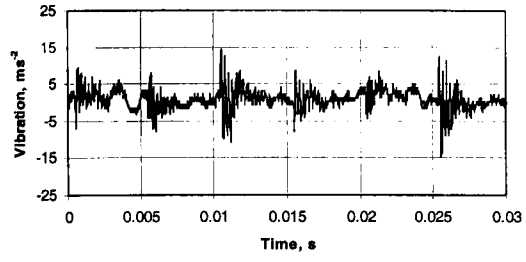

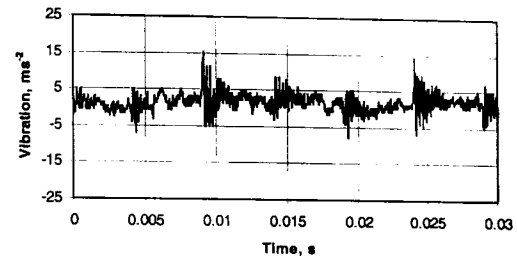

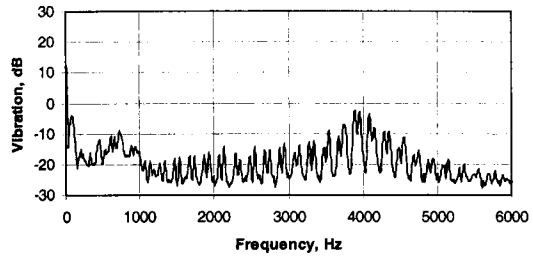

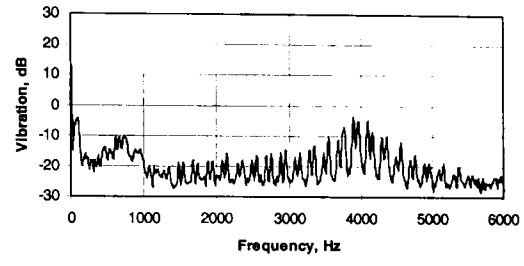

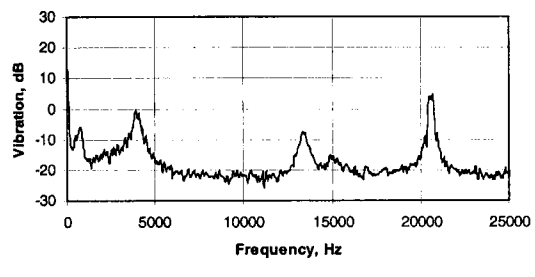

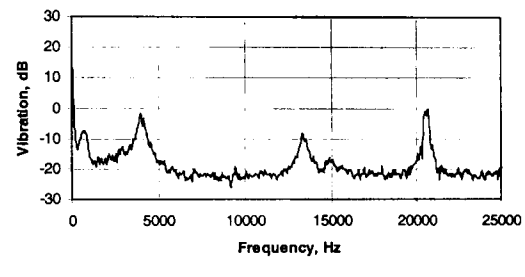

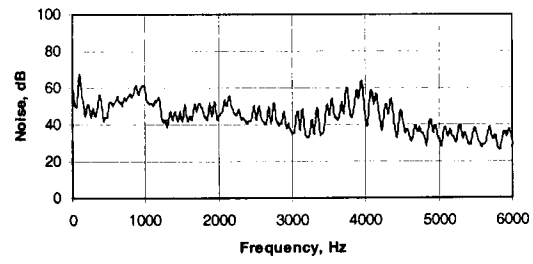

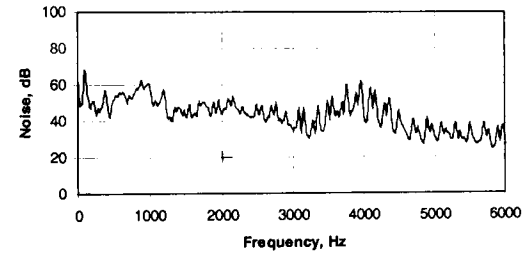

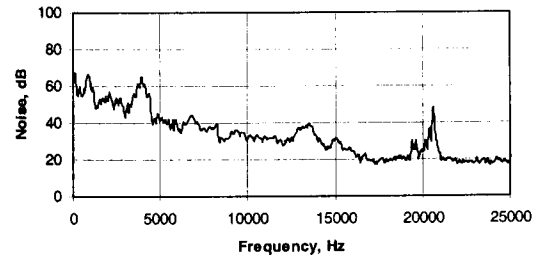

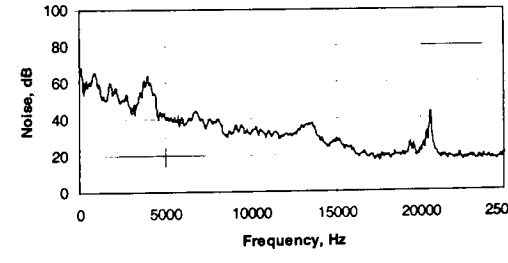

(c) *16V dc supply*

(d) *12V dc supply*

Fig. 4.36i *Influence of dc supply voltage, V_s, under voltage PWM control, no-load, 1000rpm*

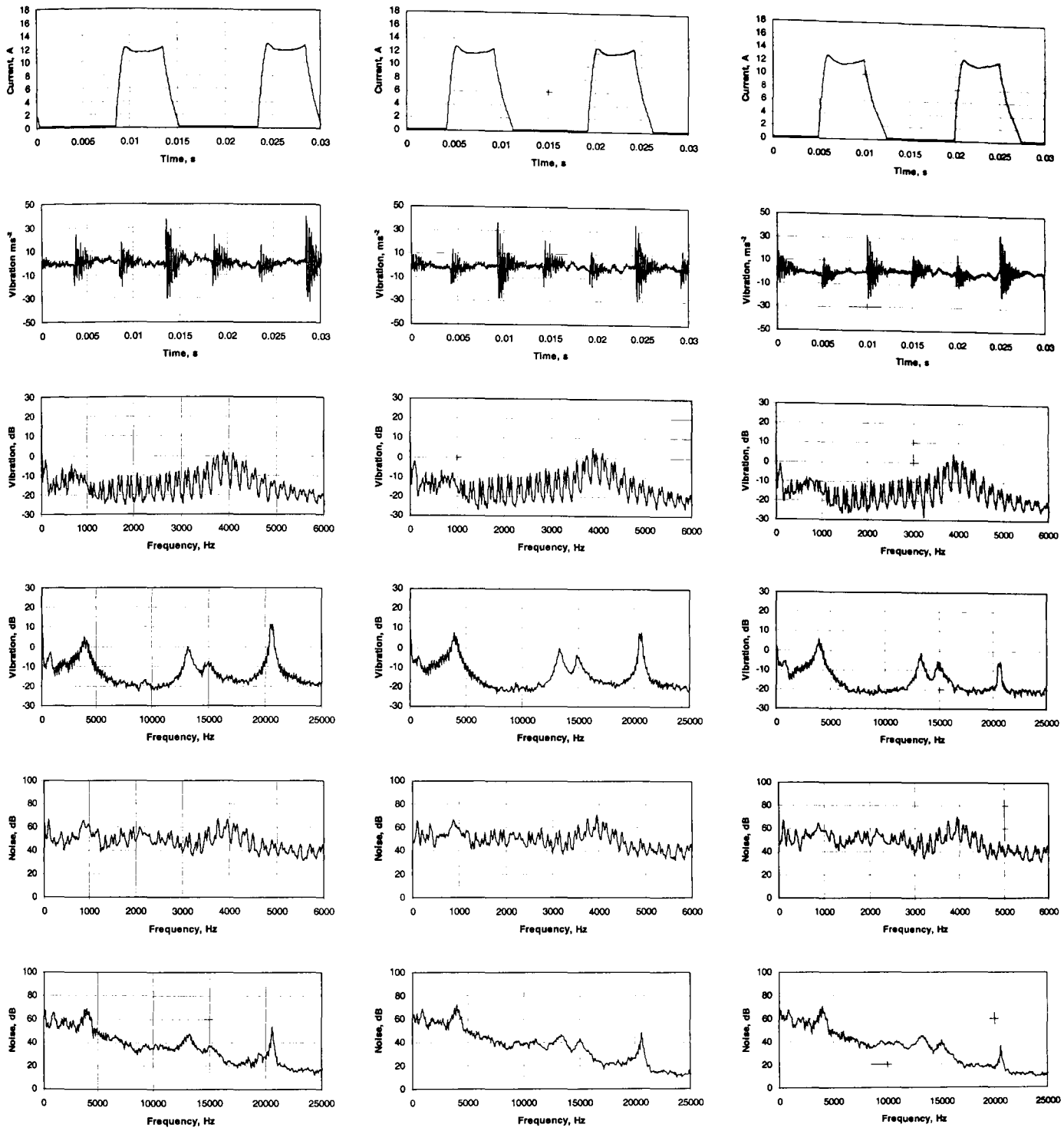

(a) *24V dc supply* **(b)** *20V dc supply* **(c)** *16V dc supply*

Fig. 4.36ii *Influence of dc supply voltage, V_s, under voltage PWM control, ≈75% load, 1000rpm*

4.6 Comparison of noise and vibration at different speeds, loads and DC link voltages

In this section a comparison is made between the noise and vibration which result with different methods of control at various speeds, whilst maintaining fixed switching angles. The time domain waveforms and associated spectra which were measured under voltage PWM control are compared to those obtained under current control, focussing specifically on soft switching, whereas the SPLs are compared for both soft and hard switching strategies. In addition, the SPL with the machine operating in single pulse mode is compared to that for both voltage PWM control and current control, under both no-load and load conditions. Finally, the switching frequency associated with each control method is evaluated to assess its influence on the stator vibration.

4.6.1 Comparison of spectra under voltage and current control

The value of the instantaneous phase currents at the point of turn-off is comparable for both control methods, **Fig. 4.37**. However, the peak current which is attained subsequent to the point of turn-on is much higher under current control due to the very high rate of rise of current. This is due to the fact that with current control the full supply voltage is available for magnetisation of the windings at turn-on until the current limit is exceeded, beyond which chopping commences. Thus, the current rise time is similar at all speeds, **Table 4.12**, whilst the increase in the rate of rise of current with speed is due to the limited action of the current controller in limiting the initial peak value of current. With voltage PWM control a limit is imposed on the magnetisation voltage, depending upon the speed error, and, hence, duty cycle of the voltage controller. Therefore, at higher speeds the current rise time decreases, and, hence, the rate of rise of current increases. The rate of decay of current is similar for the two control methods, since the same de-magnetisation voltage is available.

Table 4.12 *Comparison of rise and decay times associated with current waveforms for current and voltage control methods*

Speed (rpm)	Rise time (ms)/di/dt (As^{-1})		Decay time (ms)/di/dt (As^{-1})	
	Voltage control	Current control	Voltage control	Current control
500	2.3/3052	0.36/21408	1.3/4102	1.2/4264
1000	1.2/6717	0.28/26900	1.1/6450	1.28/5138
1500	0.9/9008	0.31/28206	1.3/5359	1.16/5834

The time domain vibration also depends on the control method. Under voltage PWM control, the excitation of mode 2 is very clear, being the most dominant oscillation at turn-off, which is also observed for the other phases with a reduced peak oscillation. Under current control, such oscillations are unclear due to the broader-band disturbance. The disturbances are rather problematic at all operating speeds. The magnitude of the oscillations which result under current control is higher than that under voltage PWM control.

The vibration peaks associated with modes 2 and 4 under current control are over 10dB larger in magnitude than those which result under voltage PWM control at all three speeds considered. This is reflected in the noise spectrums.

The vibration and noise peaks associated with the switching frequency of the PWM under voltage PWM control is absent from the current control spectra, as expected.

The vibration spectrum in the range 0-6kHz under voltage PWM control contains the pairs of harmonics associated with the duty cycle (as highlighted at the beginning of the chapter). These amalgamate when under current control, when they are engulfed by the wide-band of the vibration peak, and similarly for the 0-6kHz noise spectrum.

Throughout this investigation, current control has employed a 40kHz sampling frequency, which leads to a relatively low average switching frequency compared with that under voltage PWM control, when the switching frequency was fixed at 20.6kHz with a variable duty cycle. To further illustrate the influence of the methods of control employed, **Figs. 4.38** and **4.39** show the phase current waveforms together with the associated gate signals and time domain vibration waveforms with a shorter time base. They enable a comparison to be made between the vibration which results under single pulse mode operation to those under voltage and current control for the same operational speed and load condition. It should be noted, however, that since a 3-channel storage scope was not available, the gate signal was sampled separately from the current and vibration which were measured. Therefore, as can be seen with current control, column **(c)** of **Figs. 4.38 and 4.39**, the voltage chopping of the gate signal is not synchronised with the current ripple.

Single pulse mode operation has a significantly lower mode 2 vibration oscillation than results with the other control methods, and, has by far the minimum rate of decay of

current. Some ripple is present in the time domain vibration waveform between successive mode 2 oscillations, but this is negligible compared with the ripple associated with the PWM switching frequency under voltage PWM control.

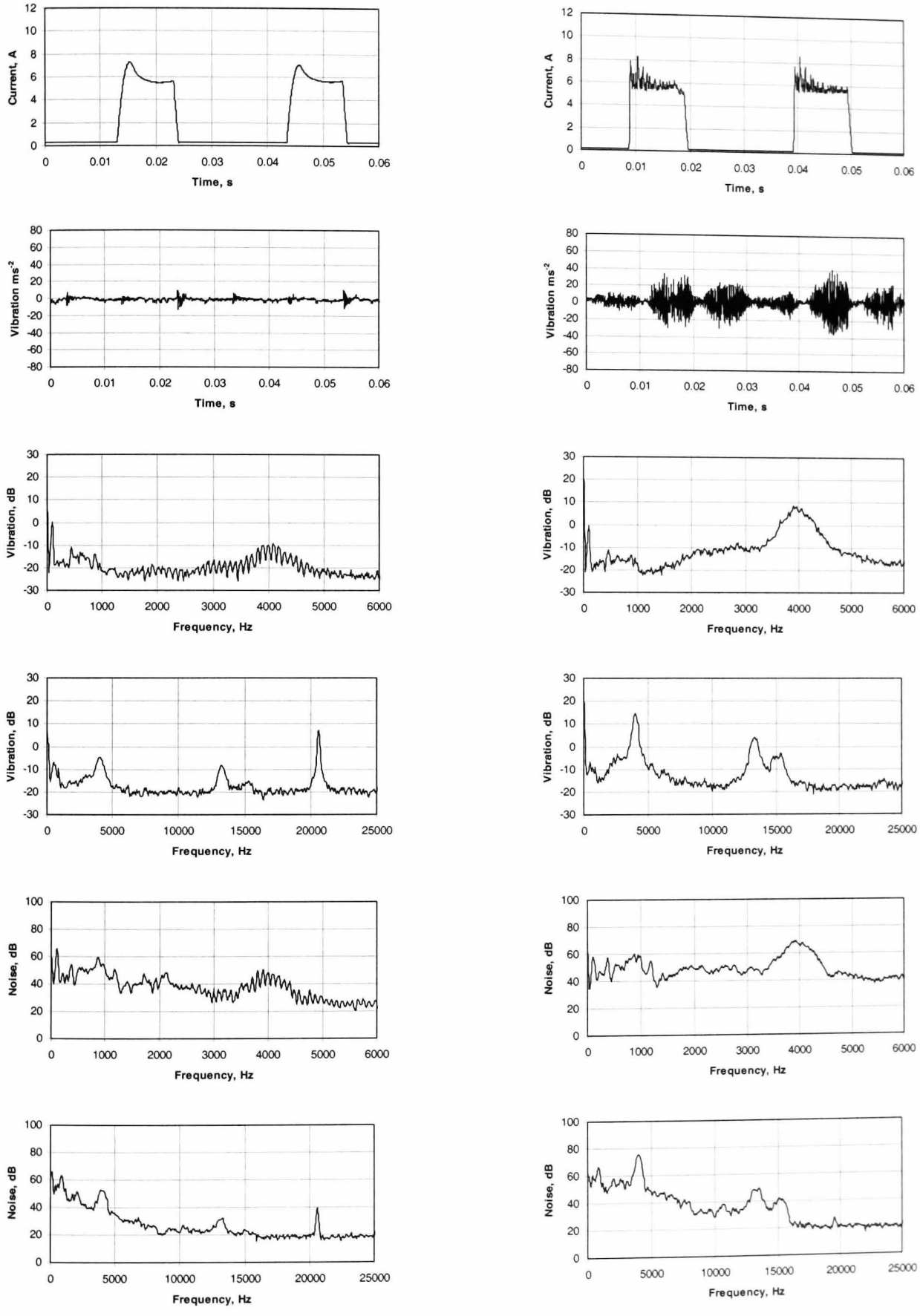

(a) *Voltage PWM control* **(b)** *Current control*

Fig. 4.37i *Comparison of voltage and current control, no-load, 500rpm*

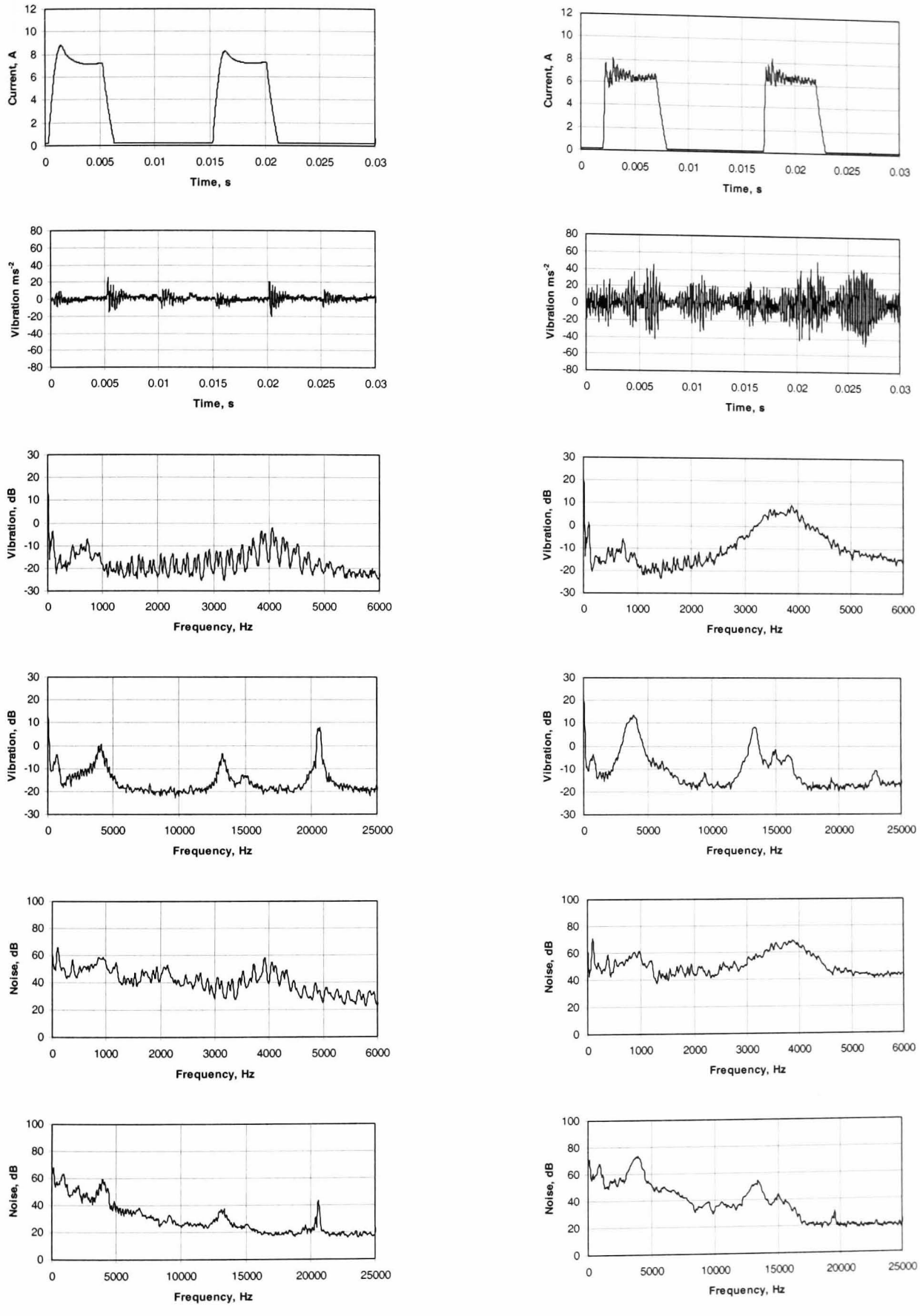

(a) *Voltage PWM control* **(b)** *Current control*

Fig. 4.37ii *Comparison of voltage and current control, no-load, 1000rpm*

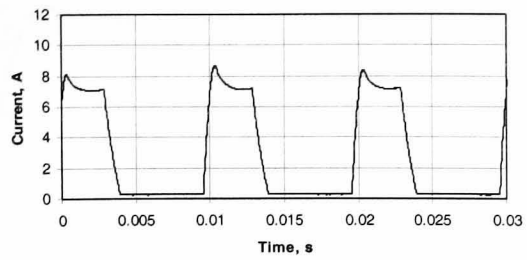

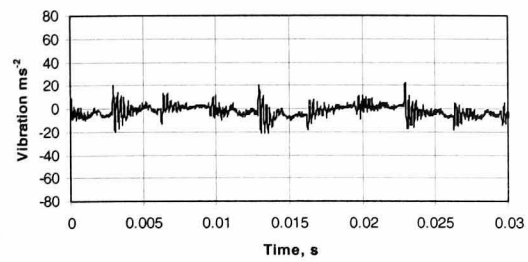

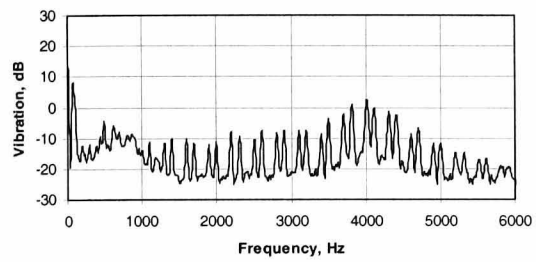

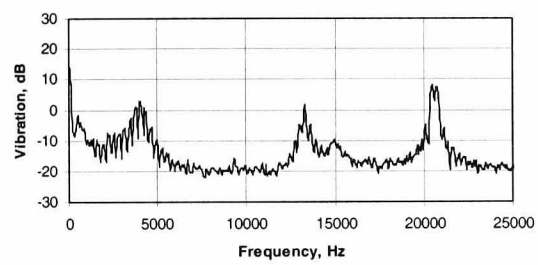

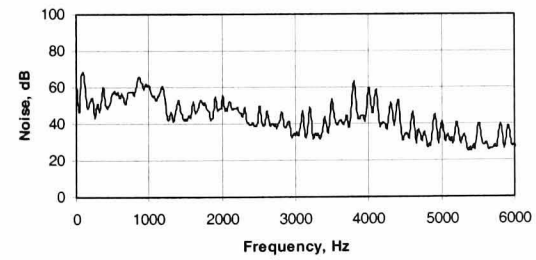

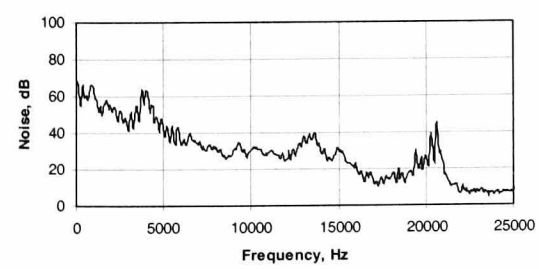

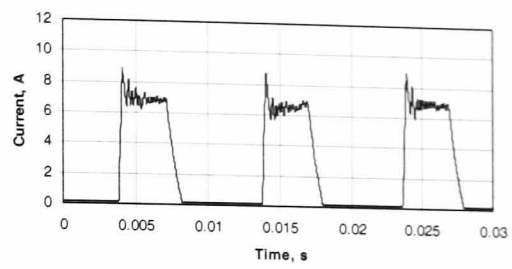

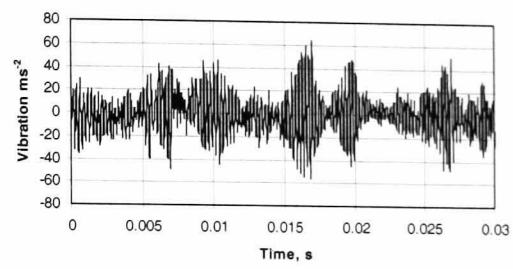

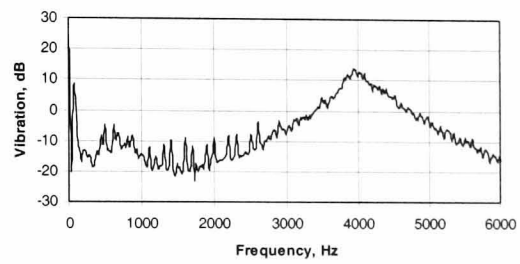

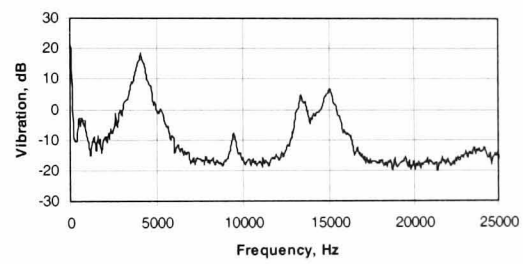

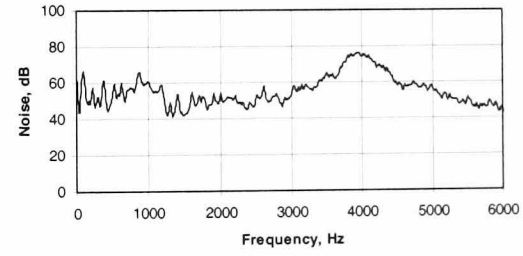

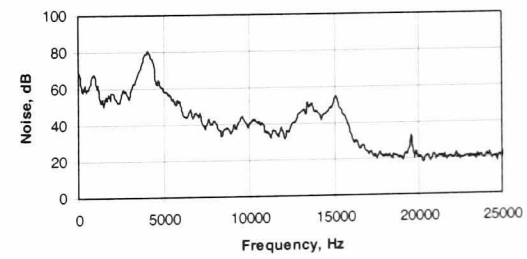

(a) *Voltage PWM control* **(b)** *Current control*

Fig. 4.37iii *Comparison of voltage and current control, no-load, 1500rpm*

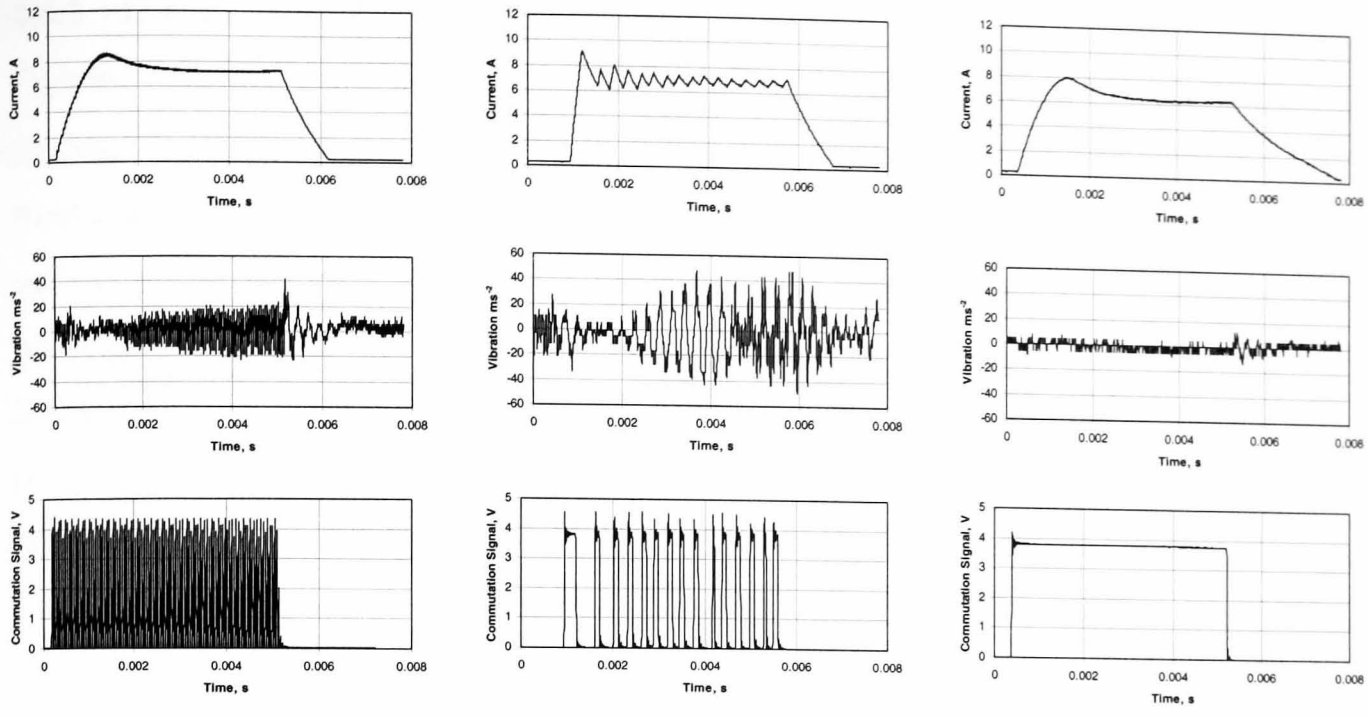

(a) *Voltage control, 20.6kHz* **(b)** *Current control* **(c)** *Single pulse mode*

Fig. 4.38 *Comparison of switching frequency for all control methods, no-load, 1000rpm*

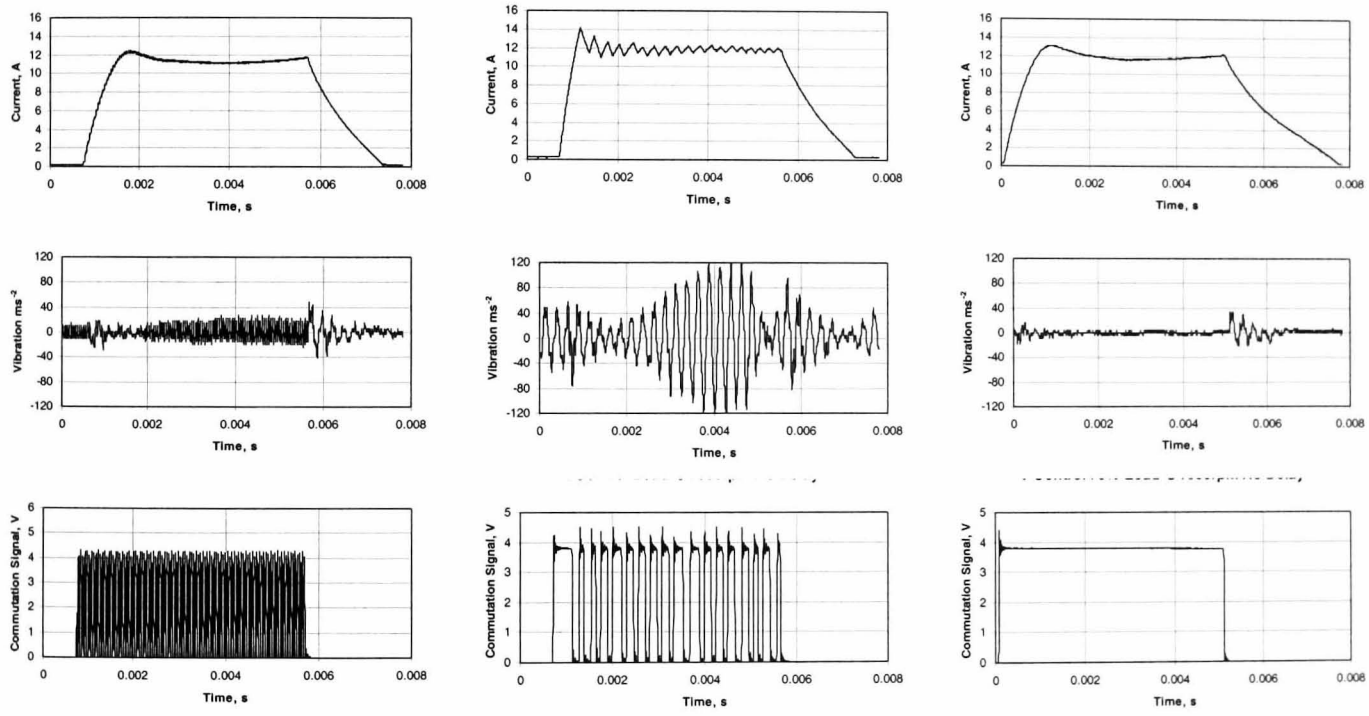

(a) *Voltage control, 20.6kHz* **(b)** *Current control* **(c)** *Single pulse mode*

Fig. 4.39 *Comparison of switching frequency for all control methods, on load, 1000rpm*

4.6.2 Comparison of SPL under voltage and current control

Figures, **4.40**, **4.41, 4.42** and **4.43** enable the SPL which results under the main operating modes, which have been considered in the chapter, to be compared. It will be observed from **Fig. 4.38** that current control generally results in a higher level of emitted noise, to such an extent that voltage PWM control under load results in a lower level of noise than when the machine is operated under current control on no-load. With the exception of 2000rpm, the sound pressure level is observed to increase as the speed is increased. This is more prominent under voltage PWM control. Current control results in a generally higher sound pressure level, and, consequently, a smaller variation over the speed range for the two load conditions. Further, under current control the SPL which results with hard chopping, is observed to be higher than with soft chopping, **Fig. 4.39**. A more significant difference occurs in the SPL in moving between current and voltage PWM control, especially at low speed, current control resulting in a higher SPL than voltage PWM control.

A comparison of the SPL obtained with the machine operating under pulse mode operation and alternative forms of voltage PWM control is shown in **Fig. 4.40**. It will be seen that single pulse and voltage PWM control follow similar trends, in that the SPL increases as the speed is increased. Thus, there is a relatively wide variation in SPL over the speed range. The similarity in the SPL is expected since the associated spectra are similar, whereas those with current control differ significantly, as discussed previously. On no-load, the single pulse mode generally results in the quietest operation, except at 2000rpm when it gives rise to the highest SPL, whilst at 2500rpm the SPL is higher than for soft chopping PWM on no-load. On-load, the single pulse mode generally results in a lower level of noise than voltage PWM control, for which hard chopping voltage generally results in the highest SPL. Single pulse mode operation is comparable to operation under voltage PWM control at higher speeds, since the demagnetisation voltage is then more comparable to that under voltage PWM control.

Fig. 4.41 compares the SPL under single pulse mode to that under alternative methods of current control, from which it is observed that, at low speed, the difference in SPL between single pulse mode and current control is very significant. The variation in SPL with the different control methods exhibits a rather different trend to that under voltage PWM control, **Fig. 4.40**, in that, regardless of load condition, single pulse mode operation results in the lowest SPL, whilst hard chopping results in the highest SPL. Furthermore, for application of load generally increases the SPL. Only at a speed of

2000rpm do these observations not apply, since the SPL with soft chopping on no-load, is then comparable to that with hard chopping on load, whilst the SPL with single pulse operation, on no-load is higher than that with single pulse operation and soft chopping on load.

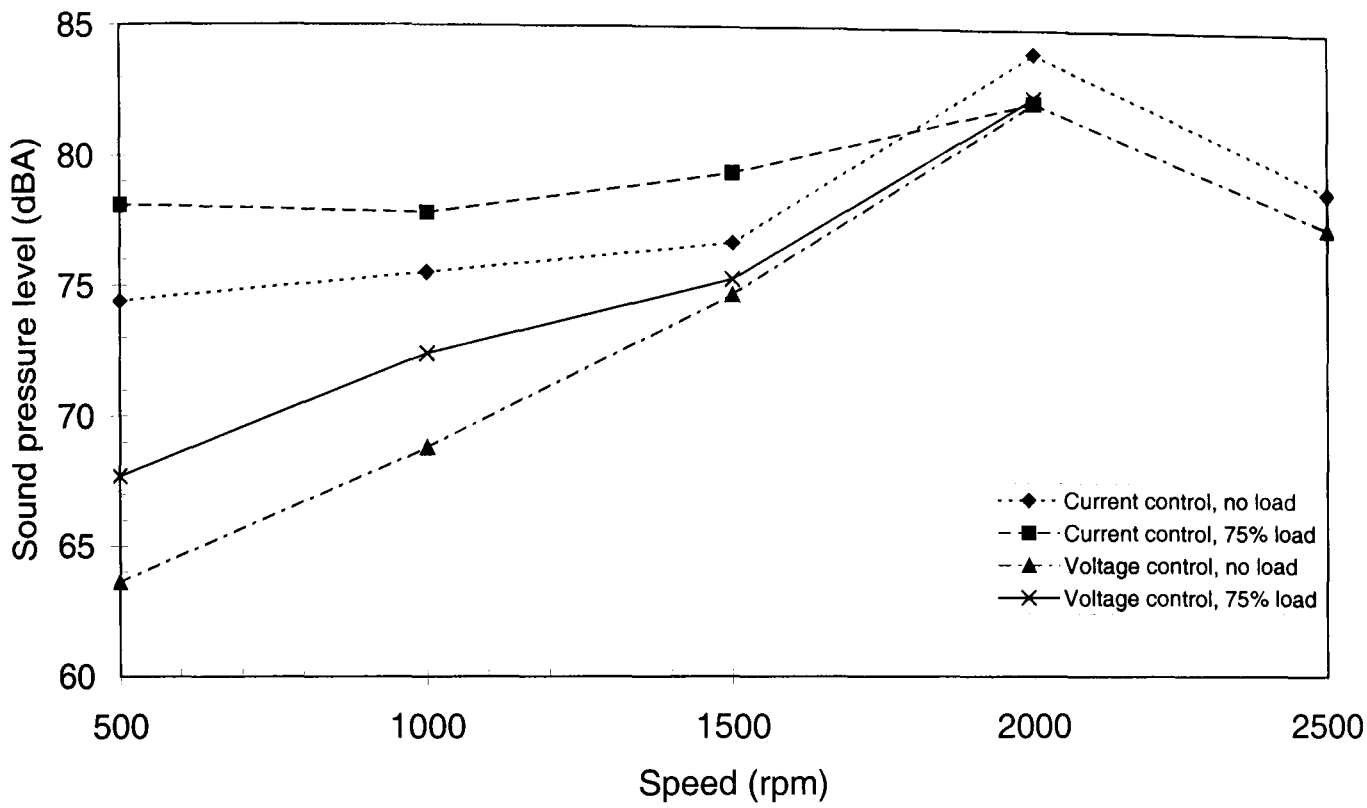

Fig. 4.40 *Comparison of soft chopping voltage and current control on sound pressure level under both no-load and load conditions*

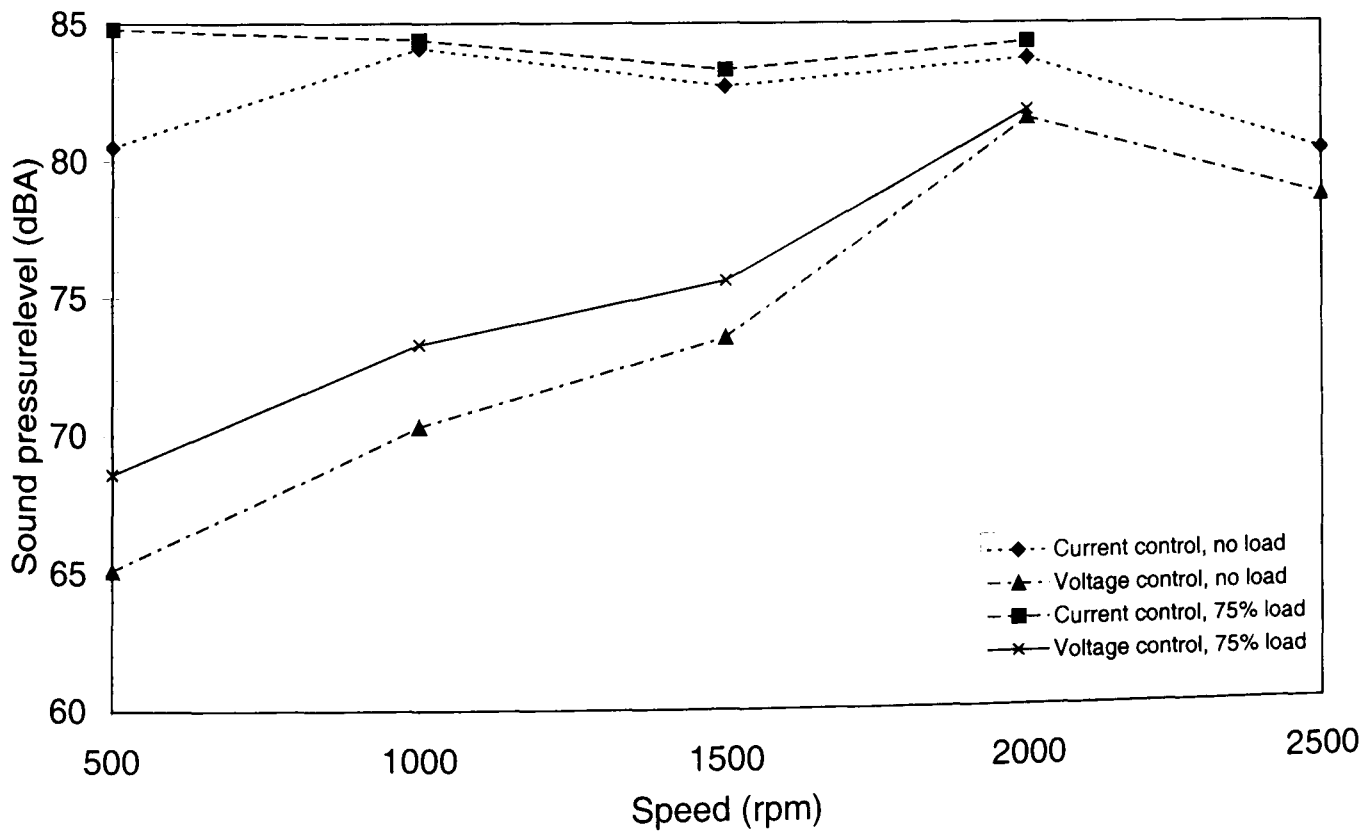

Fig. 4.41 *Comparison of hard chopping voltage and current control on sound pressure level under both no-load and load conditions*

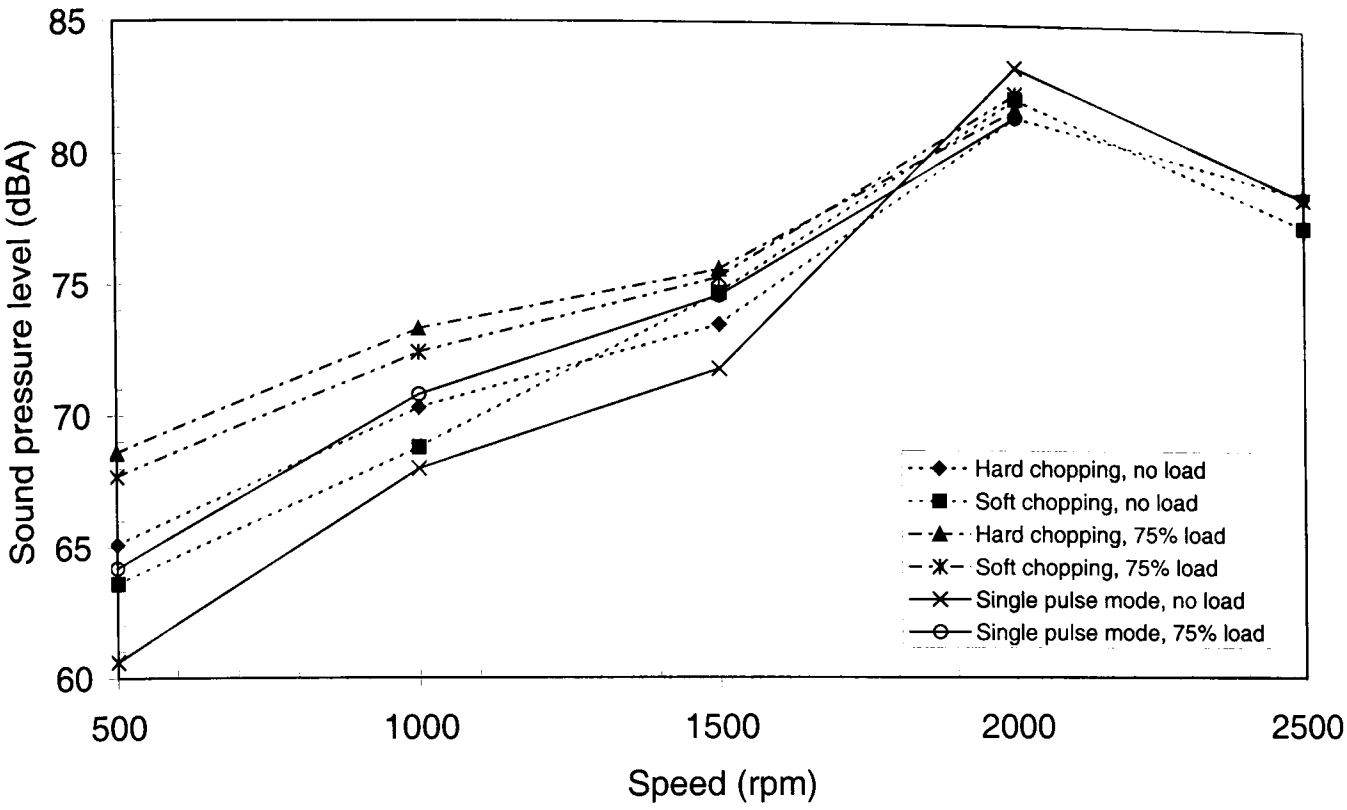

Fig. 4.42 *Comparison of single pulse mode, with soft and hard chopping voltage control, on sound pressure level under both no-load and load conditions*

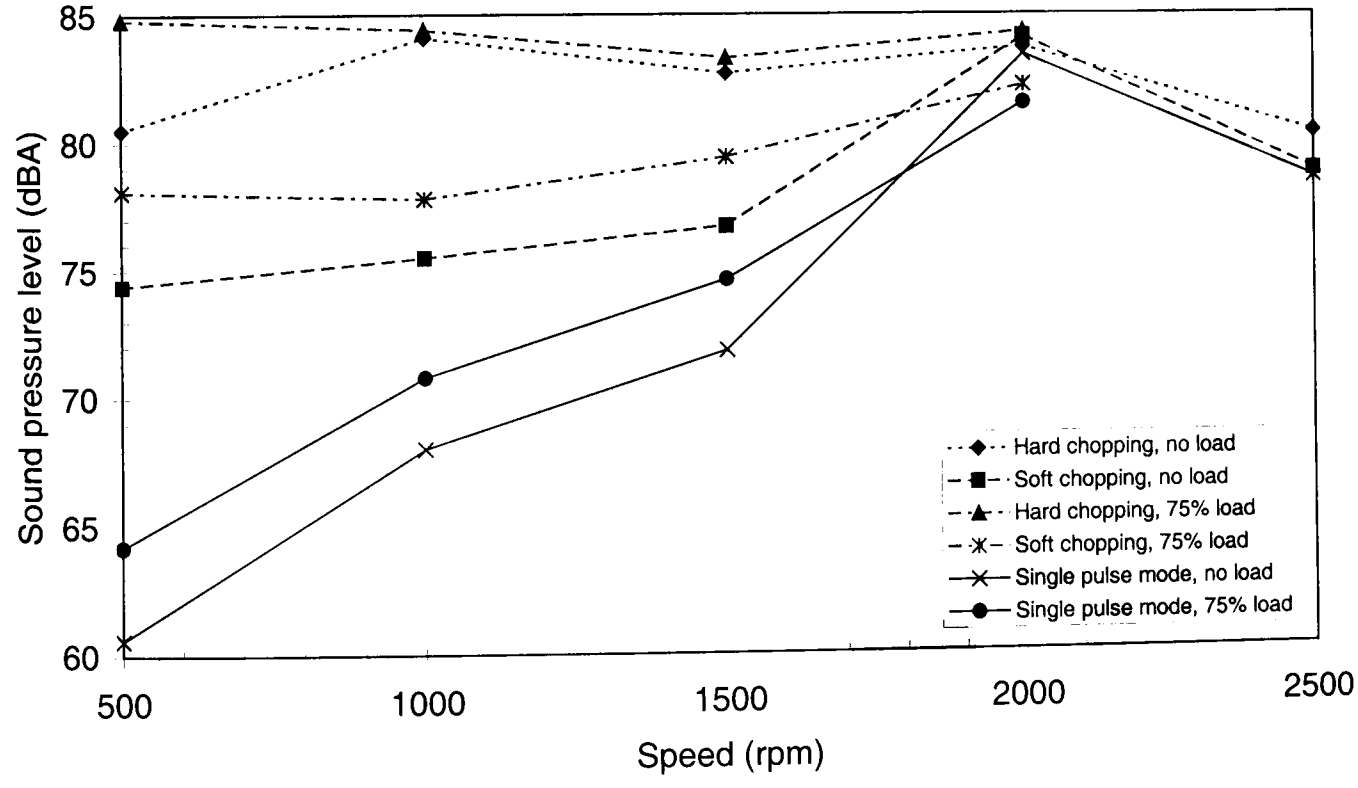

Fig. 4.43 *Comparison of single pulse mode, under soft and hard chopping current control, on sound pressure level under both no-load and load conditions*

4.7 Influence of switching angle

From the overview of the switching angles in Chapter 1 it appears that the stator vibration is more severe at turn-off than turn-on when considering the radial force. This is attributed to the larger radial force that is present at turn-off since the pair of rotor poles are closer to alignment with the excited pair of stator poles. However, in advancing both the turn-on and turn-off angles, the phase current is increased to account for the reduced flux linkage, to ensure the energy conversion is maintained for the specified operating point. Therefore, despite the fact that the radial component of force is reduced with respect to the tangential force, a larger rate of change of current will occur. Thus, it is evident that application of advance commutation may not necessarily be as effective as it may at first appear. Therefore, in order to assess the effectiveness of switching angles for noise reduction the turn-on and turn-off angles were advanced in increments of 2.5° whilst maintaining a fixed dwell of 30°. The range of angles which are summarised in **Table 4.13**, were applied for the machine operating on no-load for rotational speeds between 500rpm and 2500rpm, under both voltage and current control.

The sound pressure level measured for advanced turn-on and turn-off angles, whilst maintaining a fixed dwell angle, **Figs. 4.44** and **4.45**, show that when the machine is operating under voltage PWM control a slight increase in the sound pressure level occurs for angle advance, whereas under current control these angles have insignificant effect on the SPL. In addition, the phase current waveform and corresponding noise and vibration spectra for commutation advances of 0°, 7.5° and 15° under voltage PWM control are shown in **Fig. 4.46**, and the position of these dwell periods, relative to the idealised phase inductance is shown schematically in **Fig. 4.47**. It is observed that the current increases with switching advance, as discussed in Chapter 1, to account for the reduced flux linkage to enable the mechanical energy conversion to be maintained. As a result of the this current rise, and the lower inductance at the point of turn-off (evident from **Fig. 4.47**), the rates of decay of current are increased significantly, as is apparent from **Table 4.14**. Consequently, the level of the vibration peaks associated with modes 2 and 4 are increased, as is evident from the vibration spectra of **Fig. 4.46**. Therefore, the increased rate of decay of current more than compensates for any reduction in the radial component of force which may be achieved by switching angle advance, although this is not reflected in the corresponding noise spectra.

Table 4.13 *Range of selected switching angles*

Control parameter	Advance commutation
Turn-on angle	$37.5° \leq \theta_{on} \leq 52.5°$
Turn-off angle,	$67.5° \leq \theta_{off} \leq 82.5°$
Dwell angle,	$\theta_D = 30°$

Table 4.14 *Comparison of rise and decay times associated with current waveforms for commutation advance, voltage PWM control, no-load*

Angle advance	Rise time (ms)/di/dt (As^{-1})	Decay time (ms)/di/dt (As^{-1})
0°	0.64 / 11590	1.18 / 5841
7.5°	1.24 / 9363	0.81 / 8139
15°	1.80 / 8365	0.60 / 12428

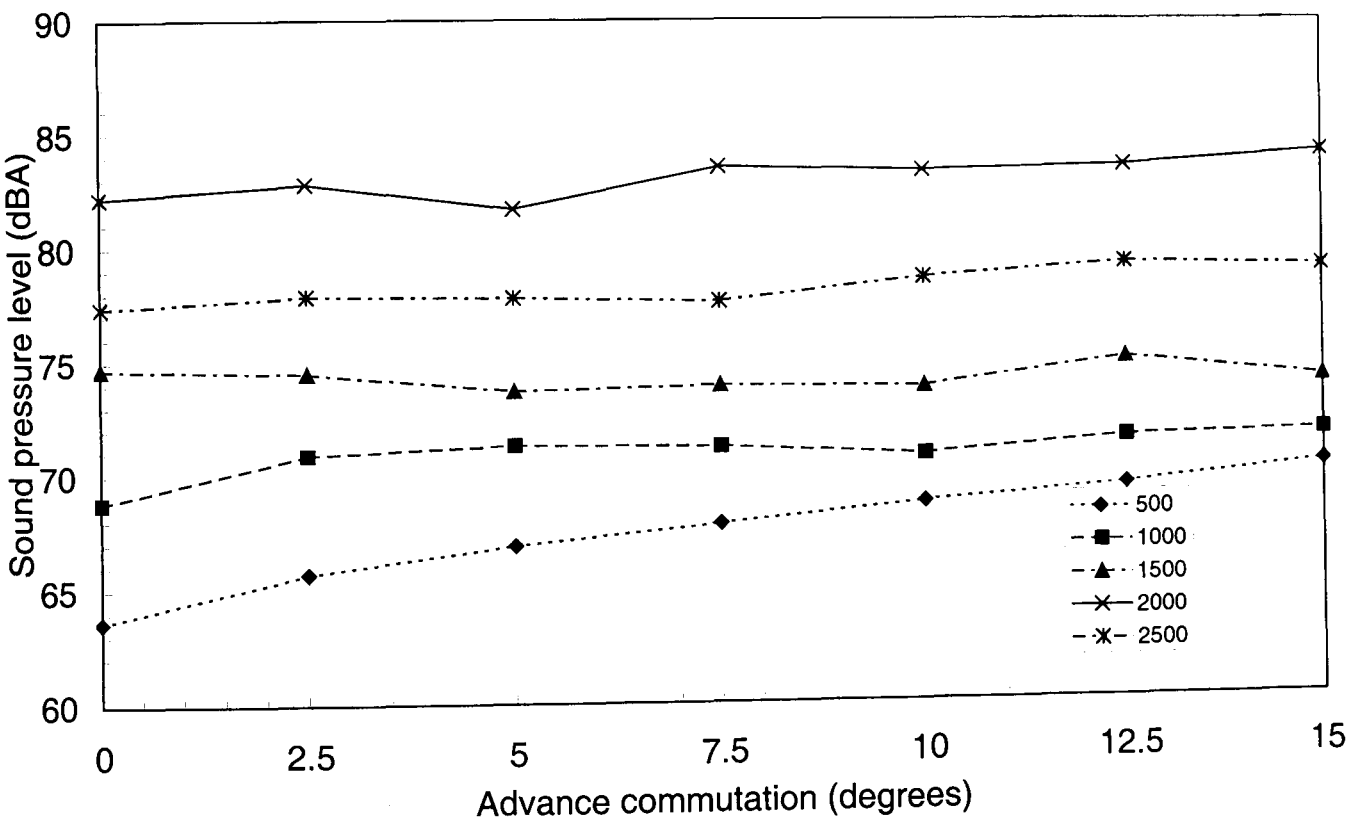

Fig. 4.44 *Variation of sound pressure level with advance of commutation angles, (fixed dwell) for voltage PWM control, no-load*

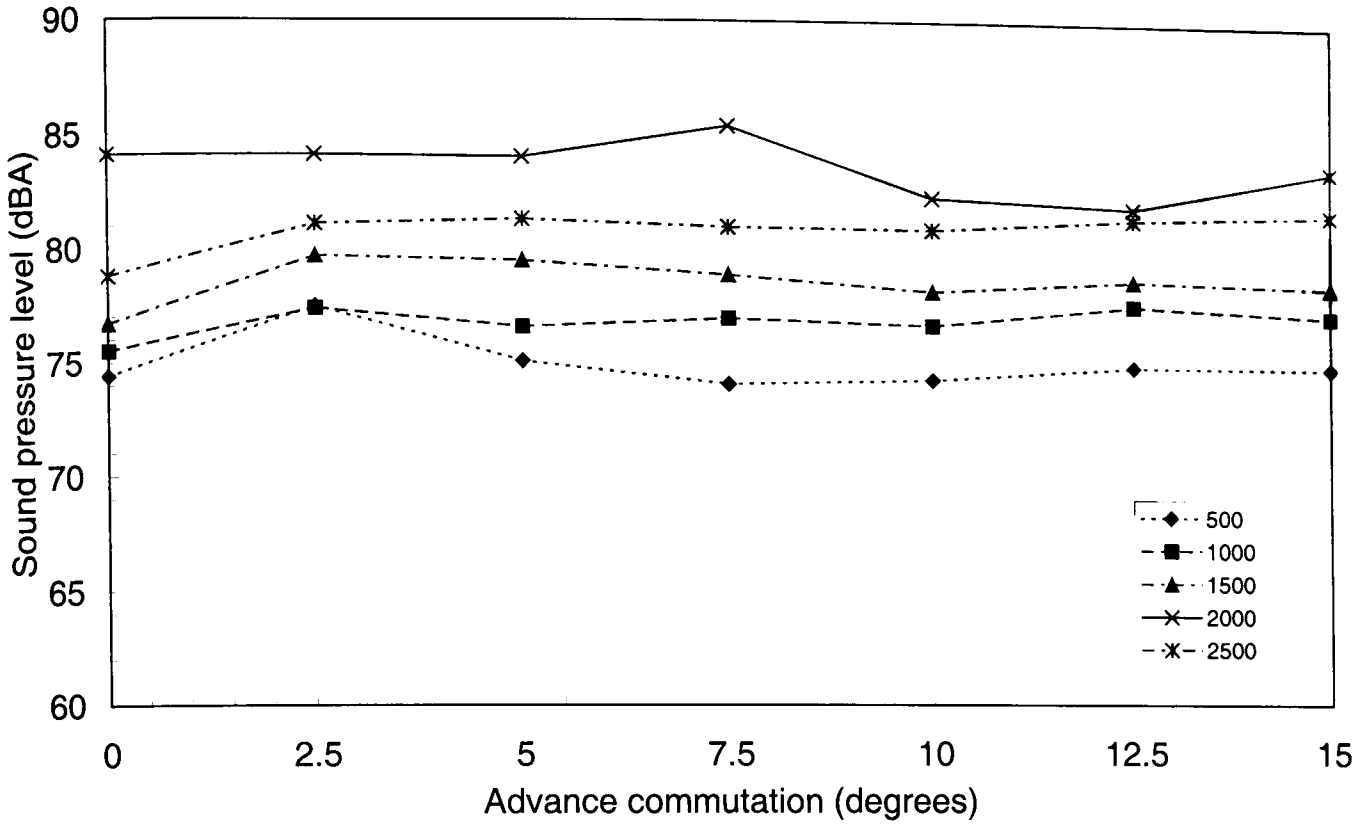

Fig. 4.45 *Variation of sound pressure level with advance of commutation angles, (fixed dwell) for current control, no-load*

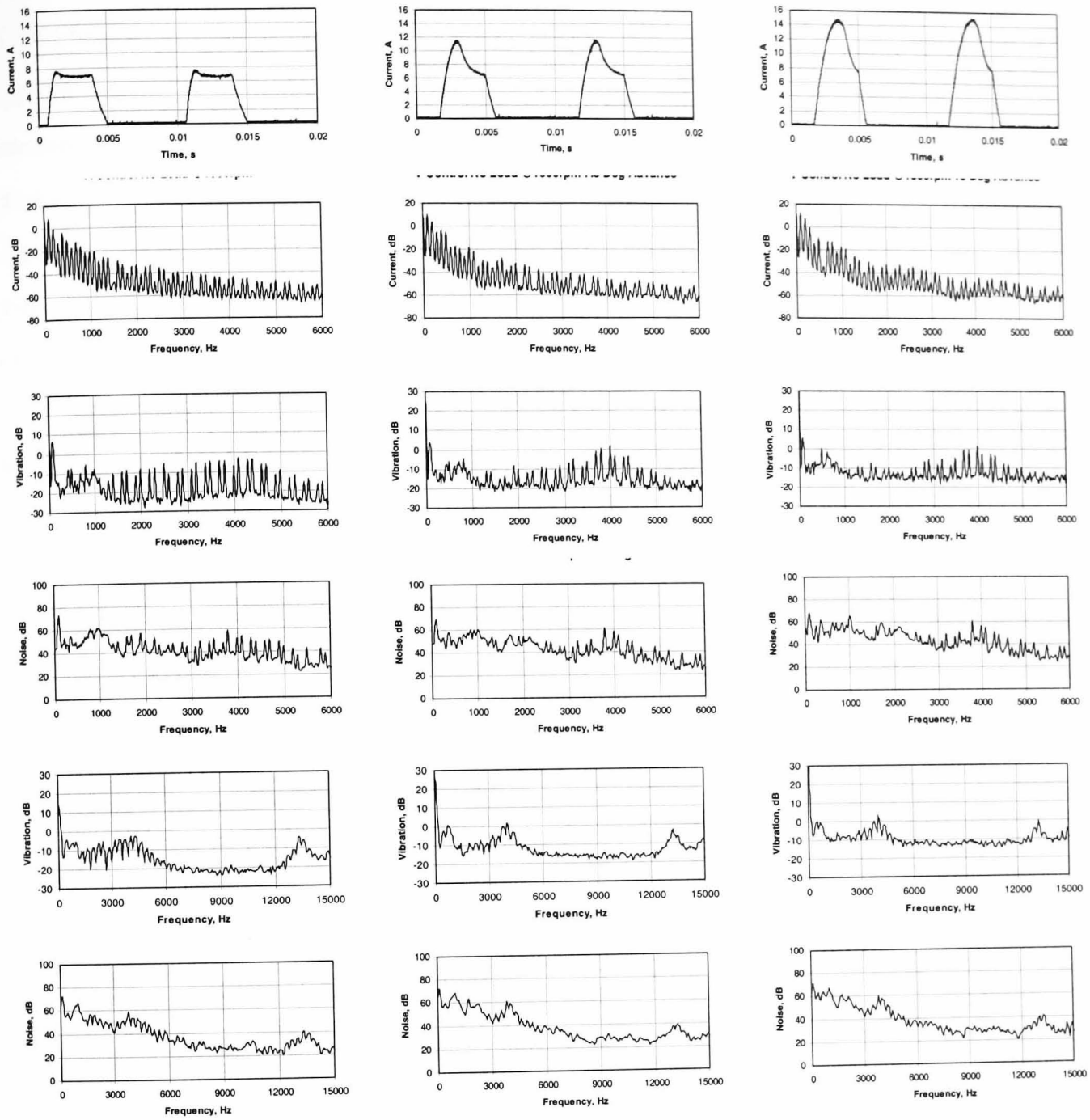

Fig. 4.46 *Fixed dwell, advanced commutation under voltage PWM control at 1500rpm, no-load (0-25kHz)*

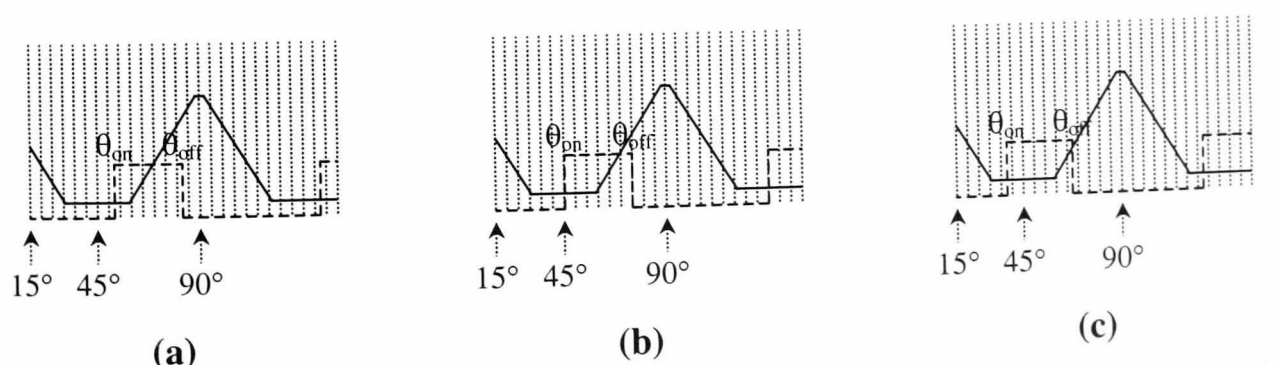

Fig. 4.47 *Position of switching angles with respect to idealised phase inductance,* **(a)** $\theta_{on}=52.5°$, $\theta_{off}=82.5°$, **(b)** $\theta_{on}=45°$, $\theta_{off}=75°$, **(c)** $\theta_{on}=37.5°$, $\theta_{off}=67.5°$,

4.8 Summary

This chapter presented a systematic study of the influence of the control parameters and typical operating modes of the switched reluctance machine on its stator vibration and emitted noise. The corresponding results have been analysed in the frequency and time domains, together with measurements of the sound pressure level. Consequently, the significance of voltage and current control has been identified with respect to the vibration and noise emissions. The conclusions drawn from this chapter will lead to the evaluation of active vibration control considered in the following chapter.

Initial noise and vibration measurements, together with measured transfer functions of the assembled SR machine, confirmed that the noise and vibration are closely associated, and that the dominant source of noise is attributed to the stator resonating at the frequencies of its even vibration modes, whereas the odd vibration modes and the additional modes attributed to the windings are generally irrelevant to noise production. This has been shown to remain true regardless of the rotational speed and operating mode.

The vibration and noise which result when a machine is operated under current control has been shown to differ significantly to that which results under voltage control and single pulse mode operation. Under current control the machine was shown to be significantly noisier, despite the fact that the rate of decay of current at turn-off is similar to that which occurs under voltage control. This is due to the fact that the random switching of the current controller induces a wide-band harmonic spectra, thus increasing the levels of all mechanical resonances. However, if fixed frequency PWM voltage control were to employ a switching frequency in the audible frequency range which also coincided with a natural frequency, the machine may then be noisier than that under current control. Further, it has been shown that hard chopping results in a noisier machine compared to that with soft chopping due to the higher current ripple, especially under current control.

When the voltage PWM switching frequency was reduced below 20kHz with the SR machine operated under voltage control, since it was then within the audible frequency range, the sound pressure level increased. Further, it has been shown that when the PWM switching frequency approaches that of a stator natural frequency, the amplitude of the natural frequency increases, and therefore coincidence with these two frequencies should be avoided.

For speeds below that which result in single pulse operation, with the SR machine operated under voltage or current control, it has been shown that the sound pressure level and the magnitude of the resonant peaks increase with speed. This is due to the increase in the rate of change of current, in response to the increase in the rotational back-emf.

Comparison of the noise and vibration under dc supply controlled single pulse mode and voltage control has shown that single pulse mode results in the quietest operation. This is also evidenced by comparing the measured sound pressure level under the various operating modes. This is attributed to the lower magnetisation voltage which is available during the tests, which have shown the strong relationship which exists between the rate of change of current at turn-off and the resulting noise and vibration. Further, a comparison of PWM voltage control for various dc supply voltages for a fixed speed operation has shown that the noise and vibration may be reduced at low speeds and loads by including an additional chopper between the dc supply and inverter to limit the de-nagnetisation voltage at turn-off.

The application of load at any rotational speed has been shown to increase the noise and vibration, due to the higher level of current and, hence, increased rate of decay of current at turn-off. Finally, for a fixed dwell period, it has been shown that the noise and vibration increases slightly as the switching angles are advanced due, again, to the increased current and, hence, increased rate of decay of current at turn-off.

Chapter 5
Reduction of Noise and Vibration

5.1 Introduction

This chapter focuses on the merits and limitations of the active cancellation technique which was proposed by Wu and Pollock, [WU95]. The investigations which have been undertaken include the application of the technique under voltage PWM control, current control and single pulse mode operation, at various operating speeds and under both no-load and load conditions. The influence of the time delay associated with the cancellation of the vibration associated with the natural frequency of mode 2 is assessed in order to evaluate the sensitivity of the technique to the delay. The influence of the time delay is also examined with regard to the vibration associated with mode 4. Throughout, current and vibration waveforms are analysed, together with the associated vibration and noise spectra and the related SPL. A summary of the investigations which have been undertaken is given in **Table 5.1**.

Table 5.1 *Summary of noise emission tests*

Test	Test Condition			
	Voltage Control		Current Control	
	No-load	75% Load	No-load	75% Load
2 main time delays*	√	√	√	√
Variation of the delay	√	√	√	√
Variation of switching frequency	√	√		
Single pulse operation	√	√	√	√

**Time delay durations of 130μs and 37μs to cancel vibration modes 2 and 4, respectively*

5.2 Principle of active noise and vibration cancellation

In their first paper which was concerned with noise and vibration of SR machines, Wu and Pollock, [WU93], outlined a number of experiments whose results were analysed in the time domain in order to identify the nature of the deformation of the stator, and, hence, the resultant noise and vibration. Their main conclusion was that the noise was greatest at turn-off of a given phase, regardless of operating mode. By means of experiments, [WU93], it was subsequently proven that by utilising appropriate control the vibration, and, hence, the emitted noise could be reduced. More recently, Wu and Pollock employed the two 4-phase 8/6 SR machines, which were used in the earlier investigations, on which to demonstrate an 'active cancellation' technique, [WU95], which was shown to be very effective.

The active cancellation technique involves switching off the phases in two stages. The first stage involves switching the dc link voltage across a phase from a positive to zero voltage by opening one of the switches in an asymmetric half-bridge inverter whilst the other remains closed. This induces a vibration having a lower magnitude than that which is induced during normal commutation, due to the reduced step change in voltage, and, hence, lower rate of change of current. The corresponding acceleration of the stator is negative, in that the stator moves away from the rotor radially to a maximum negative value one quarter of a resonant cycle after the switch is opened. Subsequently, this vibration peak reduces, and after half a resonant cycle passes through zero, before attaining a maximum positive value. When the first oscillation reaches zero, the second switch is opened, which induces a second vibration whose acceleration is negative and, therefore, in anti-phase with the first vibration which is currently entering the positive section of its cycle. This is illustrated schematically in **Fig. 5.1,** for a machine operating in single pulse mode, where the vibration period and, hence, actual time delay has been exaggerated for illustrative purposes. Due to the fact that the machine is operating in single pulse mode, the two voltage steps are of equal magnitude, thus, theoretically, the induced vibrations are in anti-phase and of equal magnitude. The delay time, t_d, is, therefore, given by equation (5.1), where f_n is usually the lowest natural frequency. In practice, t_d, is generally so small, typically several μs, that the phase current and torque waveforms will not be influenced by the introduction of the time delay.

$$t_d = \frac{1}{2}.\frac{1}{f_n} \tag{5.1}$$

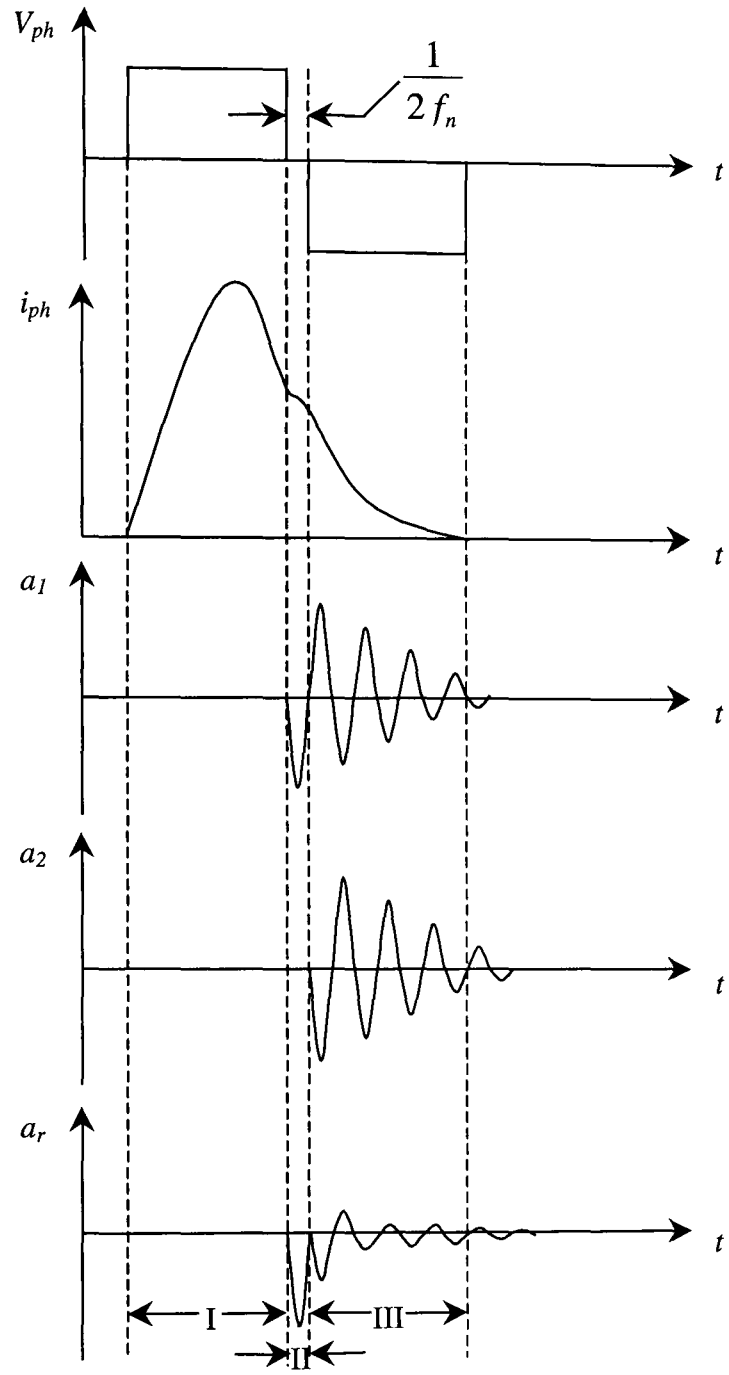

Fig. 5.1 *Active cancellation technique during single pulse mode*

To-date, voltage PWM control does not appear to have been employed with active cancellation at turn-off, since Wu and Pollock only considered the single pulse mode and current control. Furthermore, the analysis of the technique has been limited to the time domain [WU95] and backed up by only a limited number of SPL measurements for active cancellation at turn-on, [BLA94]. Therefore, the following section describes an analysis of active cancellation and current shaping techniques utilising both frequency and time domain data together with SPL measurements.

5.3 Single pulse mode operation

Standard operation of an SR machine utilises some form of chopping for speeds up to the maximum speed for rated torque, often referred to as the 'base speed'. Above this speed, it is common to employ angular position control to maintain the constant power region. However, to ensure that the methods which are considered in this chapter are consistent, i.e. maintain constant speeds and firing angles throughout, the single pulse mode is achieved by varying the dc supply voltage to maintain the required speed. Although this implies that the dc supply is not fixed throughout the various experiments, for any given speed and control technique, the average voltage which is applied to the phase windings remains consistent.

The instantaneous phase current and time domain vibration when the SR machine is operating on no-load, together with the corresponding vibration and noise frequency spectra, at various rotational speeds are shown in **Fig. 5.2**, which compares measurements without the active time delay and with the active delay to cancel vibrational mode 2, t_{d2}, (f_2=3840Hz) and, hence, $t_{d2} = \frac{1}{2}.\frac{1}{f_2} = 130\mu s$.

At all speeds, the introduction of the time delay has an insignificant effect on the current waveform, which is similar whether the machine is operated with or without active vibration cancellation. Furthermore, the maximum value of the current which is attained after turn-on and the average level of current prior to turn-off are comparable both with and without the time delay. The current rise and decay times are given in **Table 5.2,** together with their corresponding rates of change of current. The rise times and their associated rates of change of current obtained with and without the time delay are similar, as expected, since the same magnetisation voltage is available. However, the current decay times are marginally longer for operation with the time delay and, thus, the rate of current decay is lower. Again, this is expected, as is the reduction in the vibration and noise, [WU93]. Further, it is observed that at the point of turn-off, the instantaneous phase current is more 'rounded' when the machine is operated with the time delay, as can be clearly seen in the typical current waveforms shown in **Fig. 5.3**. It should be noted that whilst the quoted values of *di/dt* for the waveforms assume a simple linear variation of current, it is the initial 'rounding' of the current waveform at turn-off, where d*i/dt* is much reduced, which is of greatest significance with respect to the vibration of the stator, [WU93, GAB99a].

It will be observed that the introduction of the 130μs time delay results in a significant reduction in the time domain stator vibration, and that the cancellation method has the greatest influence on the peak oscillations associated with the natural frequency of vibration mode 2. Thus, the cancellation of vibration mode 2 is effective, although the less dominant vibrations within the spectra are generally unaffected. Further, the low frequency vibration which is associated with the shaft resonance, as discussed in the preceding chapter, is not affected by the introduction of the time delay.

Table 5.2 *Comparison of current rise and decay times, together with corresponding rates of change of current for control, with and without the delay (130μs), no-load*

Speed (rpm)	Rise time (ms)/di/dt (As^{-1})		Decay time (ms)/di/dt (As^{-1})	
	No time delay	Time delay	No time delay	Time delay
500	2.2/2928	2.18/3034	3.3/1513	3.4/1462
1000	1.16/6147	1.16/5984	2.4/2364	2.5/2278
1500	0.82/9063	0.8/10128	2.0/3016	2.17/2970
2500	0.58/14347	0.52/15834	1.5/4356	1.56/4285

Comparison of the vibration spectra in the 0-6kHz range, with and without the time delay, shows that the time delay has a significant influence on the 3840Hz frequency harmonic, which corresponds with the natural frequency of vibration mode 2. This is, by far, the dominant component when the machine is operated without the active time delay, and is almost completely eliminated at speeds of 500rpm and 1000rpm, **Fig. 5.2i & ii**. Without the time delay, this frequency component has a magnitude of ≈8dB at 2500rpm, **Fig. 5.2iv(a)**. The introduction of the time delay reduces its magnitude to <0dB, **Fig. 5.4iv(b)**. Many of the other peaks which are observed in the frequency range of 0-6kHz are also reduced, although less significantly. Thus, in the frequency spectrum 0-25kHz the vibration of mode 2 is almost indistinguishable from the background noise. In this frequency range it is observed that the influence of the time delay is negligible on the vibration peak which is associated with the natural frequency of mode 4, therefore becoming the dominant peak on the spectrum. It can also be observed in the noise spectra, that in the frequency range 0-6kHz, no significant peaks are present when the

active cancellation technique is employed. This is also the case in the 0-6kHz noise spectra, which highlights the fact that the vibration peaks other than that associated with mode 2 in the vibration spectra are insignificant as regards the emission of noise since they do not coincide with a stator natural frequency.

When the machine is loaded, the phase current waveforms are similar irrespective of whether a time delay is employed, as is the peak current which is attained after turn-on and the average current prior to turn-off, **Fig. 5.4**. The current rise and decay times, both with and without the vibration cancellation method, are given in **Table 5.3,** together with the associated average rates of change of current. The rate of change of current is similar at all speeds and, again, the rate of decay of current is consistently lower when active cancellation is employed.

The related time domain vibration waveforms of the machine on load **Fig. 5.4** confirm the effectiveness of the technique more clearly than those for no-load. Generally, the vibrational behaviour is more stable (i.e. insignificant low frequency ripple, the load constrains any shaft oscillations). At all speeds, the peak oscillation which is associated with vibration mode 2 is significantly reduced, and at a speed of 500rpm it is completely eliminated. When the machine is loaded, the vibration oscillation which is associated with the excitation of mode 2 at turn-on is more distinguishable than when the machine is on no-load. The vibrations which are induced by turn-off of the other phases, (as discussed in Chapter 4, section 4.3.1), are also observed to reduce with the introduction of the time delay, their respective oscillations appearing to be lower than that of the phase under consideration since the accelerometer is not mounted behind their respective stator poles.

The 0-6kHz vibration spectrum shows clearly that the magnitude of the 3840Hz component, which coincides with the natural frequency of mode 2, is reduced. This is especially clear at a speed of 1500rpm, at which a reduction from 8dB to –3dB is observed, **Fig. 5.4iii**. Further, at 1500rpm, it is observed that the cancellation technique results in a reduction of the noise level to such an extent that 3^{rd} harmonics associated with the current spectra, which have not been evident in all other vibration spectra analysed throughout this and the preceding chapter, are clearly visible in the vibration spectrum. The 0-6kHz noise spectra also confirms that the 3840Hz frequency component has been suppressed, the resultant spectra having no significant peaks. From the 0-

25kHz noise and vibration spectra, it will be seen that mode 4 is reduced very slightly.

Table 5.3 *Comparison of current rise and decay times, together with corresponding rates of change of current, for control with and without the delay, ≈75% load*

Speed (rpm)	Rise time (ms)/di/dt (As^{-1})		Decay time (ms)/di/dt (As^{-1})	
	No time delay	Time delay	No time delay	Time delay
500	2.01/5076	1.9/5317	3.5/2335	3.8/2171
1000	1.1/ 11820	1.13/11523	2.7/4348	2.77/4261
1500	0.7/ 20431	0.73/19567	2.1/7001	2.23/6585

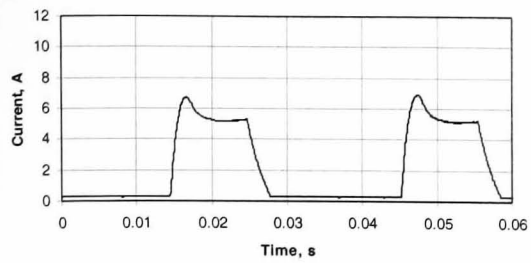

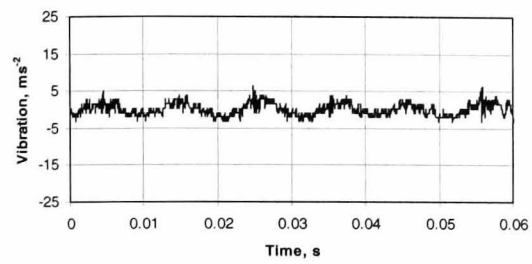

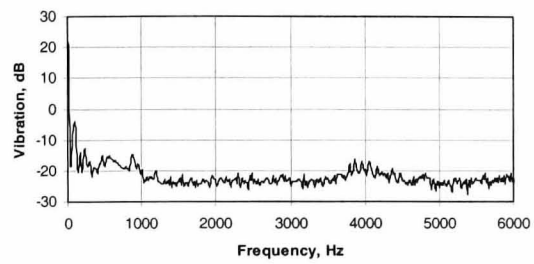

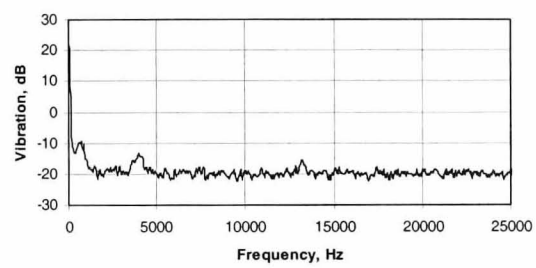

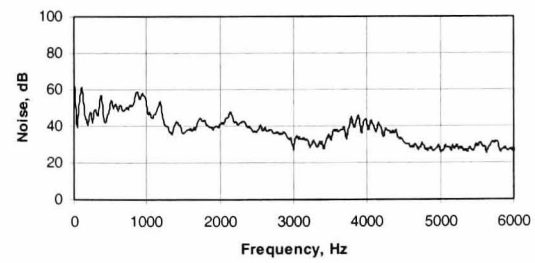

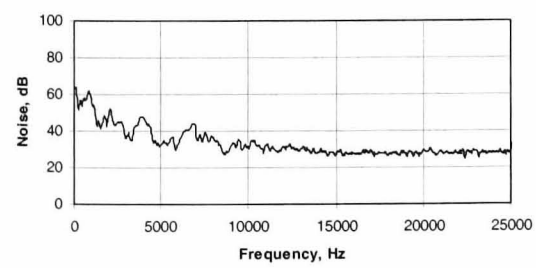

(a) *No time delay*

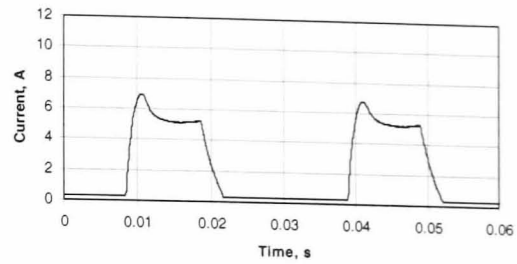

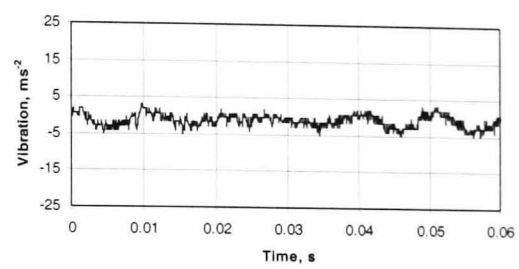

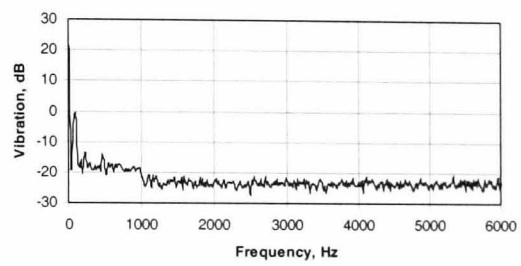

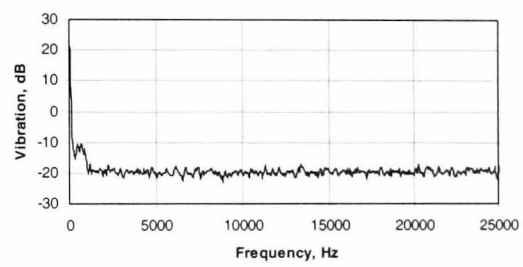

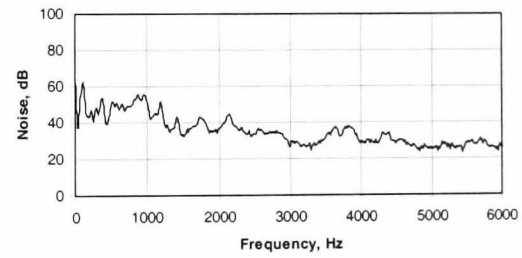

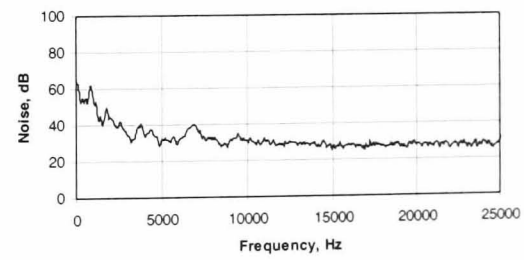

(b) *130μs time delay*

Fig. 5.2i *Single pulse mode under no-load operation at 500rpm*

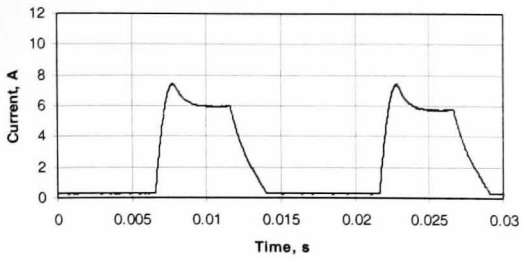

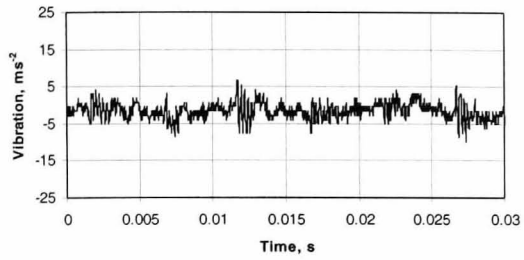

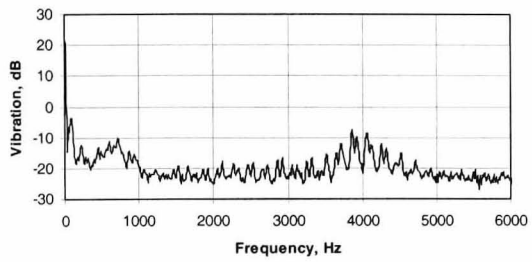

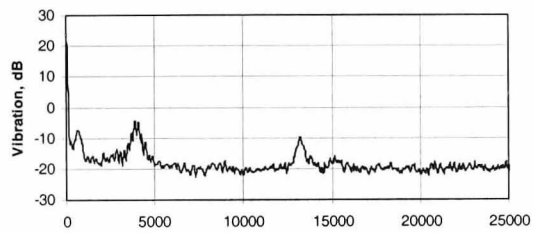

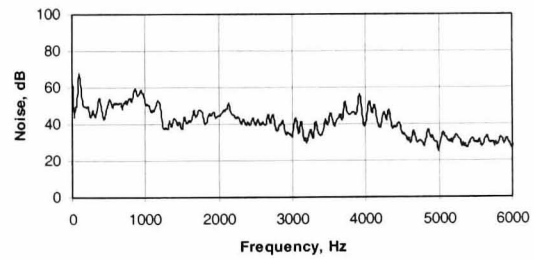

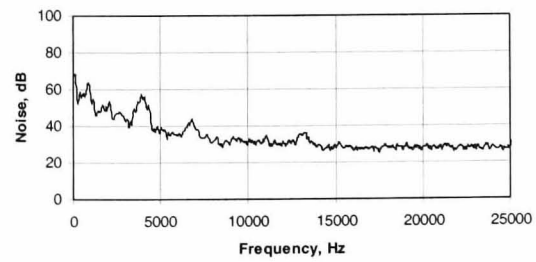

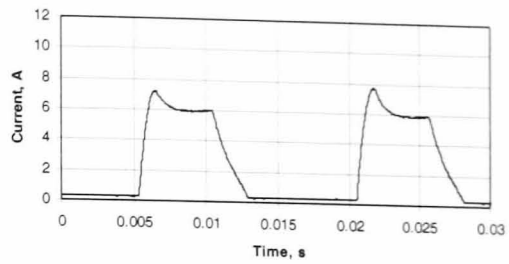

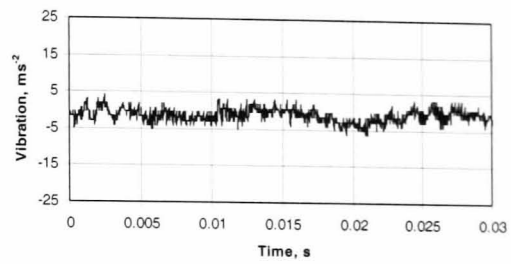

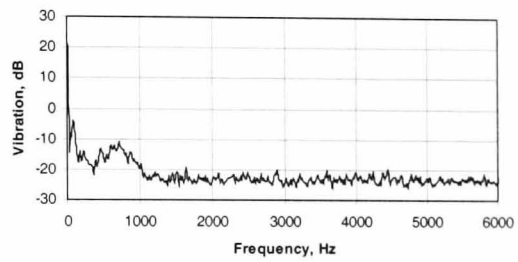

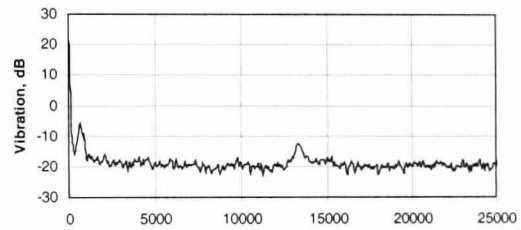

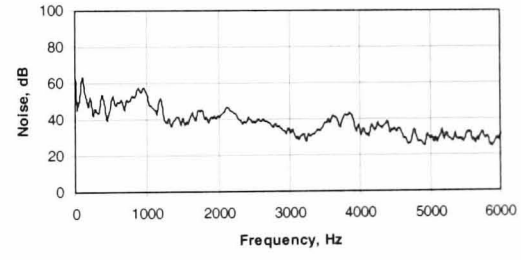

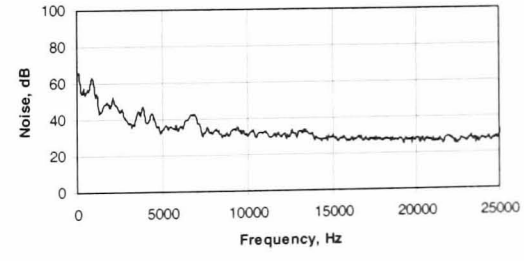

(a) *No time delay*

(b) *130μs time delay*

Fig. 5.2ii *Single pulse mode under no-load operation at 1000rpm*

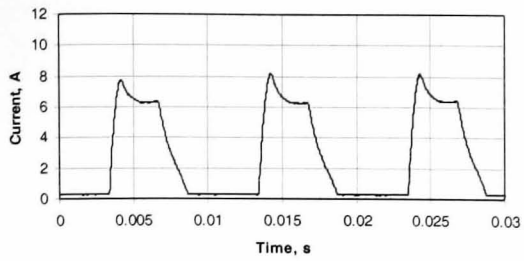

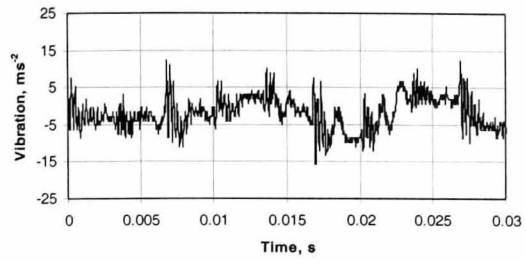

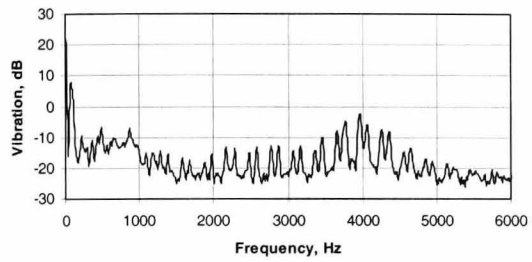

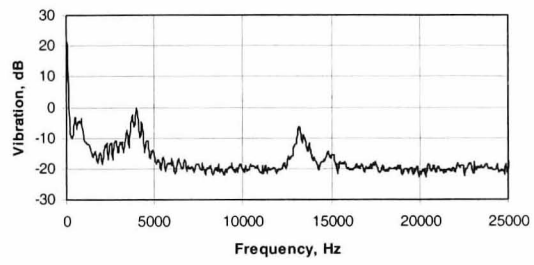

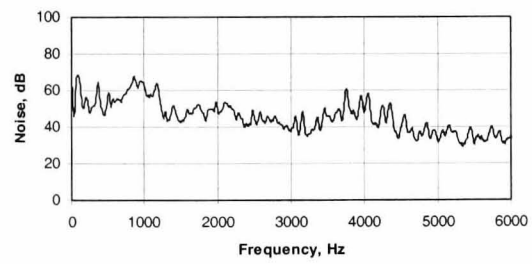

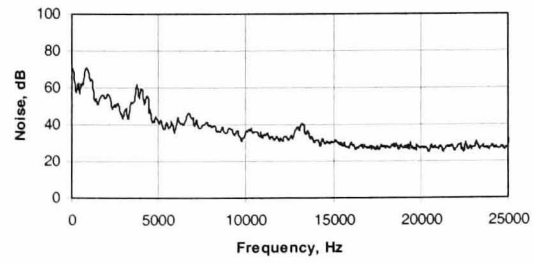

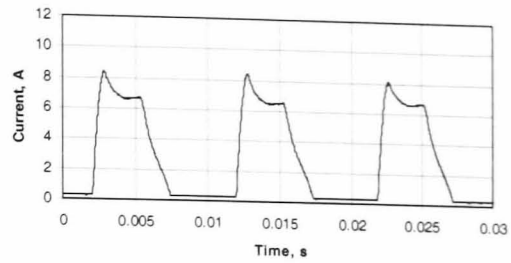

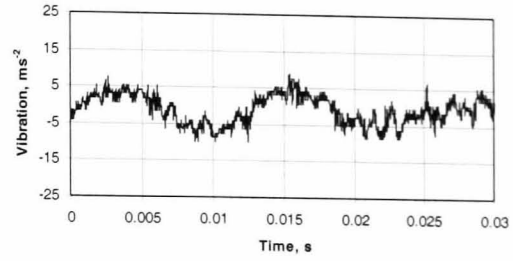

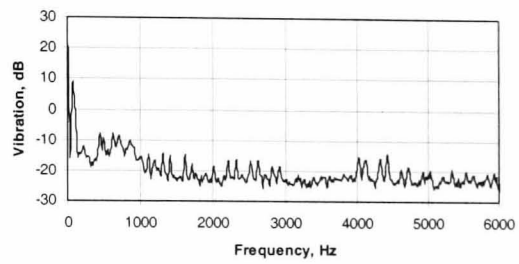

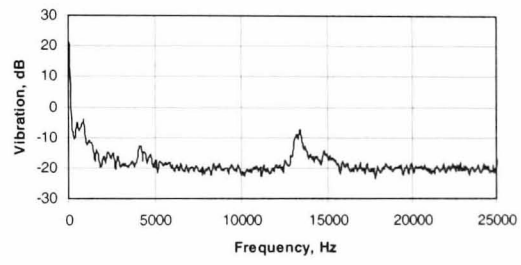

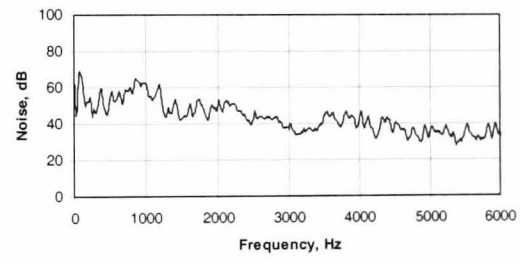

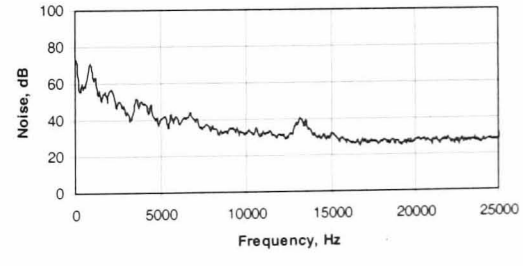

(a) *No time delay* **(b)** *130μs time delay*

Fig. 5.2iii *Single pulse mode under no-load operation at 1500rpm*

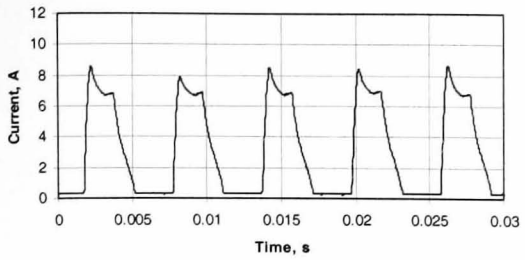

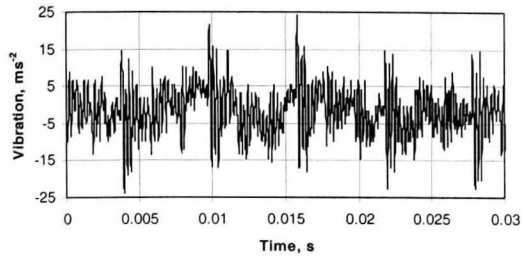

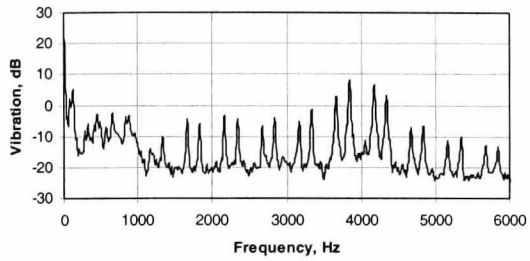

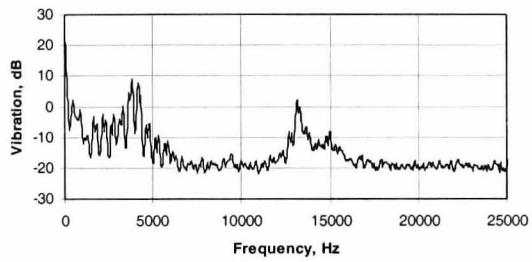

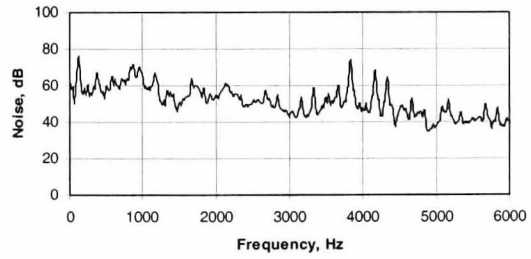

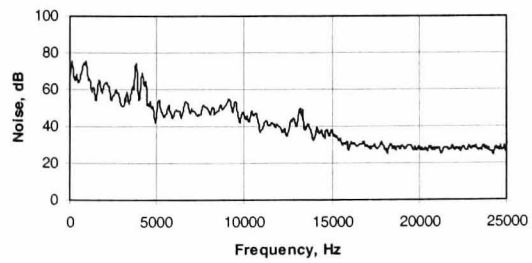

(a) *No time delay*

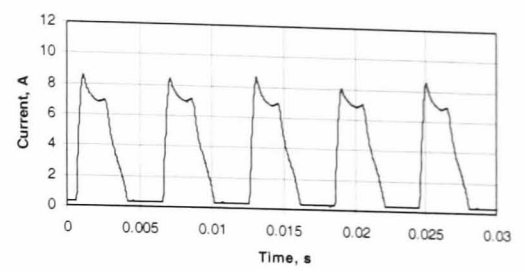

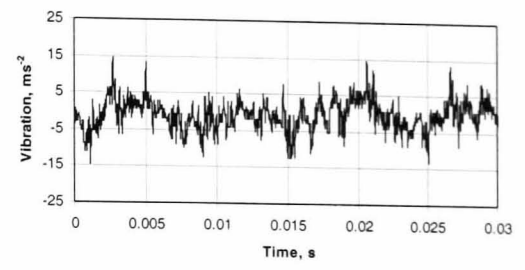

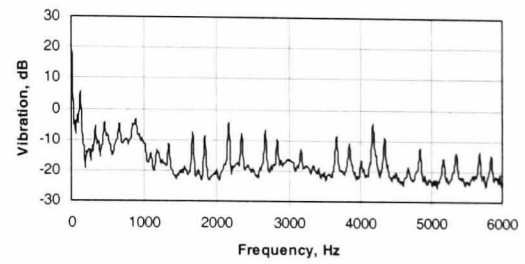

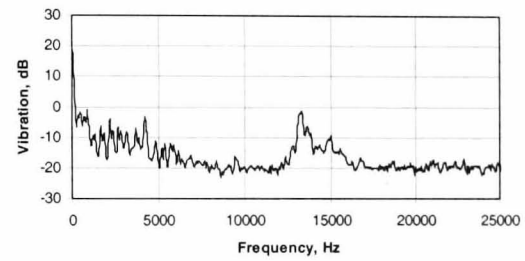

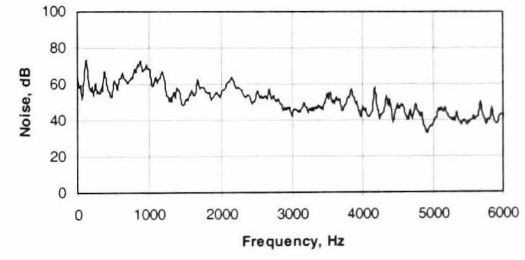

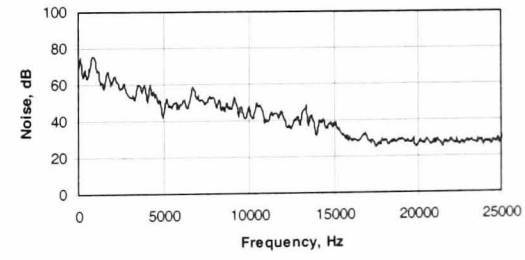

(b) *130μs time delay*

Fig. 5.2iv *Single pulse mode under no-load operation at 2500rpm*

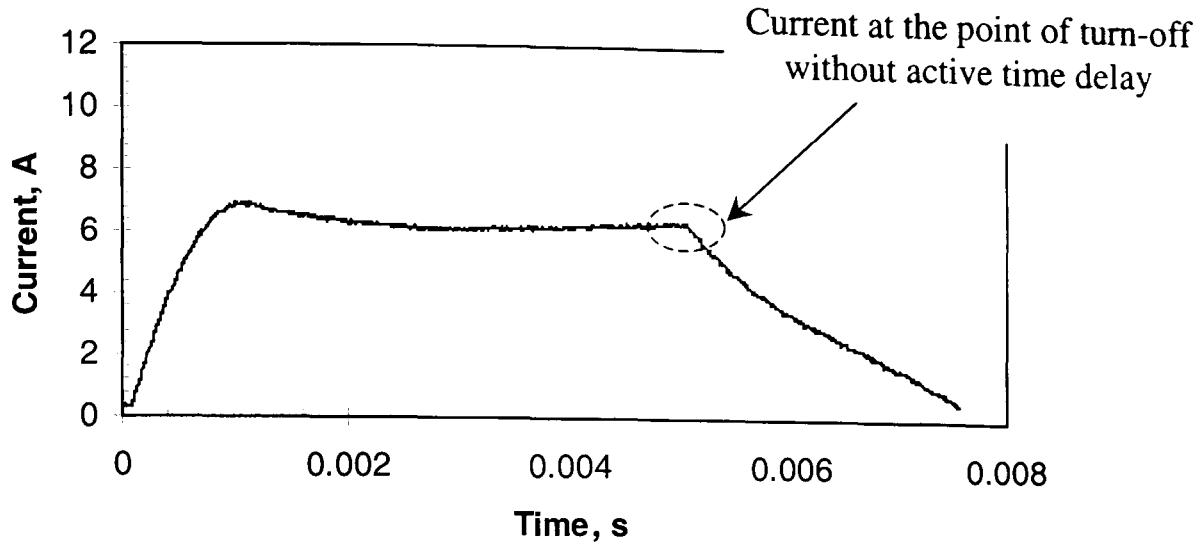

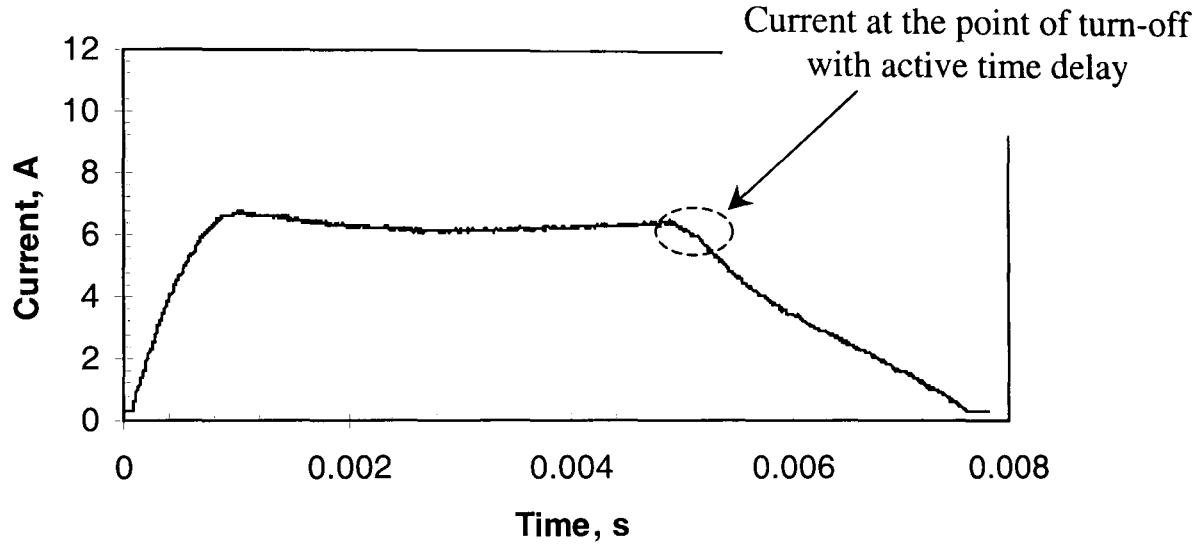

Fig. 5.3 *Influence of active time delay on initial rate of decay of current*

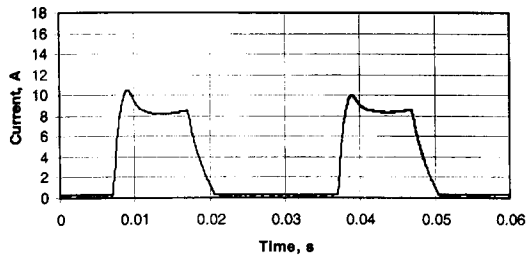

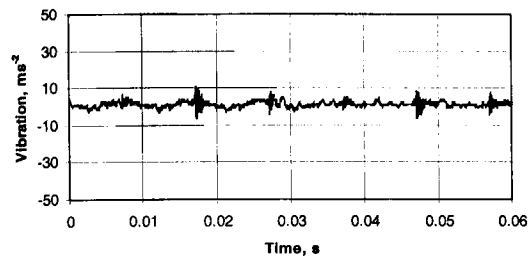

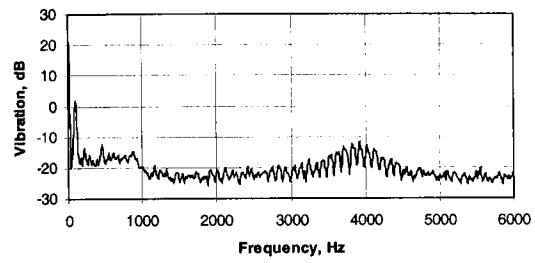

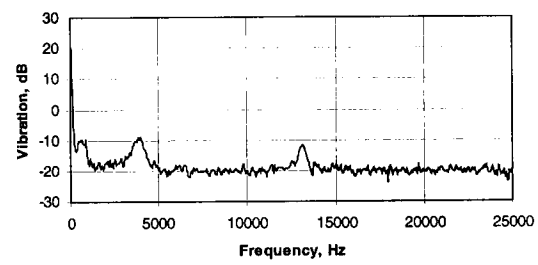

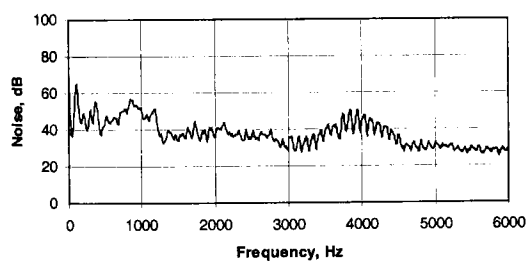

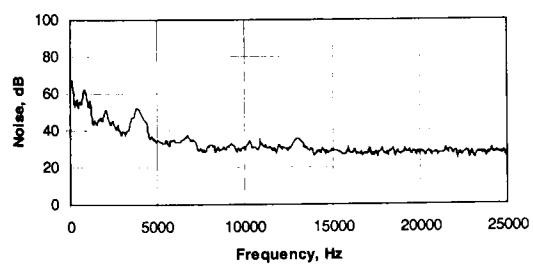

(a) *No time delay*

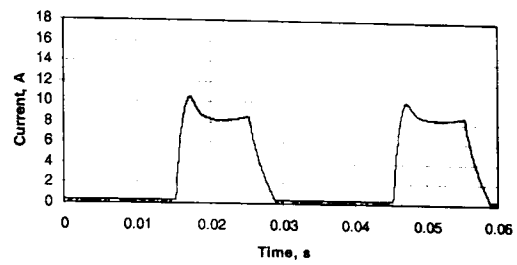

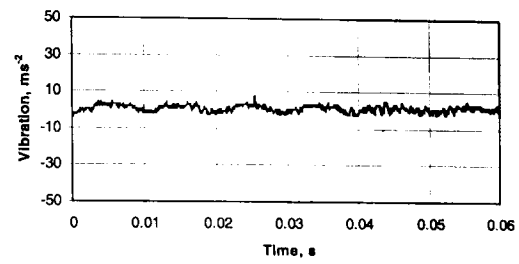

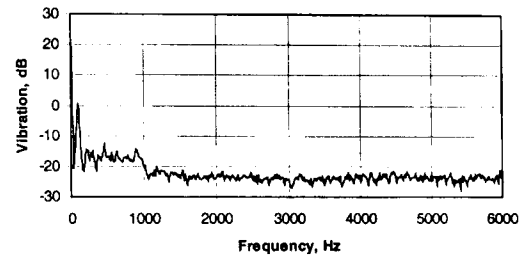

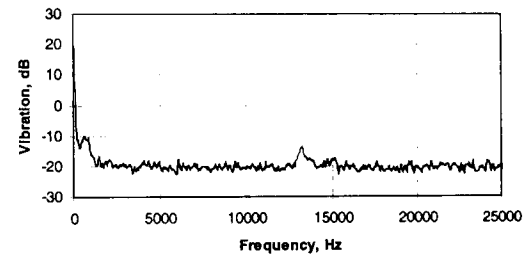

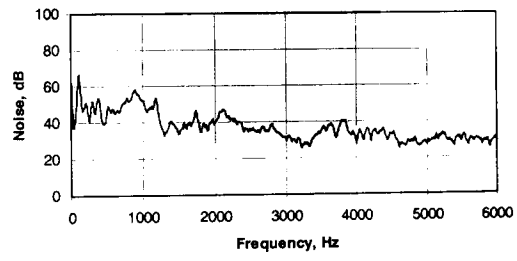

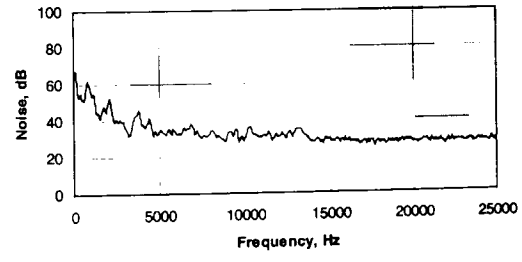

(b) *130μs time delay*

Fig. 5.4i *Single pulse mode under ≈75% load condition at 500rpm*

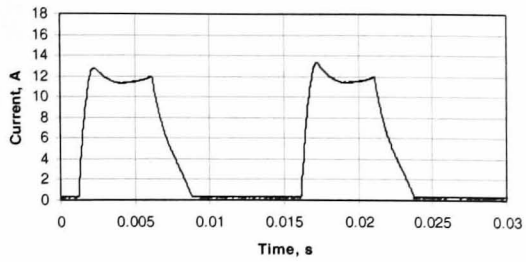

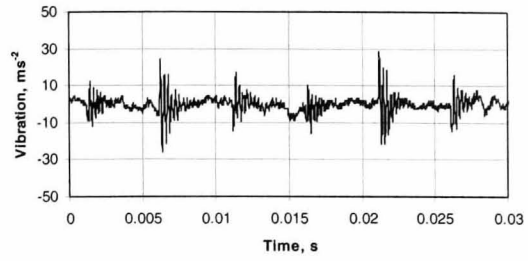

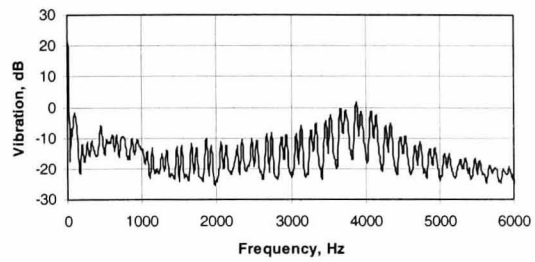

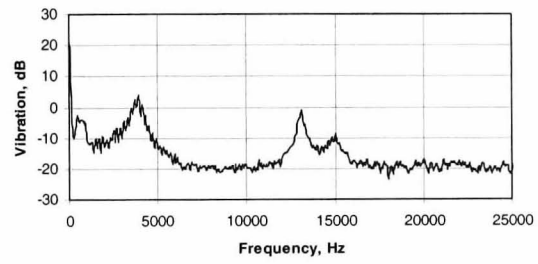

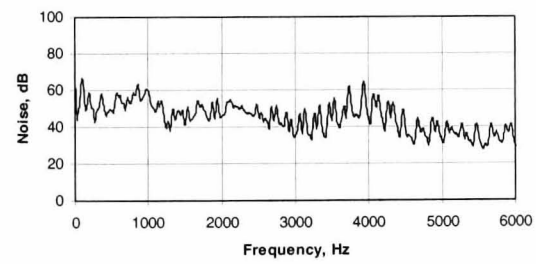

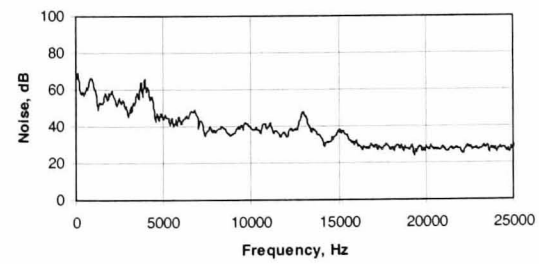

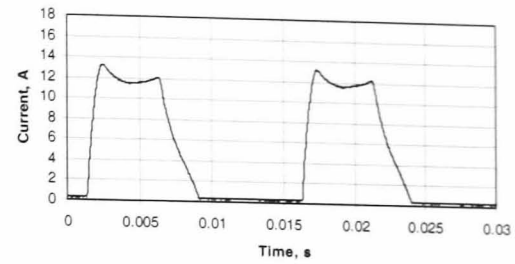

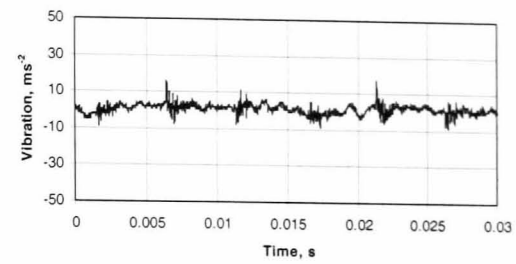

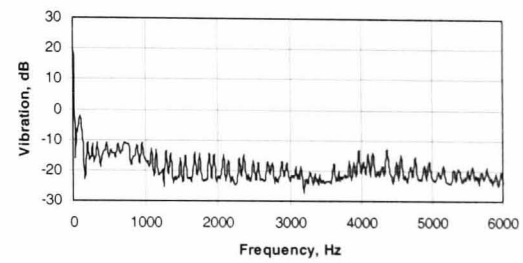

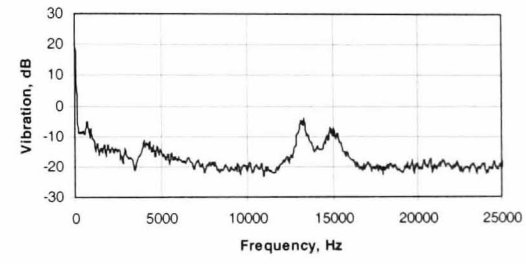

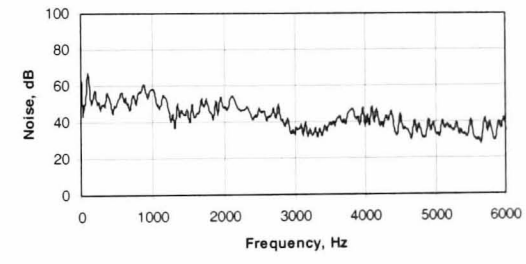

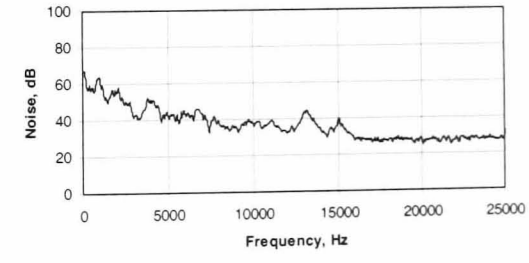

(a) *No time delay*

(b) *130μs time delay*

Fig. 5.4ii *Single pulse mode under ≈75% load condition at 1000rpm*

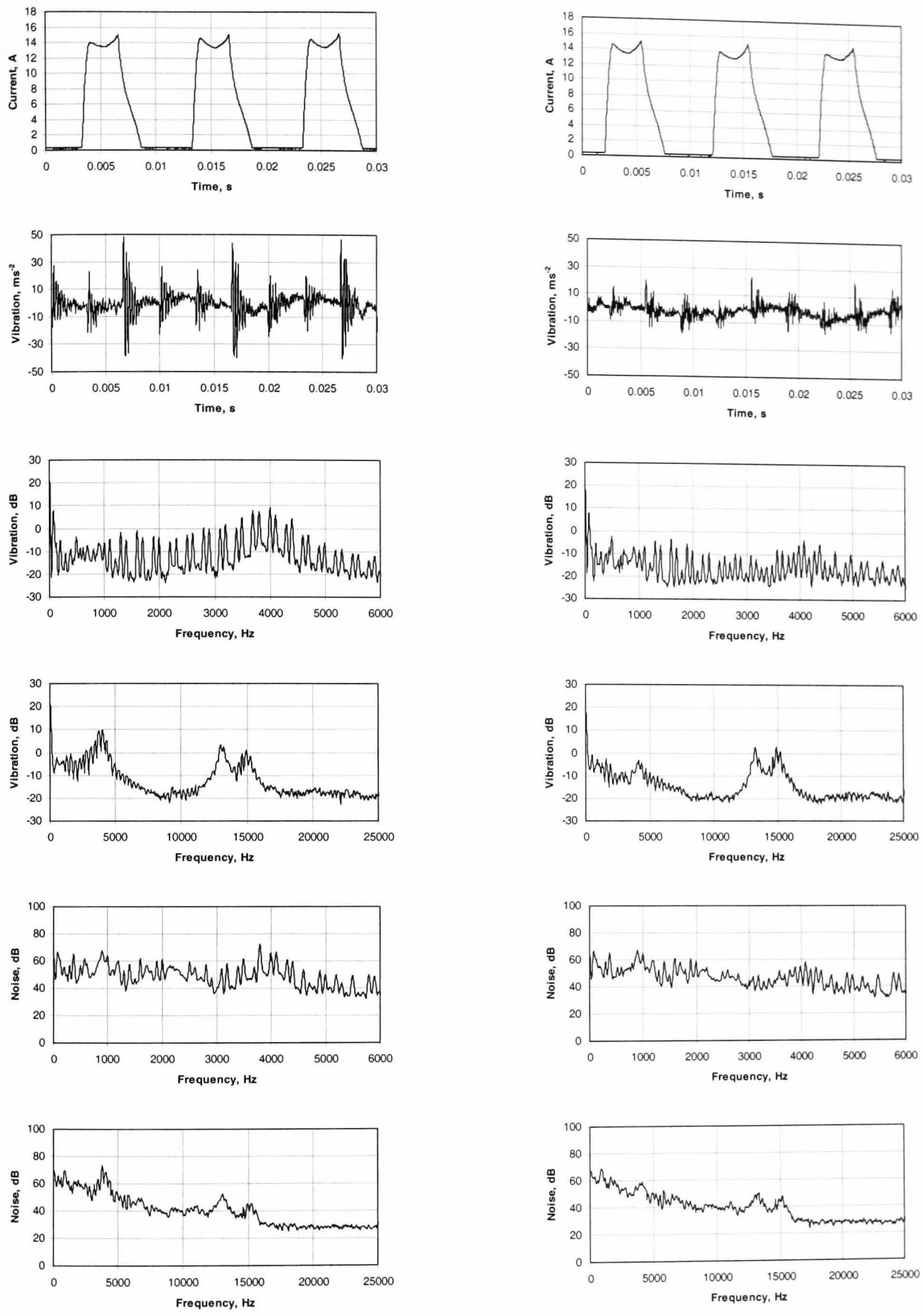

(a) *No time delay* **(b)** *130μs time delay*

Fig. 5.4iii *Single pulse mode under ≈75% load condition at 1500rpm*

5.4 Voltage PWM control

The phase current waveform, the corresponding time domain vibration waveforms, and the noise and vibration spectra, when the machine is operated with voltage PWM control. on no-load, are shown in **Fig. 5.5**, both with and without the switching delay, for speeds of 500rpm, 1000rpm and 1500rpm. It will be seen that the phase current waveforms are similar with or without the time delay, having similar peak values after turn-on and similar average values prior to turn-off. The current rise and decay times are given in **Table 5.4**, together with the associated rates of change of current. The rate of rise of current is essentially similar for operation with and without the switching time delay, since the same magnetisation voltage is available. It increases with speed due to the increased magnetisation voltage. However, the rate of decay of current is significantly lower when the time delay is introduced at all speeds, highlighting, once again, that it is the 'knee' point in the current waveform that is important as regards to the induced vibrations, and, hence, the emitted noise.

Table 5.4 *Comparison of current rise and decay times, together with corresponding rates of change of current for control with and without time delay, no-load*

Speed (rpm)	Rise time (ms)/di/dt (As^{-1})		Decay time (ms)/di/dt (As^{-1})	
	No time delay	Time delay	No time delay	Time delay
500	2.3/3052	2.3/3003	1.3/4102	1.6/3517
1000	1.2/6717	1.2/6923	1.1/6450	1.5/4499
1500	0.9/9008	0.9/9081	1.0/6956	1.2/5485

It will be observed that, at all speeds, the introduction of the time delay attenuates the peak oscillations in the time domain vibration spectra associated with the natural frequency of mode 2. However, they are not suppressed as effectively as for single pulse mode operation, for which, at all speeds, the peak oscillation associated with mode 2 was not distinguishable during no-load operation, **Fig. 5.2**. Further, similar to single pulse operation, the low frequency oscillations are unaffected by the introduction of the switching time delay.

Comparison of the vibration spectra shows that the magnitude of the vibration associated with mode 2 is reduced at all speeds, although, again, not to the extent which was achieved with single pulse operation. At 1500rpm, the vibration peak at 3840Hz, in the 0-6kHz vibration spectrum has reduced from approximately 3dB to –4dB. Further, the vibration peaks associated with the natural frequency of mode 4 and the PWM switching frequency are largely unaffected. These observations are reflected in the noise spectra, although it should be noted that the noise peaks in the 0-6kHz spectrum remain distinguishable after the introduction of the switching time delay. Further, a reduction in the PWM switching frequency, such that it falls within the audible frequency range, results in the component of PWM induced noise becoming more significant in the SPL, thereby reducing the benefits of active vibration cancellation. Typical waveforms at a PWM switching frequency of 10.3kHz, with and without the time delay, are shown in **Fig. 5.6**. It is observed that with active vibration cancellation the time domain vibration is reduced significantly, but not as much as that with a PWM switching frequency of 20.6kHz, the reason for which is explained in section 5.6. The noise and vibration peaks associated with mode 2 are clearly reduced, whilst the peak associated with the switching frequency is the most dominant peak once the time delay is implemented.

The current waveforms and noise and vibration spectra both with and without the switching time delay, are shown in **Fig. 5.7**, with the machine loaded and running at 500rpm, 1000rpm and 1500rpm. Again, the switching time delay has a insignificant influence on the current waveforms, whose rise and decay times with and without the active delay are given in **Table 5.5** together with the associated rates of change of current. As was the case for no-load operation, the rates of increase of current are similar and lower rates of decay of current result when the machine is operated with the active vibration cancellation technique, for the reasons outlined earlier. All the observations which were made for no-load operation are equally valid when operating on load.

Table 5.5 *Comparison of current rise and decay times together with corresponding rates of change of current for control with and without time delay, at ≈75% load*

Speed (rpm)	Rise time (ms)/di/dt (As^{-1})		Decay time (ms)/di/dt (As^{-1})	
	No time delay	Time delay	No time delay	Time delay
500	2.1/4813	2.0/5051	1.4/6149	1.7/5101
1000	1.01/11889	1.0/12879	1.7/7122	1.91/6586
1500	0.74/18909	0.7/19691	2.05/7606	2.2/7175

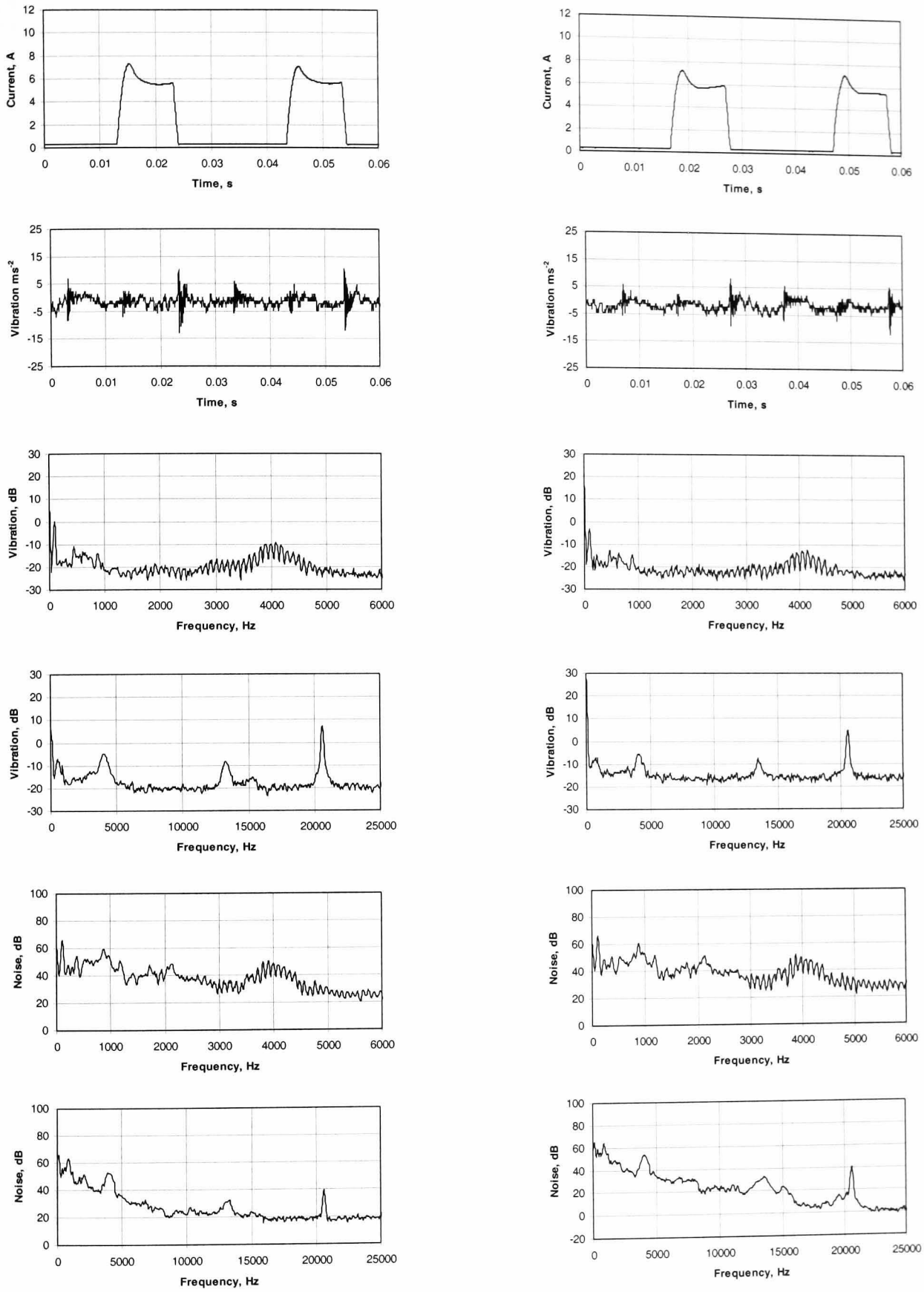

(a) *No time delay* **(b)** *130μs time delay*

Fig. 5.5i *Voltage PWM control, no-load at 500rpm*

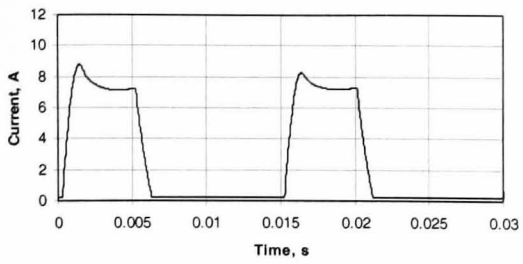

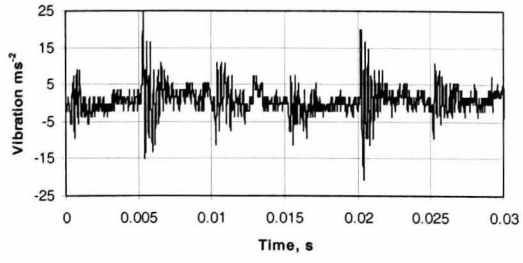

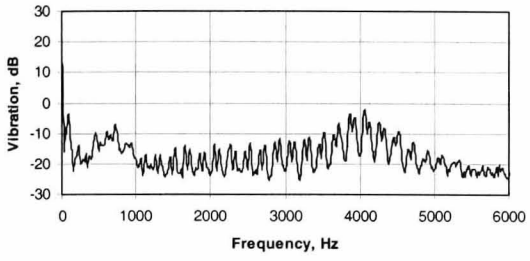

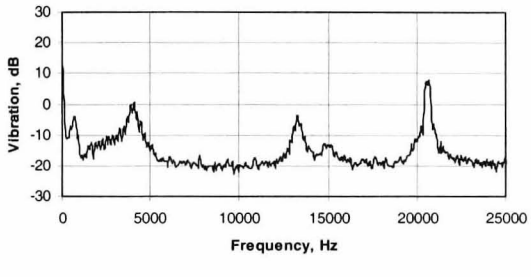

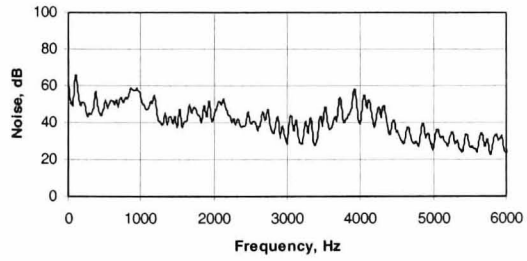

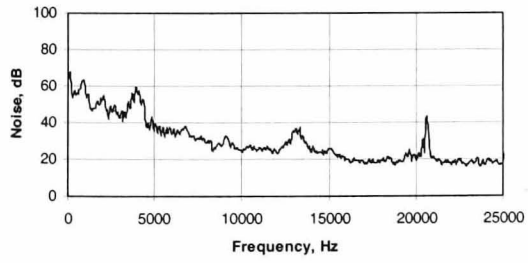

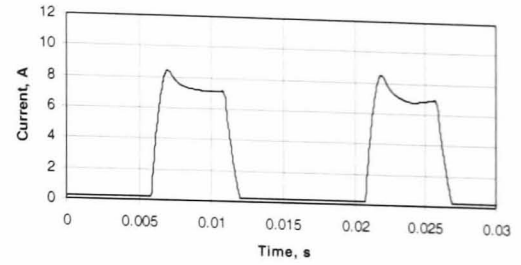

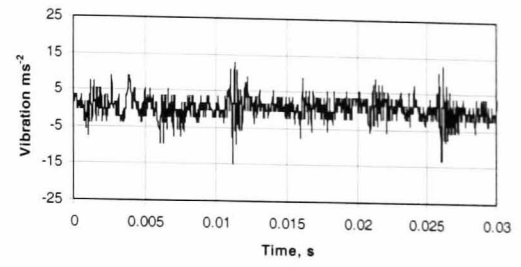

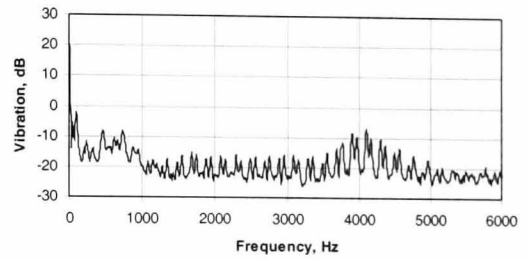

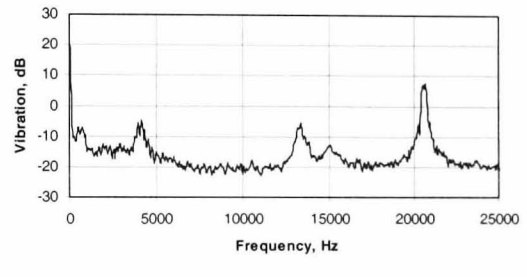

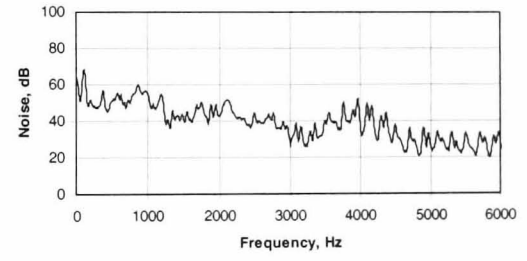

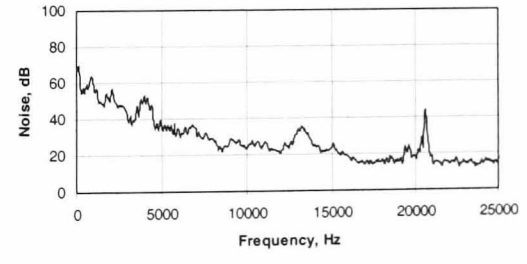

(a) *No time delay*

(b) *130μs time delay*

Fig. 5.5ii *Voltage PWM control, no-load at 1000rpm*

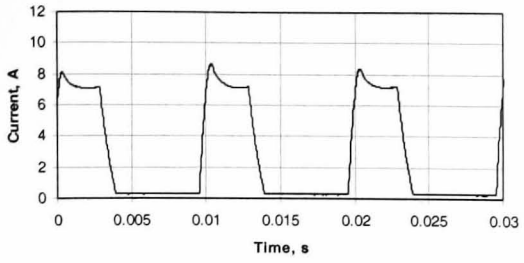

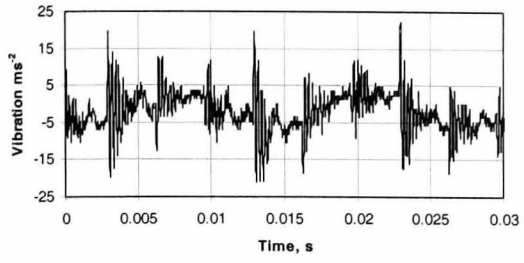

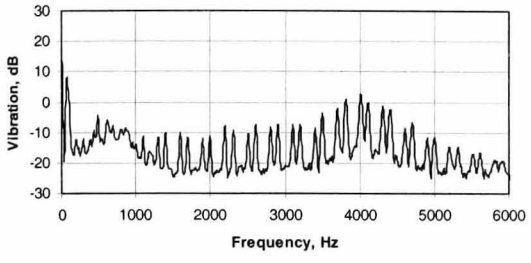

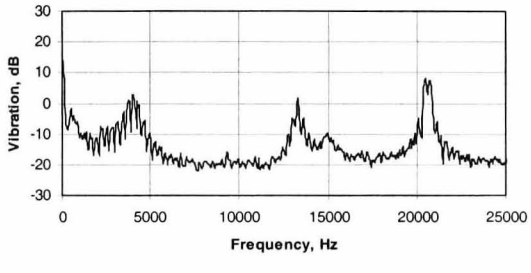

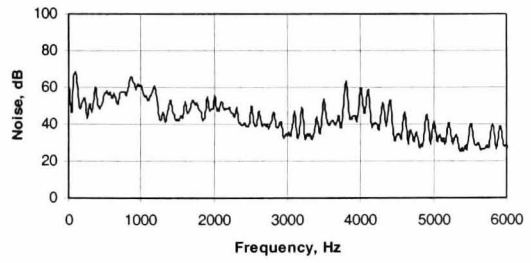

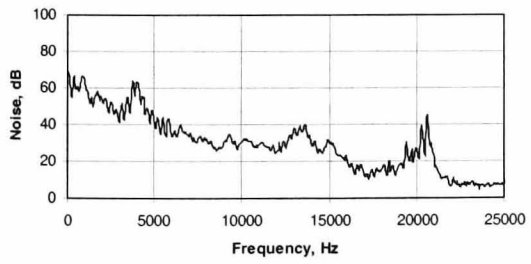

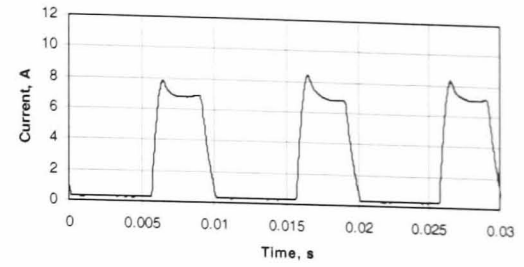

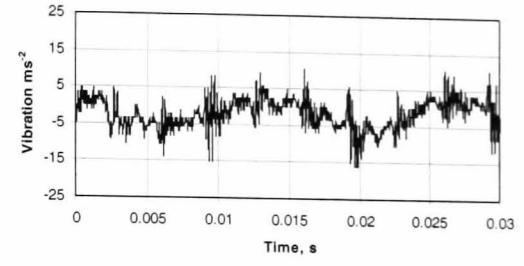

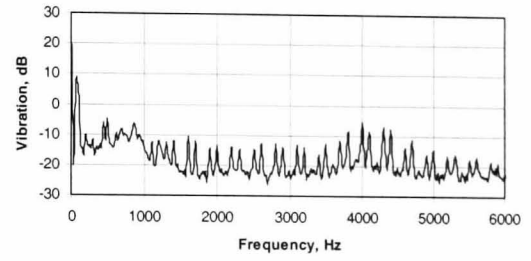

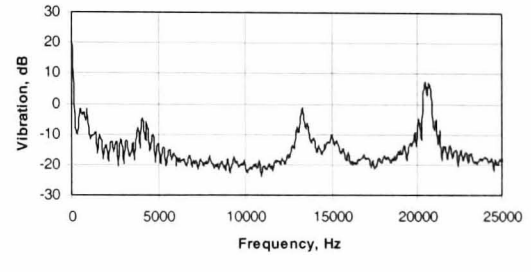

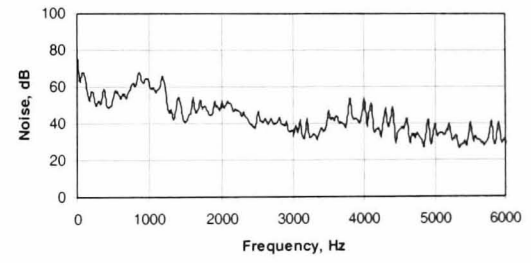

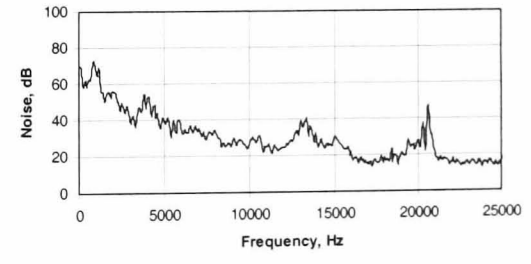

(a) *No time delay*

(b) *130μs time delay*

Fig. 5.5iii *Voltage PWM control, no-load at 1500rpm*

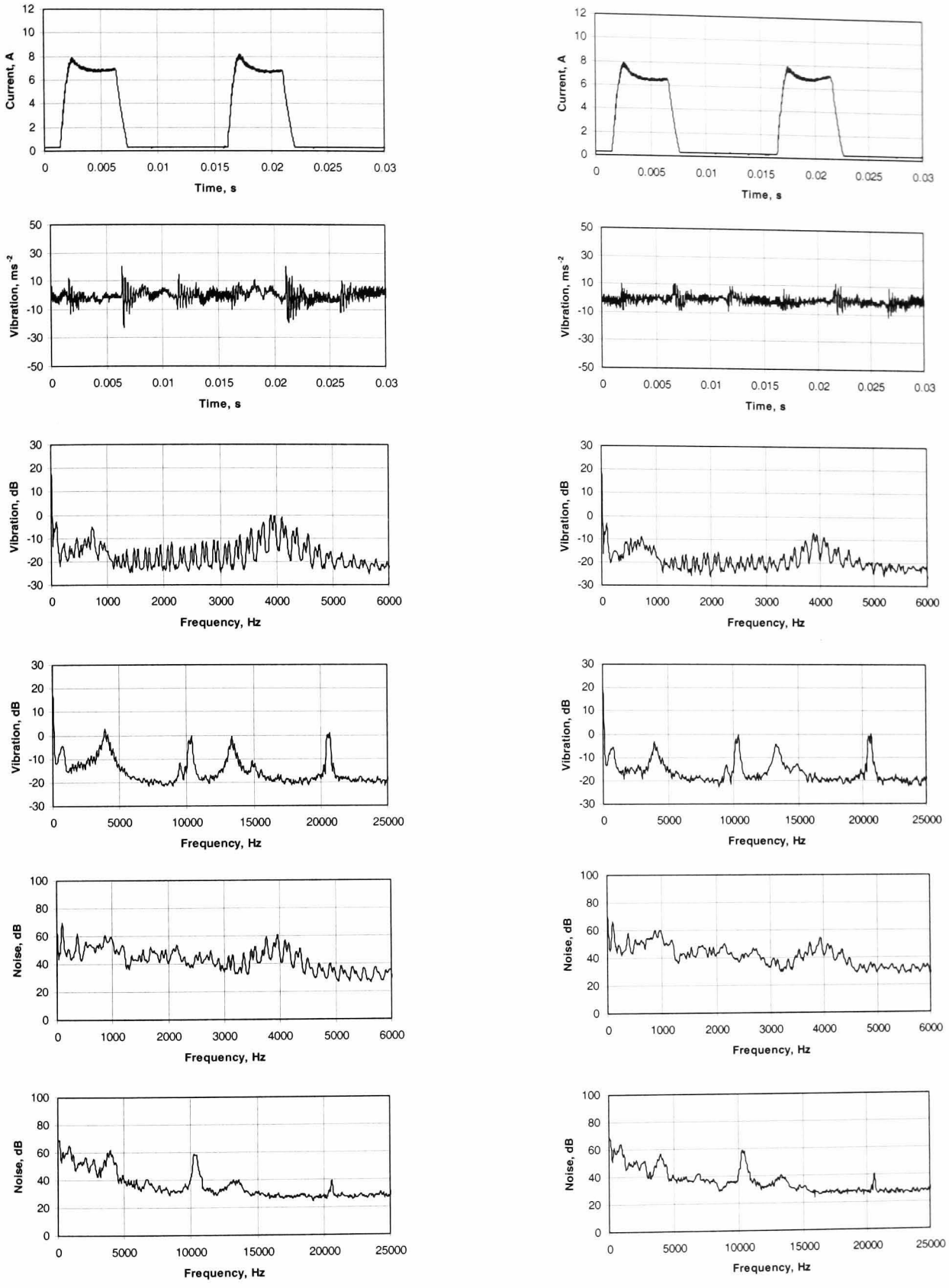

(a) *No time delay* **(b)** *130μs time delay*

Fig. 5.6 *Voltage PWM control, 10.3kHz switching frequency, no-load at 1000rpm*

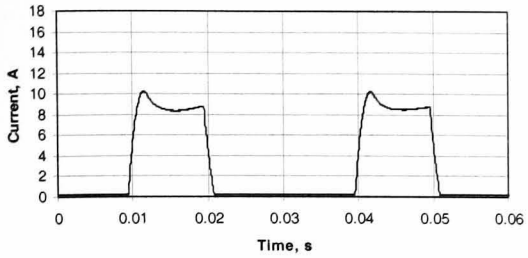

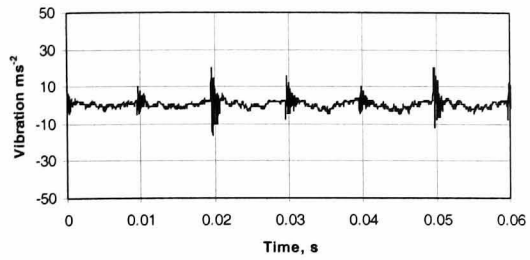

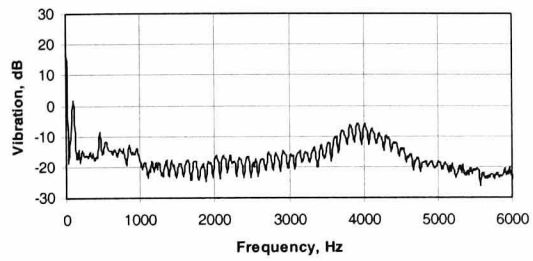

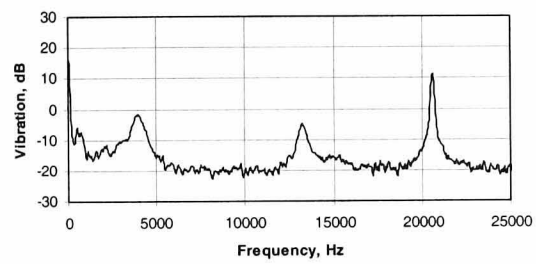

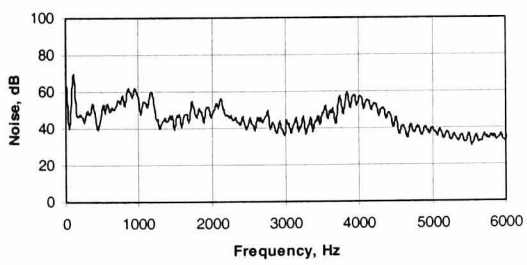

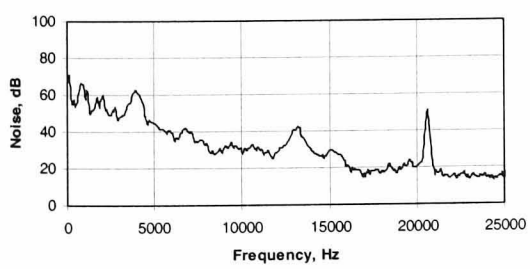

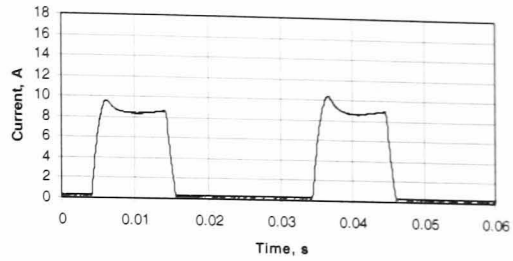

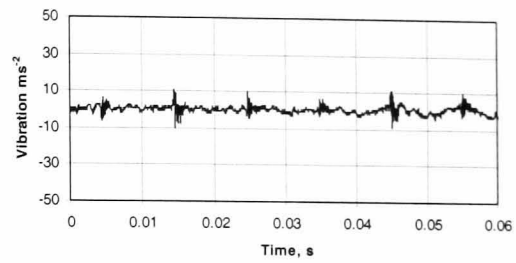

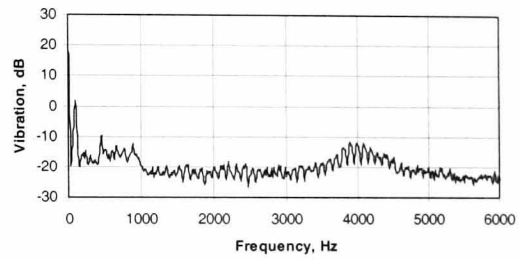

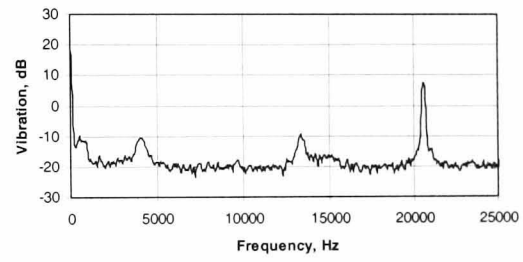

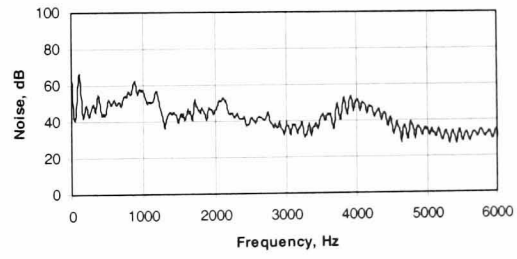

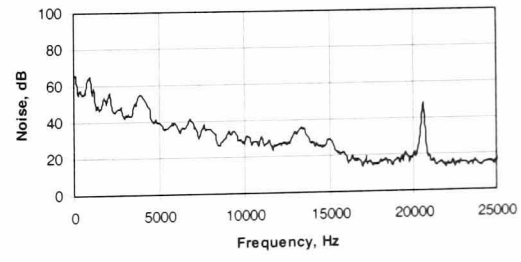

(a) *No time delay*

(b) *130μs time delay*

Fig. 5.7i *Voltage PWM control under ≈75% load condition at 500rpm*

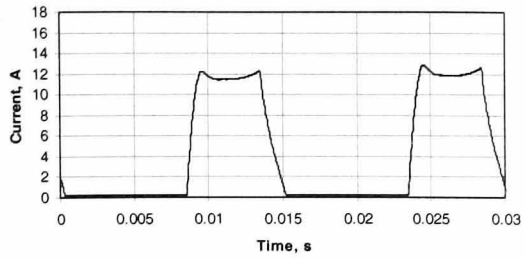

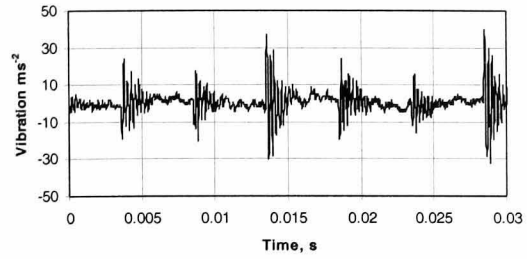

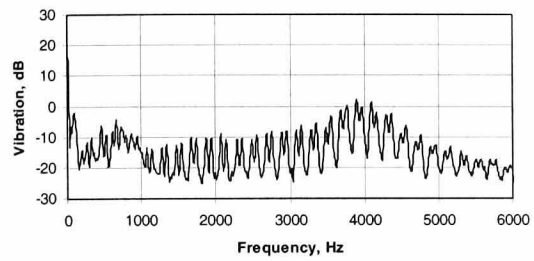

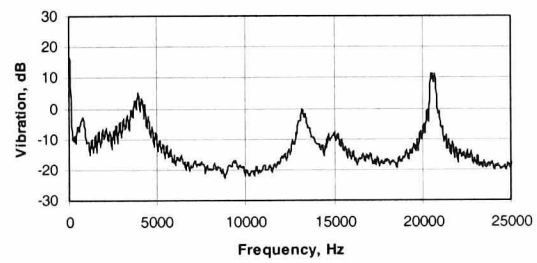

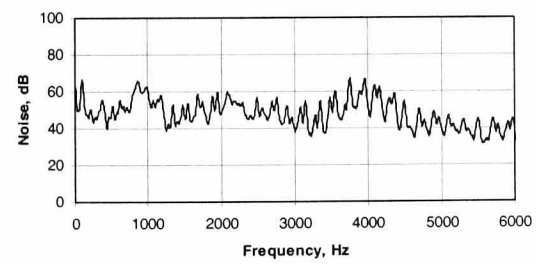

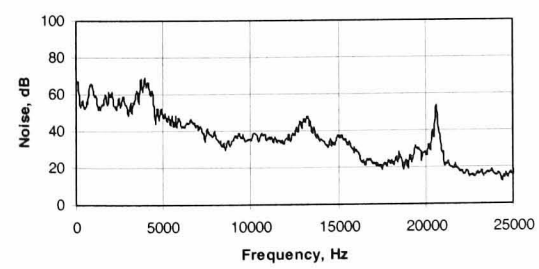

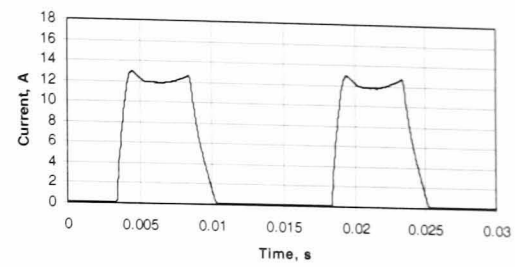

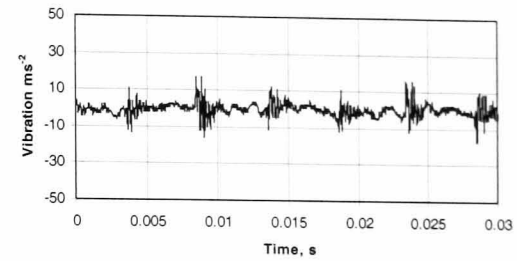

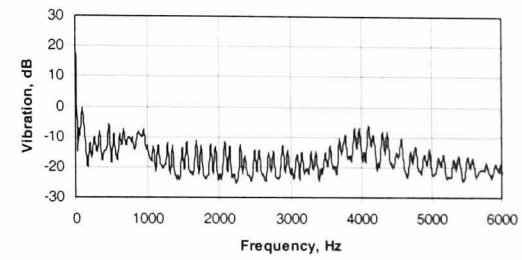

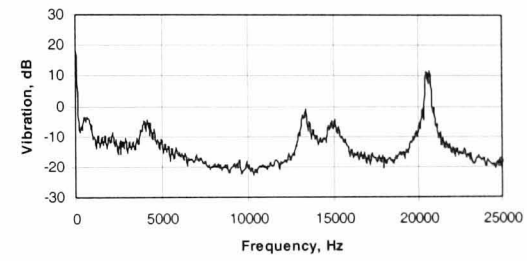

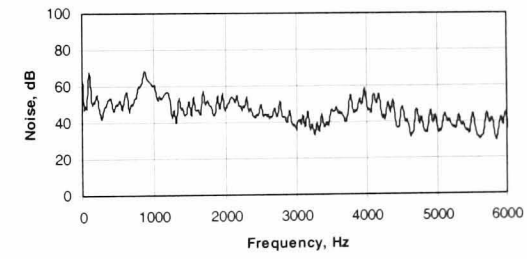

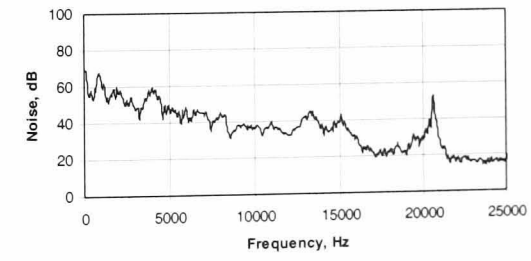

(a) *No time delay*

(b) *130μs time delay*

Fig. 5.7ii *Voltage PWM control under ≈75% load conditions at 1000rpm*

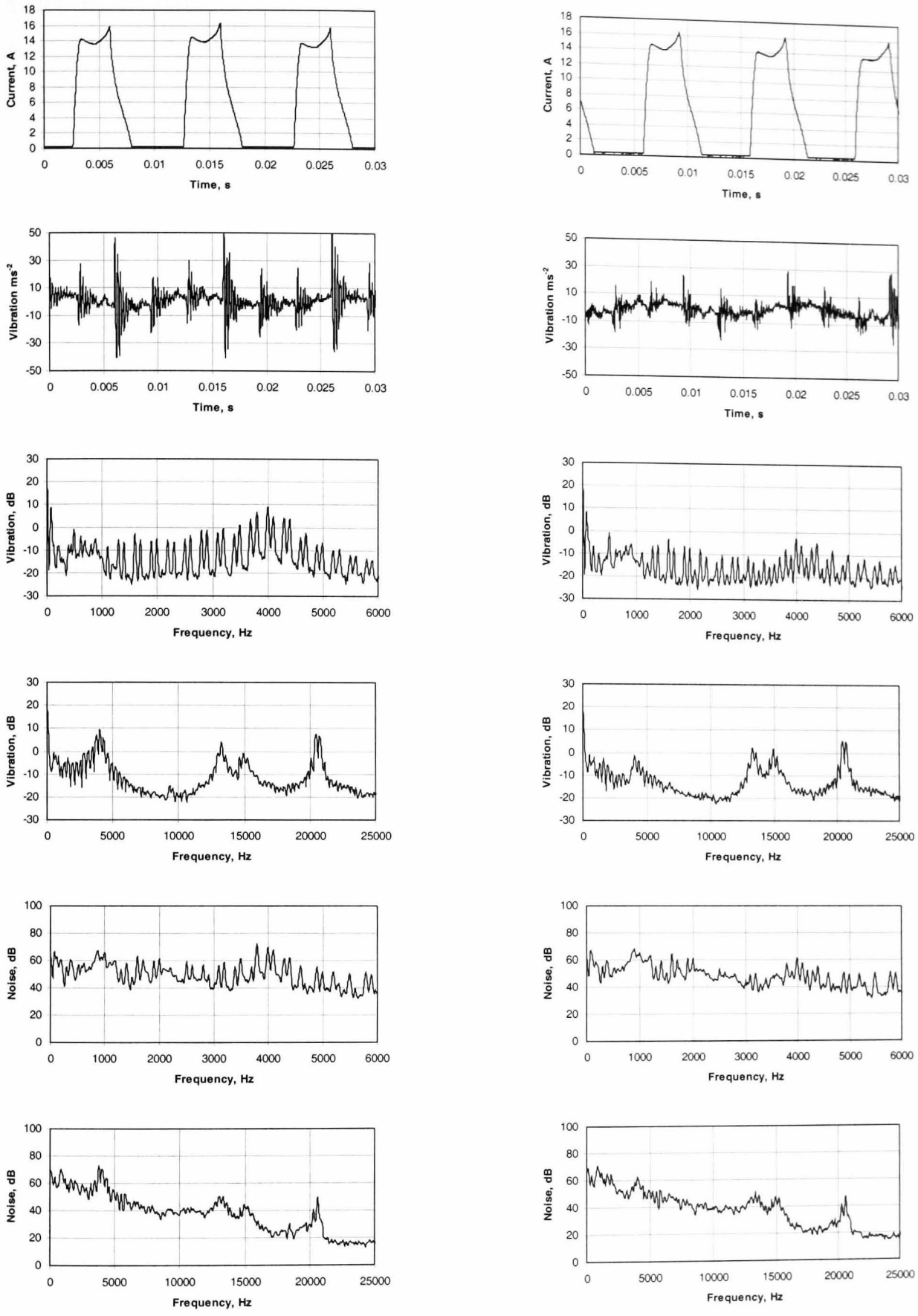

(a) *No time delay* **(b)** *130μs time delay*

Fig. 5.7iii *Voltage PWM control under ≈75% load conditions at 1500rpm*

5.5 Current Control

The phase current waveforms, the time domain vibration and the noise and vibration spectra with and without active vibration cancellation, for both no-load and load operation, are shown in **Figs. 5.8** and **5.9**, respectively. They enable the performance of the machine when operated under normal current control to be compared with that which results with the active cancellation. For all the test conditions, the phase current waveforms with and without the time delay are similar.

While running at 500rpm on no-load, **Fig. 5.8i**, it is observed that the introduction of the time delay is ineffective in reducing the time domain vibration. However, although there is a significant difference between the waveforms which are obtained with and without the time delay, they exhibit similar levels of vibration. The noise and vibration in the 0-6kHz spectra provide little, if any, detail regarding the individual peaks, as was obtained for both single pulse and voltage PWM control. This is attributed to the variable switching frequency associated with the form of current control employed, as discussed in Chapter 4. On the 0-25kHz frequency spectra, the magnitude of the vibration peak associated with mode 2 is only slightly higher when the time delay is implemented, whereas the associated noise peak is increased more significantly. Further, the magnitude of the peak associated with mode 4 in the noise and vibration spectra are essentially the same both with and without the time delay. However, a peak associated with mode 3 is introduced into the vibration spectrum when operated with the time delay, although relatively small. This is attributed to the effect of rotor eccentricity. When load is applied, **Fig. 5.9i**, the time domain vibration is generally greater when the machine is operated with the time delay. Further, the noise and vibration peaks associated with mode 2 increase significantly, whereas those associated with the natural frequency of mode 4 decrease significantly.

When operating on no-load at 1000rpm, **Fig. 5.8ii**, the oscillations in the time domain vibration are less severe after the time delay is introduced. However, it will be observed that the time domain vibration is not periodic and although the vibrations are less severe this is not attributed simply to a suppression of the mode 2 oscillation. This is reflected in the associated noise and vibration spectra in which the time delay has an insignificant influence on the peaks associated with mode 2. Further, the vibration peak associated with mode 4 is observed to reduce significantly whilst the associated noise peak reduces slightly, whereas the noise peak associated with mode 3, which is present in the

vibration spectrum, is observed to increase slightly. When the load is applied at 1000rpm, **Fig. 5.9ii**, the time domain vibration reduces significantly, as do the vibration and noise peaks associated with mode 2. Further, the introduction of the time delay does not change the magnitude of the noise and vibration peaks associated with modes 3 and 4.

At 1500rpm, the time domain vibration is observed to be lower both on no-load, **Fig. 5.8iii**, and, more significantly, when on-load, **Fig. 5.9iii**. However, when the machine is loaded the time delay has a negligible effect on the noise and vibration, whereas on no-load the noise and vibration peaks associated with mode 2 are reduced significantly. Further, the vibration peak associated with mode 3 is also reduced, whilst the peak associated with mode 4 is largely unaffected.

In summary, when the vibration cancellation method is applied under current control it is less effective than when applied under single pulse mode or voltage PWM control. Further, the influence which it has on the noise and vibration is not consistent, which reflects the unpredictable nature of the behaviour under current control. In addition, the current rise and decay times and the associated rates of change of current reflect this as will be evident from **Tables 5.6** and **5.7**. On no-load, the rate of decay of current is generally greater with the active time delay implemented, whereas it is generally smaller with the delay when load is applied. However, despite the lower rate of decay of current which results when operating under load at 500rpm with the time delay, a significantly higher vibration and noise level is produced. Although the switching noise which is associated with the method of current control, which has been employed, does influence the noise and vibration, the time delay of the zero-voltage loop actually varies to that of the applied delay, thus influencing the effectiveness of the active vibration cancellation technique. This is discussed in the next section, and although it is more significant with current control it is also an issue with voltage PWM control, especially as the PWM switching frequency is reduced.

Table 5.6 *Comparison of current rise and decay times, together with corresponding rates of change of current, for control with and without time delay, no-load*

Speed (rpm)	Rise time (ms)/di/dt (As^{-1})		Decay time (ms)/di/dt (As^{-1})	
	No time delay	Time delay	No time delay	Time delay
500	0.36/21408	0.40/17303	1.2/4264	1.3/4393
1000	0.28/26900	0.31/25319	1.28/5138	1.3/5230
1500	0.31/28206	0.40/21123	1.16/5834	1.31/5534

Table 5.7 *Comparison of current rise and decay times, together with corresponding rates of change of current for control with and without time delay, ≈75% load*

Speed (rpm)	Rise time (ms)/di/dt (As^{-1})		Decay time (ms)/di/dt (As^{-1})	
	No time delay	Time delay	No time delay	Time delay
500	0.49/21433	0.5/18686	1.6/5214	1.7/4825
1000	0.46/27437	0.52/24344	1.9/6149	1.6/5518
1500	1.04/13482	1.1/12508	2.01/7007	2.13/6319

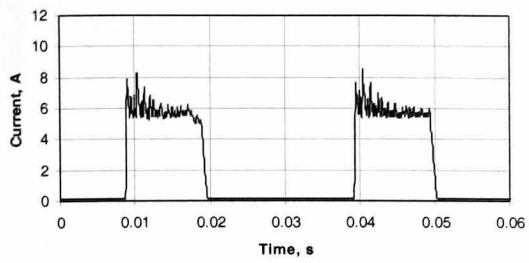

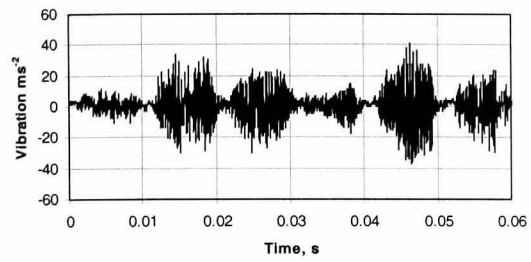

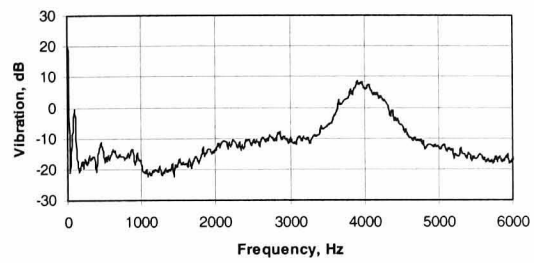

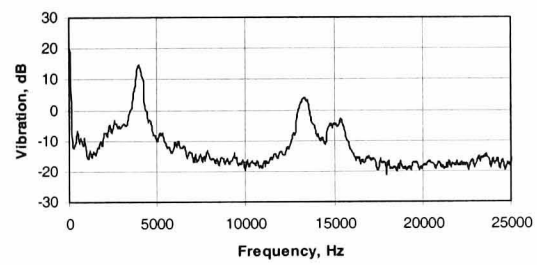

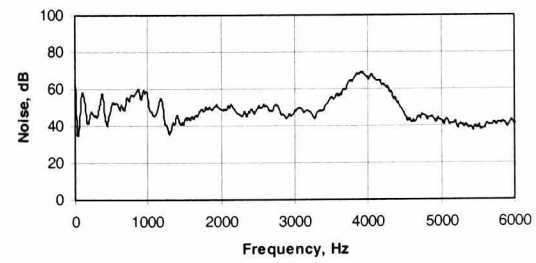

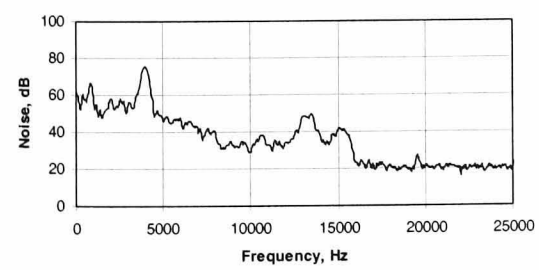

(a) *No time delay*

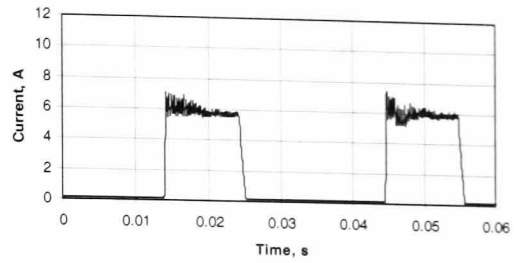

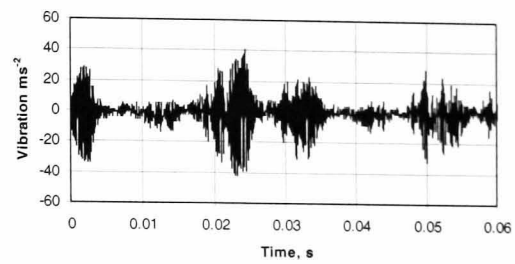

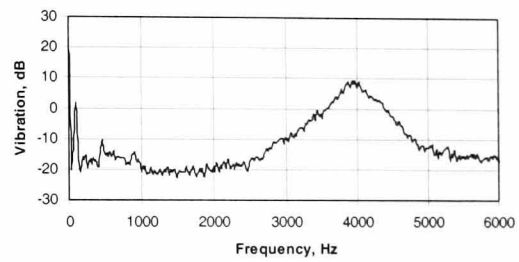

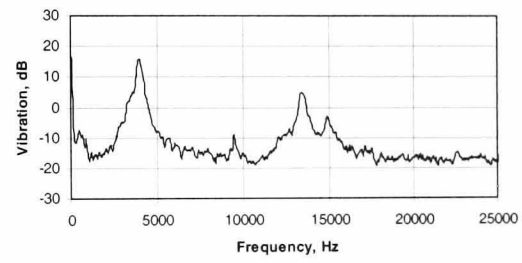

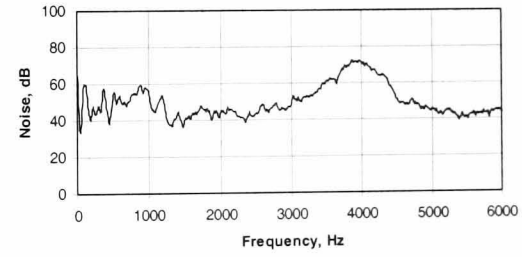

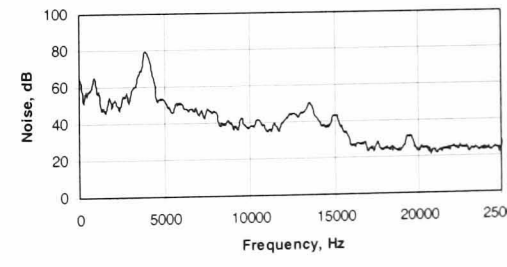

(b) *130μs time delay*

Fig. 5.8i *Current control, no-load at 500rpm*

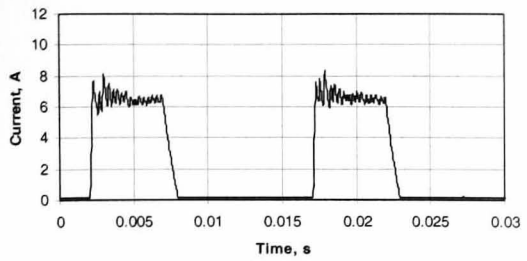

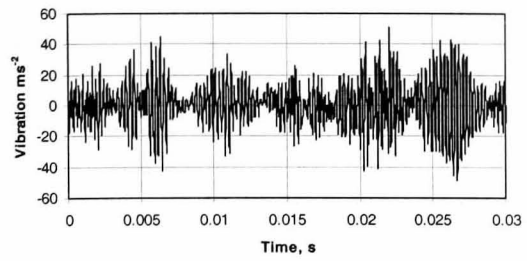

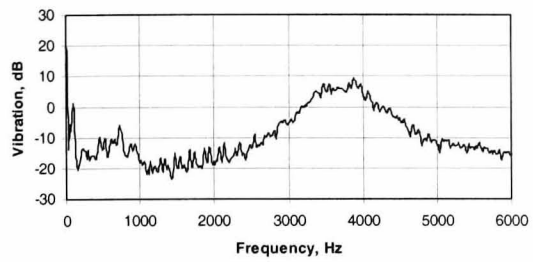

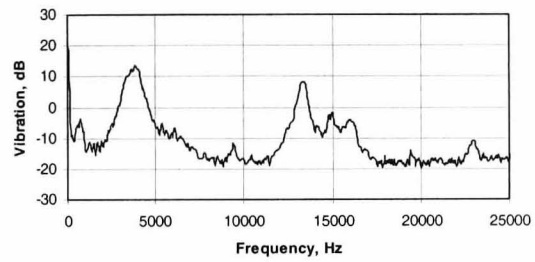

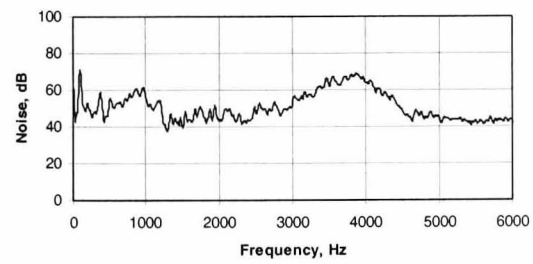

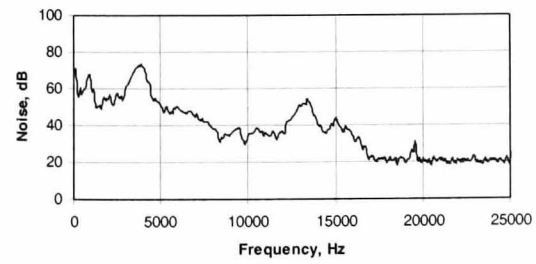

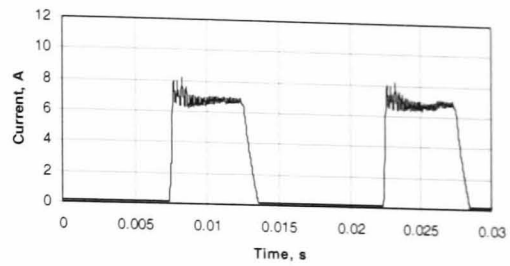

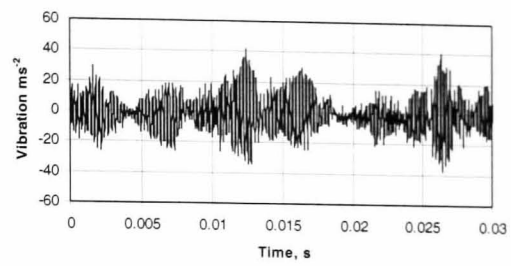

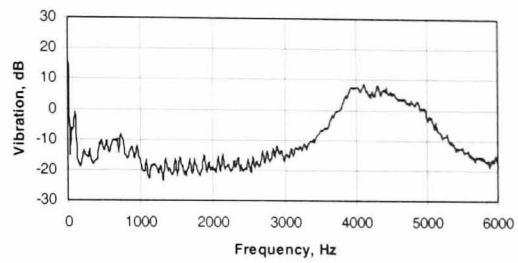

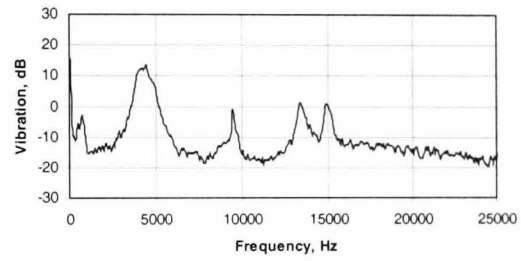

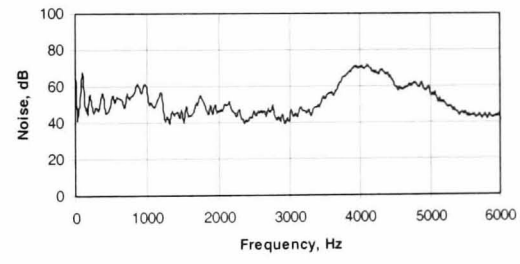

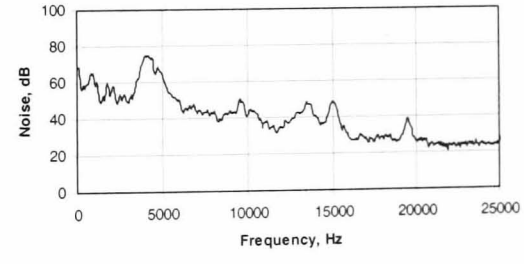

(a) *No time delay*

(b) *130μs time delay*

Fig. 5.8ii *Current control, no-load at 1000rpm*

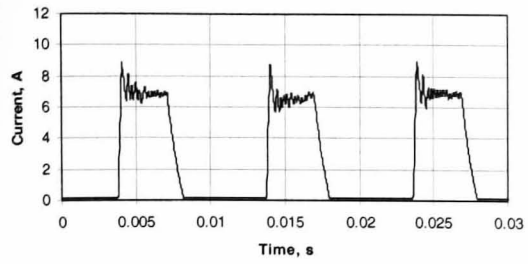

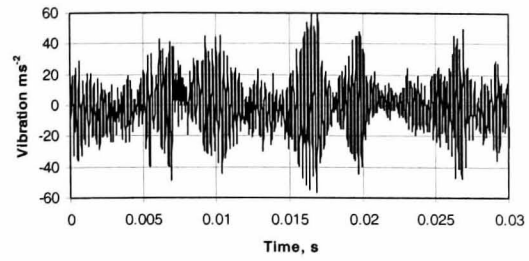

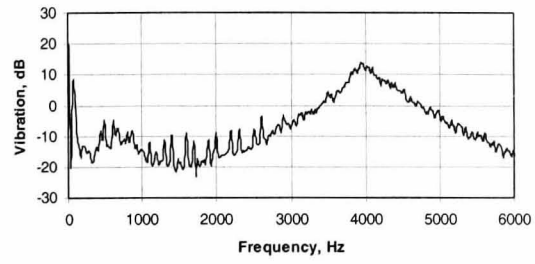

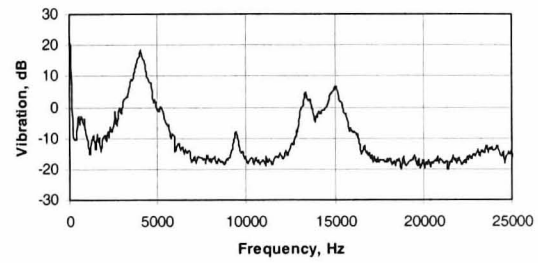

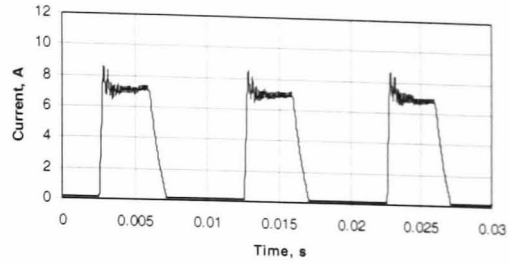

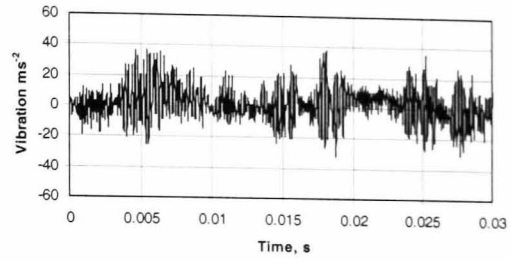

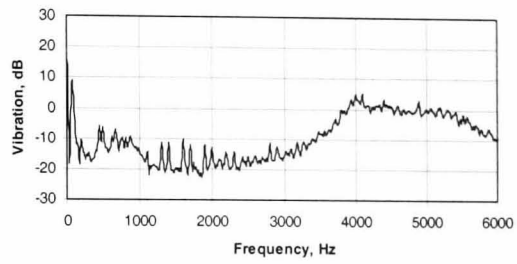

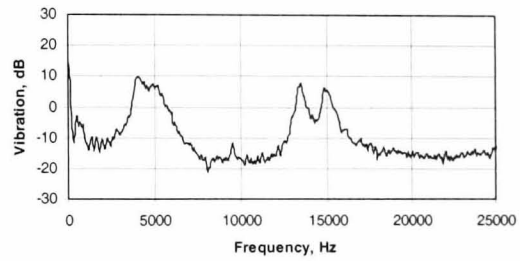

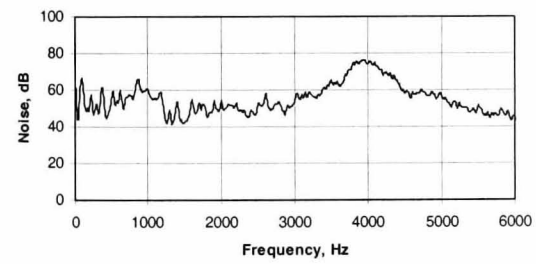

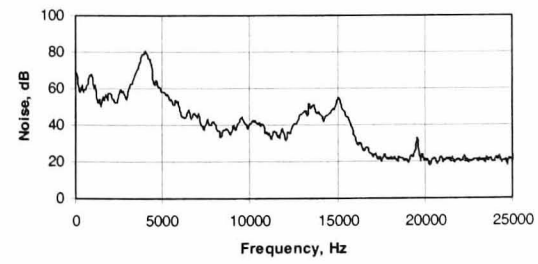

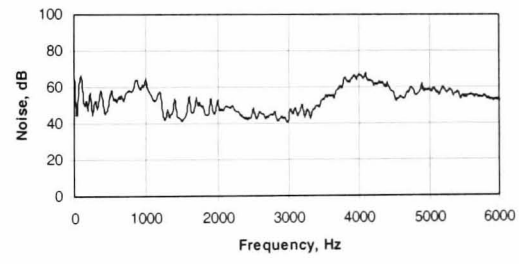

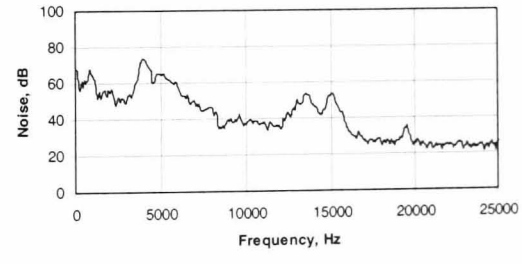

(a) *No time delay*

(b) *130μs time delay*

Fig. 5.8iii *Current control, no-load at 1500rpm*

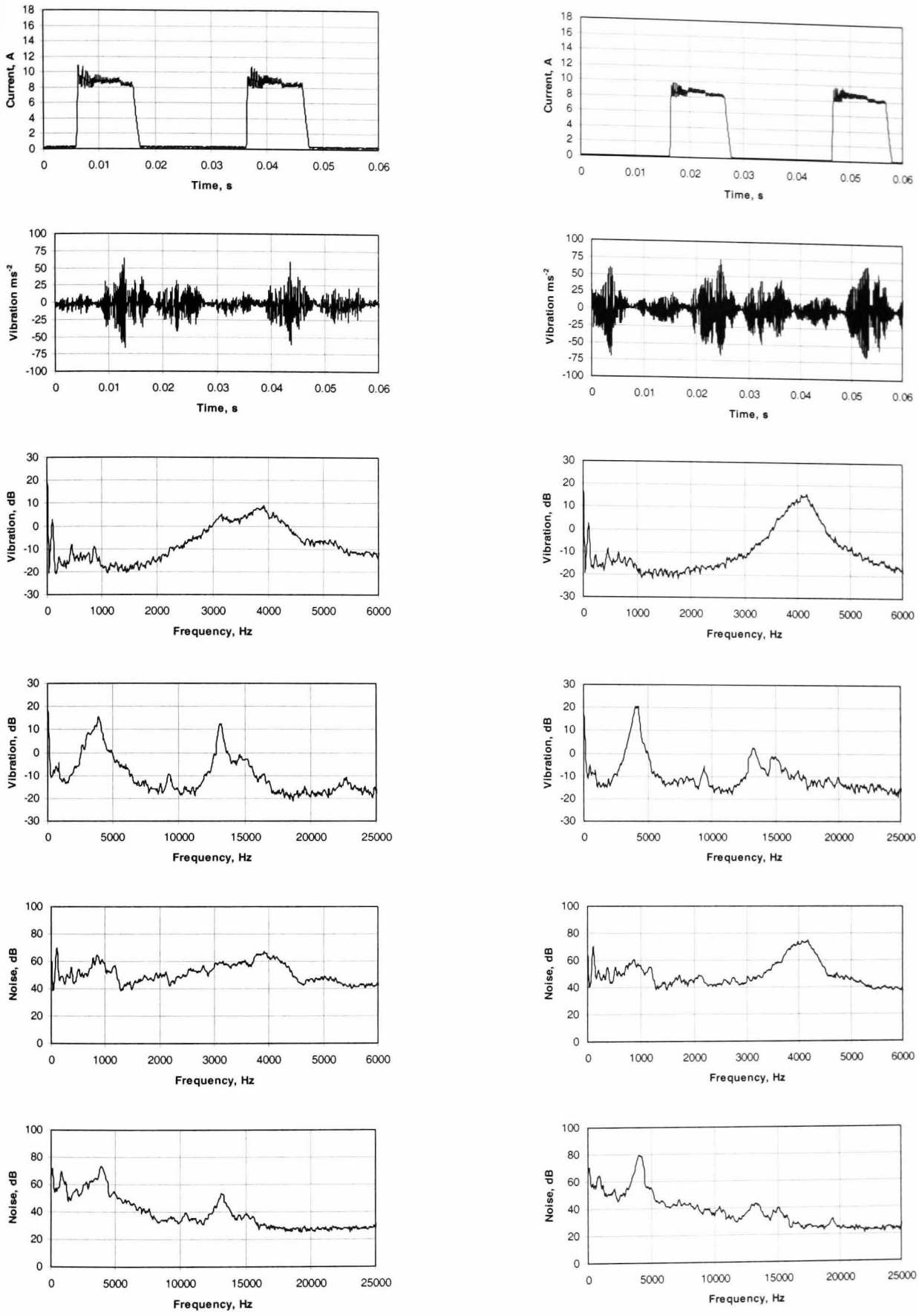

(a) *No time delay* **(b)** *130μs time delay*

Fig. 5.9i *Current control under ≈75% load condition at 500rpm*

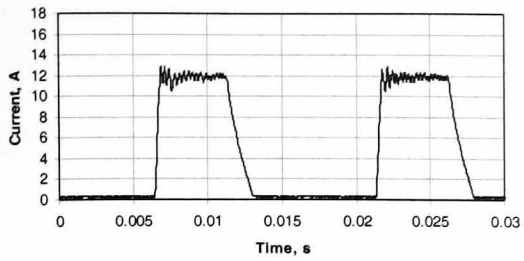

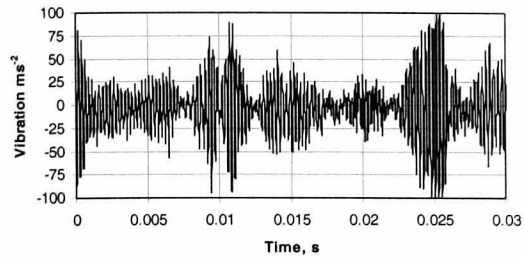

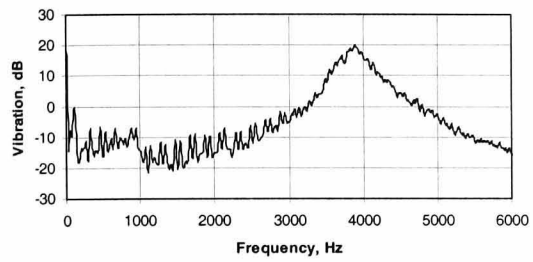

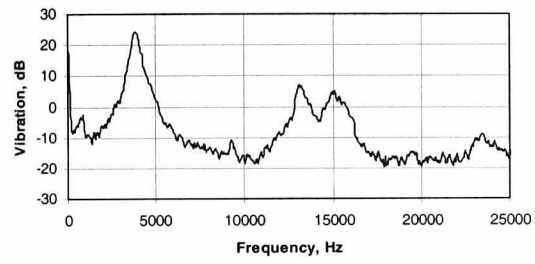

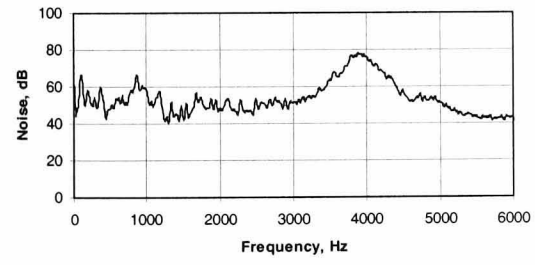

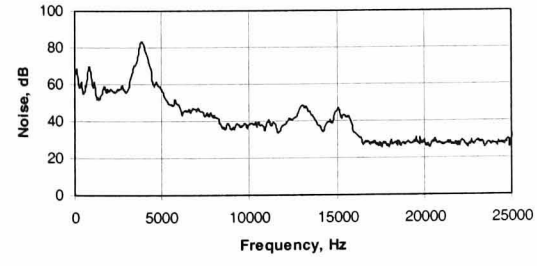

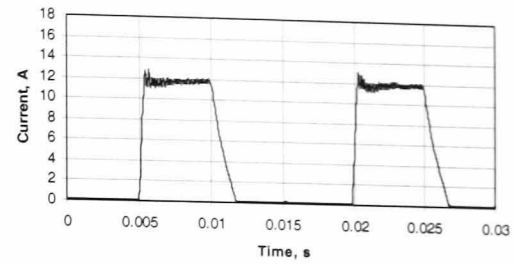

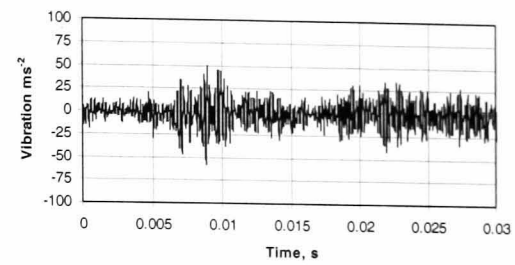

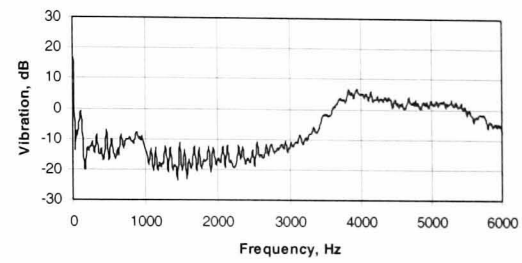

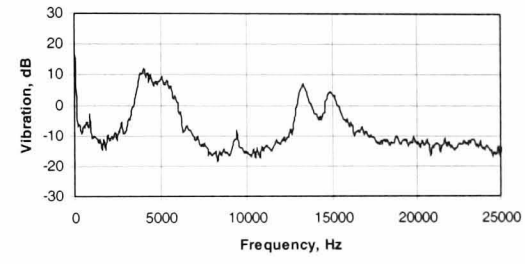

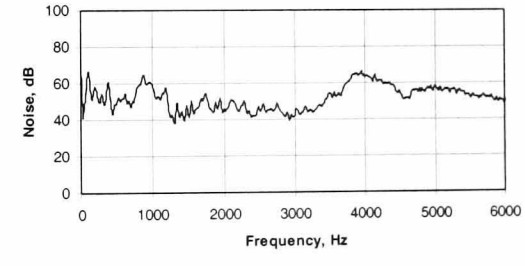

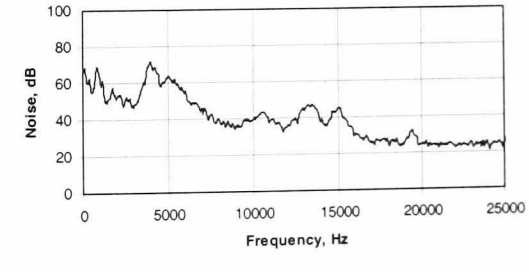

(a) *No time delay*

(b) *130μs time delay*

Fig. 5.9ii *Current control under ≈75% load conditions at 1000rpm*

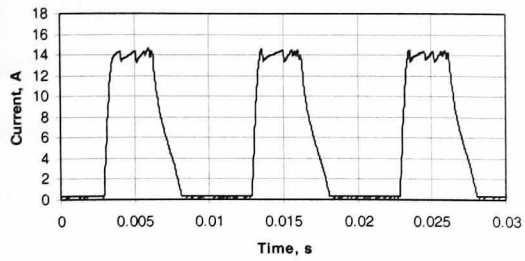

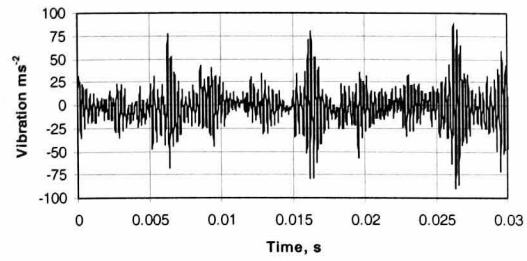

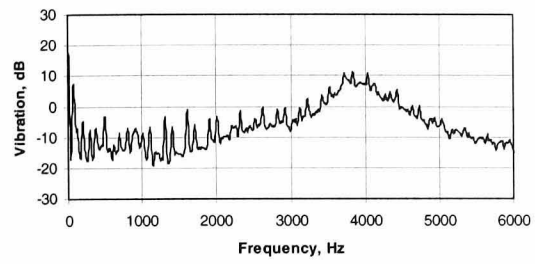

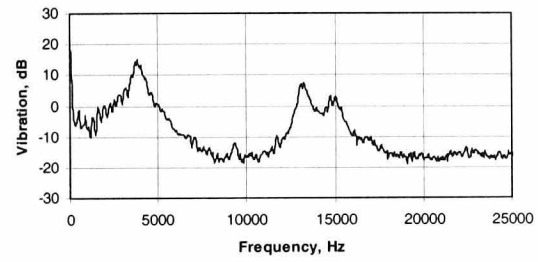

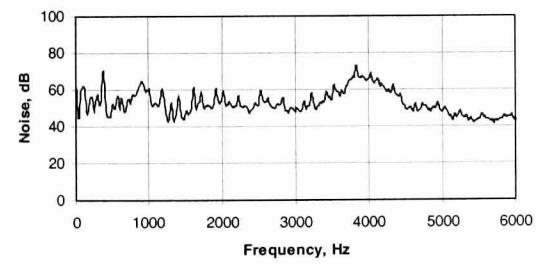

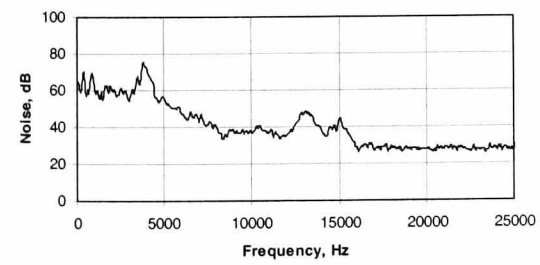

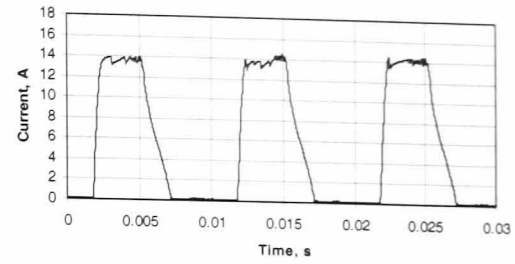

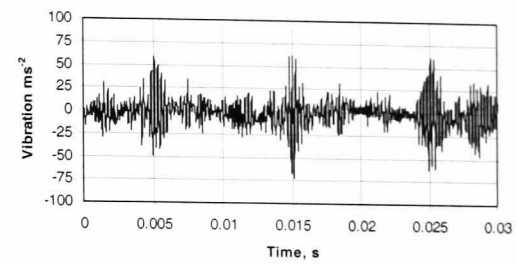

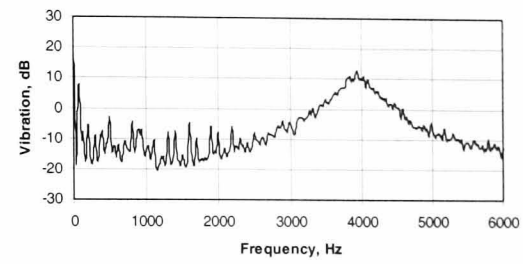

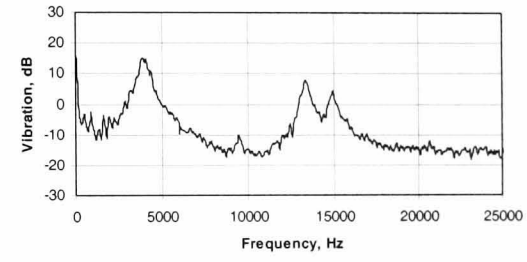

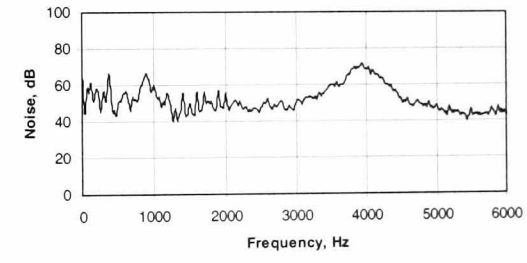

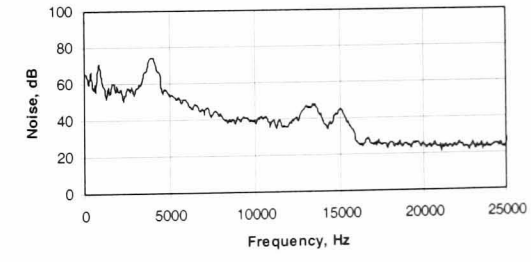

(a) *No time delay*

(b) *130μs time delay*

Fig. 5.9iii *Current control under ≈75% load conditions at 1500rpm*

5.6 Problem with active noise and vibration cancellation technique

In order to highlight the problem with the accuracy of the time delay duration, which was encountered with the active vibration cancellation technique, it is necessary to outline the software implementation and describe the control method for the power switching devices.

In the software, the state of the power switches is determined by the 'action control register', (ACTR), where bits 0-3 determine the states of the power switches of phase A, bits 4-7 determine the states of the power switches of phase B, and bits 8-11 determine the states of the power switches of phase C, as summarised in **Table 5.8**. Due to the fact that there are two active switches per phase, there are two control bits available to control each of the switches independently. This is also shown in **Table 5.8**, where S1 and S2 for each phase are configured as the commutation switch and PWM switch, respectively. These different states are defined in **Table 5.9** where 'forced high' and 'forced low' define the switches as being on or off, respectively, and are used to define the states of the commutation switches. Active high and active low enable the switch to be turned on or off depending on the value returned from the speed error to achieve voltage PWM control for operating speeds below that for single pulse operation. Once the speed demand is so high that the full dc voltage is required to magnetise the machine, the duty cycle of the PWM controller becomes 100%, when active low/active high act as commutation states.

Firstly, it is assumed that the machine is operating in single pulse mode with a conduction angle equal to $1/m_{ph}$ of the rotor pole-pitch, where m_{ph} is the number of phases. This implies that each phase of the machine is excited independently for 120° electrical. Thus, the experimental machine has a conduction period of 30° mechanical. Typical switch and phase voltages are shown in **Fig. 5.10** for a phase excitation sequence A, B, C, A, B, etc, where the turn-off point of phase A is indicated as instant 'a', at which point phase B turns on. For the implementation of the delay only one of the switches of phase A is opened at 'a' whilst the other remains closed to impose the 'zero voltage' loop, the duration of which is determined by the natural frequency of mode 2. Therefore, at instant 'b' the second switch is opened, at which point the 2^{nd} vibration is induced, as explained is section 5.1. This process is repeated for each phase, and due to the action of single pulse mode all switching instants are well defined and, thus, the time

delay duration is accurate. These tasks are undertaken by the software algorithm, which is initialised by the shaft encoder count.

When the encoder count matches that stored in the encoder compare register the commutation ISR is initiated. For operation without the active time delay this ISR routine ensures that the turn-off of a currently excited phase and the turn-on of the subsequent phase occur simultaneously. However, the active vibration cancellation technique requires the currently excited phase to be switched to the zero-voltage loop whilst the next phase is switched on, thereby necessitating the opening of only one of the power switches. Subsequently, the remaining switch needs to be turned-off at a later pre-determined instant of time. Thus, prior to the turn-on point of phase B, i.e. prior to instant 'a' in **Fig. 5.10**, the devices are configured as shown in **Table 5.10**. Subsequently, at instant 'a' the commutation ISR reconfigures the power devices as shown in **Table 5.11**, where it can be seen that phase B is initialised and phase A is forced into the zero-voltage loop. Once the value of the timer configured for the time delay matches that which is stored in the time delay compare register, the delay ISR is enabled to end the zero-voltage loop at instant 'b' in **Fig. 5.10**, by updating the power switch states to those shown in **Table 5.12**. The delay ISR flag which is set during the commutation ISR enables the software to determine which phase to disabled within the delay ISR. **Fig. 5.10** shows a schematic of the software implementation of the active vibration cancellation technique.

Table 5.8 *Control register outlining control bits for inverter switches*

ACTR	15	14	13	12	11	10	9	8	7	6	5	4	3	2	1	0
					Comm. (S1c)		PWM (S2c)		Comm. (S1b)		PWM (S2b)		Comm. (S1a)		PWM (S2a)	
					Phase C				Phase B				Phase A			

Table 5.9 *Control bits for switches*

0	0	Forced Low	(OFF)
0	1	Active Low	()
1	0	Active High	()
1	1	Forced High	(ON)

Table 5.10 *Values assigned to inverter switch control register prior to instant 'a' in* **Figs. 5.10 & 5.12**, *Phase A under normal operation*

ACTR	15	14	13	12	11	10	9	8	7	6	5	4	3	2	1	0
					0	0	0	0	0	0	0	0	1	1	1	0

Table 5.11 *Values assigned to inverter switch control register at instant 'a' in* **Figs. 5.10 & 5.12**, *to activate Phase B and impose the zero-voltage loop on Phase A (Commutation ISR)*

ACTR	15	14	13	12	11	10	9	8	7	6	5	4	3	2	1	0
					0	0	0	0	1	1	1	0	1	1	0	0

Table 5.12 *Values assigned to inverter switch control register at instant 'b' in* **Figs. 5.10 & 5.12**, *maintaining Phase B active and disabling Phase A (Delay ISR)*

ACTR	15	14	13	12	11	10	9	8	7	6	5	4	3	2	1	0
					0	0	0	0	1	1	1	0	0	0	0	0

Whilst the implementation of the technique is very effective for single pulse operation, due to the fact that the falling edge at phase turn-off is synchronised with the turn-on of the next phase, for chopping control there is potential for an error. This is attributed to the fact that the position of the final falling edge of the voltage from positive voltage to the zero-voltage loop at or around the phase turn-off point depends on the synchronism between the chopping and instant of turn-off, as illustrated in **Fig. 5.12i**, for the case of voltage PWM control. At instant 'a' in **Fig. 5.12i** only one switch is closed since this is the start of the active time delay, then at instant 'b' the 2nd switch is opened. However, due to the end of the dwell period and the chopping action being asynchronous, an

additional period of zero-voltage loop occurs prior to the main zero-voltage loop, the duration of which varies depending on the chopping frequency and the duty cycle (i.e. speed). For example, with a voltage PWM chopping frequency of 20.6kHz and at a speed which requires a duty cycle of 50%, the maximum additional time delay is ≈24μs, **Fig. 5.12ii**, i.e. the total time delay could vary between 130μs to 154μs depending on the synchronism between the PWM and dwell period. This explains the why the technique is less effective when voltage PWM control is employed at a 10.3kHz switching frequency, as highlighted earlier. However, this problem is more severe with current control since the chopping frequency is not constant, such that rather than there being a constant offset between the last falling edge and phase turn-off, the switching instants are randomly asynchronous. This asychronism depends on the speed error, the winding inductance and the sampling frequency, and, therefore, the additional time delay cannot be predicted and is constantly varying. Typical delay times measured for the zero-voltage loop duration are shown in **Figs. 5.13** and **5.14** for current and voltage PWM control respectively. Typically the time delay which results under current control varies by up to 275μs, whereas under voltage PWM control with a PWM switching frequency of 20.6kHz the correct time delay is achieved and it is no worse than 150μs with a switching frequency of 10.3kHz. The influence of the zero-voltage loop variation on the vibration cancellation is discussed further in section 5.7.

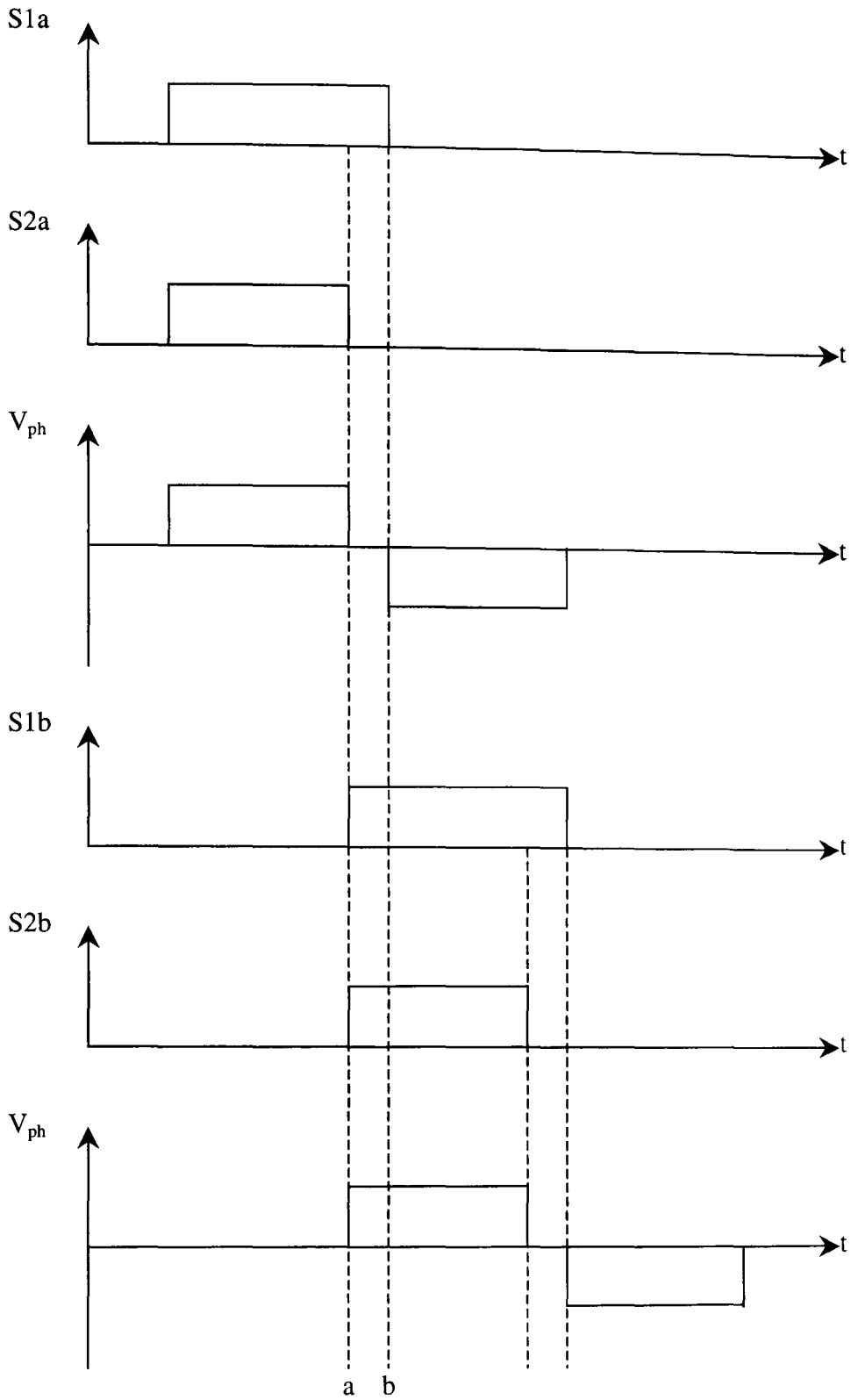

Fig. 5.10 *Active delay imposed during single pulse operation of machine*

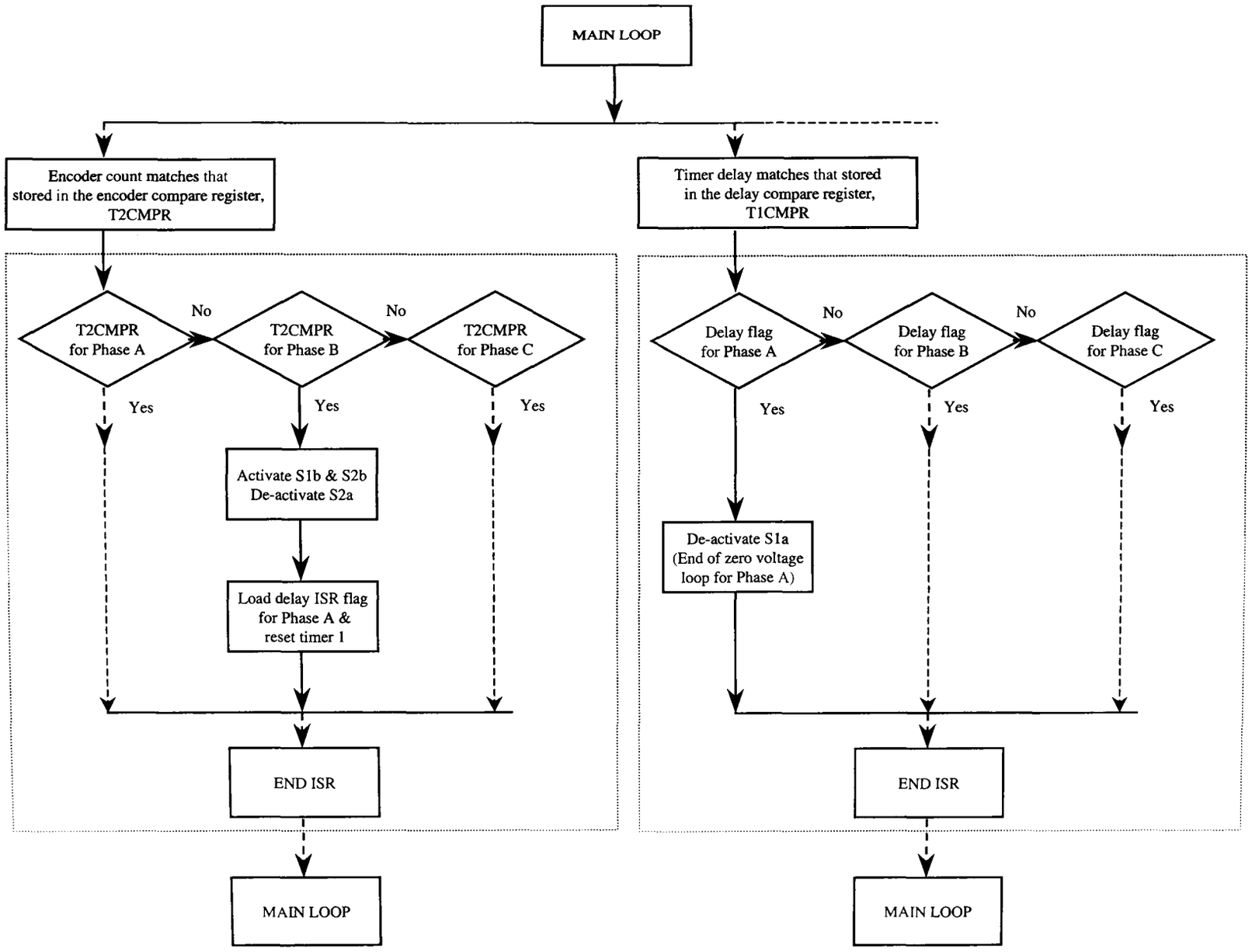

Fig. 5.11 *Flow diagram outlining the software implementation of the time delay for cancelling the mode 2 vibration induced by Phase A at turn-off*

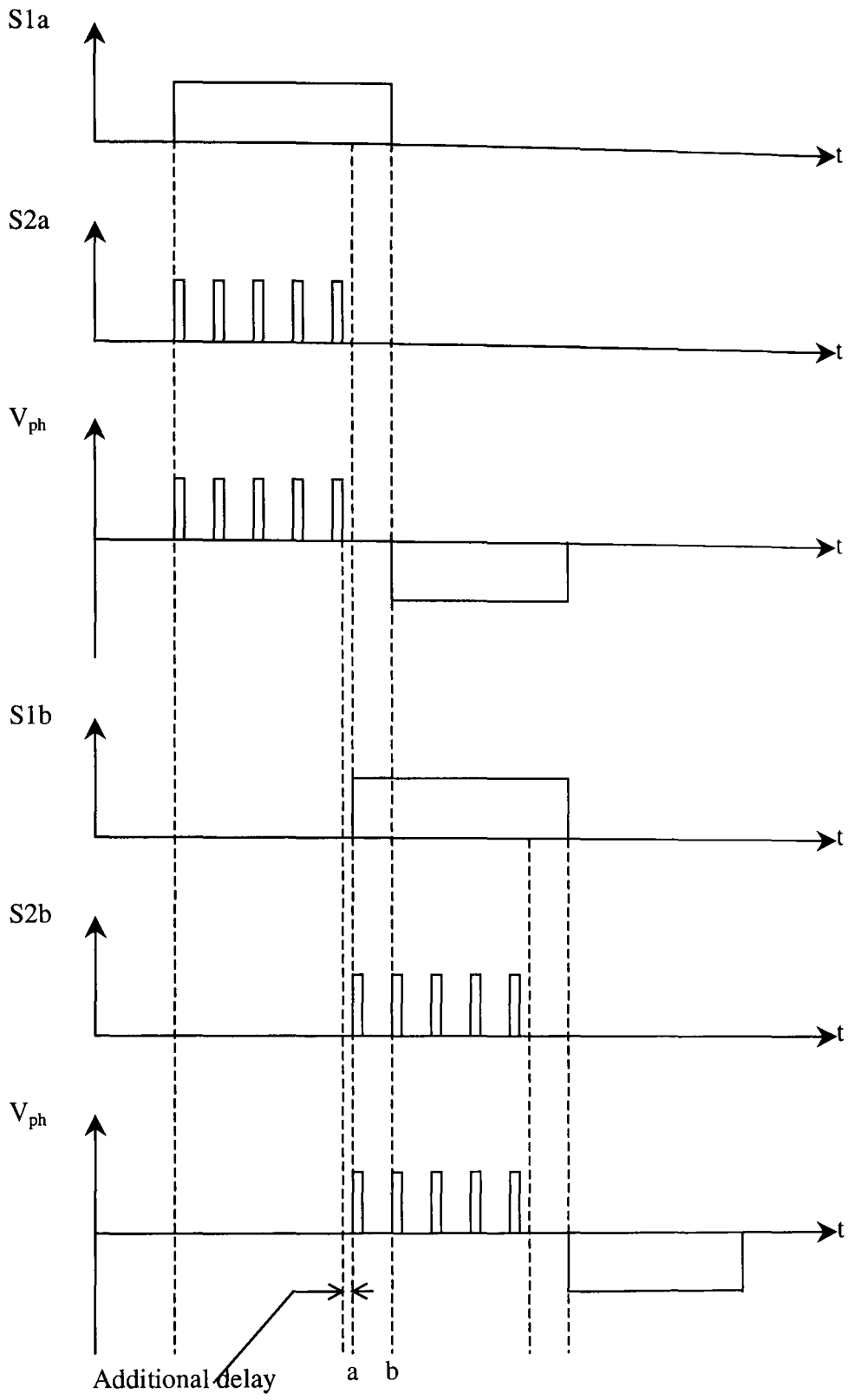

Fig. 5.12i *Active time delay together with additional time delay imposed during chopping control of machine*

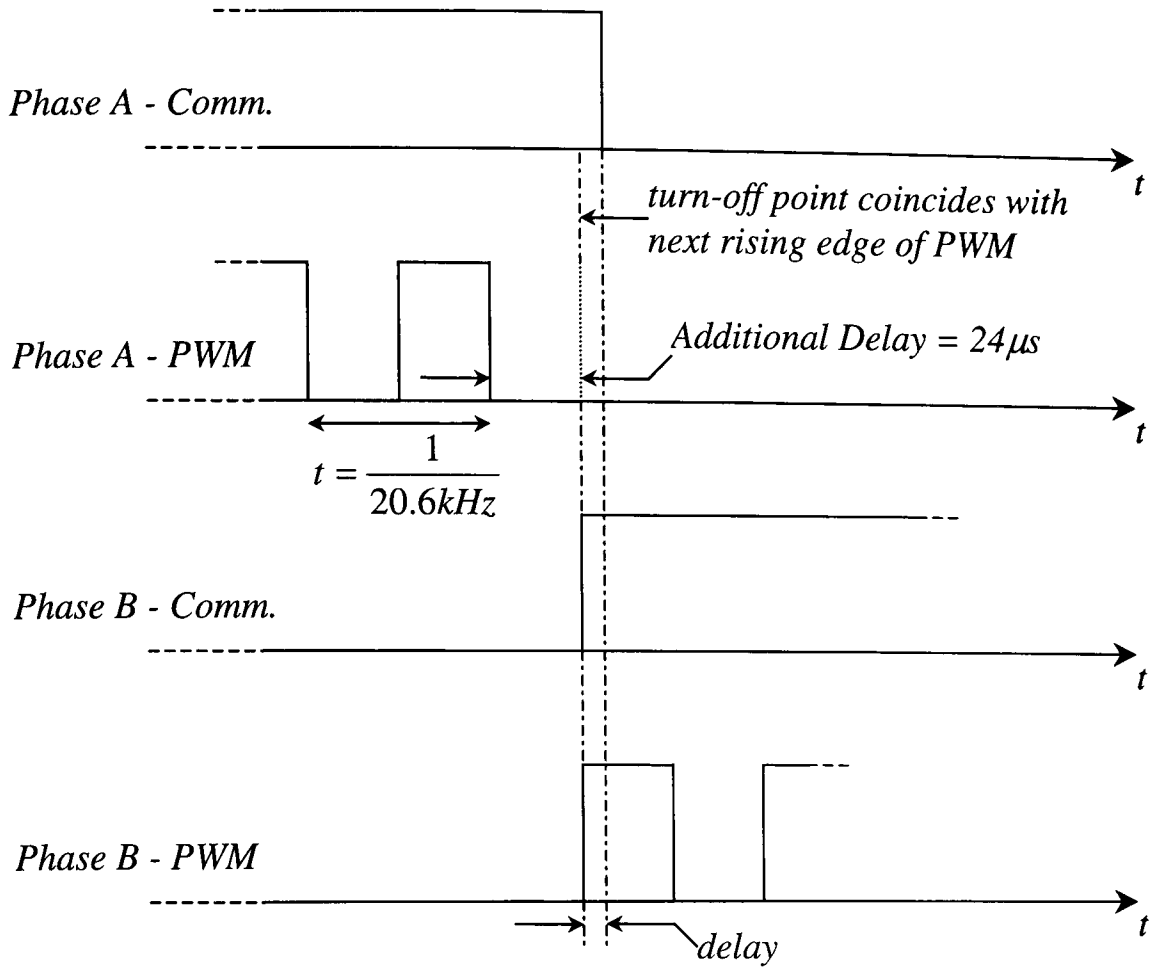

Fig. 5.12ii *Active time delay together with additional time delay imposed during chopping control of machine*

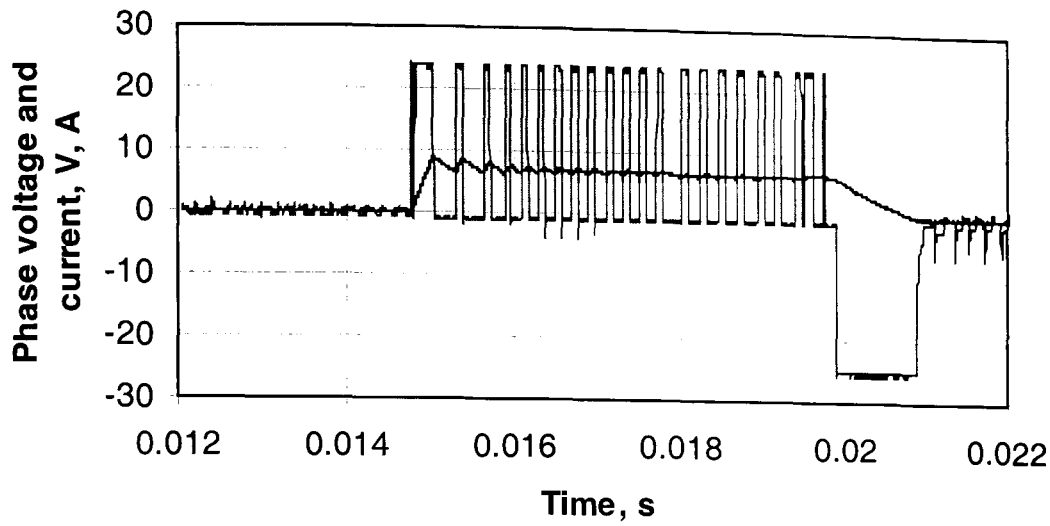

(a) *150μs delay*

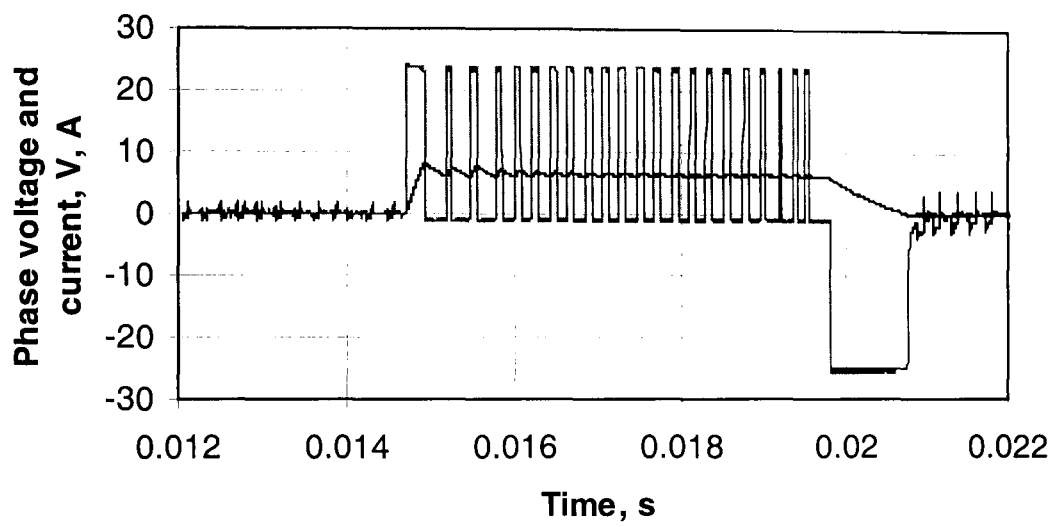

(b) *275μs delay*

Fig. 5.13 *Measured time delays under current control at 1000rpm for the same operating conditions*

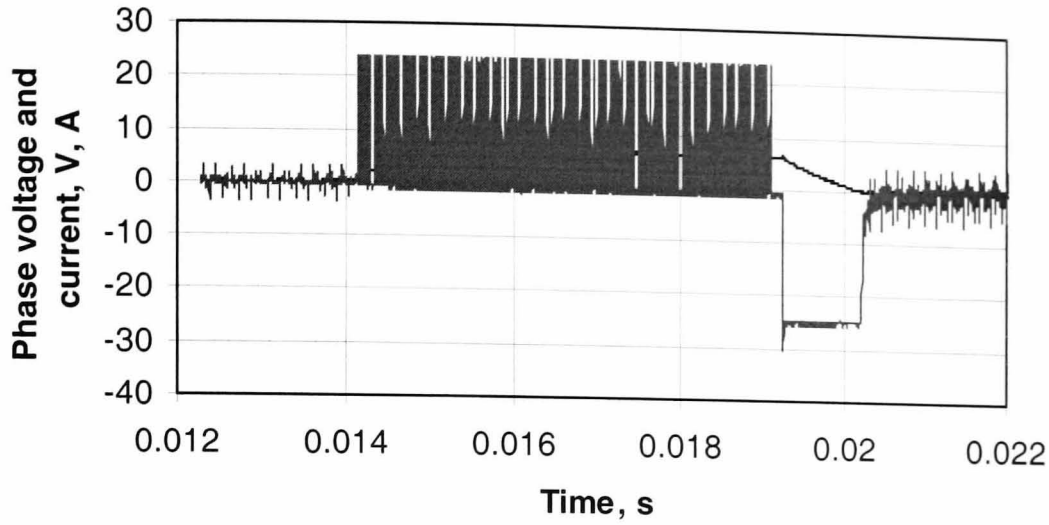

(a) *20.6kHz PWM switching frequency, 130μs time delay*

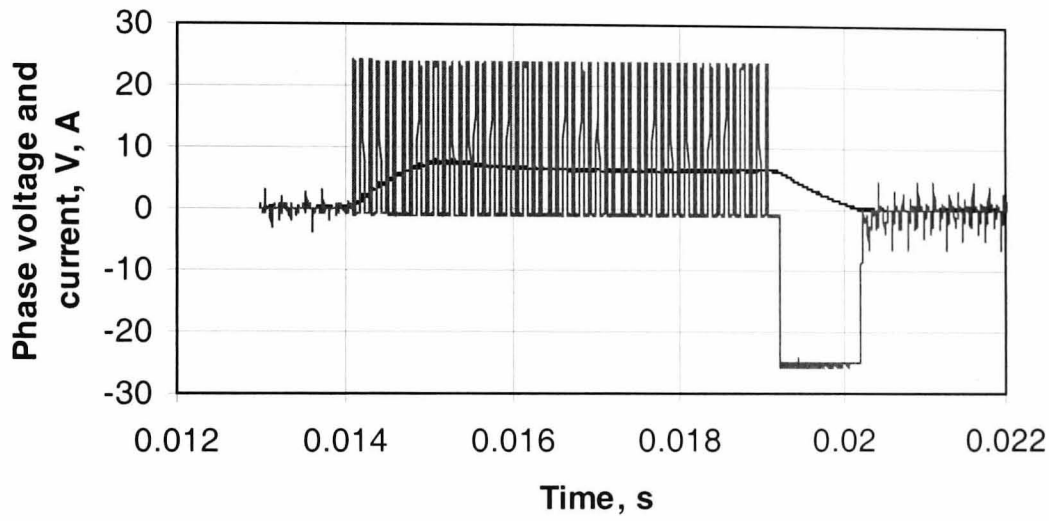

(b) *10.3kHz PWM switching frequency, 150μs time delay*

Fig. 5.14 *Measured time delays under voltage PWM control at 1000rpm for the same operating conditions*

5.7 Discussion on zero voltage duration

As discussed in Chapter 3, all the natural frequencies which are associated with even mode numbers can potentially be excited during the operation of a 6/4 SR machine. Throughout this and the previous chapter, it has been observed that vibration mode 2 and vibration mode 4 are excited during operation of the experimental machine. Further, since the associated noise lies within the audible frequency range, both contribute to the dBA noise level. This behaviour limits the 'effectiveness' of the active vibration cancellation technique, since only the vibration which is induced by the excitation of a single natural frequency is cancelled. Therefore, although the method is generally applied to cancel the vibration which is induced by the most dominant natural frequency, if there are a number of natural frequencies, which lie within the audible frequency range, and/or dual frequencies associated with them, in particular the fundamental, the technique will clearly be less effective.

5.7.1 Delay time for modes 2 and 4

In order to assess the significance of this issue, the active time delay was also selected to correspond with the vibrations associated with mode 4. The stator natural frequencies of modes 2 and 4 are given in **Table 5.13** together with their respective delay times. The machine was run on both no-load and at ≈75% load, with both voltage and current control. The measured dBA noise level which result with time delays corresponding to mode 2, and mode 4, and with no time delay are given in **Figs. 5.15 & 5.16** and **Figs. 5.17 & 5.18** for voltage and current control, respectively.

Table 5.13 *Modal frequencies and their respective delay times*

Mode	Natural frequency (Hz)	Time delay (μs)
2	3840	130
4	13370	37

Under voltage PWM control, it will be observed that when the time delay to suppress vibration mode 2 is imposed, it has the greatest effect in reducing the noise level at all speeds, both on no-load and at ≈75% load, **Figs. 5.15** and **5.16**, respectively. This is expected due to the fact that mode 2 is the fundamental stator natural frequency for the experimental machine, and does not have any dual frequency components. Further, at

the maximum speed of 2500rpm the phase excitation frequency is 167Hz, which is significantly lower than the natural frequency of mode 2, viz. 3840Hz, and even lower than that of mode 4, viz. 13370Hz. Thus, the current harmonics which coincide with the natural frequencies of modes 2 and 4 are approximately the 28^{th} and 448^{th}, respectively, thereby highlighting the greater significance of mode 2. If, however, the machine was run at a speed that resulted in an excitation frequency at or around 3840Hz, the fundamental current harmonic (and force harmonic) would be coincident with the natural frequency of mode 2 and induce the greatest vibration and noise. Similarly, if the excitation frequency was 13370Hz, the fundamental would coincide with the natural frequency of mode 4 and this would also result in a higher level of vibration and noise. This was demonstrated by Cameron and Umas, [CAM92], whose initial experiments involved applying a periodic winding excitation to a given phase over a range of frequencies. It was observed that those phase excitation frequencies that were equal in value to the stator natural frequencies resulted in the highest level of noise.

Application of the time delay for mode 4 is also observed to reduce the noise level, but not as significantly as that which results when the time delay for mode 2 is applied. However, it should be noted that implementation of the time delay for mode 4 could also influence the vibration induced by mode 2 due to the fact that the difference in the time delay durations is relatively small. In order to quantify this issue, vibration and noise spectra were measured when the machine was operated without the time delay and with a time delay which corresponds to the cancellation of mode 4. These are shown in **Figs. 5.19** and **5.20**, for the machine running under voltage PWM control at 1500rpm, for both no-load and ≈75% load**,** respectively. On no-load, **Fig. 5.19**, the vibration and noise peaks associated with mode 4 are observed to have reduced in the 0-25kHz frequency range, whereas the vibration peak of mode 2 appears to have increased. However, closer observation of the vibration spectra in the 0-6kHz range shows that the actual peak associated with the natural frequency of mode 2 has not actually increased, rather it is a number of neighbouring peaks which have increased. Therefore, due to the fact that the actual peak at the natural frequency of 3840Hz for mode 2 has not increased, the peaks associated mode 2 in the 0-6kHz and 0-25kHz noise spectra do not increase. Observation of the 0-25kHz vibration spectra when the machine is operated at ≈75% load, **Fig. 5.20**, shows that the reduction in the peak vibration associated with mode 4 is more significant than it was on no-load. This is also reflected in the 0-25kHz noise spectrum. However, both the noise and vibration spectra in the 0-6kHz range exhibit an increase in the

peaks associated with mode 2, and this is reflected in the associated 0-25kHz spectra. However, due to the reduction of the peak associated with mode 4 overall SPL level is reduced, **Fig. 5.16**. Thus, it is concluded that the reduction in dBA which results with the time delay for the cancellation of vibration mode 4 is attributed purely to the reduction of mode 4 and not to any influence it may have on the noise which is associated with the natural frequency of mode 2.

When the machine is operated under current control, the noise levels which are emitted when a time delay which corresponds to either mode 2 or mode 4 is implemented or when no time delay is employed are significantly different to those which result under voltage PWM control. On both no-load and ≈75% load, no time delay generally results in the lowest noise level, whilst a time delay of 37μs results in the highest noise. Again, this is attributed to the problems which were highlighted in section 5.5. The noise levels which result when the machine operates at ≈75% load tend to be more constant, i.e. at all speeds, the noise levels which result with the alternative time delays remain more or less same, except at 500rpm when no time delay results in the highest noise level.

The noise and vibration spectra which result under current control, on no-load at 1500rpm, are shown in **Fig. 5.21** together with the corresponding phase current waveform. It is observed that the magnitude of the vibration peak associated with mode 2 has increased with the implementation of the time delay, compared to that resulting from no-delay, although that associated with mode 4 has reduced. These observations are reflected in the associated noise spectra. When load is applied, again the vibration peak associated with mode 2, **Fig. 5.22**, is observed to increase when the time delay is introduced, whereas its influence on mode 4 is insignificant.

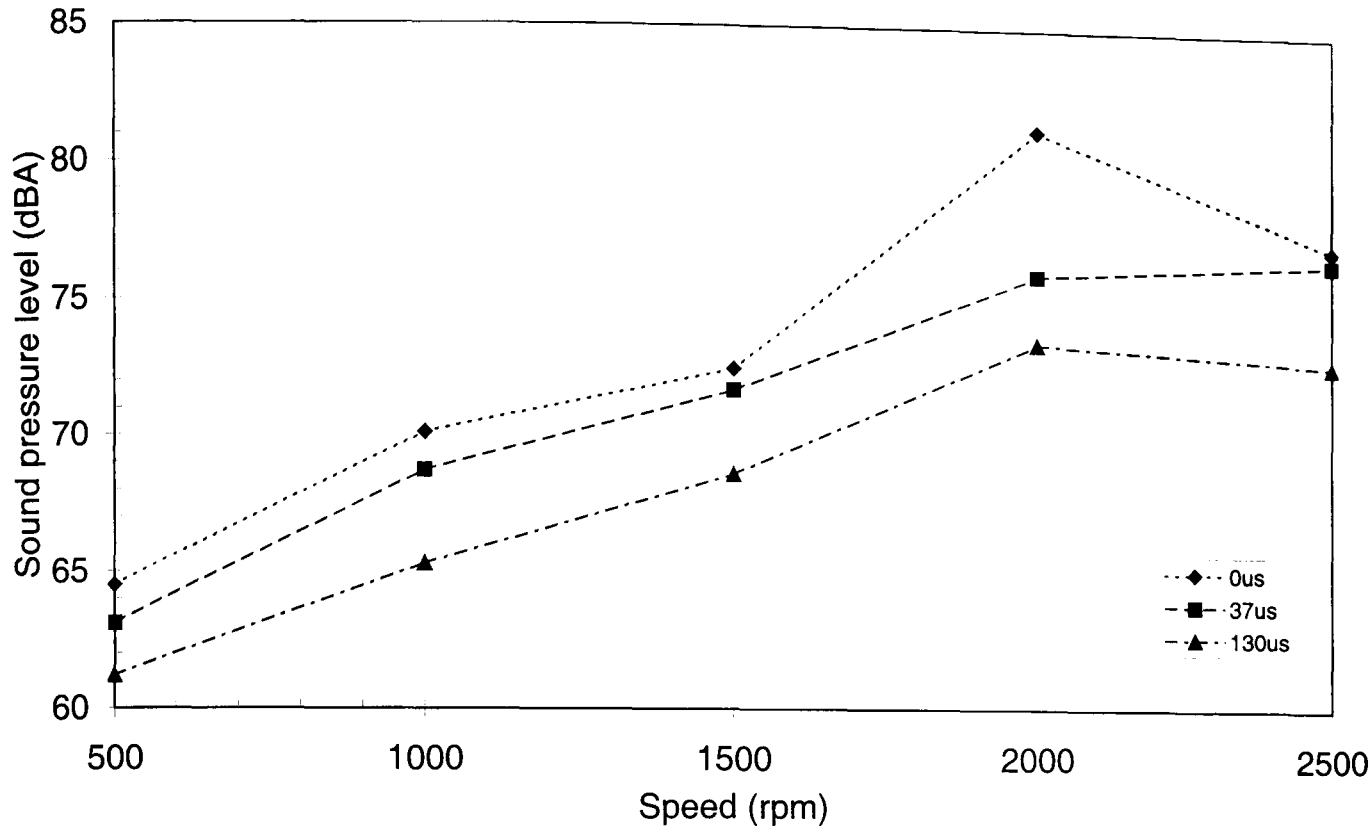

Fig. 5.15 *Comparison of sound pressure level with switching time delays implemented for main modes using voltage PWM control, on no-load*

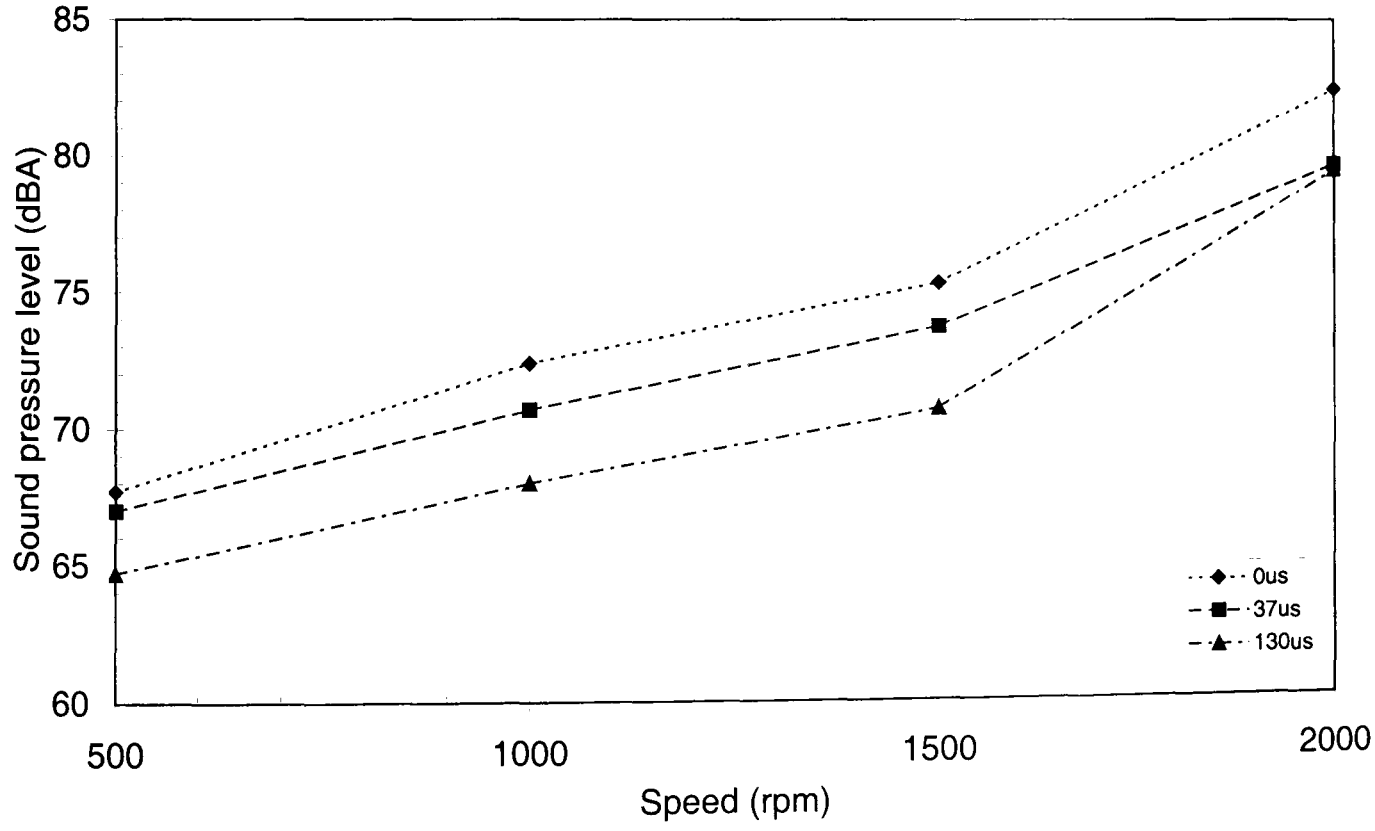

Fig. 5.16 *Comparison of sound pressure level with switching time delays implemented for main modes with voltage PWM control, at ≈75% load*

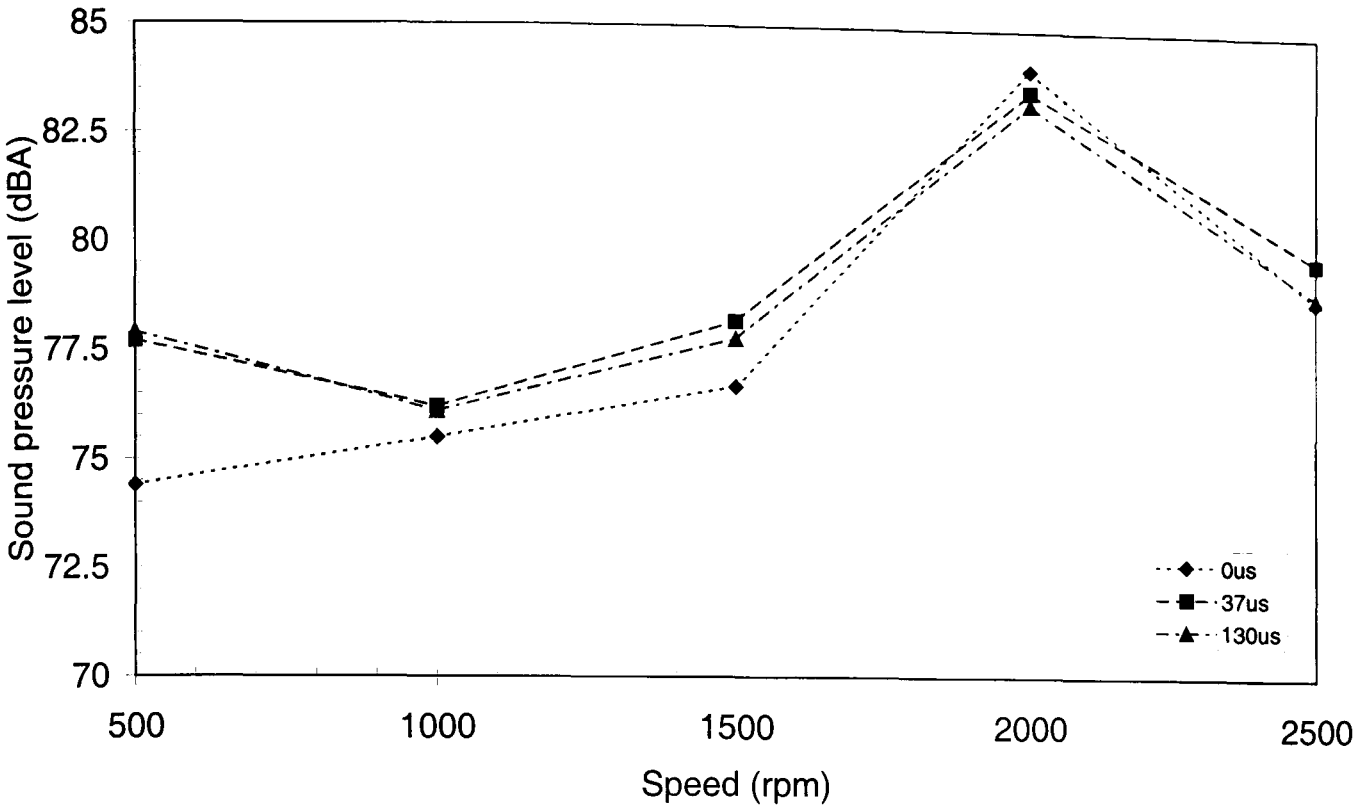

Fig. 5.17 *Comparison of sound pressure level with switching time delays implemented for main modes with current control, on no-load*

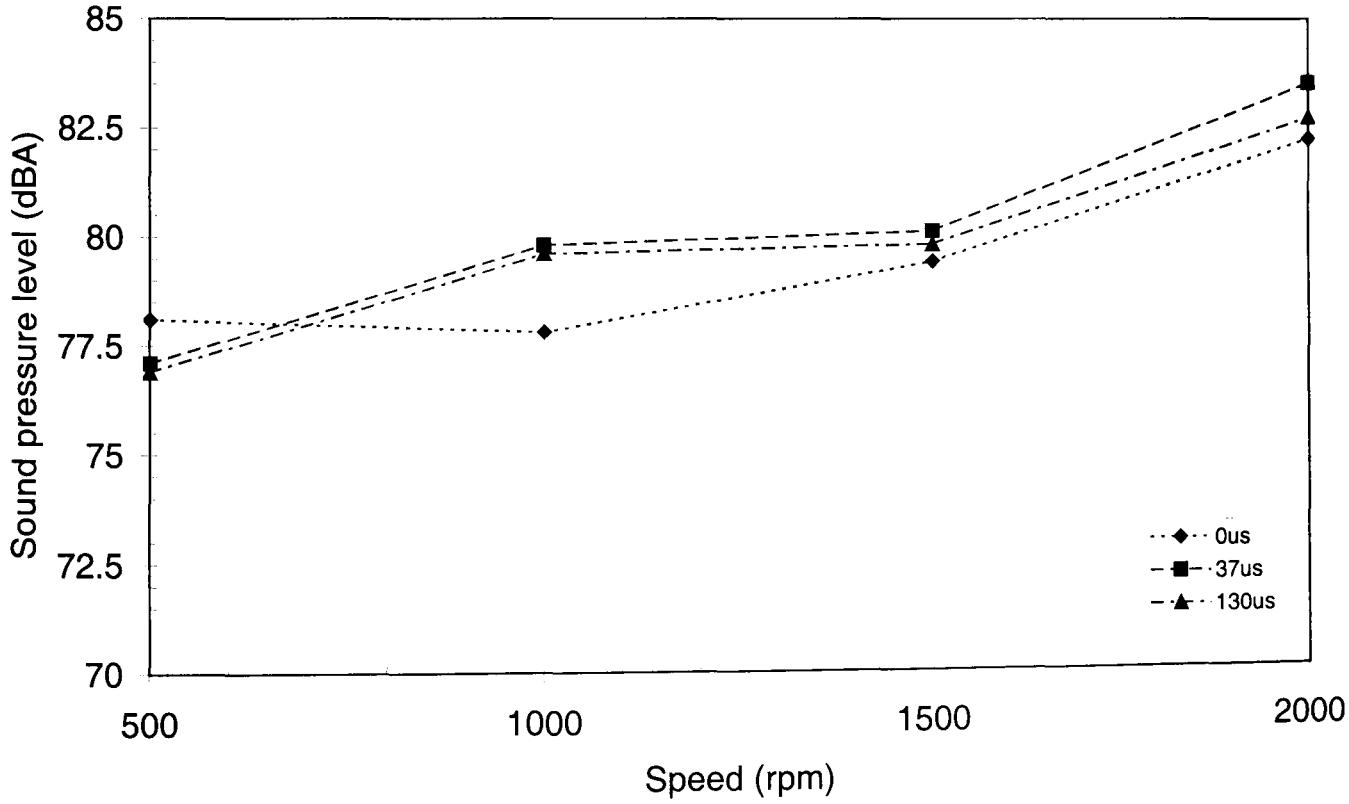

Fig. 5.18 *Comparison of sound pressure level with switching time delays implemented for main modes with current control, at ≈75% load*

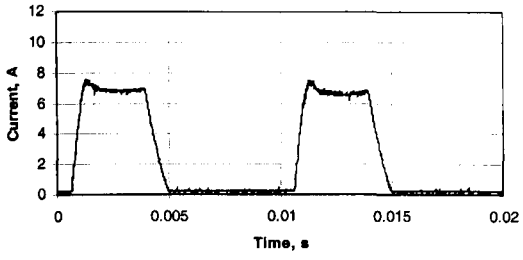

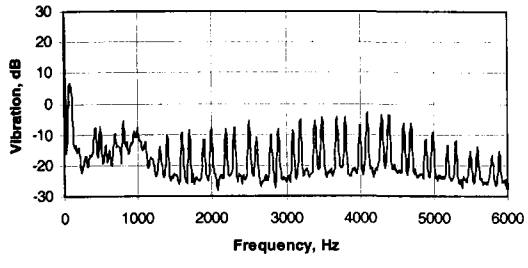

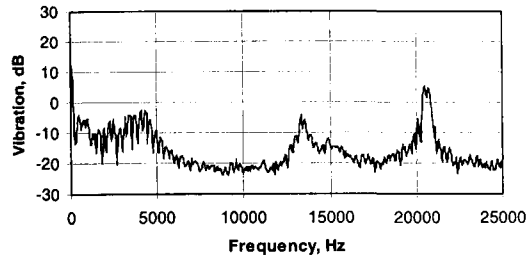

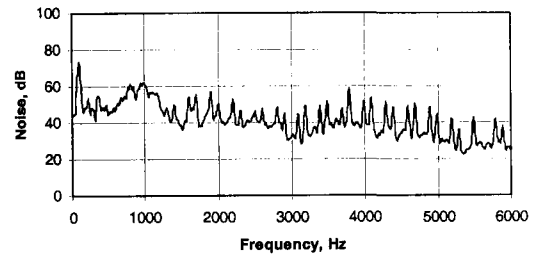

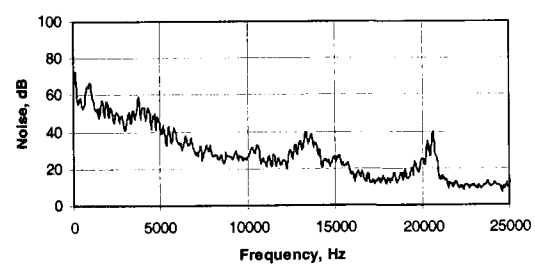

(a) *No time delay*

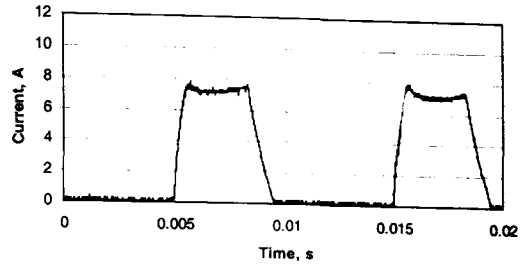

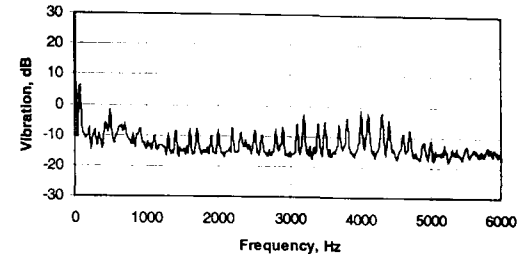

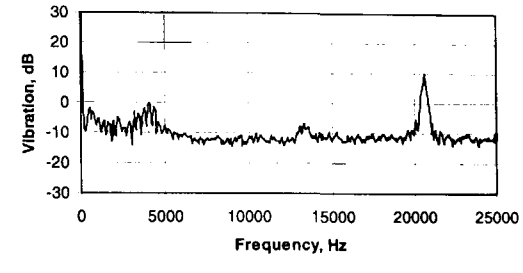

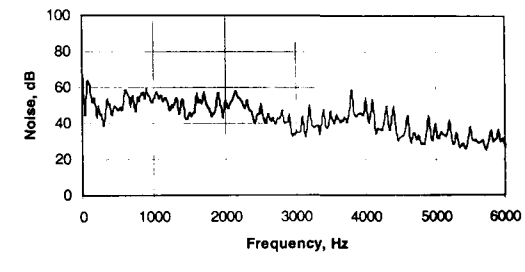

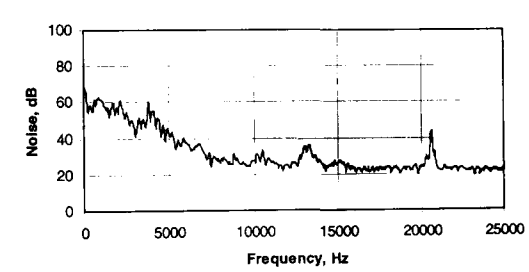

(b) *37μs time delay*

Fig. 5.19 *Voltage PWM control, no-load at 1500rpm*

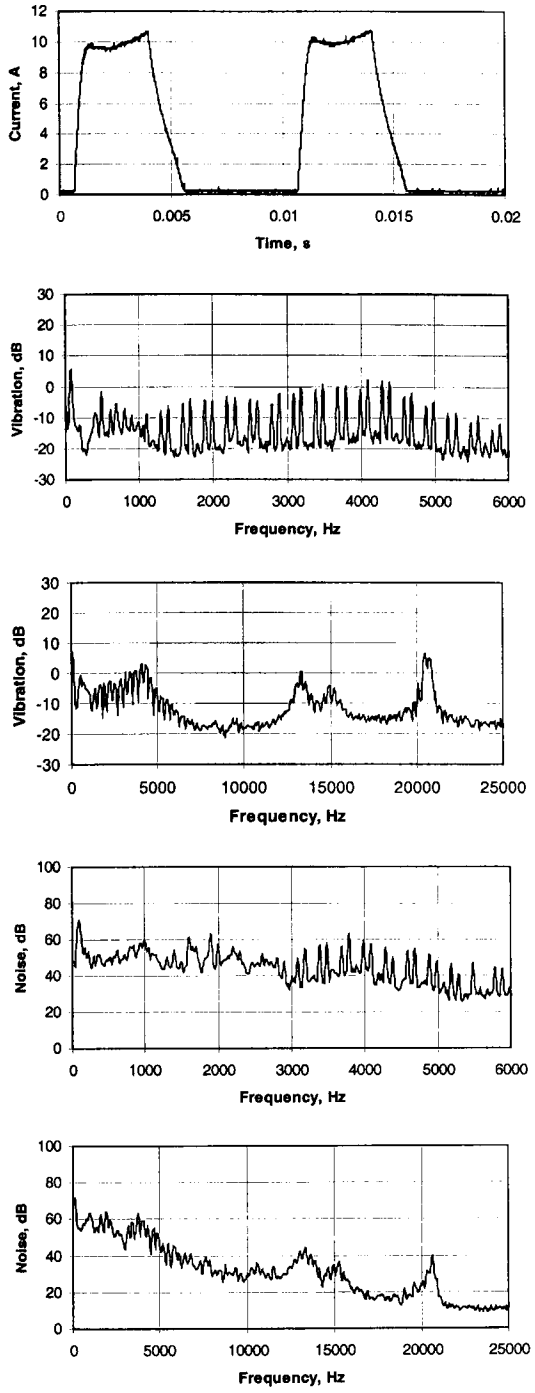

(a) *No time delay*

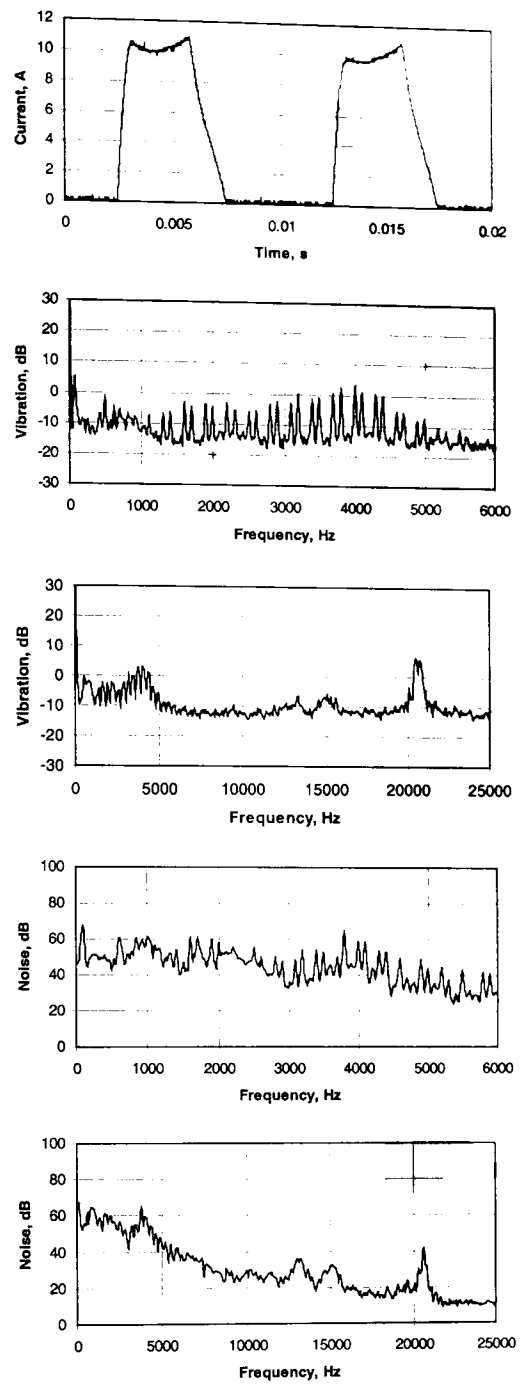

(b) *37μs time delay*

Fig. 5.20 *Voltage PWM control, ≈75% load at 1500rpm*

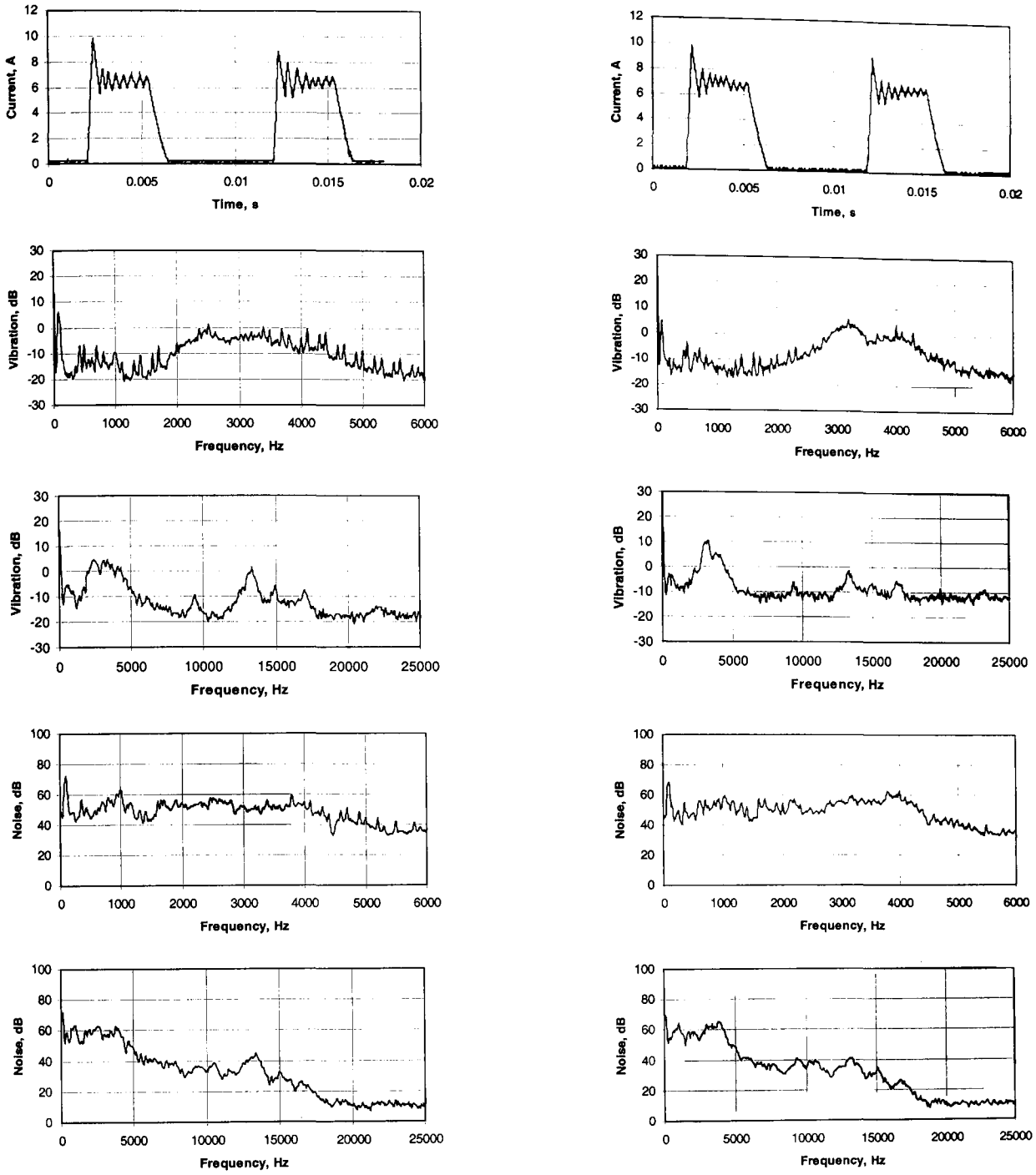

(a) *No time delay* **(b)** *37μs time delay*

Fig. 5.21 *Current control, no-load at 1500rpm*

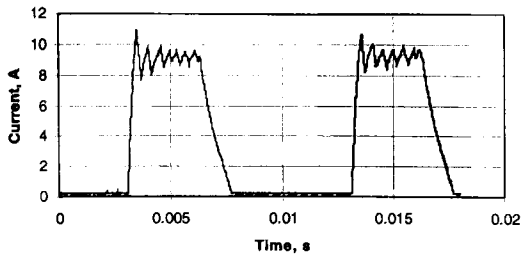

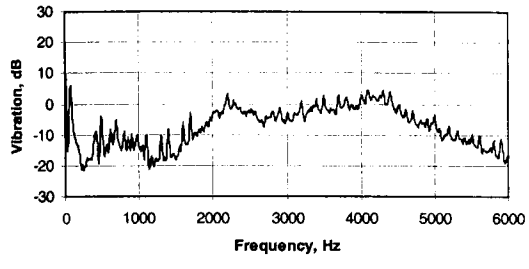

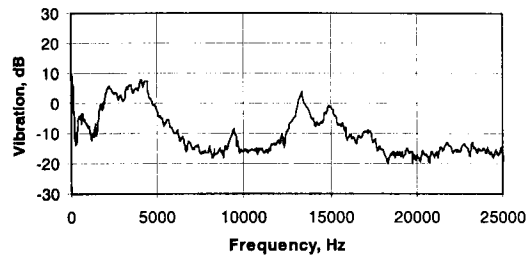

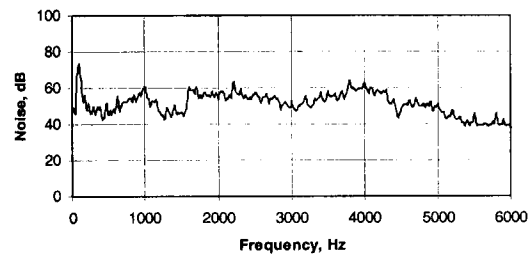

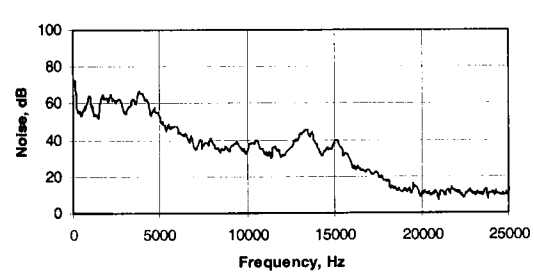

(a) *No time delay*

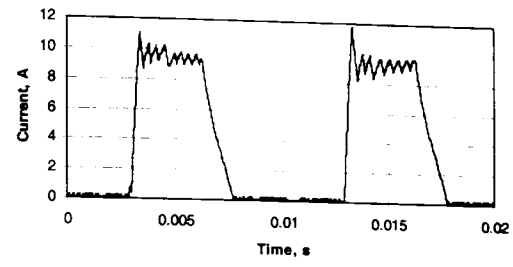

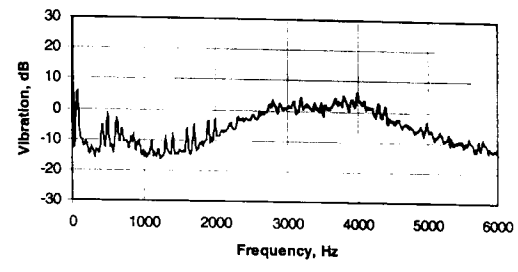

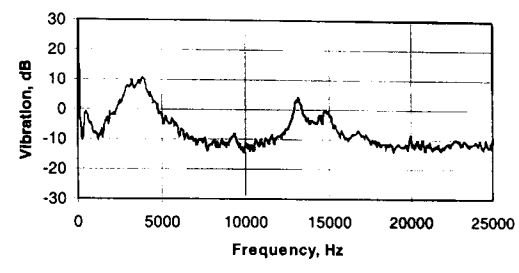

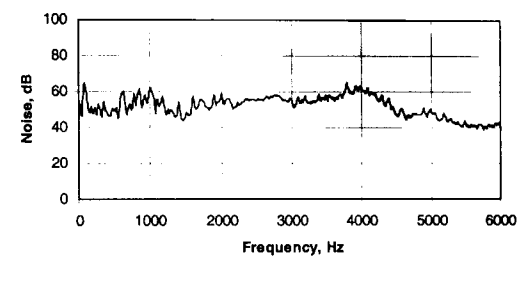

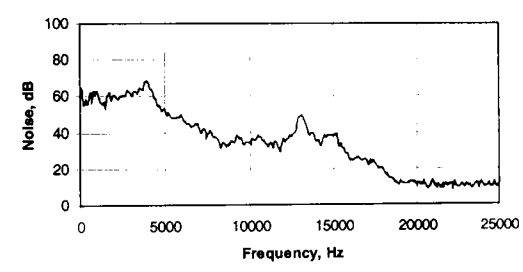

(b) *37μs time delay*

Fig. 5.22 *Current control, ≈75% load at 1500rpm*

5.7.2 Variation of Switching Delay

In the previous section the sound pressure levels emitted for the machine operating with time durations for cancellation of mode 2 and mode 4 were compared together with those measured without any delay. It was highlighted that the delay durations for the two modes are relatively close in value and there was the possibility that the delay imposed for cancellation of mode 4 could also reduce the peak of mode 2. To further this issue an assessment of the sensitivity of the noise emission with regard to the imposed delay was undertaken through variation of the of the delay duration from 0μs to 220μs. This was undertaken for conditions of no-load and ≈75% load for a range of speeds for the machine operating under voltage and current control. For the case of voltage PWM control, both without and with load, **Figs. 5.23 & 5.24** respectively, the noise level is observed to reduce steadily as the value of the delay approaches the value for cancellation of mode 2. Subsequently, the noise level increases steadily as the delay is increased further. The dBA levels measured are tabulated in Appendix I, although those with delay durations at and around that for mode 4 are summarised below in **Tables 5.14 & 5.15** for conditions no-load and load respectively. For the cancellation of mode 2 the reduction is 3.4 to 4.8dBA for no-load and 3 to 5.1 for ≈75% load, omitting the speed of 2000rpm. No dramatic reduction in the sound pressure level is observed for the cancellation of mode 4 compared to that achieved by the neighbouring delay times. For the cancellation of mode 4, with a delay of 37μs, the sound pressure level is observed to reduce by 0.8 to 1.4dBA for no-load and 0.7 to 1.6dBA for ≈75% load again with the omission of 2000rpm.

For the machine operating under current control, **Figs. 5.25 & 5.26**, the variation of the delay duration highlights the problems discussed earlier in section 5.6. The values obtained for the machine under no-load show less variation in the sound pressure level over the range of delay durations.

The reduction in the sound pressure level is limited, not only by the fact that only one natural frequency can be cancelled, but the initial vibration induced for the step change from positive voltage to the zero-voltage loop is sufficient to cause a disturbance to the surrounding air pressure.

Table 5.14 *Summary of SPL with delay times around mode 4, under voltage PWM control, no-load*

Speed (rpm)	0μs	20μs	37μs	40μs	60μs
500	64.5	64.2	63.1	63.8	62.2
1000	70.1	69.6	68.7	68.5	67.3
1500	72.5	72.4	71.7	71.4	70.4
2000	81.3	75.9	76.0	75.9	75.2
2500	77.1	75.8	76.6	76.2	75.3

Table 5.15 *Summary of SPL with delay times around mode 4, under voltage PWM control, ≈75% load*

Speed (rpm)	0μs	20μs	37μs	40μs	60μs
500	67.7	67.2	67.0	66.8	66.3
1000	72.4	71.2	70.7	70.6	70.1
1500	75.3	74.1	73.7	73.5	72.7
2000	82.4	79.8	79.6	79.2	78.7

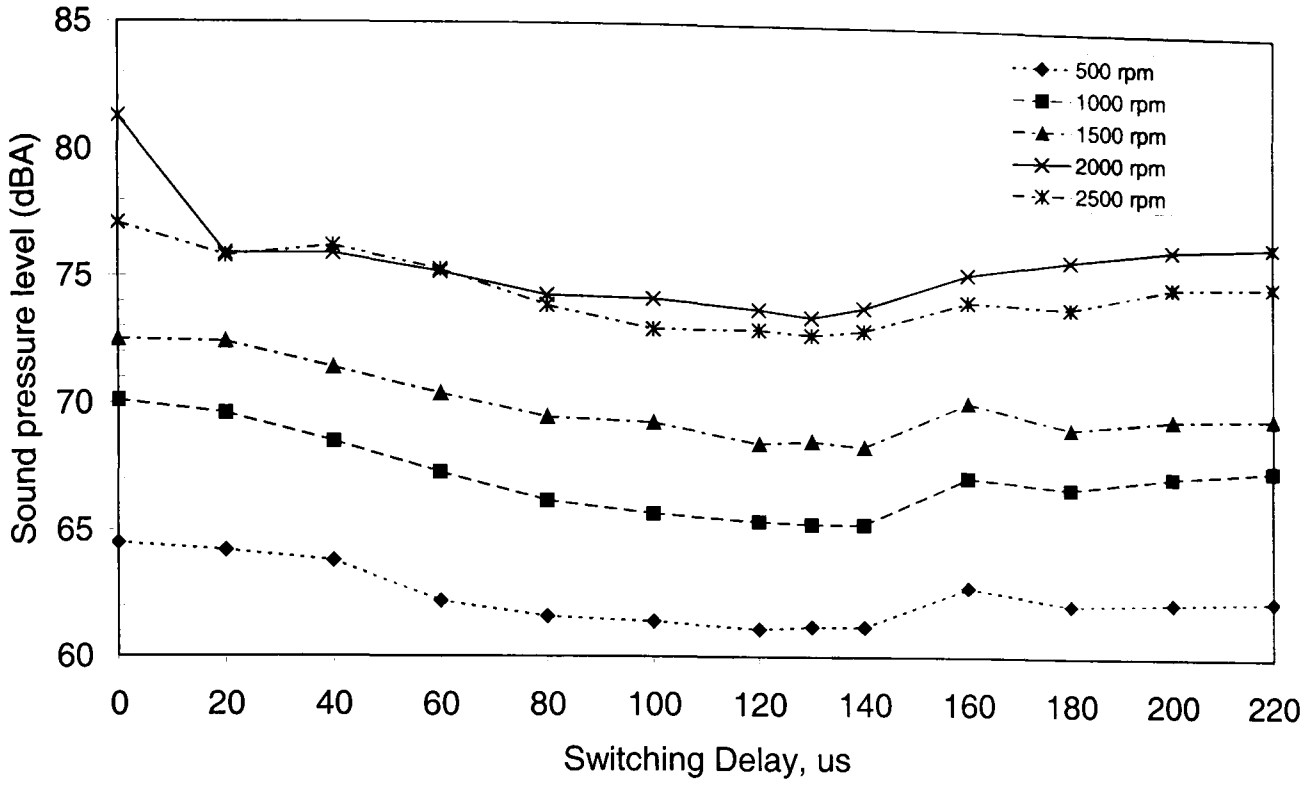

Fig. 5.23 *Variation of sound pressure level for a range of switching time delays with voltage PWM control, on no-load*

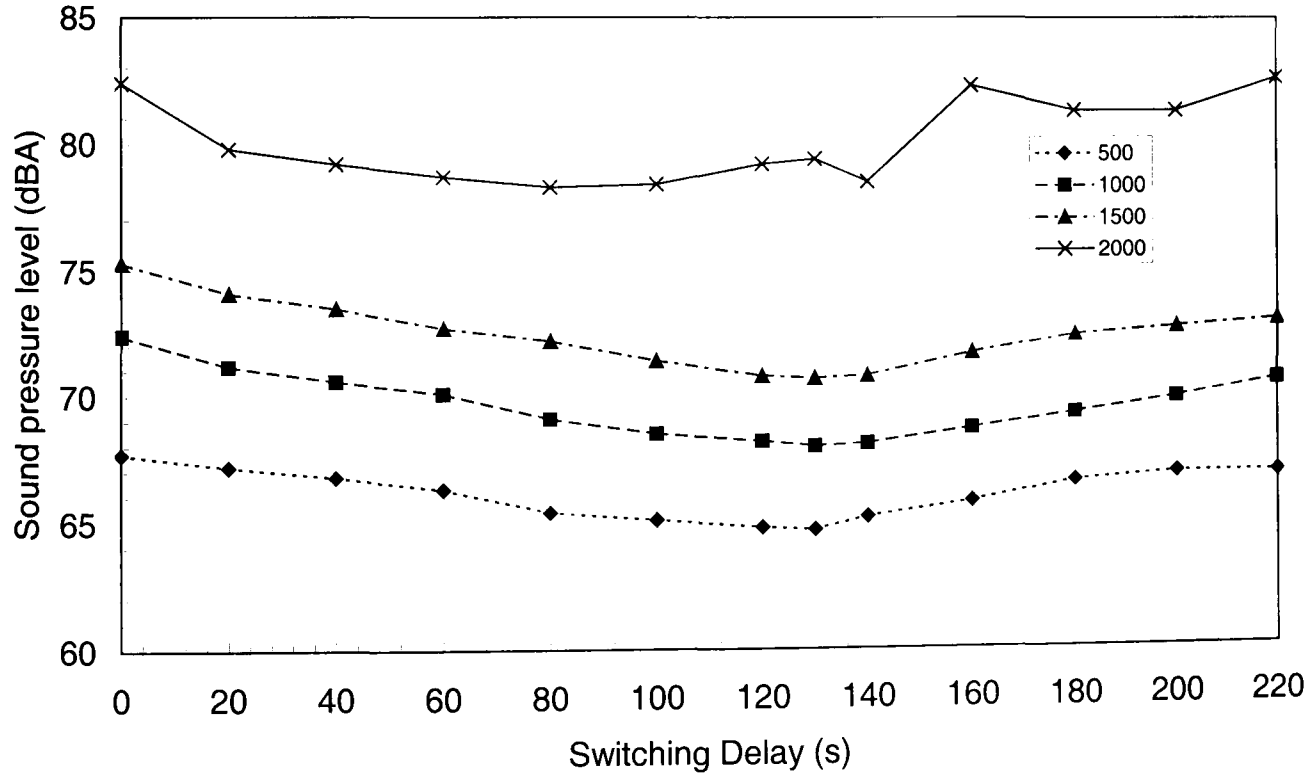

Fig. 5.24 *Variation of sound pressure level for a range of switching time delays with voltage PWM control, at ≈75% load*

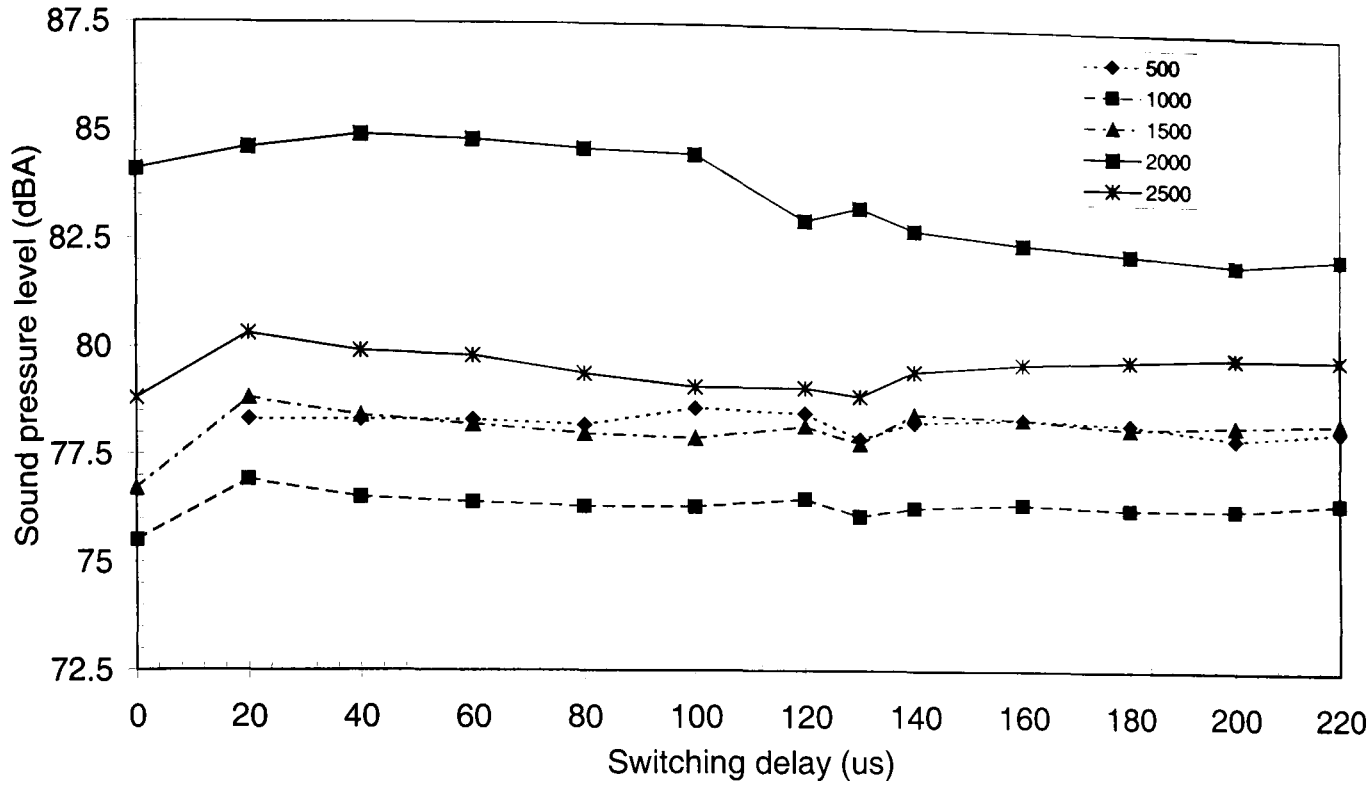

Fig. 5.25 *Variation of sound pressure level for a range of switching time delays with current control, on no-load*

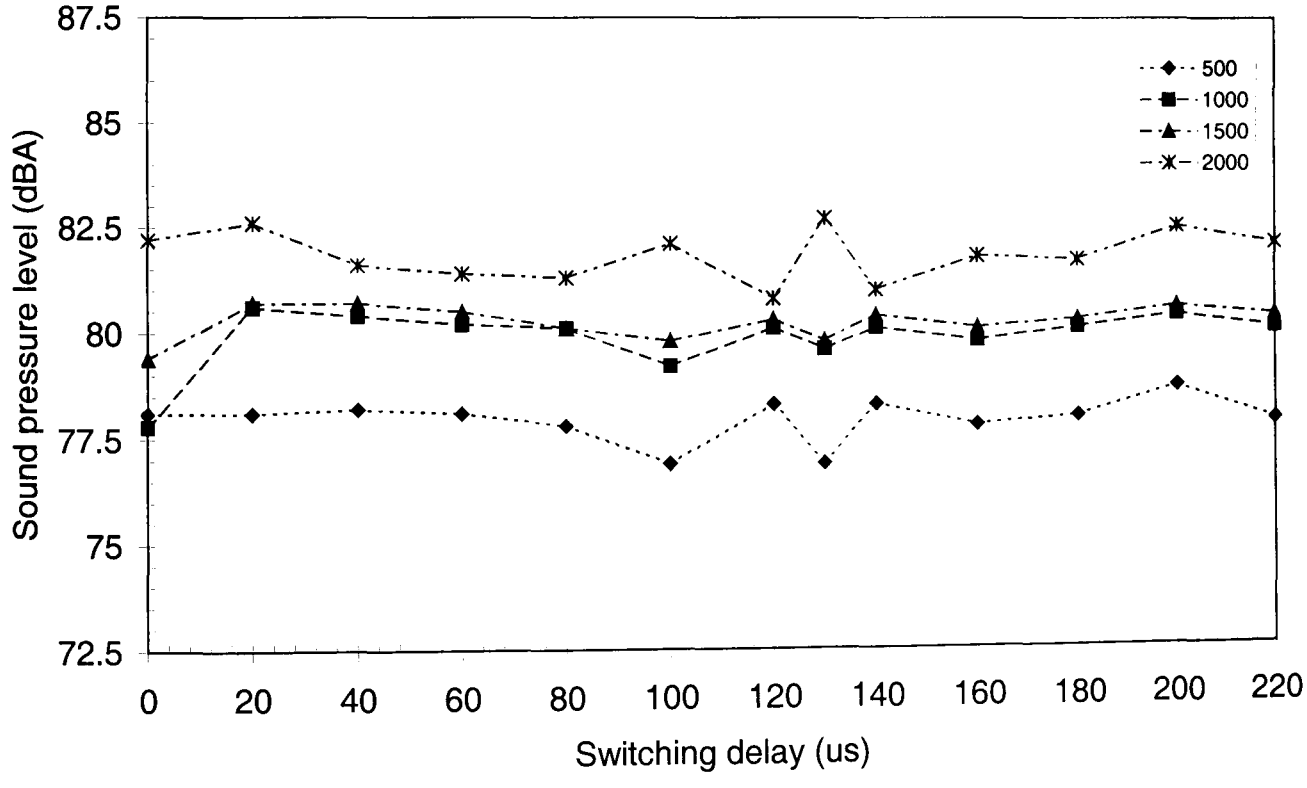

Fig. 5.26 *Variation of sound pressure level for a range of switching time delays with current control, at ≈75% load*

5.8 Summary

This chapter presented a rigorous evaluation of the effectiveness of the active vibration cancellation technique, proposed by Wu and Pollock [WU95], for reducing stator vibration and acoustic noise. For typical operating modes of the switched reluctance machine, viz. fixed frequency voltage PWM control, bang-bang current control, and single pulse mode operation, the technique was assessed for various rotational speeds on no-load and load. Furthermore, the technique was applied for cancellation of vibrations attributed to the natural frequencies of modes 2 and 4, respectively, and the influence of the time delay duration on the noise and vibration was quantified. During the above mentioned investigations the noise and vibration during active vibration cancellation were analysed, for the first time, in both frequency and time domains, together with measurements of the sound pressure level.

It has been shown that when an SR machine is operated under voltage control or single pulse mode, the major oscillation in the time domain vibration waveform is reduced significantly with the application of the time-delay. This major oscillation is attributed to the stator resonating at the natural frequency of mode 2, and, therefore, the value of the time-delay is equal to half a cycle of mode 2. The reduction in vibration is evident in both the noise and vibration spectra, by a significant reduction in the magnitude of the peaks associated with mode 2. In addition, it has been shown that the time delay does not influence the phase current, and, thus, the torque capability of the machine, although the rate of change of current at turn-off is reduced, reflecting the reduction in vibration.

Further, it has been shown that introduction of the time-delay to reduce the vibration associated with mode 2 has an insignificant influence on the vibration of mode 4, as is apparent in both the noise and vibration spectra. This is also the case when the time-delay is applied for the cancellation of vibration mode 4, in that the vibration associated with mode 2 is unaffected. This highlights the limitation of the technique for machines which have multi-resonant stators, and, although for the SR machine under investigation only modes 2 and 4 exist within the audible frequency range, larger machines may exhibit many more resonances. Further, if a machine were to comprise of dual frequencies at its fundamental vibration mode, the effectiveness of the technique may be reduced even further.

Measurement of the sound pressure level has shown that the cancellation of vibration mode 2 is more influential in reducing the acoustic noise than the cancellation of mode 4, since mode 2 is the fundamental vibration mode for the experimental SR machine which has been employed for this study.

The observation remains true irrespective of the load, although due to the application of load restraining the shaft, low frequency oscillations are reduced, thereby improving clarification of the dominant vibration mode, and the effectiveness of its attenuation by the introduction of an appropriate time delay. However, the active vibration cancellation technique has been found to be ineffective when the SR machine is operated under current control. This is apparent from time domain, frequency domain and sound pressure level measurements, and the fact that the rate of change of current at turn-off is not consistently reduced. This is attributed to the random switching nature of the phase voltage by the current controller, such that the actual time delay imposed varies to that which is required depending on the occurrence of the last switching event with respect to the turn-off point. This is highlighted further by measurements of the sound pressure level for various time delays. As the value of the applied time delay is approached, the SPL decreased gradually when the machine is operated under voltage control, and once the time delay exceeds that for cancellation of mode 2 the SPL starts to increase, the effect being consistent for different speeds and loads. However, under current control, the SPL is random, regardless of speed and load, for the reasons discussed above. This variation in the time delay is also the reason for the technique being more effective under single pulse mode than with fixed frequency PWM voltage control, and, further, explains its reduced effectiveness when the PWM frequency is reduced. In the case of single pulse mode there is no chopping, and, thus, the zero voltage loop is only defined by the applied delay time, there is no risk of additional time being added to its value.

It should be noted that for the given experimental SR machine the required time delays for modes 2 and 4 are relatively small, compared to those which may be required for larger machines. With a longer delay time, any variation in the actual time delay will be a smaller percentage of the total time delay imposed under chopping control, thus making for greater accuracy for the cancellation of the specified vibration mode. However, this does not imply that the technique will be more effective with larger machines, due to the fact that more natural frequencies may lie within the audible frequency range.

Chapter 6
Conclusions

In this thesis, the influence of the mechanical characteristics and control parameters on the vibration and acoustic noise of a switched reluctance machine has been investigated, and an active vibration cancellation technique for reducing the emitted acoustic noise has been evaluated.

6.1. Vibration behaviour of stator assembly

The influence of the stator design parameters, such as the number of poles, the pole width, the fillet radius, and the yoke thickness, as well as the stator windings, frame and end-caps, and mounting assembly, on the natural frequencies and vibration modes has been systematically investigated.

The investigation confirms that the natural frequencies increase significantly as the stator diameter is reduced and that increasing the yoke thickness increases the natural frequencies. Thus, it is concluded that they are the most influential stator parameters, as regards acoustic noise emissions.

It has been shown that the influence of geometric asymmetries in the stator are much more significant than those which may be attributed to manufacturing tolerances, and they induce dual natural frequencies for certain mode shapes. Consequently, the choice of pole number, the placement and number of notches and key-ways have been highlighted as influential factors on the number of natural frequencies a stator may possess in a given frequency range. However, through careful consideration at the design stage, these may be such as to minimise the possibility of stator resonance. For example, a 6-pole stator has been shown to possess a single frequency for modes 2 and 4 and dual frequencies for mode 3, whereas an 8-pole stator has been shown to possess a single frequency for modes 2 and 3 and dual frequencies for mode 4. However, odd vibration modes, i.e., modes 3, 5, etc, are generally not as important as even vibration modes in regard to noise generation in SR machines.

In addition, it has been highlighted that the poles should not be treated purely as an additional mass to the stator yoke, especially when higher mode numbers are of significance, since, firstly, they introduce dual frequencies, and, secondly, although they

reduce the stator natural frequencies, their stiffness effect becomes more significant for higher mode numbers. However, a variation to the pole width only influences the symmetric and anti-symmetric mode types of modes 3 and 6, for the 6-pole stator under investigation, due to the nature of their kinetic and potential energies. In addition, it has been shown that the fillet radius has an insignificant effect on the natural frequencies.

It has been shown that the fabrication of a laminated stator core has a very significant influence on its vibrational characteristics, compared to a solid equivalent. The natural frequencies are considerably reduced, despite the reduction in the mass density from that of a solid core, and are influenced by the clamping pressure and the means of affixing the laminations together. It was found that the effective Young's modulus E_z of a laminated silicon iron core had the same value as for solid silicon iron, for axial mode 0, although it had been expected to reduce slightly. However, this was partially attributed to the fact that in the experimental SR machine the laminated stator core was welded at six circumferential points along its axis. In fact, the influence of E_z was found to be insignificant for the in-plane flexural vibration, i.e. axial mode $m=0$. The shear moduli were found to have a more significant effect than the Young's moduli on the natural frequencies, the values both in the plane (G_{xy}) and normal to the laminations (G_{xz}, G_{yz}) being ≈90% and ≈33% of the values for solid silicon iron, respectively. It was also found that laminating a core significantly increases the damping, such that the axial modes, $m=1$, are suppressed significantly, although these modes are not generally relevant to noise production in SR machines.

Due to the relatively short overhang lengths, the end-winding mass and stiffness are as influential as the slot windings, in that the end-windings cannot be treated merely as an additional mass in the slots, or the complete windings as an additional mass in the poles. In fact, the influence of the winding mass is offset by their stiffness, so that their influence on the frequencies of the dominant vibration modes is relatively small. However, it was found that the presence of the stator winding introduces a large number of additional vibration modes, many of which correspond purely to end-winding movement. These increase the complexity of the winding analyses, but are not relevant to noise generation, as evidenced by the noise and vibration measurements on the experimental SR machine. Also, it should not be overlooked that the stator windings impose additional damping to the stator core, and, therefore, influence the magnitude of the vibrations, and for higher modes, their stiffness may become more apparent in

restraining the lateral movement of the stator poles. However, the most important vibration modes are usually those with low orders.

The addition of a smooth frame to the wound stator core has been shown to increase the core natural frequencies considerably, whilst the addition of end-caps causes a much further increase, due to their very high radial stiffness restraining radial movement of the axial ends of the frame. However, it was found that the assumption of an intimate contact between the end-caps and the frame, for modelling purposes, resulted in a large over-estimate of the predicted natural frequencies, and that this was more severe for the lower mode shapes. This highlighted the limitation of finite element techniques for analysing such highly complex mechanical structures, but provided an upper limit to which the end-caps may increase the natural frequencies, if for example, they were to be welded to the frame. Finally, the face-plate mounting arrangement which was employed for the experimental SR machine was shown to have an insignificant influence on the natural frequencies, since it added no further radial stiffness to that already provided by the presence of the end-caps. However, the natural frequencies generally change if foot-mounting is employed, [XU99].

6.2. Influence of drive control parameters on noise and vibration

A systematic study of the influence of the control parameters and the operating modes of a switched reluctance machine on the stator vibration and emitted noise has been undertaken. The results have been analysed in both the frequency and time domains, and correlated with measurements of the sound pressure level and related phase current waveforms.

Initial noise and vibration measurements, together with measured transfer functions of the assembled SR machine, confirmed that the noise and vibration are closely associated, and that the dominant source of noise is attributed to the stator resonating at the frequencies of its even vibration modes, whereas the odd vibration modes and the additional modes attributed to the windings are generally irrelevant to noise production. This has been shown to remain true regardless of the rotational speed and operating mode.

The vibration and noise which result when a machine is operated under current control has been shown to differ significantly to that which results under voltage control and single pulse mode operation. Under current control the machine was shown to be

significantly noisier, despite the fact that the rate of decay of current at turn-off is similar to that which occurs under voltage control. This is due to the fact that the random switching of the current controller induces a wide-band harmonic spectra, thus increasing the levels of all mechanical resonances. However, if fixed frequency PWM voltage control were to employ a switching frequency in the audible frequency range which also coincided with a natural frequency, the machine may then be noisier than that under current control. Further, it has been shown that hard chopping results in a noisier machine compared to that with soft chopping due to the higher current ripple, especially under current control.

When the voltage PWM switching frequency was reduced below 20kHz with the SR machine operated under voltage control, since it was then within the audible frequency range, the sound pressure level increased. Further, it has been shown that when the PWM switching frequency approaches that of a stator natural frequency, the amplitude of the natural frequency increases, and therefore coincidence with these two frequencies should be avoided.

For speeds below that which result in single pulse operation, with the SR machine operated under voltage or current control, it has been shown that the sound pressure level and the magnitude of the resonant peaks increase with speed. This is due to the increase in the rate of change of current, in response to the increase in the rotational back-emf.

Comparison of the noise and vibration under dc supply controlled single pulse mode and voltage control has shown that single pulse mode results in the quietest operation. This is also evidenced by comparing the measured sound pressure level under the various operating modes. This is attributed to the lower magnetisation voltage which is available during the tests, which have shown the strong relationship which exists between the rate of change of current at turn-off and the resulting noise and vibration. Further, a comparison of PWM voltage control for various dc supply voltages for a fixed speed operation has shown that the noise and vibration may be reduced at low speeds and loads by including an additional chopper between the dc supply and inverter to limit the de-nagnetisation voltage at turn-off.

The application of load at any rotational speed has been shown to increase the noise and vibration, due to the higher level of current and, hence, increased rate of decay of current at turn-off. Finally, for a fixed dwell period, it has been shown that the noise and

vibration increases slightly as the switching angles are advanced due, again, to the increased current and, hence, increased rate of decay of current at turn-off.

6.3. Evaluation of active vibration cancellation technique

The effectiveness of the active vibration cancellation technique proposed by Wu & Pollock [WU95], for reducing stator vibration and acoustic noise, has been evaluated under typical operating modes of the SR machine, viz. fixed frequency PWM voltage control, bang-bang current control, and single pulse mode operation, at various rotational speeds, both on no-load and on load. Further, the technique was applied to cancel those vibrations which are attributed to the natural frequencies of modes 2 and 4, and the influence of the time-delay duration on the noise and vibration has been quantified. During the above mentioned investigations the noise and vibration were analysed in both the frequency and time domains, and supported by measurements of the sound pressure level.

It has been shown that when an SR machine is operated under voltage control or single pulse mode, the major oscillation in the time domain vibration waveform is reduced significantly with the application of the time-delay. This major oscillation is attributed to the stator resonating at the natural frequency of mode 2, and, therefore, the value of the time-delay is equal to half a cycle of mode 2. The reduction in vibration is evident in both the noise and vibration spectra, by a significant reduction in the magnitude of the peaks associated with mode 2. In addition, it has been shown that the time delay does not influence the phase current, and, thus, the torque capability of the machine, although the rate of change of current at turn-off is reduced, reflecting the reduction in vibration.

Further, it has been shown that introduction of the time-delay to reduce the vibration associated with mode 2 has an insignificant influence on the vibration of mode 4, as is apparent in both the noise and vibration spectra. This is also the case when the time-delay is applied for the cancellation of vibration mode 4, in that the vibration associated with mode 2 is unaffected. This highlights the limitation of the technique for machines which have multi-resonant stators, and, although for the SR machine under investigation only modes 2 and 4 exist within the audible frequency range, larger machines may exhibit many more resonances. Further, if a machine were to comprise of dual frequencies at its fundamental vibration mode, the effectiveness of the technique may be reduced even further.

Measurement of the sound pressure level has shown that the cancellation of vibration mode 2 is more influential in reducing the acoustic noise than the cancellation of mode 4, since mode 2 is the fundamental vibration mode for the experimental SR machine which has been employed for this study.

The observation remains true irrespective of the load, although due to the application of load restraining the shaft, low frequency oscillations are reduced, thereby improving clarification of the dominant vibration mode, and the effectiveness of its attenuation by the introduction of an appropriate time delay.

However, the active vibration cancellation technique has been found to be ineffective when the SR machine is operated under current control. This is apparent from time domain, frequency domain and sound pressure level measurements, and the fact that the rate of change of current at turn-off is not consistently reduced. This is attributed to the random switching nature of the phase voltage by the current controller, such that the actual time delay imposed varies to that which is required depending on the occurrence of the last switching event with respect to the turn-off point. This is highlighted further by measurements of the sound pressure level for various time delays. As the value of the applied time delay is approached, the SPL decreased gradually when the machine is operated under voltage control, and once the time delay exceeds that for cancellation of mode 2 the SPL starts to increase, the effect being consistent for different speeds and loads. However, under current control, the SPL is random, regardless of speed and load, for the reasons discussed above. This variation in the time delay is also the reason for the technique being more effective under single pulse mode than with fixed frequency PWM voltage control, and, further, explains its reduced effectiveness when the PWM frequency is reduced. In the case of single pulse mode there is no chopping, and, thus, the zero voltage loop is only defined by the applied delay time, there is no risk of additional time being added to its value.

It should be noted that for the given experimental SR machine the required time delays for modes 2 and 4 are relatively small, compared to those which may be required for larger machines. With a longer delay time, any variation in the actual time delay will be a smaller percentage of the total time delay imposed under chopping control, thus making for greater accuracy for the cancellation of the specified vibration mode. However, this does not imply that the technique will be more effective with larger machines, due to the fact that more natural frequencies may lie within the audible frequency range.

6.4. Noise and vibration reduction

As a consequence of the foregoing discussion, it follows that a number of measures may be undertaken to reduce the noise and vibration of SR machines, including:

- The yoke should be made as thick as possible, although this is limited by the required slot area and volume envelope, and will also compromise the power-to-weight ratio.

- At the design stage, the pole numbers should be selected with due account of any geometric asymmetries so as to reduce the number of dual resonant frequencies that may result. For example, a 6-pole stator comprises of only a single frequency for modes 2 and 4, whereas an 8-pole stator introduces an additional frequency for mode 4.

- Lamination notches and key-ways should be avoided if at all possible, although, again, their influence may be minimised by appropriate consideration of the geometric asymmetries. For example, for the 6-pole stator of the experimental SR machine, the addition of three notches equi-spaced behind three of the stator poles did not induce dual frequencies, whereas the addition of four notches with the 8-pole stator introduced dual frequencies for mode 2.

- Fixed frequency PWM voltage control should be used in preference to current control, although current control may be more beneficial dynamically since it provides a much faster rate of rise of current. The switching frequency which is employed for voltage control should be above 20kHz, although if this is not possible due to switching loss consideration the value should be such that it does not coincide with a stator natural frequency.

- Soft chopping should be employed in preference to hard chopping, since, not only will this result in reduced noise emissions, but also a reduced switching loss.

- The application of active vibration control for reducing stator vibration and acoustic noise is a feasible means of reducing acoustic noise. However, it is best suited for fixed frequency PWM voltage control, with a high switching frequency, so as to maintain an accurate time-delay.

- Current shaping is another means of reducing noise, [GAB99a], since, although it was not evaluated in this thesis, the benefits which it may provide were evidenced by the fact that the lowest noise emissions, throughout the investigations, generally resulted with a reduced rate of change of current at turn-off.

- The inclusion of an additional chopper between the inverter and dc supply may be beneficial for noise reduction at light load. This was evidenced by the application of reduced dc supply under voltage control for a fixed speed, when the rate of change of current at turn-off and, hence, the noise were observed to reduce significantly with the reduced de-magnetisation voltage.

6.5. Future work

Suggestions for further research into noise reduction techniques for SR machines include:

- Current shaping techniques, with the aim of optimising the current waveform.
- Active vibration cancellation techniques, for machines which exhibit multiple resonances.

References

AND97 Andersen, G.K., Christiansen, H., Gurholt, R., Helle, L., Hovet, T.G., Jensen, C.H., Ritchie, E., 'Dynamic model of a switched reluctance motor for vibration analysis', *Proc. University Power Engineering Conference, (UPEC),* 1997, pp. 53-56.

ANS99 ANSYS Ver. 6.0 Manual, http:www1.ansys.com/customer/content/documentation

AYA99 Ayari, S., Besbes, M., Lecrivain, M., Gabsi, M., 'Effects of the airgap eccentricity on the SRM vibrations', *Proc. IEEE International Electrical Machines and Drives Conference, (IEMDC),* 1999, pp. 138-140.

BAR99 Bartos, F. J., 'Forward to the past with SR technology', Control Engineering, Nov/Dec. 1999, http://www.controleng.com.

BES94 Besbes, M., Ren, Z., Razek, A., Allano, S., 'Vibration diagnostic for doubly salient variable reluctance motors', *Proc. International Conference on Electrical Machines, (ICEM)* Vol. 3, 1994, pp. 415-418.

BES98 Besbes, M., Picod, C., Camus, F., Gabsi, M., 'Influence of stator geometry upon vibratory behaviour and electromagnetic performances of switched reluctance motos', *Proc. IEE Electric Power Applications*, Vol. 145, No. 5, September, 1998, pp. 462-468.

BLA94 Blaabjerg, F., Pederson, J.K., Nielsen, P., Anderson, L., Kjaer, P.C., 'Investigation and reduction of acoustical noise from switched reluctance drives in current and voltage control', *Proc. International Conference on Electrical Machines, (ICEM),* Vol.3, 1994, pp. 589-594.

BRU84 Bruel & Kjaer, 'Measuring sound', booklet, English DK BR0047-13, 1984, pp. 8.

CAI99 Cai, W., Pillay, P., 'Resonance frequencies and mode shapes of switched reluctance motors', *Proc. IEEE International Electrical Machines and Drives Conference*, 1999, pp. 44-47.

CAM92 Cameron, D.H., Lang, J.H., and Umans, S.D., 'The origin and reduction of acoustic noise in doubly salient variable-reluctance motors,' *IEEE Transactions on Industry Applications,* Vol. 26, No. 6, 1992, pp. 1250-1255.

COL96 Colby, R.S., Mottier, F., Miller, T.J.E., 'Vibration modes and acoustic noise in a four-phase switched reluctance motor', *IEEE Transactions on Industry Applications*, Vol. 32, No. 6, 1996, pp. 1357-1364.

EHS87 Ehsani, M., Bass, J.T., Miller, T J.E., Steigerwald, R. L. 'Development of a unipolar converter for variable reluctance motor drives,' *IEEE Transactions on Industry Applications*, Vol. 23, No. 3, May-June, 1987, pp. 545-553.

ELL71 Ellison, A., and Yang, S.J., 'Natural frequencies of stators of small electric

machines', *Proc. IEE*, Vol. 118, No. 1, January, 1971, pp. 185-190.

ERD57 Erdelyi, E., Horvay, G., 'Vibration modes of stators of induction motors,' *ASME Trans.*, [E], Vol. 24, 1957, pp. 39-45.

EWI00 Ewins, D.J., 'Modal Testing, theory, practice and application', *second ed., Research Studies Pres Ltd*, Baldock, Hertforshire, England, 2000.

GAB97 Gabsi, M., Camus, F., Humeau, B., Besbes, M., 'Vibrations in the switched reluctance motor. Influence of the feeder mode', *Proc. European Power Electronics Conference, (EPE)*, 1997 pp. 2.495-2.499.

GAB99a Gabsi, M., Camus, F., Loyau, T., Barbry, J.L., 'Noise reduction of switched reluctance machine', *Proc. IEEE International Electric Machines and Drives Conference, (IEMDC)*, Piscataway, NJ, USA, 1999, pp. 263-265.

GAB99b Gabsi, M., Camus, F., Besbes, M., 'Computation and measurement of magnetically induced vibrations of a switched reluctance machine,' *Proc. IEE Electric Power Applications*, Vol. 146, No. 5, September 1999, pp. 463-470.

GAR89 Garvey, S.D., 'The vibrational behaviour of laminated components in electrical machines,' *Proc. IEE Electric Machines and Drives, (EMD)*, 1989, pp. 226-231.

GIR79 Girgis, R.S., and Verma, S.P., 'Resonant frequencies and vibration behaviour of stators of elecetrical machines as affected by teeth, windings, frame and laminations,' *IEEE Transactions on Power Apparatus and Systems*, 1979, pp. 1446-1455.

HAR56 DEN HARTOG, J.P., 'Mechanical vibrations', *McGraw-Hill Book Company*, 1956.

HEW88 Hewlett-Packard Company, 'HP 35660A operating manual set', July, 1988, Manual part no. 35660-90000

HUL96 Hull, D., Clyne, T.W., 'An Introduction to composite materials', *Cambridge University Press*, 1996.

HUS00 Husain, I., Radun, A., Nairus, J., 'Unbalanced force calculation in switched reluctance machines', *IEEE Transactions on Magnetics*, Vol. 36, No. 1, January 2000, pp. 330-338.

KAI53 Kaiser, E.R., 'Acoustical vibration of rings', J. *Acoust. Soc. Am.*, 1953, Vol. 25, No. 4, pp. 617-622.

KIR76 Kirkthorpe, J., 'Simple frequency expression for the in-plane vibration of thick circular rings', *J. Acoust. Soc. Am.*, 1976, Vol. 59, No. 1, pp. 86-89.

KRI87 Krishnan, R., Aravind, S, and Materu, P., 'Computer-aided design of electrical machines for variable speed applications', *Proc. IEEE International Conference on Industrial Electronics, Control and Instrumentation, (IECON)*, Cambridge, Vol. 2, 1989, pp. 756-763.

LOV94 Lovatt, H.C., Stephenson, J.M., 'Computer-optimised current waveforms for switched-reluctance motors', *Proc. IEE Electric Power Applications*, Vol. 141, No. 2, March 1994, pp. 45-51.

MAH96 Mahn, J., Williams, D., Wung, P., Horst, G., Lloyd, J., Randall, S., 'A systematic approach toward studying noise and vibration in switched reluctance machines: Preliminary results', *Proceedings on IEEE Industry Applications Conference*, Vol. 2, 1996, pp. 779-785.

MEH92 Moallem, M., Ong, C., Unnewehr, L.E., 'Effect of rotor profiles on the torque of a switched reluctance motor', *IEEE Transactions on Industry Applications*, Vol. 28, No. 2, March/April, 1992, pp. 364-369.

MIL85 Miller, T.J.E., 'Converter volt-ampere requirements of the switched reluctance motor drive,' *IEEE Transactions Industry Applications*, Vol. 21, No. 5, 1985, pp. 1136-1144.

MIL87a Miller, T.J.E., McGilp, M., 'PC CAD for switched reluctance drives,' *Proc. IEE Conference on Electrical Machines and Drives*, No. 282, 1987, pp. 360-366.

MIL87b Miller, T.J.E., 'Brushless Reluctance Motor Drives,' *IEE Power Engineering Journal*, Vol. 1, November, No.6, 1987, pp. 325-331.

MIL88 Miller, T.J.E., Bower, P.G., Becerra, R., and Ehsani, M., 'Four quadrant brushless reluctance motor drive,' *Proc. IEE Conference on Power Electronics and Variable Speed Drives* (London), July 1988, pp. 273-276.

MIL90 Miller, T.J.E., 'Nonlinear theory of the switched reluctance motor for rapid computer-aided design', *IEE Proceedings-B (Electric Power applications)*, Vol. 137, No. 6, November 1990, pp. 337-347.

MIL93 Miller, T.J.E., 'Switched reluctance motors and their control', *Magna Physics, Oxford*, 1993.

MIL95 Miller, T.J.E., 'Faults and unbalanced forces in the switched reluctance machine,' *IEEE Transactions on Industry Applications*, Vol. 31, No. 2, 1995, pp. 319-328.

NEV97 Neves, C.G.C., Carlson, R., Sadowski, N., Bastos, J.P.A., Nau, S.L., 'The influence prediction of the current waveforms on the vibrational behavior of switched reluctance motors', *IEEE*, 1999, pp. TB1-7.1-TB1-7.3.

NOD87 Noda, S., Mori, S., Ishibashi, F., and Itomi, K., 'Effect of coils on natural frequencies of stator cores in small induction motors,' *IEEE Transactions on Energy Conversion*, Vol. 2, No. 1, March, 1987, pp. 93-99.

PHI90 Philips, D.A., 'A novel high performance – low noise switched reluctance motor', *Proc. International Conference on Electric Machines, (ICEM)*, 1990, pp. 801-805.

PIL95 Pillay, P., Samudio, R.M., Ahmed, M., Patel, R.T., 'A chopper-controlled SRM Drive for reduced acoustic noise and improved ride-through

capability using supercapacitors', *IEEE Transactions on Industry Applications*, Vol. 31, No. 5, 1995, pp. 1029-1038.

PIL99 Pillay, P., Cai, W., 'An investigation into vibration in switched reluctance motors', *IEEE Transactions on Industry Applications*, Vol. 35, No. 3, May/June 1999, pp. 589-596.

POL97 Pollock, C., Wu, C., 'Acoustic noise cancellation techniques for switched reluctance drives', *IEEE Transactions on Industry Applications*, Vol. 33, No. 2, 1997, pp. 477-484.

PUL93 Pulle, D.W.J., Lai, J.C.S., Milthorpe, J.F. and Huynh, N., 'Quantification and analysis of acoustic noise in switched reluctance motors', *Proc. European Conference on Power Electronics and Applications, (EPE)*, 1993, pp. 65-70.

RAD92 Radun, A.V., 'High-power density switched reluctance motor drive for aerospace applications,' *IEEE Transactions on Industry Applications*, Vol. 28, No. 1, 1992, pp. 113-119.

RAS99 Rasmussen, P.O., Blaabjerg, F., Pedersen, J.K., Kjaer, P.C., Miller, T.J.E., 'Acoustic noise simulation for switched reluctance motors with audible output', *Proc. CD-ROM EPE'99*, Lausuanne, Switzerland, 1999.

SAD96 Sadowski, N., Lefevre, Y., Neves, C.G.C., Carlson, R., 'Finite elements coupled to electrical circuit equations in the simulation of switched reluctance drives: attention to mechanical behaviour', *IEEE Transactions on Magnetics*, Vol. 32, No. 3, 1996, pp. 1086-1089.

SCH97 Schofield, N., 'Brushless permanent magnet traction machines with extended speed capability', *Ph.D Thesis, University of Sheffield*, 1997.

SOO92 Sood P., ESCD Emerson Electric, St. Louis, MO, 'Power converter for switched reluctance motor,' Patent number 5,115,181, 1992.

STE89 Stephenson, J.M., El-Khazendar, M.A., 'Saturation in doubly salient reluctance motors', *IEE Proceedings-B*, Vol. 136, No. 1, 1989, pp. 50-58.

TAN97 Tang, Y., 'Characterization, numerical analysis, and design of switched reluctance motors', *IEEE Transactions on Industry Applications*, Vol. 33, No. 6, 1997, pp. 1544-1552.

TEX97 Texas Instruments, 'Reference set, volume 2: Peripheral library and specific devices', TMS320C24x DSP Controllers, 1997, literature number. SPRU161B.

TIM74 Timoshenko, S.P., 'Vibration problems in engineering', *fourth ed., New York, London, Wiley*, 1974.

TUR98 Turner, J.M., 'Output smoothing in a switched reluctance machine', Patent, GB2313498.

VER81a Verma, S.P, Girgis, R.S., 'Experimental verification of resonant frequencies and vibration behaviour of stators of electrical machines. Part

1 – Models, experimental procedure and apparatus,' *IEE Proceedings-B.*, Vol. 128, No. 1, January 1981, pp. 12-21.

VER81b Verma, S.P, Girgis, R.S., 'Experimental verification of resonant frequencies and vibration behaviour of stators of electrical machines, Part 2 – Experimental investigations and results,' *IEE Proceedings-B.*, Vol. 128, No. 1, January 1981, pp. 22-32.

VER89a Verma, S.P, Williams, K., and Signal, R.K., 'Vibrations of long and short laminated stators of electrical machines, Part 1 – Theory, experimental models, procedure and set-up,' *Journal of Sound and Vibration*, Vol. 129, No. 1, 1989, pp. 1-13.

VER89b Verma, S.P, Williams, K., and Signal, R.K., 'Vibrations of long and short laminated stators of electrical machines, Part 2 – Results for long stators,' *Journal of Sound and Vibration*, Vol. 129, No. 1, 1989, pp. 15-29.

VUK91 Vukosavic, S., Stefanovic, V.R., 'SRM inverter topologies: A comparative study,' *IEEE Transactions on Industry Applications*, Vol. 27, No. 6, 1991, pp. 1034-1047.

WAL90 Wallace, A.K., Spee, R., and Martin, L.G., 'Current harmonics and acoustic noise in AC adjustable-speed drives', *IEEE Transactions on Industry Applications*, Vol. 26, No. 2, March/April 1990, pp. 267-273.

WAN97 Wang, H., Williams, K., 'Effects of laminations on the vibrational behaviour of electrical machine stators', *Journal of Sound and Vibration*, Vol. 202, No. 5, 1997, pp. 703-715.

WAT83 Watanabe, S., Kenjo, S., Ide, K., Sato, F., Yamamoto, M., 'Natural frequencies and vibration behavior of motor stators,' *IEEE Transactions on Power Apparatus and Systems*, Vol. 102, No. 4, 1983, pp. 949-956.

WIL89 Williams, K., Signal, R.K., and Verma, S.P., 'Vibrations of long and short laminated structures of electrical machines Part II - Results for long stators', *Journal of Sound and Vibration*, Vol.129, 1989, pp.15-29.

WU93 Wu, C.Y., Pollock, C., 'Time domain analysis of vibration and acoustic noise in the switched reluctance drive', *Proc. International Conference on Electrical Machines and Drives, (EMD)*, 1993, pp. 558-563.

WU95 Wu, C.Y., and Pollock, C., 'Analysis and reduction of acoustic noise in the switched reluctance drive', *IEEE Transactions on Industry Applications*, Vol. 31, No.6, 1995, pp. 91-98.

WU96 Wu, X., Haramura, S., Ueda, J., 'Development of switched reluctance motor for electric vehicle – acoustic noise reduction', *Proc. Drives and Controls Conference*, 1996, pp. 1-5.

XU99 Xu, L., 'Influence of PWM and control trategies on acoustic noise and EMI emissions from induction motor drives', *Ph.D Thesis, University of Sheffield*, 1999.

YAN78 Yang, S.J., 'Finite element method in evaluating the stator natural

frequencies of small machines,' *Proc. International Conference on Electrical Machines (ICEM)*, 1978, pp. G3-G8.

YAN81 Yang, S.J., 'Low noise electrical motors', *Oxford Claredon Press*, 1981

YON86 Yong-Xiao, C., Zhu, Z.Q., 'Study of the natural frequencies and modes of stators of electrical machines,' *Proc. International Conference on Electric Machines, (ICEM)*, Germany 1986, pp. 301-304.

YON97 Yong-Xiao, C., Jianhua, W., Jun, H., 'Analytical calculation of natural frequencies of stator switched reluctance motor', *Proc. Electric Machines and Drives conference, (EMD)*, 1997, pp. 81-85.

ZHU87 Zhu, Z.Q., Chen, Y.X., 'The analysis of natural frequencies and modes of electrical machine stators by finite element method', *Trans. Chinese Electrotechnology*, No. 4, 1987, pp. 39-46.

ZHU89 Zhu, Z,Q., Howe, D., 'Effects of end-shields and rotor on natural frequencies and modes of stator of small electrical machines,' *Proc. Electric Machines and Drives Conference, (EMD)*, 1989, pp. 232-236.

ZHU93 Zhu, Z.Q., Howe, D., 'Electromagnetic noise radiated by brushless permanent magnet DC drives,' *Proc. Electric Machines and Drives Conference, (EMD)*, 1993, pp. 606-611.

List of Publications

1. Long, S.A., Zhu, Z.Q., Howe, D., 'Influence of Stator Laminations on Natural Frequencies of Switched Reluctance Motors', *Proceedings of International Seminar on Vibrations and Acoustic Noise of Electrical Machinary, (VANEM)*, Bethune, France, 25-26th May 1998, pp. 135-139.

2. Long, S.A., Zhu, Z.Q., Howe, D., 'Vibrational Behaviour of Switched Reluctance Motors', *Proceedings of International Conference on electrical Machines (ICEM)*, Instanbul, Turkey, 2-4th September 1998, pp. 2122-2127.

3. Long, S.A., Zhu, Z.Q., Howe, D., 'Influence of Windings on the Natural Frequencies of Switched Reluctance Motors', *Proceedings of International Seminar on Vibration and Acoustic Noise of Electric Machinery, (VANEM)*, Lodz, Poland, June 2000, pp. 103-107.

4. Long, S.A., Zhu, Z.Q., Howe, D., 'Vibration Behaviour of Stators of Switched Reluctance Motors', *IEE Proceedings of Electric Power Applications*, Vol. 148, No. 3, May 2001, pp. 257-264.

5. Long, S.A., Zhu, Z.Q., Howe, D., 'Influence of Load on Noise and Vibration of Voltage and Current Controlled Switched Reluctance Machines', Accepted for *International Conference on Power Electronics, Machines and Drives, (ICPEMD)*, Bath 16-18 April 2002.

6. Long, S.A., Zhu, Z.Q., Howe, D., 'Effectiveness of Active Noise and Vibration Cancellation of Switched Reluctance Machines Under Alternative Control Strategies', Accepted for *International Conference on Electric Machines, (ICEM) 2002*.

Appendices

Appendix A: Alternative inverter topologies for switched reluctance machines

The phase current associated with the operation of the SR machine is always unipolar and therefore the inverter only requires at most a half H-bridge configuration. The active switching devices are separated by the machine phase windings which avoids the problem 'shoot through' associated with standard H-bridge configurations and hence there is no requirement of dead-time generation. Although there are a number of different inverter topologies available for switching the supply current in the phases of SR machines, all need to fulfil a number of criteria to enable sufficient operation of the machine. The capability to provide pulse width modulation (PWM) of the applied voltage is necessary at low speeds to limit the winding current, whereas, since at high speeds the time available for injecting the current into the winding is limited, a sufficiently high forcing voltage is required. When a phase is switched off this high forcing voltage is required for demagnetisation to ensure the current tail is extinguished quickly to avoid negative torque production. Ultimately the choice of topology and power rating of components depend upon the application of the machine. The following text provides a brief description of the operation of common SRM inverters divided into two main categories viz. single rail and dual rail inverters.

A.1. Single Rail Inverters

The 'Classic' Circuit

The 'classic' circuit or half-asymmetric H-bridge configuration shown below in **Fig. A.1** is probably the most common topology used for SR machines and has been addressed in many publications, [RAD92, VUK91, MIL87b]. This circuit is very reliable and robust since it comprises of two active switches per phase such that all phases are totally independent, i.e. if one phase fails, operation of the remaining phases is unaffected and the machine continue operating, although at a lower power. The voltage available for the de-magnetisation of the phase windings is the same as that available for magnetisation due to the asymmetric configuration and the inverter configuration allows flexibility of machine operation through the use of simple control algorithms, using the three main switching states outlined below for phase 1.

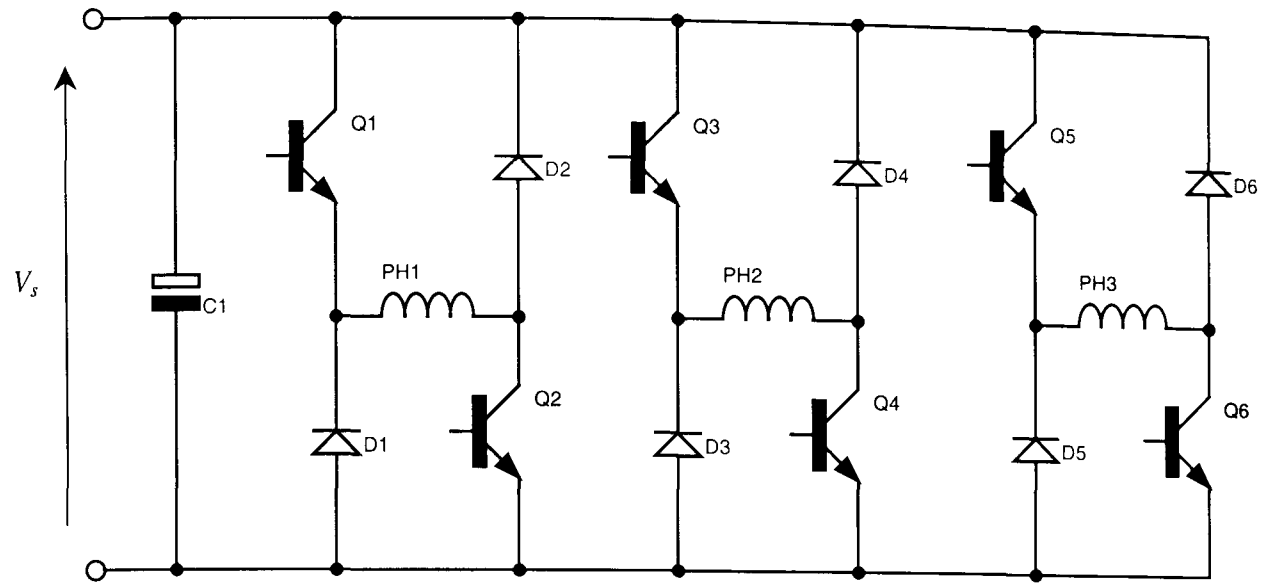

Fig. A.1 The 'Classic' Circuit

(i) When the switches Q1 and Q2 are turned on, full supply voltage, V_s, is dropped across phase 1 and the current takes the path Q1, PH1, Q2.

(ii) If Q1 switched off whilst Q2 remains on, the current freewheels via D1 taking the path D1, PH1, Q2 and hence zero volts are dropped across phase 1, and the freewheeling current decays as energy is returned to the supply via C1. Note that current flow through the phase winding remains in the same direction.

(iii) When Q1 and Q2 are both switched off negative supply voltage, V_s, is imposed across phase 1, forcing the current to freewheel via D1, PH1 and D2. Again, current flow remains in same direction, but the negative voltage is de-fluxing the machine and hence the current is forced to zero whilst the stored field energy is returned to the supply.

At high speeds where the back-emf is large enough to limit the current, 'single pulse' operation is employed, whereby stage (i) is applied at the start of the working stroke and stage (iii) is applied at the end. For lower speeds, where current limiting is required, PWM is used, be it voltage or current controlled, whereby stage (i) and (ii) are used to maintain the current within a particular band or below a limiting value. This is known as 'soft chopping,' since only the dc voltage supply is chopped across the winding between these two stages. At the end of the working stroke, stage (iii) is then applied. Hard chopping can be implemented utilising stages (i) and (iii) to maintain the current, during which twice the supply voltage is 'chopped' across the windings.

Single Switching Device Circuits

A number of single device solutions have been proposed, [EHS87, MIL93], some of which are impractical for many applications and generally limit the machine operation, and therefore only a brief description of these is presented. The circuit diagrams shown in **Fig. A.2** show circuit configurations for a single phase leg for description purposes.

Freewheeling Circuit (Fig. A.2a)

When Q1 is on, full supply voltage is dropped across the winding. When Q2 turns off the diode provides a freewheel path for the current. However during this freewheel period zero voltage is dropped across the windings and hence there is no voltage to force de-magnetisation of the windings, which is provided by the resistance of the windings and the volts dropped across the diode.

Suppression Resistor Circuit (Fig. A.2b)

This is an extension of **Fig. A.2a** with the additional resistance to enhance the available de-fluxing capability. This is unsatisfactory since the suppression voltage decreases with decrease in current, and hence the extinction of current is still prolonged.

Zener Diode Circuit (Fig. A.2c)

The addition of the zener diode enables **Fig. A.2b** to sustain a higher level of suppression voltage.

Bifolar Windings (Fig. A.2d)

When Q1 turns off, the current in the primary transfers to the secondary and freewheels via D1. Unlike circuits **Figs. A.2a, b and c**, this circuit provides negative supply voltage when Q1 is switched off, but a zero voltage loop is not attainable. The coupling between the primary and secondary windings will not be perfect, and so a transient voltage may occur.

(m+1)-Switch Circuit

Otherwise known as the Miller circuit, [MIL87b, MIL88], this guarantees a total number of $m_{ph}+1$ switches, where m_{ph} is the number of phases. Each phase comprises of a single switch to necessitate the commutation of phases, whereas QA, **Fig. A.3**, is a common chopping switch for all phases together with the freewheel diode DA. Likewise, for the classic half-asymmetric H-bridge, this circuit can perform soft and hard switching incorporating the three stages outlined earlier. For normal operation this can match the

performance of the classic circuit with the same component ratings. However, when increased dwell commutation is introduced and hence phase overlap occurs, QA will be carrying twice as much current compared to the classic circuit, therefore increasing the rating requirement of QA and DA. Another obvious weakness associated with this configuration is the loss of phase independence, i.e. if QA fails then all the phases are disabled.

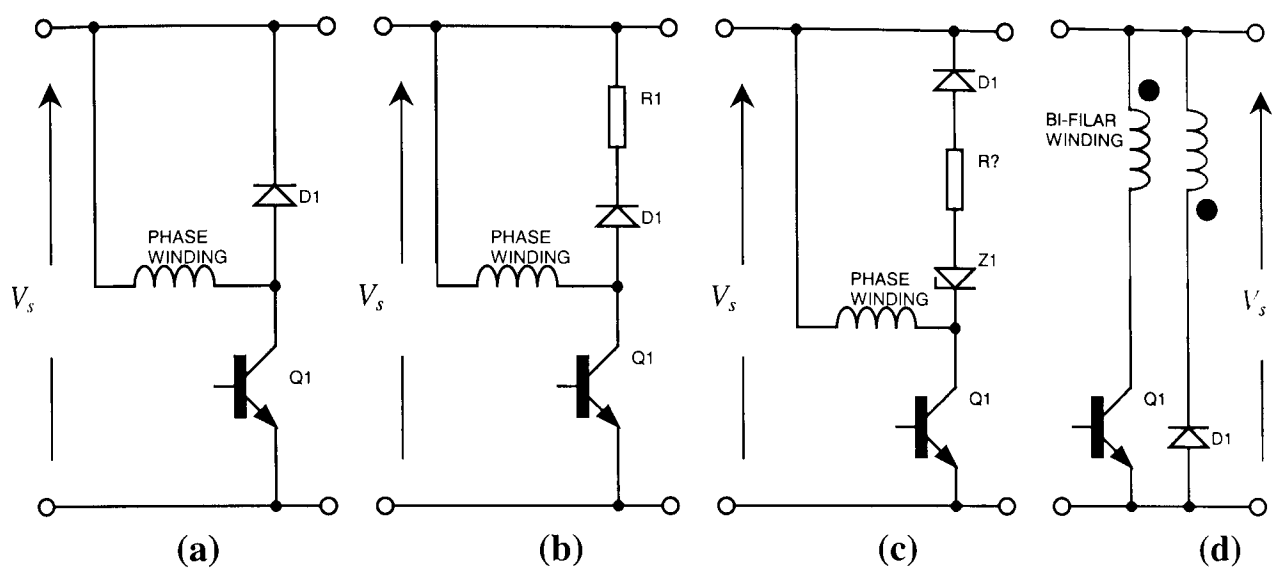

Fig. A.2 Single Switching Device Topologies

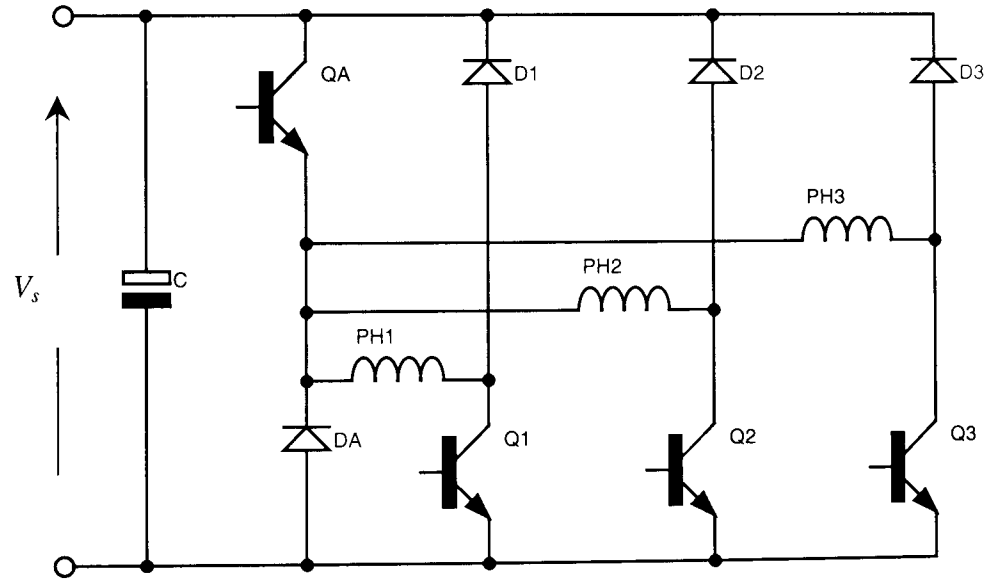

Fig. A.3 The (m_{ph}+*1*) Switch Circuit

The 2(m_{ph}+*1*) Switch Circuit

This is an extension of the m_{ph}+1 circuit, whereby, instead of one common chopper switch and freewheel diode being shared between all phases, each pair of phases share, [KRI87, STE89], **Fig. A.4**. Therefore this topology is limited to machine topologies comprising of even phase numbers and once again, operation is the same as outlined for the classic circuit. This topology has two distinct advantages over the (m_{ph}+*1*) configuration. Firstly, owing to phases 1 and 3 sharing common chopping devices and phases 2 and 4 sharing the chopping devices, neither chopping device carries double

current during overlap. Quite simply QA and QB will be overlapping, and hence their ratings remain the same as the other switching devices. Secondly, this circuit is more fault tolerant than the $m_{ph}+1$ circuit since if one chopper fails only two phases are disabled.

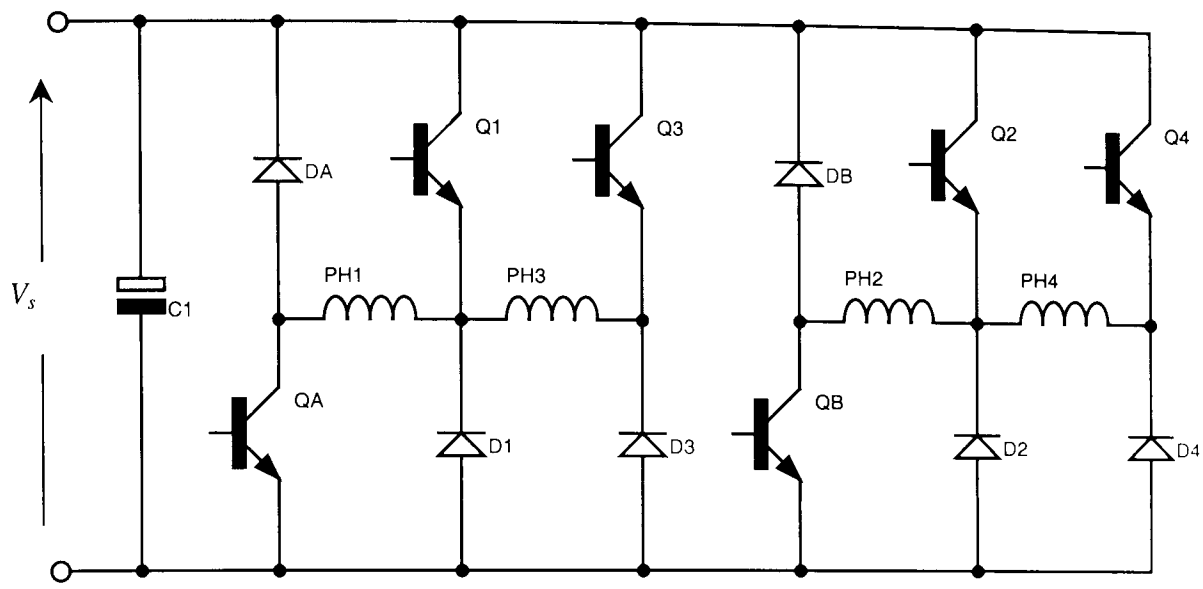

Fig. A.4 The 2($m_{ph}+1$) Switch Circuit

Oulton Circuit

This utilises the minimum possible number of switching devices, [MIL93], one per phase, whilst maintaining full flux reversal, unlike the circuits discussed earlier in **Fig. A.2**. This incorporates a split dc supply, **Fig. A.5**, and thus, for viable operation of the machine a good balance is required between the pairs of phases and again is limited to machines with an even number of phases. The operation is as follows.

(i) If Q1 is on, half the supply voltage is dropped across phase 1, and the current takes the path Q1, PH1, C1, but no current flows through phase 2.

(ii) When Q1 switched off, the current freewheels through phase 1 via D2, PH1, C2 and negative half of the supply voltage is dropped across phase 1 for demagnetisation.

(iii) The operation is the same for phase 2, by utilising Q2, D1 and C2.

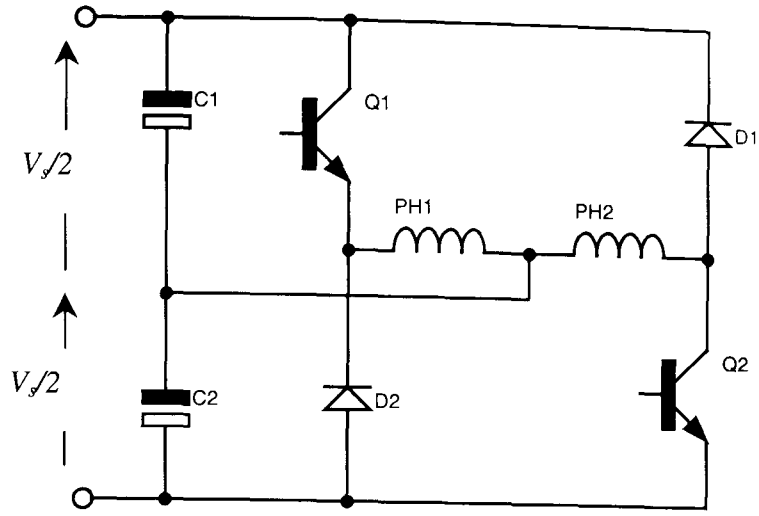

Fig. A.5 Oulton Circuit

A.2. Dual Rail Inverters

C-Dump Circuit (Capacitive Supression)

A number of these are discussed in detail [EHS87], viz. with damped energy recovery. with resonant energy recovery and with chopper energy recovery. The general philosophy behind this circuit is based upon sharing the freewheel circuit as opposed to the chopping device, **Fig. A.6**. The capacitor voltage is controlled with the converter and most energy is recovered, as described below.

(i) When Q1 is switched on, the supply voltage is dropped across phase 1, and the current takes the path PH1, Q1, C.

(ii) When Q1 turns off, the current freewheels into the dump capacitor, CD, via D1, which consequently discharges into the dump inductor, LD.

(iii) When QA is turned on, the energy in L is returned to supply via DA.

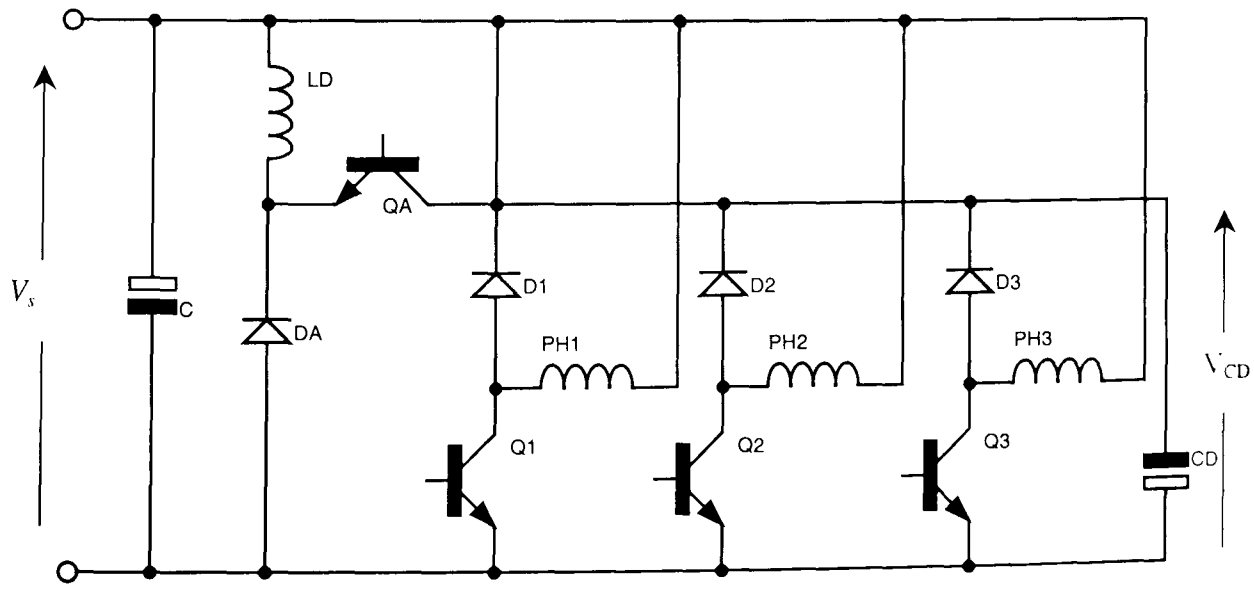

Fig. A.6 C-Dump Circuit with chopper energy recovery

Buck-Boost Inverter

This is so named because the components C1, QA, L, DA and C2 are arranged in the form of a buck-boost converter, **Fig. A.7**, and is outlined in [VUK91]. The stages of operation are outlined below:

(i) With Q1 switched on a current path is provided through phase 1 via C2 and Q1.

(ii) When Q1 is switched off, diode D1 freewheels and the current takes the path PH1, D1 and C1. The voltage dropped across Q1 at this point is $V_{c1}+V_{c2}$.

(iii) When QA is turned on, it acts like a buck-boost inverter and the current builds up in L from C1 and hence C1 discharges into L.

(iv) When QA turned off, the energy stored in L is now transferred to C2 ready for stage (i). During this period, the voltage across QA is $V_{c1}+V_{c2}$.

(v)

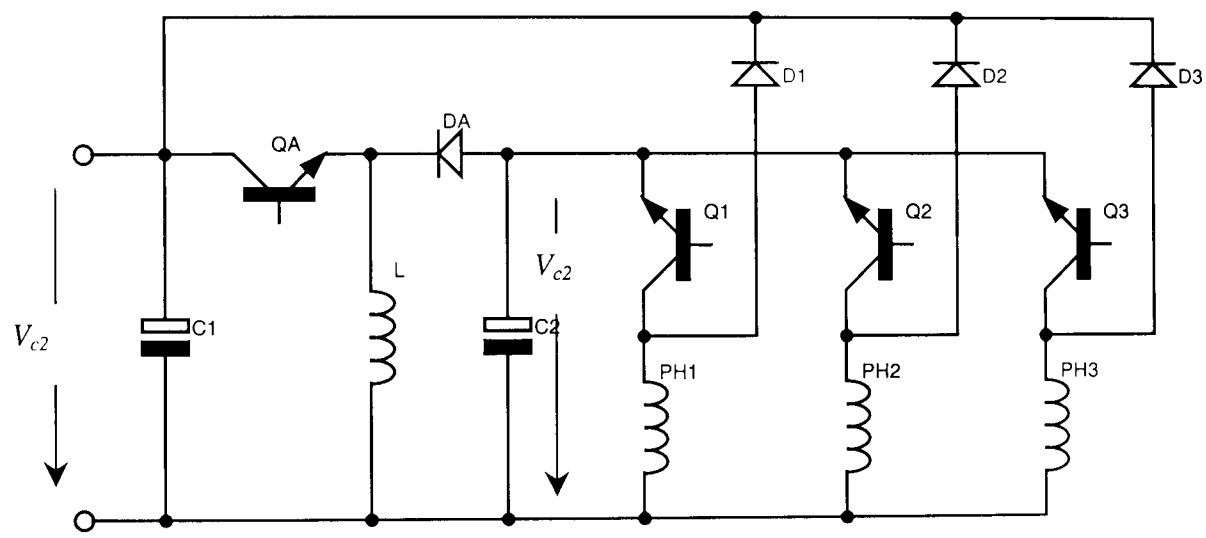

Fig. A.7 Buck-boost converter

Sood Inverter

This circuit is relatively new compared with the other topologies discussed above, and when presented [VUK91] the circuit was patent pending, [SOO92]. The circuit configuration is similar to that of the c-dump and buck-boost already discussed, however, this circuit eliminates the requirement of a dc link inductance and capacitor and provides a direct transfer of the capacitor energy to the machine windings, **Fig. A.8**. The operation, which is more complex than for the other circuits, is summarised below.

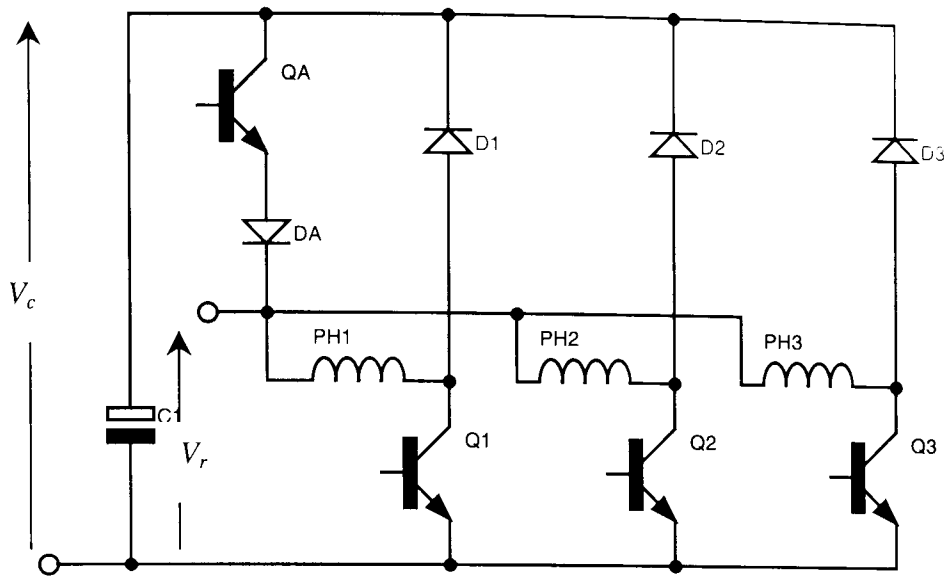

Fig. A.8 Sood Inverter

(i) Q1 is on and the phase winding is connected directly to the unfiltered rectified voltage, V_r.

(ii) Q1 and QA are on, thus magnetising the windings from the capacitor voltage, V_c. This is larger than the rectified voltage, V_r and hence the input rectifier is reverse biased and the energy flows form the capacitor to the winding. Note, that if $V_c < V_r$ then QA would be reverse biased and the operation would return to (i).

(iii) Q1 is turned off whilst QA remains on, initiating a freewheel state through QA, DA and D1. The energy is returned to the supply as phase 1 is de-magnetised.

(iv) Q1 is now also turned off and a proportion of the available energy is returned to the capacitor whilst the winding is de-magnetised through the path D1, input rectifier and capacitor.

Appendix B: Mesh density convergence data

Table B.1 *Element type 42 – 2D 4-node structural solid element*

Number of elements	Vibrational mode shape				RMS error	Normalised wavefront^2
	0	2	3	4		
12	19780	3534	12498	31250	1.588	1.00
16	19583	3091	9499	20425	1.208	1.00
24	19444	2899	8338	16424	1.073	1.00
48	19444	2906	8362	16367	1.073	1.19
96	19361	2813	7846	14769	1.018	1.19
144	19361	2809	7826	14711	1.016	1.40
288	19340	2787	7709	14347	1.003	1.40
384	19340	2786	7700	14323	1.002	1.62
576	19336	2782	7679	14257	1.000	1.62
720	19336	2781	7674	14245	1.000	1.86
1440	19334	2778	7661	14204	0.998	2.12
1760	19333	2777	7652	14178	0.997	4.00
Measured values	19072	2816	7680	14272		

Table B.2 *Element type 82 – 2D 8-node structural solid element*

Number of elements	Vibrational modes				RMS error	Normalised wavefront^2
	0	2	3	4		
8	19345	2859	8383	17453	1.089	1.51
12	19335	2800	7833	14982	1.020	1.51
24	19333	2781	7692	14322	1.002	1.51
48	19333	2778	7663	14278	1.000	1.99
96	19333	2776	7652	14179	0.997	1.99
144	19333	2776	7650	14174	0.997	2.53
288	19333	2776	7650	14170	0.997	2.53
384	19333	2776	7650	14170	0.997	3.14
720	19333	2776	7650	14170	0.997	3.82
1440	19333	2776	7649	14169	0.997	10.42
Measured values	19072	2816	7680	14272		

Table B.3 *Element type 45 – 3D 8-node structural solid element, axial mode, m=0*

Element Size	Number of elements	Vibrational modes			RMS error	Normalised Wavefront^2
		2	3	4		
0.02	72	2966	8561	16838	1.117	4.37
0.015	96	2963	8552	16818	1.116	5.59
0.01	180	2888	8140	15506	1.058	6.95
0.009	216	2887	8137	15500	1.057	8.46
0.008	576	2871	8029	15139	1.042	15.46
0.007	672	2870	8026	15135	1.042	18.84
0.006	960	2858	7963	14942	1.033	22.56
0.005	1200	2857	7961	14937	1.033	31.00
0.0045	1584	2850	7927	14834	1.028	35.73
0.004	3024	2843	7887	14713	1.023	68.81
0.003	5184	2838	7863	14644	1.019	109.77
Measured values		2816	7680	14272		

Table B.4 *Element type 45 – 3D 8-node structural solid element, axial mode, m=1*

Element size	Number of elements	Vibrational modes				RMS error	Normalised Wavefront^2
		1	2	3	4		
0.02	72	18152	4763	12076	21183	1.089	4.37
0.015	96	18070	4724	11951	20934	1.079	5.59
0.01	180	17863	4657	11568	19688	1.046	6.95
0.009	216	17839	4642	11531	19626	1.043	8.46
0.008	576	17782	4629	11429	19275	1.035	15.46
0.007	672	17767	4619	11407	19245	1.033	18.84
0.006	960	17730	4606	11349	19069	1.028	22.56
0.005	1200	17718	4595	11326	19036	1.026	31.00
0.0045	1584	17699	4589	11296	18945	1.024	35.73
0.004	3024	17686	4569	11227	18782	1.019	68.81
0.003	5184	17669	4560	11198	18709	1.016	109.77
Measured values		17536	4480	11008	18304		

Table B.5 *Element type 73 – 3D 8-node structural solid element with rotations, axial mode, m=0*

Element size	Number of elements	Vibrational modes			RMS error	Normalised Wavefront^2
		2	3	4		
0.02	72	2877	8074	15288	1.048	8.46
0.015	96	2877	8070	15277	1.048	11.93
0.01	180	2847	7928	14865	1.028	16.00
0.009	216	2847	7928	14863	1.028	20.66
0.008	576	2838	7865	14662	1.020	43.44
0.007	672	2838	7865	14661	1.020	54.89
0.006	960	2832	7839	14587	1.016	67.69
0.005	1200	2832	7839	14586	1.016	97.29
0.0045	1584	2829	7825	14545	1.014	113.62
0.004	3024	2827	7814	14517	1.013	234.65
Measured values		2816	7680	14272		

Table B.6 *Element type 73 – 3D 8-noded structural solid element with rotations, axial mode, m=1*

Element size	Number of elements	Vibrational modes				RMS error	Normalised Wavefront^2
		1	2	3	4		
0.02	72	17825	4633	11461	19184	1.035	8.46
0.015	96	17821	4625	11431	19184	1.034	11.93
0.01	180	17747	4602	11324	19001	1.027	16.00
0.009	216	17746	4600	11316	18984	1.026	20.66
0.008	576	17719	4568	11203	18711	1.018	43.44
0.007	672	17718	4567	11200	18704	1.017	54.89
0.006	960	17706	4563	11182	18649	1.016	67.69
0.005	1200	17706	4562	11181	18646	1.016	97.29
0.0045	1584	17700	4560	11172	18562	1.014	113.62
0.004	3024	17686	4558	11162	18591	1.014	234.65
Measured values		17536	4480	11008	18304		

Table B.7 *Element type 95 – 3D 20-node structural solid element, axial mode, m=0*

Element size	Number of elements	Vibrational modes			RMS error	Normalised Wavefront^2
		2	3	4		
0.02	72	2860	7938	14825	1.029	16.00
0.015	96	2858	7933	14812	1.029	21.92
0.01	180	2843	7873	14657	1.021	28.77
0.009	216	2842	7872	14654	1.020	36.55
0.008	576	2830	7816	14503	1.013	80.59
0.007	672	2830	7815	14501	1.013	101.37
0.006	960	2829	7812	14493	1.012	124.53
0.005	1200	2829	7812	14492	1.012	177.98
0.0045	1584	2829	7811	14489	1.012	208.28
Measured values		2816	7680	14272		

Table B.8 *Element type 95 – 3D 20-node structural solid element, axial mode, m=1*

Element size	Number of elements	Vibrational modes				RMS error	Normalised Wavefront^2
		1	2	3	4		
0.02	72	17661	4607	11333	18986	1.026	16.00
0.015	96	17654	4591	11296	18924	1.023	21.92
0.01	180	17651	4576	11242	18784	1.019	28.77
0.009	216	17649	4571	11231	18766	1.018	36.55
0.008	576	17646	4542	11132	18544	1.011	80.59
0.007	672	17645	4539	11125	18534	1.011	101.37
0.006	960	17645	4537	11120	18522	1.010	124.53
0.005	1200	17644	4535	11115	18516	1.010	177.98
0.0045	1584	17644	4535	11114	18512	1.010	208.28
Measured values		17536	4480	11008	18304		

Table B.9 *Convergence of elements in z-direction, element type 73 – 3D 8-node structural solid element with rotations, axial mode, m=0*

Element size	Number of elements	Vibrational modes			RMS error	Normalised Wavefront^2
		2	3	4		
1	96	2791	7717	14344	1.000	8.46
2	192	2850	7905	14747	1.025	14.93
3	288	2847	7893	14718	1.023	21.92
4	384	2845	7888	14706	1.023	30.25
5	480	2845	7886	14700	1.022	39.92
6	576	2845	7885	14698	1.022	50.93
Measured value		2816	7680	14272		

Table B.10 *Convergence of elements in z-direction, element type 73 – 3D 8-node structural solid element with rotations, axial mode, m=1*

Element size	Number of elements	Vibrational modes				RMS error	Normalised Wavefront^2
		1	2	3	4		
1	96	18070	4695	11487	19131	1.042	8.46
2	192	17710	4592	11279	18856	1.022	14.93
3	288	17685	4557	11205	18750	1.017	21.92
4	384	17680	4550	11181	18703	1.015	30.25
5	480	17679	4547	11170	18679	1.015	39.92
6	576	17678	4545	11164	18667	1.014	50.93
Measured value		17536	4480	11008	18304		

Appendix C: Mesh density scaling

The following defines the ratio of element area to model area based on that of the simple annular ring, from which the appropriate element size is derived for the simple dc motor stator modelled in Chapter 3, section 3.2.2.

The area per element is calculated from equation (C.1) and the ratio of element area to area of model given by equation (C.2) is 2.6e-03m^2, where the variables are defined in **Table C-1** together with their corresponding values.

$$\text{Area per element, } A_E = \frac{A_{ring}}{E_{ring}} \tag{C.1}$$

$$\text{Ratio, } R = \frac{A_E}{A_{ring}} \tag{C.2}$$

Table C.1 *Variables of annular ring*

Area of annular ring, A_{ring}	2.1808e-03m^2
Number of elements in annular ring, E_{ring}	384

By application of the ratio, R, the element area for the dc motor stator and thus the element length to be specified for the mesh is calculated by equation (C.3) where the variables and their corresponding values are defined in **Table C-2**.

$$\text{Element area} = R \times A_{yoke} \tag{C.3}$$

Table C.2 *Variables of dc motor stator*

Area of yoke of dc motor stator, A_{yoke}	21.837e-03m^2
Element area	5.69e-05m^2
Element length	0.0075m

Appendix D: Model dimensions

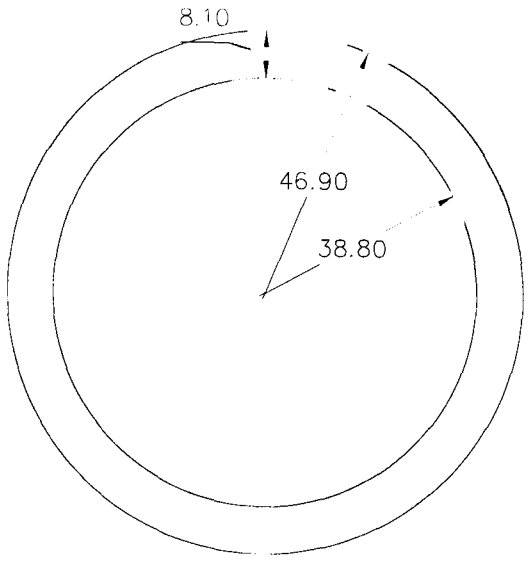

(a) Model Ia/b

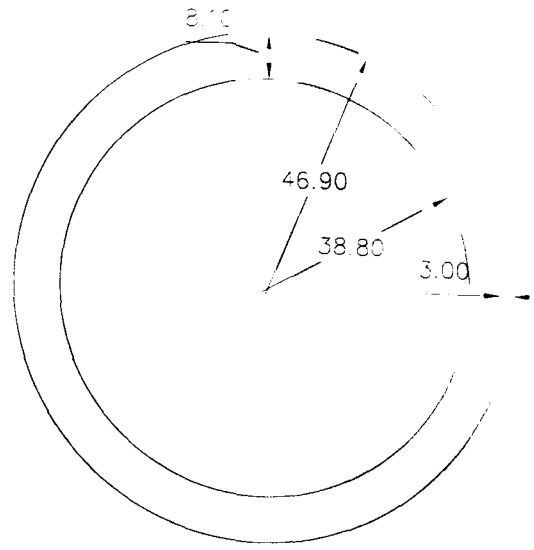

(b) Model II

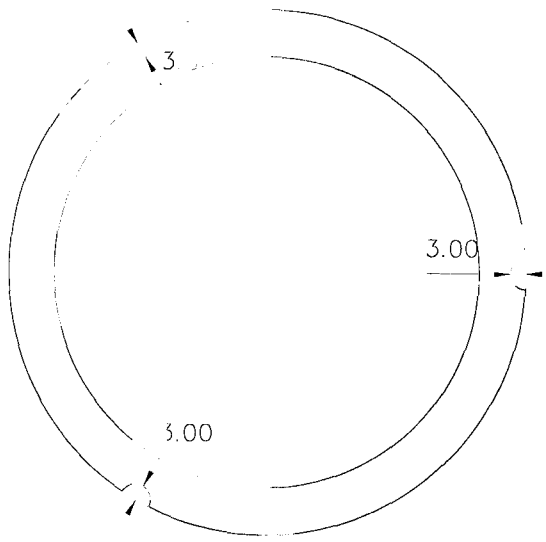

(c) Model III

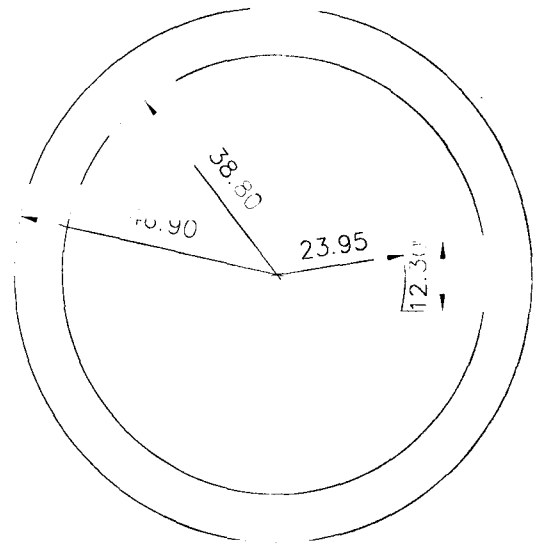

(d) Model IV

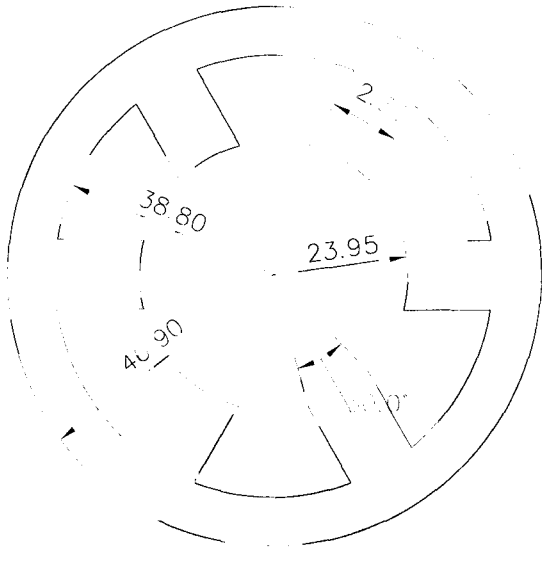

(e) Model V

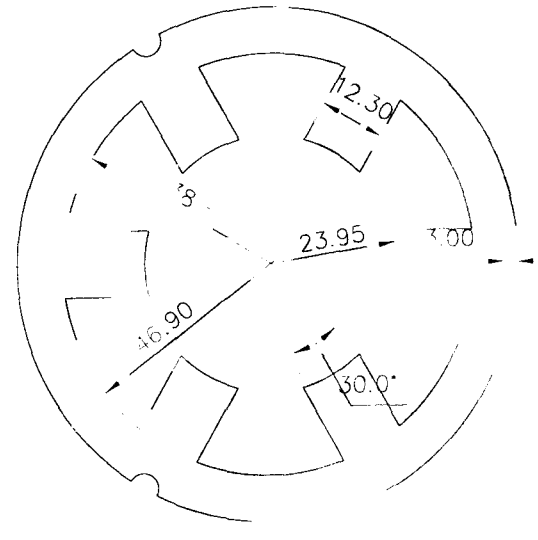

(f) Model VIa/b

Fig. D.1 *Details of geometric parameters, all dimensions in mm, axial length = 46.9mm*

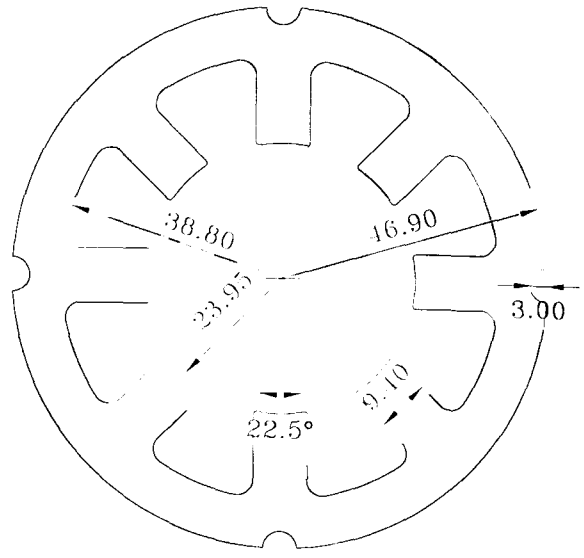

Fig. D2 *Details of 8-pole stator, Model VIIIa/b axial length 46.9mm, all dimensions in mm*

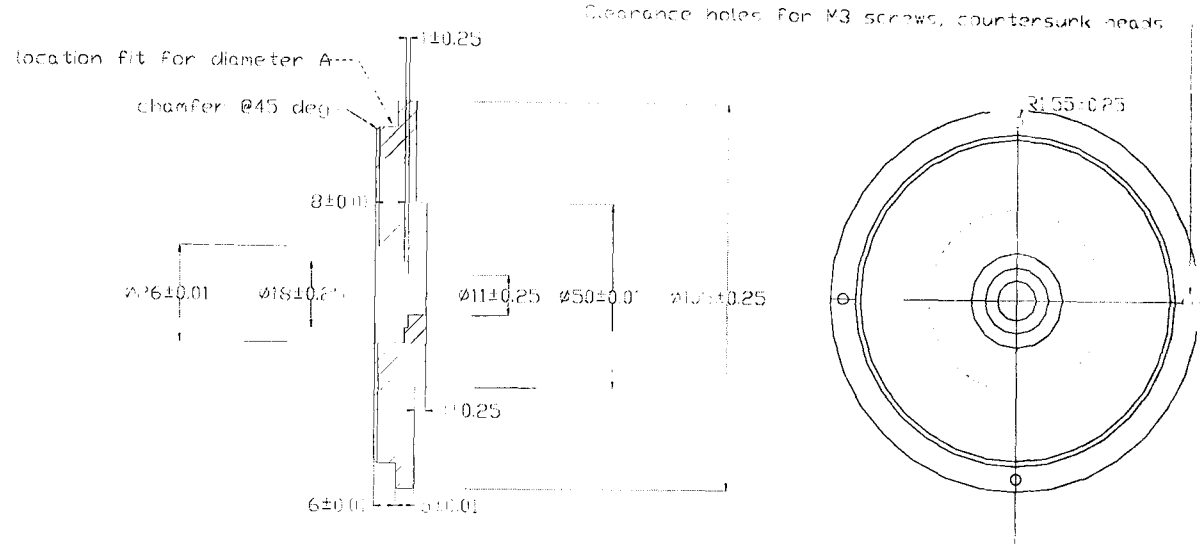

(a)

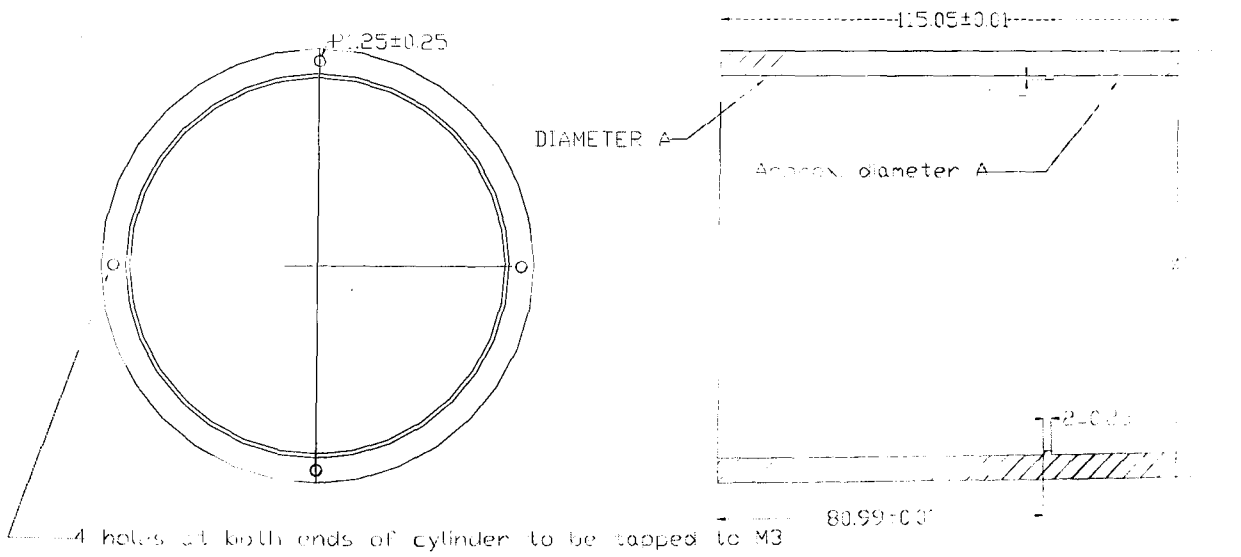

(b)

Fig. D3 *Details of (a) End-caps, (b) Frame, all dimensions in mm*

Table D.1 *Mass of stator components*

Stator component	Mass (kg)
Stator slot windings	0.340
Stator end-windings	0.165
Frame	0.554
End-caps (total)	0.446

Appendix E: Lamination convergence data

Table E.1 $G_{xz}=G_{yz}=82.69GPa$

Modulus of shear G_{xy} (GPa)	Young's modulus E_z (GPa)	mode 2	error (%)	mode 3	error (%)	mode 4	error (%)
70	2.15E+11	2931	-9.04	8002	-7.79	14904	-8.31
60	2.15E+11	2886	-7.37	7767	-4.62	14441	-4.95

Table E.2 $G_{xz}=G_{yz}=11GPa$

Modulus of shear G_{xy} (GPa)	Young's modulus E_z (GPa)	mode 2	error (%)	mode 3	error (%)	mode 4	error (%)
60	215	2697	-0.33	7675	-3.38	14253	-3.58
58.5	215	2677	0.41	7637	-2.87	14178	-3.04
57.5	215	2664	0.89	7611	-2.52	14127	-2.67
57.5	172	2673	0.56	7637	-2.87	14176	-3.02
55.5	215	2636	1.93	7558	-1.80	14020	-1.89
55	215	2628	2.23	7544	-1.62	13993	-1.69
55	172	2637	1.90	7569	-1.95	14041	-2.04

Table E.3 $G_{xz}=G_{yz}=9GPa$

Modulus of shear G_{xy} (GPa)	Young's modulus E_z (GPa)	mode 2	error (%)	mode 3	error (%)	mode 4	error (%)
55	215	2627	2.27	7537	-1.52		
55	151	2640	1.79	7577	-2.06		
57.5	151	2676	0.45	7645	-2.98		
57.5	172	2670	0.67	7627	-2.73		

Table E.4 $G_{xy}=G_{yz}=8GPa$

Modulus of shear G_{xy} (GPa)	Young's modulus E_z (GPa)	mode 2	error (%)	mode 3	error (%)	mode 4	error (%)
55	215	2626	2.31	7533	-1.47		
55	172	2633	2.05	7554	-1.75	14010	-1.82
55.5	215	2633	2.05	7547	-1.66	13998	-1.73
56	215	2640	1.79	7560	-1.83	14025	-1.93
57.5	215	2661	1.00	7600	-2.37	14104	-2.50
57.5	172	2668	0.74	7622	-2.67	14144	-2.79
58.5	215	2674	0.52	7626	-2.72	14155	-2.87
58.5	172	2682	0.22	7684	-3.50	14195	-3.16
60	215	2694	-0.22	7664	-3.23	14248	-3.55
60	172	2702	-0.52	7686	-3.53	14288	-3.84
70	215	2813	-4.65	7888	-6.25	14674	-6.64
80	215	2914	-8.41	8076	-8.78	15029	-9.22
82.69	215	2938	-9.30	8121	-9.39	15115	-9.85

Appendix F: Winding convergence data

Table F.1 *Convergence of Young's Modulii, E_x=E_y for machine windings*

Young's Modulus	Vibration modes				
	2a	2b	3a	3b	4a
1.20E+11	8958	9234	21308	22157	35078
6.00E+10	7374	7548	17370	17954	28557
3.00E+10	5927	6041	13910	14245	22672
1.50E+10	4713	4801	11169	11205	18541
1.20E+10	4379	4464	10375	10443	17348
6.00E+09	3517	3599	8231	8605	14248
3.00E+09	2893	2979	6676	7147	11988
1.50E+09	2463	2554	5608	7679	11242
1.30E+09	2394	2487	5436	7474	10724
1.25E+09	2376	2469	5391	7422	10598
1.20E+09	2357	2451	5346	7370	10464
1.15E+09	2340	2433	5300	7317	10333
1.10E+09	2321	2415	5253	7265	10200
1.05E+09	2302	2396	5204	7211	10064
1.00E+09	2283	2377	5156	7157	9923
9.50E+08	2263	2358	5106	7101	9778
9.00E+08	2243	2338	5055	7044	9625
8.50E+08	2223	2318	5002	6986	9463

Appendix G: Scaling of measured data from spectrum analyser

The following describes the Hewlett-Packard dynamic spectrum analyser, model HP35660A, employed for frequency domain and time domain analyses within the thesis, together with the accelerometer and sound pressure meter employed for measurement of the noise and vibration.

G.1. Spectrum Analyser

In order to establish a reference of the data displayed on the dynamic signal analyser, the screen display obtained for a sinusoidal waveform from a signal generator of 500Hz with a 2V peak and offset of 2V, is shown in **Fig.G.1**. This signal may be represented by equation (G.1), where ω is the frequency in rads^{-1} and t the time is seconds.

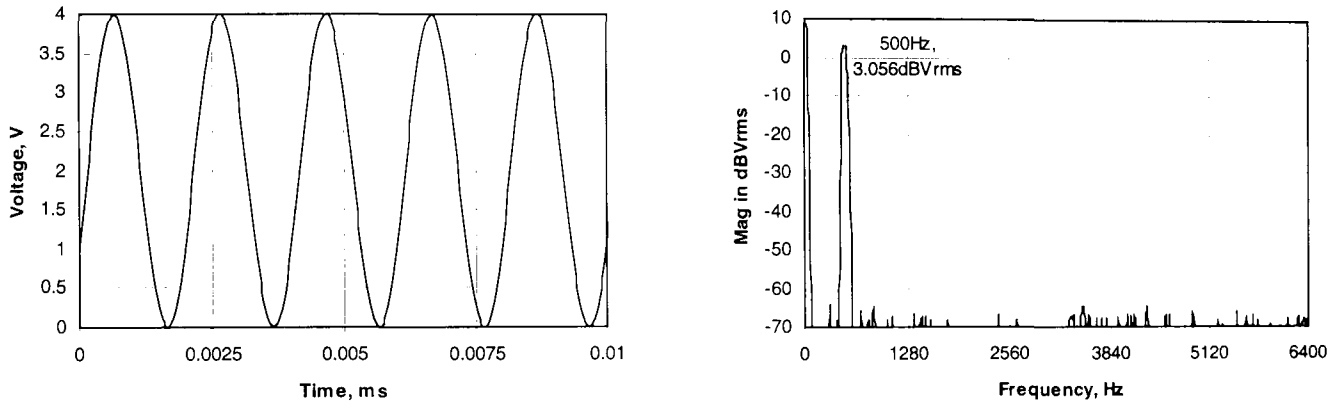

(a) **(b)**

Fig. G.1 *Measurement of sinusoidal signal; (a) time domain output from signal generator, (b) frequency spectrum displayed on signal analyser screen*

$$signal = 2 + 2\sin\omega t \tag{G.1}$$

From **Fig. G.1(b)** it is observed that the magnitude is represented by the value dBVrms, a value which is defined by equation (G.2), where V is voltage input to the spectrum analyser, and $1V_{rms}$ is $\sqrt{2}$. Thus, application of equation (G.2) for the 2V peak sinusoidal example above results in a magnitude of 3.056dBVrms, as is evidenced from the output of the spectrum analyser.

$$\text{dBVrms} = 20\log_{10}\left(\frac{V}{1V_{rms}}\right) \tag{G.2}$$

Finally, the dynamic spectrum analyser comprises of 401 discrete points to produce the continuous data, such that the resolution deteriorates with an increase in the chosen

frequency range, [HEW88]. Typical examples of the frequency resolution for a number of frequency ranges are shown in **Table G.1**.

Table G.1 *Resolution achieved with typical selections of the frequency range*

Frequency range (kHz)	Resolution (Hz)
25.6	64
12.8	32
6.4	16

G.2. Sound Pressure Level Meter

The following describes the calibration and necessary output scaling of the sound pressure level meter, B&K Type 2221, employed for measurements of the sound pressure level and the spectral analysis of the acoustic noise emitted by the experimental SR machine. The calibrator, supplied with the sound pressure meter produces a pure tone output at 1000Hz, 94 decibels (dB). The spectrum output displayed on the screen of the signal analyser is shown in **Fig. G.2(a)**, from which it is apparent that the value of –6.402bDVrms is meaningless in terms of noise in dB, and, therefore, requires scaling appropriately to obtain the magnitude of 94dB output by the calibrator, as displayed on the dial of the sound pressure level meter.

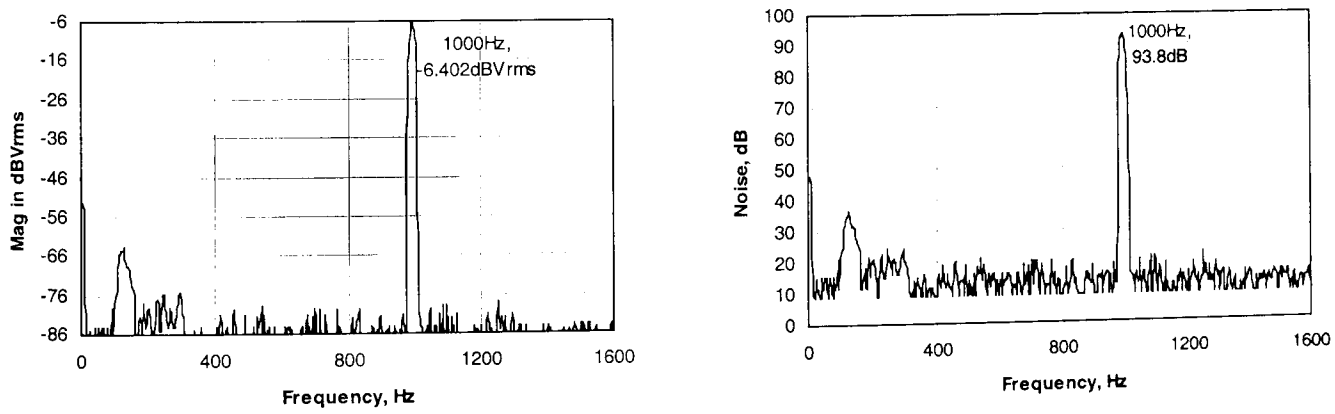

(a) **(b)**

Fig. G.2 *Sound pressure level meter measurement of calibrator signal; (a) output on spectrum analyser screen, (b) spectrum resulting from appropriate scaling of spectrum analyser data*

The appropriate scaling is provided by the offset values in **Table G.2**, where the Leq range is selected on the sound pressure level meter by the user. For calibration this was

set to the range of 45-105dB and therefore a value of 100 is added to the spectrum analyser data, thus resulting in a magnitude of 93.8dB, **Fig. G.2(b)**.

Table G.2 *Offset required for range settings of sound pressure meter*

Leq Range, dB(A)	Offset, dB(A)
85-145	140
65-125	120
45-105	100
25-85	80

G.3. Accelerometer

The accelerometer employed for vibration measurements is a quartz precision pezoelectronics accelerometer, with a calibrated sensitivity of 10mV/g suitable for frequencies beyond 10KHz, model 480(B). This is connected to the dynamic signal analyser via a pre-amp, model 480B02, of unity gain to match the output impedance of the accelerometer to the input impedance of the spectrum analyser. Given that the accelerometer, together with the pre-amp provides an output of 10mV/g, it follows that the acceleration is derived from the voltage output by equation (G.3).

$$acceleration = \frac{output\ voltage}{1.019e10^{-3}} (ms^{-2}) \qquad \text{(G.3)}$$

Appendix H: Fourier series of gate signals

The nominal switching angles employed for operation of the experimental 3-phase 6/4 SR machine result in a dwell period of 120°electrical, equivalent to 30° mechanical. The resulting commutation signals for the 3-phases is shown in **Fig. H-1**, where τ represents the dwell period.

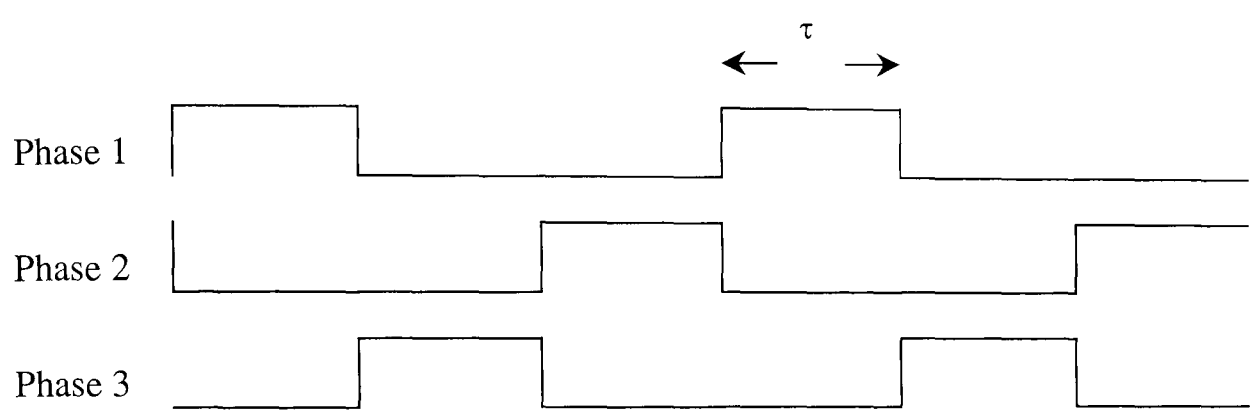

Fig. H.1 *Nominal commutation signals for experimental 3-phase 6/4 SR machine*

Thus, considering a single phase, the commutation signal has the form of the pulse train shown in **Fig. H-2**, where E is the magnitude of the pulses, and T is the period between successive pulses. The harmonics associated with the commutation signal may be determined from the general equation of the Fourier series, equation (H-1), and due to the fact that the signal is zero except within the region τ, this simplifies to equation (H-2).

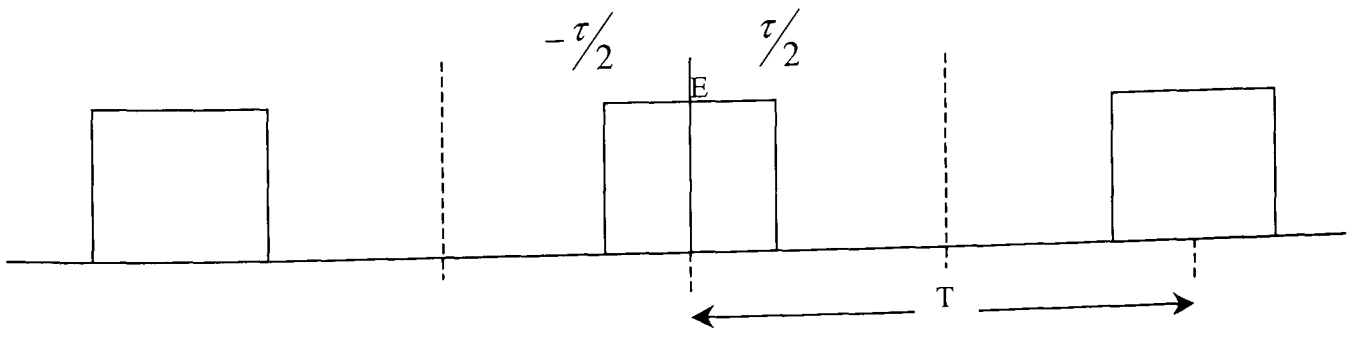

Fig. H.2 *Definition of variables for pulse train associated with single commutation signal*

$$C_n = \frac{1}{T}\int_{-T/2}^{T/2} f(t)\exp(-jn\omega_o t)dt \qquad \text{(H.1)}$$

$$C_n = \frac{2}{T}\int_{0}^{\tau/2} E\exp(-jn\omega_o t)dt \qquad \text{(H.2)}$$

Since it is a symmetric function only cosine terms are present and therefore solving equation (H-2) results with equation (H-3), and due to the fact that it is a 3-phase machine with nominal switching angles, the relationship between T and τ, equation (H-4), leads to equation (H-5), where n is the harmonic number, 1, 2, 3.....n^{th}. It can therefore be seen that when $n=3,6,9$, i.e. $n=3$ and multiples thereof, $C_n=0$.

$$C_n = \frac{E\tau}{T}\frac{\sin(\pi n f_o \tau)}{(\pi n f_o \tau)} \tag{H.3}$$

$$\frac{\tau}{T} = \frac{1}{3} = \tau T \tag{H.4}$$

$$C_n = \frac{E}{3}\frac{\sin(\pi n/3)}{(\pi n/3)} \tag{H.5}$$

Appendix I: Sound pressure level test data

Table I.1 *Sound pressure level, (dBA), no-load*

Speed (rpm)	Voltage control		Current control		Single pulse mode
	Soft	Hard	Soft	Hard	
500	63.6	65.1	74.4	80.5	60.6
1000	68.8	70.3	75.5	84.1	68.0
1500	74.7	73.5	76.7	82.7	71.8
2000	82.2	81.5	84.1	83.7	83.4
2500	77.4	78.6	78.8	80.3	78.5

Table I.2 *Sound pressure level, (dBA), ≈75% load*

Speed (rpm)	Voltage control		Current control		Single pulse mode
	Soft	Hard	Soft	Hard	
500	67.7	68.6	78.1	84.8	64.2
1000	72.4	73.3	77.8	84.4	70.8
1500	75.3	75.6	79.4	83.3	74.6
2000	82.4	81.8	82.2	84.3	81.5

Table I.3 *Variation of sound pressure level, (dBA), with PWM switching frequency at 1000rpm*

	7.5kHz	10.3kHz	12.5kHz	15.0kHz	17.5kHz	20.6kHz
No-load	72.9	72.6	72.7	72.7	72.3	72.4
75% load	76.4	76.7	76.5	76.4	76.1	76.0

Table I.4 *Variation of sound pressure level, (dBA), with sampling frequency, no-load*

Speed (rpm)	40kHz	30kHz	20kHz	10kHz
500	79.6	79.6	74.4	72.6
1000	79.9	78.7	75.5	75.6
1500	84.9	82.6	76.7	78.3
2000	86	83.8	84.1	81.8
2500	81.4	81.6	78.8	80.3

Table I.5 *Variation of sound pressure level, (dBA), with sampling frequency, ≈75% load*

Speed (rpm)	40kHz	30kHz	20kHz	10kHz
500	80.8	78.7	78.1	77.1
1000	88	84.9	77.8	79.2
1500	84.4	83.6	79.4	79.5
1750	83.5	83.5		80.6
2000	83.3	83.6	82.2	82.5

Table I.6 *Variation of sound pressure level, (dBA), with advance commutation (mechanical degrees), fixed dwell angle, no-load, voltage control*

Advance	Speed (rpm)				
	500	1000	1500	2000	2500
0.0°	63.6	68.8	74.7	82.2	77.4
2.5°	65.7	70.9	74.5	82.8	77.9
5.0°	66.9	71.3	73.7	81.7	77.8
7.5°	67.8	71.2	73.9	83.5	77.6
10.0°	68.7	70.8	73.8	83.3	78.6
12.5°	69.4	71.5	75	83.5	79.2
15.0°	70.3	71.7	74.1	84.1	79

Table I.7 *Variation of sound pressure level, (dBA), with advance commutation (mechanical degrees), fixed dwell, no-load, current control*

Advance	Speed (rpm)				
	500	1000	1500	2000	2500
0.0°	74.4	75.5	76.7	84.1	78.8
2.5°	77.5	77.4	79.7	84.1	81.1
5.0°	75.1	76.6	79.5	84	81.3
7.5°	74.1	77	78.9	85.4	81
10.0°	74.3	76.7	78.2	82.3	80.9
12.5°	74.9	77.6	78.7	81.9	81.4
15.0°	74.9	77.2	78.5	83.6	81.7

Table I.10 *Variation of sound pressure level, (dBA), with time-delays for modes 2 and 4, voltage control, no-load*

Speed (rpm)	Time-delay (μs)		
	0	37	130
500	64.5	63.1	61.2
1000	70.1	68.7	65.3
1500	72.5	71.7	68.6
2000	81.3	76.0	73.5
2500	77.1	76.6	72.8

Table I.11 *Variation of sound pressure level, (dBA), with time-delays for modes 2 and 4, voltage control, ≈75% load*

Speed (rpm)	Time-delay (μs)		
	0	37	130
500	67.7	67.0	64.7
1000	72.4	70.7	68.0
1500	75.3	73.7	70.7
2000	82.4	79.6	79.4

Table I.12 *Variation of sound pressure level, (dBA), with time-delays for modes 2 and 4, current control, no-load*

Speed (rpm)	Time-delay (μs)		
	0	37	130
500	74.4	77.7	77.9
1000	75.5	76.2	76.1
1500	76.7	78.2	77.8
2000	84.1	83.6	83.3
2500	78.8	79.7	78.9

Table I.13 *Variation of sound pressure level, (dBA), with time-delays for modes 2 and 4, current control, ≈75% load*

Speed (rpm)	Time-delay (μs)		
	0	37	130
500	78.1	77.1	76.9
1000	77.8	79.8	79.6
1500	79.4	80.1	79.8
2000	82.2	83.5	82.7

Table I.14 *Variation of sound pressure level, (dBA), with time-delay, voltage control, no-load*

Delay (μs)	Speed (rpm)				
	500	1000	1500	2000	2500
0	64.5	70.1	72.5	81.3	77.1
20	64.2	69.6	72.4	75.9	75.8
40	63.8	68.5	71.4	75.9	76.2
60	62.2	67.3	70.4	75.2	75.3
80	61.6	66.2	69.5	74.3	73.9
100	61.4	65.7	69.3	74.2	73
120	61.1	65.4	68.5	73.8	73
130	61.2	65.3	68.6	73.5	72.8
140	61.2	65.3	68.4	73.9	73
160	62.8	67.2	70.2	75.3	74.2
180	62.1	66.8	69.2	75.9	74
200	62.2	67.3	69.6	76.4	74.9
220	62.3	67.6	69.7	76.6	75

Table I.15 *Variation of sound pressure level, (dBA), with time-delay, voltage control, ≈75% load*

Delay (μs)	Speed (rpm)				
	500	1000	1500	1750	2000
0	67.7	73.1	75.3	77.8	82.0
20	67.2	71.2	74.1	75.5	79.8
40	66.8	70.6	73.5	75.2	79.2
60	66.3	70.1	72.7	74.6	78.7
80	65.4	69.1	72.2	74.2	78.3
100	65.1	68.5	71.4	73.6	78.4
120	64.8	68.2	70.8	72.9	79.2
130	64.7	68	70.7	73.5	79.4
140	65.2	68.1	70.8	73.8	78.5
160	65.8	68.7	71.7	73.9	82.3
180	66.6	69.3	72.4	73.1	81.3
200	66.9	69.9	72.7	73.7	81.3
220	66.9	70.6	73	74.1	82.6

Table I.16 *Variation of sound pressure level, (dBA), with time-delay, current control, no-load*

Delay (μs)	Speed (rpm)				
	500	1000	1500	2000	2500
0	74.4	75.5	76.7	84.1	78.8
20	78.3	76.9	78.8	84.6	80.3
40	78.3	76.5	78.4	84.9	79.9
60	78.3	76.4	78.2	84.8	79.8
80	78.2	76.3	78	84.6	79.4
100	78.6	76.3	77.9	84.5	79.1
120	78.5	76.5	78.2	83	79.1
130	77.9	76.1	77.8	83.3	78.9
140	78.3	76.3	78.5	82.8	79.5
160	78.4	76.4	78.4	82.5	79.7
180	78.3	76.3	78.2	82.3	79.8
200	78	76.3	78.3	82.1	79.9
220	78.2	76.5	78.4	82.3	79.9

Table I.17 *Variation of sound pressure level, (dBA), with time-delay, current control, ≈75% load*

Delay (μs)	Speed (rpm)				
	500	1000	1500	1750	2000
0	78.1	77.8	79.4		82.2
20	78.1	80.6	80.7		82.6
40	78.2	80.4	80.7	81.5	81.6
60	78.1	80.2	80.5	80.7	81.4
80	77.8	80.1	80.1	80.3	81.3
100	76.9	79.2	79.8	80.8	82.1
120	78.3	80.1	80.3	81	80.8
130	76.9	79.6	79.8		82.7
140	78.3	80.1	80.4	80.6	81
160	77.8	79.8	80.1	81.4	81.8
180	78	80.1	80.3	81.2	81.7
200	78.7	80.4	80.6	80.8	82.5
220	77.9	80.1	80.4	81.4	82.1